The Tribological Performance of Gas Turbine Lubricants

By

Jake Christopher Airey

A thesis submitted to

The University of Birmingham

For the degree of

DOCTOR OF ENGINEERING

School of Chemical Engineering,

The University of Birmingham,

Edgbaston,

Birmingham,

B15 2TT,

UK

April 2020

Abstract

This thesis is a study of the tribological properties of gas turbine lubricants with the aim of understanding how variations in the formulation of this product can affect friction and wear under different operating conditions. In particular, the focus is on understanding whether current aviation lubricants are capable of protecting and lubricating in new highly loaded gear environment inside the Power GearBox (PGB) in the new Rolls-Royce engine; the UltraFan©. This will be the largest planetary gearbox in the aviation industry to date and hence, introduces a new tribological challenge for the lubricant that needs to be investigated.

Modern gas turbine lubricants are an entirely synthetic formulated product and each component is tailored to optimise the performance within the engine. The majority component: the base oil usually comprises ~95 % of the lubricant formulation and as a result, it governs most of the viscometric properties and acts as the carrier for the other additives in the formulation. Work was done to understand how variation in the molecular structure of base oils affects friction across different operational conditions. It was found that for polyol ester base oils, increasing the chain length, the number of ester groups and decreasing the amount of molecular branching decreases friction across all lubrication regimes. This effect was also seen independent of viscosity by conducting tests for each oil at the same kinematic viscosity by varying the temperature. This effect was attributed to larger and more linear molecules possessing an improved packing efficiency, thus enabling an improved load bearing capability.

Another component of the lubricant is the anti-wear additive, this is responsible for protecting machine element surfaces in the absence of a sufficient lubricant fluid film. The introduction of a new gear environment motivated research into understanding whether current anti-wear additives in aviation could influence micropitting like other automotive anti-wear additives;

this is the prevalent wear mechanism commonly found on the dedenda of gear teeth. It was demonstrated that aviation anti-wear wear additives promote micropitting much less than a common automotive anti-wear additive Zinc Dialkyl DithioPhosphate (ZDDP). The ashless anti-wear additives allow the "running-in" of a surface due to their slower tribofilm formation than ZDDP and this prevents high asperity contact pressures being maintained that accelerate micropitting.

Finally, current fully formulated gas turbine lubricants were evaluated with respect PGB conditions and four commercially available lubricants were tested. It was found that the lowest viscosity candidate resulted in the best protection giving rise to lower friction and less micropitting. This has the potential of offering other efficiency benefits, however, its promising tribological properties will need to be balanced with its thermal capability. It would also have to challenge current industry specifications that require kinematic viscosity in the range 4.9 cSt to 5.4 cSt at 100 °C, and this lubricant is ~ 3 cSt at 100 °C. The next best lubricant was 5 cSt lubricant with high thermal capability, this showed marginally worse micropitting performance with higher friction but was still better than the other two lubricants that overall performed more poorly. A gear lubricant containing an EP additive was found to promote micropitting more slowly but introduced another wear mechanism; polishing wear that still resulted in substantial material loss most likely through a softening mechanism. The highest viscosity lubricant also gave rise to higher friction and more micropitting than the other candidates. This study showed that viscosity has limited effect in boundary lubrication regimes and confirmed the importance of a specific anti-wear additive package.

Acknowledgements

Dedication

This thesis is dedicated to my Mum, Licia Wolff, who taught me to strive for the best and never to settle.

Contents

X

List of Figures

XII

XIV

XX

List of Tables

Nomenclature

AC   Advisory Circular

CI   Corrosion Inhibitor

CLE   Civil Large Engine

cP   Centipoise

cSt   Centistoke

DLC   Diamond Like Carbon

DODPA   Dioctyl Diphenylamine

EASA   European Aviation Safety Agency

ECR   Electrical Contact Resistance

EHD   ElastoHydroDynamic

EP   Extreme Pressure

FAA   Federal Aviation Administration

FOHE   Fuel Oil Heat Exchanger

HPC   High Performance Capability lubricants according to SAE AS5780

HTHS   High-Temperature High Shear

HTS   High Thermal Stability Aviation Lubricants within MIL-PRF-23699

IP   Intellectual Property

IPT	Intermediate Pressure Turbine
MoD	Ministry of Defence
MONOPE	MONO-PentaErythritol
MPR	MicroPitting Rig
MTM	Mini Traction Machine
NPG	NeoPentyl Glycol
OEM	Original Engine Manufacturer
OPAN	OctylPhenyl-α-Napthylamine
PAN	Phenyl-α-Napthylamine
PGB	Power GearBox
PRI	Performance Review Institute
PVD	Physical Vapour Deposition
QPG	Qualified Products Group
SAE	Society of Automotive Engineers
SLIM	Spacer Layer Imaging
SPC	Standard Performance Capability lubricants according to SAE AS5780
SRR	Slide-Roll Ratio
STD	Standard Class of Aviation Lubricants within MIL-PRF-23699
TAN	Total Acid Number

TCP   TriCresyl Phosphate

TMP   TriMethylol Propane

VI   Viscosity Index

ZDDP   Zinc Dialkyl DithioPhosphate

Chapter 1.   Introduction

1.1 Background

1.1.1 The Gas Turbine

Gas turbines are heat engines that burn fuel to convert their energy into thrust, but whereas a piston engine uses this energy to rotate a crankshaft, a Turbojet or Turbofan gas turbine expels a jet of air out of the back of a turbine. This propels the engine and the body it is connected to (i.e. the body of the aircraft) forwards thus, obeying Newton's third law of motion that "for every force acting on a body, there is an equal and opposite reaction" (1).

The basic principle of the operation of a gas turbine is that air is sucked in through the fan, compressed in the compressor stages, mixed with fuel and ignited in the combustor and then this air not only rotates the turbine to power the aircraft and rotate all the other components, but also provides thrust to propel the aircraft as it is ejected out the back of the gas turbine. This is the principle of operation of a Turbojet; a Turbofan differs in that some of the air sucked in through the fan bypasses the core of the engine through a duct around the core of the engine. This is advantageous for several reasons including an increased propulsive efficiency due to utilising bypass air as thrust as well as core air, so that this engine can have a lower fuel burn, and this also results in a reduction in noise. Although thrust is sacrificed to increase efficiency, the Turbofan engine is the main type of engine employed by the civil aerospace. However, there are other types of gas turbines that use the energy to rotate a shaft such as Rolls-Royce's M250 TurboShaft engine used to rotate helicopter blades or to rotate a propeller such as on a Rolls-Royce AE 2100 TurboProp engine (1).

1.1.2   Aviation Lubricants

Lubricants are used across a wide variety of industries and can be solids, liquid and gases (2). Aviation lubricants are organic liquids and are tailored to meet the many demanding conditions within the gas turbine (3). They are a formulated product comprising mostly of an organic ester therefore, classifying them as an oil. At room temperature they remain as a viscous liquid and they are surface active. The natural properties of oils resulted in these substances finding use as lubricants especially because of their tendency to be more viscous than aqueous substances and have a superior load carrying capacity. The load-carrying capacity of a lubricant is the maximum load or pressure that can be sustained by the lubricant without failure of the sliding contact surfaces as evidenced by adhesive wear or localized welding (4). They also contain additives to further optimize performance and are a vital component of an engine.

Aviation lubricants have a variety of roles which, can be (5):

- To provide a thin layer to separate surfaces.

- to reduce friction and wear in various bearings and gearboxes.

- to act as a coolant/ heat dissipater throughout the oil system and this heat is also utilised to heat the fuel in the Fuel Oil Heat Exchanger (FOHE).

- to protect against corrosion

- to carry away debris particles.

Therefore, the formulation is tailored to optimise their performance across all these roles but can often lead to challenges as improving a certain property can decrease the performance of another and so consequently, the lubricant formulation needs careful consideration.

Modern aviation lubricants are composed of a base oil and additional chemical additives. They generally consist of ~95% base oil and therefore, this governs most of its physical fluid properties.

The base oil is responsible for most of the lubricant's lubricating properties at high speed, by providing a fluid layer to separate the two moving surfaces. This regime of lubrication is known as hydrodynamic or elastohydrodynamic lubrication (hydrodynamic if the interacting surfaces are conformal and elastohydrodynamic if the interacting surfaces are non-conformal) and is governed mostly by the viscous properties of the base oil.

1.1.3   Tribology

Tribology is defined as the science and technology of interacting surfaces in relative motion and encompasses wear, friction, lubrication and contact mechanics (5). The term was coined for the first time by Prof H Peter Jost in the "JOST report" in 1966 where he outlined the problems that wear, friction and corrosion were causing in the field of engineering and the huge potential cost savings that could be gained (6). It has been estimated that potential costs associated with tribological issues are around 1-1.5% GDP and the UK total of these issues were calculated to be £515 million in 1965 and around £4 billion in present day (6). Therefore, Tribology has long been studied to optimise machine elements with the aims of optimising efficiency, reducing or increasing friction for a particular application, reducing and preventing wear with the goal of economically prolonging component life (7).

Lubricants have long been a crucial component to any engine and play an important role in lubricating many components throughout the oil system. Understanding the tribological influence of the formulation of these lubricants both from a physical property and chemical standpoint are paramount in optimising the lubrication for the new conditions expected within the PGB of the UltraFan©.

1.1.4 Friction

The frictional force is a tangential component to the external normal force in the direction of the motion that needs to be overcome to initiate and sustain movement between contacting bodies. Frictional force (F) is directly proportional to the normal force (W) and this ratio is called the coefficient of friction (μ) as shown in (1-1).

$$\mu = \frac{F}{W}$$

(1-1)

The two-term model of friction explains that frictional forces arise from two components (and sometimes three depending on the elasticity of the material) and these are (8):

- Adhesion – Asperities contact to form junctions that need to be sheared to allow movement.
- Deformation – The displacement of material is required which, can be plastic or elastic to allow motion.
- Hysteresis losses – Only for deformable surfaces such as viscoelastic materials that have a lag in deformation response after a stress is applied.

These mechanisms of friction do not always result in wear. With adhesion, if shearing occurs at the interface between two surfaces there will be no wear. With deformation, wear results directly from cutting or plastic deformation. Only 10% of the energy dissipated by friction actually goes into wear with the rest of the energy being released as heat and noise (5,7).

There are three laws of friction known as Amontons' Laws (9) (although these were actually first stated in by Leonardo da Vinci in 1493) which, are:

1. F is proportional to W.
2. F is independent of the apparent area of contact.
3. F is independent of sliding speed.

4

The first law is obeyed experimentally as shown by Bowden and Taylor (1954) where they showed that a constant coefficient of friction was obtained over a range of normal loads for unlubricated sliding steel on aluminium in air (10). This law is obeyed well for most metals and other materials but not for polymers.

The second law of friction is also obeyed for most material except polymers and was verified by showing that the coefficient of friction of wooden sliders on an unlubricated steel surface was constant as the apparent area of contact was increased by a factor of approximately 250 under a constant load. Therefore, this demonstrates that friction is generally independent of the apparent area of contact (11).

The third law is less well obeyed but is usually a good guide. It has been commonly observed that the frictional force needed to initiate motion is usually larger than the force required to maintain motion and therefore, the coefficient of static friction (μ_s) is usually larger that the coefficient of dynamic friction (μ_d).

1.1.5 Wear

Wear is defined as progressive damage, involving material loss, which, occurs on the surface of a component as a result of its motion relative to the adjacent working parts (5). Thus, wear can propagate in a variety of ways with a range of different severities depending on the conditions of the contact. Wear can be broken down into four scenarios: sliding, rolling, impact and single or repeated cycle mechanisms. These situations can all occur in the transmissions system of a gas turbine although certain types of wear occur more often than others, especially rolling and sliding as expected due to the function of bearings and gears. It is expected that as wear progresses, it could introduce reciprocating vibrational mechanisms introduced by uneven, worn surfaces and impact scenarios are much rarer occurrences.

There are many wear mechanisms, but, the main types of behaviour are adhesive, abrasive, impact, erosive, oxidative, thermal and fatigue mechanisms. Whilst most of these wear mechanisms are seen within a gas turbine engine, this thesis will focus on wear mechanisms seen within lubricated contacts under normal operating conditions and which, are expected to be present on gears; adhesive, abrasive and fatigue wear. It is common for wear mechanisms to compete, coexist and merge with one another as certain mechanisms could be acting independently or they could be different stages of a wear process where one has propagated onto another.

Table 1-1 – Table distinguishing different severities of wear (5).

Mild Wear	Severe Wear	Catastrophic Wear
• Wear rate 10^{-4} – 10^{-3} mg/m	• Wear rate 10^{-3} – 10^{-2} mg/m	• Wear rate $>10^{-2}$ mg/m
• Results in smooth surfaces, sometimes smoother than the original.	• Results in rough and deeply torn surfaces, rougher than the starting material	• Creates extremely rough surfaces.
• Wear debris very small, ~100 nm	• Wear debris much larger, ~0.01 mm	• Usually caused by high temperatures.
• High electrical contact resistance as there is only a small amount of metallic contact	• Low electrical contact resistance due to the formation of true metallic junctions.	

Many components often require "running-in", this is when they require a process of preconditioning to improve conformity to a specific environment and this consequently improves their load carrying capacity. There is a gauge of severity with wear which, is outlined in Table 1-1 based upon the rate at of material loss from the surface (wear rate).

Adhesive Wear

Adhesive wear occurs when opposing surface asperities bond at discrete points and when the surfaces shear, these junctions are broken, and it can produce wear if the junction does not break at the interface on the bound asperities. Depending on the ductility of the bound materials, brittle or ductile fracture can occur as shown in Figure 1-1. This can sometime result in the production of wear debris which, could give rise to three-body abrasive wear, tips off the softer asperity could become lodged in the harder opposing asperity and in severe contacts, galling can result where large macroscopic chunks are torn away from the surface.
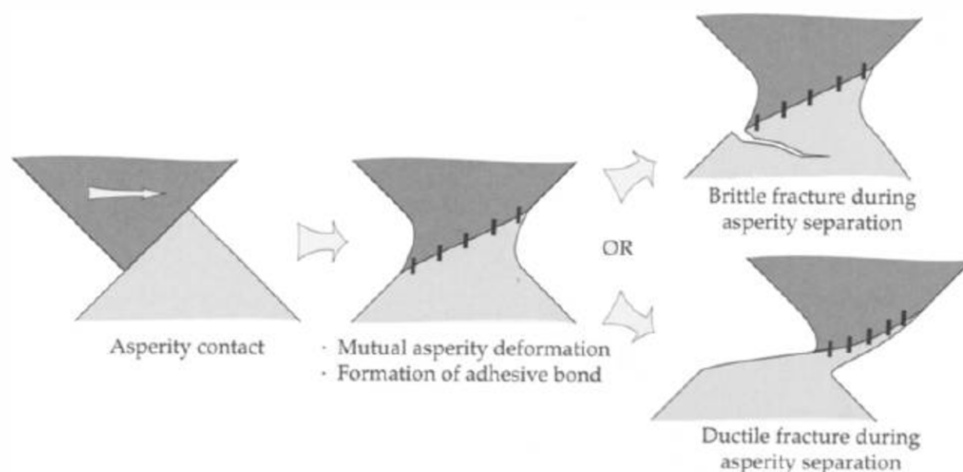
Figure 1-1 – Model of the mechanism of adhesive wear (12).

Abrasive Wear

Abrasive wear is damage to a component that occurs when another harder material deforms the surface of another material and the mechanisms are shown in Figure 1-2 and Figure 1-3. It can

either be two or three-body abrasive wear as shown in Figure 1-3 (three bodies if wear debris or other hard contaminants are present), however, if no other third body is present, all other abrasive wear is two-body (so all the mechanisms shown in Figure 1-2 and Figure 1-3 are classed as two-body abrasive wear). A characteristic of abrasive wear is that the surface topography shows long parallel grooves running in the sliding direction and the volume of these grooves can vary significantly.
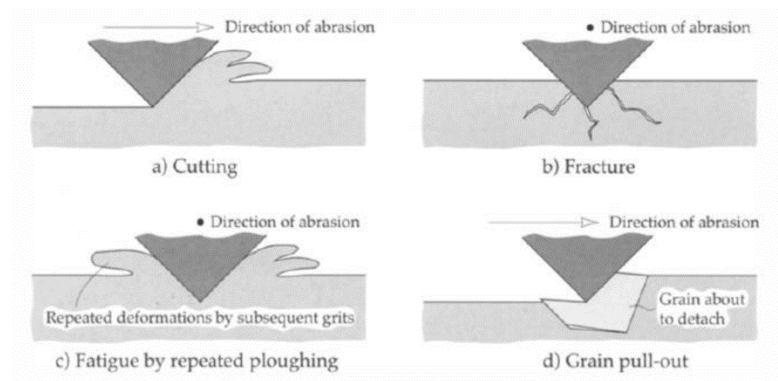
Figure 1-2 – Mechanisms of abrasive wear (12).
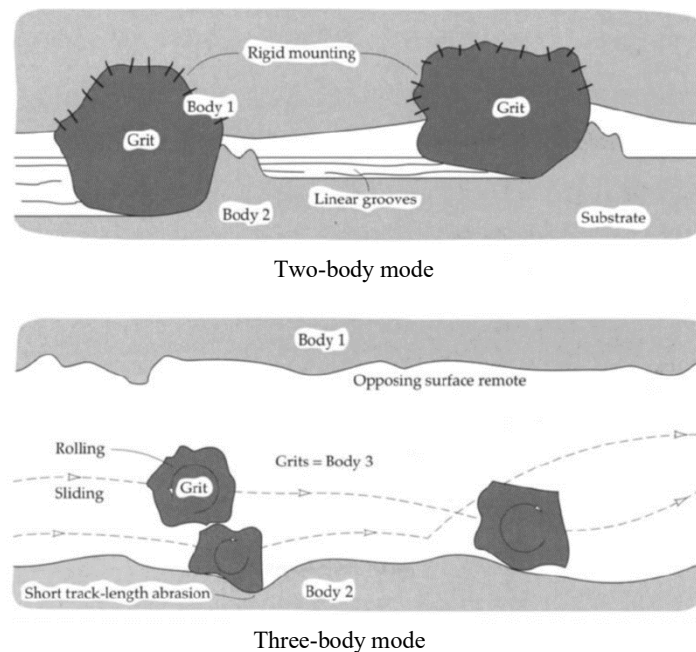
Figure 1-3 – Diagrams of two body and three body abrasive wear (12).

Micropitting

As well as lubricants reducing friction, it also needs to be understood how lubricants influence different wear mechanisms and one mechanism of particular focus in this thesis is micropitting. Micropitting is a type of surface contact fatigue that occurs in rolling contacts under thin film conditions and is commonly seen in gears and bearings. Fatigue itself can be defined as material weakening and damage due to the repeat stresses. Due to the formation of micropits, this increases the amount of vibration and noise in these components and gives rise to increased peak stresses that can propagate micropitting into more severe wear mechanisms such as macropitting, tooth breakage (after deviations in the tooth profile) in gears and ultimately catastrophic failure. It can occur after a relatively short period of operation quite often less than 10^6 cycles and therefore, it is of great interest to prevent the initiation of this wear mechanism completely in order to prolong component life and therefore, engine life (13–16).

Characteristics of micropitting are a field of very fine micropits that usually have a depth, width and length of around 1-30 μm and are typically initiated by a crack at or very close to the surface which, propagates until the crack reaches the surface again causing material to fragment off leaving a shallow pit. It is known throughout the literature that micropitting is affecting by the SRR, the speed, the roughness, the hardness, the load, temperature and the lubricant itself (17).

Figure 1-4 shows an image of micropitting on the dedendum of gear (a.), a magnified wear track showing the characteristic "v" shape of micropits with respect to frictional direction and rolling direction (b.) and the mechanism the formation of a micropit (c.).

The diagram is labelled with numbers to show the series of steps that lead to a micropit. 1 shows that a crack is initiated from the surface or close to the surface through fatigue due to repeated loading and then the crack grows at an inclination angle to the surface between 5-50 °. After growth the crack branches with one crack propagating parallel to the surface (2 to 3) and the

other one continuing to grow into the bulk (2 to 5) and this could potentially be the point at which, the formation of a macropit is initiated. The crack parallel to the surface propagates parallel for a short distance and then turns back up to the surface which, forms the micropit as material is lost (13–16).
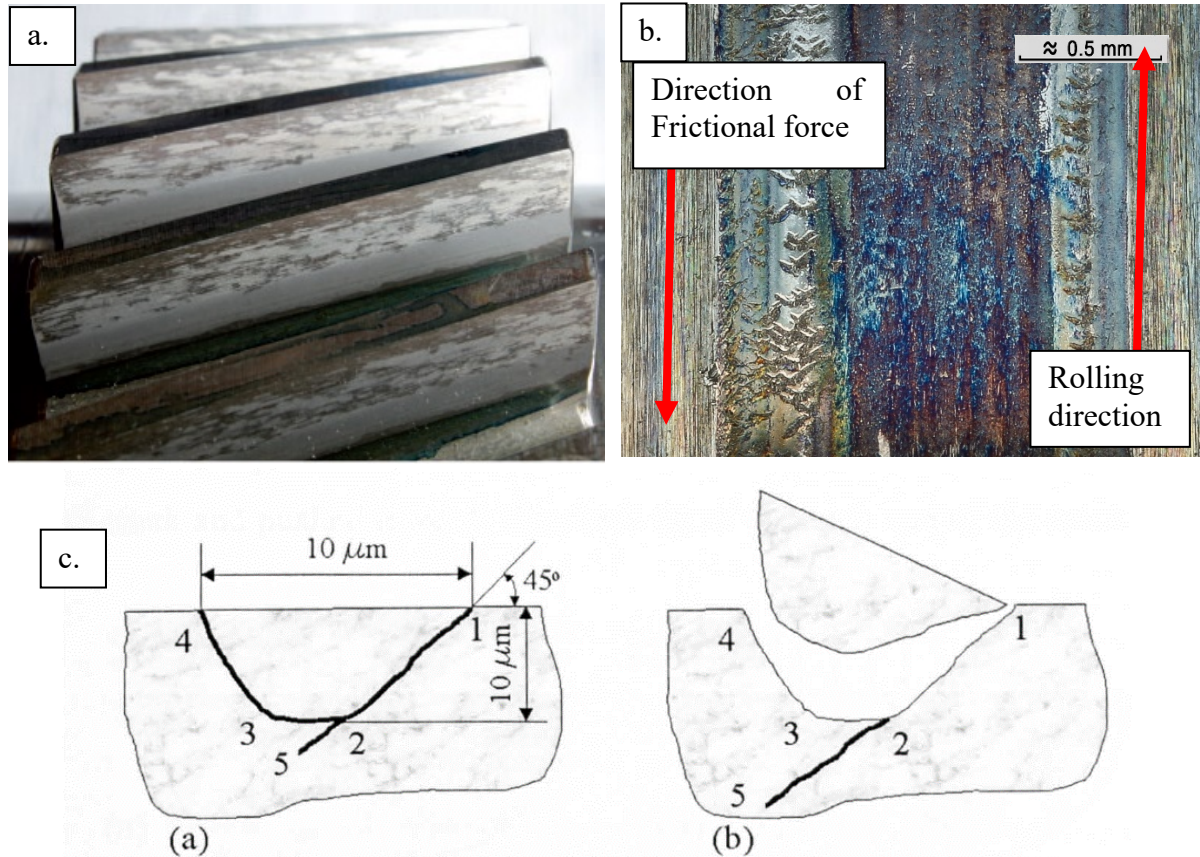
Figure 1-4 – a. Image showing micropitting on the dedenda of helical gear teeth, b. zoomed in photograph showing the characteristic "v" shape of micropits with respect to frictional direction and rolling direction and c. shows the mechanism by which, micropits are believed to form (13,18).

Scuffing

Another wear mechanism that is more severe than micropitting is scuffing. Scuffing (also known as scoring) is "gross damage characterised by the formation of local welds between sliding surfaces" (19). This type of wear results from excessive adhesion and causes a dragged/ torn appearance on one or both contacting surfaces. For this to occur, the lubricant film separating the surfaces must collapse and the scuffing starts at a singular point and spreads until

10

the surface becomes damaged, heating disrupts the lubricant film completely and the surfaces weld. It is also classed as a catastrophic rather than an accumulating mechanism (19,20).

Scuffing is usually caused by high loads, high sliding speeds and it is sensitive to lubricant chemistry (especially additives), roughness and material properties. It can be characterised in a tribology test by a sudden increase in friction coupled with extensive damage on the surface (3,7,20).

1.2   Business Case and Motivation

Rolls-Royce Plc is developing a new civil large engine (CLE) which, features a drastically different architecture to current gas turbines. This engine is called the UltraFan© and features a new sub-system called the Power Gearbox (PGB) which, will enable a huge efficiency benefit; 25% more efficient than the Trent 700. This will form a new family of engines for Rolls-Royce plc to maintain a competitive advantage in the marketplace. As a result, current aviation lubricants need to be evaluated for their ability to sufficiently lubricate and protect the contacting surfaces in this new environment. It is expected to involve higher loads than previously experienced in other gas turbine oil system contacts despite having lower temperatures than in other areas of the engine, hence, the ability of current aviation lubricants needs to be evaluated. The decision to create a higher loaded gearbox was to drive efficiency by making the turbine operate hotter and spin faster. These high loads will then be transmitted to the PGB distributed across the large contact area to give a lower contact pressure than other tribological contacts in the engine such as ball bearings.

The purpose of this thesis is to investigate the tribological performance of aviation lubricants using novel and current commercially available formulations, however, specifications within the industry have to be considered as deviation outside of current civil aviation specified limits or introduction of new compounds would be difficult to get into the market. This is due to a

variety of reasons; firstly, a new product would need to satisfy all of the requirements of the current specification in order to prove adequate performance throughout all areas of an engine oil system. It also needs to be compatible with all the materials used throughout the oil system. Moreover, oil systems are designed for a certain set of physical characteristics and therefore, deviation away from the design parameters would be difficult to adapt to.

Concurrently, any improvements in tribological performance of the lubricant must be monitored alongside their thermal stability as the demanding core oil system temperatures cause lubricant degradation to occur. Therefore, tribological and thermal performance are often opposing properties as improvements in one will cause a decrease in performance in the other; hence, performance improvements need to be extensively investigated and balanced. This is simply a consequence of certain additives with good tribological properties often having poor thermal capabilities and vice versa. Consequently, lubricants have been evaluated with respect to the newly defined conditions whilst understanding the limitations of the research by considering the implications on other areas of the engines as well as on the industry.

1.3 PGB Test Plan

Due to the substantial design change with the UltraFan© and the PGB compared to current aviation gas turbines, the PGB sub-system needs to be extensively studied. Rolls-Royce have adopted a test plan to evaluate lubricant performance, incorporating various scales of testing which, include:

- Small scale rig testing on an MTM and MPR *forming the core of this EngD project* to study the fundamental behaviour of different lubricant formulations and how these influence friction and micropitting.

- A small geared rig under lubrication at Newcastle University operated by the Design Unit which, conducts tribological testing of the gears and should provide insight into the wear and potential failure mechanisms of the gears in the PGB.

- A full size PGB rig in Dahlewitz in Germany operated by Rolls-Royce, this is the final testing of the gears under lubrication that will provide information on the operation of the gearbox itself as well as observing any potential tribological issues.

This project utilises small-scale rig tests that provide insight into potential tribological challenges in the new power gearbox environment within the UltraFan$^©$ engine allowing simulation of operating conditions as a method of easily screening and comparing lubricants for the larger scale rig tests (21). Small scale rig testing for this program has several advantages and disadvantages as shown in Table 1-2.

Table 1-2 – The advantages and disadvantages of small-scale rig testing.

Advantages	Disadvantages
• Cheap and fast testing. • Simple method of testing a range of lubricants and choosing the most appropriate candidates. • Tribology rigs such as the Mini Traction Machine (MTM) and MicroPitting Rig (MPR) allow the measurement of many parameters that cannot be measured in larger scale tests.	• The MTM and MPR in this project are not geared geometries and therefore, the exact contact condition cannot be replicated. • Contact conditions limited by the capability of the small-scale rigs and therefore, exact contact environments may not be achievable (i.e. maximum temperature of the MTM is 150 °C and so cannot simulate the temperatures of the oil in the core of the engine).

1.4   Objectives

The objectives of this thesis are:

1. To develop laboratory scale test methods to evaluate the tribological capability of a range of commercially available and novel aviation lubricant formulations focusing on:

    a. Their effect on friction across different lubrication regimes.

    b. Their influence on wear and micropitting.

2. To understand how the tribological behaviour of aviation lubricant formulations is affected by the following individual components:

    a. The base oil as this comprises most of the formulation and hence, governs the bulk properties of the fluid.

    b. The boundary additives as these are surface active and will therefore, influence boundary lubrication conditions.

3. To deduce whether currently available lubricant formulations are suitable for the PGB environment of the UltraFan© and understand how they interact with different candidate steels by assessing:

    a. Their effect on friction across different lubrication regimes.

    b. Their influence on wear and micropitting.

1.5   Thesis Structure

This thesis is structured as follows. Chapter 2 explores the literature on aviation lubricants, their role within the gas turbine engine and the fundamentals of tribology and rheology which, are applicable to these areas. Chapter 3 outlines the methods and materials used in this thesis and also reviews the development of the test procedures.

The results chapters focus initially on the different components within the aviation lubricant formulation with the later chapters focusing on the full formulation. Chapter 4 explores the tribological characteristics of the base oil and specifically how variation in the molecular structure of the base oils influence the lubricants' physical fluid properties and therefore, friction, which, in turn relates to engine efficiency. Chapter 5 investigates different boundary additives used in the aviation lubricants mainly focusing on anti-wear additives. They are compared with a commonly used and well researched automotive additive to understand how they affect friction and how they influence different wear mechanisms; especially for a common failure mode called micropitting.

Chapter 6 and Chapter 7 investigate fully formulated commercially available aviation lubricants using the MTM-SLIM and MPR methods respectively. They evaluate their suitability to support the PGB in the UltraFan©, primarily focusing on friction, tribofilm formation and how they influence wear mechanisms.

Chapter 8 outlines the conclusions drawn from the discussed results and contains suggestions for future work.

1.6   Achievements and Publications

Journal Papers:

Airey J, Spencer M, Greenwood R, Simmons M. The Effect of Gas Turbine Lubricant Base Oil Molecular Structure on Friction. Tribology International. 2020; 146 (June):11, DOI: 10.1016/j.triboint.2019.106052 (22) (Appendix 1).

Oral Presentations (Speaker Underlined):

<u>Airey J</u>, Spencer M, Greenwood R, Simmons M., The Evaluation of Anti-wear Additives on Micropitting Propensity and Tribofilm Thickness, 74th STLE Annual Meeting & Exhibition, 2019, Nashville, TN, USA

Airey J, Spencer M, Greenwood R, Simmons M., *The Tribological Performance of Gas Turbine Lubricants,* 5th Rolls-Royce Engineering Doctorate Conference, 2018, Derby, UK

Airey J, Spencer M, Greenwood R, Simmons M., *The Effect of Gas Turbine Lubricant Base Oil Molecular Structure on Friction,* 74th STLE Annual Meeting & Exhibition, 2018, Minneapolis, MN, USA

Airey J, Spencer M, Greenwood R, Simmons M., *The Tribological Performance of Gas Turbine Lubricants,* 44th Leeds-Lyon Symposium on Tribology, 2017, Lyon, France

Airey J, Spencer M, Greenwood R, Simmons M., *The Tribological Performance of Gas Turbine Lubricants,* 3rd Rolls-Royce Engineering Doctorate Conference, 2016, Derby, UK

Poster Presentations:

Airey J, Spencer M, Greenwood R, Simmons M., *The Tribological Performance of Gas Turbine Lubricants,* TriboUK, 2016, Leeds, UK

Airey J, Spencer M, Greenwood R, Simmons M., *The Tribological Performance of Gas Turbine Lubricants,* IET New Challenges in Tribology, 2016, Birmingham, UK

Airey J, Spencer M, Greenwood R, Simmons M., *The Tribological Performance of Gas Turbine Lubricants,* ChemEngDayUK, 2017, Birmingham, UK

Airey J, Spencer M, Greenwood R, Simmons M., *The Tribological Performance of Gas Turbine Lubricants,* IET New Challenges in Tribology, 2017, Birmingham, UK

Airey J, Spencer M, Greenwood R, Simmons M., *The Tribological Performance of Gas Turbine Lubricants,* 4th Rolls-Royce Engineering Doctorate Conference, 2017, Birmingham, UK

Chapter 2. Literature Review

This literature review will explore the fundamental theory underpinning research into aviation lubricants, tribology and the transmissions systems in aviation gas turbine engines and discuss the relevant progress that has been made in the field. Firstly, the purpose and properties of aviation lubricants will be outlined giving rise to why a specific formulation of base oils and various additives are required to satisfy the demanding conditions within the gas turbine oil system. Following this, the specifications that the oils must abide by within the civil aviation industry will be discussed to understand the current limitations in changing oil formulations.

Next, the new Turbofan gas turbine engine; the UltraFan© by Rolls-Royce Plc will be introduced outlining the differences with previous Trent gas turbine engines with a specific focus on understanding the new challenges for the lubricant. Discussion of the UltraFan© will prompt elucidation of the new lubricant challenges presented by the novel Power Gearbox whilst understanding the necessity to balance improvements in tribological performance with other challenges throughout the oil system such as the high temperatures faced in the core of the engine.

Following this, an overview of tribology will be introduced and its importance to lubricant formulation will be examined. The key mechanical and material parameters and the fundamental tribological knowledge will be defined that has been used to evaluate lubricant performance. This will give rise to review of the types of wear mechanism seen in the research presented in in this thesis that are also seen in lubricated gear environments.

Finally, the rheology of turbine lubricants will be introduced with emphasis on how the physical properties of the lubricants affect deformation and flow and the consequentially friction performance.

Each of the following results chapters will build upon this literature review with more specific literature relevant to the corresponding chapter.

2.1 Gas Turbine Lubricants

Great demands are placed on the lubricant to sufficiently perform across a wide range pressures, temperatures and timescales within gas turbines. Historically lubricant development has focused on high temperature performance to enable gas turbines to run hotter and faster to improve efficiency (1,23).

Gas turbines can be considered as simpler to lubricate than piston engines since there are no moving parts in the combustion chambers and therefore, the lubricant is not directly exposed to extremely high combustion temperatures. However, one of the main challenges for the lubricant is exposure to high temperatures in the oil system in the core of the engine. Modern bulk temperatures range from 80-100 °C for the oil system feed and peak at 190 °C on the scavenge side (3). Oil vented out of the bearing chambers can reach a temperature of 250 °C through the vent pipe (24,25). They can be exposed to even higher temperatures between 300-400 °C when in contact with metal walls, which, can subsequently lead to lubricant degradation and therefore, coking (26). Despite there being no combustion products to deal with, coke deposits can still form due to exposure to the high temperature. These deposits must be prevented from building up and causing blockages which, highlights the advantage of more thermally stable lubricants.

This challenge, along with aircraft operators' desire to extend the time between major overhauls even further (currently more than 40,000 operating hours for some civil engines) means lubricants need to be developed with the stability to last the operating cycle of the engine. The lubricant does not last for the entire operating period and regular topping up is needed to replace a gradual loss of oil from vents in bearing chambers and expelling overboard out of the centrifugal breather pipe. Extremely low temperatures can be reached as well such as -40 °C

in cold climates which, is where the lubricants pour point properties are vital in ensure that the oil can still flow at low temperatures (3).

Another major challenge is the tribological demands on the oil. Throughout the gas turbine oil system there are many high contact pressure environments which, the lubricant needs to sufficiently lubricate across this wide range of temperatures whilst also being compatible with other materials throughout the oil system such as various alloys and elastomer seals. The lubricant needs to be capable of sustaining a protective fluid film to separate sufficiently opposing asperities to prevent wear and ultimately prolong component life. This is the focus of this thesis.

2.1.1   Aviation Lubricant Formulation

Base oils

Base oils can generally be classified into two categories:

- Those refined from petroleum
- Synthetic base oils

The first lubricants for aero-engines were refined mineral oils derived from petroleum due to having good performance, good availability and a low price. As these were derived from crude oil, they required many chemical refining steps to isolate the hydrocarbon components which, had good lubricating properties (3). These were also used in the automotive industry at the time but, aero-engines required low temperature capability such as for cold starts or re-lights at high altitude. Therefore, lower viscosity straight chain mineral oils were developed through further refinement. The demand for lower viscosity straight mineral oils has diminished due to the need for lubricants with a greater tolerance for extreme conditions.

As more powerful engines were produced resulting in higher thrusts and compression ratios, mineral oils could not withstand these high temperatures for an appropriate length of time resulting in rapid degradation, deposition of coke and excessive volatility (3). To improve their high temperature capability, aviation lubricants switched to synthetic base oils; the first being a diester and were considered as the 1st generation of aviation synthetic lubricants. These had better oxidative and thermal stability and did not require pour-point depressant additives that prevents thickening and maintain fluidity at low temperatures, a common issue for mineral oils. But their poor load carrying capacity led to the addition of additives known as thickeners (usually a complex ester). Although synthetic oils were beginning to show promising performance, they lacked some of the lubricating properties that mineral oils naturally contained. This was due to the multicomponent nature of mineral oils as they contain many components that could not be removed via the refining process from crude oil, but some of these were beneficial to lubrication. Therefore, synthetic oils had to incorporate additive packages to enhance performance specifically to prevent thermal and oxidative degradation to preserve the oil life and to maintain engine cleanliness.

Diesters were formed from di-carboxylic acids and reacted with alcohols, this reaction is called esterification and choice of acids and alcohols determine the final properties of the oil. As an example, longer chain di-acids improve the viscosity index (VI) (increasing VI results in a smaller change in viscosity with temperature) but can reduce the pour point (3).

However, even with anti-oxidant additives present, di-ester based lubricants were still limited in their high temperature capabilities due to a degradation process known as β-hydrogen abstraction. This mechanism proceeds via the β carbon hydrogen bonding to the ester's carbonyl group allowing a pericyclic elimination to take place, giving rise to alkene and aldehyde products (3) as shown in Figure 2-1.
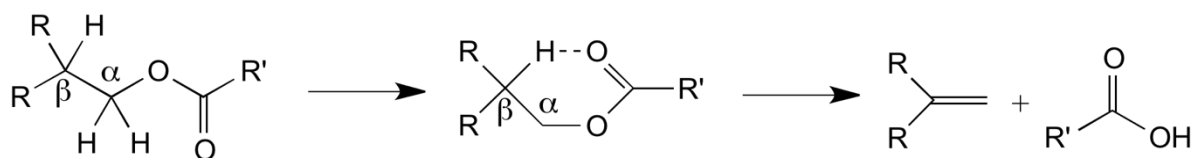
Figure 2-1 – Mechanism of the breakdown of di-ester lubricants at high temperature by β-hydrogen abstraction.

As a result, current lubricants progressed onto 2nd generation synthetic oils which, are polyol esters which, have no β-hydrogen in the molecular structure thus preventing β-hydrogen abstraction; they also typically have multiple alkyl chains which, protect the vulnerable ester groups via steric hindrance. Polyols are produced by reacting polyhydric alcohols (mono-pentaerythritol (MONOPE), trimethylolpropane (TMP) and neopentyl glycol (NPG) as shown in Figure 2-2) with monoacids ranging from nC_5-nC_{10}.
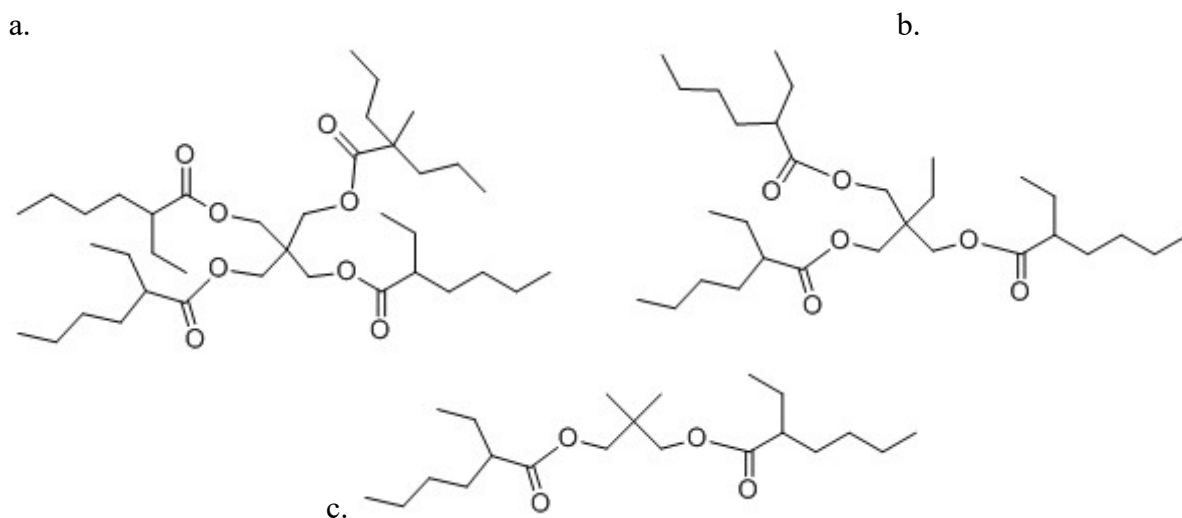
Figure 2-2 – Molecular structures or polyol esters, a. a polyol ester derived from pentaerythritol, b. an ester derived from trimethylol propane and c. an ester derived from neopentyl glycol with side chains of 2-ethylhexyl.

.

Modern polyol base oils are often a mixture of these with the more viscous oils being predominantly pentaerythritol based and the less viscous oils being mostly neopentyl glycol based.

These were developed as larger, higher powered gas turbines emerged that required oil with better performance under higher loads and temperatures and the hindered structure of the polyols gave rise to better thermal capability.

But further advancement of gas turbines continued giving rise to aero-engines with improved fuel consumption, but this caused more severe oil operating conditions, higher pressures and temperatures. The 2nd generation synthetic oil proved not stable enough at these elevated conditions which, lead to the 3rd generation synthetic lubricant being developed with improved thermal capabilities. These are also known as High Thermal Stability (HTS) lubricants which, were generated through improved purity of the base oils and an improved additive package that had a more effective anti-oxidant.

Additive Chemistry

The properties of the lubricant can be enhanced by the addition of chemical additives to give many additional benefits. The base fluid also acts as a carrier for these additives and therefore, needs to be able to maintain them in solution under normal working conditions (3). The additives in aviation lubricants can be separated into boundary additives (i.e. additives that interact that the surface or boundary) and those that do not. Due to the boundary additives interacting at the surface, these have the most tribological influence when the bulk lubricant film is too thin to separate the surface asperities. Such boundary additives include anti-wear and load carrying additives, extreme pressure (EP) additives, metal deactivators and corrosion inhibitors. They also contain anti-oxidants to improve thermal capability and anti-foamants to prevent foaming. However, for this thesis, only the anti-wear and EP additives will be discussed as these have the largest impact on the tribological performance.

Anti-Wear and Load Carrying Additives

Anti-wear additives are used to reduce wear by protecting surface asperities when a lubricant film is not thick enough to separate opposing asperities where asperities are the protruding parts of a surface that contact an opposing surface. They are an essential component to lubricant formulations to provide protection in boundary and mixed lubrication conditions which, improve load carrying capacity. Boundary and Extreme Pressure (EP) (more severe conditions than boundary) lubrication can be broken down into categories depending on their temperature and load. The type of boundary lubrication present in gas turbine oil system conditions are classified as high temperature and high-pressure contacts. Therefore, the mechanism of boundary lubrication involves a chemical reaction between the anti-wear additives and the metal surface to create a chemisorbed tribofilm that serves as a sacrificial film that is preferentially sheared off instead of the substrate metal (3,27).

These additives are vital to the performance of the lubricant as the oil system will operate across a variety of lubrication regimes during flight operation due to varying component speeds, such as cold starts, cruise and landing. Therefore, as these surfaces may be moving slower, this means the lubricant fluid film thickness is insufficient to protect surface asperities and therefore, relies on anti-wear additives to mitigate wear.

One of the most common anti-wear additives is zinc dialkyl dithiophosphate (ZDDP, shown in Figure 2-3 a.) which, is an anti-wear additive commonly used in automotive lubricants and this has been extensively studied in the literature (17,28–37).
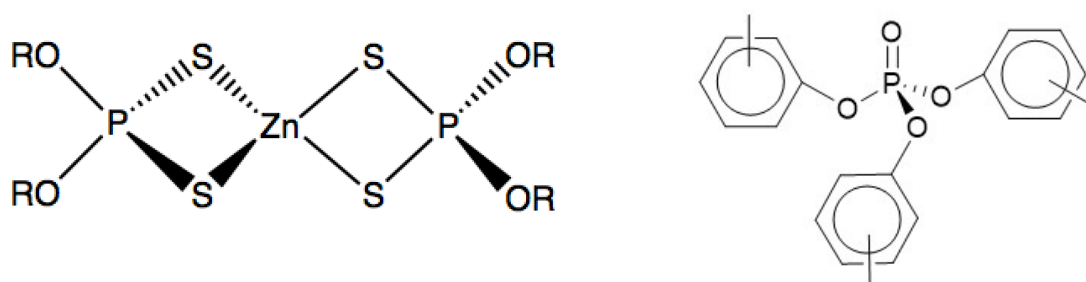
Figure 2-3 – Molecular structures of ZDDP indicating the location of the alkyl groups that can be varied and TCP.

However, aerospace lubricants prohibit the use of ZDDP due to its poor temperature stability which, would lead to the formation of toxic and corrosive species. These include hydrogen sulphide, mercaptans and olefins. Metal containing additives can cause corrosion problems due to the catalytic nature of metals promoting lubricant breakdown.

Consequently, aerospace lubricants use "ashless" anti-wear additives (metal free additives) that are more temperature stable. The most common aviation anti-wear additive is Tri Cresyl Phosphate (TCP, shown in Figure 2-3 b.) and is usually added in concentrations of ~1-3% in the lubricant formulation (3). This is an effective anti-wear additive but forms much thinner tribofilms films than ZDDP and therefore, provides less wear protection (38). It has been found in the literature that ZDDP tribofilms stabilise at a thickness of approximately 120 nm and TCP films tend to form additive films around 30 nm thick (29,38). However, it is more stable at the higher temperatures experienced within a gas turbine oil system (3). It has been frequently observed that TCP forms a coloured film on the surface of the metal and this film has been attributed to the reduction of wear and friction in the boundary lubrication regime (39–42).

The exact chemical composition of the tribofilm formed on the surface is not currently known due to difficulty in analysing the thin tribofilm but it is believed to be rich in phosphorus and oxygen species (39,43–45). These tribofilms are often described as a phosphate-glass referring to them being relatively hard but also fragmenting off under high shear (46). Initial findings suggested that iron phosphate was deposited onto the bearing material surface but it has now been reported that it may be polyphosphate that formed onto the surface or a combination of both (39,41,43,44).

Extreme Pressure Additives

Load carrying capacity can be further improved with the addition of Extreme Pressure (EP) additives. They are commonly used in helicopter transmissions and industrial gearboxes but

have limited use in civil aviation gas turbines. They prevent adhesive wear when the lubricant fluid film is insufficient to separate asperities by forming a protective tribofilm under conditions that traditional anti-wear additives are unable to survive. They can be broken down into two types: temperature dependent and non-temperature dependent. Temperature dependent EP additives include boron, chlorine, phosphorus, sulphur and/or nitrogen-based compounds which, only react with the metal surface at elevated temperatures caused by extreme pressure and friction. These typically form metal salts such as iron chlorides, iron phosphides and iron sulphides that form a "soap-like" film that reduces friction and therefore, wear, scoring and surface welding.

Non-temperature dependent EP additives can form without the need for elevated temperatures such as over-based sulphonates which, contain a colloidal carbonate salt dispersed within the excess sulfonate. This colloidal carbonate forms a film that can act as a barrier between metal surfaces (47,48).

However, they have some limitations including poor low temperature and low speed protection due to the necessity of harsh conditions to initiate the reaction with the metal surface. They can cause a polishing type of wear which, alters tolerances between components including gear tooth profile wear. Sulphur-phosphorus types specifically have been shown to be too chemically reactive which, results in polishing wear (49).

There has also been evidence of sulphur and chlorine-based EP additives being too chemically aggressive resulting in the softening of lower hardness alloys such as brass and bronze which, can result in pitting, spall formation and eventually premature failure. This is accelerated further at higher temperatures and hard abrasive compounds can form on the surface of the metal (e.g. copper sulphide and disulphide from the copper in the brass and bronze) which, can damage softer machine surfaces (50,51).

The detrimental effects of EP additives have been reported in the literature (52,53). However, sulphur and phosphorus based EP have been shown not to attack grain boundaries in case carburized 8119 steel (54). Whilst these alloys are not used in aerospace components, further understanding is required to deduce whether these limitations in exist aerospace components via a similar mechanism.

2.1.2 Aviation Lubricant Regulations and Specifications

Historically all aviation lubricants were controlled by a military specification from the U.S. Navy called MIL-PRF-23699 (formerly MIL-L-23699) to govern their 5 cSt at 100 °C synthetic lubricants. This specification is still used today and the latest version of this specification is MIL-PRF-23699G and this now covers standard class (STD), the corrosion inhibited class (C/I), the HTS class and the Enhanced Ester (EE) class (40).

However, these specifications did not address the commercial requirements for the lubrication of civil engines especially with the main requirement that civil engines require oil lives of up to 30,000 hours. Therefore, Rolls-Royce plc. and the UK Ministry of Defence (MoD) launched an initiative to develop a specification to better satisfy both the regulatory authority and the original engine manufacturers (OEMs) and the specification is called SAE AS5780. This adopts the Performance Review Institute (PRI) best practice for an industry managed solution to this issue to better address the concerns of the regulatory authorities. This specification is governed by the SAE E-34 Propulsion Lubricant Technical Standards Committee and qualifications to this specification are managed by a Qualified Products Group (QPG) which, is under the control of the PRI. The QPG consists of OEM's and government agencies only. AS5780 covers over 95 % of all OEM rig and laboratory testing requirements, however, it does not relinquish the responsibility of the OEM to approve specific lubricants for certain engines. It also does not remove the right for OEM's to perform additional non-AS5780 testing.

This specification covers two classes of lubricant:

- Standard Performance Capability (SPC)

- High Performance Capability (HPC) (higher temperature capability)

SAE AS5780 outlines a range of different criteria some of which, the lubricant must abide to specific limits (depending on the class) and some of which, are report only and the definitions of these parameters are shown in Table 2-1.

Table 2-1 – List of lubricant properties covered in the civil aviation specification SAE AS5780

Property	Definition
Coking Propensity	The tendency of a lubricant to form carbonaceous deposits when exposed to high temperatures.
Density	The mass per unit volume at a certain temperature.
Deposition Formation	A measure of a lubricants resistance to forming deposits.
Elastomer Compatibility	An evaluation of a lubricant's chemical compatibility with elastomeric materials.
Electrical Conductivity	A measure of a substances ability to conduct an electric current.
Evaporation	A measure of the volatility of a substance therefore, indicating the tendency of a substance to change phase from the liquid to the gaseous phase.
Flash Point	The lowest temperature at which, the substance gives off enough vapour to ignite in air.
Foaming Tendency	A measure of the tendency of a substance to form foam when aerated or mechanically agitated.
Heat Capacity	The amount of heat energy required to increase the temperature of one-unit mass of a substance by one kelvin.
Hydrolytic Stability	A measure of a lubricants resistance to degradation when exposed to water.
Kinematic Viscosity	The dynamic viscosity per unit of density where the dynamic viscosity is a measure of the force required to overcome internal friction to initiate motion.
Load Carrying Properties	An evaluation of a lubricants ability to reduce mechanical wear under load carrying conditions.
Lubricant Compatibility	An evaluation of a lubricant's compatibility with a selection of other lubricant types.
Pour-Point	The lowest temperature at which, a liquid will continue to flow and maintain its fluidity.
Pressure-Viscosity Coefficient	A parameter that specifies the effect pressure has on lubricant viscosity.

Sediment/ Ash	The quantity of solid particulate present within the substance.
Shear Stability	A measure of a lubricant's variation in viscosity with shear stress.
Thermal and Oxidative Stability	A measure of a lubricant's resistance to oxidation in the presence of elevated temperatures and oxygen.
Thermal Conductivity	A measure of a substances ability to conduct heat.
Total Acid Number (TAN)	A measure of lubricant acidity determined by the mass of potassium hydroxide required to neutralize one gram of oil.
Trace Metals	The concentration of specific metallic elements within a specific quantity of a substance.
Viscosity Index	An arbitrary value which, indicates the extent of change in viscosity with temperature. The lower the VI, the greater the change in viscosity with temperature.
Viscosity Stability	A measure of a lubricants change in viscosity over time.

Throughout this thesis, the SAE AS5780 definitions of performance capability are used although the tribological testing was not limited to lubricants within this main specification (3,55).

Safety regulations for the approval of lubricating oils governed by the Federal Aviation Administration (FAA) are stated in Advisory Circular (AC) 20-24D and the European Aviation Safety Agency (EASA) in CS-E section 570 (g) (56,57).

2.2 The UltraFan©

This project primarily focuses on Rolls-Royce's new engine; the UltraFan© which, can be seen in Figure 2-4.
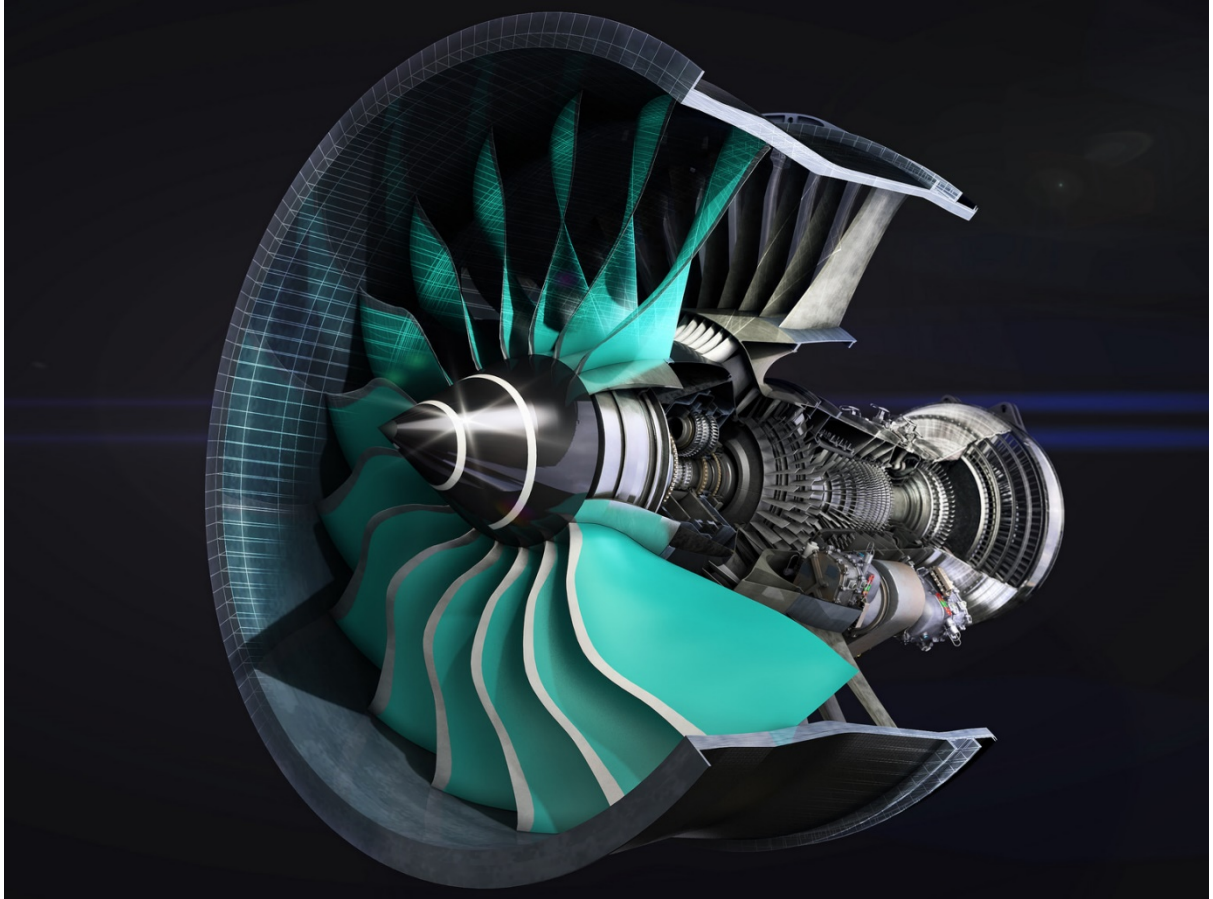
Figure 2-4 – Rolls-Royce's new Turbofan engine the UltraFan© (58).

The UltraFan© has a different architecture to current turbofan engines as it employs a new addition to the transmission system called the Power GearBox (PGB). This allows a huge predicted efficiency benefit of 25% compared with Rolls-Royce's Trent 700 turbofan engine. It is expected to be in service by 2025 (58).

The PGB has a planetary (epicyclic) gear arrangement as shown in Figure 2-5, and this allows the fan blades driven by the intermediate pressure turbine (IPT) to rotate much slower than the IPT. This consequently enables optimisation of both the speed of the fan and the IPT. It allows

the IPT to rotate faster and hotter, therefore, meaning it can be made smaller which, results in an efficiency benefit. By slowing the fan speed, this results in a reduction in noise and turbulence.
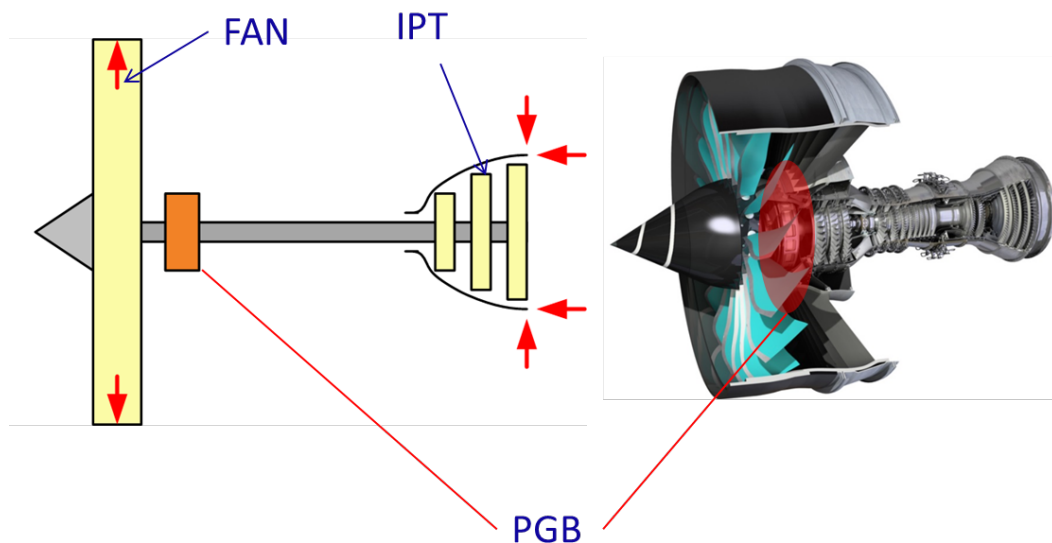
Figure 2-5 - Schematic showing that the PGB is connected the both the Fan and the IPT system and the location of the PGB in the engine (58).

Figure 2-5 illustrates that the PGB is connected to both the fan and IPT systems and that the PGB is located near the front of the engine just behind the fan. The central sun gear of the PGB is connected to the IPT and the fan is connected to the carrier of the five planetary gears.

The PGB presents a new tribological challenge for the lubricant due to the very high loads transmitted between the gear teeth although it is at a lower temperature than the core of the engine. The main challenge is deducing if current aviation lubricants can satisfy both the tribological challenges at the front of the engine in the PGB as well as being able to survive the high temperatures (more than 200 °C) in the core of the engine (where oil degradation is an issue). These are often opposing properties in that increasing tribological performance causes a reduction in thermal capability or increasing the lubricant viscosity. Consequently, a single shared oil system presents a significant challenge and therefore, a dual oil system could be a

preferable option if current lubrication solutions are unsuitable (58). However, this comes with additional challenges as a dual oil system would increase the complexity of the oil system and introduce the potential for operator error from putting the wrong oil into the wrong oil circuit. This would also have business and marketing implications as it is less desirable for airlines to purchase an engine either with different specific lubricating requirements or being limited to specific oils approved for the UltraFan©. This is especially true given that competitor PGB containing engines can use current lubricants to satisfy their lubrication requirements.

2.2.1 Business case for the UltraFan©

A geared turbofan engine offers a great efficiency saving due to allowing optimisation of the fan and turbine speeds. There are currently a few geared turbofan engines in service as shown in Table 2-2 but these are mostly for smaller business jet aircraft and Pratt & Whitney's PW1000G family of engines are currently operating in a range of medium sized civil aircrafts. Pratt & Whitney also claim this engine offers reduction in fuel burn, environmental emissions, engine noise and operating costs. Therefore, there is a gap in the market for a large geared turbofan for the large civil aerospace market which, Rolls-Royce hopes to exploit.

Table 2-2 – Geared turbofan engines that are currently in service along with some engine specification and examples of planes that utilise the engine (59,60).

Engine	Diameter Fan (inches)	Thrust (lbf)	Planes implemented in
Honeywell TFE731 (formerly Garrett TFE731)	40	~4500	Business Jets/ Military trainers – CASA C-101, Cessna Citation III, Dassault Falcon 900
Lycoming ALF 502 (Honeywell owned)	40.25	6970	Business Jets –British Aerospace 146, Bombardier Challenger 600.
Pratt & Whitney PW1000G	56 – 81	13K - 31K	Business Jets/ Civil Aircrafts – Mitsubishi Regional Jet, Bombardier CSeries, Airbus A320neo, Embraer E-Jet E2, Irkut MC-21.

2.2.2 Gas Turbine Oil System

The main requirements for a lubricant in the oil system are to provide lubrication and cooling for various ball and roller bearings, gear meshes, mechanical seals, and splined couplings and more specifically for the UltraFan©, the PGB. Other roles are to provide vibration damping using squeeze films and the heat in the oil is also transferred to the fuel system to prevent ice formation and to retain the heat energy efficiency benefits (1).

Oil System Arrangement
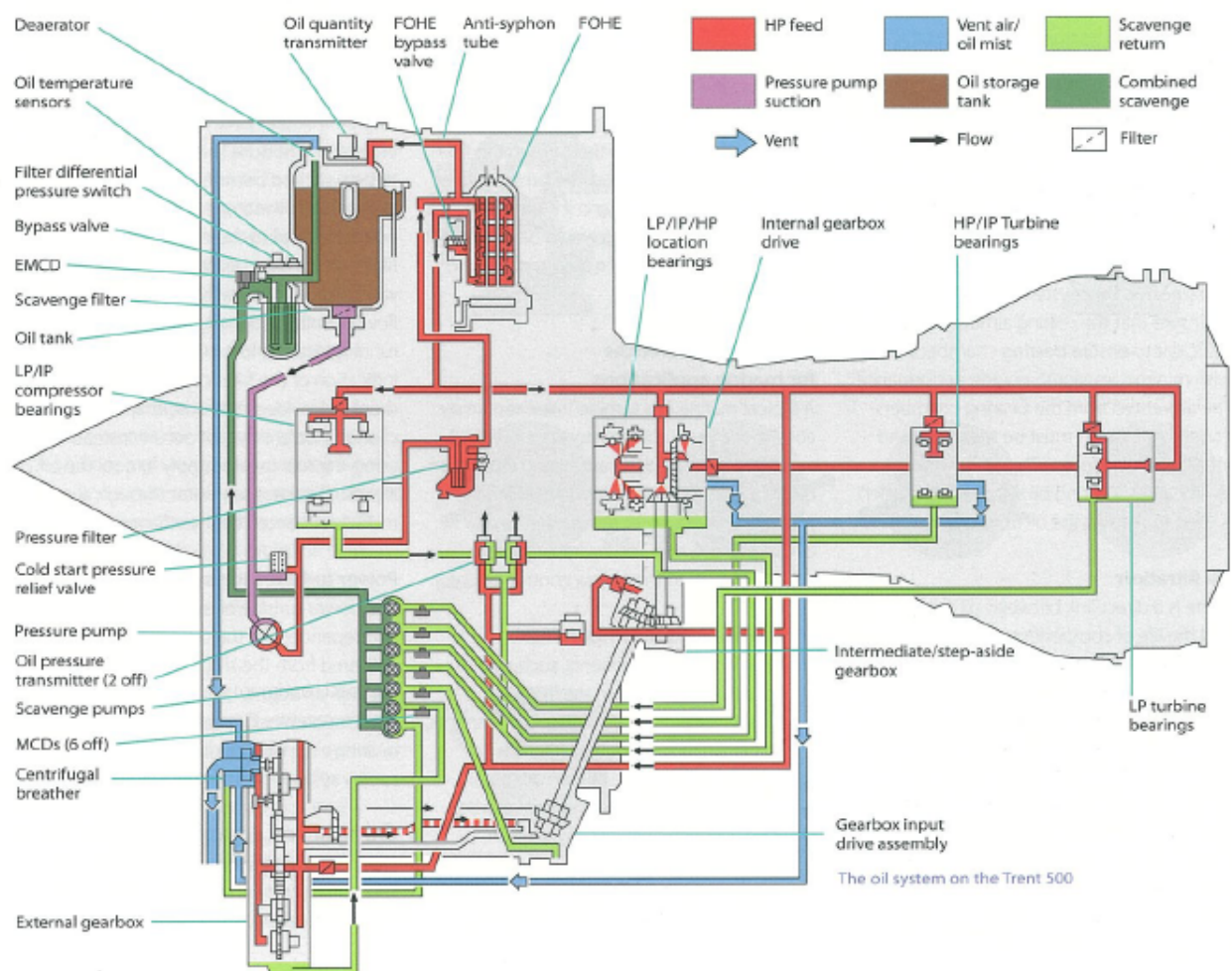
Figure 2-6 – Generalised gas turbine oil system schematic (1).

A gas turbine oil system from a Trent 500 is shown in Figure 2-6 and the basic operation is (1,61):

1. Oil is drawn through a strainer to protect from potential contaminants that may have gathered in the tank from a previous cycle (not shown on the diagram however, is part of the pipe that extracts the oil from the tank).

2. The pressurised oil then passes through a filter after a pressure limiting valve that opens if a blockage occurs, usually due to high viscosity oil at cold starting temperatures.

3. The oil then flows to the Fuel Oil Heat Exchanger (FOHE) where the heat in the oil is transferred to the fuel and in turn cools the oil before being separated into individual lines that are directed to the various bearing chambers and gearboxes.

4. Oil jets and distributors meter and direct the flow as necessary.

5. After lubricating and cooling the bearings and gearboxes, the oil goes into the sumps (individual sump for each chamber).

6. Scavenge pumps (which, also have strainers to filter out contaminants and wear debris) return the oil from the sumps to the oil tank via the scavenge filter.

7. As the oil enters the oil tank, it is deaerated.

8. The air that is removed from the vent systems is exhausted overboard via the centrifugal breather that recovers oil that may be dispersed in the air (although some oil is still lost overboard).

2.2.3 Tribological Contacts in the Oil System

Throughout the oil system of a gas turbine there are a variety of different metal-metal contacts that require lubrication to decrease friction and wear resulting in prolonged component life. Such contacts include different types of gears, roller and ball bearings, splines and couplings,

pumps which, all have specific conditions. These conditions include temperature, speed, the ratio of sliding to rolling, load and the materials properties.

As one of the aims of the project was to investigate whether current lubricants are suitable for the PGB environment in the UltraFan©, the focus of test conditions has been on those for gears. Gears are machine elements that transmit motion by teeth from one element contacting and pushing the teeth of another machine element similar to the action of small levers. Gears can be classified into three different types; gears for connecting parallel shafts, gears connecting intersecting shafts and neither parallel or intersecting shafts (Figure 2-7). The geometry and orientation of the teeth can also vary and Figure 2-7 gives examples of some different types including spur, bevel and helical gear teeth . The PGB is a helical gear system of connected parallel shafts. Some of the common terminology for gears can be seen in Figure 2-8.

Spur Gears

Rack and Pinion

Gears for connecting
parallel shafts

Straight Bevel Gear

Spiral Bevel Gear

Gears connecting
intersecting shafts

Crossed Helical Gear

Worm and worm gear

Gears with neither parallel
nor intersecting shafts
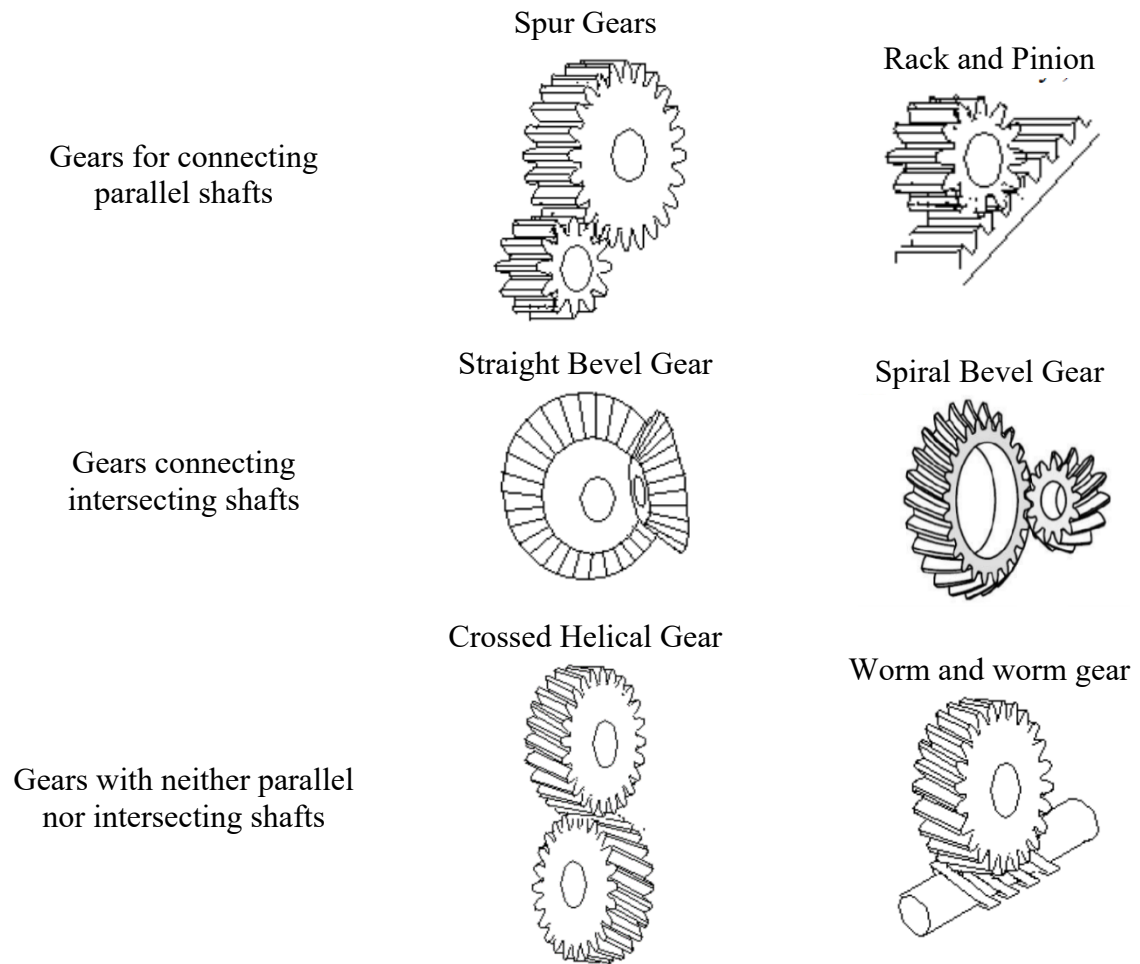
Figure 2-7 - Images showing different gear types (62,63).

Addendum
Circle

Face
Width

Space Width

Addendum

Circular
Thickness

Face

Flank

Fillet

Clearance

Pitch Circle

Root Circle

Dedendum
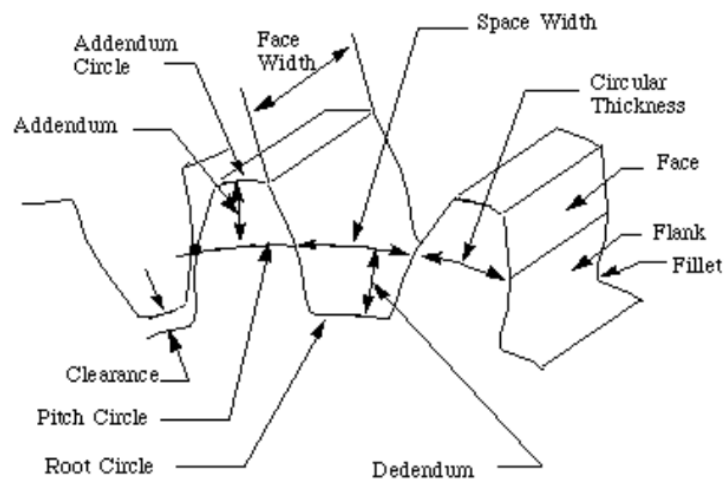
Figure 2-8 – Schematic of gear teeth showing some of the common terminology for gears (62).

36

Many factors can contribute to gear failure and a reduction in gear life such as the load, operating environment, the speed and contamination. Some of the design parameters that can influence gear failure are the Hertzian strength (ability of a gear tooth to withstand repeated loadings), thermal rating (maximum speed, reduction ratio and horsepower of a gear set), the backlash (the distance between the back of one gear tooth and the front of the next mating tooth) and the clearance (the distance between the top of a gear tooth and the base of the tooth on the other gear).

These parameters can influence a wide range of different gear failure modes have been summarised in Figure 2-9 and are also listed in ISO10825 (64).
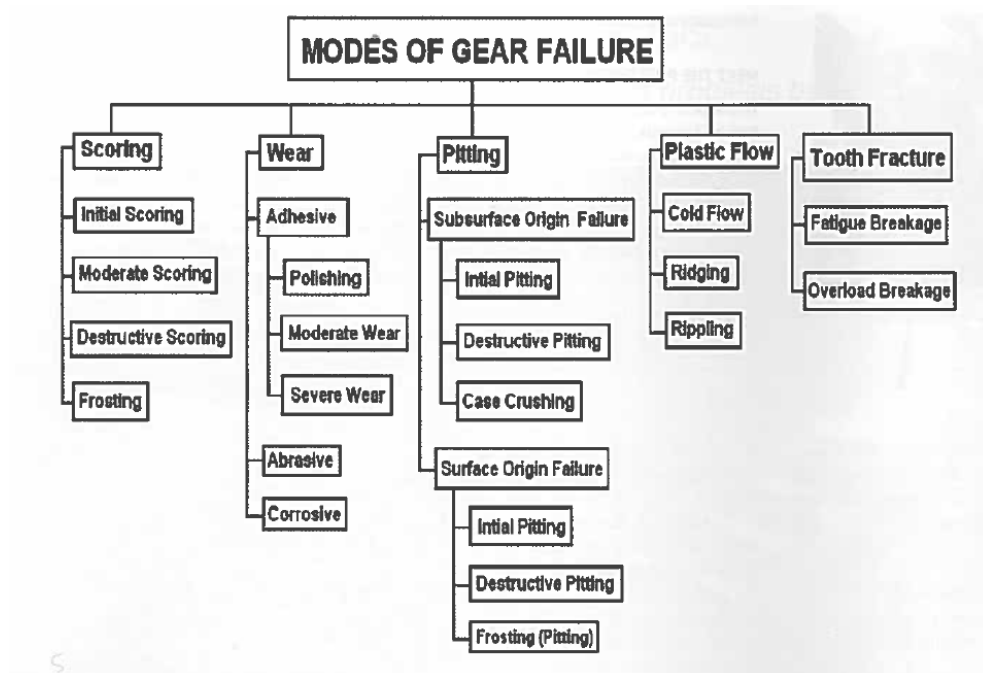
Figure 2-9 – Gear failure modes can be separated into five different modes each with their further corresponding subcategories of failure (64,65).

Whilst there are many factors in the gear design and operating conditions that contribute to failure, the lubricant also influences gear life. Both the physical properties of the lubricant and its chemistry can influence certain failures. A common wear mechanism associated with gears is micropitting (described in more detail in the Micropitting section) and this usually begins on

the dedendum of gear teeth as shown in Figure 1-4. Hence, the work in this thesis will aim to improve understanding on how lubricants used in aerospace influence micropitting (13,66–69).

2.3 Tribology Fundamentals

2.3.1 Stribeck and Traction Curves

Stribeck curves are a plot of entrainment speed (the speed at which, the surfaces are moving over one another) versus traction coefficient (or friction coefficient, μ) whilst maintaining a constant slide-to-roll ratio (SRR) and can be seen in Figure 2-10.
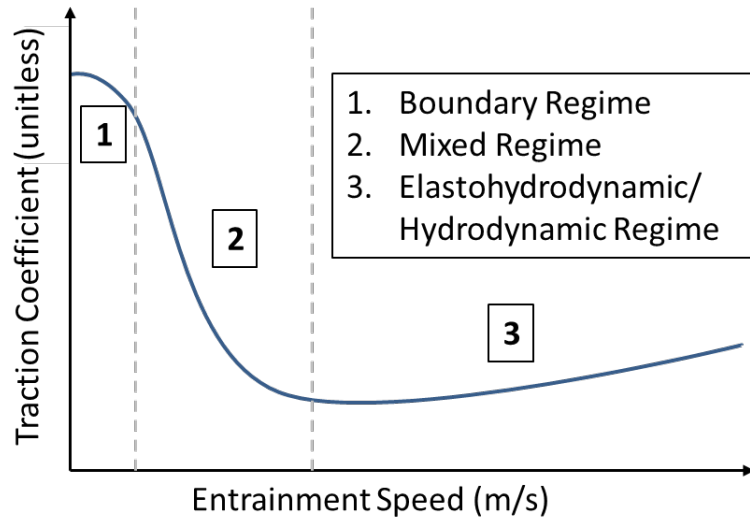
Figure 2-10 – A typical Stribeck Curve.

The equations for entrainment speed and SRR can be seen in (2-1) and (2-2) where U_1 and U_2 are the speeds of surfaces 1 and 2 respectively.

$$Entrainment\ Speed = \frac{U_1 + U_2}{2} \quad\quad (2\text{-}1)$$

$$SRR = \frac{U_1 - U_2}{Entrainment\ Speed} \times 100\% \quad\quad (2\text{-}2)$$

Stribeck curves can also be normalised for viscosity by plotting the traction coefficient against a dimensionless number called the Hersey number shown in (2-3), where N is the entrainment

speed in revolutions per second, μ is the dynamic viscosity and p_0 is the maximum contact pressure.

$$Hersey\ Number = \frac{\mu \times N}{p_0}$$ (2-3)

The Stribeck curves are fundamental to the tribology as they can show the various lubrication regimes and therefore, indicate lubricating performance. The regions/ lubricating regimes on a Stribeck curve can be broken down into the boundary regime at low entrainment speeds, the mixed regime at slightly higher entrainment speeds and finally either the hydrodynamic regime in conformal contacts or the elastohydrodynamic (EHD) regime in non-conformal contacts at high entrainment speeds. These regions are illustrated in Figure 2-10 where 1 is the boundary regime, 2 is the mixed regime and 3 is either the hydrodynamic or elastohydrodynamic regime. (5,7)

The boundary lubrication regime describes the conditions where high friction occurs due to asperity-asperity contact meaning there is either no lubricant film present, or the film thickness is insufficient to separate asperities. The mixed regime shows a decrease in traction coefficient as lubricant entrains between the surfaces and begins to separate asperities, but there is still some asperity-asperity interaction present. Finally, in the hydrodynamic/ elastohydrodynamic regime, the lubricant film thickness is enough to separate surface asperities giving rise initially to a lower traction coefficient again, but this begins to rise again as the viscous effects of the lubricant dominate. Another way of indicating the regime of lubrication is to look at the lambda ratio (λ) which, is a ratio of the lubricant film thickness (h) to the average of the surface roughness's (σ) as shown in (2-4) (70,71). Table 2-3 describes how the lambda ratio corresponds to the lubrication regime (5,7).

$$\lambda = \frac{h}{\sqrt{\sigma_1^2 + \sigma_2^2}}$$

<div align="right">(2-4)</div>

Table 2-3 – Table indication the lubrication regime according to the Lambda ratio (5,7).

Lambda Value	Lubrication Regime/Information
$\lambda > 3$	Full fluid film separation
$1 < \lambda < 3$	Partial or Mixed EHL (some asperity contact
$\lambda < 1$	Asperity contact
$\lambda < 3$	Most counterformal contacts

A traction curve is another analytical tribological graph which, is a plot of slide-to-roll ratio (SRR) against traction coefficient whilst maintaining a constant entrainment speed. It can be seen in Figure 2-11 that a traction curve can be broken down into three regions; the linear region, the non-linear region and the thermal region. The linear region shows an increase in traction coefficient as the SRR increases and this shows that the lubricant is Newtonian (constant viscosity) and it depends on the pressure in the contact. A further increase in the SRR causes the curve to gradually level out until a maximum traction coefficient is reached and here the lubricant displays non-Newtonian behaviour and depends on the rheology of the lubricant. A further increase again in SRR causes the traction coefficient to decrease as heat is generated in the contact which, causes the viscosity to decrease which, therefore, reduces the traction coefficient. (5,7)
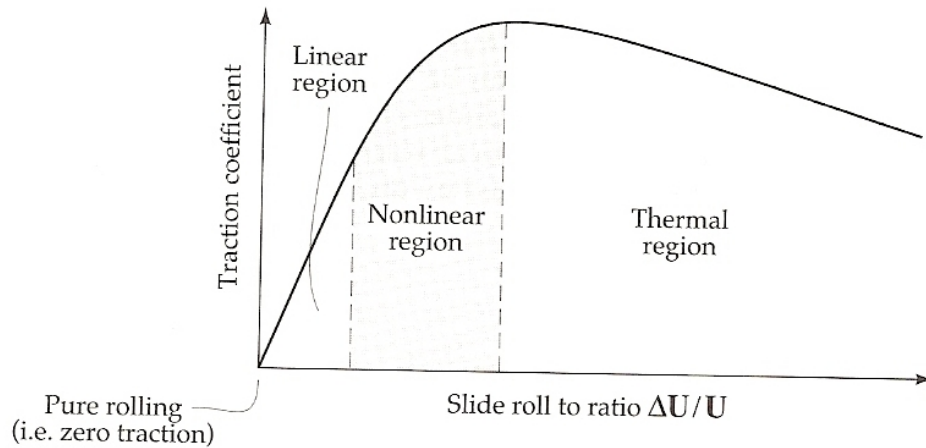
Figure 2-11 – A graph of a traction curve and its regions.(5)

2.3.2 Roughness

Surface finish or roughness is an important aspect to consider in a tribological problem. It is highly unlikely that even the smoothest opposing surfaces will be completely flat and thus make perfect contact with each other. A surface can be considered as an uneven plane with protruding parts and craters. The protruding parts that contact the opposing surface are commonly referred to as asperities. The roughness of the surface will determine how many of these surface asperities will contact the opposing surface and rougher surfaces will lead to less contacting asperities, which, will decrease the contact area and therefore, increase the contact pressure. Higher contact pressures apply higher stresses to a surface which, can ultimately lead to increasing wear and friction.

The deviation from an ideal surface can be described in terms of lay, flaws, waviness and roughness as shown in Figure 2-12 (72). There are many parameters used to define roughness and these should always be considered with each other as surfaces can have similar values for one parameter and yet different ones for others. The more parameters that are measured, the better the complete view of the surface profile. The two most widely used are centre-line average roughness, R_a and the root-mean-square roughness, R_q which, can be described by (

41

2-5) and (2-6). L is the measurement length; z is the height of the surface above the mean level and x is a coordinate in the surface. These roughness values are usually reported in μm or nm.

$$R_a = \frac{1}{L} \int_0^L |z| \, dx \qquad\qquad (\,2\text{-}5\,)$$

$$R_q = \sqrt{\frac{1}{L} \int_0^L z^2 \, dx} \qquad\qquad (\,2\text{-}6\,)$$

R_q is deemed to be more accurate than R_a as R_a cannot distinguish between a gentle undulating surface and a surface with more rigid and sharp asperities. R_q addresses this as the squared term gives a greater significance to surface variations some way from the average surface level.
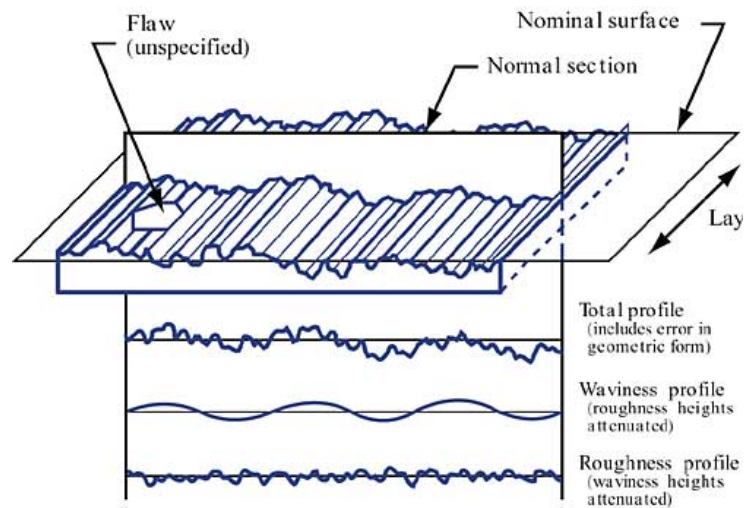
Figure 2-12 – Illustration showing the various quantifiable components of a real surface (72).

2.3.3 Hardness

Hardness of a given material is a material property and this has a large influence on wear. Generally, the harder the material, the more resistant it is to wear. The hardness of a material is defined by a specific measurement procedure which, is usually determined from the size of an impression by a very hard specimen (not deforming itself) of a specific shape set time and force. The three most common methods for measuring hardness are Brinell, Rockwell and Vickers

which, each have a specific indenter geometry and equation for giving a value for the hardness. The method utilised here is Vickers hardness.

Vickers hardness uses a diamond square-based pyramidal indenter that is included at an angle of 136 ° and then the square based impression it measured under a microscope. The dimensions (diagonal lengths, d) of the impression and the load (F) applied are used to give a Vickers hardness value using equation (2-7) (5,7).

$$H_V = \frac{1.854W}{D^2}$$ (2-7)

A schematic of the indenter and the impression can be seen in Figure 2-13.
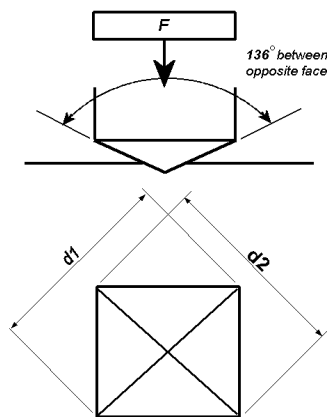
Figure 2-13 – Diagram showing the geometry of the indenter and impression for a Vickers hardness test (73).

2.3.4 Contact Mechanics

The principles of contact mechanics describe how surfaces contact and how loads are concentrated onto a small area where the opposing surfaces meet; this is known as the contact area. The actual contact area is greatly affected by the roughness as opposing surfaces will only contact at asperity junctures and therefore, the contact area is usually much smaller than the respective components. As the contact pressure is the load divided by the contact area, the contact pressure increases as the contact area decreases (and increases further as the roughness increases). Therefore, engineers aim to design components to have a larger contact area with a

smooth surface finish to lower the contact pressure to decrease the stress on the component, but this may be limited by the size of the component and the cost of creating a smooth surface finish.

The contact of two curved bodies loaded against one another can be described by Hertzian contact theory which, was proposed by Heinrich Hertz in 1881. Hertzian contact theory assumes the following:

1. The materials in contact are homogenous and the yield stress of the materials is not exceeded.
2. The contact load is caused by the load that is normal to the contact.
3. The size of the contact area is much smaller than the size of the bodies in contact.
4. The contacting bodies are at rest and in equilibrium (bodies are static).
5. Surface roughness is negligible.

Hertzian contact defines solutions for circular, line and elliptical contacts.

Circular Point Contact

Circular point contacts can form between two contacting balls or a ball on a flat surface as shown in Figure 2-14. The Mini-Traction Machine (MTM) is an example of this ball on flat contact geometry.
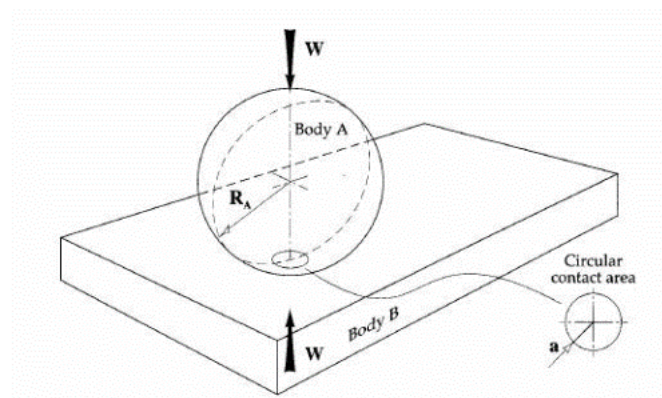
Figure 2-14 – An example of a circular point contact where ball is contacting a flat surface (12).

44

The contact area, a, the maximum contact pressure, p_0, the average contact pressure, p_{avg} and the contact pressure distribution, $p(r)$ can be calculated by equations (2-8), (2-9), (2-10) and (2-11) respectively:

$$a = \sqrt[3]{\frac{3PR'}{4E^*}} \tag{2-8}$$

$$p_0 = \frac{3P}{2\pi a^2} \tag{2-9}$$

$$p_{avg} = \frac{P}{\pi a^2} \tag{2-10}$$

$$p(r) = p_0 \sqrt{1 - \frac{r^2}{a^2}} \tag{2-11}$$

Where P is the normal load (N), r is the radius of the contact area, R' is the reduced radius of the contact (m) and E^* is the reduced elastic modulus (N/m²). To acquire the pressure distribution across the length of the radius, $r = 0$ in the centre of the point contact and $r = a$ at the outer circumference of the point contact (the full radius). R' and E^* can be calculated by (2-12) and (2-13).

$$\frac{1}{R'} = \frac{1}{R_1} + \frac{1}{R_2} \tag{2-12}$$

$$\frac{1}{E^*} = \left(\frac{1 - v_1^2}{E_1} + \frac{1 - v_2^2}{E_2} \right) \tag{2-13}$$

Where R_1 and R_2 and the radii of curved bodies 1 and 2 (m), v_1 and v_2 are the Poisson ratios of bodies 1 and 2 (unitless) and E_1 and E_2 are the elastic moduli of bodies 1 and 2 (Pa). It should also be noted that if a surface is concave, the radius is a negative curvature, if it is convex the radius is positive and if the surface is flat, the radius is infinity (∞).

Line Contact

Line contacts can occur between parallel contacting cylinders or a cylinder within a cylinder like a journal bearing. The MPR is another example of a line contact and the outer rings contact the central roller along a line.
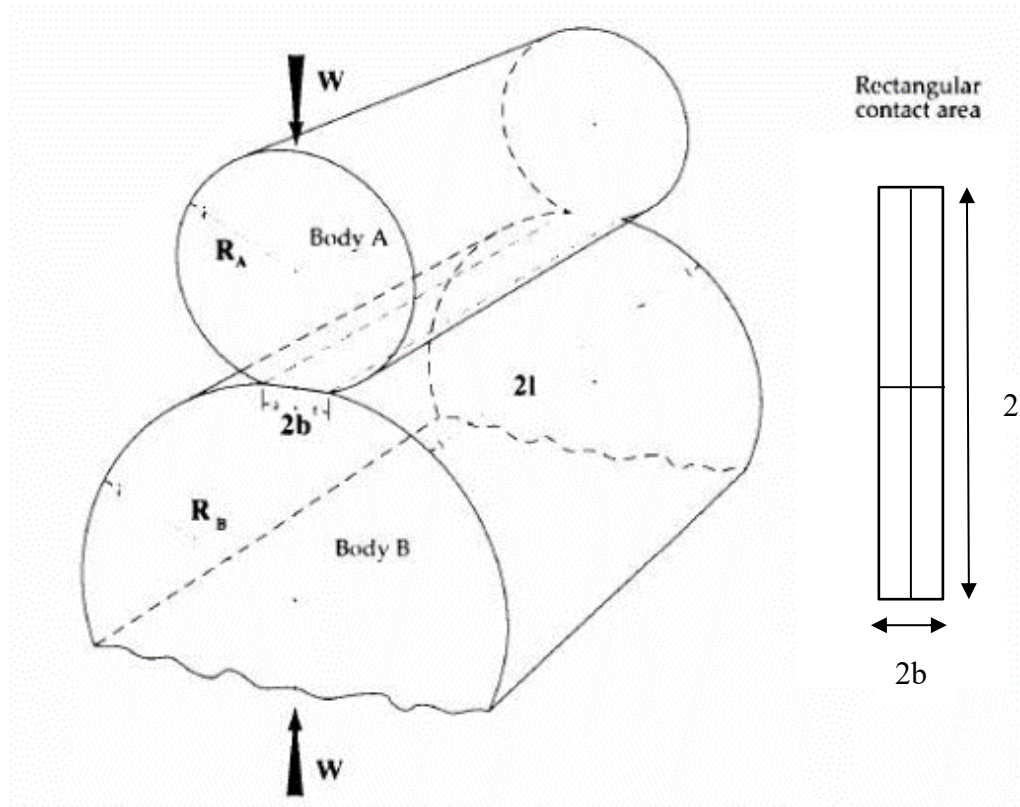
Figure 2-15 – An example of a line contact with two parallel contacting cylinders (12).

The contact area, *a*, the maximum contact pressure, p_0, the average contact pressure, p_{avg} and the contact pressure distribution, *p(r)* can be calculated by equations (2-14), (2-15), (2-16) and (2-17) respectively.

$$b = \sqrt{\frac{4P'R'}{\pi E^*}} \qquad (2\text{-}14)$$

$$p_0 = \frac{2P'}{b\pi} \qquad (2\text{-}15)$$

$$p_{avg} = \frac{P'}{2b} \qquad (2\text{-}16)$$

$$p(x) = p_0 \sqrt{1 - \frac{x^2}{b^2}} \qquad\qquad (\,2\text{-}17\,)$$

Where P' is the normal load per unit length of the cylinder (N/m), x is the length of the contact area (m) (for pressure distribution, x is 0 to b to get the distribution) and b is the half width of the rectangle.

Elliptical Contact

Elliptical contacts can occur when two cylinders are crossed, when a ball is in a bearing raceway as shown in Figure 2-16 or even two gear teeth in contact.
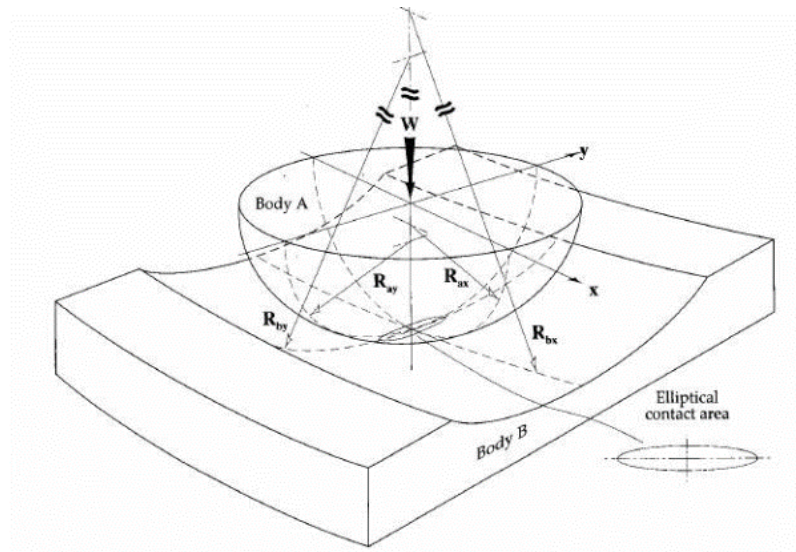
Figure 2-16 – An example of an elliptical contact area with a convex ball contacting a concave bearing raceway (12).

The gear tooth on each gear in the PGB will therefore, have an elliptical contact area. They are considered an elliptical contact due to the curvature of the teeth, the gear alignment and the direction of motion the size of shape of the elliptical contact also changes throughout the gear teeth meshing cycle. The tribology rigs cannot replicate a gear contact exactly which presents a limitation of the MTM and MPR in understanding the tribological behaviour of gears. However, despite the exact geometry of the contact not being replicated, many of the other conditions experienced can, such as the contact pressure, the temperature (if not over 150 °C

maximum temperature of the MTM), the SRR, the entrainment speed, the metallurgy of the surfaces and the oil which, can all be tailored to mimic PGB conditions.

The contact radii, a and b, the maximum contact pressure, p_0, the average contact pressure, p_{avg} and the contact pressure distribution, $p(r)$ can be calculated by equations (2-18), (2-19), (2-20), (2-21) and (2-22) respectively.

$$a = \sqrt[3]{\frac{3k^2 EPR'}{\pi E^*}}$$
(2-18)

$$b = \sqrt[3]{\frac{3EPR'}{\pi k E^*}}$$
(2-19)

$$p_0 = \frac{3P}{2\pi ab}$$
(2-20)

$$p_{avg} = \frac{P}{\pi ab}$$
(2-21)

$$p(x,y) = p_0 \sqrt{1 - \frac{x^2}{a^2} - \frac{y^2}{b^2}}$$
(2-22)

2.3.5   Film Thickness in Elastohydrodynamic Lubrication

As shown in the Stribeck curve (Figure 2-10), at high entrainment speeds and providing the surfaces are smooth enough, full fluid film separation of the surfaces can be achieved. As mentioned earlier, if this film is between two non-conformal surfaces, this regime is known as the ElastoHydroDynamic (EHD) regime. Many environments within the oil system are non-conformal contacts such as meshing gear teeth. These contacts are typically characterised by having the load concentration on a smaller contact area that results in:

- A very high contact pressure like what is present in gear teeth contacts and in a ball on flat contact (point contact, like the arrangement of the MTM).

- The surfaces elastically deform.

- The viscosity on the oil increases due to the increased pressure (as shown by the Barus equation in (2-23)) which, shows that viscosity increases with pressure, where η_0 is the viscosity at atmospheric pressure, α is the pressure-viscosity coefficient and p is the pressure), this is known as piezo-viscosity.

$$\eta = \eta_0 \exp(\alpha p) \qquad (\,2\text{-}23\,)$$

Due to the high pressures present, this causes elastic deformation of the contacting surfaces and consequently results in different film geometry in the contact. This deformation is small in comparison to the size of the components themselves but is large when compared to the film geometry and therefore, need to be take into consideration. It can be seen in Figure 2-17 that there is a spike in pressure at the exit of the contact that is caused by the constriction near the exit of the contacts due to deformation of the surfaces (5,7).
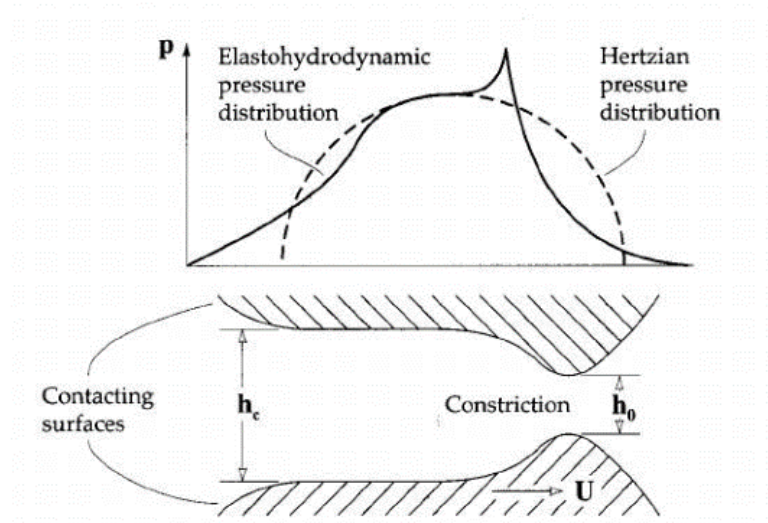
Figure 2-17 – Graph showing the pressure distribution in the contact and a diagram showing the film geometry in between the deformed surfaces in the EHD contact where h_c is the central film thickness and h_0 in the minimum film thickness (12).

There are a few different methods for calculating of the lubricant film thickness in the EHD contact that were deduced numerically such as Dowson-Hamrock and Ertel-Grubin, but the equation used in this thesis is the Dowson-Higginson formula shown in (2-24).

$$\frac{h_{min}}{R_x} = 2.65(2\alpha E^*)^{0.54}\left(\frac{\bar{U}\eta_0}{2E^*R_x}\right)^{0.7}\left(\frac{W}{2E^*R_xL}\right)^{-0.13} \qquad (\,2\text{-}24\,)$$

Where $2\alpha E^*$ is known as the material parameter, $\frac{\bar{U}\eta_0}{2E^*R}$ is known at the speed parameter and

$\frac{W}{2E^*RL}$ is known at the load parameter. R_x is the reduced radius in the x direction, α is the pressure-viscosity coefficient, E^* is the reduced elastic modulus, $\bar{U}$ is the average speed of the two moving surfaces, η_0 is the viscosity at atmospheric pressure, W is the load and L is the length of the contact (74).

2.3.6 Current aviation tribological test methods

There are few tribology methods that are used to test aviation lubricants for specification approval and reporting purposes (26). In the current civil aviation lubricant specification, SAE AS5780, the only mandatory tribological test method is the method for measuring load carrying capacity using the Ryder gear method; method 6508 in FED-STD-791 (the federal standard testing methods of lubricants, liquid fuels and related products) (55,75). The test involves gradually increasing the pressure between mating gears and the resultant scuffing is measured. The capability of the lubricant to mitigate scuffing is measured by the maximum pressure when operating at 10,000 rpm.

SAE AS5780 also lists some other tribological test methods that are either under development or the data is not understood enough for the method to be a requirement of the specification. Therefore, these items are referred to as "report only" and are not routinely supplied by aviation lubricant manufacturers. The first is the Aviation Lubricant Tribology Evaluator (ALTE) which, assesses the lubricating capacity of gas turbine lubricants in which, the method is listed in SAE ARP6255 (76). This test involves a non-rotating steel ball which, is vertically mounted and loaded against a steel cylinder via a weight. The cylinder rotates at a fixed speed whilst partially immersed in a lubricant reservoir which, results in lubricant continuously being

entrained into the contact. The diameter of the wear scar on the ball is measured and is the indicator for a lubricants wear performance.

The other report only method is the Wedeven Associates Inc. Machine (WAM) which, measures a lubricant's load carrying capability as shown in SAE ARP6156 (77). The WAM wear test consists of a rotating ball contacting a rotating disc under lubrication. The speeds of the surfaces can be controlled to give a range of sliding and rolling conditions and the test measures the lubricant performance through the resultant wear and also through measuring the traction coefficient.

Another method that is not currently used to assess lubricants but is one of the most common gear test methods in the gear industry is the FZG test which, is a back-to-back spur gear test rig which, conducts a lubricated wear test under controllable conditions.

2.4 Rheology

The rheology of a lubricant (how the lubricant deforms and flows) also influences the tribological performance. This is because how a lubricant deforms, and flows will affect its viscosity) under certain conditions and will typically have more of an effect in the EHD regime due to the traction coefficient being influenced mostly by the bulk viscometric properties of the lubricant at high speeds. As the lubricant flows around the oil system, it is subjected to a wide range of different shear stresses and speeds which, result in strain (or deformation) on the oil which, is dissipated through the viscous fluid.
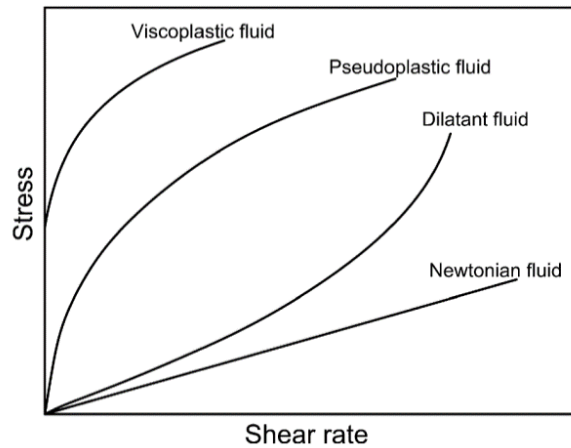
Figure 2-18 - Flows curves showing types of rheological behaviour; Newtonian and non-Newtonian fluid behaviour (78).

Rheological properties are often described using flow curves to observe rheological behaviour seen in Figure 2-18 whereby the fluid (the lubricant) is subjected to ascending or descending shear rates, and the corresponding shear stress and therefore, viscosity are measured (79).

A Newtonian fluid (or Newton-Stokes fluid) is a fluid in which, the viscosity remains constant with increasing shear stress and is represented by a straight line on a flow curve as shown in Figure 2-18 and by equation (2-25) where σ is shear stress, η is the shear viscosity and $\dot{\gamma}$ is the shear/ deformation rate.

$$\sigma = \eta\dot{\gamma} \qquad (\text{2-25})$$

It can be shown that the shear rate is proportional to the velocity gradient. This is exploited in a rheometer where the velocity gradient can be taken as linear, or theoretically derived, as in for example a Couette, cone and plate or parallel plate geometry. The other curves on the graph are considered non-Newtonian as the shear stress is not proportional to the shear rate and the ratio of shear stress to shear rate is the apparent viscosity. Therefore, equation (2-25) becomes invalid and other equations of state are required for each non-Newtonian fluid. Non-Newtonian fluids can either be a viscous or viscoelastic. For a viscous fluid, the work of deformation

52

dissipates throughout the fluid and for a viscoelastic fluid, the work of deformation is stored as elastic energy and released as elastic deformation.

However, conventional rheology often has the limitation of not being capable of reaching the shear rates experienced in certain parts of a gas turbine oil system such as in a high-speed bearings and as a result, it is more difficult in deducing the rheology in EHD conditions. For example, in parallel plate rheometers, the fluid is flung out of the contact as the centrifugal force is too high (80–83).

Consequently, engine manufacturers use High-Temperature High-Shear rate (HTHS) viscosity as a measure of the lubricant's resistance to flow in the narrow confines between hot and fast-moving engine components. However, current standard methods are tailored for automotive applications (84,85). Whilst the rheology is an important parameter to understand a lubricants' tribological performance, research has shown that the base oils used in aviation lubricants are Newtonian as shown by *Moore 1997* and hence, should not cause any adverse effects in the EHD regime. (81)*.*

Chapter 3.   Methods and Materials

3.1 Methods

3.1.1 Mini Traction Machine

A Mini Traction Machine (MTM, developed by PCS instruments) was used to evaluate the tribological performance of the oils (86). The MTM uses a ball on a disc configuration, each component with a separately controlled rotational speed (and therefore, entrainment speed (U)) to achieve the defined slide-roll ratio (SRR).

The contact between the ball and the disc is submerged in a reservoir of lubricant (approximately 35 mL) and the ball rotates against the disc at an inclined axis to eliminate spin in the contact. The load and lubricant temperature can also be controlled and the traction coefficient (friction) is measured. Under normal operation of the MTM the ball rotates anti-clockwise and the disc rotates clockwise as shown in Figure 3-1.
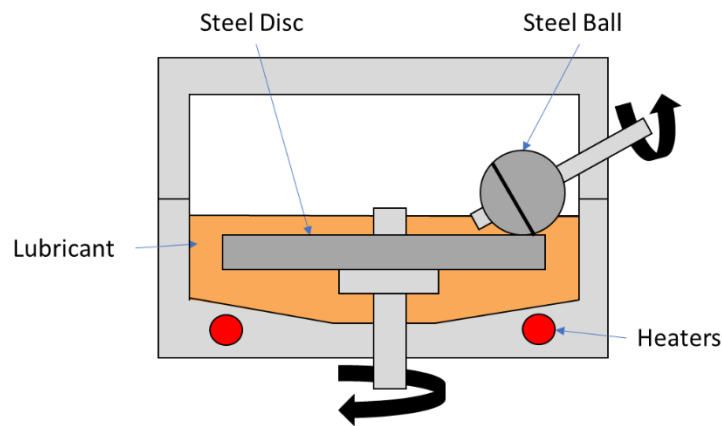
Figure 3-1 - Configuration of the MTM showing the rotational directions of the ball and disc.

Final Test Conditions

The MTM was used to produce Stribeck curves over a range of temperatures. Each of these tests was completed three times to confirm repeatability and all Stribeck curves have been plotted with error bars of one standard deviation for each data point. Representative gas turbine oil system contact conditions were used for Stribeck analysis are shown in Table 3-1. It should be noted that the exact conditions in use in the PGB cannot be disclosed for Intellectual Property (IP) reasons but are considered representative of a point contact within the meshing of the gears in that environment.

Table 3-1- Conditions used for Stribeck analysis.

Parameter	Value
Applied Load	40 N
Contact Pressure	1.01 GPa
Contact area	0.062 mm^2
Slide-to-Roll Ratio (SRR)	50 %
Entrainment Speed	0 – 3 m/s

The type of EHD lubrication seen in these tests at high entrainment speeds was hard viscous EHD lubrication as the steel specimens used have a high elastic modulus; the viscosity changes in the contact due to the high contact pressures and the contact is elastically deformed due to the high contact pressure in the non-conformal contact (87,88). The test also starts at high speed and progresses to low speed. Two different methods of normalising for viscosity were applied to the tests to isolate the effect of the molecular structure on friction. The first method involved plotting the measured traction coefficient against the Hersey number (as discussed in 2.3.1 Stribeck and Traction Curves section). The dynamic viscosities were calculated using the supplied densities and can be seen in Appendix 5.

The second method involved testing each lubricant by carrying out experiments at different temperatures for each oil so that they all had the same kinematic viscosity. This was done using data from measurements of kinematic viscosity and ASTM D341 which, is a standard method

that allows the prediction of viscosities of liquid petroleum products over a range of temperatures using the Walther Equation (the equation for this can be seen in Appendix 4) (89). The viscosities selected were chosen as the calculated test temperature required for each oil was within the temperature range capability of the MTM. The calculated temperatures for each base oil can be seen in Appendix 4.

Another consideration worth noting is shear stability of the base oil molecules. Walker et al. showed by sampling the base oil through a small hole, that polymeric base oils can break down into smaller molecules in EHD contacts (90). They suggested that polymeric scission will begin to occur in linear hydrocarbon polymers if shear stress × molecular weight^2 > 1 × 10^{13} Pa, but this is generally only a concern for much larger base oil molecules. Hence, for the base oils tested in this study the shear stability was assumed not to be an issue (91).

Also, due to the low roughness of the superfinished specimens (R_a < 0.01 μm for the disc and R_a < 0.02 μm for the ball), very minimal wear was produced for all tests and therefore, the wear was not investigated.

Development of Test Conditions

It was necessary to develop test conditions that allowed a comparison of different lubricants whilst also understanding of their performance under representative conditions of contact environment (in this case the PGB).

The technical specifications of the MTM are shown in Table 3-2.

Table 3-2 – Specifications of the MTM including the range of conditions that can be replicated.

Load	0 to 75 N.
Contact Pressures	0 to 1.25 GPa (standard 3/4" steel ball specimens) up to 3.1 GPa with alternative specimens.
Speed	-4 to 4 m s^{-1}
Slide/Roll Ratio	0 to 200 %
Temperature Range	Ambient to 150 °C (lower with optional oil cooler)
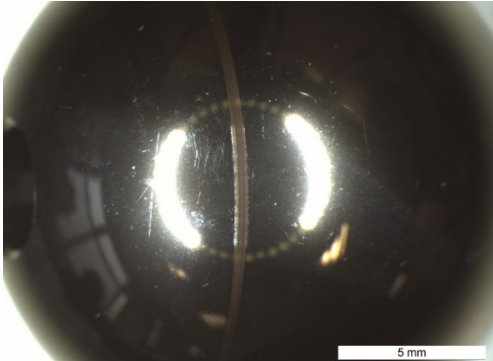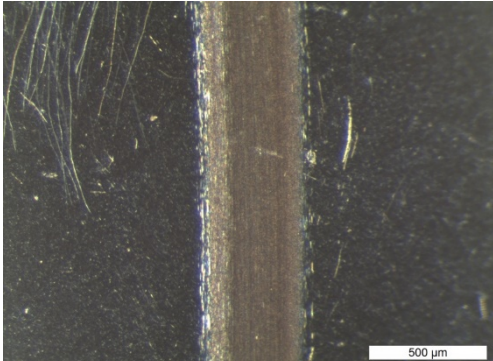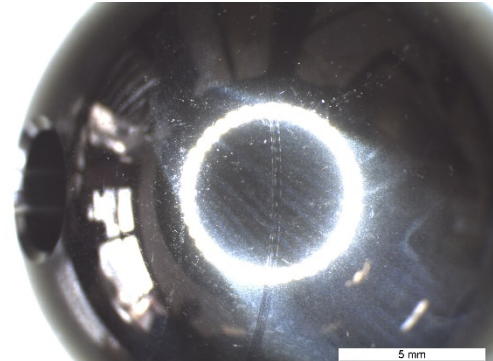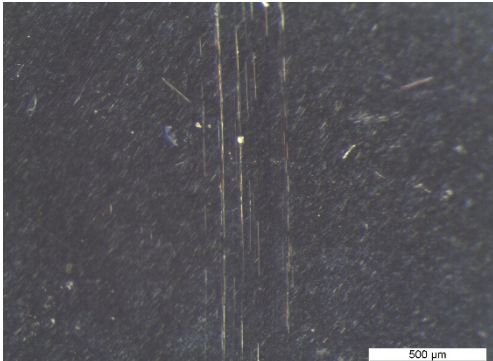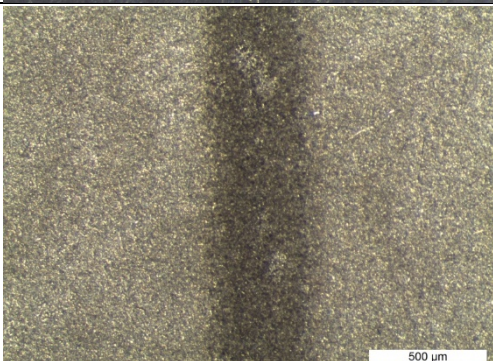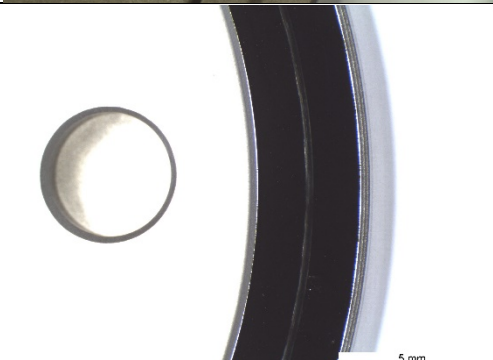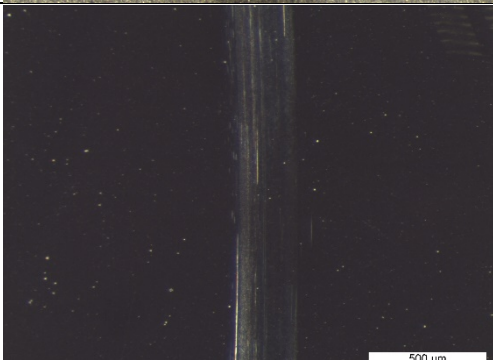
Test Sample Volume	35 mL

The expected conditions between gear teeth in the PGB are within the limits in Table 3-2. The high load and SRR shown in Table 3-1 were chosen to understand how the lubricants behave under the more challenging conditions and the range temperatures were chosen to understand how the behaviour changes with the range of temperatures the PGB could experience. A Stribeck curve is especially useful for understanding how the behaviour of the lubricant changes over different speeds seen in the PGB under different operational modes of the aircraft. These include slow entrainment speeds during start up and high entrainment speeds during ascension to high altitudes. Hence, this covers the range of conditions expected within the tribological contacts in the PGB as it covers a range of lubrication regimes.

Superfinished smooth specimens were chosen to allow comparison of the frictional behaviour of the lubricants despite these not being representative of the rougher gears expected in the real application. Rougher specimens were tested but this resulted in inconsistent and unrepeatable results until the rough surfaces had been sufficiently run in. The images showing the effect of the roughness can be seen in Table 3-3 which, shows that a rougher disc produces a more severe wear than a smooth disc specimen. The Stribeck curves showing how the friction changes throughout multiple runs with the rougher disc can be seen in Figure 3-2, Figure 3-3, Figure 3-4 and Figure 3-5. This would therefore, introduce another variable and unnecessary complexity to the comparison of lubricant performance. Also, if too much wear has occurred, the risk of abrasive wear particles contributing to the wear would also distort the results as can be seen from Table 3-3 with rougher specimens producing excessive wear.

Table 3-3 – Table showing the microscopy images demonstrating the effect of roughness on the wear produced on both the ball and disc specimens.

	Overview image	Magnified Image (x 10)
<0.02 µm Ball tested against 0.3 µm Disc		
<0.02 µm Ball tested against Smooth <0.01 µm Disc		
0.3 µm Disc tested against <0.02 µm Ball		
<0.01 µm Disc tested against <0.02 µm Ball		
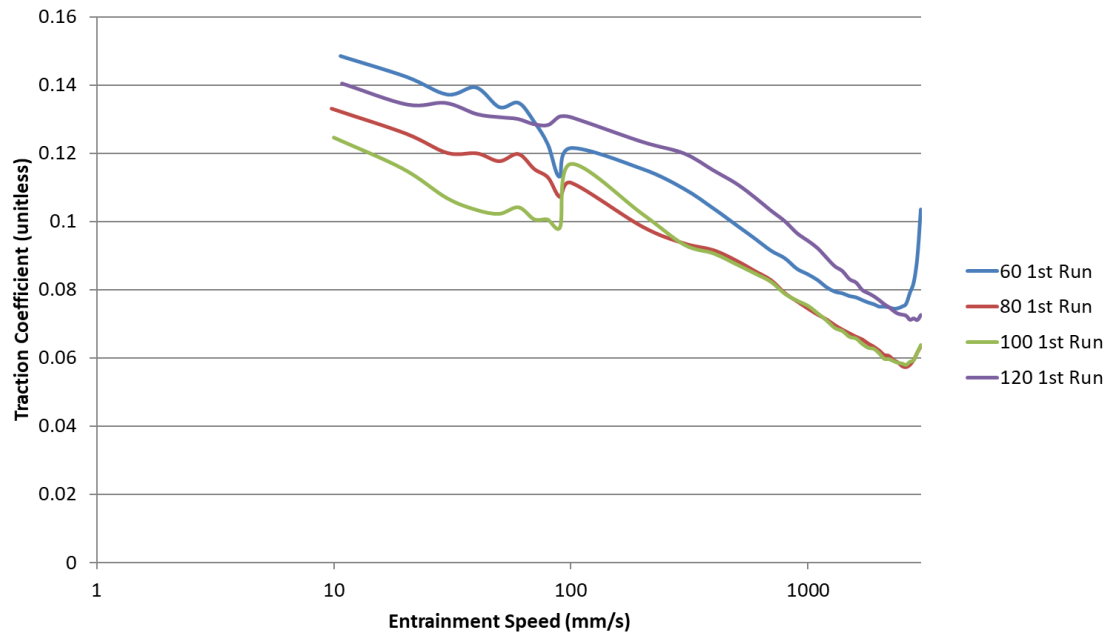
Figure 3-2 – Stribeck curves showing the first run of Stribeck tests in the following order; 60 °C, 80 °C, 100 °C and 120 °C with Lubricant A with a disc specimen of roughness R_a 0.3 μm and ball roughness <0.01 μm.
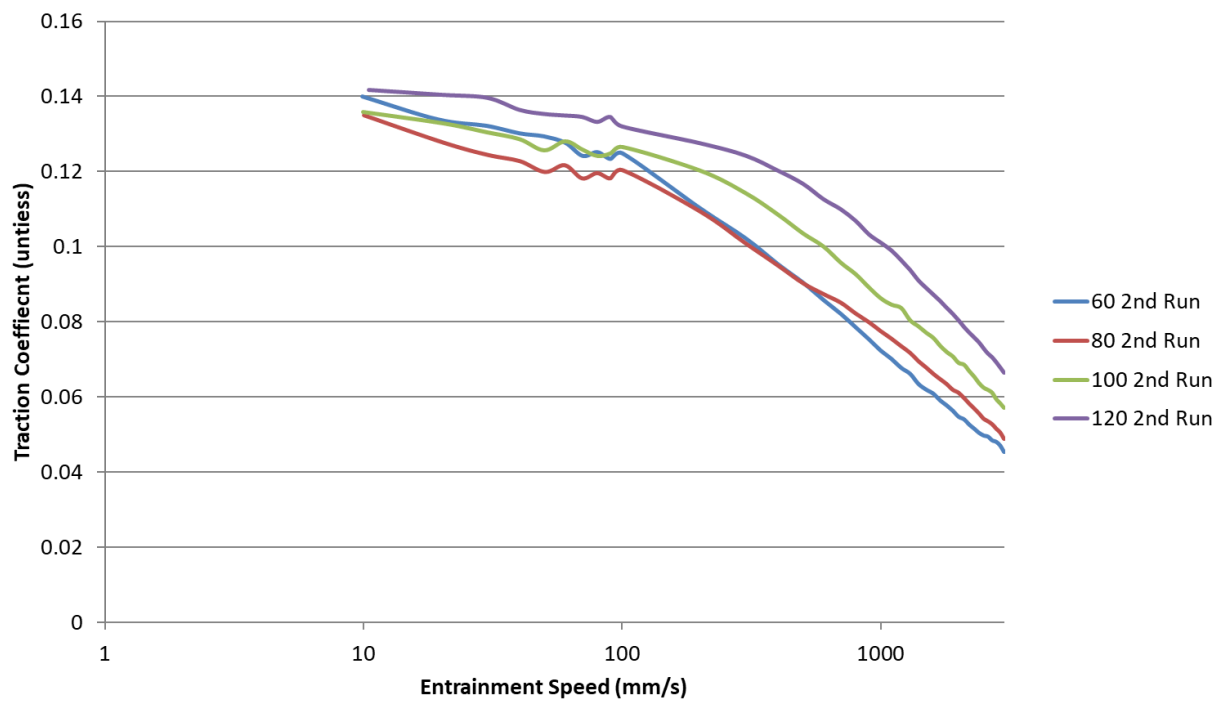
Figure 3-3 – Stribeck curves showing the second run of Stribeck tests in the following order; 60 °C, 80 °C, 100 °C and 120 °C with Lubricant A with a disc specimen of roughness R_a 0.3 μm and ball roughness <0.01 μm.
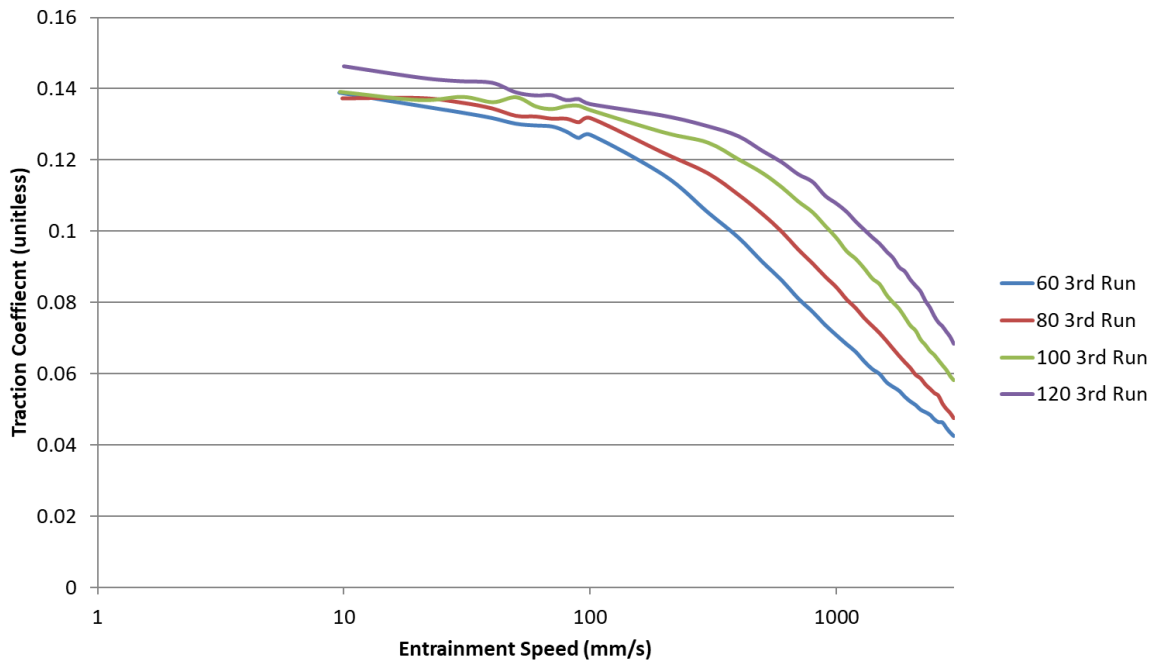
Figure 3-4 – Stribeck curves showing the third run of Stribeck tests in the following order; 60 °C, 80 °C, 100 °C and 120 °C with Lubricant A with a disc specimen of roughness R_a 0.3 μm and ball roughness <0.01 μm.
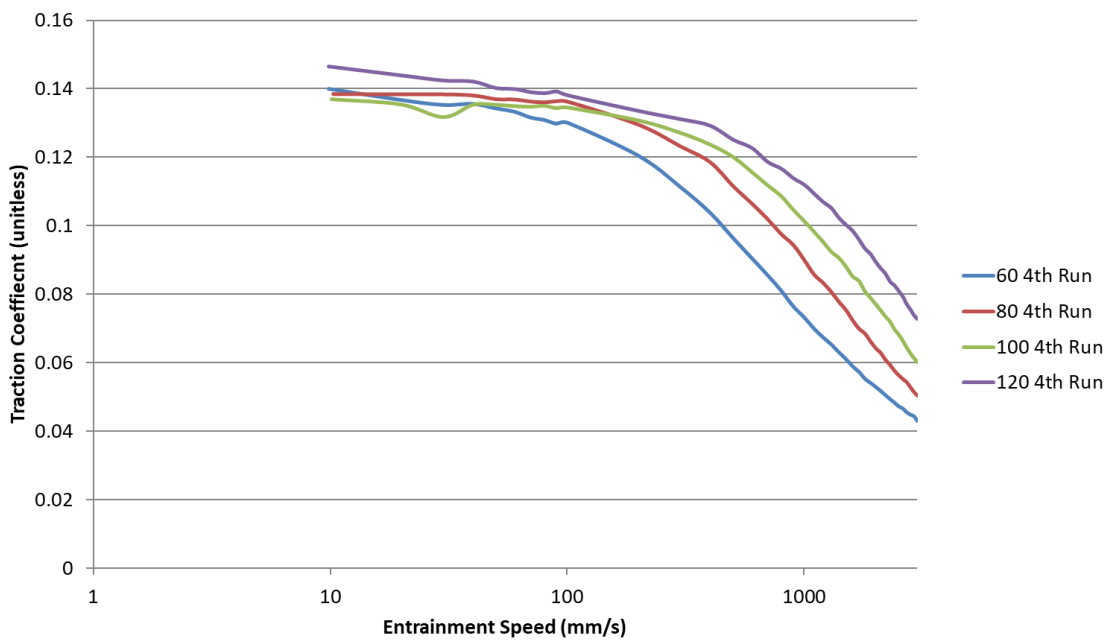
Figure 3-5 - – Stribeck curves showing the fourth run of Stribeck tests in the following order; 60 °C, 80 °C, 100 °C and 120 °C with Lubricant A with a disc specimen of roughness R_a 0.3 μm and ball roughness <0.01 μm.

Error Analysis

Understanding the repeatability and reproducibility the MTM was paramount in understanding the results. Hence, a Gage R & R study was completed to understand the accuracy between multiple repeats of the same test for the same user but also to look for differences between users. A gage R&R study was conducted between 2 operators (Operator A and Operator B), 4 different lubricants (Lubricants A-D shown in 3.2.2 Commercially Available Full Formulation Lubricants section) on one MTM. Whilst Stribeck curves were produced for all of these test following the conditions outline in Table 3-1, traction coefficient was selected at three different entrainment speeds 200 mm/s, 500 mm/s and 2000 mm/s at the four different test temperatures; 60 °C, 80 °C, 100 °C and 120 °C (92).
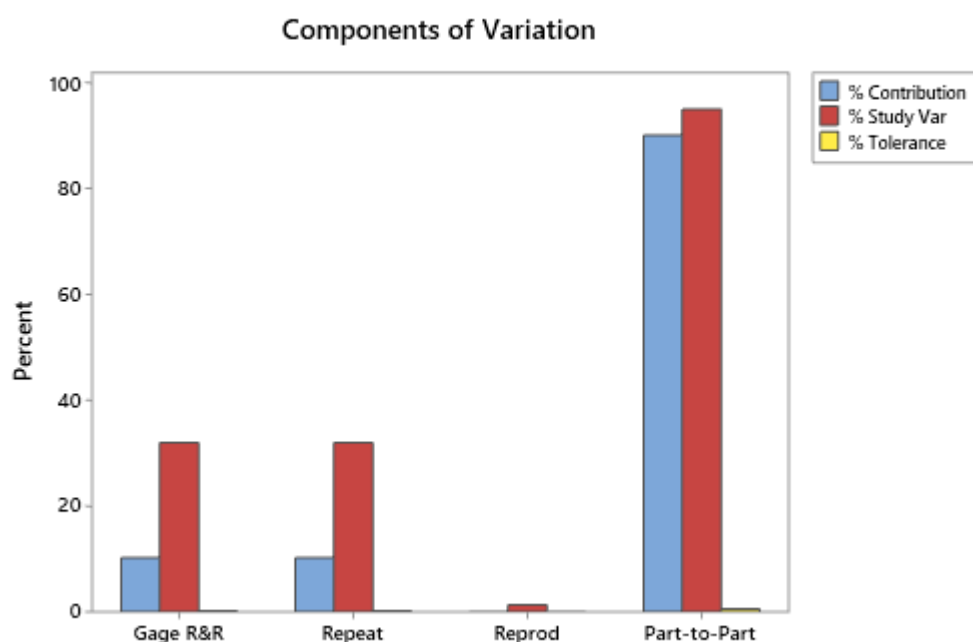
Figure 3-6 - Graph summarising the Gage R&R study showing the results for each of the components of variation.

Figure 3-6 showing the results summarising the Gage R&R study highlight the different sources of variation. The Total Gage R&R is the variation due to the measuring system including multiple operators using the same gage. Repeatability is the variability in measurements

obtained when the same part is measured multiple times by the same operator on the same machine.   Reproducibility is the variability in measurements obtained when the same part is measured by different operators but also on different machines, however, this study was only performed on one MTM and could be improved in the future through reproducing the results on a second machine. Part-to-Part is the variability in measurements across different parts.

The graph also separates these sources of variation into multiple bars; the contribution, study variation and the tolerance and are defined in equations (3-1), (3-2) and (3-3) (92).

$$Contribution\ \% = \frac{Component\ Variance}{Total\ Variance} \times 100 \qquad (3\text{-}1)$$

$$Study\ Variation\ \% = \frac{Component\ Study\ Variation}{Total\ Study\ Variation} \times 100 \qquad (3\text{-}2)$$

$$Tolerance\ \% = \frac{Study\ Variation}{Process\ Tolerance} \times 100 \qquad (3\text{-}3)$$

Hence, from this graph the largest variation is from the part to part. This is expected as there is a large variation in traction's coefficients measured at different speeds, temperatures and different lubricants and therefore, a lot of variation is expected (92).

Figure 3-7 and Figure 3-8 show the X bar and R charts for the Gage R & R study. The x axis cannot be read too well after listing all 192 data points; however, these charts are evaluating all the data points in the study. The X bar chart shows the mean average measurement on each part where the green line is the overall mean average for traction coefficient for both operators and the red control limits are based on the repeatability estimate and the number of measurements for each average. Due to measuring a range of traction coefficients in different regimes and temperatures, it is expected that this graph has a lot of data outside of the control limits (92).

Xbar Chart by Operators
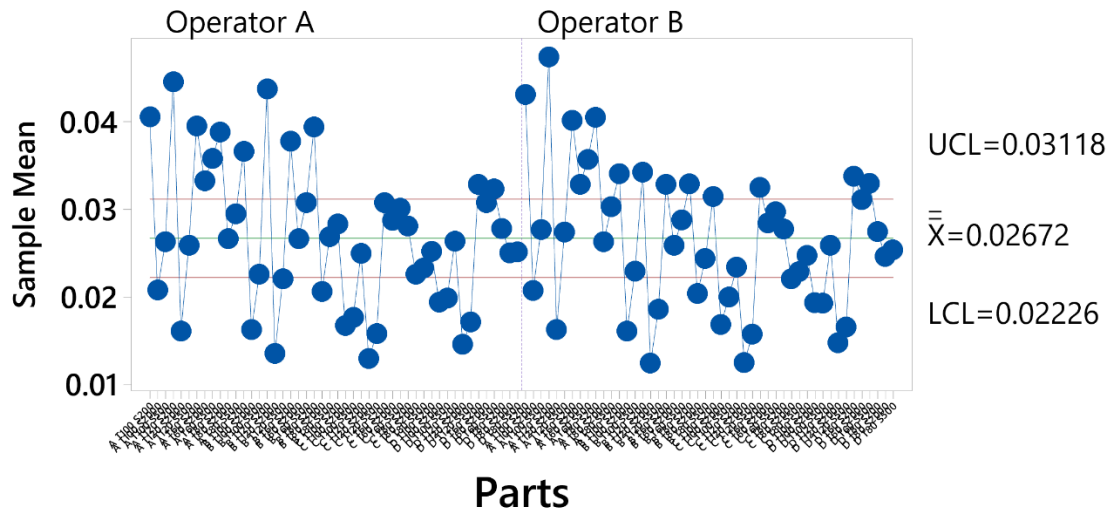
Figure 3-7 – Xbar chart from the Gage R&R Study.

R Chart by Operators
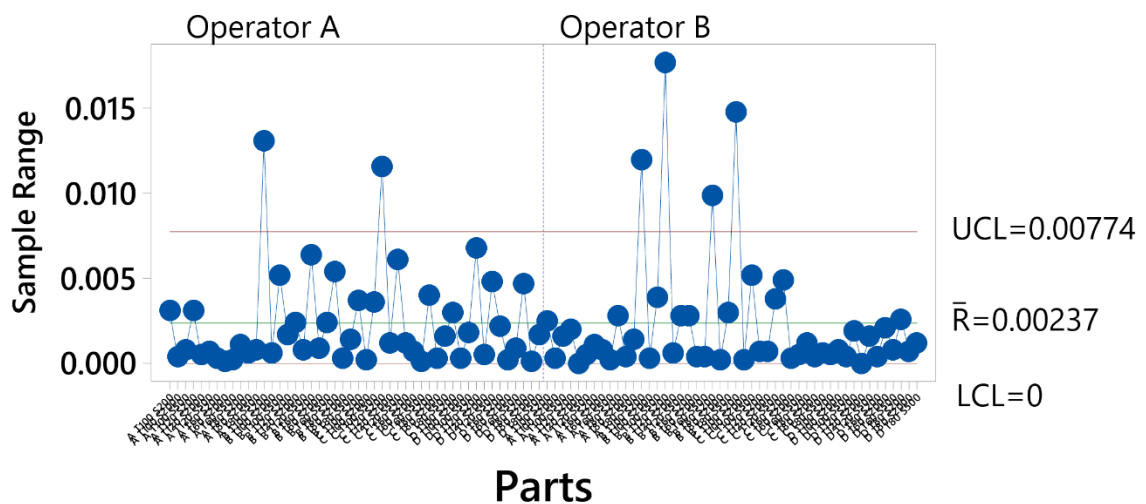
Figure 3-8 – R chart from the Gage R&R study.

The R chart represents the difference between the largest and smallest measurements on each part (traction coefficient) for each operator. The green line is the mean average of all the traction coefficient ranges for repeats and the red lines are the control limits which, represent the amount of variation expected for the repeat measurement ranges. These limits are calculated using the

63

variation within subgroups. Therefore, operator A is marginally more consistent with repeat results than operator B but both operators on the whole produce repeat results within the control limits (92).

Gage R&R (ANOVA) for Traction
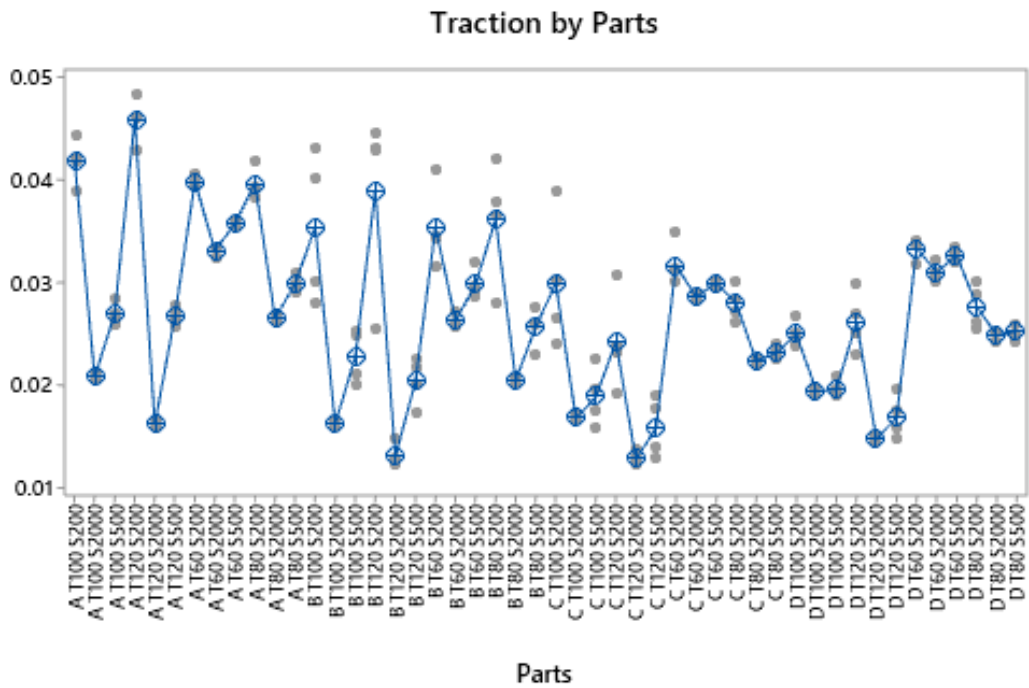
Figure 3-9 – Graph showing the scatter of repeat traction coefficient values for each part (grey) and the average (blue circle with a cross in it) for each part.

Figure 3-9 shows the scatter of repeat traction coefficient values for each part (grey) and the mean average (blue circle with a cross in it) for each part. The blue line connects the mean average measurements for each part. Ideally there would be very little variation between traction coefficient for repeats and whilst some points look like there is a lot of variation, the y-axis need to be considered showing there is very little variation between repeats (92).

Gage R&R (ANOVA) for Traction

Parts * Operators Interaction
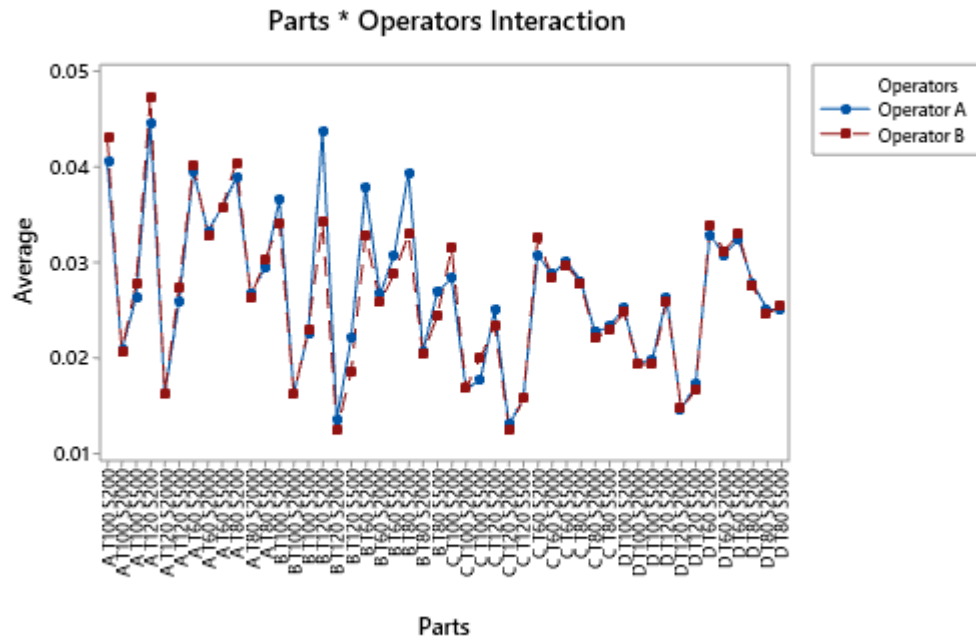
Figure 3-10 – Graph showing the difference in results between different operators.

Figure 3-10 shows the mean average of all the measurements in the study compared for both operators. Hence, it shows that there is very little variation between operators as the lines show the same pattern and the part average vary such that differences between parts are clear (92). Figure 3-11 shows a box plot for all of the measurements comparing each operator. It can be seen that the means (cross-circle symbol) are very similar for both as well as the median (centre line in the box), the upper and lower quartiles are similar (the top and bottom part of the boxes) and the upper and lower whiskers (the lines) are similar. The only difference is an outlier for operator B but as this it only one, this is not a concern as this is negligible due to the amount of other data points in the study (92).

Gage R&R (ANOVA) for Traction

Traction by Operators
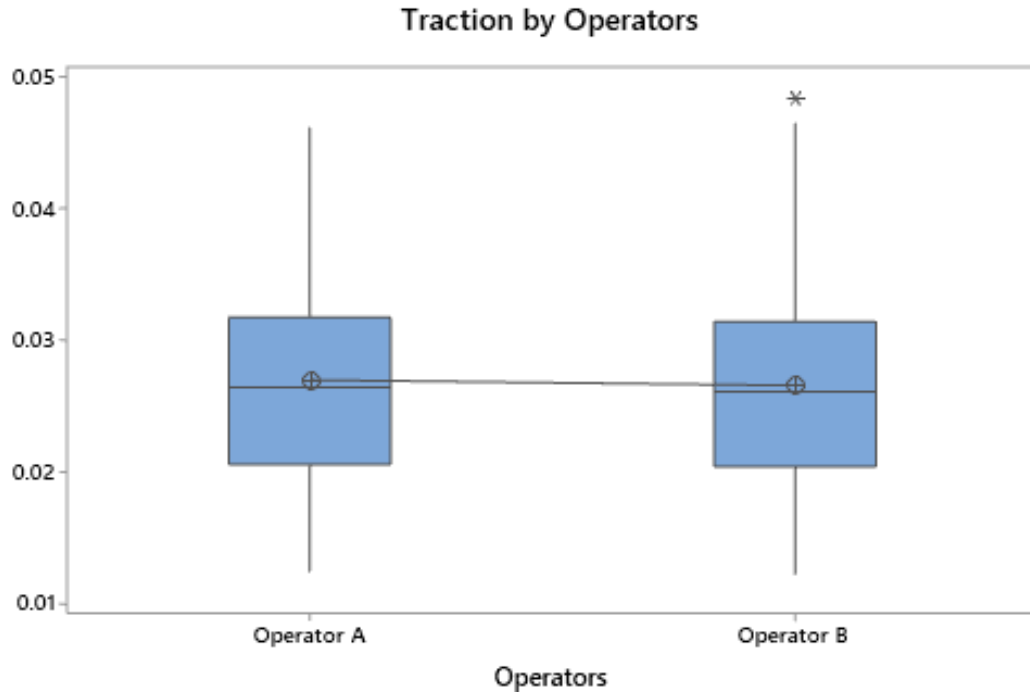
Figure 3-11 – Box plot of all of the traction coefficient measurements the study for each operator.

Overall is can be seen that the MTM is an instrument that produces repeatable and reproducible results as the gage R&R has shown very little variation between repeats and operator over the range of conditions that are used in the Stribeck analysis in this thesis. This study could be further improved by also comparing the results to another MTM to compare the results from different MTMs (92).

3.1.2 Mini Traction Machine with Spacer Layer Imaging

The boundary additive films produced by these lubricants were studied using an extension to the MTM called Spacer Layer IMaging (SLIM). SLIM uses optical interferometry to measure the thickness and topography of boundary additive films that form within the contact of the moving surfaces. These additives are essential in boundary lubricated conditions as they can

minimise wear, lower friction and ultimately prevent seizure by providing a low shear strength film which, is preferentially sheared rather than the material surface.

A schematic showing how the MTM-SLIM works can be seen in Figure 3-12.
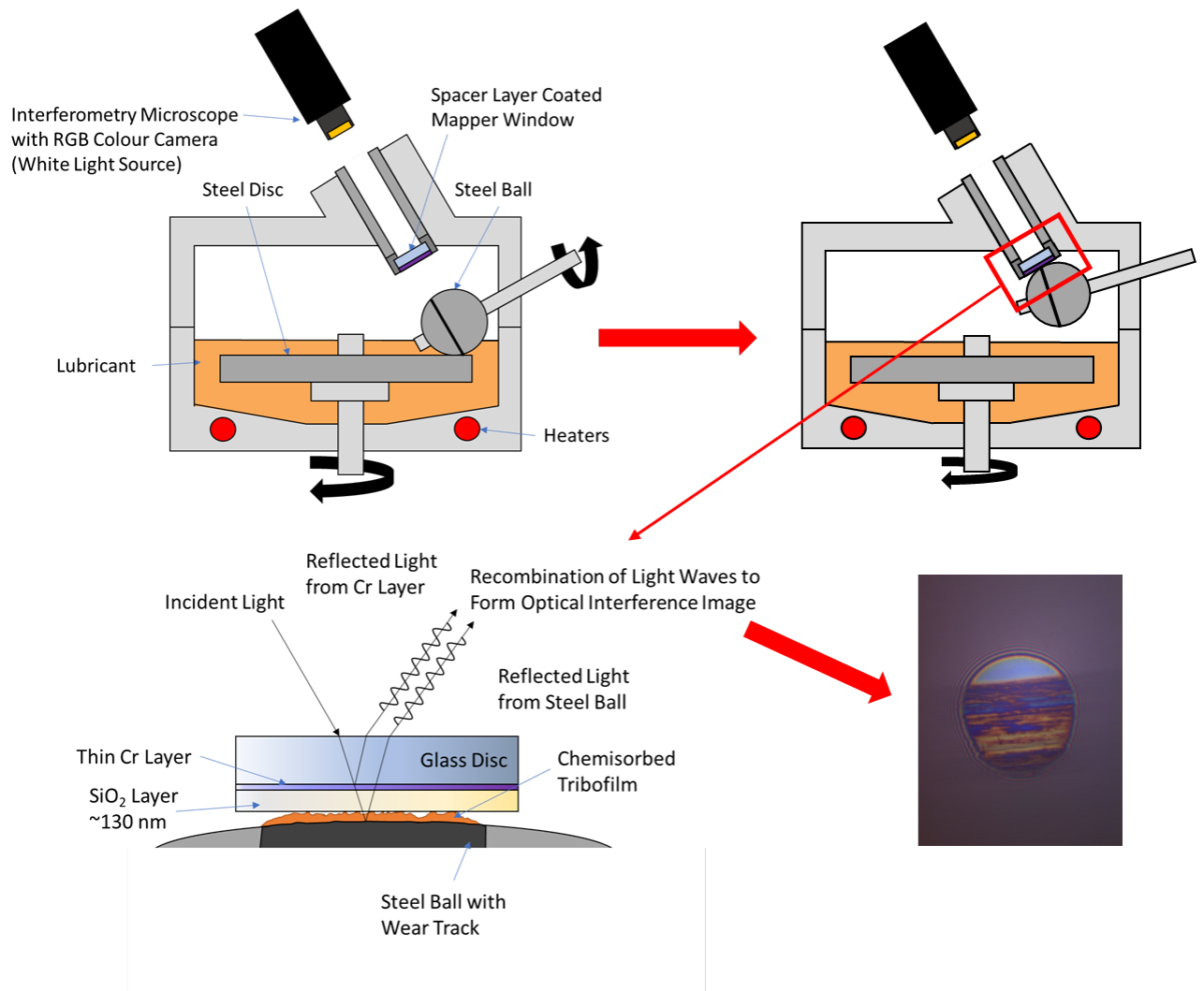
Figure 3-12 – Schematic demonstrating the functionality of the MTM-SLIM technique.

As shown in Figure 3-12, a lubricated wear test is conducted between the ball and disc specimen. After a defined wear test interval, the ball specimen periodically lifts off the disc and contacts the mapper window of the interferometric microscope with the wear track on the ball specimen. An interferometric image is then taken of the Hertzian contact which, produces an image where the colours can be interpreted as a tribofilm thickness using the film thickness/ colour calibration that is pre-set in the instrument.

There are other instruments that utilise similar SLIM technology to measure the lubricant film thickness in the EHD regime. However, in these experiments, this technique has been applied to a stationary ball to find the boundary additive thickness rather than the full fluid lubricant film separating the two moving surfaces.

Principle of Interferometry

The principle of interferometry is also described in Figure 3-12. The window (which, the ball contacts) is composed of a flat glass surface which, is coated with a thin semi-reflective chromium layer followed by a "spacer-layer" of transparent silicon dioxide of known thickness. Previous optical interferometry techniques were limited to a film thickness range of 80 nm to 1 μm as the minimum detectable thickness was related to the interference wavelength which, was 80 -130 nm. For polychromatic/ multi coloured interferometry, 130 nm is taken as the lower limit and the thickness resolution is 25-30 nm. In SLIM, the silica spacer layer augments the oil film and hence, removes the lower limit limitation (35,93,94). It does this by creating a larger difference between the recombined light waves and hence, the minimum wavelength can be overcome, and the thin film thickness deduced by deducting the known thickness of the silica layer from the thickness of the silica layer and the lubricant film. This is illustrated in Figure 3-12.

At the beginning of each test the spacer layer film thickness is measured to set the zero value for film thickness, and this is subsequently subtracted from the later film thickness measurements to determine the true film thickness. The steel ball is then loaded against the steel disc and rubbing is resumed under mixed rolling/sliding. The MTM-SLIM is fully computer-programmable, which, allows for monitoring film thickness and friction simultaneously via automated test protocols that control ball and disc speed, load, slide-roll ratio and test temperature.

Whilst the ball is reverse loaded onto the glass screen, light is directed through the glass onto the contact area. The light itself after it has passed through the glass, undergoes a division of amplitude with one beam being reflected directly back from the semi-reflective chromium layer and the other being reflected back from the steel surface after it has passed through the additive film. Therefore, the beam that is reflected from the steel surface will have travelled through two film thicknesses (through to the steel surface and then back through towards the camera). The two beams (light waves) will therefore, be out of phase and then they will recombine (interfere), and this can be constructive or destructive depending on how each light wave corresponds to the other (types of interference shown in Figure 3-13).
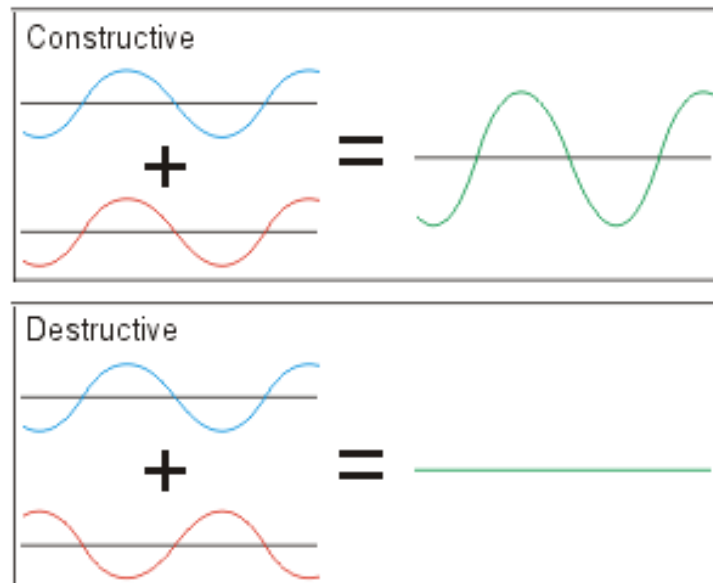
Figure 3-13 – Constructive and destructive interference of combining light waves (95).

Constructive and destructive interference can be described by equations (3-4) and (3-5) where h_{oil} is the spatial thickness of the oil anti-wear film (the optical film thickness divided by the oil refractive index, n), λ is the wavelength, θ is the angle of incidence of the beam (this is usually 0), Φ is any net change that occurs on reflection and N is the fringe order. Φ also known as the phase change, can be found by calibration from a static contact.

Constructive Interference:
$$h_{oil} = \frac{(N - \Phi)\lambda}{2n \cos \theta} \quad N = 0,1,2,\ldots \qquad (\,3\text{-}4\,)$$

Destructive Interference
$$h_{oil} = \frac{(N + 1/2 - \Phi)\lambda}{2n \cos \theta} \quad N = 0,1,2,\ldots \qquad (\,3\text{-}5\,)$$

SLIM produces an interference fringe pattern which, gives a detailed "map" of the surface separation over the contact area. With the spacer layer, additive film thicknesses can be measured accurately below 10 nm (31).

Anti-wear film thickness values are then calculated using equation (3-6) and as the interferometry operates under vertical illumination from a collimated light source (parallel light rays with low beam divergence), $\theta = 0\,°$ and therefore, cos $\theta = 1$.

$$h_{oil} = \frac{\left(N_{sp+oil} - \Phi\right)\lambda_{sp+oil} - (N_{sp} - \Phi)\lambda_{sp}}{2n_{oil} \cos \theta} \quad N = 0,1,2,\ldots \qquad (\,3\text{-}6\,)$$

It should also be noted that "sp + oil" indicates the value is for both the spacer layer and the oil anti-wear film whereas "sp" values refers to the spacer layer only.

The image is frame grabbed by a RGB colour camera and the red, green and blue colour pixel is converted to give a film thickness map across the surface of the contact (93,94).

Final Test Conditions

The same test specimens used in standard Mini Traction Machine tests were used for the SLIM experiments. It is necessary to use a superfinished ball specimen for the technique to work such that a smooth contact is made with the mapper window and so the tribofilm is easily distinguishable from the excessive wear that would prevail on a rougher ball specimen. The conditions used for the test are outlined in Table 3-4.

Table 3-4 – SLIM wear test conditions.

Parameter	Value
Load (N)	35
Contact Pressure* (GPa)	0.96
Contact area (mm^2)	0.056
Window Load (N)	20
Contact Pressure* (GPa)	0.51
Contact area (mm^2)	0.060
Wear test entrainment speed (mm/s)	35
Test Duration (h)	12
Temperature (°C)	100
SRR (%)	100
Stribeck Intervals	Every 2 hours

* Calculated using the Hertzian contact pressure calculation for a point contact.

The test consists of a series of constant speed and SRR wear steps, Stribeck curve steps (seven Stribeck curves in total per test) and interferometric imaging steps. This occurs in-situ without any rinsing or cooling of the ball as it has been shown that the action of the ball contacting the window squeezes out any residual oil leaving only the chemisorbed tribofilm (94). The wear test uses a fixed, slow entrainment speed of 35 mm s^{-1} to ensure that the test operates in the boundary to mixed lubrication regimes to ensure asperity contact, giving rise to the contact conditions necessary to initiate boundary film formation. The calculated lambda ratio for the constant wear test is approximately 0.11 for the lubricants with different types and concentrations of anti-wear additives, 0.106 for lubricant A and 0.062 for lubricant B (further information can be seen in the Test Lubricants section.

Prior to the start-up of each test, the test specimens were cleaned to remove their protective anti-corrosive coating which, is applied by the manufacturer for protection and preservation of the specimens. They were cleaned by consecutive immersion in an ultrasonic bath with acetone for 10 minutes and then for a further 10 minutes in petroleum ether. Each test was performed using fresh unworn specimens and at the end of the test the specimens were cleaned with petroleum ether in an ultrasonic bath for 10 minutes and then stored in a sealed plastic wallet to preserve the tribofilm build-up and thus allow further surface analysis to be performed.

As well as conducting wear tests at constant entrainment speeds and SRRs, Stribeck tests were also performed throughout the procedure. Seven Stribeck curves were recorded for each test which, allows the variation over time to be observed. The conditions for the Stribeck curve (constant SRR and varying entrainment speed) are shown in Table 3-5. The Stribeck curves will follow the lambda curves shown in Figure 3-29 and Figure 3-30.

Table 3-5 - Conditions used for Stribeck analysis

Parameter	Value
Applied Load (N)	35
Contact Pressure (GPa)	0.96
Slide-to-Roll Ratio (SRR)	50
Entrainment Speed (mm/s)	0 – 3000
Temperature (°C)	100

The films were measured using the SLIM film thickness software on the MTM PC that enables selection of a specific area on each SLIM image to deduce the anti-wear film as shown in Figure 3-14. A mean average is taken on each image by selecting three circular areas; a circular area of an appropriate radius will measure the RGB values of every pixel to give a single RGB value that will correspond to a specific film thickness in the pre-set calibration file.

Figure 3-14 – Illustration demonstrating how specific areas of the SLIM image were selected using the SLIM film thickness software to measure the film thickness.

Development of Test Conditions

As mentioned previously, appropriate test conditions were needed to visually produce a tribofilm visible on the interferometry images with a measurable thickness. Therefore, as shown in many other papers using the SLIM to explore mostly ZDDP films and some other additives, boundary regime conditions were used to generate the tribofilm films as they require harsh conditions to initiate their formation. The role of "Mechanochemistry" has been discussed by Spikes (96) which, refers to how mechanical forces can promote chemical reactions (96). Whilst previously it was believed that high contact stress via normal pressure and high temperatures were needed for ZDDP tribofilm formation, Zhang and Spikes (37) showed that is ZDDP tribofilm formation was in fact driven by purely stress. This was shown by monitoring the formation of a ZDDP tribofilm under EHD conditions where a tribofilm formed even in the absence of asperity contact using a high friction traction fluid which, produced high shear stress in the EHD regime. This test was also compared with ZDDP in PAO and no film was observed in the EHD regime (37,96).

Therefore, high friction and therefore, high shear stress is necessary into initiate tribofilm formation. Aviation base oils and lubricants typically have relatively low friction in the EHD regime and therefore, boundary conditions were chosen to supply the high friction for tribofilm formation.

This was done using a slow entrainment speed but with a high SRR along with other representative PGB conditions. Shimizu and Spikes (97) showed that under mixed-sliding and rolling, tribofilm formation forms at a similar rate over a wide range of SRRs as long as pure sliding is avoided which, results in excessive damage.

It was necessary to use smooth superfinished specimens (R_a <0.02) for the MTM SLIM test as the ball specimen needs a smooth surface to contact the mapper window to produce a perfectly

circular Hertzian contact with the window such that minimal wear is produced. It is important to minimise the wear on the ball in these tests such that wear is not mistaken for an anti-wear film. Table 3-6 shows how wear can be misinterpreted as an anti-wear film due to the dark colour produced which, correspond to a high film thickness in the calibration file. The test with the base oil and no anti-wear additives gives a very worn and pitted surface and this can be seen in the SLIM image as well. The SLIM image looks elongated and dark patches can be seen showing that the wear depth could be confused for tribofilm thickness. This is due to the worn surface being rough and uneven which, therefore, prevents full contact with the mapper window. However, the SLIM image for the ZDDP and base oil maintains the circular Hertzian contact and no wear features have transferred onto the SLIM image which, would affect the thickness measurement. Tribofilms can be rough and patchy, but usually on a smaller scale (nm) as long as the circular Hertzian contact is maintained on the mapper window, it can be assumed there is minimal wear and the differential colours are due to tribofilm.

Initially, shorter tests and faster entrainment speeds were used but this resulted in little to no visible TCP tribofilm being produced as shown in Figure 3-15. This may infer that there is little to no protection of the steel surfaces in the engine under these conditions, but as there is no wear (as shown in Table 3-6), the additives are still providing enough protection to prevent excessive wear. Therefore, longer tests with slower entrainment speeds were used to move further into the boundary regime and allow more time for thicker ashless tribofilm formation. A lower load was also used to as it was postulated that higher loads may be shearing off the tribofilm.
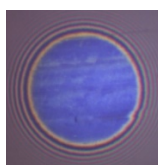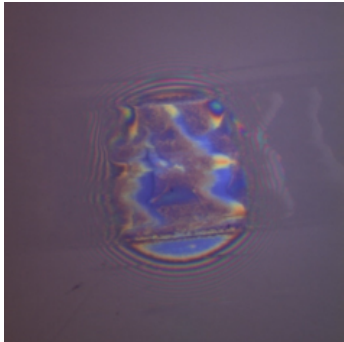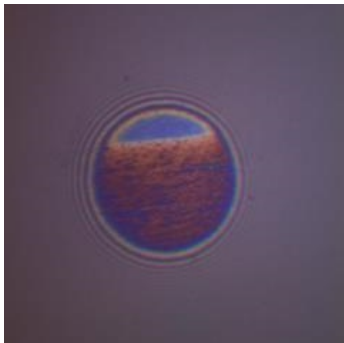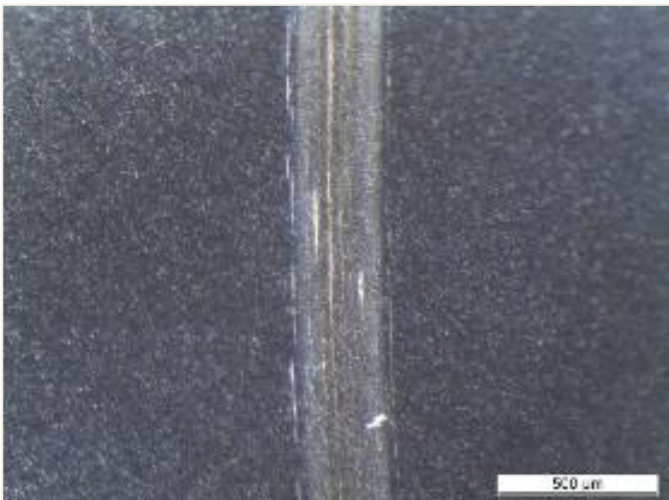
Figure 3-15 – SLIM image with TCP and Base Oil at 100 m s^{-1}, 50 % SRR, 100 °C, 50 N, over 5 hours.

Table 3-6 – Table demonstrating how wear can be misinterpreted as wear through comparing a test with base oil and test with ZDDP and Base oil comparing both the SLIM image and ball optical wear track image.

	SLIM Image and Measured Film Thickness	Optical Microscope Image
Base Oil		
ZDDP + Base Oil		

Error Analysis

As the SLIM technique is an addition to the MTM, the Error Analysis for the MTM in section 3.1.1 also applies to the friction results for these tests. However, the measurement of the film thickness is another source of error, one potential being the refractive index. The refractive index was pre-set to 1.60 for all SLIM measurements to convert the measured film thickness from the SLIM measurement into an absolute film thickness. The optical properties of various tribofilms have been explored including some zinc phosphate glasses such zinc methaphosphate

75

(n = 1.5) and zinc orthophosphate (n = 1.65) (38,98). As this thesis also explores zinc free ashless anti-wear additives, using a single refractive index value will introduce error into the calculation of true film thickness. However, is has been shown that for most transparent materials, the refractive indices are spread across a relatively narrow range of ~1.4 to ~1.8. Therefore, despite the refractive index being more accurate for zinc phosphate glass tribofilm (from ZDDP), using this for ashless tribofilm should not introduce an error in excess of approximately 15%. Previous studies by Fujita et al. found this error was less than the experimental scatter of different methods of measuring very thin tribofilms (99). Also, as mentioned earlier, the ambiguity in determining whether a colour is due to wear or tribofilm could be another potential source of error.

However, despite the issues in the accuracy of the film thickness measurements, the SLIM technique is useful for detecting tribofilm formation, monitoring the progression of its formation with rubbing time and also providing an indication of potential tribofilm morphology (38).

Another method of measuring the thickness of ZDDP tribofilms was completed by Rydel et al (100). In which, an Atomic Force Microscope (AFM) was used measure the thickness of a ZDDP tribofilm on the surface of an MTM disc wear track. This was done by measuring the surface profile using the AFM, then chemically removing the tribofilm using EthyleneDiamineTetraacetic Acid (EDTA) and oxalic acid and then remeasuring the same profile thus allowing deduction of the thickness through the height difference. Nanoindentation was used to mark either side of the wear track to ensure the profile was measured in the same place after the tribofilm had been removed. This technique could potentially be applied to ashless tribofilm but could prove more difficult as the film tends to be thinner. However, this technique does avoid the need to know the films refractive index to accurately calculate the tribofilm (36,100,101).

3.1.3 Micropitting Rig

Micropitting experiments were completed using a Micropitting Rig (MPR) developed by PCS instruments. The MPR (shown in Figure 3-16) is a rolling contact fatigue rig that measures friction under a range of sliding and rolling conditions under lubrication. The contact geometry incorporates a central roller surrounded by three counter-face rings spaced 120 ° apart. Equal loads are applied at each of the three contact points and the contact geometries are line contacts. The load is applied via a stepper motor driven ball-screw which, transfers the load via the load beam to the top counter-face ring. Both the disc and roller specimens are driven by independent electric motors which, enables a range of SRR to be achieved and the assembly is dip lubricated from a temperature-controlled oil sump which, allows a smaller quantity of oil to be used for each test.
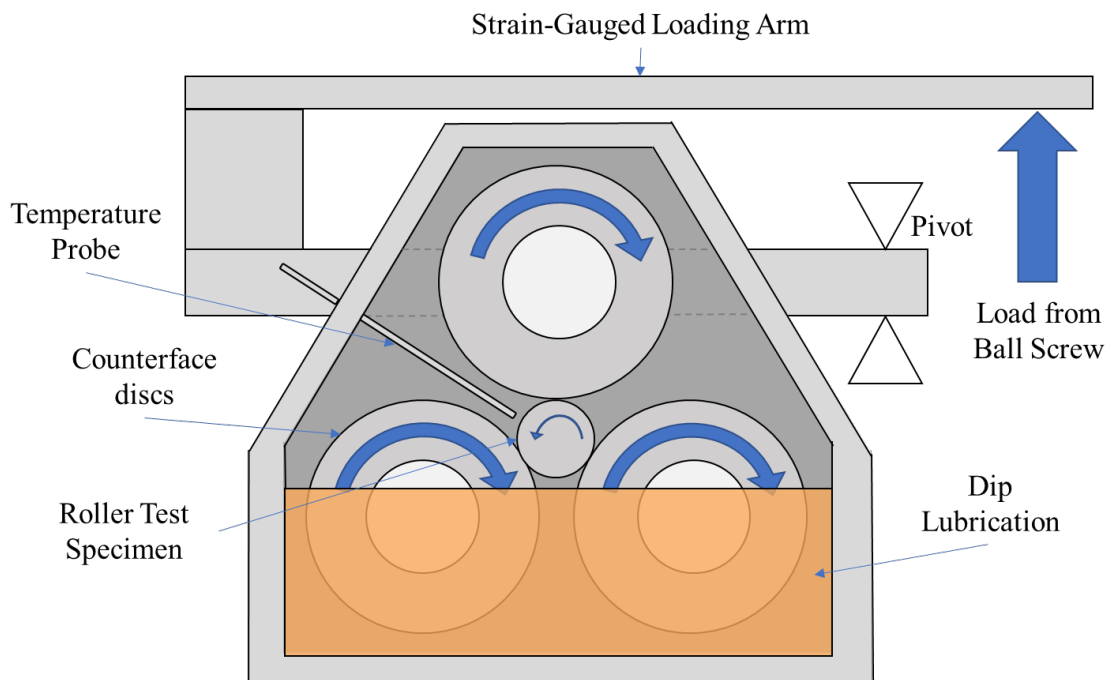
Figure 3-16 – Diagram illustrating the layout of the MPR showing how the rings and roller rotate and how the load is exerted on the roller specimen.

This rig can be used to assess lubricant performance by simulating lifetime wear and allows observation of micropitting progression. In particular the MPR focuses on micropitting by

having the roller specimen rotate slower than the conunterface rings and the roller specimen is also softer and smoother than the counterface rigs. As a result, micropitting damage is directed onto the roller specimen. This rig allows the central roller to be taken out in between tests to enable observation and measurements of the roller to be acquired. Having three rings in contact with the roller allows accelerated testing due to the use of the three rings tripling the amount of contact cycles within a certain time.

The load, the rotational speed of the rollers and rings, the lubricant temperature and the SRR can be controlled. A variety of outputs are measured such as the acceleration signal (essentially a measure of vibration), the friction/ traction coefficient, the wear and the torque.   The specifications of the rig can be seen in Table 3-7.

Table 3-7 – Table listing the specifications of the MPR.

Parameter	Value
Maximum Load	1250 N
Maximum Speed	4 m / s (depending on slide roll ratio)
Slide Roll Ratio	0 % (pure rolling) to +/- 200 % (pure sliding)
Maximum Temperature	135 °C
Maximum Roller Torque	20 Nm (total of all 3 contacts)

Final Test Conditions

Again, it should be noted that the exact conditions in used in the PGB cannot be disclosed for Intellectual Property (IP) reasons, but are considered representative of a line contact within the meshing of the gears in that environment. Test conditions were chosen to evaluate lubricant performance under representative PGB conditions but also used boundary regime to promote micropitting formation and initiate boundary additive reactions with the surface. This test procedure was completed two or three times for each lubricant candidate depending on the availability of specific steels manufactured specifically for this testing.

The conditions are representative worst-case conditions expected during operation of the PGB. However, due to the range of speeds, temperatures and variation in the meshing of the gear

teeth during different parts of the engine cycle, the gears will undergo a range of tribological environments. A gear tooth typically experiences a range of SRR throughout the process of the gear teeth meshing together due to certain in contact points rolling over one another and other points sliding across the opposing surface. The test followed a series of constant speed wear steps shown in Table 3-8 and the conditions are shown in Table 3-9. A series of wear steps allows intermittent observation of the central roller using optical microscopy and an oil change was done after the first step to remove any initial wear metal generated from running in the specimens to prevent other wear mechanisms not caused directly by the oil formulation. Previous studies have shown that wear debris can lead to other surface-initiated fatigue mechanisms and third body abrasive wear in the EHD and boundary regimes. Sayles and Macpherson (102) found a sevenfold increase in L_{10} bearing life and a result of changing the filter size from 40 μm to 3 μm. L_{10} bearing life is the number of cycles that a 90% group of apparently identical bearings will complete prior to the initiation of fatigue and therefore, 10 % of the bearings are not expected to achieve the L_{10} life. Presence of more larger debris was found to lead to debris indentations on the contacting surfaces and which, create new fatigue initiation sites (102). Nikas et al. (22) also showed that wear debris can also be responsible for scuffing caused by agglomeration of wear debris in the inlet of the EHD contact area and localised melting as a result of the heat created from friction of sliding wear debris (103).

Table 3-8 - The steps in the MPR test describing when the oil is changed and the duration of each step.

Step	Oil	Number of Contact Cycles	Time of Step (Hr:min:sec)
1	Fresh Oil	73000	00:05:07
1'	No change	Stribeck Curve	n/a
2	Change Oil	440000	00:30:48
3	No Change	880000	01:01:35
4	No Change	1320000	01:32:23
5	No Change	1760000	02:03:11
6	No Change	2200000	02:33:58
7	No Change	2640000	03:04:46
8	No Change	3080000	03:35:34
9	No Change	3520000	04:06:21
10	No Change	3960000	04:37:09
11	No Change	4400000	05:07:57
11'	No Change	Stribeck Curve	n/a

Table 3-9 – Table showing the MPR test conditions.

Parameter	Value
Load	165 N
Contact Pressure	1.1 GPa
SRR	10 %
Entrainment Speed	3.15 m/s
Average PGB Bulk Oil Temperature	100 °C

Using the Hertzian contact pressure calculation for a line contact, it was calculated that a load of 165 N is required to achieve a contact pressure of 1.1 GPa. Using the Dowson-Higginson calculation for film thickness, it was calculated that the test has a minimum lubricant film thickness of ~52 nm for lubricant A and hence, the test has a lambda ratio of ~0.13 and ~31 nm and 0.05 for lubricant B. Again, lubricant C can be assumed to be like lubricant A due to having a similar viscosity and lubricant D will have a higher lambda ratio due to having a higher viscosity. This shows that the test operates in the boundary regime meaning the lubricant film thickness is insufficient to prevent asperity contact (5,74).

80

It should also be noted that for this calculation, the accuracy was improved by using Jaegers theory of moving hotspots to calculate the inlet temperature between the ring and roller and then the Walther equation (used in ASTM D341) was used to calculate the exact viscosity in the contact by accounting for this temperature increase in the contact (104,105). These equations can be seen in Appendix 4. Stribeck curves were also completed at the beginning and end of the test again to look for changes due to differences in the specimens due to wear and due to changes in the lubricant. The Stribeck curves also used the same conditions shown in Table 3-9 except the entrainment speed was varied from 0 m/s to 3.5 m/s. Tests have shown that the base oils tested are Newtonian up to shear rates of 200 s^{-1} due to the measurement limitation of the cone and plate rheometer ejecting the low viscosity fluid samples due to centrifugal forces at high shear rates. It is assumed that these base oils are all Newtonian in the EHD regime as well as shown by Moore (1997) (81).

Development of Test Conditions

It was necessary to develop a set of test conditions that were representative of expected PGB conditions but also allowed comparison of different lubricants. Whilst it is understood that the contact geometry of the MPR contact is different to a gear contact, the MPR can be used to replicate a specific contact line at a specific point between the meshing of gear teeth. In comparison to the MTM which, was described earlier, the MPR has a line contact in comparison to the point contact between the MTM ball and disc. The main implication this has is that it becomes more difficult to reach the EHD regime due to having a larger contact area and therefore, a large entrainment speed would be required to reach EHD. However, boundary conditions are preferred for these tests to understand whether different lubricants can protect surfaces under the harshest operational conditions and to provide the conditions needed to initiate boundary additive action.

Testing began using representative worst case PGB conditions, but this results in rapid excessive wear which, made distinguishing wear features produced by different lubricants difficult. Therefore, the SRR was reduced to 10 % as shown in Table 3-9. Previous studies have discussed the influence of SRR on micropitting and found that micropitting is accelerated when the SRR is increased as the contact experiences an increased number of contact cycles (106,107). The entrainment speed, load and temperature were kept constant as the reduction of the SRR was sufficient enough to enable lubricant comparison whilst keeping the conditions representative to the PGB. It is understood that throughout the gear meshing cycle of actual gears, a range of positive and negative SRR are achieved. However, one SRR and the other fixed test parameters were chosen to enable lubricant formulation comparison and to allow micropitting to progress in a monitorable way under relatively representative conditions. This limitation is understood and taken into account in the interpretation of the results.

Error Analysis

Each MPR test was repeated three times in order to take a mean average and standard deviation but for certain tests, only two repeats could be completely due to the number of available test specimens.

To evaluate the repeatability and reproducibility of the MPR, a small round robin was conducted between another MPR and our MPR. These are labelled MPR A and B respectively in the following results. Both MPRs followed the procedure set out in the MPR Final Test Conditions section and the tests were evaluated of the wear produced (visual analysis using optical microscopy), mass loss, track width increase/ roller radius, friction measurement and ring roughness measurement.

The results for the track width increase can be seen in Figure 3-17. The rate of track width increase for both MPRs is very similar showing that both MPRs were reporting a similar rate

of wear. However, MPR B has a larger track width than MPR A, but this is due to both MPRs using different methods to measure the width increase and therefore, this is a difference in how each technique decides where the wear track begins and ends. MPR A used a tactile profilometer to measure the track width as specified in 3.1.6 Talysurf section whereas MPR B uses the optical microscope specified in 3.1.4 Optical Microscopy. Therefore, the results are comparable as the rate of track width increase is very similar.

Figure 3-18 shows the overall mean average friction comparison for each step for each MPR. This shows that there is a significant difference in friction coefficient of 0.3-0.4. This same difference was also seen in the Stribeck curves in Figure 3-19.

Figure 3-20 shows the difference in ring roughness measurement between both MPRs. MPR B only has initial and final mean average ring roughness as the roughness could not be measured on site and therefore, could only be measured before and after the test. However, both test houses show a similar smoothening of the ring specimen for all tests.

Therefore, the only data that deviated between MPRs was the friction data. Further investigation revealed that MPR A was using an older version of the MPR that gave lower traction coefficient value and this was rectified when a test was performed on a latest model of the MPR (MPR B was also the latest model). Therefore, the MPR was shown to be repeatable and reproducible.
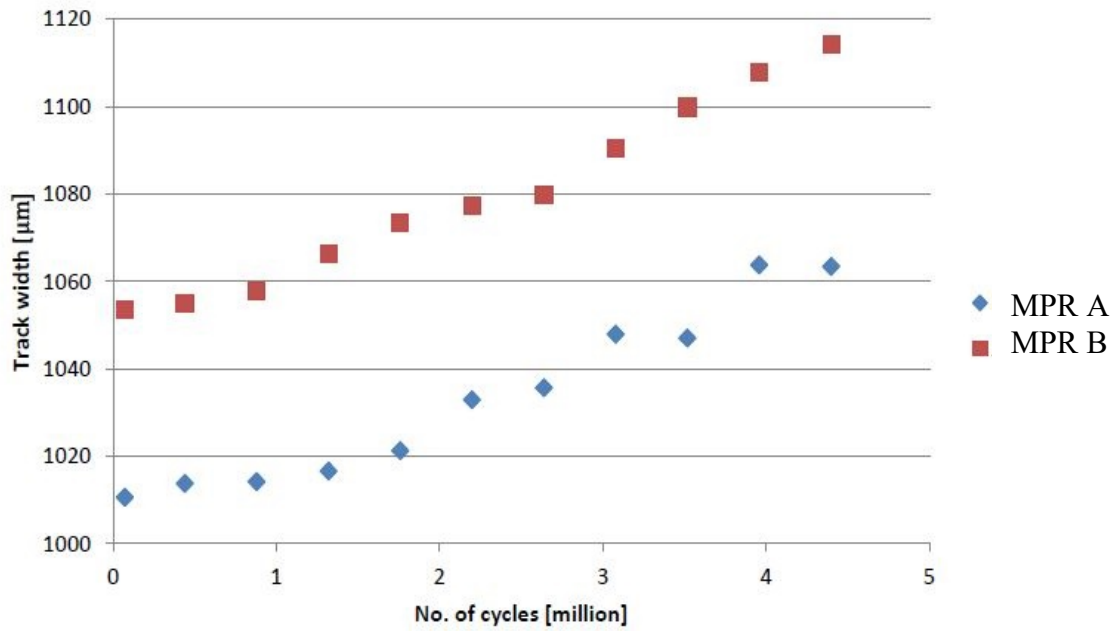
Figure 3-17 - Graph comparing the results of the MPR Round Robin results showing the difference in mean average track width increase of the MPR roller between two different MPRs.
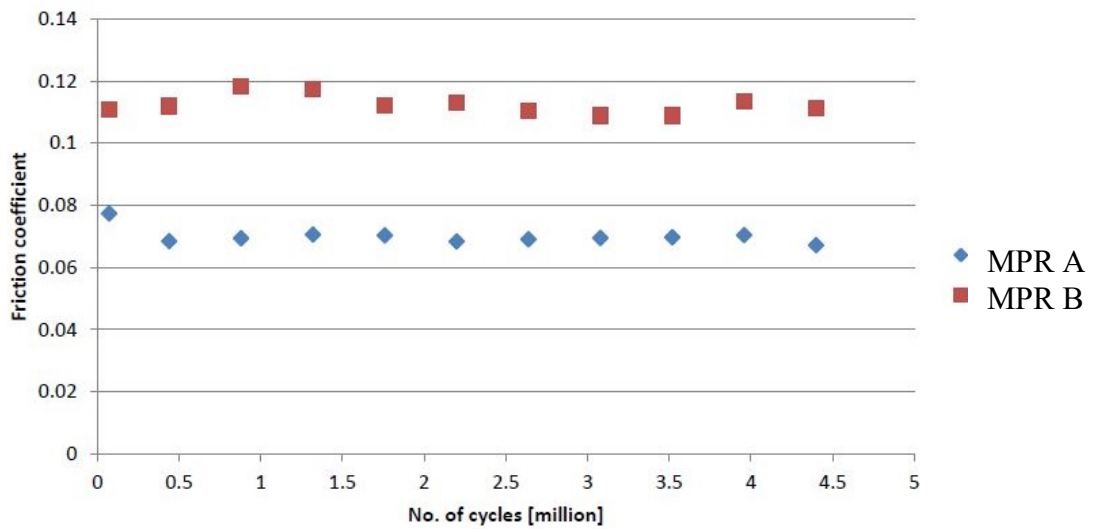
Figure 3-18 - Graph comparing the results of the MPR Round Robin results showing the difference in overall friction between two different MPRs.

a.
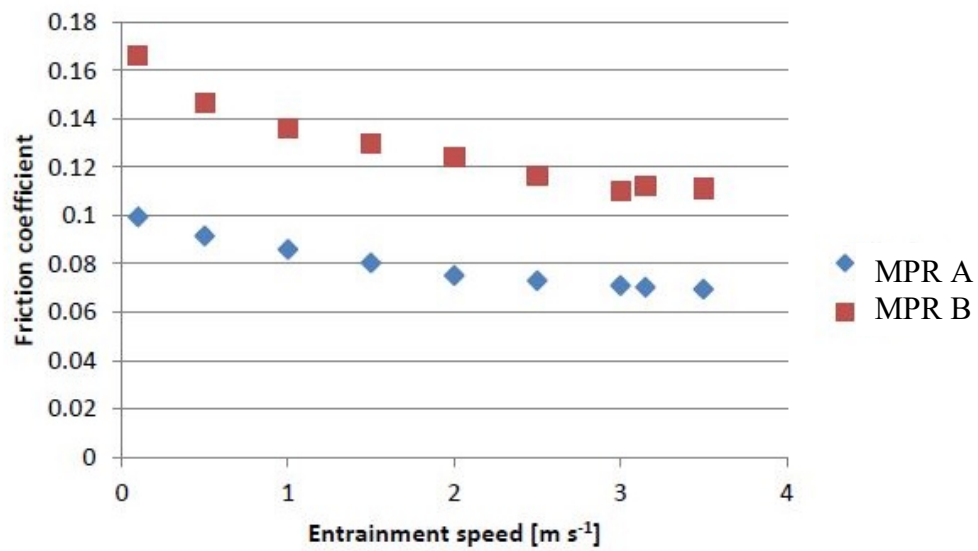
b.
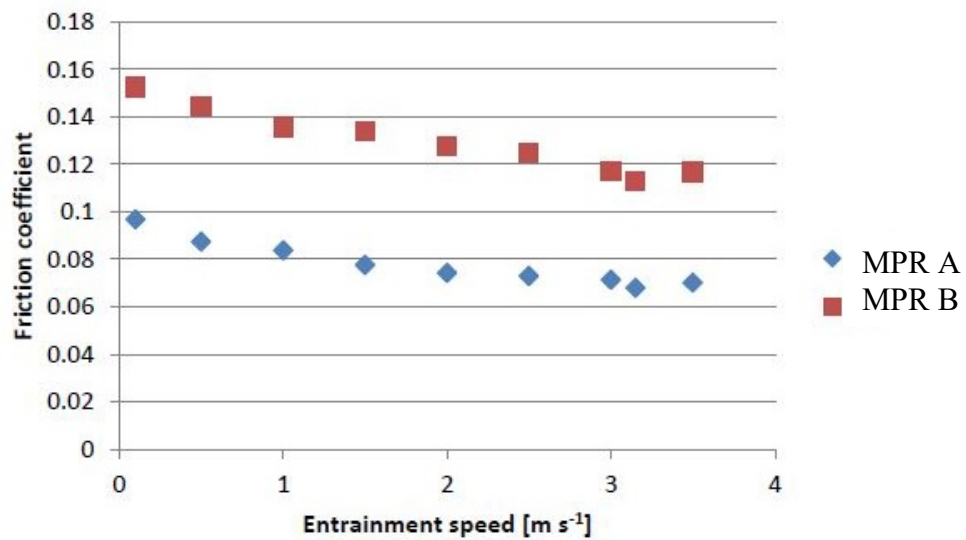
Figure 3-19 - Graph comparing the results of the MPR Round Robin results Stribeck curves after the first (**a.**) and last (**b.**)

step for the two different MPRs.

a.
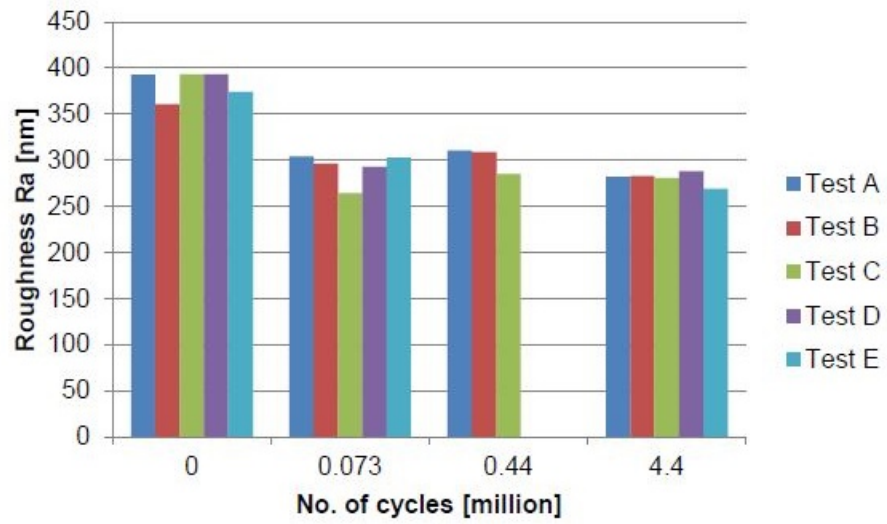
b.
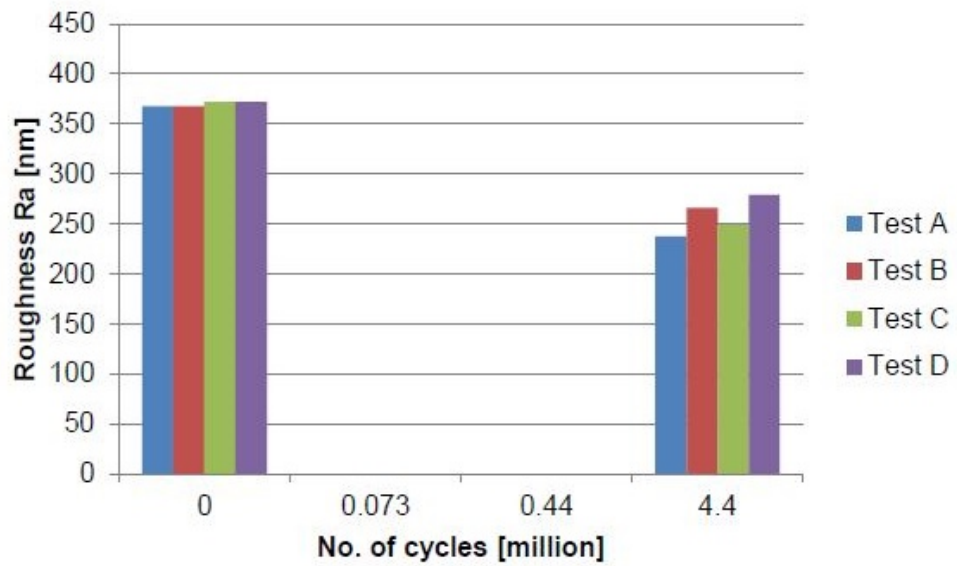
Figure 3-20 - Graph comparing the results of the MPR Round Robin results showing the difference in average MPR ring

roughness for the two different MPRs; MPR A (**a.**) and MPR B (**b.**).

3.1.4 Optical Microscopy

As it can be seen from Figure 3-21, the roller has a chamfer at either side of the wear track and as a result, wear causes an increase in wear track width and this can be monitored after each step by capturing an image using an optical microscope.
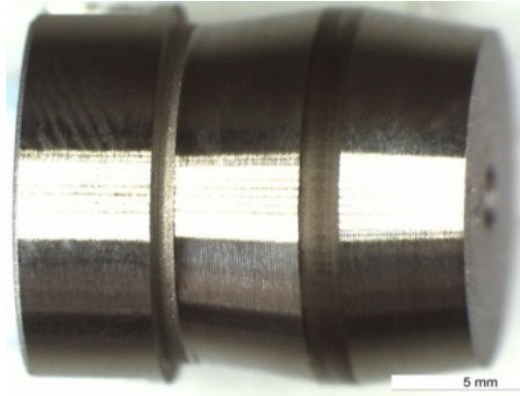
Figure 3-21 – An optical microscope image of a used MPR roller showing the wear track around the circumference of the roller.

Images of the roller specimens are taken using a Leica MZ75 optical microscope produced by Meyer instruments and then computer software called Image Access was used to measure the width of the wear track on images of the specimens. The precision of this measurement at a magnification level of ×50 (the magnification at which, the wear track widths were measured) has a 95% confidence interval of ± 4 µm due to limitations in the optical resolution at high magnification.

It should be noted that some other MPR studies monitor radius loss instead of track width increase. The geometry of the chamfered roller mean that an increase in track width also results in an increase in radius loss and both of these directly correlate (17).

3.1.5 Mass Loss Measurement

The mass of the roller specimens was measured using a Mettler Toledo XP205 analytic balance. The uncertainty of measurement for the mass balance is ± 0.000320 g.

3.1.6 Talysurf

Roughness measurements on MPR Specimens were performed using a Form Talysurf Series 2 made by Taylor-Hobson which, measures roughness by detecting the deflection of a pin which, is being rastered across a surface. Wear tracks on both the roller and rings were measured in four places and a mean average was taken. The cut-off wavelength was 0.25 mm, data length was 3 mm and the filter was Gaussian.

3.1.7 X-Ray Photoelectron Spectroscopy

X-Ray Photoelectron Spectroscopy (XPS) analyses were performed on a ThermoFisher Scientific Instruments (East Grinstead, UK) K-Alpha$^+$ spectrometer. XPS spectra were acquired using a monochromated Al Kα X-ray source (hν = 1486.6 eV). An X-ray spot of ~400 μm radius was employed. Survey spectra were acquired employing a Pass Energy of 200 eV. High resolution, core level spectra for all elements were acquired with a Pass Energy of 50 eV. All spectra were charge referenced against the C1s peak at 285 eV to correct for charging effects during acquisition. Quantitative surface chemical analyses were calculated from the high resolution, core level spectra following the removal of a non-linear (Shirley) background. The manufacturers Avantage software was used which, incorporates the appropriate sensitivity factors and corrects for the electron energy analyser transmission function.

Also, the depth of analysis is ~5-6 nm and only one X-ray spot was measured on each wear track and on each body of each specimen.

3.1.8 Image Analysis with ImageJ

To quantify the amount of micropitting on the surface of the MPR roller specimens, a method was developed using the image analysis freeware ImageJ. This can be seen in Figure 3-22.
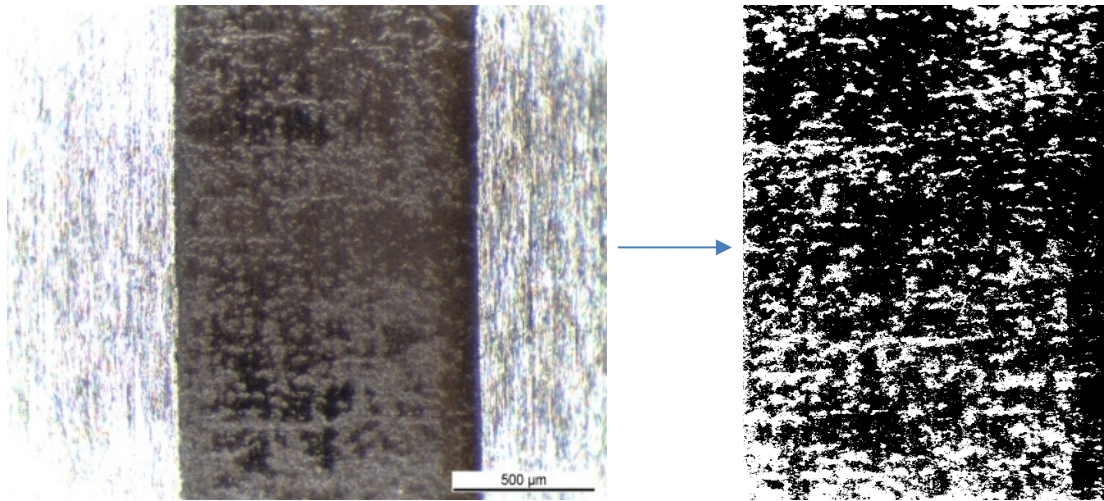
Figure 3-22 – Image showing how an optical microscope image was converted to allow quantification of micropitting.

This method involved converting the optical microscope image to the greyscale, cropping the image leaving just the wear track and then applying a binary threshold. Particle analysis can then be applied to count the amount of micropits which, have been converted into white areas and a percentage micropitted area was also deduced.

3.2   Materials

3.2.1   Wear Specimens

MTM Specimens

Specifications of the MTM test specimens are shown in Table 3-10, both of which, showed minimal wear throughout the Stribeck tests.

Table 3-10– Specification of test specimens.

Property	MTM Standard Disc	MTM Drilled Ball
Dimensions (diameter)	46 mm	¾" (19.05 mm)
Material	AISI 52100	AISI 52100
Surface Finish, R_a	<0.01 μm	<0.02 μm
Hardness, H_v	720-780	800-920

Despite not using MTM specimens made of the proposed PGB gear steels, boundary additives are designed to function with iron and therefore, it is assumed they will perform similarly with PCS standard specimens.

MPR Specimens

The specification of the standard PCS test specimens can be seen in Table 3-11. Two sets of different MPR test specimens have been used to compare two different steel candidates for the PGB, MSRR 6010 and Pyrowear 53 (P53). The specifications of the MSRR 6010 and P53 test specimens used in the test are shown Table 3-12 and Table 3-13 respectively. It should be noted that typically, roller specimens are designed to be softer and smoother than the ring specimens to concentrate the damage onto the roller specimen. However, despite the roller specimens being slightly softer and smoother than the ring specimens for the gear steel specimens, standard specimens usually have a larger differential hardness and roughness, therefore, this is considered during interpretation of these results and before comparison to the MPR results shown in Chapter 5.

Table 3-11 - Table listing the specifications of the Standard PCS 16MnCr5 test specimens.

Property	MPR Roller	MPR Ring
Dimensions (diameter)	12 mm cylinder	54.15 mm
Material	16MnCr5	16MnCr5
Surface Finish, Ra	~0.1 μm	~0.4 μm
Hardness	709 HV (58.8 HRC)	784 HV (61.9 HRC)

Table 3-12 - Table listing the specifications of the MSRR 6010 test specimens.

Property	MPR Roller	MPR Ring
Dimensions (diameter)	12 mm cylinder	54.15 mm
Material	MSRR 6010 Steel	MSRR 6010 Steel
Surface Finish, Ra	~0.1 μm	~0.4 μm
Hardness	804 HV (62.7 HRC)	816 HV (63.1 HRC)

Table 3-13 – Table listing the specifications of the P53 test specimens.

Property	MPR Roller	MPR Ring
Dimensions (diameter)	12 mm cylinder	54.15 mm
Material	P53 Steel	P53 Steel
Surface Finish, Ra	~0.1 μm	~0.3 μm
Hardness	753 HV (60.6 HRC)	770 HV (61.3 HRC)

3.2.2 Test Lubricants

Oils for Aviation Base Oil Evaluation

Varied Chain Length and Number of Ester Groups Base Oils

A variety of group V base oils were acquired of known chemical composition and molecular structure with no additives. The five pure base oils can be seen in Figure 3-23.
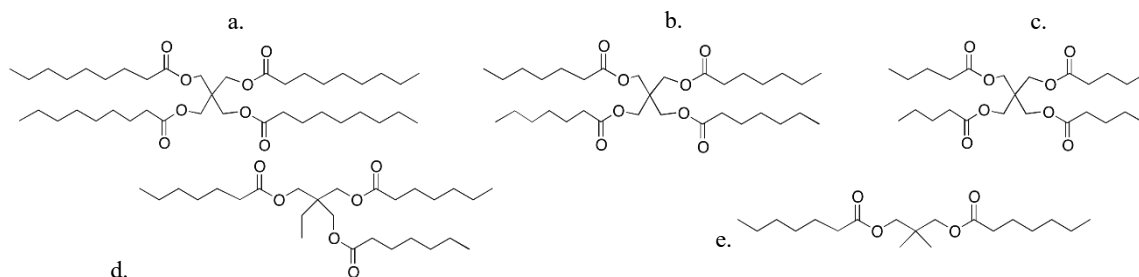
Figure 3-23 - Molecular structure of the base oils tested. a. polyol ester made from pentaerythritol with chains of n-C9 (MONOPE C9), b. polyol ester made from pentaerythritol with chains of n-C7 (MONOPE C7), c. polyol ester made from pentaerythritol with chains of n-C5 (MONOPE C5), d. polyol made from trimethylol propyl with chains of n-C7 (TMP C7) and e. polyol ester made neopentyl glycol with chains of n-C7 (NPG C7).

The base oils represent esters typically seen in aerospace lubricants and have representative chain lengths. The two parameters considered are the chain length of the substituent end groups on the esters and the amount of ester groups on the molecule. The chain lengths of the pentaerythritol base oils vary by increments of two carbons. These variations were selected as they were readily available from the supplier.

Extra data for these base oils both measured and calculated can be seen in Appendix 3. The base oils tested are Newtonian up to shear rates of 200 s^{-1} due to the measurement limitation of the cone and plate rheometer ejecting the low viscosity fluid samples due to centrifugal forces at high shear rates. It is assumed that these base oils are all Newtonian in the EHD regime as well as shown by *Moore 1997* (Appendix 7) (81).

Varied Degree of Branching Base Oils

More group V base oils of known chemical composition and molecular structure were acquired that had a varied degree of molecular branching and contained no additives. The molecular structure of these base oils can be seen in Figure 3-24. This was done by synthesising polyol pentaerythritol esters with different ratios of straight and branched acids to vary the amount of branching in the final lubricant formulation. The acids used were octanoic acid (NC8) for the linear chains and 2-ethyl hexanoic acid (EH) for the branched chains. However, it is difficult

to direct esterification at a specific alcohol group on a pentaerythritol. Therefore, whilst base oils **g.**, **h.** and **i.** are most likely structures, each of these base oils will be a mixture of other combinations depending on the available alcohols during esterification reaction. However, due to controlling the ratios of the alcohol reactants, the total ratio of linear to branched chains will still be the percentages stated.
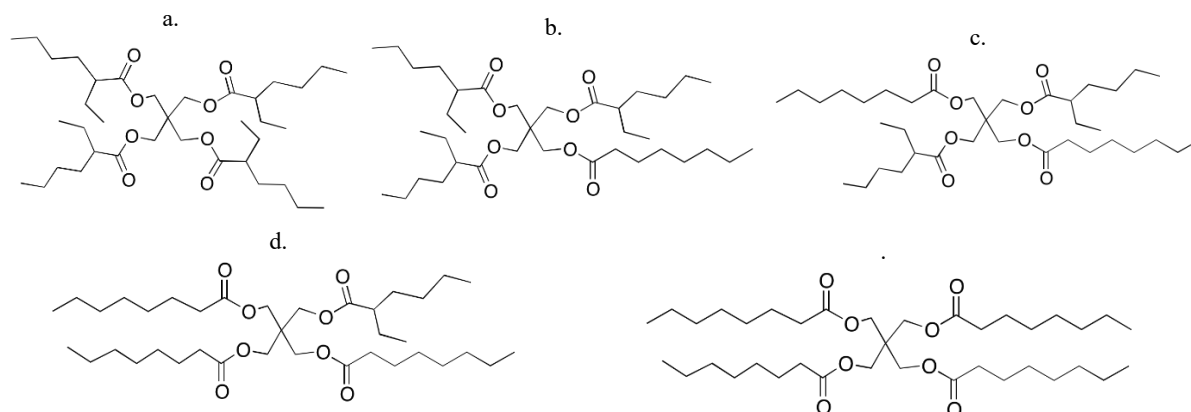

Figure 3-24 - Molecular structure of the base oils used to observe the tribological effect of molecular branching, a. polyol ester made from pentaerythritol with chains of all EH, b. polyol ester made from pentaerythritol with 25 % chains being NC8 and 75% of chains being EH (NC8 EH 25 75), c. polyol ester made from pentaerythritol with a 50:50 ratio of EH and NC8 chains (NC8 EH 50 50), d. polyol ester made from pentaerythritol with 75 % chains being NC8 and 25% of chains being EH (NC8 EH 75 25) and e. polyol ester made from pentaerythritol with chains of all NC8 chains (NC8).

Fully formulated pure base oil blends

Fully formulated lubricants based on commercially available aviation lubricants were acquired which, all contain the same additive package but have different amounts and types of group V base oils (A, B, C and D) to alter their viscosity.

The base oils used contain varying amounts of different polyol esters to vary the viscosity; they differ in the proportion of base oils with a different number of ester groups (Figure 3-25). Typically, the alkyl chain branching is 2-ethylhexyl but there may be some low level of iso C9 branching.
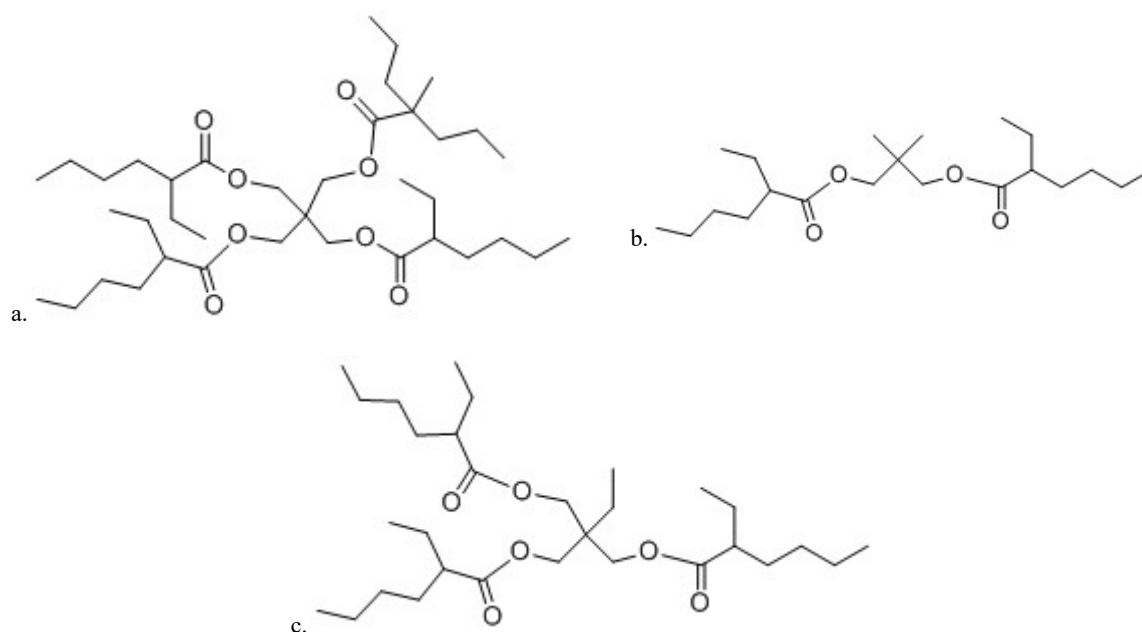
Figure 3-25 – Molecular structure of the base oils used in the formulated oils tested. a. polyol ester made from pentaerythritol with chains of 2-ethylhexyl and some iso C9, b. polyol ester derived from neopentyl glycol with side chains of 2-ethylhexyl and c. polyol ester derived from trimethylol propane with side chains of 2-ethylhexyl.

The High viscosity oils (made from base oil D) are predominantly pentaerythritol based (4a) and the Low viscosity oils (from base oil A) are mostly neopentyl glycol (4b) based but also contain some trimethylol-propane-based ester (4c).

Both Medium viscosity oils (made from base oils B, C and D) are a blend of polyol esters (pentaerythritol and neopentyl glycol) with the Medium High containing more pentaerythritol esters and less neopentyl glycol ester esters than Medium Low. Exact formulation details of oils are unavailable. The composition of each formulated lubricant tested in terms of additives and base oil can be seen in Table 3-14.

Table 3-14 – Table showing oil compositions.

	Oil A (v/v %)	Oil B (v/v %)	Oil C (v/v %)	Oil D (v/v (%)	Additives (v/v %)	Kinematic Viscosity @ 100°C (cSt)
High	-	-	-	94.8	5.2	8.0
Medium High	-	-	28.0	66.8	5.2	6.9
Medium Low	-	10.0	84.8	-	5.2	5.0
Low	94.8	-	-	-	5.2	3.1

Test Lubrication Regimes

94

Using the supplied pressure-viscosity coefficients, the fluid film thickness and therefore, lambda ratio, the lubrication regimes can be estimated for each oil over the range of speeds seen in the Stribeck test. The equations used to calculate the contact pressure, film thickness and the lambda ratio can be seen in section 2.3.4 and 2.3.5. These calculations utilised the data provided by the manufacturer to calculate the dynamic viscosity at each test temperature to give a more accurate estimate of the film thickness and therefore, the lambda ratio.

As shown in the Appendix 3, all of these oils have different viscosity and will therefore, have different lambda ratios at different speeds. Therefore, a plot of Hersey number vs. lambda ratio, seen in Figure 3-26 for the lowest viscosity base oil NPG C7 and the base oil, will reach higher lambda ratios and lower Hersey numbers at the same test temperature. It can be seen that NPG C7 base oil does not reach the EHD regime with the conditions used and it can also be seen when lambda ratio is plotted against the Hersey number, the curves overlap as Hersey number normalises for viscosity. Therefore, whilst previous studies have only compared the effect of base oil structure on EHD friction, the results presented in this thesis observe the effect of the molecular structure across a range of lubrication regimes as not all the oils will reach the EHD regime. This is due to certain fluids requiring higher entrainment speeds to reach the EHD regime which, cannot be reached with the current test conditions. However, the results across the range of conditions seen in this study give an insight into the behaviour of different base oils on friction.
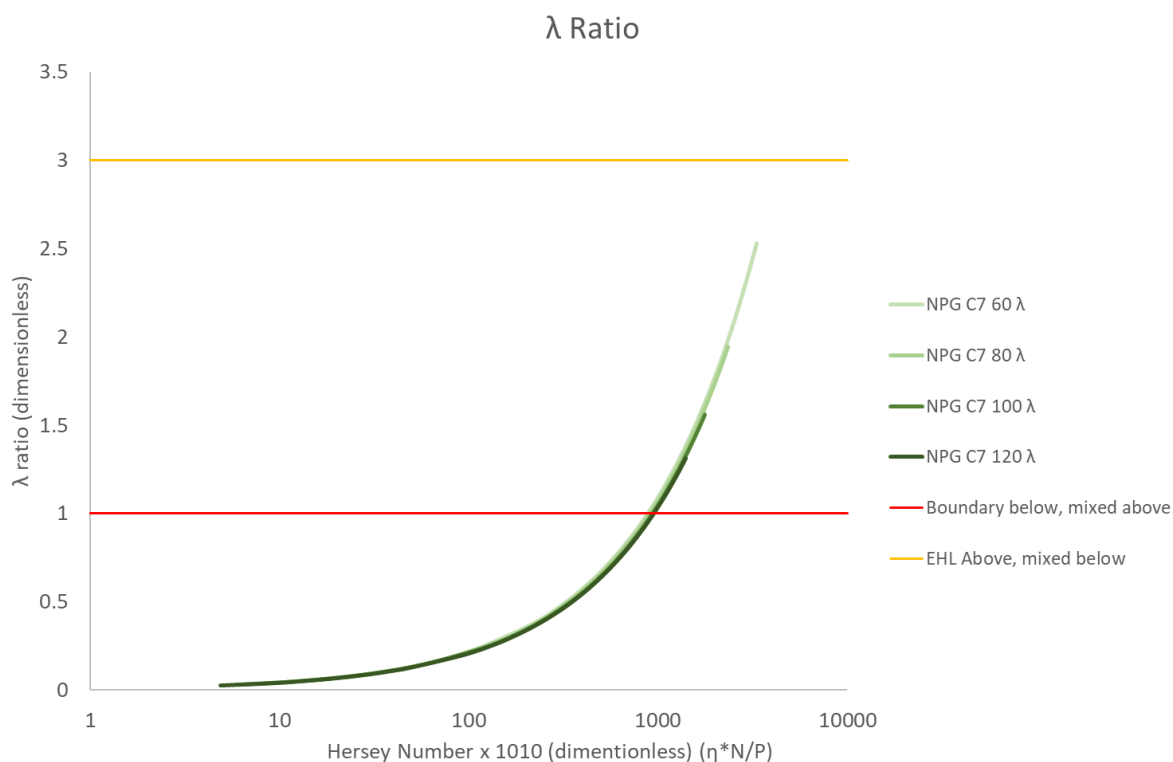
Figure 3-26 – Lambda ratio against the Hersey number for the NPG C7 base oil showing that it does not reach the EHD at any test temperature for the test conditions used.

Anti-wear Additives with Base Oil

To investigate the effect of anti-wear additives on wear and friction, formulations were acquired with different anti-wear additives over a range of concentrations in a standard base oil package used in a commercially available aviation lubricant. Three different anti-wear additives were tested; Zinc Dialkyl Dithio Phosphate (ZDDP), TriCresyl Phosphate (TCP) and another ashless phosphorus-based additive called "Additive X" (the details cannot be shared as it is commercially sensitive). The molecular structures of ZDDP and TCP can be seen in Figure 3-27. A summary of the test oils can be seen in Table 3-15 showing the concentrations of the produced test solutions.
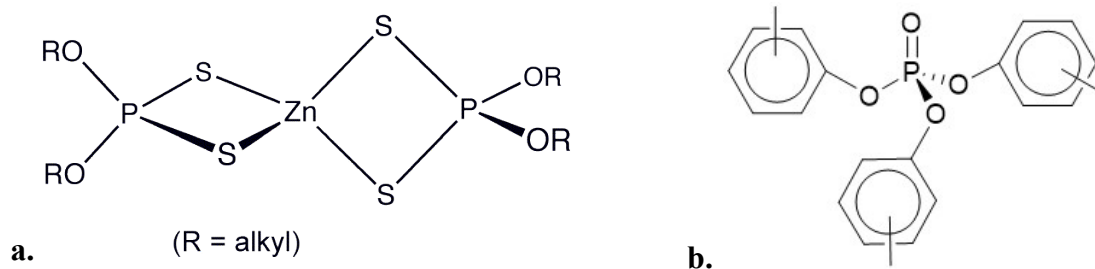
Figure 3-27 – Anti-wear additives; **a**. ZDDP and **b**. TCP.

Table 3-15 – Table showing the test blends with different concentrations of different anti-wear additives.

Oils for Anti-wear Additive Study
Pure Base oil
800 ppm P (TCP) + Base oil
2000 ppm P (TCP) + Base oil
4200 ppm P (TCP) + Base oil
800 ppm P (X) + Base oil
2000 ppm P (X) + Base oil
4200 ppm P (X) + Base oil
800 ppm P (ZDDP) + Base oil
2000 ppm P (ZDDP) + Base oil

Test Lubrication Regimes

Using the supplied pressure-viscosity coefficients, the fluid film thickness and therefore, lambda ratio, the lubrication regimes can be estimated for each oil over the range of speeds seen in the Stribeck test. These calculations utilised the data provided by the manufacturer to calculate the dynamic viscosity at each test temperature to give a more accurate estimate of the film thickness and therefore, the lambda ratio. Hence, from Figure 3-28 it can be seen from the plot of lambda ratio against the entrainment speed these formulations will reach the EHD regime with the conditions used. It should be noted that all the formulations in Table 3-15 are expected to have similar pressure-viscosity coefficients and viscosities, as they all have the same base oil package which, dominates the viscometric behaviour due to it being the bulk

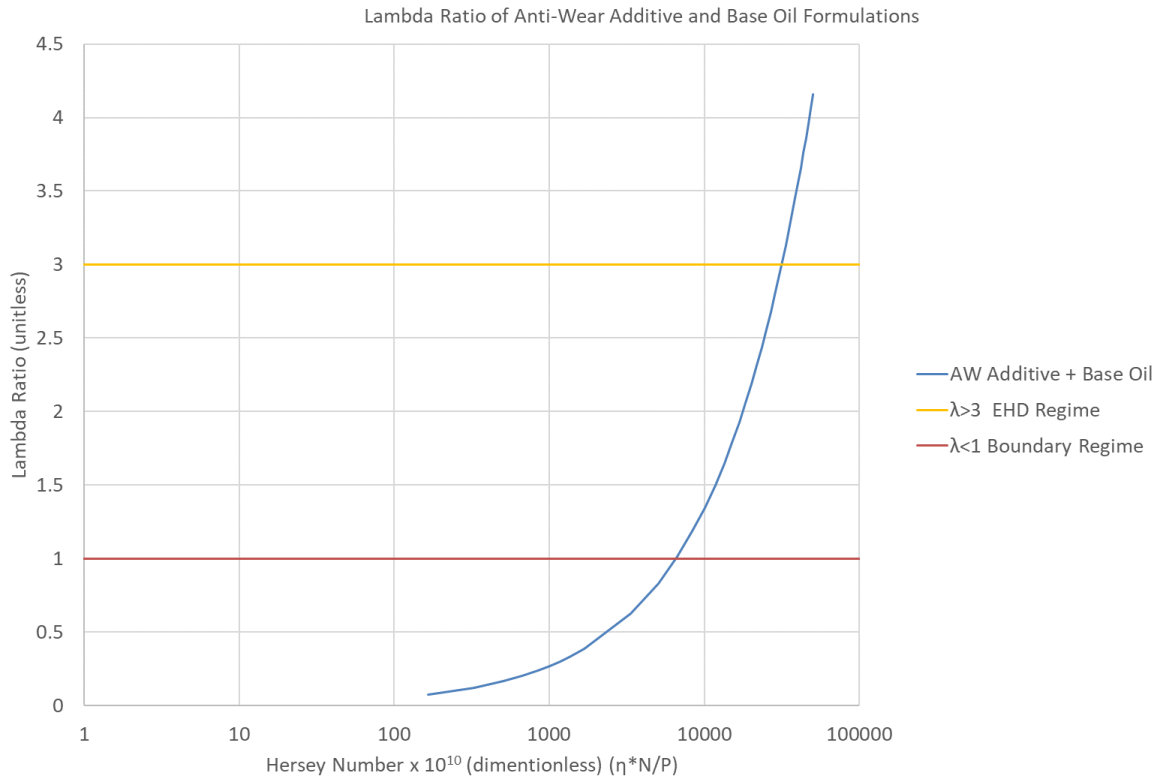component of each formulation. The extra data used to calculate these can be seen in the Appendix.

Figure 3-28 – Lambda ratio against the entrainment speed for the anti-wear additive and base oil formulations.

Commercially Available Full Formulation Lubricants

Most of the lubricants tested are gas turbine lubricants, but one is a helicopter gear oil, as shown in Table 3-16. The table shows a list of the lubricants tested, their kinematic viscosities at 100 °C and the specification and classification of their current approval. Table 3-17 also details some base oil information about the full formulated lubricants.

Table 3-16 – Table listing the different lubricants tested with their kinematic viscosities at 100 °C and their corresponding specification and classification.

Lubricant	Kinematic Viscosity (cSt @100 °C)	Specification and Classification	Description
A	5.220	SAE AS5780 HPC	A HPC which, has higher thermal capabilities than SPC lubricants due to better antioxidants, but this usually compromises tribological performance.
B	3.173	MIL PRF 7808 Grade 3	Lower viscosity APU oil with the same AW additive as Lubricant A. Expected to enable improved efficiency with a lower viscosity but compromised thermal and tribological capabilities.
C	5.208	MIL PRF 85734 EP	An EP oil that contains extra load carrying additives as well as AW additives for improved tribological performance but poorer thermal capabilities.
D	8.806	AIR STANDARD ACS 4035	Higher viscosity gear oil that has a range of AW and EP additives for better tribological performance but poorer thermal capabilities than the other turbine oils tested.

Table 3-17– Table showing the base oil packages in the test lubricants.

Lubricant	**Base oil package**
A	• Pentaerythritol with chains of C5-C10.
B	• NPG & TMP esters (C5-C10 straight chain acid). • Neopentyl glycol dipelargonate.
C	• MONOPE and DIPE esters.
D	• TMP polyol ester (but has chains made with high molecular weight acids used to give a higher kinematic viscosity).

Lubrication Regimes of Lubricant Candidates under Proposed Test Conditions

The lubrication regimes with the proposed test conditions for lubricants A and B were deduced from calculation of the lambda ratio using the physical properties of the lubricants, the test specimens and the chosen test conditions. Plots of the Hersey Number versus lambda ratio can be seen in Figure 3-29 and Figure 3-30.

Figure 3-29 and Figure 3-30 show that not all the Stribeck curves will reach the EHD regime as the increase in temperature results in a decrease in viscosity thus showing that at high speeds, there will be insufficient fluid film thickness to completely separate opposing asperities. It can be seen that as lubricant B is a lower viscosity oil than lubricant A, it does not reach the EHD in the 100 °C test as well as the 120 °C test. Despite not having the PVC data for lubricants C and D, it can be assumed that lubricant C will behave similarly to lubricant A and as lubricant D is the most viscous oil, it would potentially reach the EHD even at the highest test temperature.
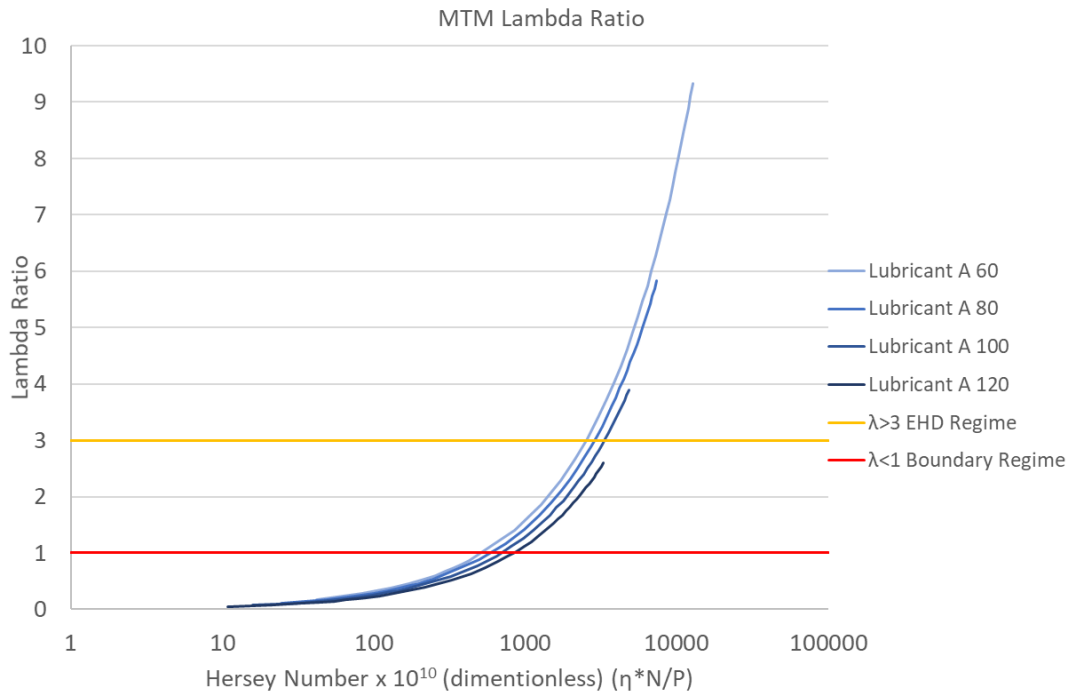
Figure 3-29 – Graph showing the lambda ratios against the Hersey number for lubricant A under the chosen test conditions at the range of test temperature used. The graph also displays, the boundaries for the lubrication regimes (7).
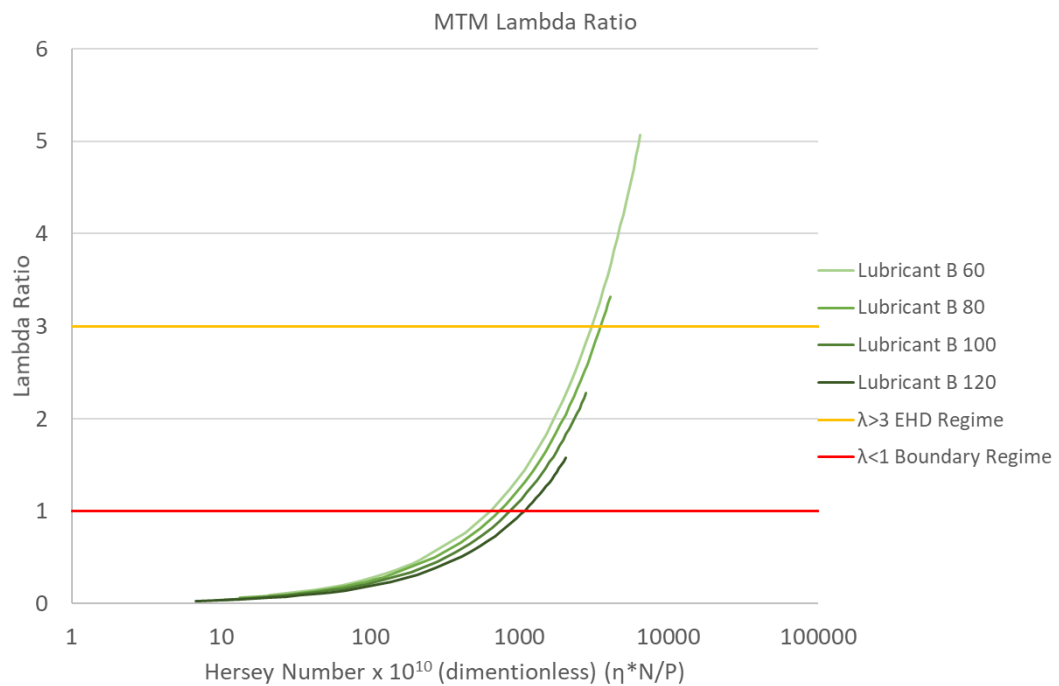

Figure 3-30 - Graph showing the lambda ratios for lubricant B under the chosen test conditions at the range of test temperature used. The graph also displays, the boundaries for the lubrication regimes (7).

Chapter 4.   The Effect of Gas Turbine Lubricant Base Oil Molecular Structure on Friction[1]

4.1 Introduction

The formulation of a lubricant requires a careful balance of different chemistries to tailor it to a specific environment thus ensuring optimal performance. Whilst there are many requirements in which, additives are needed to boost capability, the largest proportion of the formulation of a gas turbine lubricant is the base oil; approximately 95% of the total formulation. Hence, the base oil governs most of the physical characteristics of the lubricant and is the focus of this chapter.

In most mechanical systems, low friction is desired to improve machine efficiency and limit component wear. It has been highlighted in many industries that frictional losses are a major source of energy loss and by understanding the tribology, changes can be implemented to conserve energy and therefore, improve efficiency (108). This is especially relevant within a gas turbine oil system where it is vital that the oil lubricates the many different components such as bearings and gears to ensure component life but also to decrease friction and therefore, optimise the efficiency of the engine.

As discussed later in section 4.2, modern aviation base oils have advanced from crude oil derived mineral oils to entirely synthetic group V polyol base oils due to the need for lubricant with better temperature stability. This is due to the rise in oil system temperatures with the advancement in gas turbine technology. Whilst offering improved thermal stability, they

---

[1]The work presented in this chapter have been published in the following journal publication, cited as: Airey, J., Spencer, M., Greenwood R.W, Simmons, M.J.H. The effect of gas turbine lubricant base oil molecular structure on friction, Tribology International, https://doi.org/10.1016/j.triboint.2019.106052. Also in Appendix Appendix 1.

require supplementing with additives to improve oxidative stability further as well as improving other load carrying capabilities.

This chapter explores how the molecular chemistry of polyol base oils can greatly influence friction therefore, demonstrating the importance in furthering understanding on how to optimise base oils for engine efficiency.

4.2   Base Oil Literature Review

Lubricant base oils are categorized by the American Petroleum institute (API) and are used in many lubricant specifications worldwide (109). The base oil categories are:

- Group I – Mineral oil-based containing <90 % saturates and/ or >0.03 % sulphur with a viscosity index ≥80 and <120.

- Group II – Mineral oil-based containing ≥90 % saturates and/ or ≤0.03 % sulphur with a viscosity index ≥80 and <120.

- Group III – Mineral oil-based containing ≥90 % saturates and/ or ≤0.03 % sulphur with a viscosity index ≥80 and ≥120.

- Group IV – Polyalphaolefin (PAO) base oils.

- Group V – All other synthetic base stocks not included in the other groups. Therefore, aviation polyol esters are part of this group.

Research on how the molecular structure of the latest generation of aviation base oils influences friction is limited and inconclusive due to difficulty in acquiring base oils with a specific molecular chemistry. This is due to the standard production of base oils containing mixture of chain lengths which, would require a costly separation process to isolate specific components. However, a mixture of chain lengths is beneficial as it lowers the pour point giving enhanced lower temperature capabilities as a mixture of molecule sizes hinders the close packing

necessary for freezing to occur at low temperatures. Previous research in this area has mostly used base oils containing a mixture of molecules therefore, resulting in general conclusions based on assumed differences between tested oils. There is also the added challenge that it is not always possible to reproduce a base oil mixture exactly. Conversely, base oils with a mixture of chain lengths are more relevant to lubricants used in real applications and hence, trends drawn from simplified single molecule compounds have to be balanced with understanding how mixtures of different size base oil molecules synergistically affect friction (110).

Previous trends in the effect of base oil types on friction have been reviewed. It is well known that a higher kinematic viscosity results in higher elastohydrodynamic (EHD) friction due to the higher viscosity fluid having more resistance to shear (3,5). However, this research focuses on the effect of molecular chemistry on friction when the effect of viscosity is removed by testing the oils at the same viscosity by varying the test temperature for each oil.

Most papers evaluating base oils relate the molecular characteristics to EHD friction as this is the regime where additives have little influence and the properties of the base oil dominate (81,110–118). It is also useful to understand how various fluids behave in high speed conditions. Conversely, there has also been extensive work looking at how the molecular structure of fatty acid friction modifier (FAFM) additives affect friction, but this is mostly for the boundary regime as they are added as boundary additives to reduce boundary and mixed friction beyond the capabilities of low viscosity grade oils (108,119). Consequently, by considering the effect of base oils' properties in the EHD regime and FAFM in the boundary regime, these trends provide a useful insight into the expected behaviour of polyol base oils across a range of lubrication regimes.

FAFM are believed to readily adsorb on to a surface either via dipole interactions (Frewing (120,121)) or via hydrogen bonding interaction (Beltzer *et al* (122–124) and also by Davidson

et al (125)). Friction trends for FAFM are well documented and it has been shown that friction decreases as chain length increases (126,127), in unsaturated chains, trans isomers give rise to lower friction than cis isomer due to straighter chains (128) and that polarity is also a dominant factor (120,121). It has also been demonstrated that branching leads to higher friction due to creating an irregular profile of molecular repulsion and deep interaction zone that gives rise to high friction and has weak cohesive forces between adjacent chains in the monolayer resulting in increased vulnerability to shear (120–124,128). It has also been shown the adsorption of FAFM additives is easier with branched base oils owing to their irregular profile, which, results in a decrease in traction coefficient in the boundary regime (129). Hence, despite this paper observing the effect of different base oil molecular structures on friction, their behaviour with additives should also be considered when creating a lubricant formulation. Kus and Kalin (130) also showed that the molecular structure affects not only the friction but the wettability of PAO lubricants containing FAFM. It was shown that FAFMs with only one carboxyl group, longer saturated chains and a more polar head group decreased the wettability of the oil resulting in enhanced friction reducing properties more than ones with two carboxyl groups, with shorter, less saturated chains and less polar head groups (130).

Consequently, some of the trends seen with friction modifiers may be synonymous to polyol ester base oils, however, due to the difference in structure, location of the polar functional group in the molecule and the difference in reactivity between a carboxylic acid and an ester group, care needs to be taken in how transferrable these trends are. Polyol esters associate with metal surfaces due to their polarity as well and increasing chain length and decreasing branching also decreases boundary friction. However, the shielding from attached carbon chains around the ester group will result in a decrease in their surface activity and could hinder monolayer formation leading to a decrease in the applicability of the branching trend seen with FAFMs (131).

Contrariwise, there has been a wide range of research investigating base oils, but this mostly related to EHD performance (81,110–118). Tsubouchi proposed five molecular properties that are likely to increase friction in traction fluids (132). The first is high molecular stiffness caused by structures with restricted molecular mobility due to a high proportion of unsaturated bonds or complex ring structures as this hinders molecular slip as molecules cannot deform and rotate easily which, can also give rise to molecular entanglement. Through various studies, it is believed that EHD friction is influenced mostly by the flexibility and structure of individual molecules as this will affect how molecular layers shear over one another under high pressure. Washizu and Ohmori confirmed this using molecular dynamics simulations (133). This was seen by Zhang *et al* where it was shown that flexible groups and linear molecules favoured low friction which, allowed more free movement and prevented molecular entanglement (110). Synthetic esters are an example of a flexible molecule as the ester bond allows free rotation of substituents. Hentschel et al. also discovered that bulkier and more irregular shaped cyclic structures gave rise to more steric hindrance hindering fluidity due to neighbouring molecule interlocking resulting in higher friction in comparison to regular spherical and ellipsoidal rings (111).

The second was large molecule size as it was believed this produces more steric hindrance. More specifically, this is referring to the degree of branching and linearity of molecule, how much free space a molecule occupies and how it interacts with neighbouring layers. Zhang et al. showed that bulky cyclo-hexyl rings and methyl branches gave higher EHD friction due to hindering movement against neighbouring layers (110). While linear chains favour low friction as they interact less with neighbouring layers. An NPG based polyol ester with a branched substituent gave higher friction than a linear one containing a double bond. It was also found that the friction of polyglycols was strongly influenced by the amount of branching, with more propylene instead of ethylene units resulting in more branching and therefore, higher friction

(110). This was confirmed by Hentschel who suggested the low friction of polyglycols was caused by the low degree of branching resulting in a thread-like structure which, allowed the polyglycols chains to align which, minimizing interaction with other layers (112). These results were confirmed by Hirst and Moore (113). Further confirming that bulkier molecules give a higher EHD friction, Hammann *et al* showed that molecules with one or two cyclohexyl rings gave high EHD friction (134). Cecil *et al* confirmed this result by finding that paraffinic mineral oils gave a lower EHD friction than naphthenic, the latter having more saturated rings substituents (135). The paper also showed that glycol compounds produced a lower friction than the mineral oils tested. A similar study was also performed by Hirst and Moore where EHD friction was higher for molecules containing multiple side chains and saturated rings, but it was found to be lower for polyglycols (113). It was also found that friction was found to be lower for benzene ring containing base oils where the substituents were located para to one another (substituents on opposite carbons on the 6-membered ring) as opposed to ortho and meta (substituents on the adjacent carbon or the second carbon around the 6-membered ring) due to the molecule being more linear (113). Another study discovered that EHD friction increased with increased degree of branching. Friction data was analysed using a viscoelastic Eyring model and it was noted that the Eyring stress decreased with the degree of branching and with molecular volume (80). LaFountain *et al* measured the EHD friction properties of three base oils a found that the EHD friction increased from PAO (polyalphaolefins) to diesters to alkylated aromatic base oils (116). This again confirmed that bulkier molecules can give rise to higher friction. Zhang et al reported a general trend with base oil group with group 1 having the highest friction, then group 2 and then groups 3 and 4 which, also follows the trend of decreasing proportion of cyclic and branched components (110).

However, an increase in the size of the molecule can also decrease friction if the larger molecule can pack more efficiently than the smaller molecule. With regards to base oils seen in aviation

lubricants, Chang utilized an in-contact temperature rise mapping method to measure the shear stress properties of a range of ester base oils and it was found that pentaerythritol esters had a lower shear stress than trimethylolpropane (TMP) based esters. The paper also noted that more branching lead to an increase in shear stress (118).

The third molecular characteristic was short alkyl chains resulting in a poor molecular packing efficiency. Zhang et al showed an increase in chain length from adipic to azelaic to sebacic acid results in decreasing friction (110,132).

The fourth factor was a high melting point, but this may just be due to larger molecules and molecules with more polar atoms resulting in stronger intermolecular bonding as they inherently have a higher melting point (132).

The fifth molecular characteristic is low molecular polarity as high polarity gives rise to repulsion between neighbouring molecules preventing close packing and aiding the molecules sliding over one another (132). It was found that solvent treated mineral base oils gave a higher friction than hydrotreated oils and that the lowest friction was produced by group III and group IV base oils therefore, showing that the introduction of polar water resulted in lower friction than those treated with organic non-polar solvents (117).

Other studies have also observed the loss of torque and efficiency of real bearings and gears and found that the synthetic base oils tested; PAOs, polyglycols and esters produced a reduction in torque in comparison to other mineral oils. This could be due to characteristics such as molecular packing efficiency, polarity or bulky substituents. Although it is difficult to make further deductions without more detail on the molecular chemistry of the mineral oils, it is likely to be due to a higher proportion of cyclic and branched substituents (136–140). When comparing the synthetic base oils to each other, the literature sources found opposing results in that Yoshizaki et al. found PAO to give a lower friction than polyglycols whereas the opposite

was found by Höhn et al. This may be due to differences in the PAOs and polyglycols tested hence, the reason for the difficulty in understanding a trend with base oils and the necessity for control of base oil production for research purposes (136,137).

The above literature shows that the effect of molecular structure on base oils in the EHD regime and FAFM in the boundary regime have similar trends but differ in the mechanism behind the frictional effects. The literature suggests that low friction is favoured by longer chain lengths, linear molecules, less branching and therefore, less bulky molecules. The aim of this chapter is to deduce whether the molecular structure of the aviation derived base oils influences friction, following the trends previously outlined in the literature, but also to further confirm the trends seen in the literature with lubricants with known specific molecular structures. Specifically, the effect of varying the alkyl chain length on the end groups on the polyol esters, the number of ester groups in the polyol ester and the introduction of branching to these structures on friction is explored. This was done by producing Stribeck curves to compare the different base oils over a range of temperatures. To deduce whether the molecular structure still influences friction when independent of viscosity, the different base oils were compared by testing each oil at a specific temperature to attain the same kinematic viscosity.

For this testing a Mini-Traction Machine (MTM) was chosen as shown in 3.1.1 Mini Traction Machine section as it allowed the quick production of Stribeck curves at specific temperatures under specific point contact conditions representative of the cooler gearbox environments near the front of the engine.

4.3　Results & Discussion

4.3.1　The Effect of Chain length and the Number of Ester Groups on Friction

This section will interpret the tribological properties of the base oils in Figure 3-23 in which, the chain length and the number of ester groups in the polyol ester have been varied.

Effect of Temperature

The normalised Stribeck curves solely showing the MONOPE C7 base oil are shown in Figure 4-1. The other base oils displayed similar trends.

Generally, it is known that a higher viscosity results a lower traction coefficient in the boundary regime due to the fluid forming a thicker oil film to protect asperities, but a lower viscosity will result in a lower traction coefficient at high speeds as a thinner fluid is sheared more easily (7). As the temperature is varied, this results in a viscosity change, which, alters the performance in the boundary and EHD regimes and the general trend is the friction decreases from low to high temperature due to the difference in viscosity and temperature effects. The calculated kinematic viscosities of these oils can be seen in Table 8-6.

Normalisation of the Stribeck curves would lead to a single master curve if viscosity was the sole parameter governing frictional characteristics, but the fact that there is still separation of results in Figure 4-1 shows that another variable as well as viscosity is contributing to the underlying tribological behaviour. Also, it should be noted that this method of normalising for viscosity can only shift curves laterally on the Stribeck graph and can therefore, not account for the lower traction coefficients produced for the higher temperature tests as a result of the decreased viscosity.

Therefore, Figure 4-1 shows a decrease in traction coefficient as the temperature is increased which, is due to the increased temperature resulting in a decrease in viscosity and hence, the

fluids are sheared more easily. Prior to normalisation of the Stribeck curves, higher viscosities would favour a lower traction coefficient in the boundary regime however, normalisation results in shifting of the curves as the tests have been normalised for viscosity. The separation in the curves is also larger for the test fluids that have a larger difference in viscosity across the range of test temperatures.
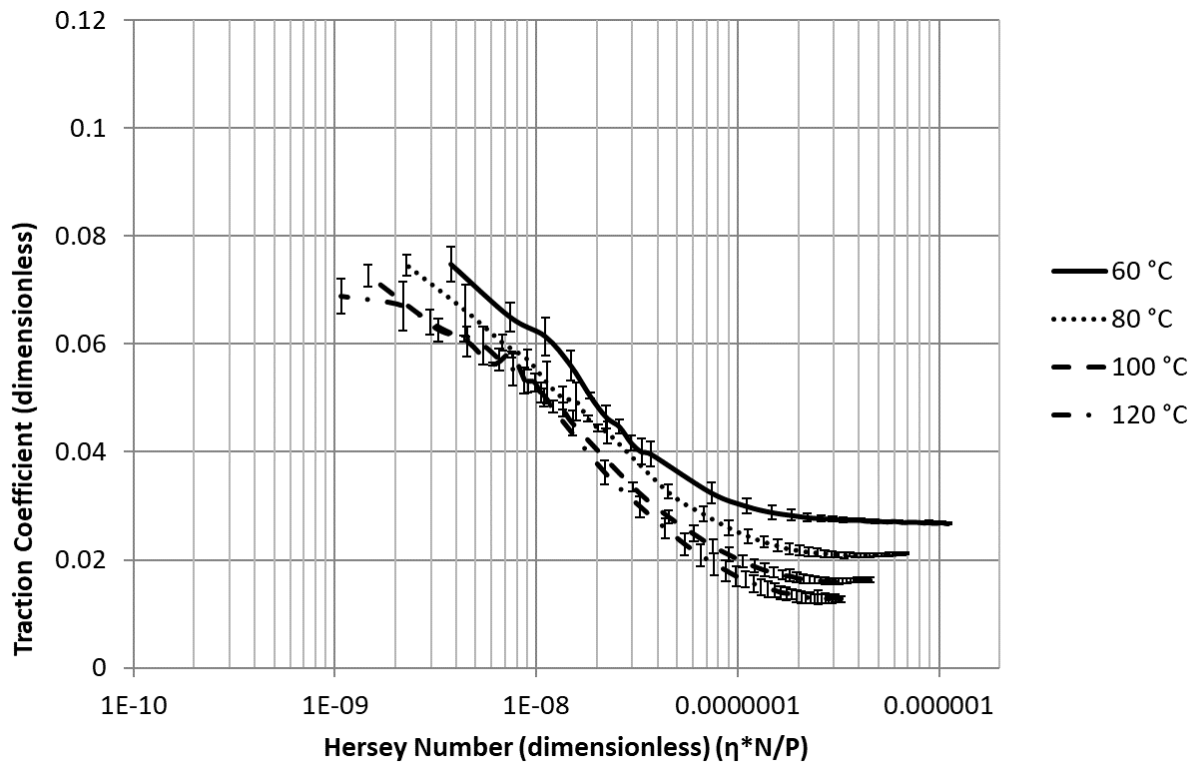
Figure 4-1 – Normalised Stribeck curves of the MONOPE C7 base oil at a range of temperatures.

Comparison at Constant Temperature

Figure 4-2 shows that when the base oils are compared at a constant temperature, separation of the Stribeck curves only emerges at the higher temperatures (120 °C). At the lower test temperature of 60 °C there is no significant trend. By considering the viscosities of each of these oils at each test temperature, there is a larger difference in kinematic viscosity at the lower test temperature. Hence, it can be seen that at 120 °C, this has the smallest range of viscosities of 2.83 cSt whereas at 60 °C the range is 12.04 cSt. Consequently, at low temperatures, viscosity

dominates the behaviour leading to similar curves due to normalising for viscosity by plotting the traction coefficient against the Hersey number. When the difference in viscosity is minimised, a difference in friction emerges due to other underlying variables in the system, namely the difference in molecular structure.

The order of the friction decreased from NPG C7 to TMP C7 to MONOPE C5 to MONOPE C7 and then to MONOPE C9. Hence, this indicates an effect of molecular structure on friction. The results show that friction decreases with an increase in both the number of ester groups and the chain length. It is likely this is due to the larger molecules being able to pack more efficiently and separate the surfaces due to their larger size. Larger chains can better separate surfaces since they take up more space thus providing improved support, but this can often come with increased friction if larger bulkier molecules have more difficulty moving which, can mask this effect.

However, at high test temperatures at high entrainment speeds, the pentaerythritol base oils converge, and the neopentyl and trimethylol base oils remain separated from them. This suggests that the pentaerythritol base oils behave similarly at higher entrainment speeds regardless of their difference in chain length as they reach the EHD regime and that the neopentyl and trimethylol base oils require higher speeds to reach the same traction coefficient. Hence, this shows that the effect of the number of ester groups potentially has a larger impact on the molecular packing than differences in substituent chain length.

Stribeck Curves at 60°C

Stribeck Curves at 120 °C

Figure 4-2 – Normalised Stribeck curves comparing the different base oils at 60 °C and 120 °C.

Comparison at Constant Kinematic Viscosity

When tested at a constant viscosity, there is a clear separation of Stribeck curves across each of the different test viscosities, but there appears to be a slightly larger separation on the lowest viscosity graph; Figure 4-3. The order from high to low friction is marginally different to the same temperature Stribeck curves as the trend now goes NPG C7, PE C5, TMP C7, PE C7 and then PE C9. Therefore, the PE C5 and TMP C7 have swapped. However, this is due to the fact that they have very similar molecular weights and therefore, viscosity (as shown in Table 8-2) and have performed very similarly throughout all the tests.

Despite this marginal change in frictional order, the same trend can clearly be observed, showing that as both chain length, and the number of ester groups increases, the friction decreases. This reinforces the theory that viscosity is not the only factor influencing friction and that the molecular structure has a substantial effect which, is revealed after viscosity has been eliminated as a variable. It is likely this is due to the larger molecules being able to pack more efficiently, which, results in less frictional resistance and be able to separate the rubbing surfaces more effectively because of their increasing size.

Another observation is that the pentaerythritol base oils do not completely converge at high entrainment speeds as they did when all compared at the same test temperature. This could be due to increasing chain length effect being more apparent at the same viscosity and potentially requires higher entrainment speeds to converge. Again, the effect of the number of ester groups potentially has a larger impact on the molecular packing than differences in substituent chain length as there is a larger separation between the NPG C7, TMP C7 and MONOPE C7 than each of the MONOPE curves.
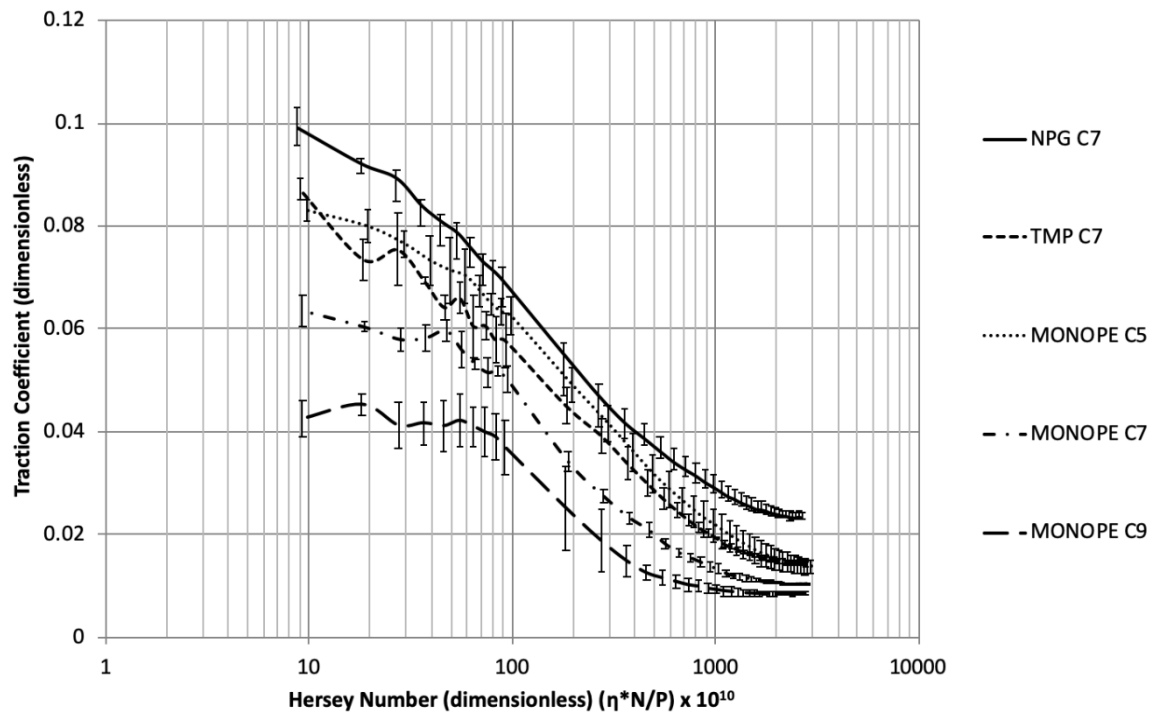
Figure 4-3 – Normalised Stribeck curves comparing the different base oils at a kinematic viscosity of 2.9 cSt by varying the test temperature for each base oil.

4.3.2 The Effect of Molecular Branching on Friction

This section will discuss the tribological properties of the base oils in Figure 3-24 in which, the amount of molecular branching has been varied.

Effect of Temperature

Figure 4-4 shows Stribeck curves for the NC8:EH 25:75 base oil at a range of test temperatures (the other base oils display similar trends). Again typically, friction decreases as the temperature increases, which, is due to the viscosity decreasing with increasing temperature and results in less friction (due to lower viscosity fluids having a lower resistance to shear). There is also more separation in the EHD regime due to the physical properties of the lubricant like viscosity having more influence in the EHD regime than in the boundary regime. However, just as in Figure 4-1, normalisation of the Stribeck curves would lead to a single master curve

115

if viscosity was the only factor governing frictional characteristics, but the fact that there is still separation of results shows that another variable as well as viscosity is contributing to the underlying tribological behaviour. However, this method of normalising for viscosity can only shift curves laterally on the Stribeck graph and can therefore, not account for the lower traction coefficients produced for the higher temperature tests as a result of the decreased viscosity. Hence, these Stribeck curves still show a trend of decreasing friction with increasing temperature and therefore, viscosity.
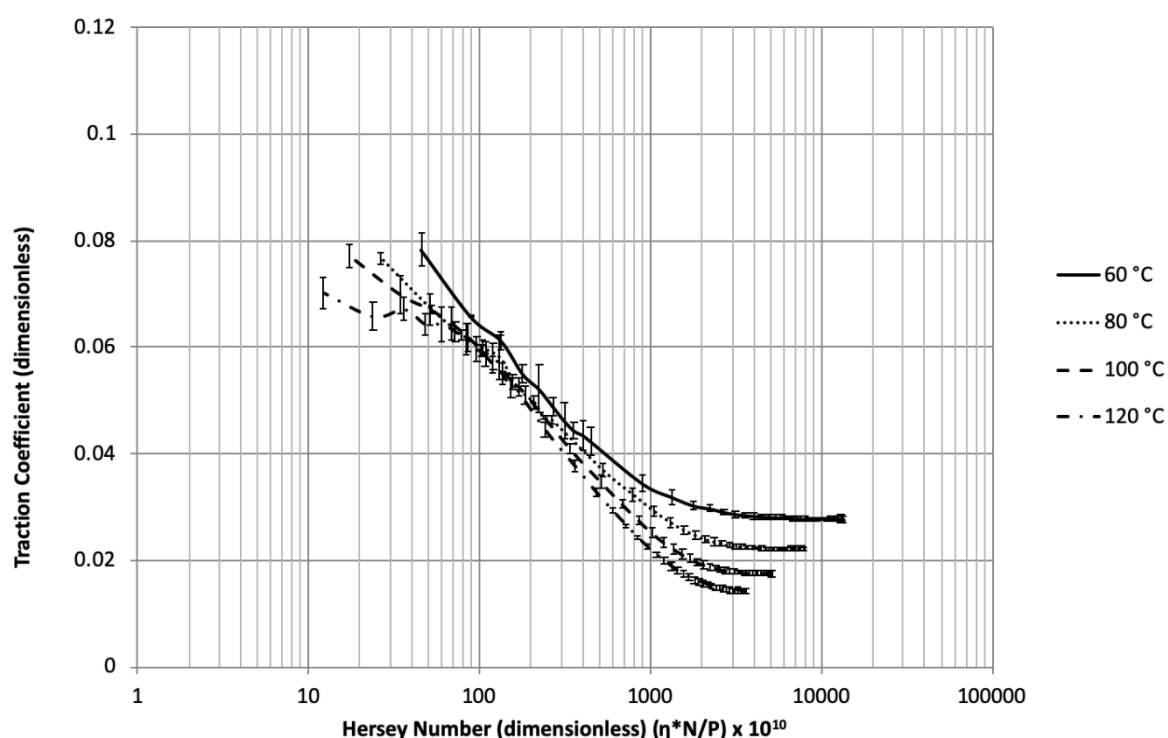
Figure 4-4 – Stribeck curves for NC8:EH 27:25 at a range of test temperatures.

Comparison at Constant Temperature

When comparing the base oils at the same temperature, there is a distinct and repeatable separation between the Stribeck curves following a trend of low to high friction as the proportion of branching (from EH chains) increases (as shown in Figure 4-5 for both 60 °C and 120 °C).
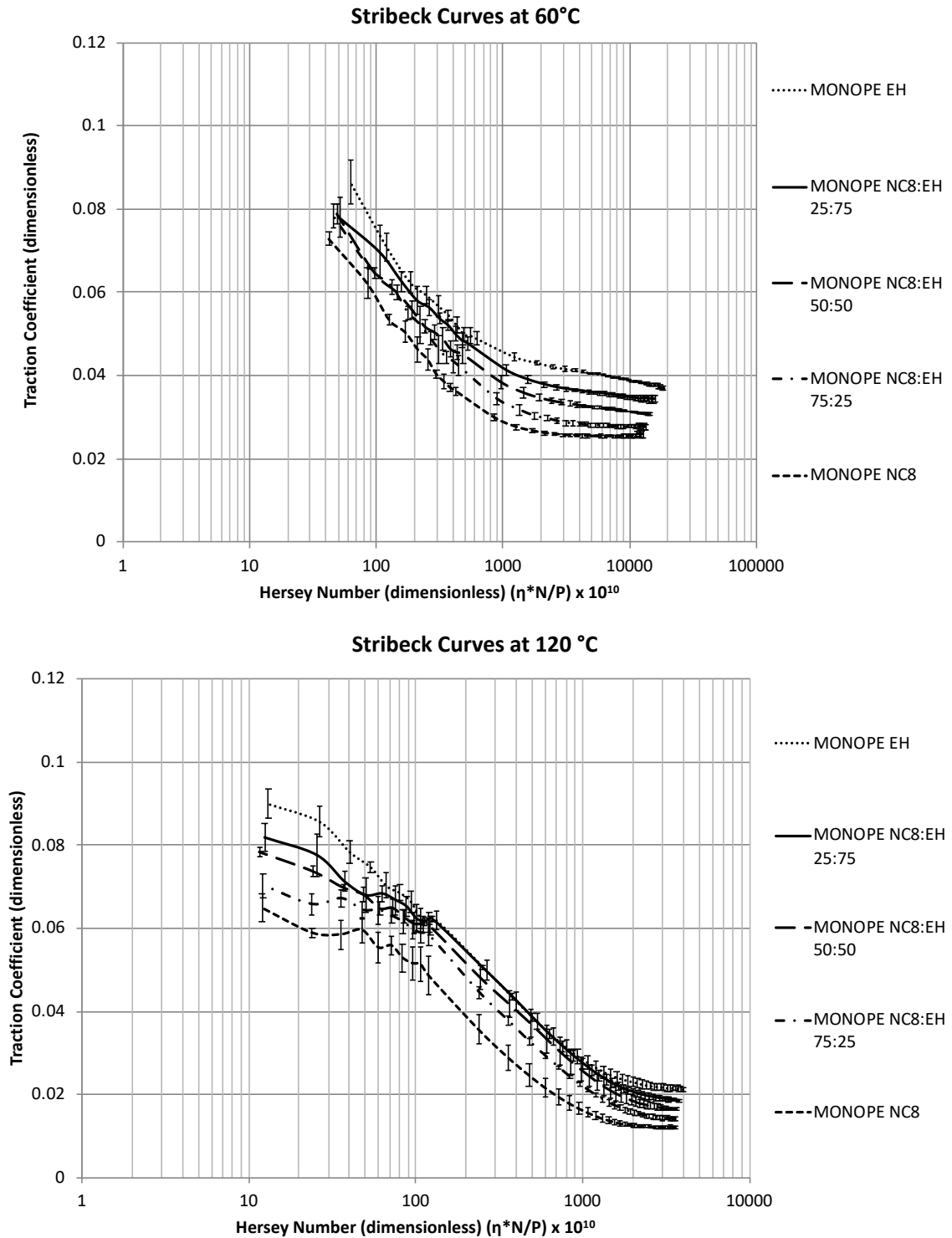
Figure 4-5 – Normalised Stribeck curves comparing the linear vs. branched base oils at 60 °C and 120 °C.

At constant test temperatures, each of the test fluids has a different kinematic viscosity (as it can be seen in Table 8-8) however, plotting against the Hersey number normalises for viscosity and hence, the trends seen must be due to differences in molecular chemistry. In this case, as

the amount of molecular branching increases, the friction increases across all lubrication regimes. Unlike in Figure 4-2, this trend can be seen at the lower and higher test temperatures although more observable at lower test temperatures. This could potentially suggest that branching may have a more significant effect on friction than the molecular variables studied earlier.

Comparison at Constant Kinematic Viscosity

There is clear separation of Stribeck curves when tested at a constant kinematic viscosity across each of the different test viscosities, but unlike in Figure 4-3, this separation remains present at each of the test kinematic viscosities as shown in Figure 4-6. Again, friction increases with the amount of branching present in the base oil. This reinforces the theory that viscosity is not the only factor influencing friction and that the molecular structure has a substantial effect. Branching leads to more interference with molecular packing, which, results in more frictional resistance. It is also clear that this effect is present across all lubrication regimes.

These results show that the inclusion of branching may inverse the trends seen with the previous oils where increasing chain length and increasing the number of ester groups decreased friction, potentially due to larger molecules being able to pack more efficiently and better support load. It may be that the inclusion of branched side chains prevents the larger molecules packing as efficiently giving rise to more steric hindrance as the molecules get larger with more branching.
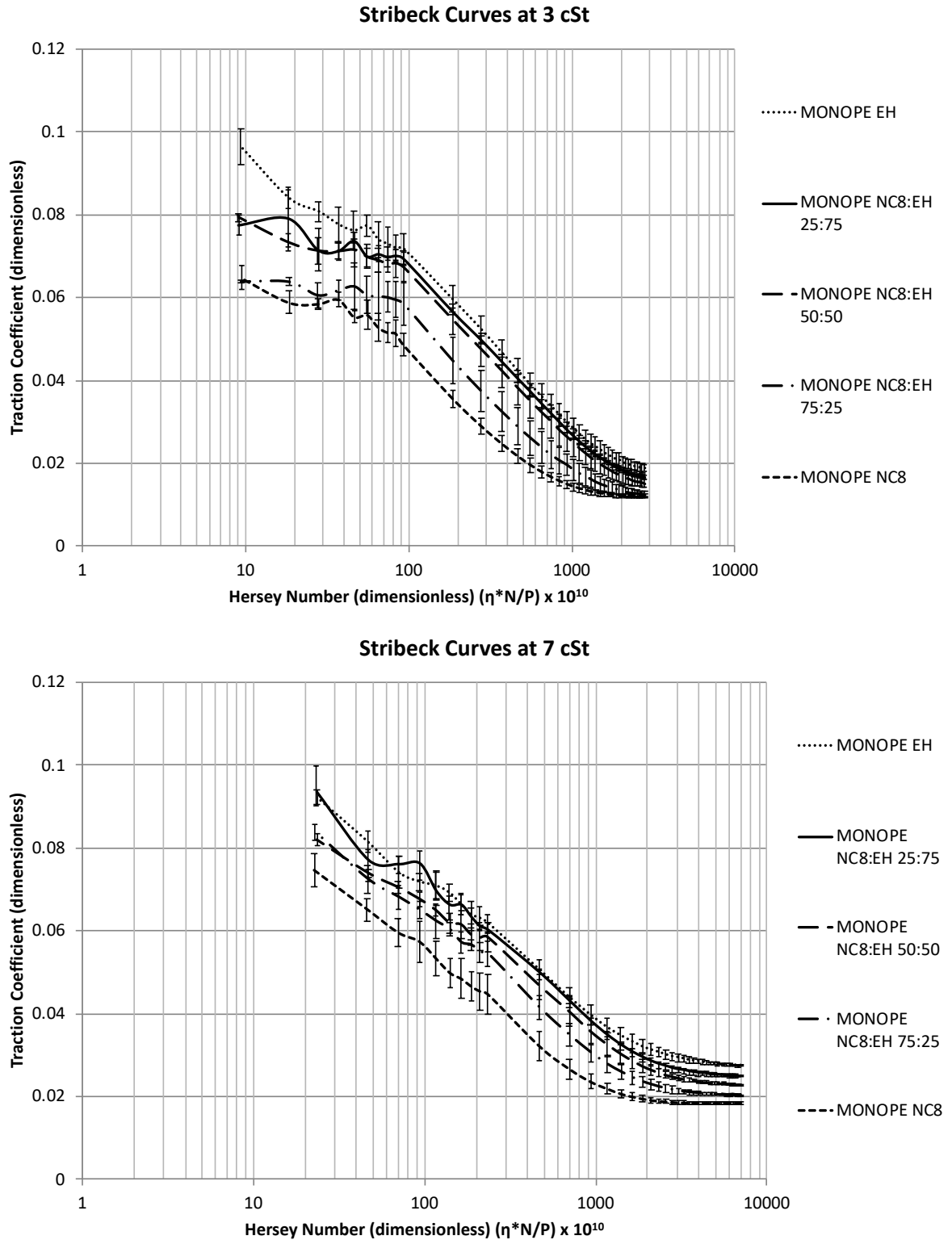
Figure 4-6 – Normalised Stribeck curves comparing the different base oils at kinematic viscosities of 3 cSt and 7 cSt by varying the test temperature for each base oil.

4.3.3 Fully Formulated Base Oil Analysis

The section will show the results of the fully formulated lubricants each with the same additive package and all have a controlled mixture of different structure base oils to vary viscosity.

Effect of Temperature

The Stribeck curves for the high viscosity formulation are shown in Figure 4-7 (the other formulations are not shown as they show a similar trend). There is a trend showing that traction coefficient decreases with increasing temperature as shown with the pure base oils.

The difference in traction coefficient in the boundary regime is smaller than the difference in traction coefficient in the EHD regime. This is because the boundary region is affected much more by additive performance and as all the oils contain the same additive package, similar performance is expected. As it is the base oil which, is being varied and not the additives, it is expected that the main differences will be seen in the EHD regime and this is confirmed in the presented results. But the differences that are seen in the boundary regime must be due to higher viscosity oils forming thicker films and therefore, they can separate the surface asperities more than lower viscosity blends (5). It is likely that the additives will introduce some surface chemistry effects that could interact with the base oils creating a different frictional response in comparison to the unadditised oils. However, it is not expected these effects will be significantly different between each of the fully formulated lubricants.

Figure 4-7 shows that the Stribeck curves for the higher viscosity oils do not flatten off. This could be a possible effect of shear heating. Shear heating occurs when shearing of high viscosity fluids results in friction which, generates heat as the molecules shear over one another and as a result causes a decrease in viscosity. Higher entrainment speeds may cause more shearing resulting in a thinner film and therefore, lower friction. But it is also possible that a higher entrainment is needed for the more viscous oils to reach a minimum traction in the EHD regime.
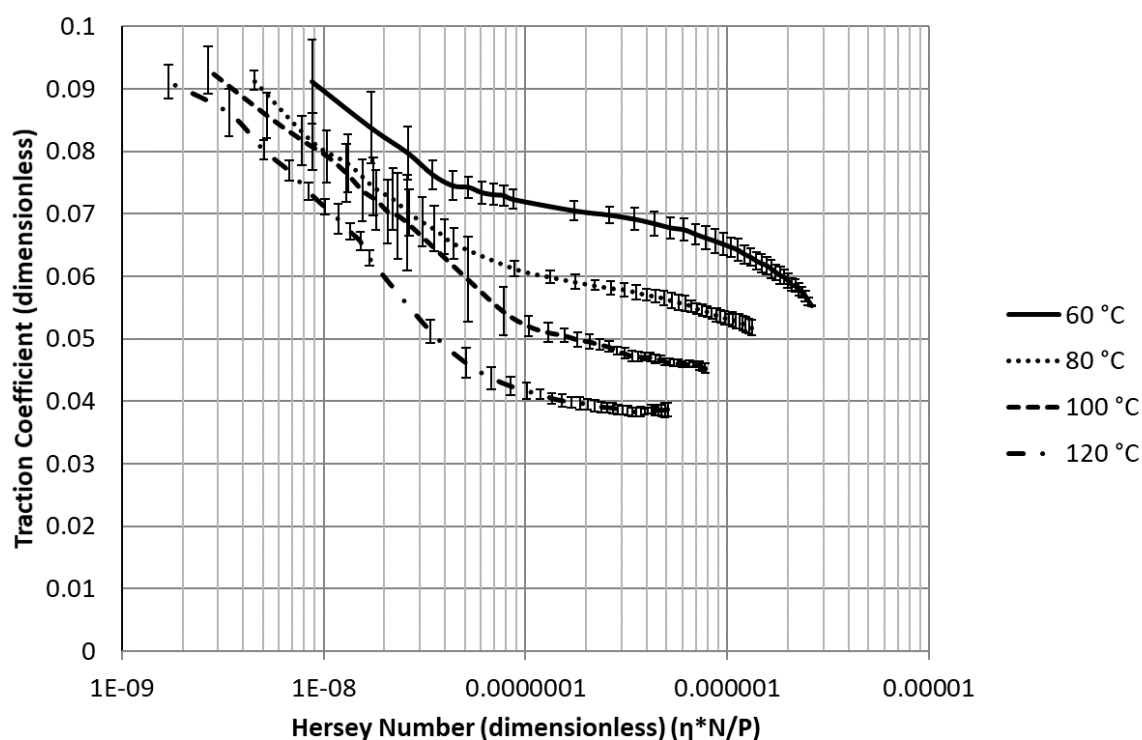
Figure 4-7 – Stribeck curves of the High Formulation at a range of temperatures.

Effect of Base Oil Structure at Constant Temperature

Figure 4-8 shows the Stribeck curves comparing the fully formulated oils at the 120 °C (the other test temperatures show a similar trend). Despite the kinematic viscosities of these oils ranging from 2.33 cSt for the "Low" lubricant to 5.28 cSt for the "High" lubricant as shown in Table 8-10, there is a clear trend of decreasing friction from the High to the Low viscosity blends. This is most likely due to differences in base oil molecular structure as the Stribeck curves have been normalised for viscosity. However, the high viscosity formulations have a higher proportion of esters due to the higher proportion of pentaerythritol esters which, in Figure 4-8 leads to higher friction, an opposite trend to the previous Stribeck curves in Sections 4.3.1. However, as shown from Figure 3-25, these esters are branched and therefore, as the pentaerythritol esters have more chains, there are a higher proportion of branching in the higher

viscosity blends. Therefore, these results show that branching has a stronger effect on friction in comparison to the number of ester groups. The presence of the standard additive package does not appear to influence the frictional trends showing the base oil molecular has the dominant effect on friction.
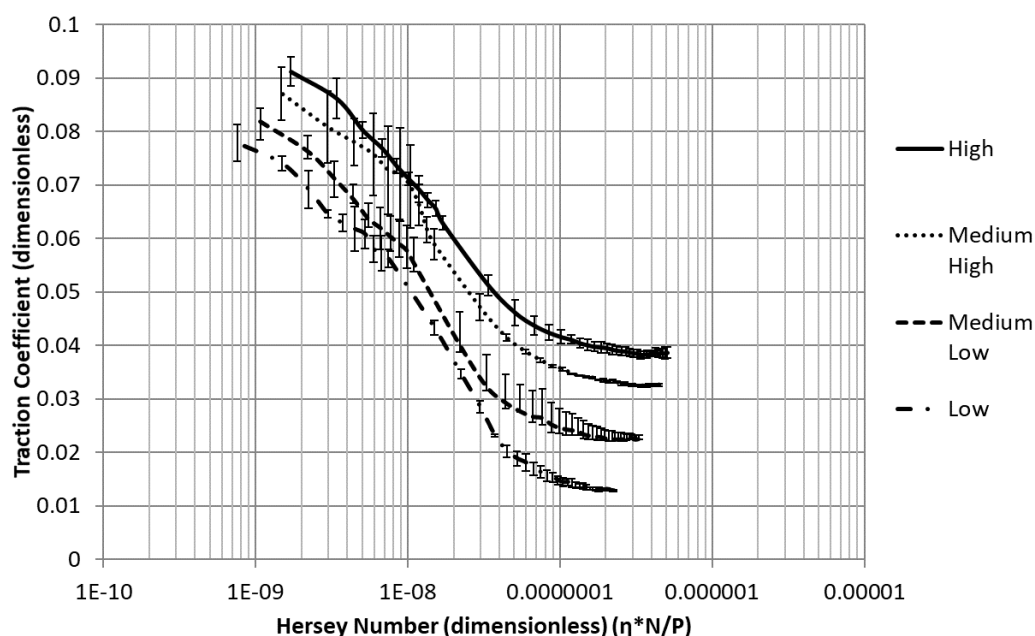
Figure 4-8 – Normalised Stribeck curves of the fully formulated blends with different base oils at 120 °C.

Effect of Base Oil Structure at Constant Viscosity

The Stribeck curves at 5 cSt and results shown are in Figure 4-9. There is a clear trend showing that friction decreases moving from the high viscosity to the low viscosity formulations even when all of them have the same kinematic viscosity. Therefore, if the viscosity is not the main influence behind the tribological effects, the only other difference between the oils is difference in base oil chemistry. This graph demonstrates the opposite to Figure 4-3 as the oils with a larger size now result in higher friction.

As mentioned earlier, the low viscosity oil is mainly composed of polyol esters from NPG and TMP and the high viscosity oil is predominantly polyol esters from pentaerythritol, but these

esters are now branched too. Therefore, from the low to the high viscosity formulations, there is an increase in the number of esters with more branching. Consequently, this increase in branching, has led to more interference with molecular packing giving rise to higher friction.

Hence, this shows that the inclusion of branching inverses the trends seen with the previous oils where increasing chain length and increasing the number of ester groups decreased friction potentially due to larger molecules being able to pack more efficiently. It may be that the inclusion of branched side chain prevents the larger molecule packing as efficiently giving rise to more steric hindrance as the molecules get larger with more branching. Again, the presence of the standard additive package does not appear to influence to frictional trends showing the base oil molecular structure has the dominant effect on friction.
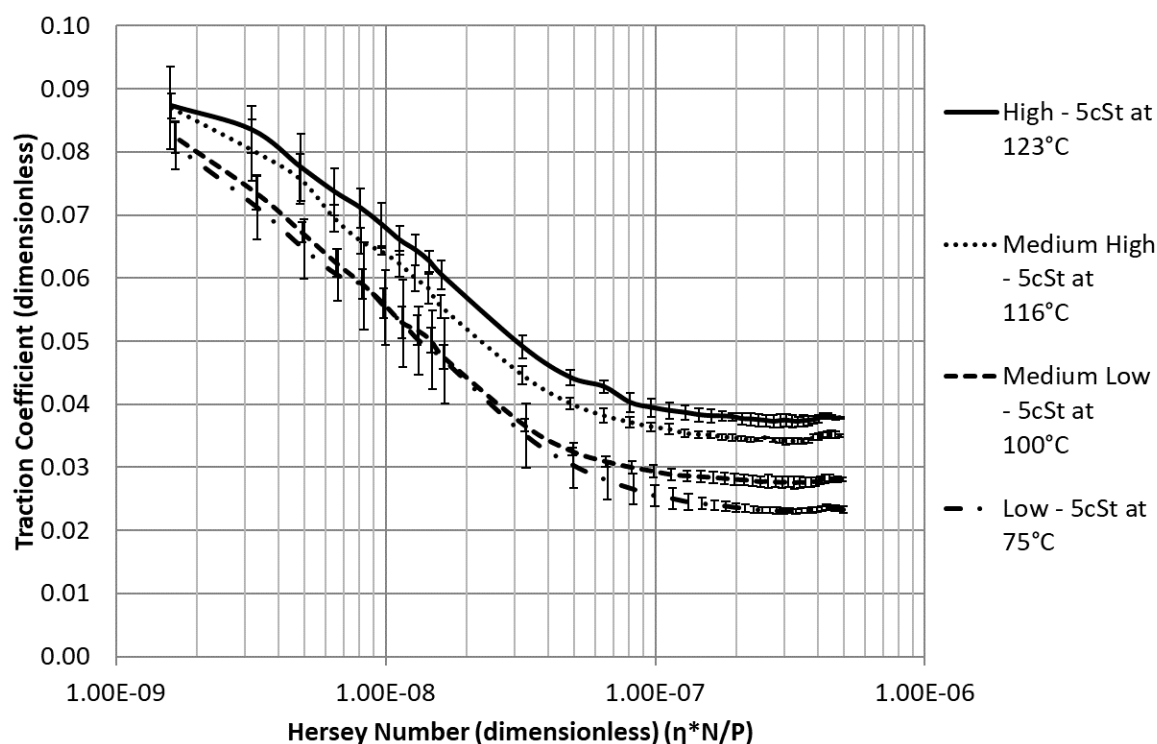
Figure 4-9 – Normalised Stribeck curves comparing fully formulated lubricants with different base oils at the same kinematic viscosity of 5 cSt by varying the test temperature for each base oil.

4.4 Conclusions

Stribeck curves have been produced for a range of base oils with specific molecular structures to understand the effect of molecular structure on friction. Whilst changes to molecular structure influence the viscosity of the fluid, the base oils were also tested at the same viscosity by varying the temperature of each test.

The results showed the molecular structure has a substantial impact on the measured friction across all lubrication regimes. The viscosity behaviour is as expected with an increase in viscosity leading to an increase in friction as a higher viscosity fluid incurs more resistance to shear. After viscosity was eliminated as a variable through plotting traction coefficient against the Hersey number and by conducting wears tests at the same viscosity, the first two molecular variables explored were; the effect of chain length and the influence of the number of ester groups on friction. It was shown that the friction decreases across all lubrication regimes as the chain length increases and by increasing the number of ester groups which, is most likely due to larger molecules being able to pack more efficiently and separate the contacting surfaces.

Larger chains can separate surfaces better since they take up more space thus providing improved support, but this can often come with increased friction if larger bulkier molecules have more difficulty moving which, can mask this effect. It was also seen that the number of ester groups potentially has more of an effect on friction that the substituent chain length as the pentaerythritol base oils converge when compared at the same temperature, but the TMP and NPG oils remain separated. This suggested that the pentaerythritol base oils behave very similarly at high entrainment speeds regardless of their difference in chain length. In addition, the effect of molecular branching was explored which, showed that the friction increased as the proportion of branching on the ester substituents increased. Consequently, the inclusion of branched side chains prevents the larger molecules packing as efficiently, giving rise to more

124

steric hindrance as the molecules get larger with more branching giving rise to increased friction.

When fully formulated lubricants were investigated, the results demonstrated that branching has a stronger influence on friction in comparison to the number of ester groups. This could potentially be due to branching having a larger effect in disrupting molecular packing due to having more interaction with neighbouring layers. Whereas increasing the number of esters does not prevent the molecule from maintaining linearity but provides more linear chains to improve load carrying capacity resulting in a decrease in friction.

Overall, these results agree with the literature in that low friction is favoured by longer chain lengths, increasing the number of ester groups (within a polyol ester) and maintaining a linear molecule. Branching leads to producing a bulkier molecule which, gives rise to high friction whereas, whilst increasing the chain length and the number of ester groups increases the size of the molecule, the molecule remains linear and flexible giving rise to improved load carrying capacity and packing efficiency which, reduces friction.

Chapter 5. The Evaluation of Anti-Wear Additives on Micropitting Propensity and Tribofilm Thickness

5.1 Introduction

Modern aviation lubricants have evolved from mineral oil-based compounds to entirely synthetic compounds. The tribological performance of mineral oils is mostly due to naturally occurring different sulphur species which, impart some wear protection. These species were not separated out due to cost, but also due to the mixture performing well without the need for further purification (3,23). As gas turbine technology has progressed, there was a need for superior high temperature stability which, subsequently led to the use of synthetic group V polyol esters (as mentioned in Chapter 4). Consequently, the natural tribological properties imparted from the crude oil were absent in these synthetic formulations and as a result, additives were used to give the required wear protection. Anti-wear additives have become an essential component of most lubricant formulations, as they are vital in ensuring protection under extreme pressure, boundary and mixed lubrication regimes.

Boundary and extreme pressure lubrication can be broken down into categories depending on their temperature and load. The type of boundary lubrication present in these conditions is categorised by high temperature and high-pressure contacts. Therefore, the mechanism of boundary lubrication involves a reaction between the anti-wear additives and the metal surface to create a chemisorbed tribofilm that serves as a sacrificial film which, is preferentially sheared off instead of the substrate metal (3,27).

Whilst anti-wear additives are known to be proficient in protecting against wear, their effect on less severe wear mechanisms such as micropitting, which, is a common wear mechanism seen in gear environments, has been less studied. This study will thus focus on the influence of

different anti-wear additives on micropitting. This is motivated by the development on the PGB in the UltraFan© as it needs to be understood whether current lubricants can adequately protect the new tribological environment.

Micropitting has been shown to be influenced by a wide range of different parameters including load, roughness, SRR, the speed of the surfaces, the hardness, the temperature and type of lubricant and additives present in the formulation as summarised by Laine *et al* (141). It has also been found that the fluid pressure in the contact also contributes to opening the crack therefore, contributing to accelerating micropitting (142,143).

They found that the above parameters influenced micropitting in the following ways (14,144–156):

- Micropitting could be reduced or prevented by increasing the lambda ratio by decreasing the surface roughness (by superfinishing for example) or increasing the fluid film thickness (through controlling the test conditions or controlling the viscosity of the lubricant).
- Increasing the SRR (reduces the micropitting initiation life but has limited effect on the wear rate) (150).
- Not having a differential hardness between meshing components. Softer surfaces are more susceptible to micropitting which, is why MPR test specimens are designed to have a softer roller specimen in comparison to the counterface rings (150).
- The slower moving component is more likely to be micropitted.
- Certain anti-wear additives have been shown to promote micropitting (146,147,153,155).

Hence, to study micropitting, a wear test need to be conducted in the boundary regime with a low lambda ratio, with sliding (a higher SRR) such that the central roller is slower, there needs to be a differential hardness between the test specimens. The effect of the addition of anti-wear additives can then be monitored showing whether they hinder or promote micropitting like some other anti-wear additives.

Some anti-wear additives are known to promote micropitting (141,146,147,153,155,157). In particular many of these studies have observed the effect of one of the most common anti-wear additives; zinc dialkyl dithiophosphate (ZDDP), however, there have been limited studies that have investigated whether ashless additives like TCP used in aviation lubricants also influences micropitting (28,158). Trivedi *et al* demonstrated that TCP actually had a positive effect on rolling contact fatigue (RCF) life, however, these tests were done on a ball on rod rig, with a 3 cSt formulation, contact pressure of 5.5 GPa, lambda 0.04 on a range of bearing steels (159). Hence, this suggests TCP may not promote micropitting like ZDDP, however, this study uses different conditions to the gear conditions in this thesis. Therefore, it needs to be understood whether ashless anti-wear additives used in aviation lubricants like TCP also promote micropitting as this could be a potential failure mode for the PGB.

To evaluate the performance of anti-wear additives, it is important to understand the mechanism by which, they chemically react with the surface to form a tribofilm, but also to understand what the mechanical drivers are for tribofilm formation and growth. It is well known that ZDDP forms relatively thick tribofilms that have a rough and patchy topography, often being described as "pad-like" as confirmed by Atomic Force Microscopy and SLIM (31,32,35,160–164). It has also been noted this patchy thick film comprises of a multilayer film of iron phosphate and iron sulphide, followed by sulphide in the bulk and then topped off with a zinc sulphide and organic sulphide on the top (28,165). TCP films are usually only described as being thin in comparison to the likes of ZDDP and therefore, do not incur any notable morphological features that have the same effect as the ZDDP tribofilm (28,38,166).

The mechanism of ZDDP tribofilm formation has been extensively studied, however, it was only recently found that ZDDP tribofilm formation does not need solid asperity-asperity contact to drive film formation (37,96). This was found by conducting a test with a high-EHD friction fluid and no asperity contact using an MTM-SLIM, and it was found that a ZDDP tribofilm still

formed. The applied shear stress was sufficient to reduce the thermal activation energy to initiate film formation. Consequently, it confirmed that sliding is required for tribofilm formation as it generates the applied shear stress which, is not being created in pure rolling conditions. This proposed mechanism explains many of the tribological behaviours produced from ZDDP, including the rough pad like topography and morphology of ZDDP. Tribofilm formation will occur at the asperity conjunctions where the contact pressure and, therefore, the shear stress is the highest. The tribofilm will continue to grow at these locations as they will bear the majority of the load. This results in deep valleys in between the pads where minimal tribofilm will grow as there is negligible shear stress in those areas (35,37,167). It has been shown in many studies that ZDDP tribofilms form rapidly and then level out at a maximum tribofilm thickness (31,32,35,160–162). This levelling out was suggested to be due to the phosphate-glass tribofilm plastically deforming, which, increases the contact area such that the shear stress decreases and eventually reached a point where it is too low to further drive tribofilm growth (37). It was previously believed that an equilibrium was eventually reached where the rate of tribofilm formation equalled the rate of removal. However, Fujita *et al* (31,99) demonstrated that there was no ZDDP tribofilm loss after a tribofilm was produced and then the lubricant was replaced with base oil for the remainder of the test.

ZDDP tribofilm formation is not highly dependent on the surface material as long as the surfaces have a high hardness and elastic moduli to sustain the applied shear stress. There may be some chemical surface influence to promote the initial adhesion of ZDDP to the surface, but the mechanism of growth of the ZDDP tribofilm is believed to be an oligomerisation process (168).

The chemistry behind the reaction of how ZDDP breaks down to form a phosphate tribofilm is still poorly understood. There are two theories for this; the first postulates that the alkyl-oxygen bond breakage gives rise to the formation of the phosphate glass tribofilm. This has been backed

through showing that secondary alkyl ZDDP forms a tribofilm faster than primary ones and also has lower thermal stability. This therefore, implies this strength of that bond directly relates to the rate of ZDDP decomposition (37,99). The second theory was that the shearing conditions exploits ZDDP's ability to stretch the S-Zn bond and O-Zn bond which, results in the bonds becoming more polar and less covalent. This gives rise to increased nucleophilicity of the corresponding thiophosphate or phosphate ion which, results in promoting polymerisation into a phosphate glass tribofilm and also reduces the solubility of ZDDP (168). Consequently, it is clear that is it difficult to study the underlying chemistry of the additive breaking down to form the phosphate glass tribofilm. However, the mechanochemical mechanism has been proven for ZDDP and shows a clear driver behind film formation which, is potentially transferrable to ashless additives too. However, the slower formation and thinner thickness of these tribofilms further increases the difficulty in understanding their formation, composition and mechanical properties.

The mechanism of TCP tribofilm formation is less understood but there have been a few theories suggested supported by experimental evidence (166). Godfrey (43) proposed that TCP breaks down to produce an iron phosphate film formed by the reaction of phosphoric acid with the steel surface. The phosphoric acid is present either as an impurity in commercial TCP or it is formed by the TCP under wear conditions (by hydrolysis of the TCP). The phosphoric acid then reacts with the iron in the steel to form iron (II) phosphate which, eventually forms a layer (43).

Sung and Gellman (169) and Saba and Forster (170) both suggested the tribofilms form via thermal decomposition of TCP. As the temperature increases from 180 K to 700 K, the TCP undergoes adsorption onto the steel surface and as the temperature increases towards 700 K, the TCP decomposes until a phosphate or metal phosphate layer is formed. It is believed to decompose via homolytic cleavage of either the P-O or O-tolyl bond depending on the degree

of oxidation of the steel surface (44,169). Godfrey (43) also suggested that TCP film formation was enhanced by the presence of oxygen as confirmed by Goldblatt and Appeldorn (171). It is not known exactly whether this occurs via direct oxidation of the TCP or via oxidation at the iron surface, but experimental evidence shows that film formation is better in oxygen than in inert nitrogen or argon and is also hindered by moisture (43,171). The work of Klaus and Bieber (172) hypothesised that the polar water molecules and TCP adsorbed onto the metal surface of the bearing. This would then activate the P=O of the TCP and the O-H of the water in order to allow nucleophilic attack with the electron rich oxygen atom on the water molecule at the electrophilic (electron deficient) phosphorus atom on the TCP. Their results showed that hydrolysed TCP with mono and di-cresyl phosphate gave equal or superior anti-wear performance. But contradictory results have been obtained by Goldblatt and Appledoorn (171) where the TCP was pre-treated with silica-gel to remove phosphoric acid and water and apparently give similar anti-wear results (171,173–175).

Other studies believe that the TCP film formation is metal catalysed in which, TCP coordinates with the metal surface resulting in activation of the P=O bond causing the P to become more electrophilic. This increases its susceptibility for nucleophilic attack by a surface O^{2-} (present as an oxide of iron on the surface) and results in the loss of cresol (176,177).

Studies have also shown that the chemistry and morphology of the film formed is heavily dependent on the type of metal surface present. This is most likely the main reason for the difficulty in understanding the exact mechanism by which, TCP forms a film. Due to the slight differences in metal surface composition between studies, this could have led to different results. This is especially important as Sheasby and colleagues (40) suggested that wear is more of a chemical than mechanical process, implying that surface composition plays a role in film formation.

Numerous theories have been discussed for the role of the metal in TCP film formation under boundary conditions. One is that collision of opposing asperities could result in roughness fracturing which, exposes nascent surfaces that act as active sites for the catalysis of film formation (32). Another is that the heat energy generated in the wear process created hot spots that also catalyse TCP film formation (32,40). Another study showed that TCP adsorbs much more strongly onto a chromium-nickel-iron alloy than silicon nitride and silicon carbide (176). This suggests the TCP has chemically reacted with the surface. Saba and Forster (44) demonstrated that TCP was more stable in the presence of iron, copper, aluminium, nickel and chromium than in the presence of their oxides. They also found that higher oxidation states gave a higher degree of TCP decomposition concluding that the TCP decomposition was dependent on the Lewis acidity of the metal oxides.

Hence, it can be seen there are a wide variety of proposed mechanisms for TCP tribofilm formation which, are somewhat less conclusive than ZDDP perhaps due to it being studied less, but, also due to the increased difficulty in studying a tribofilm that forms slowly and is thinner.

Now that the mechanisms behind tribofilm formation have been discussed, these can be used to aid the understanding of how these additives may promote micropitting. ZDDP has been shown to promote micropitting in comparison to base oils (141,153,157,178,179). The mechanism by which, this is believed to occur is that the additive prevents initial smoothening of components as they "run-in" by protecting asperities too early, thereby, maintaining many high asperity contact pressures which, encourages micropitting (141,153,157,178,179).

This mechanism was investigated by Ueda *et al* (157) using an optical interferometry technique on a ball on disc tribometer that allowed the in-situ measurement of the thickness of a tribofilm (MTM-SLIM, also used in this thesis). This technique monitored tribofilm formation and noted that film formation coincided with an increase in friction which, was attributed to both the patchy morphology of the ZDDP tribofilm, and also the maintained surface roughness as

asperities were protected and prevented from running in. It was also found that that the ZDDP tribofilm formation reached a steady state where the friction remained constant and the thickness of the tribofilm remained constant, which, could potentially indicate the rate of formation and removal of the tribofilm had reached a steady state(28,163,164). However, this could now be due to the plastic deformation of the phosphate glass tribofilm leading to an increased contract area which, could decrease the shear stress below the minimum required to drive tribofilm formation (96,163). It has also been found that by adding the ZDDP after the initial running in of components completely mitigates the accelerated micropitting seen previously (17,180).

Therefore, this chapter explores the effect of different additives on micropitting using an MPR to observe the progression of micropitting from different additives and with different concentrations. An MTM-SLIM was also used to understand the tribofilms produced by the additives at different concentrations in order to provide fundamental understanding how these tribofilms contributed to the micropitting seen from different additives. Details of this apparatus and test method can be seen in section 3.1.2.

5.2 Results & Discussion

This section will discuss the effect of different additives and different concentrations of anti-wear additives on micropitting using an MPR and then an MTM-SLIM was used to further understand fundamentally how the tribofilms created by these solutions contributed to the micropitting damage produced.

5.2.1 MPR results

Wear Track Image Analysis

The wear track images for the MPR tests of the anti-wear additised solutions can be seen in Figure 5-1, Figure 5-4 and Figure 5-5 and all show that the amount of micropitting increases as the number of cycles increases. It should be noted that only one repeat was shown for each concentration despite the repeat tests not showing very repeatable amounts of micropitting, but this is accounted for in the Micropitting Quantification Using Image Analysis in section 5.2.1 and in the discussion.

Figure 5-1 shows the progression of micropitting damage for 800 ppm P (TCP), 2000 ppm P (TCP) and 4200 ppm P (TCP) which, appear to show that not only does the micropitting initiate earlier at higher concentrations, but results in more micropitting damage over time. However, as shown in the Micropitting Quantification Using Image Analysis section, the amount of micropitting was not repeatable and in fact revealed neither no effect of concentration nor that 2000 ppm P (TCP) was the concentration that results in the most micropitting, but this would need to be studied further. In addition, the size of the micropits are consistent between concentrations.

High definition camera images of the roller specimens were also acquired to better visualise the wear produced and to identify the true colour of the wear tracks and these can be seen in Figure 5-2. No significant wear features are distinguished between concentrations, however, there appears to be the introduction of an array of colours in some areas of the wear track in comparison to just base oil showing the anti-wear additive appears coloured on the surface. It could be that the presence of the anti-wear additive film disperses white light splitting it into its component colours.

It can also be seen from Figure 5-3 that the directions of the micropits differ to the HD images, but this was just due to the difference in orientation of the roller when the image was

taken. This was unintentional and a result of an external source taking the camera images. The impact this has on the image is that the micropits are opposite way round for each method.
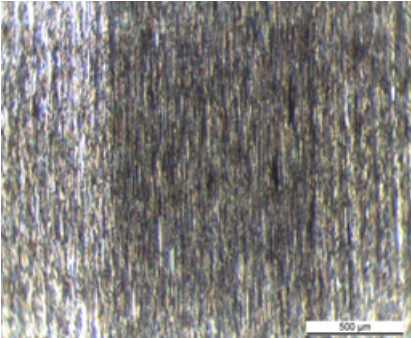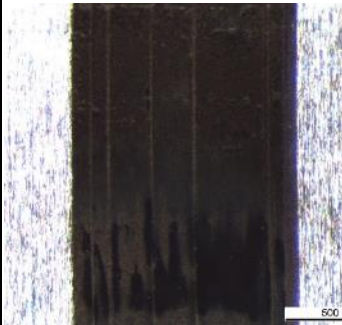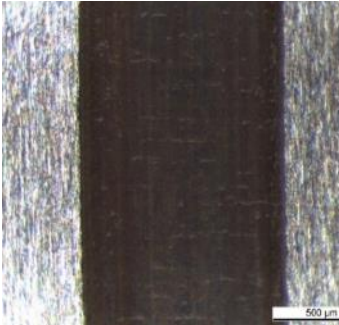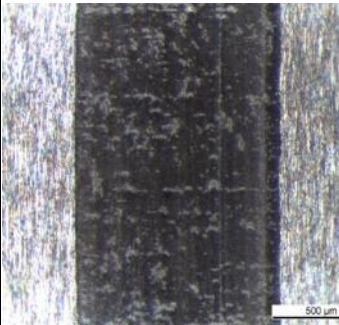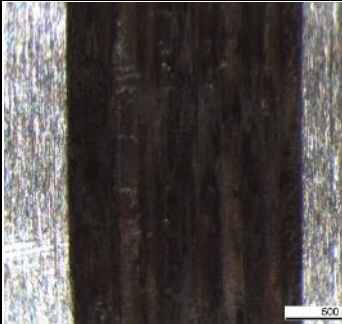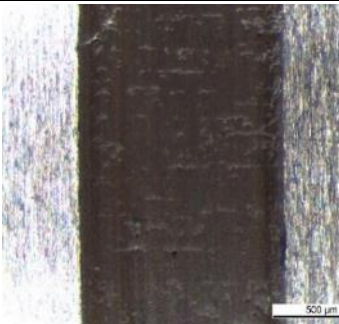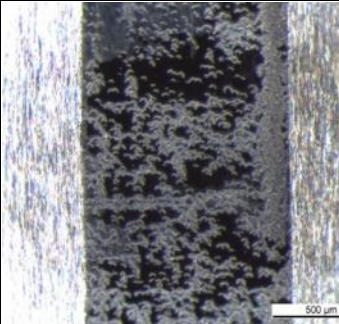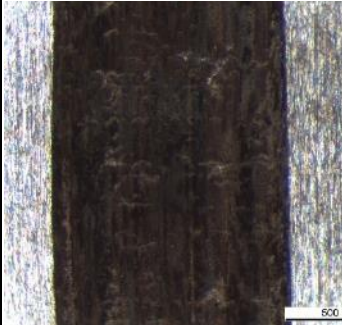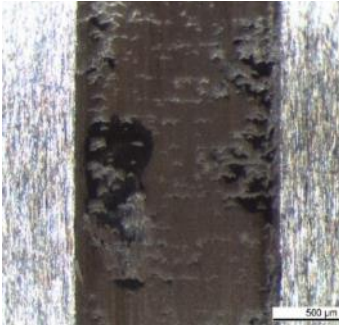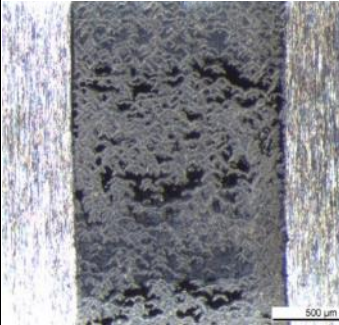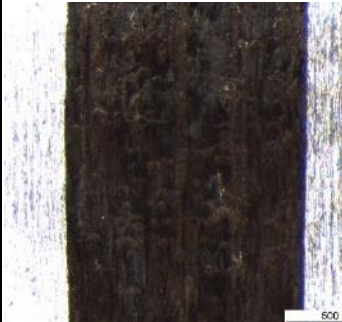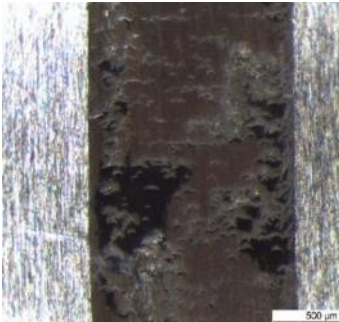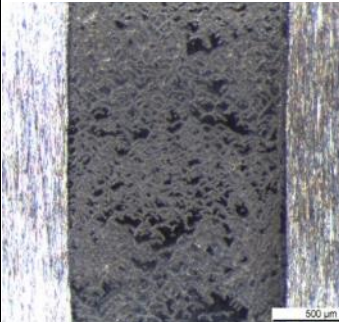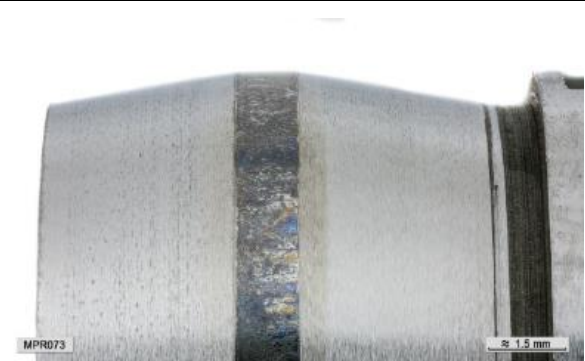
Lubricant	800 ppm P (TCP) + base oil	2000 ppm P (TCP) + base oil	4200 ppm P (TCP) + base oil
Unworn Specimen			
Step 2 – 440 k cycles			
Step 5 – 1760 k cycles			
Step 8 – 3080 k cycles			
Step 11 – 4400 k cycles			

Figure 5-1 - Table showing the optical microscope images of the wear track of the 16MnCr5 chamfered rollers for the range

of TCP additised oils.

Lubricants	Wear track Image	Zoomed in Wear track image
Base oil		
800 ppm P (TCP) + Base oil		
2000 ppm P (TCP) + Base oil		
42000 ppm P (TCP) + Base oil		

137
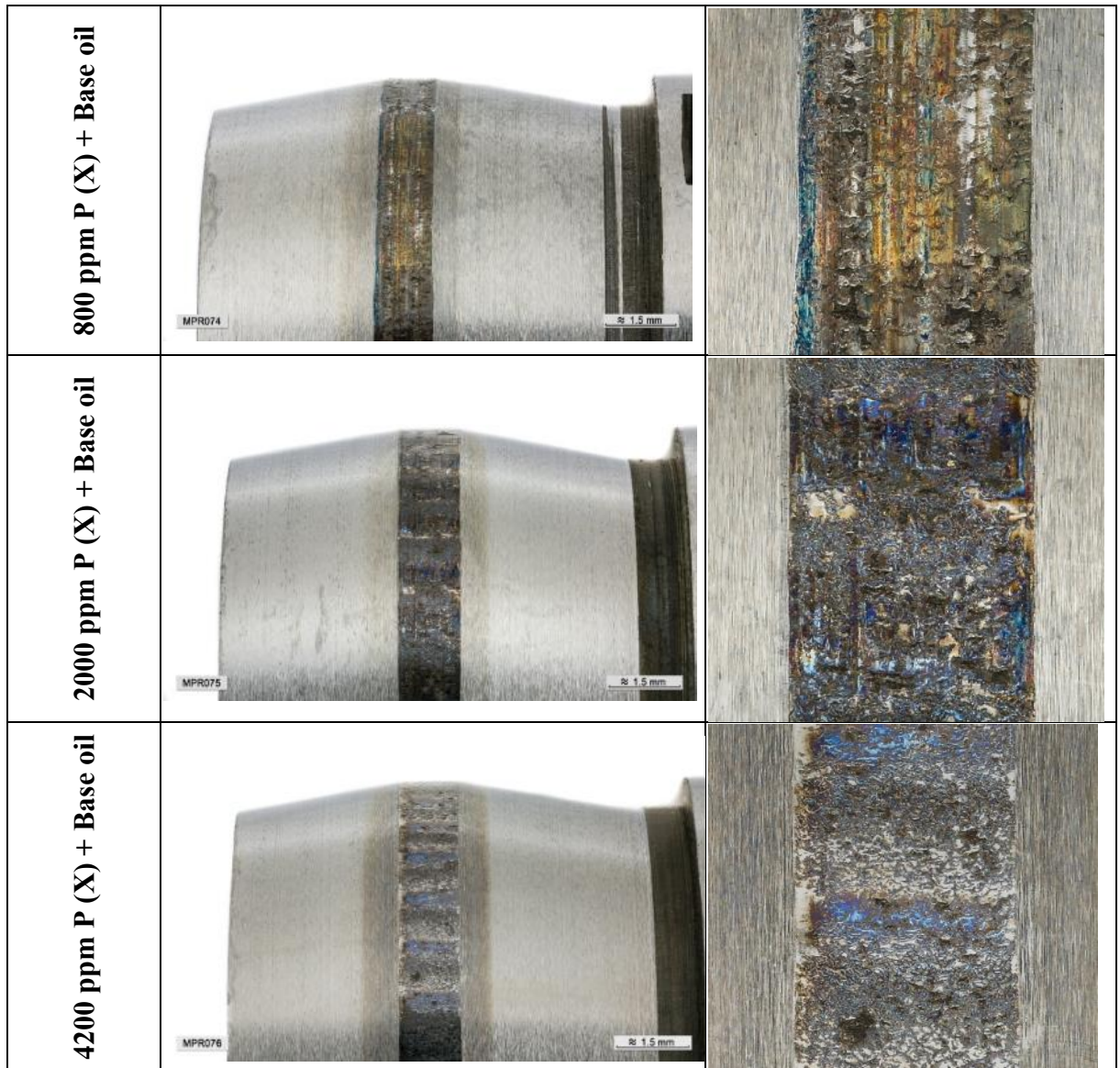
Figure 5-2 – High definition images of the wear tracks of the 16MnCr5 roller specimens from the MPR tests with different

anti-wear additives at different concentrations.

Optical Microscope Image	Rolling direction and direction of fatigue crack growth Direction of Frictional force
HD Camera Image	Direction of Frictional force and direction of fatigue crack growth Rolling direction
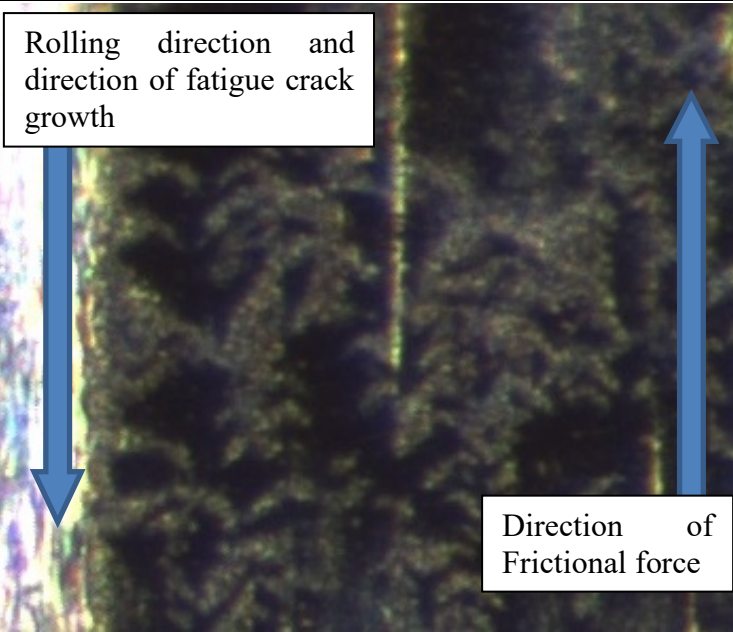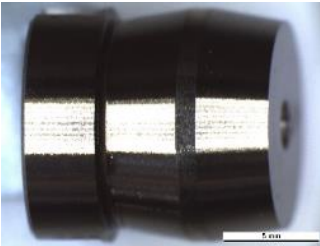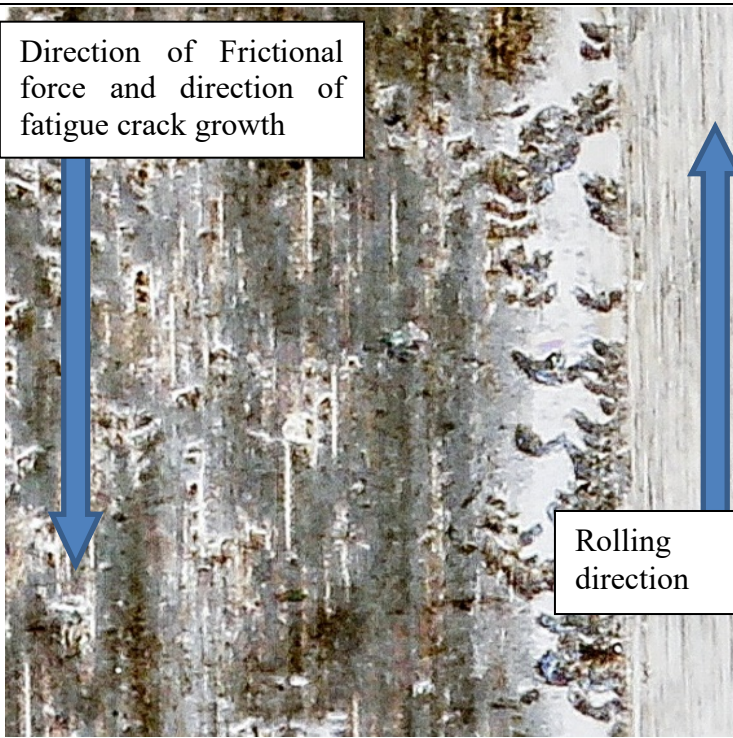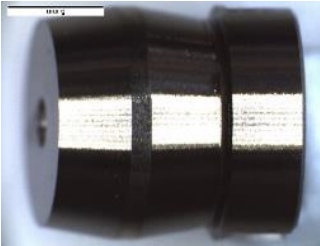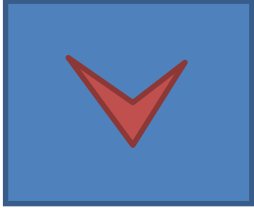
Figure 5-3 – Table showing the orientation of micropitting with respect to roller orientation, rolling direction, frictional force and direction of fatigue crack propagation.

Figure 5-4 shows the progression of micropitting for different concentrations of additive X. Again, micropitting appears to initiate earlier and progress further at higher concentrations, however, this is backed up by results which, shows micropitting increasing as the concentration increases. Additive X gives rise to marginally higher amounts of micropitting in comparison

to TCP as shown from the images, but also the slightly higher amount of micropitting, see Figure 5-6, however, these differences are still within the overlap of error bars.

Micropitting sometimes initiates at the edge of the wear track where the chamfer begins, this is expected due to edge effects that are commonly seen with these type of micropitting experiments where there is a higher stress concentration at the edge of the wear track (179,181). This potentially suggests that additive X is more active than TCP at protecting asperities earlier which, results in the fast formation of micropitting even at equivalent phosphorus concentrations. The size of the micropits are also comparable with TCP.

The effect of concentration on the amounts of micropitting can also be seen in Figure 5-2 which, also shows once again that the additive gives rise to the dispersion colour effect on the surface in comparison to just base oil.

Figure 5-5 shows the progression of micropitting for different concentrations of ZDDP and also for base oil only. It can clearly be seen that ZDDP gives rise to the early onset of micropitting and leads to extensive micropitting throughout the test across the entire wear track. The micropits appear smaller than the other ashless additives. The amounts of micropitting also increases from 800 ppm P (ZDDP) to 2000 ppm P (ZDDP) showing that more ZDDP leads to a stronger effect of early asperities protection leading to more micropitting. The micropitting observed by ZDDP is much more progressive than the ashless additives as it is evident that the micropitting is progated through multiple layers of material rather than just at the surface. This is also reinforced in the Wear Track Width Increase section and clearly shows how detrimental ZDDP is in comparison to the other additives.
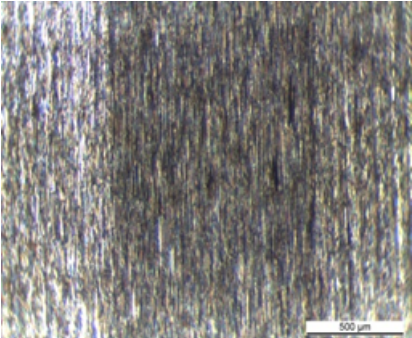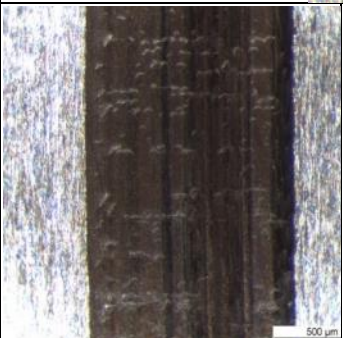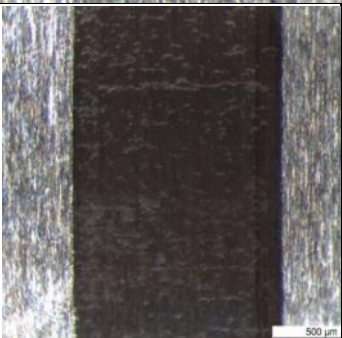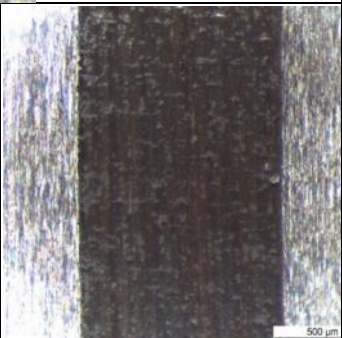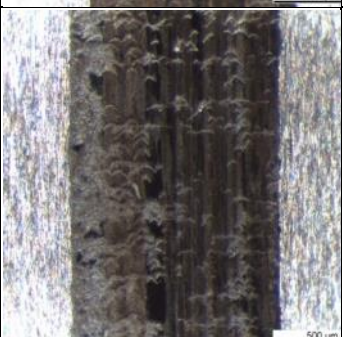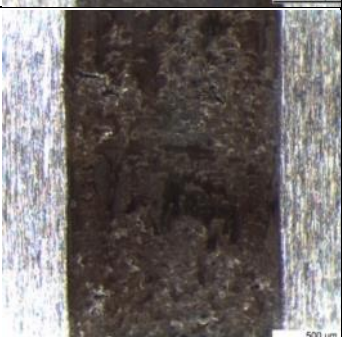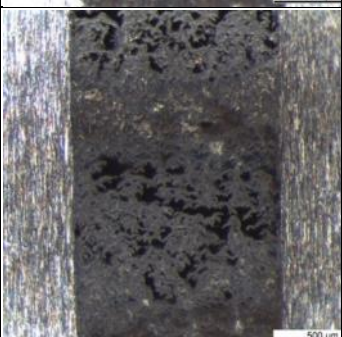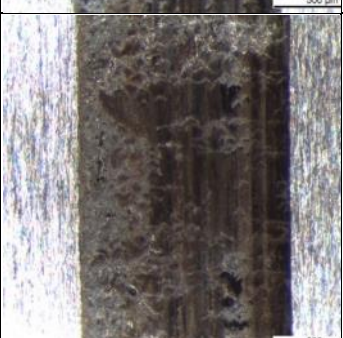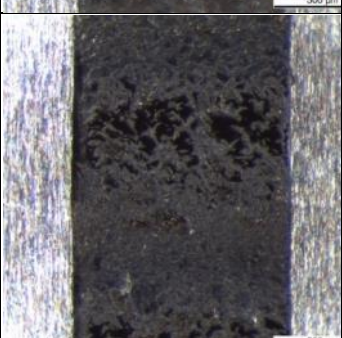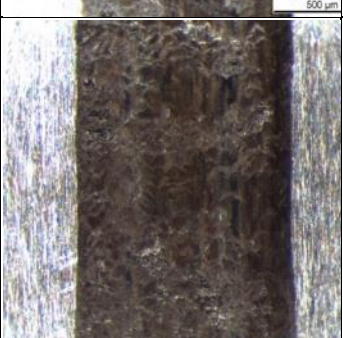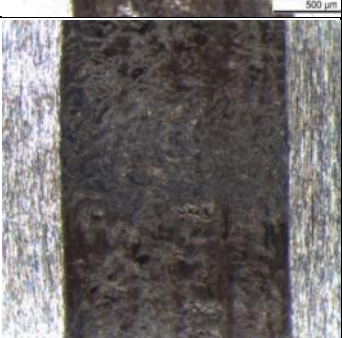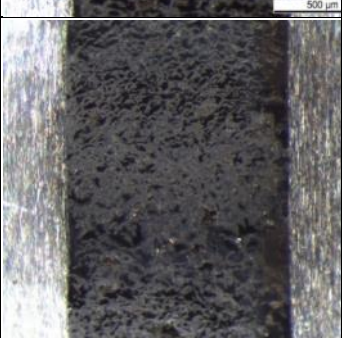
Lubricant	800 ppm P (X) + base oil	2000 ppm P (X) + base oil	4200 ppm P (X) + base oil
Unworn Specimen			
Step 2 – 440 k cycles			
Step 5 – 1760 k cycles			
Step 8 – 3080 k cycles			
Step 11 – 4400 k cycles			

Figure 5-4 - Table showing the optical microscope images of the wear track of the 16MnCr5 chamfered rollers for the range of X additised oils.
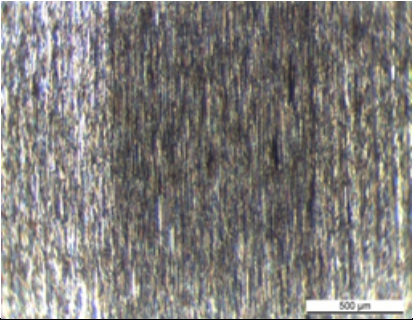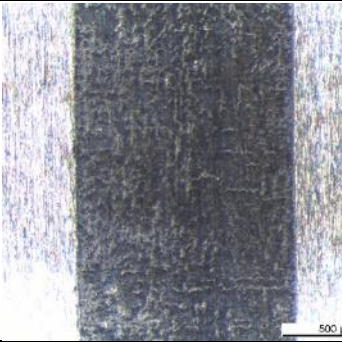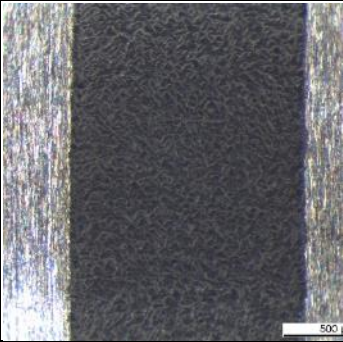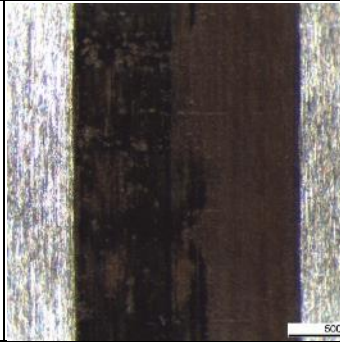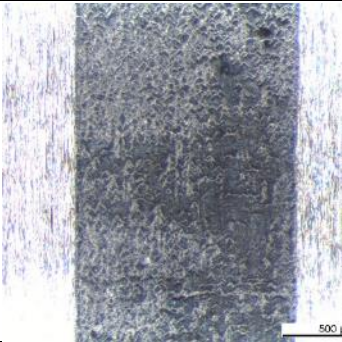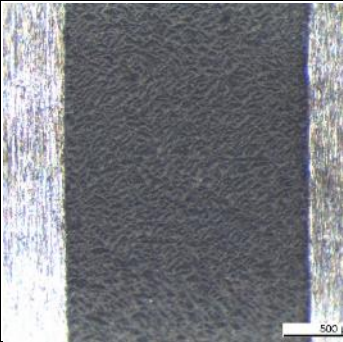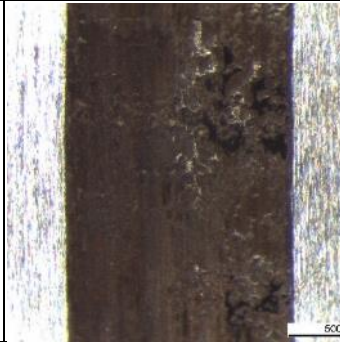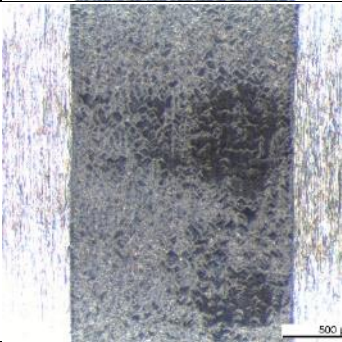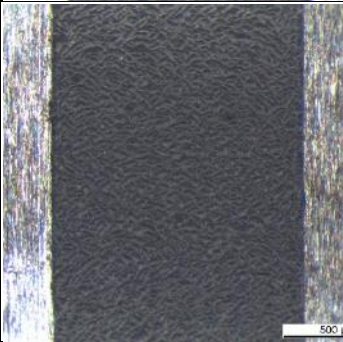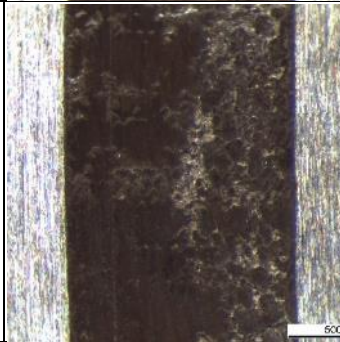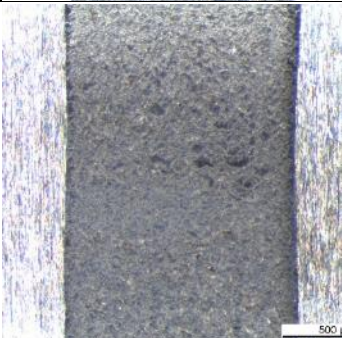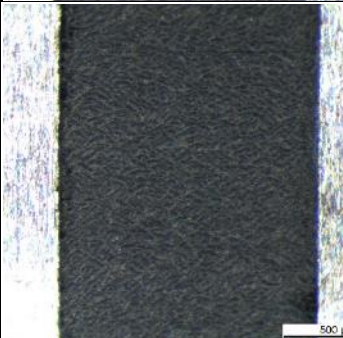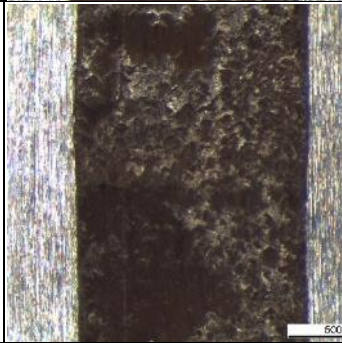
Lubricant	800 ppm P (ZDDP) + base oil	2000 ppm P (ZDDP) + base oil	Base oil
Unworn Specimen			
Step 2 – 440 k cycles			
Step 5 – 1760 k cycles			
Step 8 – 3080 k cycles			
Step 11 – 4400 k cycles			

Figure 5-5 - Table showing the optical microscope images of the wear track of the 16MnCr5 chamfered rollers for the range

of ZDDP additised oils and the test with only base oil.

142

Conversely, the test with just base oil showed very minimal micropitting earlier on in the test and quickly progressed from micropitting to more severe macropitting failures. These results are further confirmed in Figure 5-6 where the base oil has very minimal micropitting, but the ZDDP much higher amounts of micropitting which, increases with concentration. Unfortunately, there were no high definition images taken of the ZDDP tests, but the base oil wear track image shows extensive micropitting and macropitting damage with no dispersion colour effect showing the presence of additives.

Micropitting Quantification Using Image Analysis

Figure 5-6 shows the bar chart which, quantifies the amounts of micropitting as deduced from image analysis using Image J. The base oil results in the lowest amount of micropitting after step 2 and potentially showed that anti-wear additives in general give rise to an earlier onset of micropitting.

For TCP, there appears to be no effect of concentration, but the amount of micropitting is still higher than base oil alone. It also potentially shows there could be an optimum amount of TCP for more micropitting, however, the error bars are large.

For additive X, there is more micropitting in comparison to TCP potentially suggesting this ashless additive is more active in adhering to asperities and protecting surfaces quicker than TCP leading to the faster formation of micropitting. There is also an effect of concentration in that showing more micropitting is seen as the concentration of additive X increases, however, again the error bars are large suggesting this is a weak trend.

ZDDP clearly results in a lot more micropitting than the ashless additives with the 800 ppm P (ZDDP) showing similar levels of micropitting to the highest concentration of additive X and then the 2000 ppm P (ZDDP) showing the highest amounts of micropitting seen in these experiments.
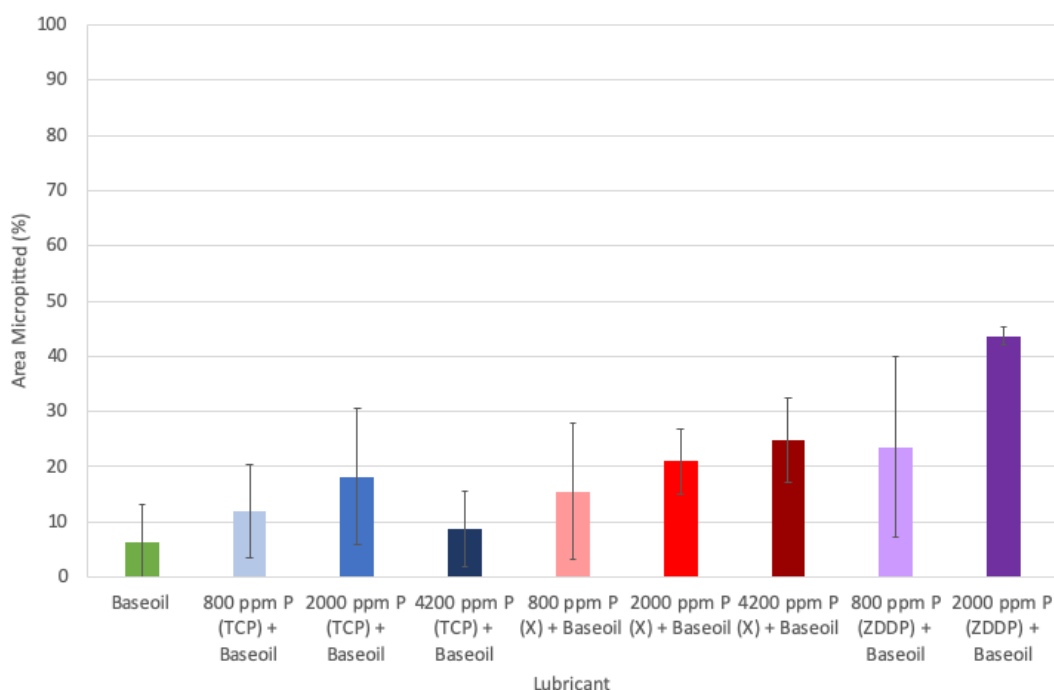
Figure 5-6 – Quantification of the amount of micropitting after Step 2 in the MPR test generated using Image J analysis.

Friction

The average measured friction throughout the MPR tests are shown in Figure 5-7. The friction coefficients are all in a similar range close to 0.1. However, TCP appears to have a higher friction coefficient than additive X and both of these are higher than ZDDP. It has been shown previously that ZDDP leads to an increase in friction in comparison to base oil due to maintaining asperity roughness, however, this was not seen (157,182).

There is no trend with TCP concentration and friction, which, is comparable to the micropitting quantification results. Additive X shows a slight trend with concentration as the friction increases as the concentration increases. Whereas, as the ZDDP concentration increases, the friction decreases. The base oil friction remains lower than all the other tests except ZDDP.

144
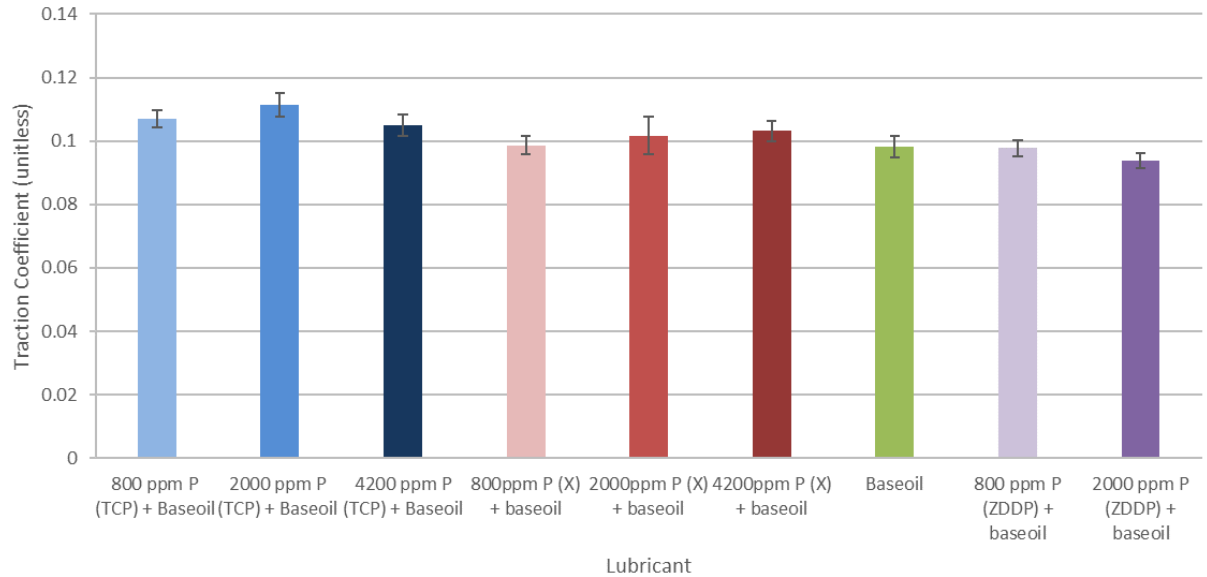
Figure 5-7 - The average traction coefficient for the micropitting tests with anti-wear additive formulations of a range of concentrations on 16MnCr5.

Wear Track Width Increase

The results for the average increase in wear track width of the chamfered rollers are shown in Figure 5-8. TCP has the lowest track width increase overall. There is also a slight decrease in as the concentration of TCP increases. Additive X has a higher wear track width increase and shows the reverse trend of increasing track width with increasing concentration. The wear track increase from ZDDP also increases with concentration and 2000 ppm P (ZDDP) has the highest track width increase despite having the lowest boundary friction as discussed in the previous section. However, in general, these are weak trends due to the large error bars. The base oil test also has the second highest track width increase. These results reinforce the importance of why a less severe wear mechanism like micropitting should be carefully studied as ZDDP has clearly promoted micropitting to such an extent that the amount of wear has surpassed the base oil with no additive protection. The 800 ppm P (ZDDP) could have potentially had a similar magnitude, but the significant error between repeats resulted in a reduction in the average as shown from Figure 5-8. It was expected that the base oil test would result in a large track width

145

increase since the wear in this test progresses more quickly due to having no additive protection as shown from the earlier images.
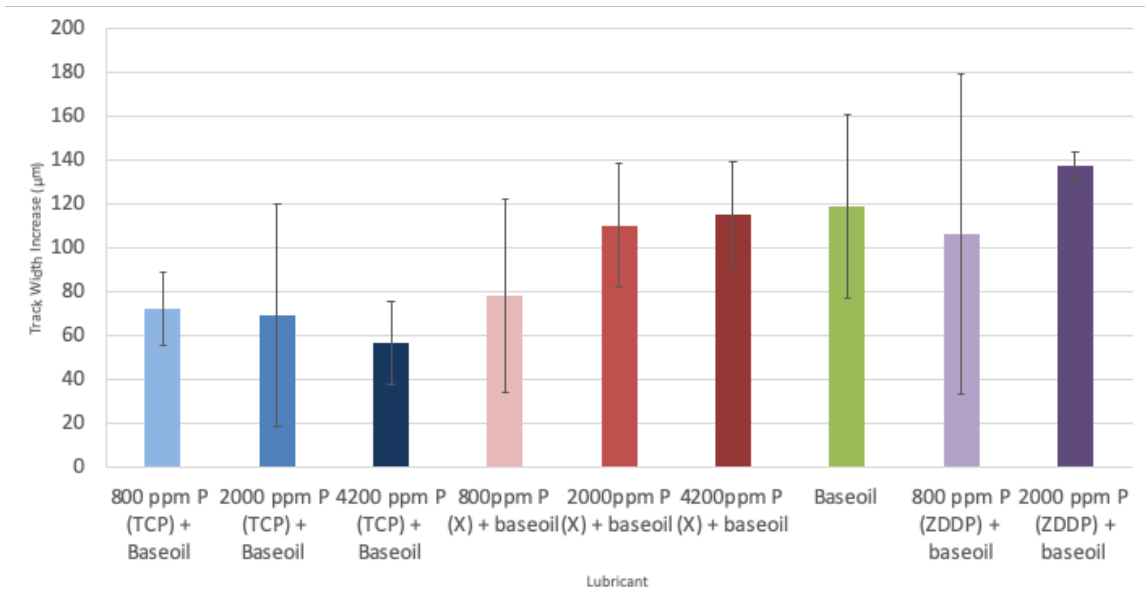
Figure 5-8 – Mean wear track increase results for the different concentrations of different anti-wear additive lubricant formulations.

Mass Loss

The mean mass loss results are shown in Figure 5-9. These results show a very similar trend to the Wear Track Width Increase results with the exception that the scale of these results are very small as the mass loss was small for all tests. It is expected that these results should closely correlate as the material lost should directly correlate to change in geometric profile (wear track width in the case) and consequently loss of mass. The TCP tests showed a decrease in mass loss with increasing concentration, whereas additive X showed an increase in mass loss as the concentration increased. The 2000 ppm P (ZDDP) had the highest mass loss followed by the base oil test, but the 800 ppm P (ZDDP) was relatively small in comparison. It can be seen that the size of the error bars for the 800 ppm P (ZDDP) vary between the mass loss and track width increase results. For the repeats of this test, one test resulted in a lot less micropitting and therefore track width increase and mass loss than there other 2 repeats. However, this resulted

in a larger variation in final track with rather than the final mass which accounts for this difference. Also, the scale of the mass loss results is different the track with increase graph which also accounts for the size difference. These results highlight again that the severity of micropitting has led to the largest mass loss, more than base oil alone therefore, showing the importance of limiting the promotion of micropitting.
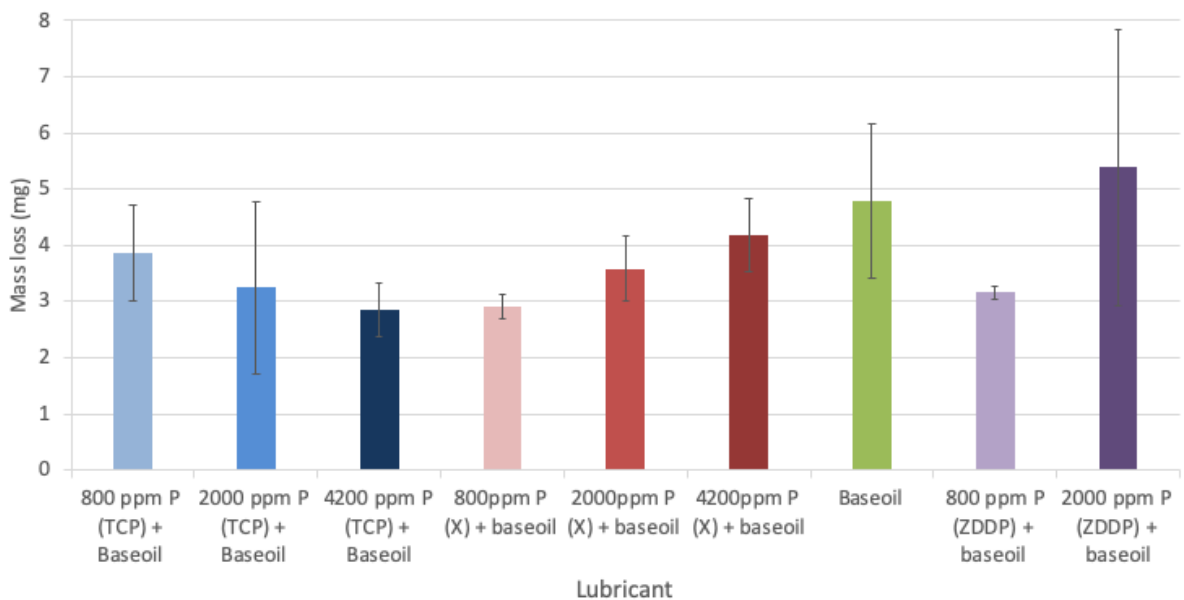
Figure 5-9 – Mean mass loss results for the different concentrations of different anti-wear additive lubricant formulations.

Stribeck Analysis

This section interprets the Stribeck curves from the MPR tests. The initial and final average Stribeck curves for TCP and base oil can be seen in Figure 5-10 and Figure 5-11. There is a close grouping of traction coefficients and all tests show a small decrease in traction coefficient from the beginning to the end of the test. In general, the base oil test consistently has the lowest traction coefficient and then the different concentration of TCP shows little variation outside of the error bar range. At the start of the test it could be argued that 4200 ppm P (TCP) has the highest friction, but this decreases and has a similar traction coefficient as the other concentrations as the Hersey number increases.

147
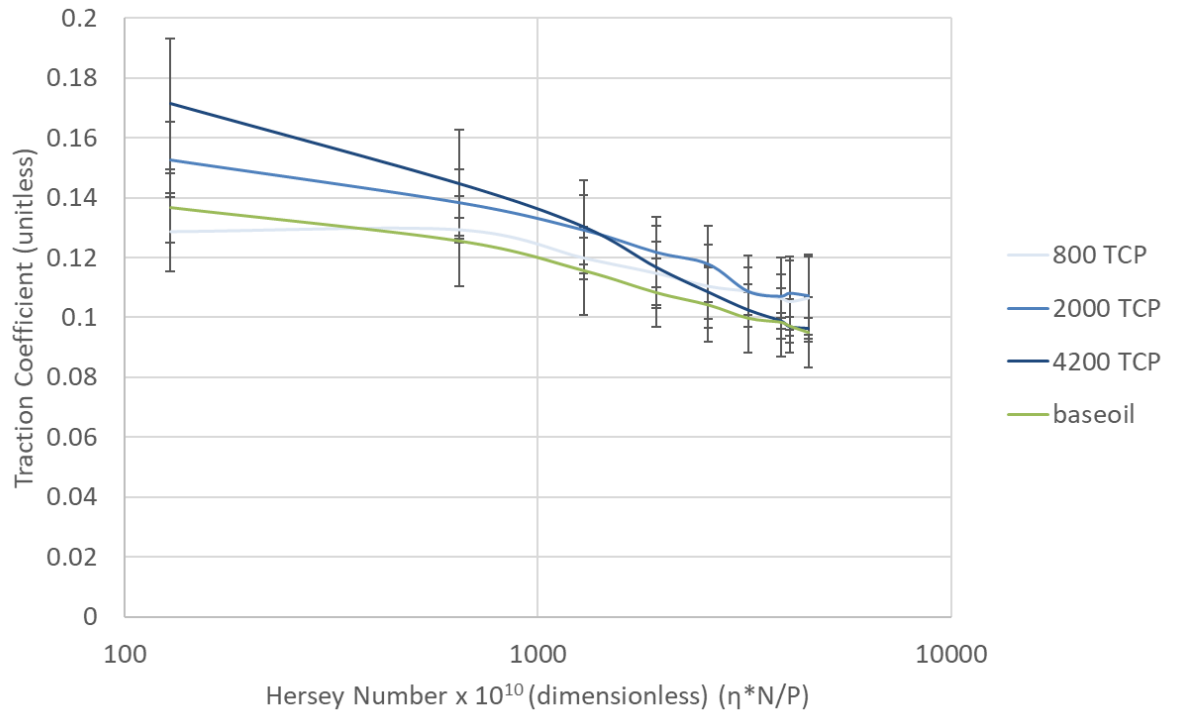
Figure 5-10 – Mean average Stribeck curves for the different concentrations of TCP and base oil at the beginning of the test.
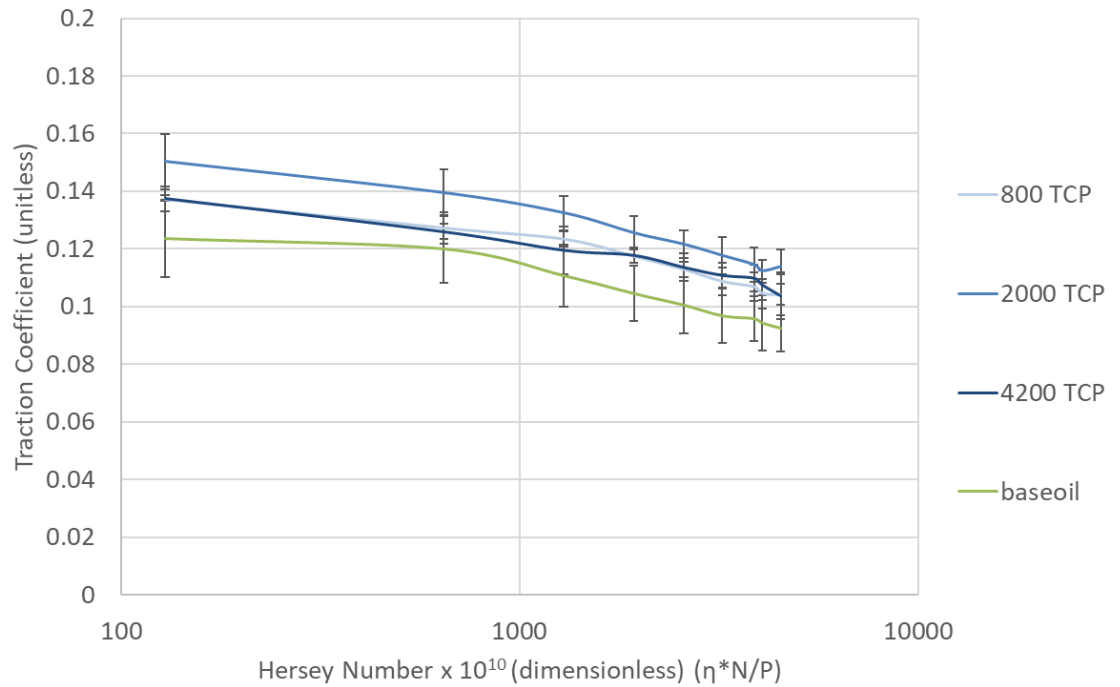
Figure 5-11 – Mean average Stribeck curves for the different concentrations of TCP and base oil at the end of the test.

The initial and final mean average Stribeck curves for additive X and base oil can be seen in Figure 5-12 and Figure 5-13. For both graphs, there is little to no variation in traction coefficient between the different concentrations and base oil and there is only a slight decrease in friction from the initial to the final Stribeck curves.
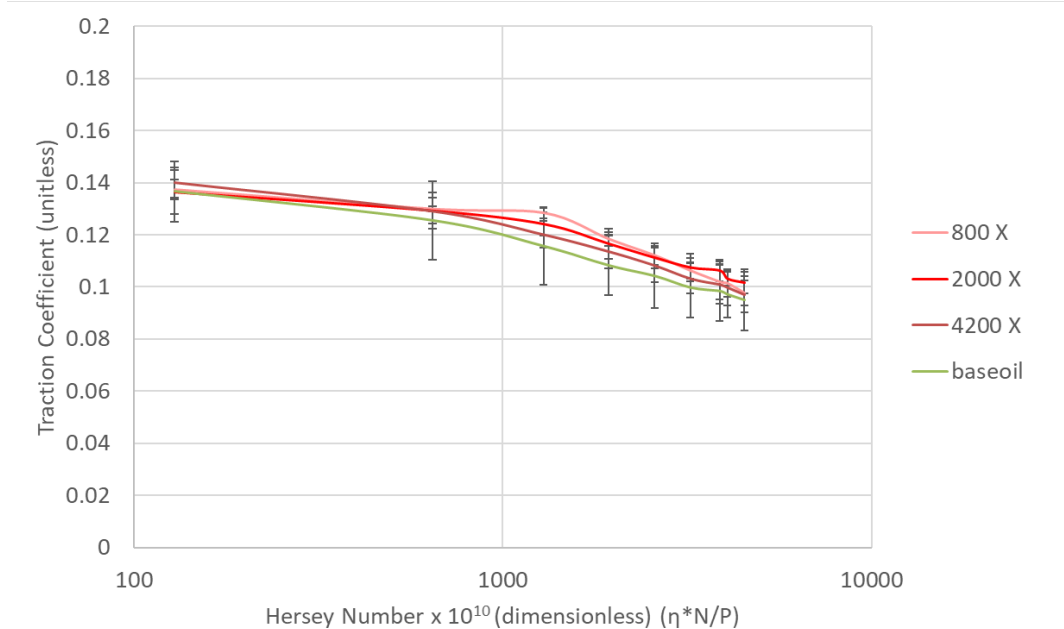
Figure 5-12 – Mean average Stribeck curves for the different concentrations of additive X and base oil at the beginning of the test.
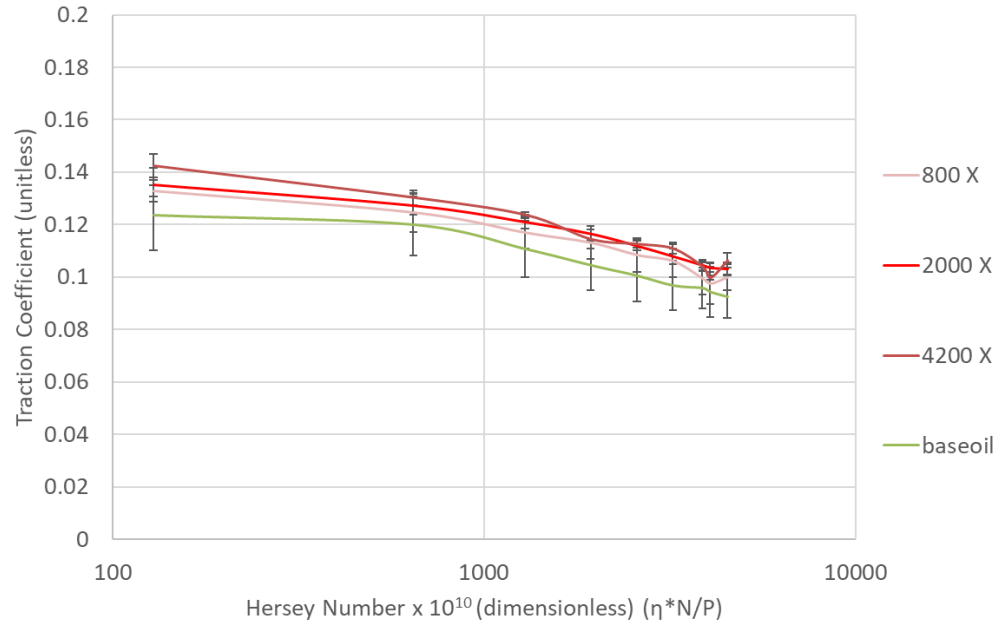
Figure 5-13 – Mean average Stribeck curves for the different concentrations of additive X and base oil at the end of the test.

149

The initial and final average Stribeck curves for ZDDP and base oil can be seen in Figure 5-14 and Figure 5-15. For both graphs, there is only a slight decrease in friction from the initial to final Stribeck curves. However, in comparison to TCP, ZDDP has a lower traction coefficient at both concentrations than base oil at lower Hersey numbers and they all converge as the Hersey number increases. This is a surprising result given the amount of wear on the surface and the amount of micropitting seen from ZDDP. It could be that as the ZDDP results in the quick formation of small micropits and maintains this wear mechanism throughout the test. The roughness remains lower than that created for more severe wear and pitting which, leads to a lower friction. However, the initial Stribeck curve would not have micropitted that quickly and it is likely the lower friction is a function of the tribofilm giving rise to a lower friction.

The initial and final average Stribeck curves comparing the TCP, additive X and ZDDP at 800 ppm P can be seen in Figure 5-16 and Figure 5-17. The traction coefficient for all the additives decreases from the initial to final curve. ZDDP again has a lower traction coefficient than the other additives and the two ashless additives consistently have very similar friction on both graphs.
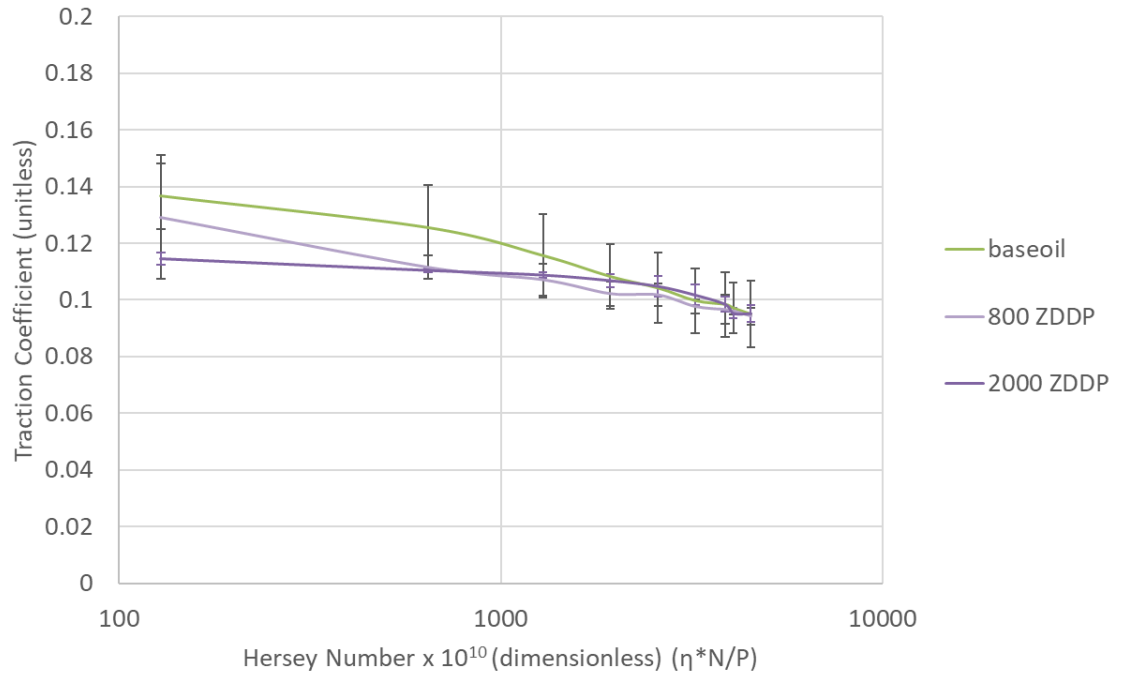
Figure 5-14 – Mean average Stribeck curves for the different concentrations of ZDDP and base oil at the beginning of the test.
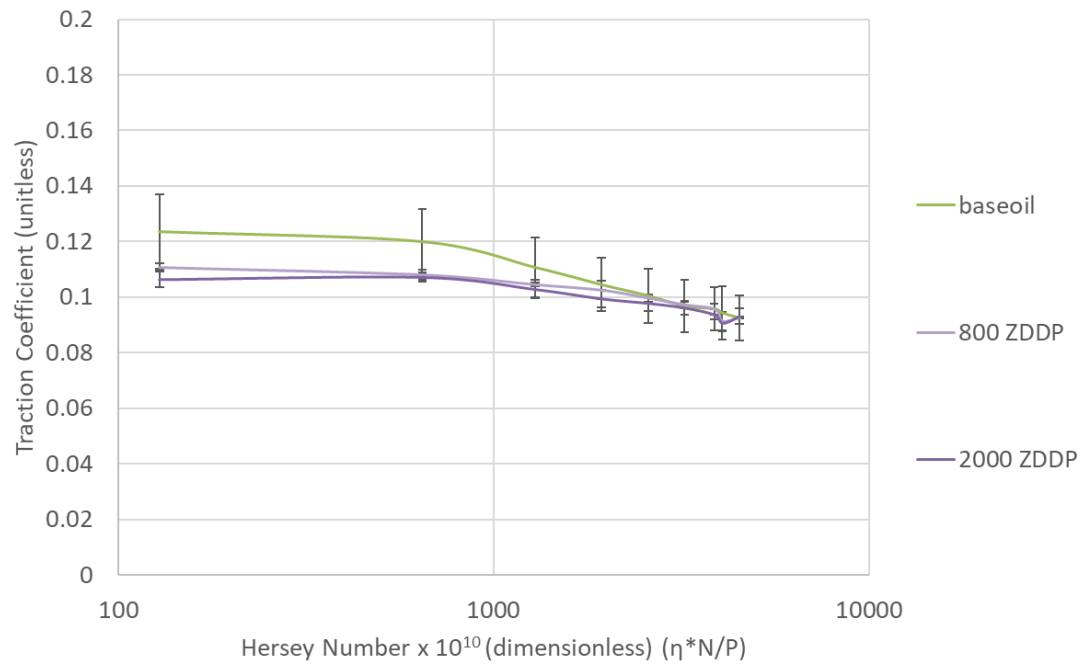
Figure 5-15 – Mean average Stribeck curves for the different concentrations of ZDDP and base oil at the end of the test.
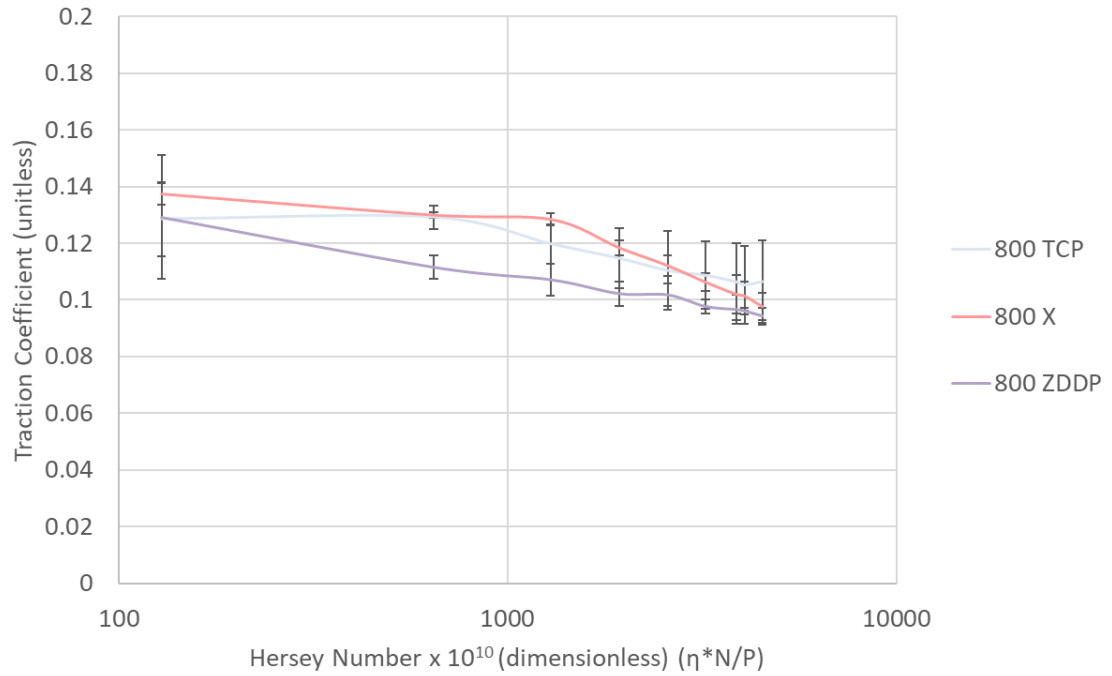
Figure 5-16 – Mean average Stribeck curves comparing the TCP, additive X and ZDDP at an equivalent phosphorus concentration of 800 ppm at the beginning of the test.
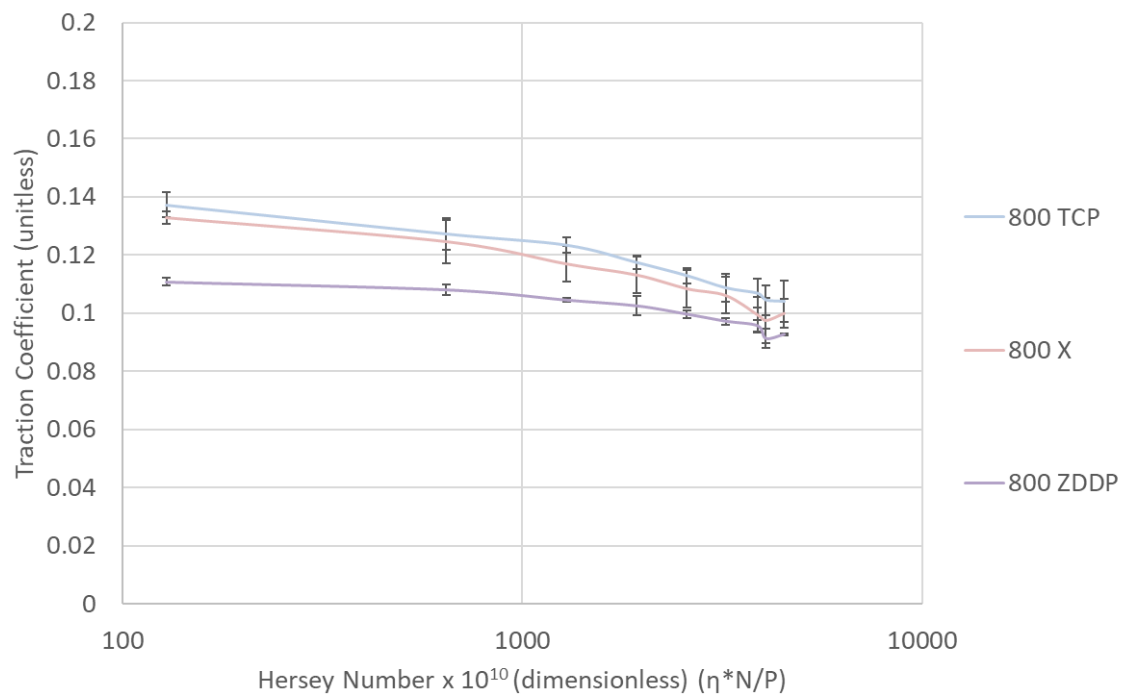
Figure 5-17 – Mean average Stribeck curves comparing the TCP, additive X and ZDDP at an equivalent phosphorus concentration of 800 ppm at the end of the test.

152

The initial and final mean average Stribeck curves comparing the TCP, additive X and ZDDP at 2000 ppm P can be seen in Figure 5-18 and Figure 5-19. There is very little change between the initial and final change curves for these additives at 2000 ppm P. The separation in traction coefficient is more prominent than for 800 ppm showing a clear difference between all the additives. ZDDP has the lowest traction coefficient followed by additive X and then TCP which, has the highest traction coefficient. This difference in friction could be related to the magnitude of micropitting promotion. It was be expected that due to the proposed mechanism of ZDDP promoting micropitting through early protection of asperities maintaining a rougher surface for longer, that the friction would in fact be higher, however, this is not seen.

It is possible the initial roughness of the surface may be contributing to whether ZDDP makes a surface rougher or smoother. Siavash (182) demonstrated that friction increased with ZDDP in comparison to base oil in an MPR using a ring and roller of roughness of R_q 500 ± 50 nm and 50 ± 5nm respectively but on 52100 steel. Here a smoother roller and rougher ring is used in comparison to the tests in this thesis. It is possible that the smoother roller could be the reason for the increase in friction, however, a lot of additional parameters were varied when compared with the MPR tests in comparison to this thesis. Friction has also been shown to increase with ZDDP in MTM tests by other workers (34,157,161,164).
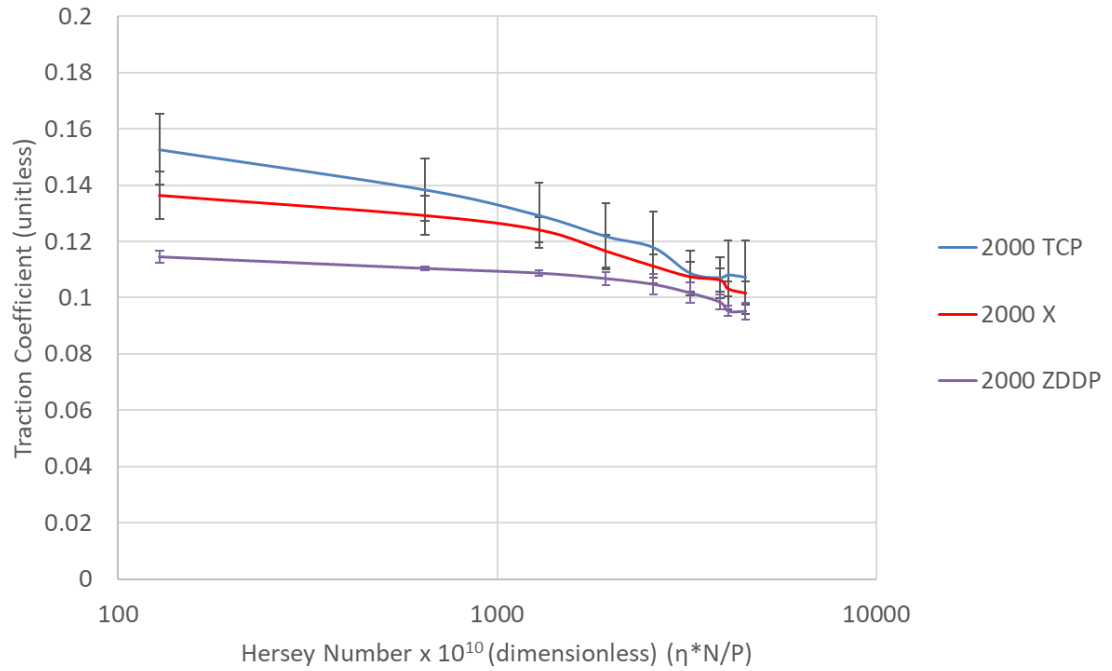
Figure 5-18 – Mean average Stribeck curves comparing the TCP, additive X and ZDDP at an equivalent phosphorus concentration of 2000 ppm at the beginning of the test.
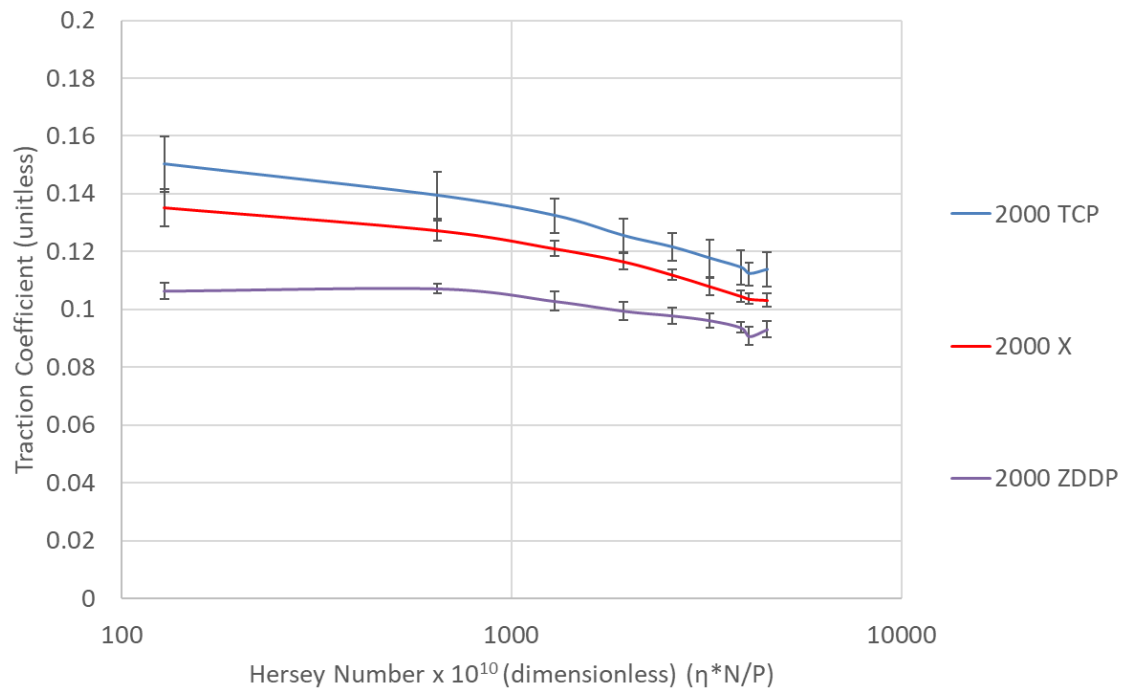
Figure 5-19 – Mean average Stribeck curves comparing the TCP, additive X and ZDDP at an equivalent phosphorus concentration of 2000 ppm at the end of the test.

154

Roughness

Bar charts showing the measured R_a roughness for the ring and the roller can be seen in Figure 5-20 and Figure 5-21. Figure 5-20 shows there is a substantial decrease in roughness in comparison to a fresh unworn specimen for all oils. Unfortunately, there is no roughness measurement for 800 ppm P (ZDDP). ZDDP appears to have maintained the highest roughness which, coincides with the theory that ZDDP protects and maintains asperity roughness as part of its micropitting promotion mechanism. These results for additive X are less rough and do not show any trend with concentration. The lower concentration TCP blends at 800 ppm P and 2000 ppm P have the lowest roughness followed by the base oil. These results follow a similar trend in the order ZDDP, additive X and TCP, which, show decreasing micropitting promotion (from ZDDP to TCP), reflecting how effective the additive is at maintaining asperity roughness.

It can also be seen from these results that the error in Ra is less than in Chapter 6, which, could potentially infer there is less variation in tribological performance from simpler formulations, however, this would need to be investigated further. In addition, there were less repeats of some of the tests in the full formulation studies due to limited number of specimens which, could contribute to this increase in error.

Figure 5-21 shows there is a lot of variation in roller roughness in comparison to a new roller as expected from the different amounts on wear in each test. Four profiles were taken from four points around the circumference of the wear track all 90 ° apart using the Talysurf profilometer and a mean value was taken. Therefore, if a large pit happened to be at any of these points, this could dramatically influence the measured value and produce large errors. However, the roller roughness results show that for some tests there is a large increase in roughness which, coincides with the excess damage seen in these tests. However, the test for ZDDP shows a decrease in roughness with very low amounts of error. This is potentially due to the formation of the very small micropits resulting in a lower roughness value despite having

excessive wear. A collection of many very small micropits could still produce a relatively smooth surface in comparison to less but larger micropits.
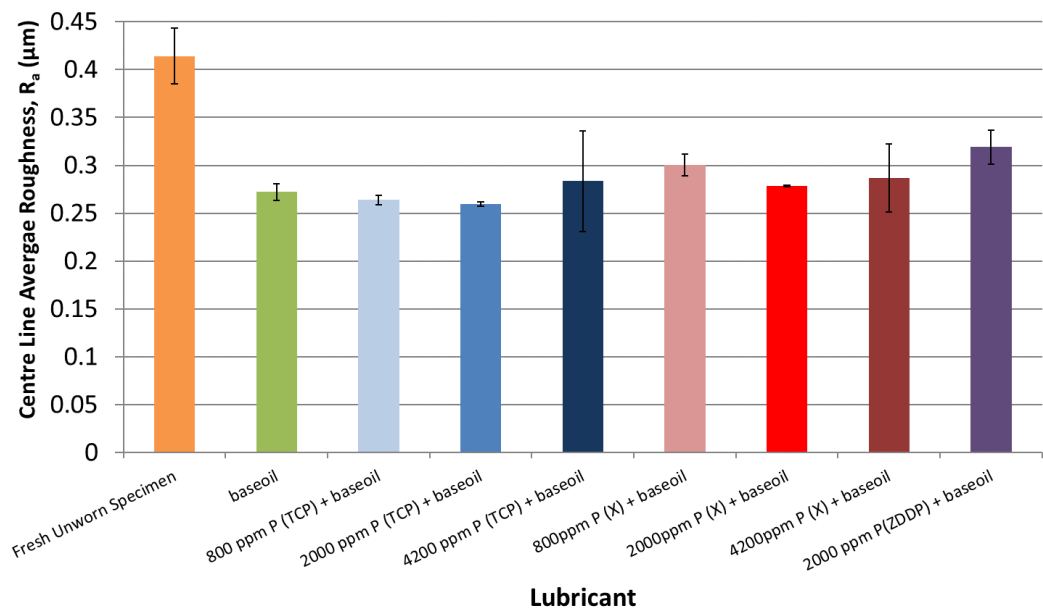
Figure 5-20 - Bar chart showing the mean centre line average roughness (Ra) of the ring specimens for the wear tests for the different types and concentrations of anti-wear additives, base oil only and a new ring.
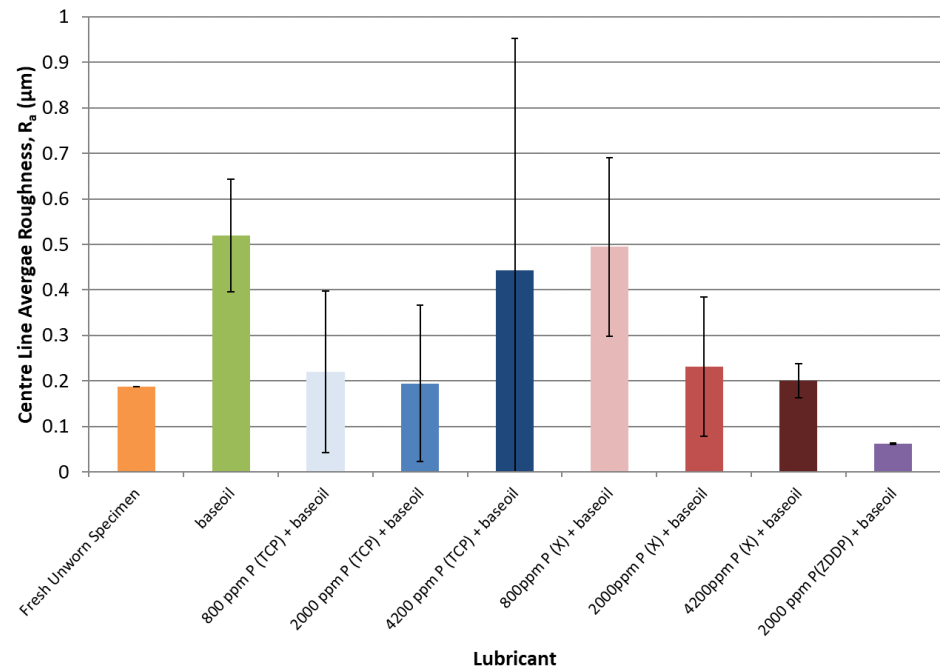
Figure 5-21 - Bar chart showing the mean centre line average roughness (Ra) of the roller specimens for the wear tests for the different types and concentrations of anti-wear additives, base oil only and a new roller.

156

5.2.2 SLIM Results

This section will discuss the results produced by the MTM-SLIM to further understand how the tribofilm formation contributes to the wear and micropitting produced.

Optical Microscope Wear Track Image Analysis
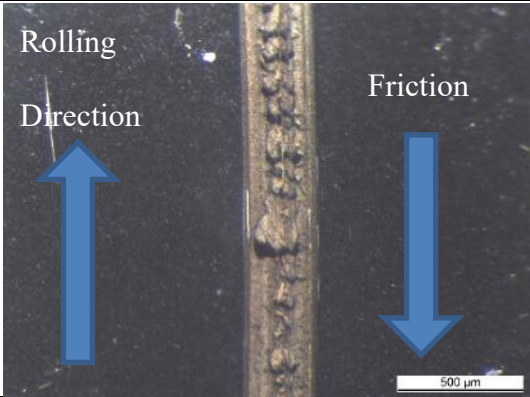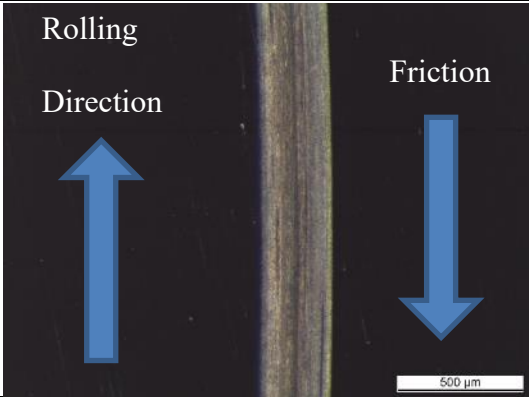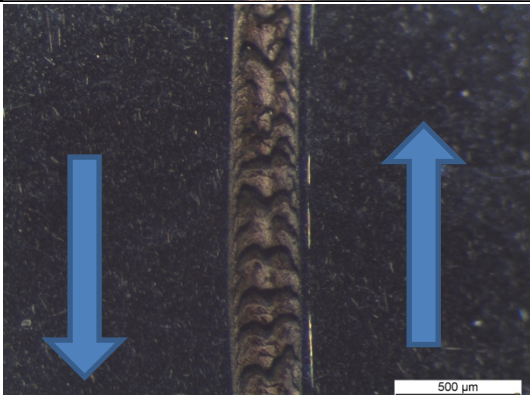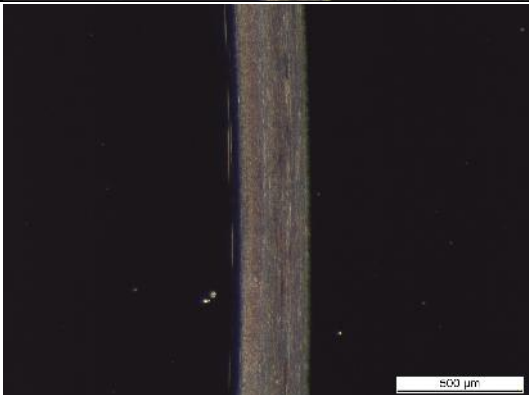
Figure 5-22 shows the wear track images for the ball and the disc for all of the wear tests with base oil and different concentrations of anti-wear additives. This Figure is also labelled with the rolling direction and direction of friction. Note these are directions can be reversed between images due to imaging the ball at different angles for different tests. However, the direction is only important when considering the characteristic shape of a pit. The direction can be deduced by looking at the curvature of the wear track. It is immediately obvious from these results that the base oil test performs very differently to the additised blends as the ball surface shows severe wear and pitting and both the ball and disc exhibit an orange-brown discolouration at the surface.
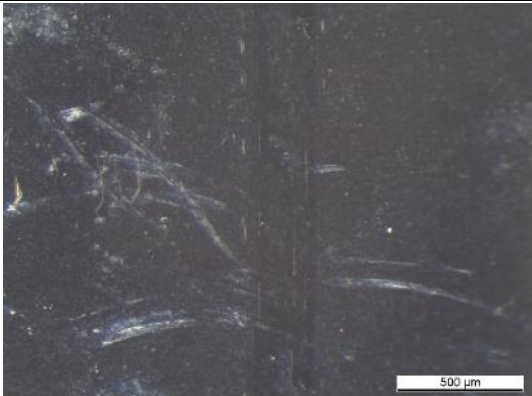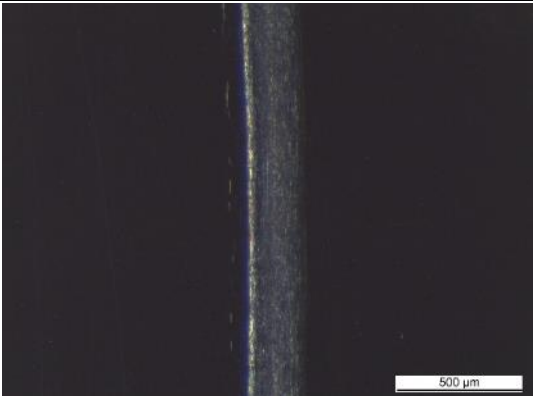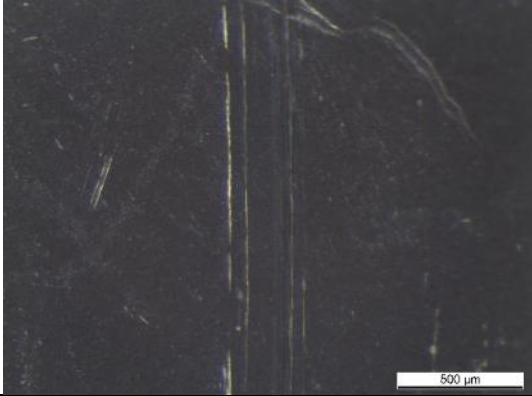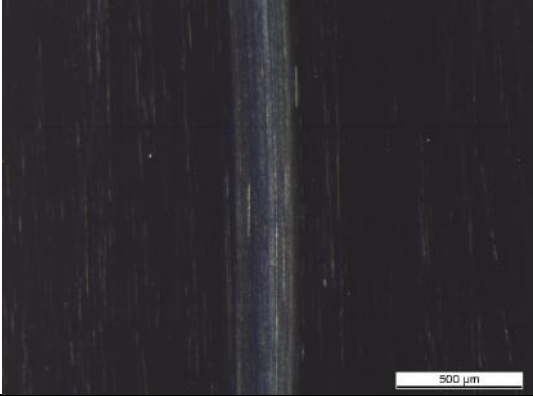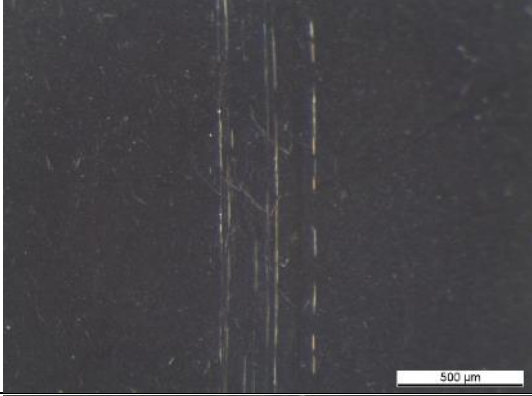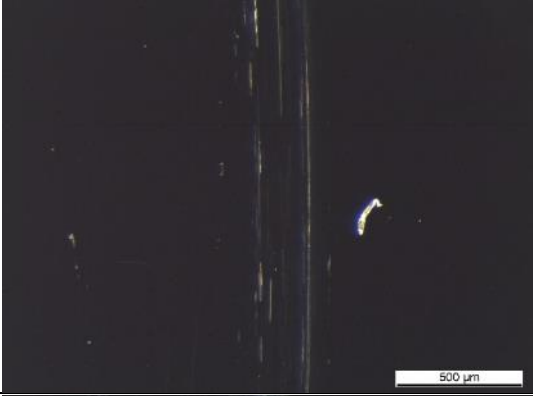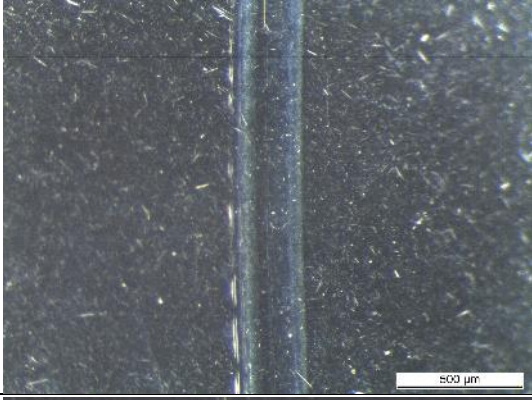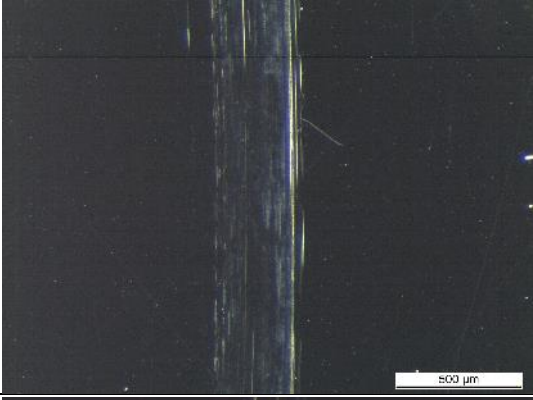
Using the ashless anti-wear additive formulations at the same concentrations as the MPR tests (800 ppm P, 2000 ppm P and 4200 ppm P) there is very minimal wear and discolouration and no effect of concentration is seen. There is only some very faint abrasion in the wear track in the form of narrow scores and white tracks.

To deduce if there was a minimum concentration required for protection for ashless additives, the concentration was diluted with more base oil to create blends with a lower concentration; 200 ppm P and 100 ppm P. It was found with TCP there was sufficient protection at 200 ppm P however, 100 ppm P resulted in a surface appearing very similar to the base oil test with large amounts of wear, pitting and an orange-brown discolouration. Whereas for additive X, whilst there was still sufficient protection for 200 ppm P, at 100 ppm P, some wear was starting to
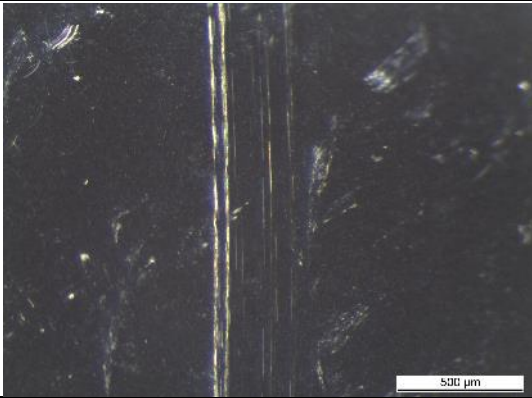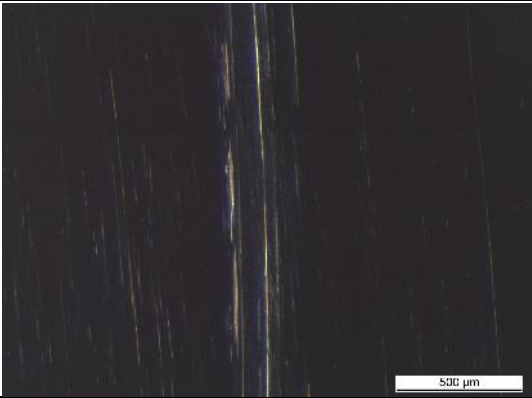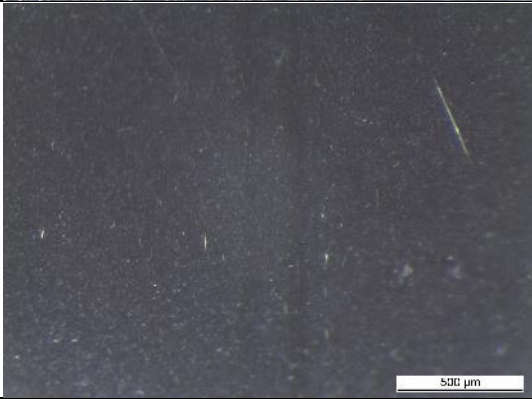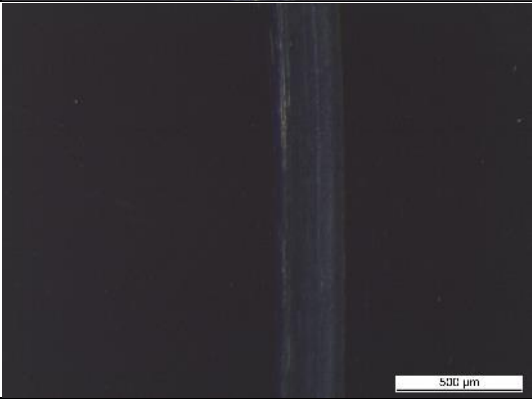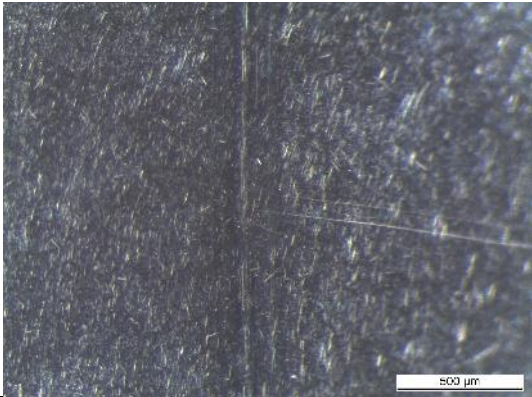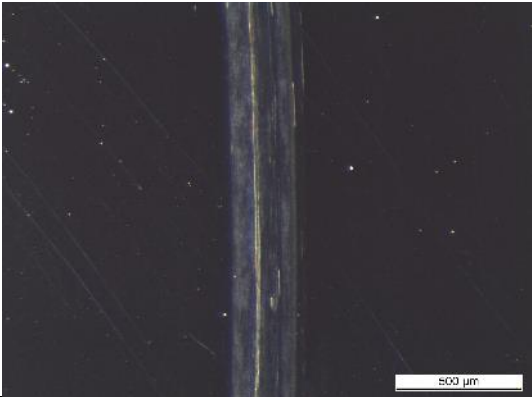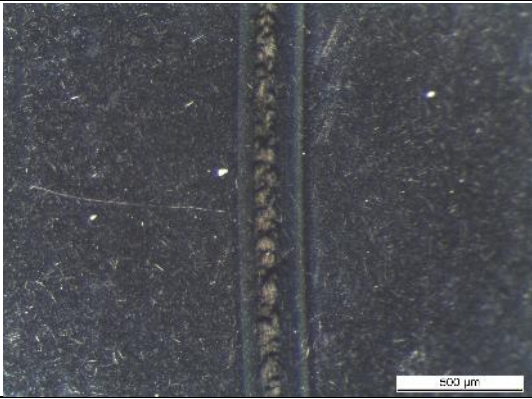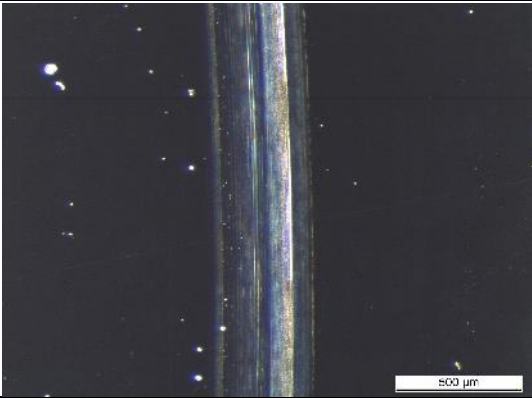
initiate with some orange-brown discolouration. This shows that additive is more active than TCP as it can still offer protection at a lower phosphorus concentration. ZDDP, however, appears different to the other additives in that there is a lot more discolouration in the wear track. It is likely the majority of this colour has come from the additive producing a visible tribofilm on the surface.

It should be noted that due to using superfinished smooth specimens, there was very minimal wear in these tests that could not be quantified using mass loss or wear track width increase (like for the MPR).

200 ppm P (TCP) + Base oil		
800 ppm P (TCP) + Base oil		
2000 ppm P (TCP) + Base oil		
42000 ppm P (TCP) + Base oil		

159
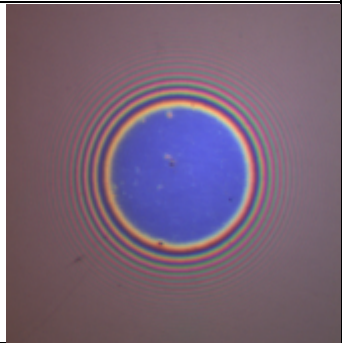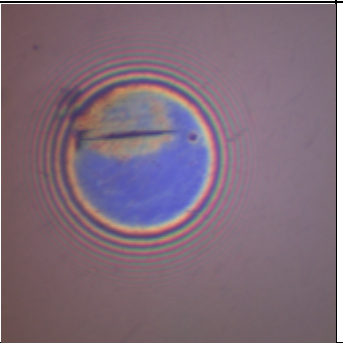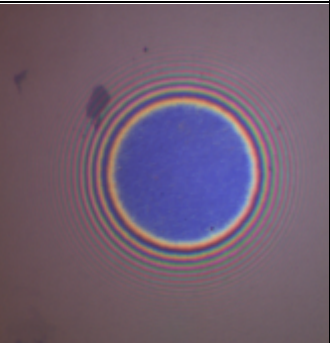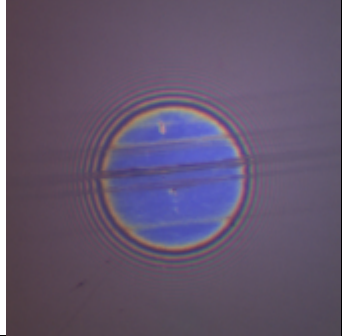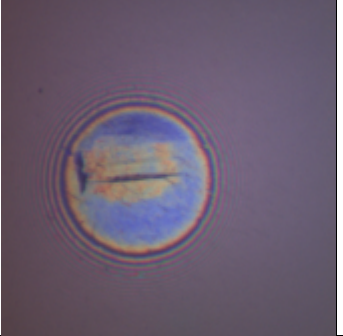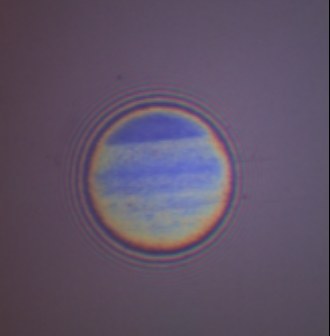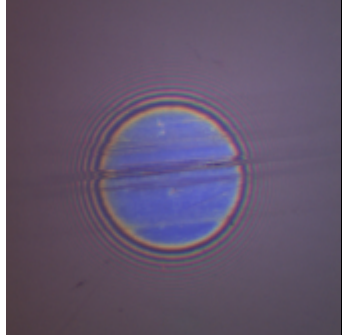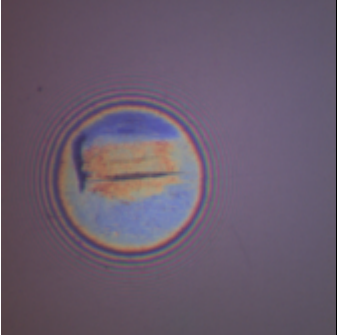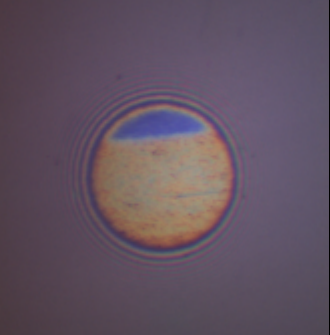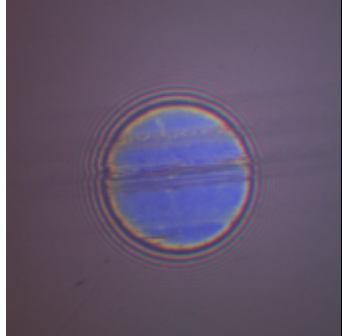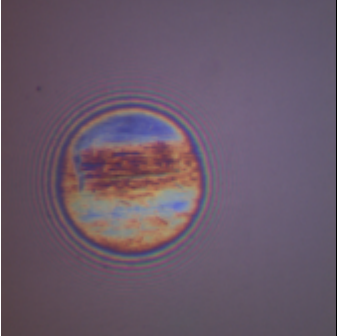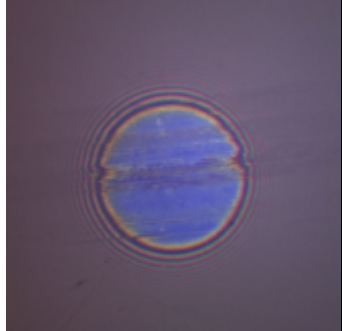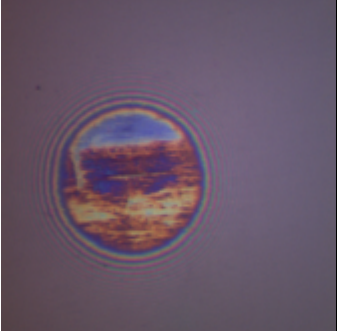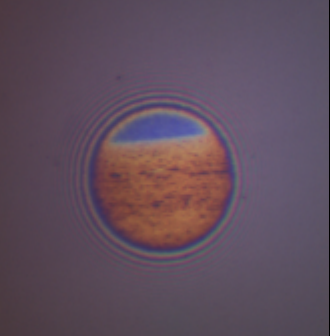
Figure 5-22 – Wear track optical microscope images of ball and disc specimens from the MTM-SLIM tests
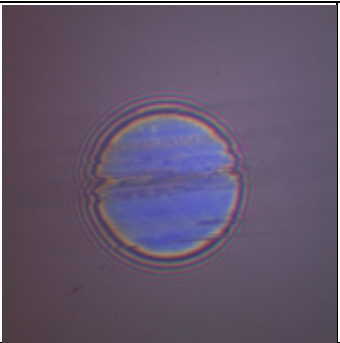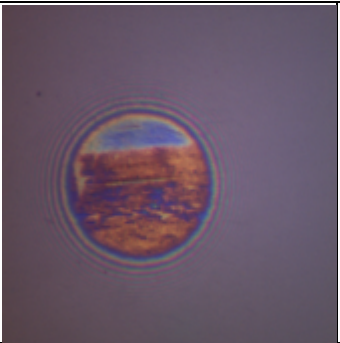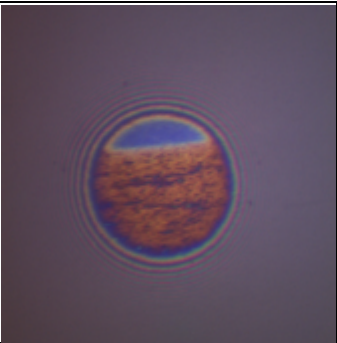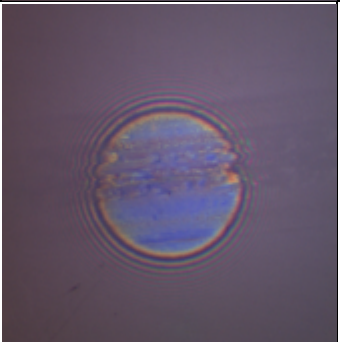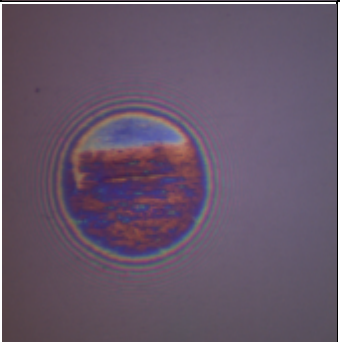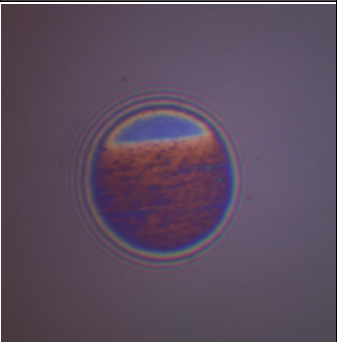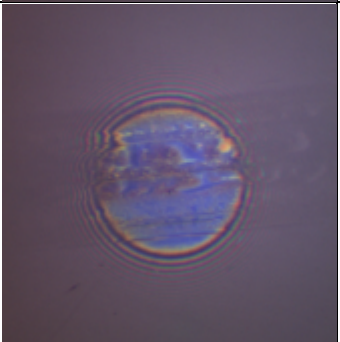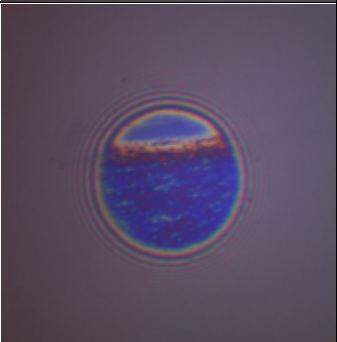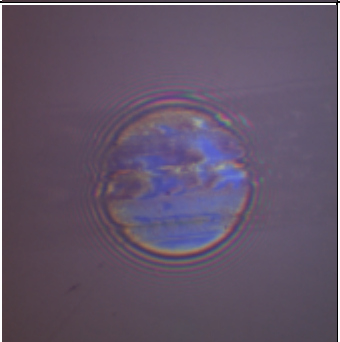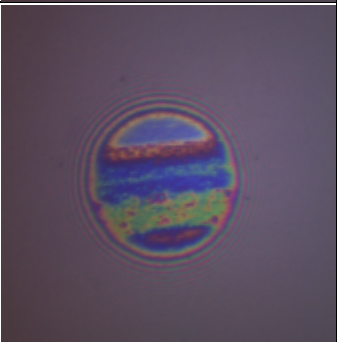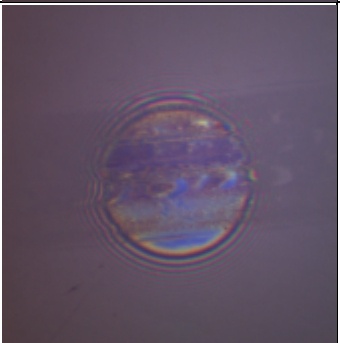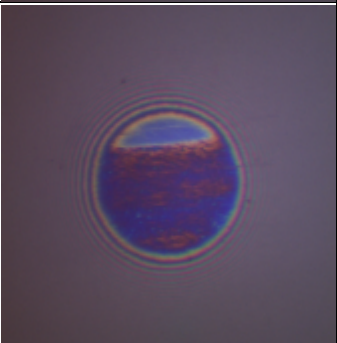
Interferometry Tribofilm Analysis
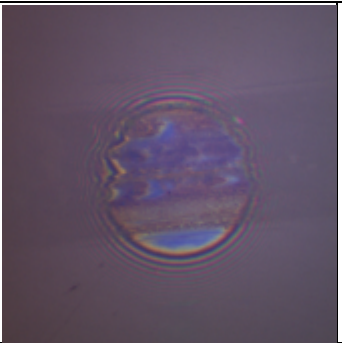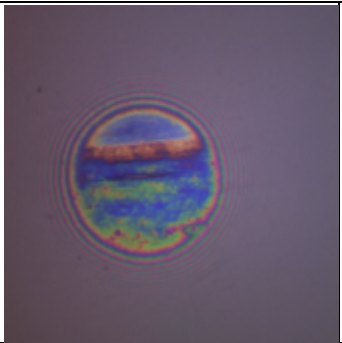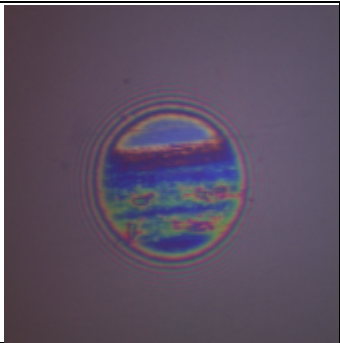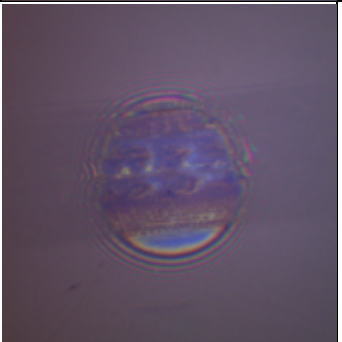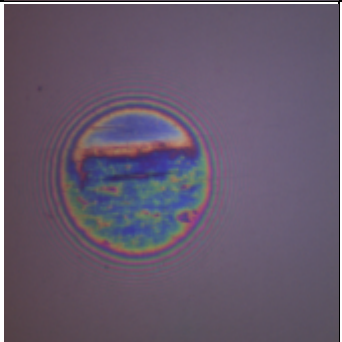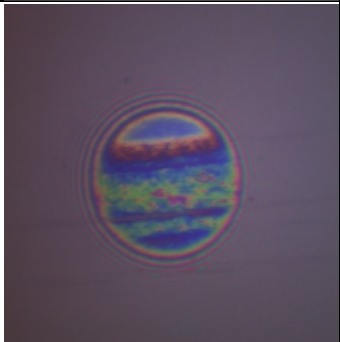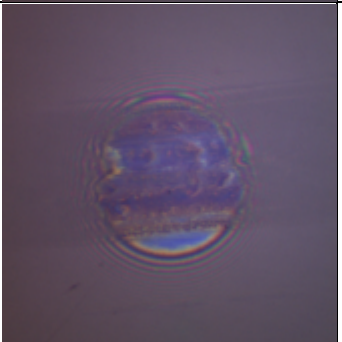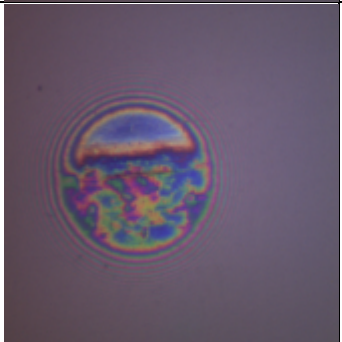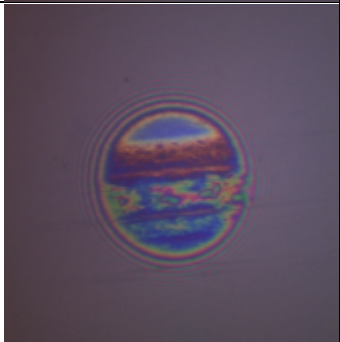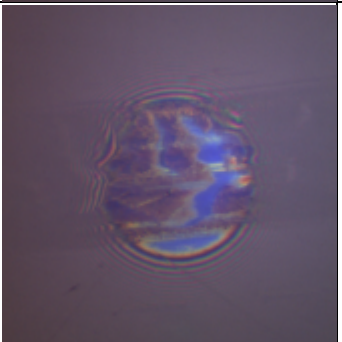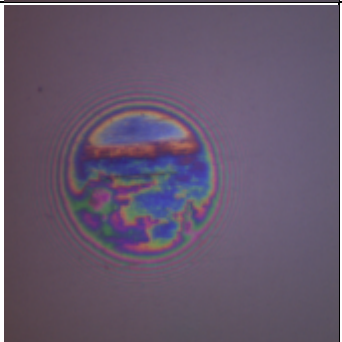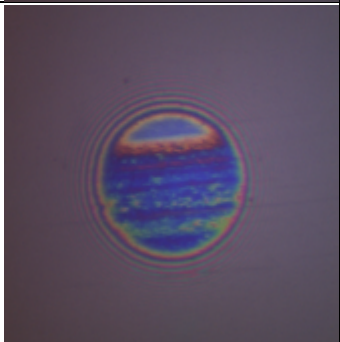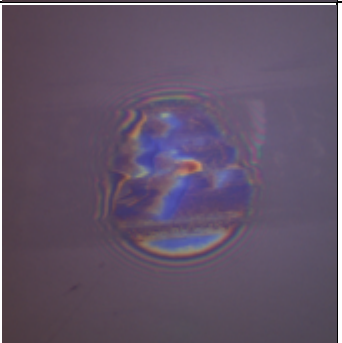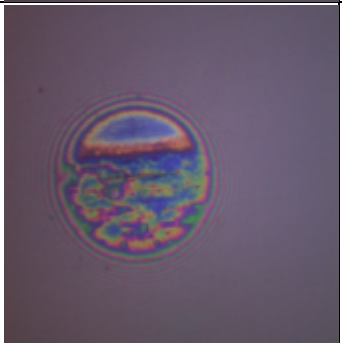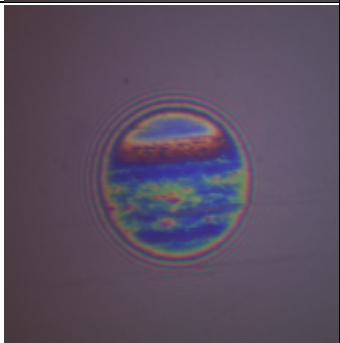
This section discusses the interferometry images throughout the MTM-SLIM tests for all the oils. Figure 5-23 shows the interferometry images for base oil and the different concentrations of ZDDP in base oil whilst Figure 5-24 shows the measured film thickness. There are no error bars for 800 ppm P (ZDDP) as only one test was completed. The base oil shows excessive wear, pitting and a misshapen contact on the mapper window and therefore, the film thickness was not measured as it would be interpreted as film thickness as shown from Figure 5-22. Both

161

ZDDP concentrations had a very thick tribofilm in comparison to the ashless additives with max film thicknesses between 120 nm to 140 nm. For the 800 ppm P (ZDDP) test, there is a small amount of damage on the window that remains throughout the test, however, this area was not measured when measuring the tribofilm thickness. There is a marginal effect of concentration, with the 2000 ppm having a higher tribofilm thickness than that for 800 ppm. Despite the error bars being large, the difference is outside of the error bar range. There is a plateau of film thickness which, may back up the theory of Zhang et al. (163) on the plastic deformation of the tribofilm leading to an increase in contact area which, consequently decreases the shear stress enough to prevent tribofilm formation. However, even though subsequent images from this plateau region of Figure 5-24 have subtle differences in features in the interferometry images, it is unclear whether these are due to new tribofilm formation or tribofilm removal. The thickness of these films could be responsible for the difference in wear track appearance in Figure 5-22; ZDDP appears to affect the surface more than the ashless additives, but still provides wear protection. But this test does not produce large amounts of wear, so the wear performance cannot be justified as much as from the MPR.

Test time (seconds) / Test Oil	Base oil	800 ppm P (ZDDP) + Base oil	2000 ppm P (ZDDP) + Base oil
0			
621			
1521			
2421			
3321			

4221			
7821			
12042			
15642			
19863			

23463			
27684			
31284			
35505			
39105			

43326			
46926			

Figure 5-23 - Interferometer images from the MTM-SLIM for different concentrations of ZDDP in base oil and also for the

pure base oil test
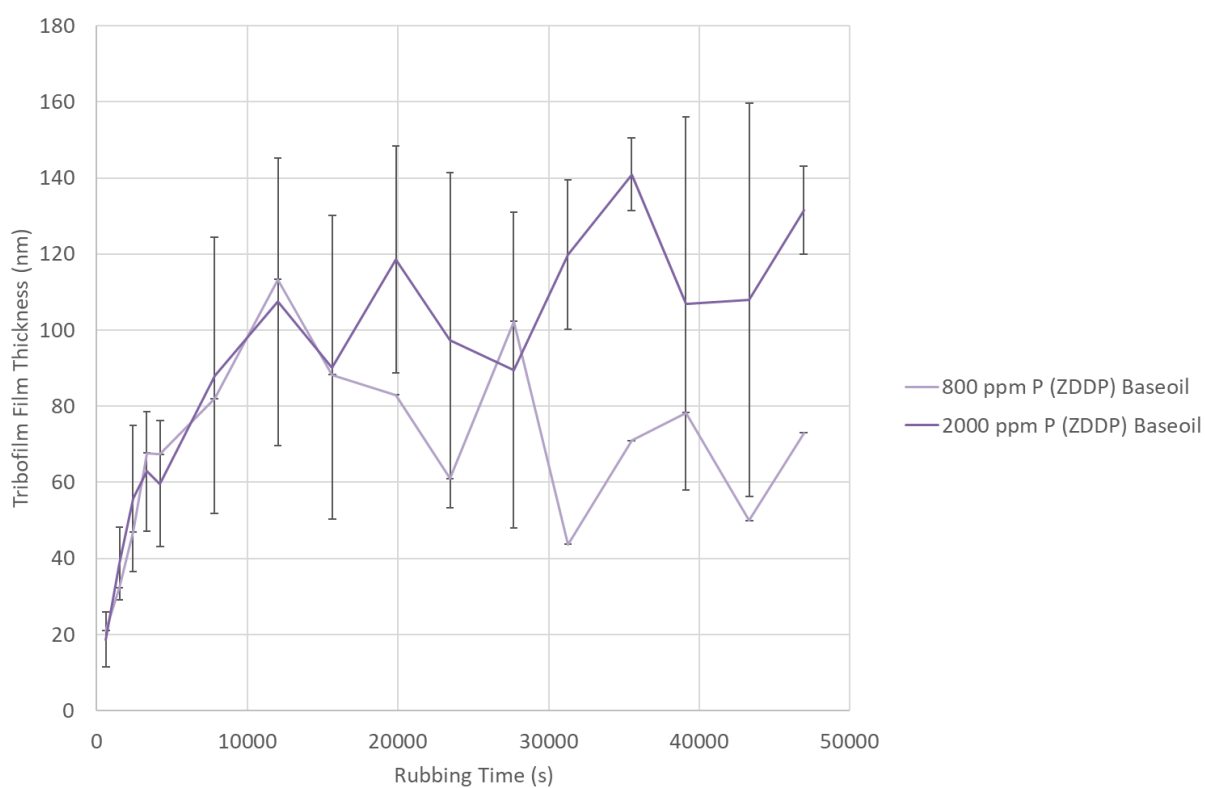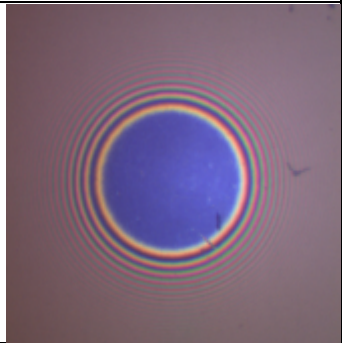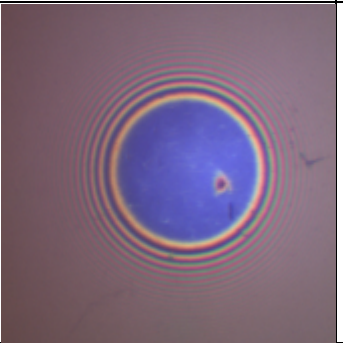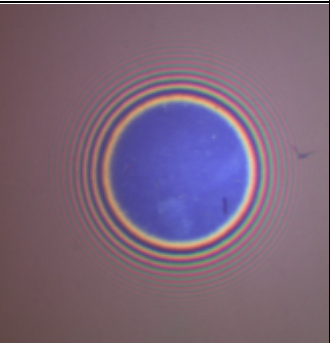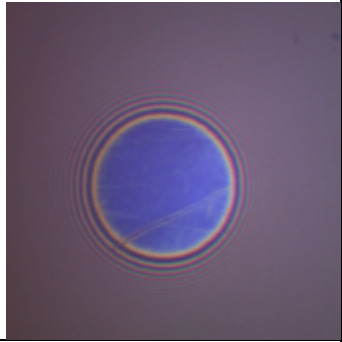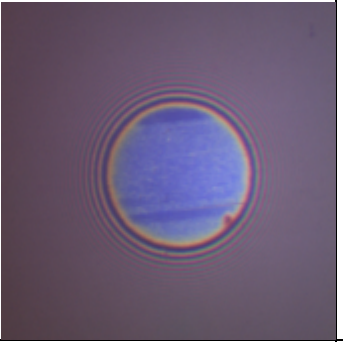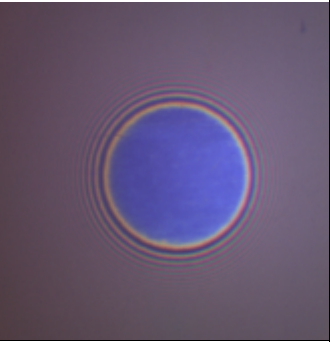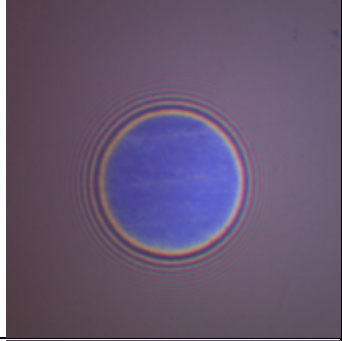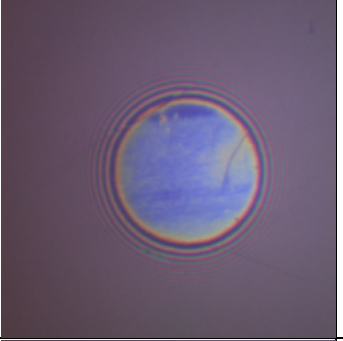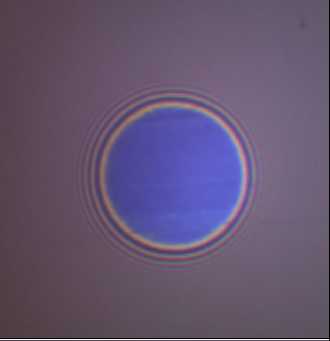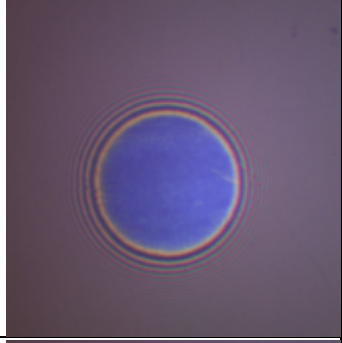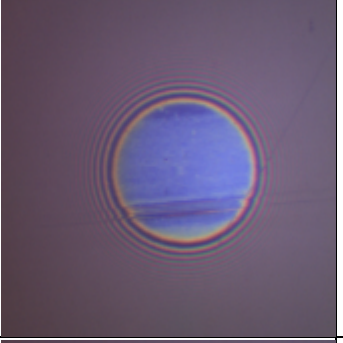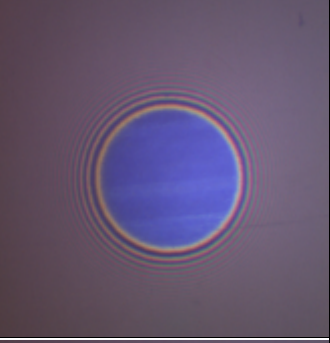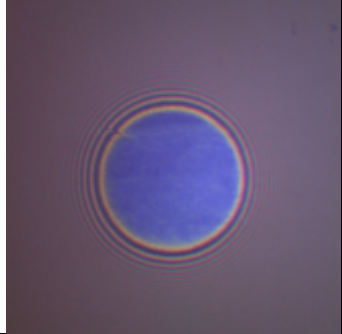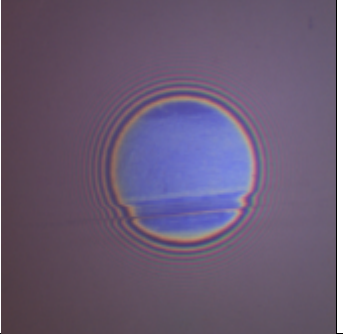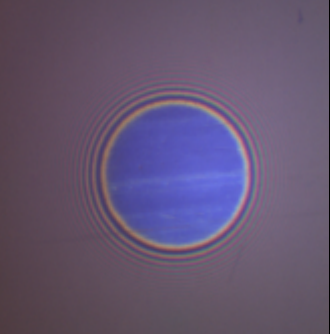
Figure 5-24 – Mean film thickness of ZDDP tribofilms from different concentration solutions against the rubbing time.
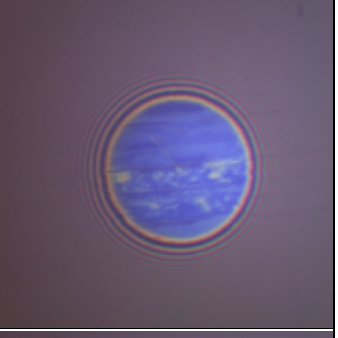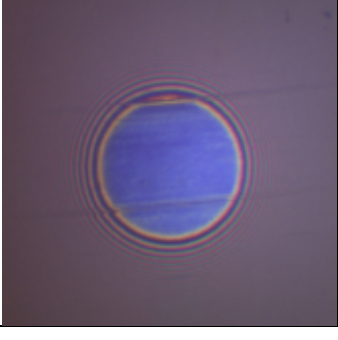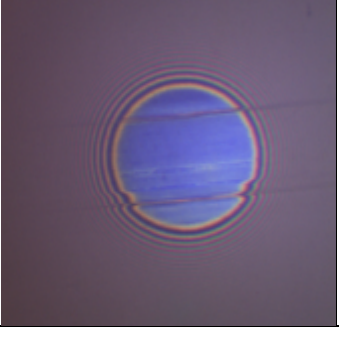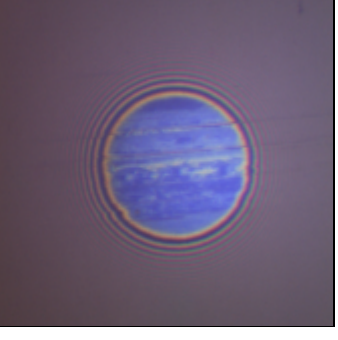
166
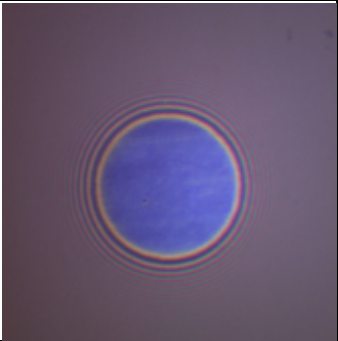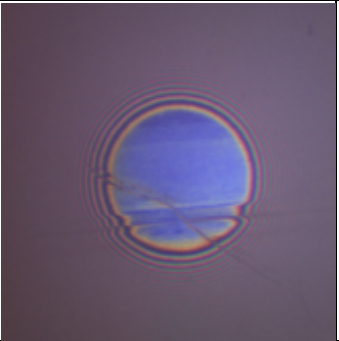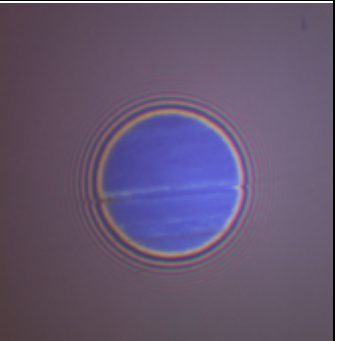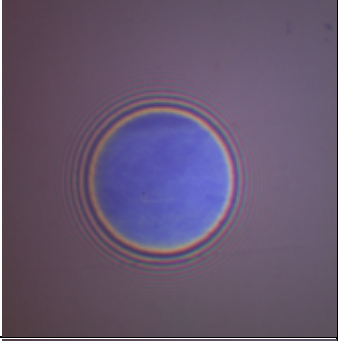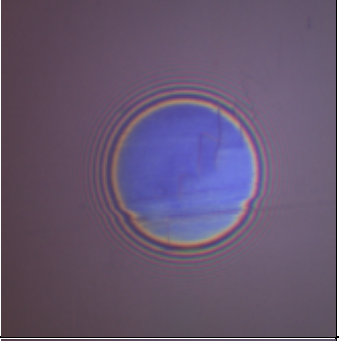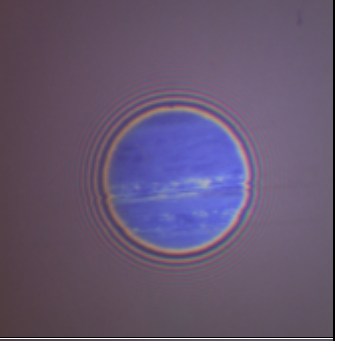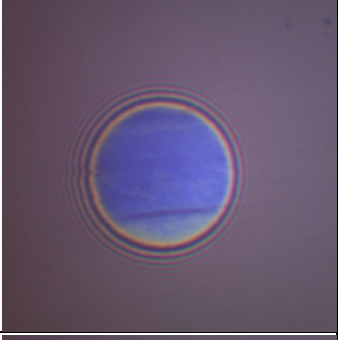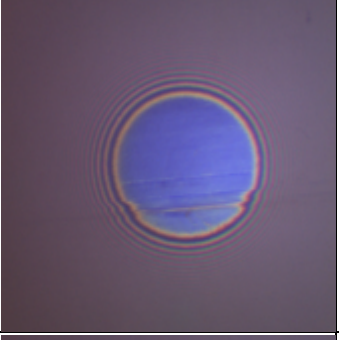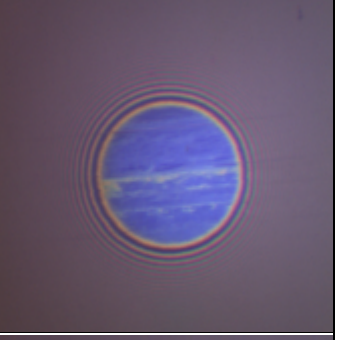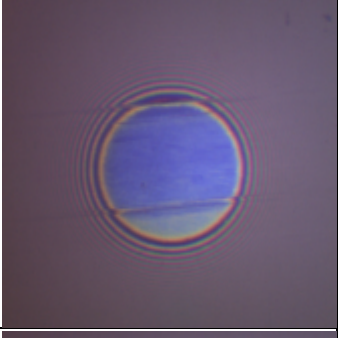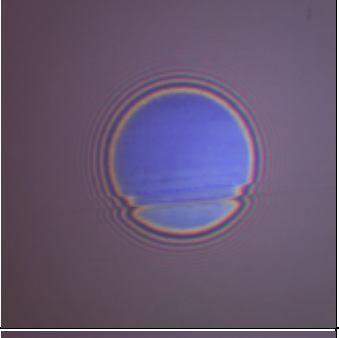
Figure 5-25 shows the interferometry images for TCP at phosphorus concentrations of 800 ppm, 2000 ppm and 4200 ppm and Figure 5-26 shows the interferometry images for TCP at the lower phosphorus concentrations of 100 ppm and 200 ppm. For all concentrations, the Hertzian contact on the mapper window remains blue for most of the test with only a very faint and thin film forming towards the end of the test.
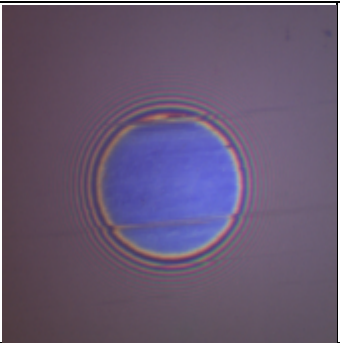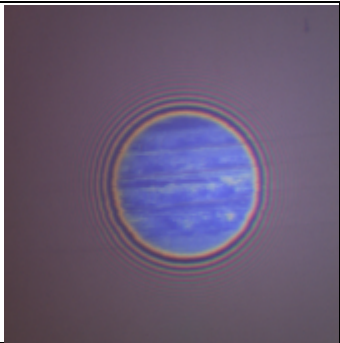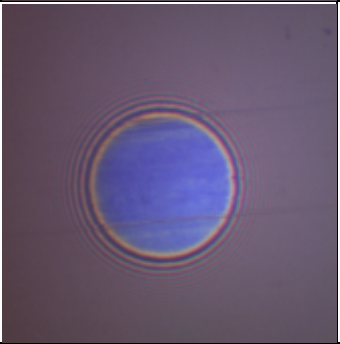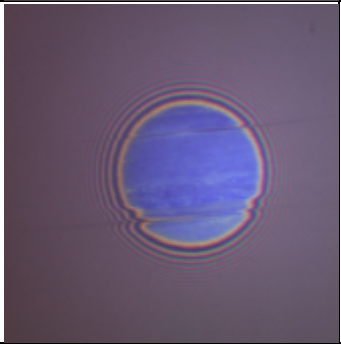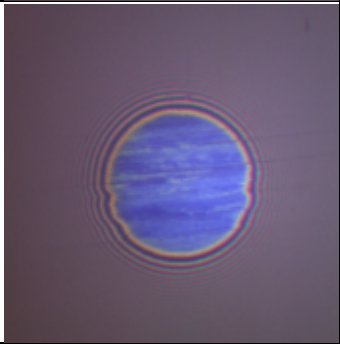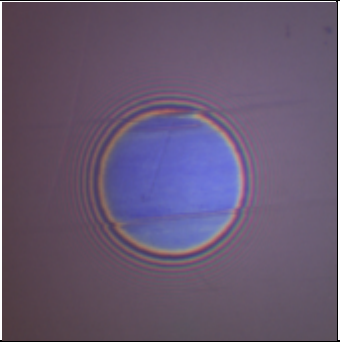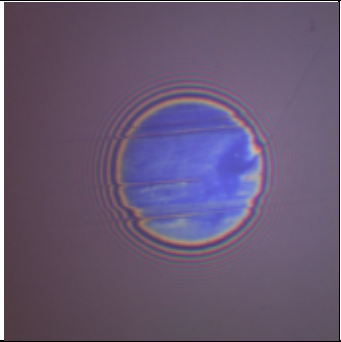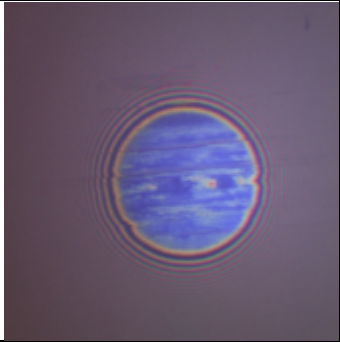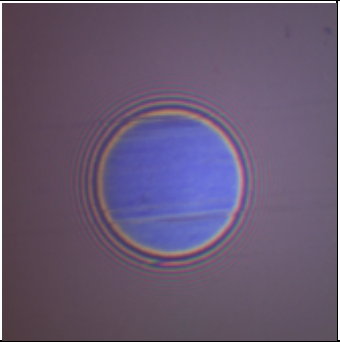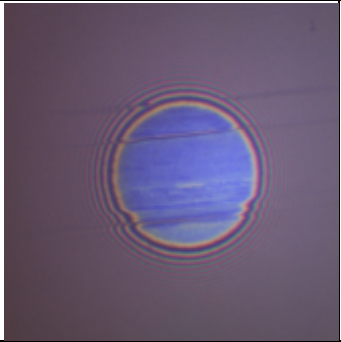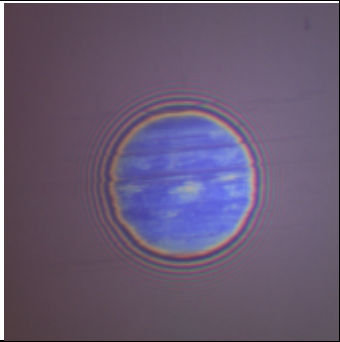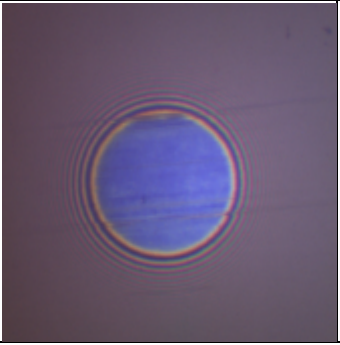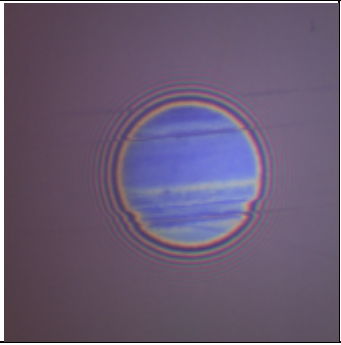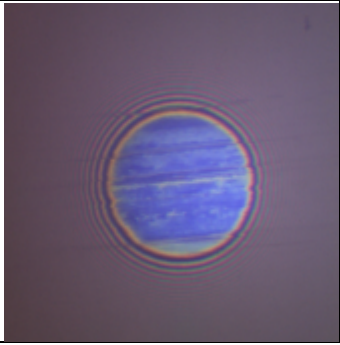
Figure 5-27 shows that only very thin films are formed of maximum thickness ~30 nm with no trend with concentration. The film thickness for the 100 ppm test was not measured due to it producing a surface resembling the test for base oil, thus it could not protect the surface at that concentration. It has been discussed how SLIM should not be used to measure film thickness when there are large amounts of wear as it cannot distinguish wear from film thickness. However, clearly whilst the tribofilms formed are very thin, there is no wear like that produced with the base oil alone as shown in Figure 5-23. This shows that TCP is still offering adequate protection despite not having a thick tribofilm. From observing the progression of the images, it appears the subtle changes in the images in subsequent steps are as a result of removal and reformation of tribofilm. This opposes the theory suggested for ZDDP where plastic deformation of the tribofilm results in a larger contact area decreasing the shear stress below that required for tribofilm formation (96,163,183). However, it could be that thinner ashless additives are weaker and therefore, more susceptible to being sheared off.

Test time (seconds) / Test Oil	800 ppm P (TCP) + Base oil	2000 ppm P (TCP) + Base oil	4200 ppm P (TCP) + Base oil
0			
621			
1521			
2421			
3321			

		169	
4221			
7821			
12042			
15642			
19863			

23463			
27684			
31284			
35505			
39105			

		171	
43326			
46926			
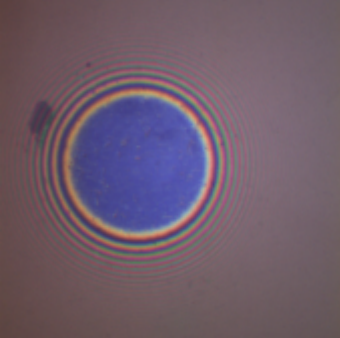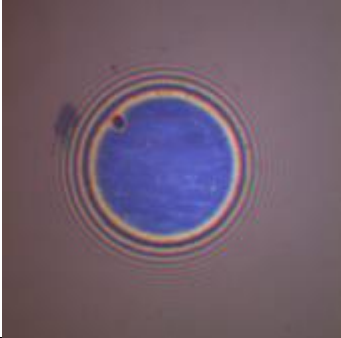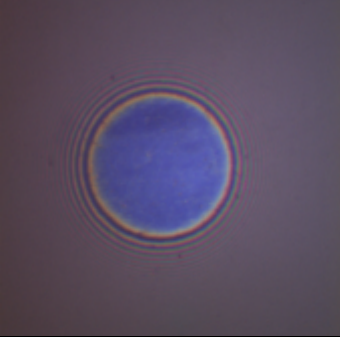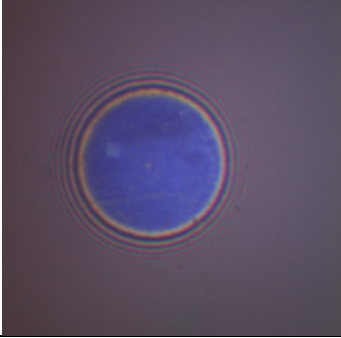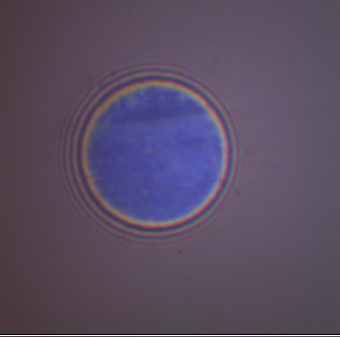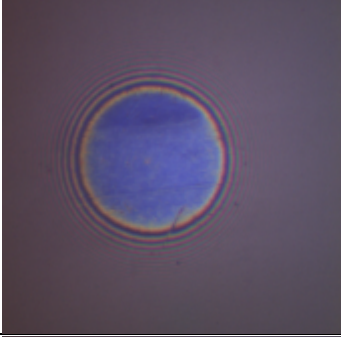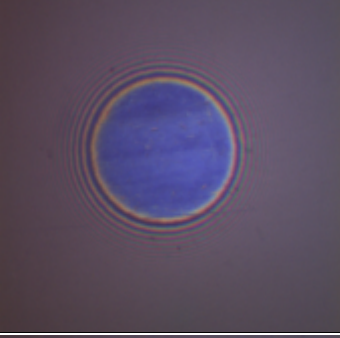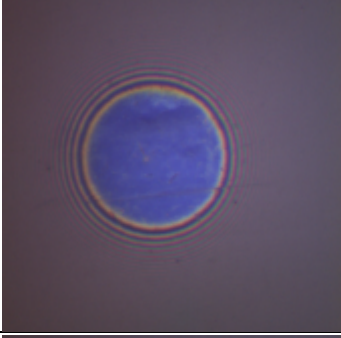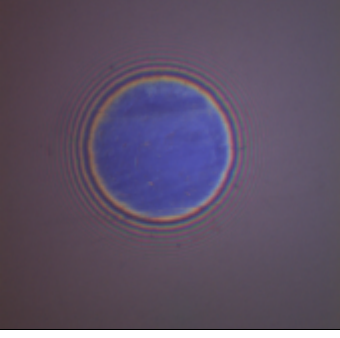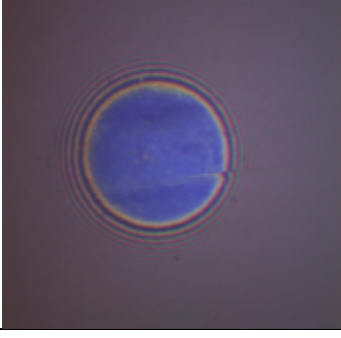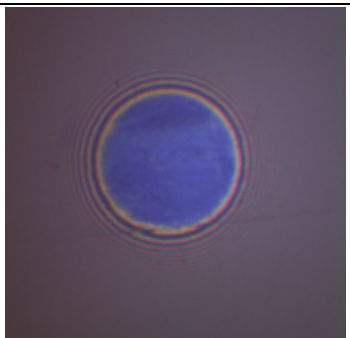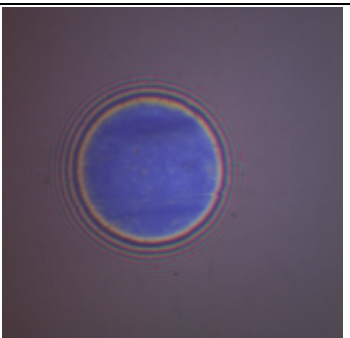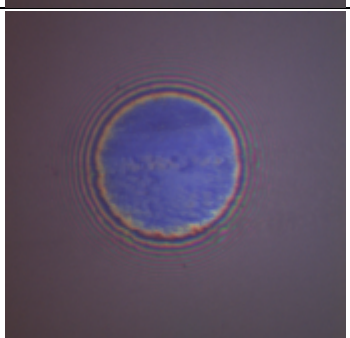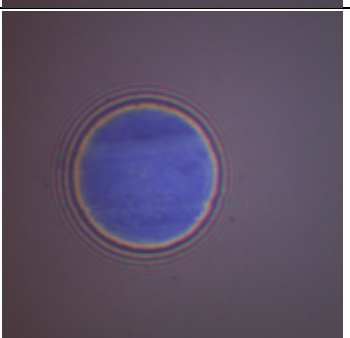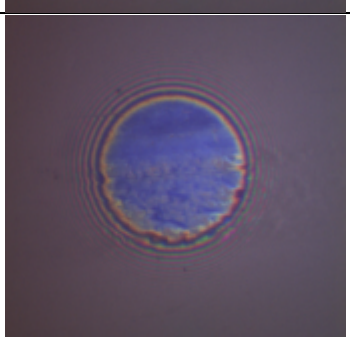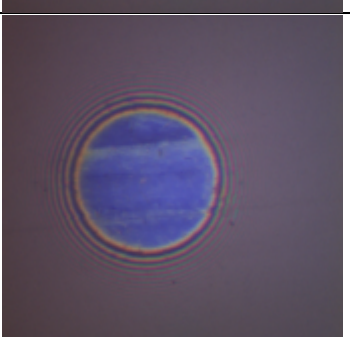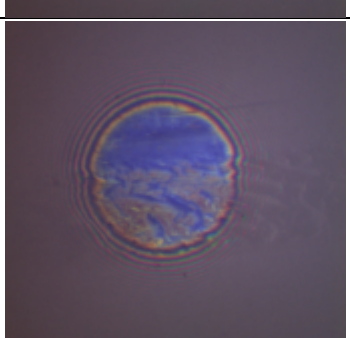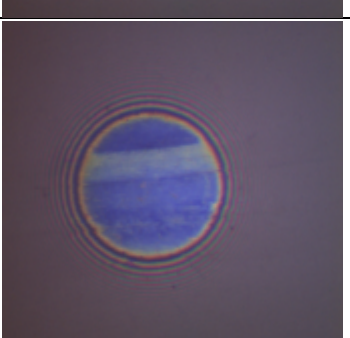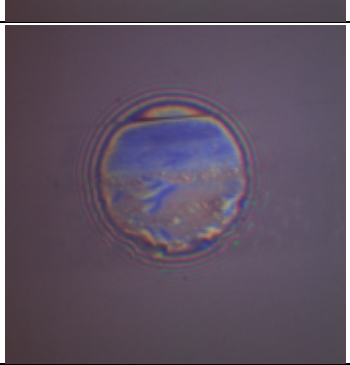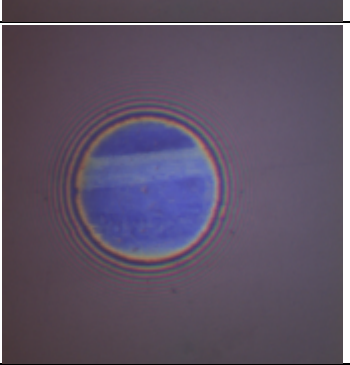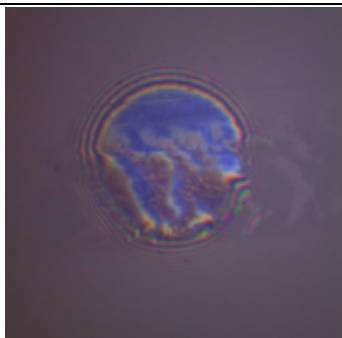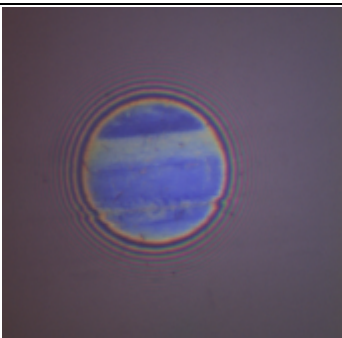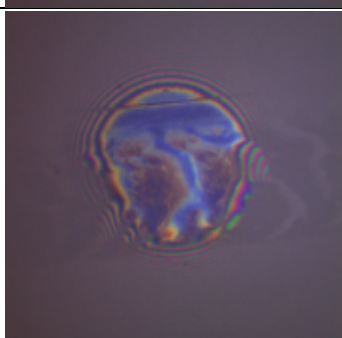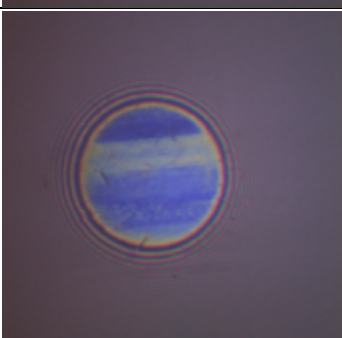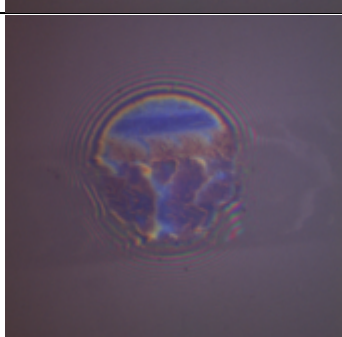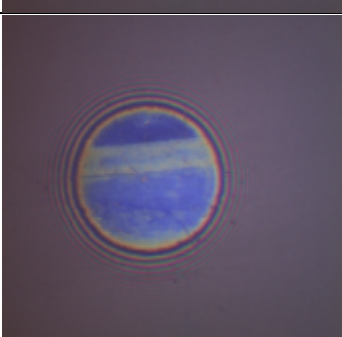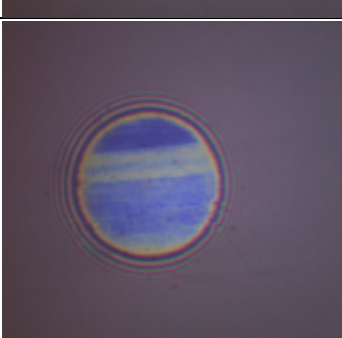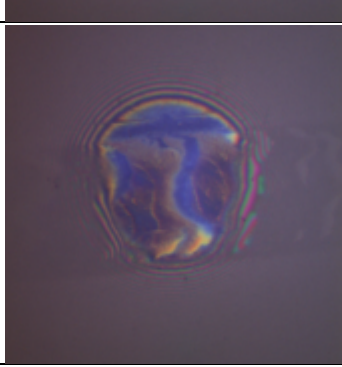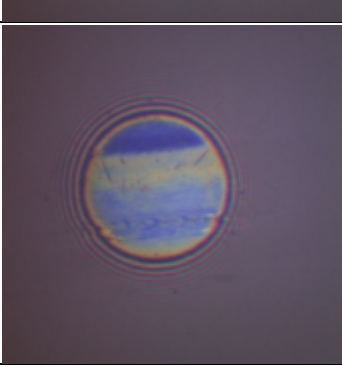
Figure 5-25 - Interferometer images from the MTM-SLIM for different concentrations of TCP.

Test time (seconds)/ Test Oil	100 ppm P (TCP) + Base oil	200 ppm P (TCP) + Base oil
0		
621		
1521		
2421		
3321		

4221		
7821		
12042		
15642		
19863		

23463		
27684		
31284		
35505		
39105		

| 43326 | | |
| 46926 | | |

Figure 5-26 - Interferometer images from the MTM-SLIM for different concentrations of TCP.
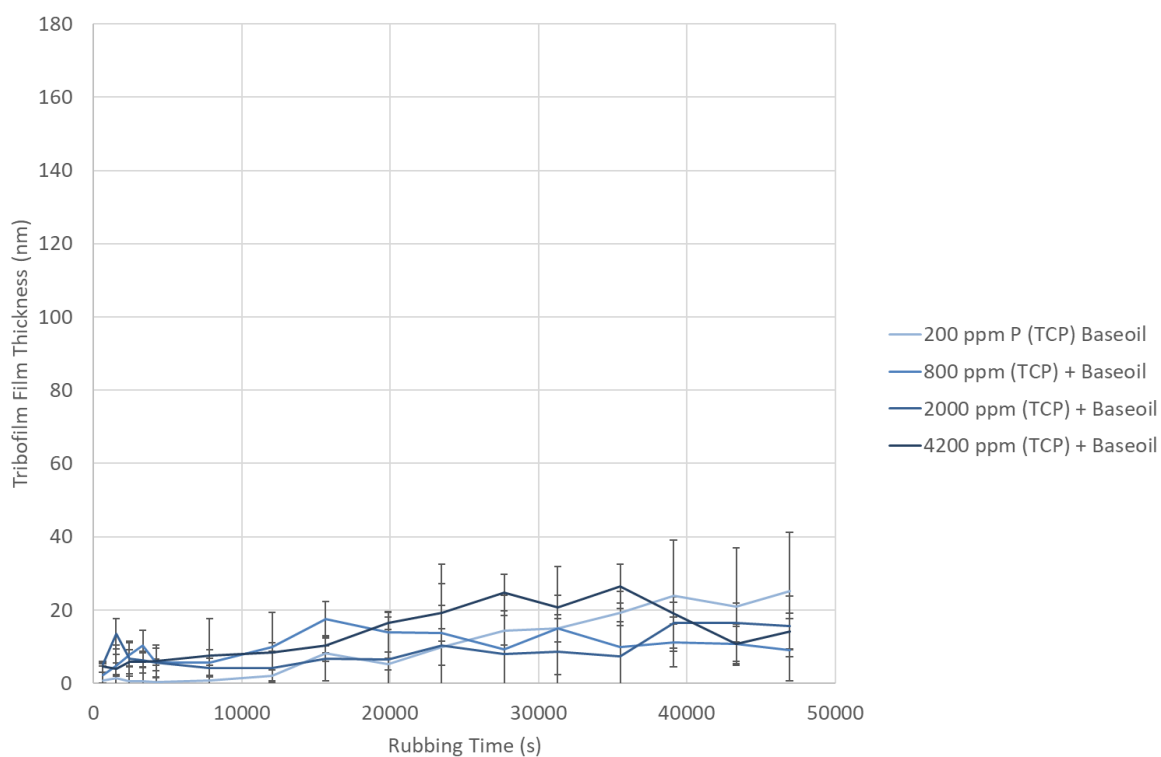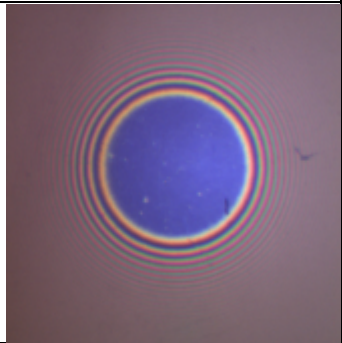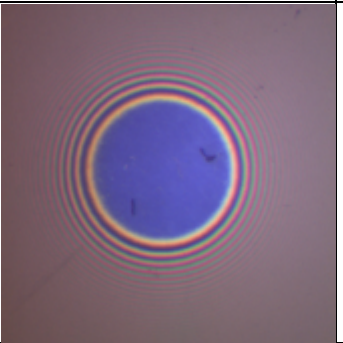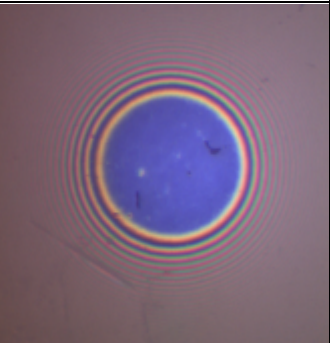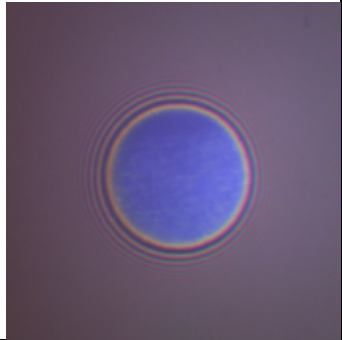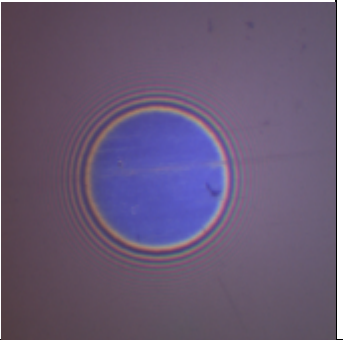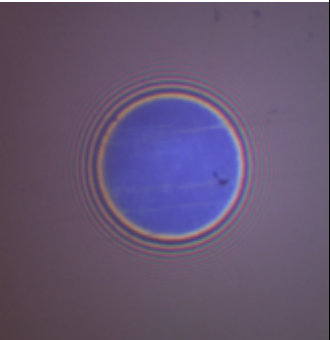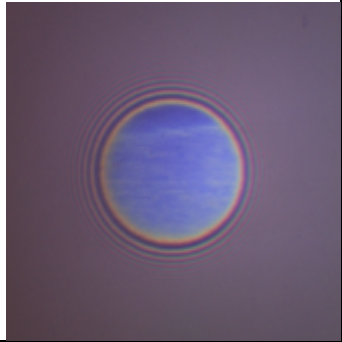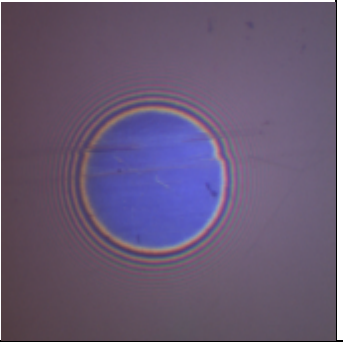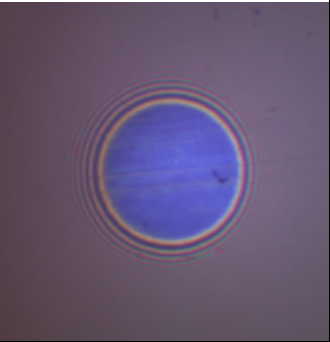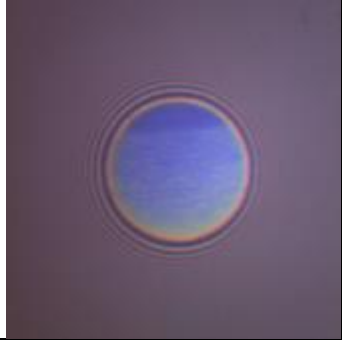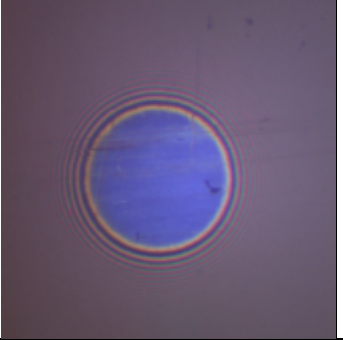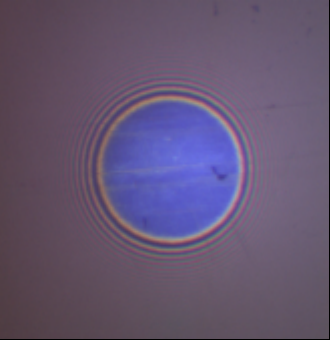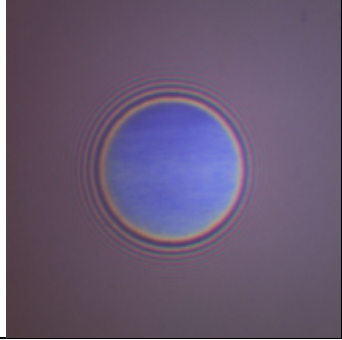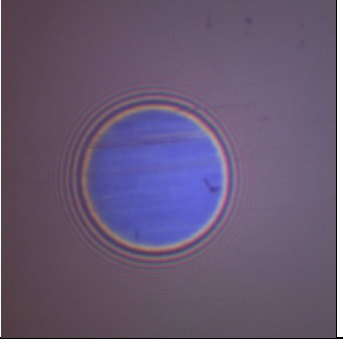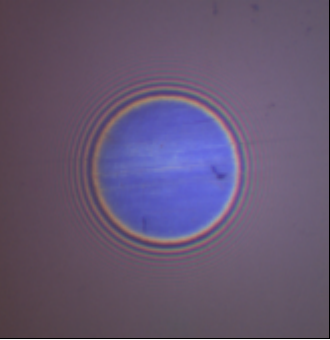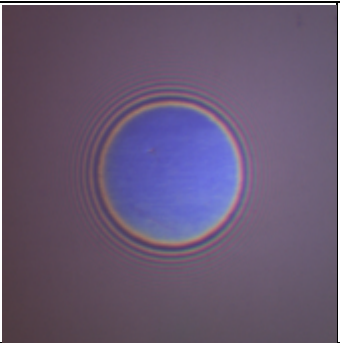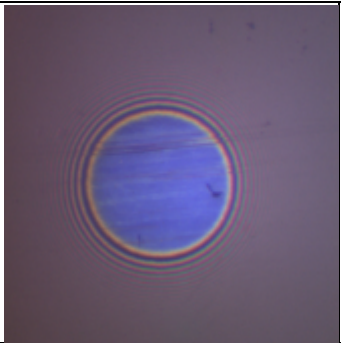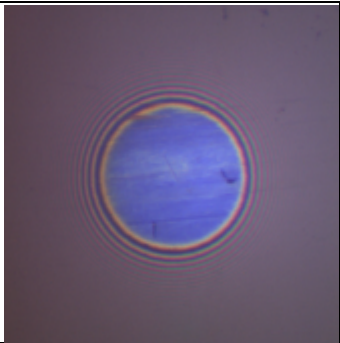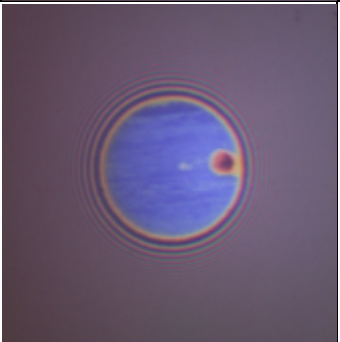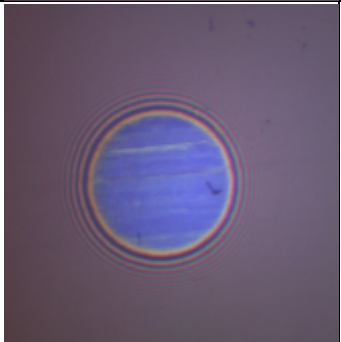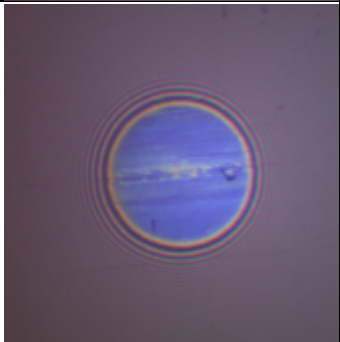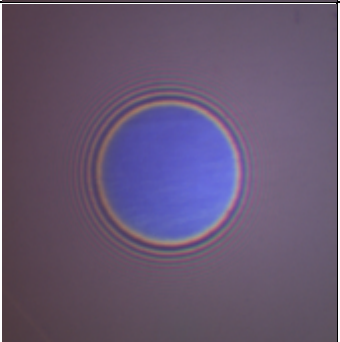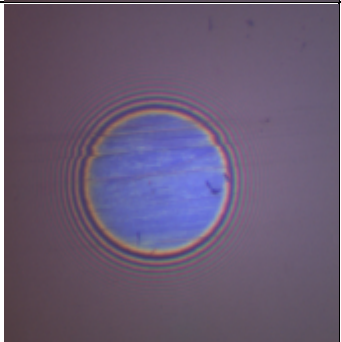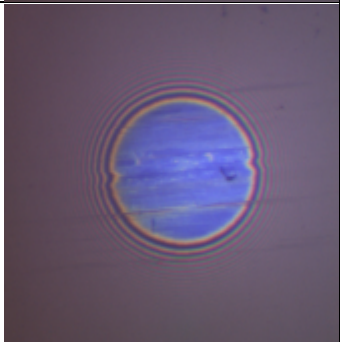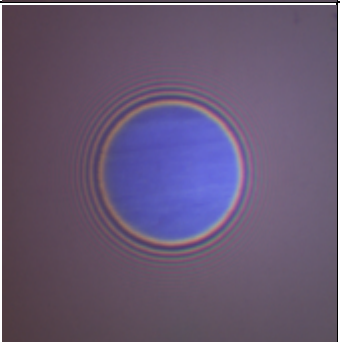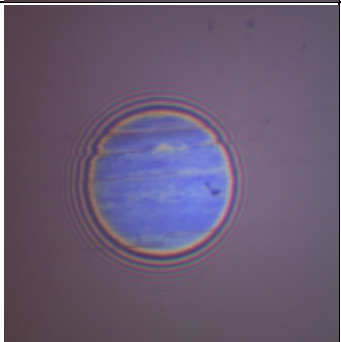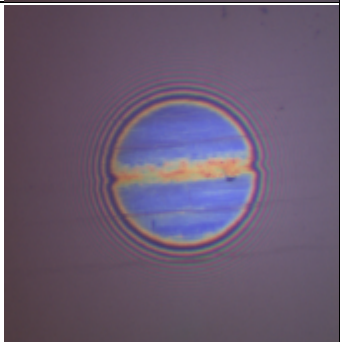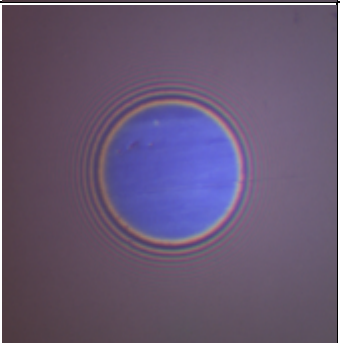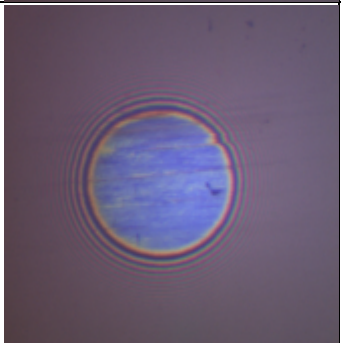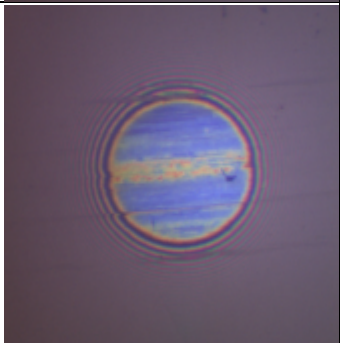
Figure 5-27 – Mean film thickness of TCP tribofilms from different concentration solutions against the rubbing time.

Figure 5-28 shows the interferometry images for additive X at phosphorus concentrations of 800 ppm, 2000 ppm and 4200 ppm and Figure 5-29 shows the interferometry images for additive X at the lower phosphorus concentrations of 100 ppm and 200 ppm. Figure 5-30 shows the tribofilm thickness measured for additive X throughout the wear test. The higher concentrations of 2000 ppm P and 4200 ppm P have a slightly higher film thickness; however, they are not outside of the error bar range of the other concentrations. Therefore, there does not appear to be a strong effect of concentration. The images appear to show a marginally thicker tribofilm than TCP as shown from the more concentrated yellow areas however, the measured values are still in the 30 nm range. However, the measurement may incur some error as discussed in Chapter 3 due to the assumption that the optical characteristics of ashless phosphorus based tribofilms are similar to phosphorus tribofilms derived from ZDDP. These images also appear to show removal and reformation mechanisms as shown from the subtle changes in tribofilm topography from step to step. These also show good protection as the surface does not become heavily worn and pitted like the base oil test despite only having a thin tribofilm.
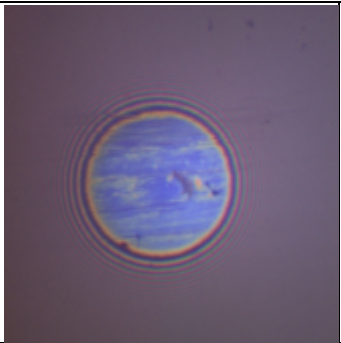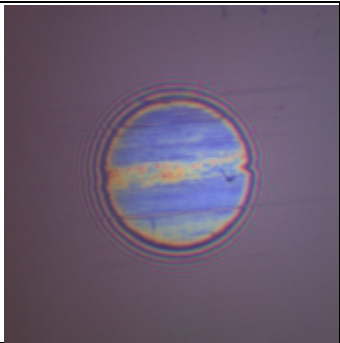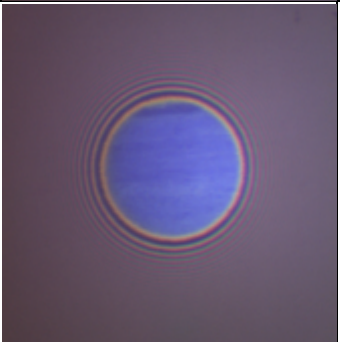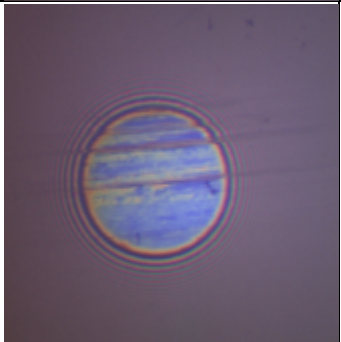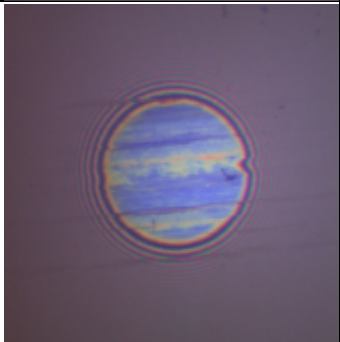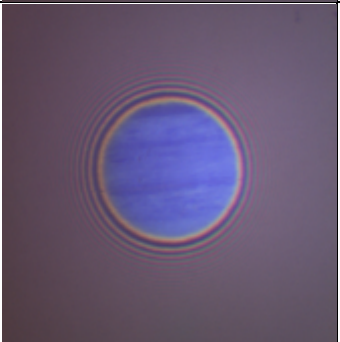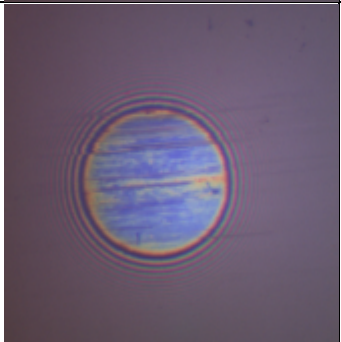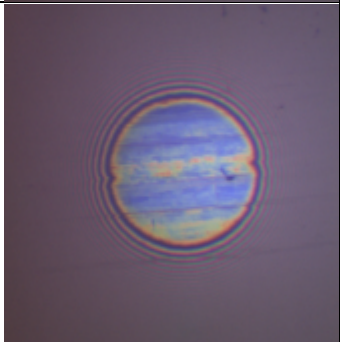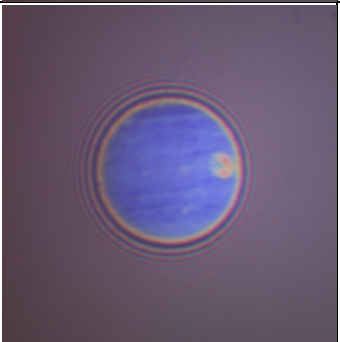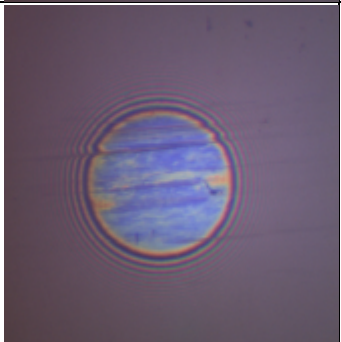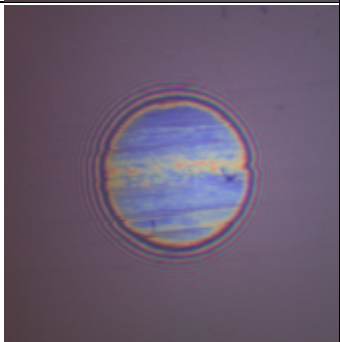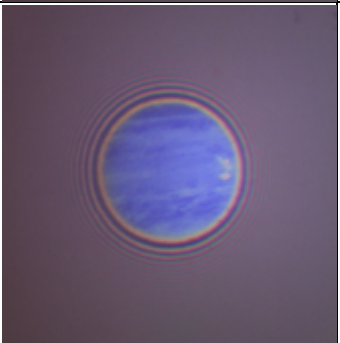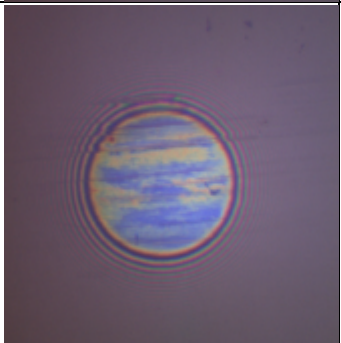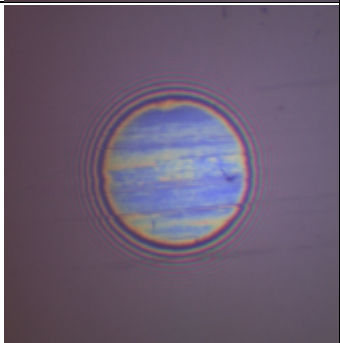
When tested at even lower concentrations, Figure 5-29 shows that there is still sufficient protection at 200 ppm P, but at 100 ppm P, the wear initiates similarly to the base oil with the formation of a strip of orange-brown wear with pitting as shown in Figure 5-22. The tribofilm thickness of 100 ppm was not measured due to the wear being on the surface. However, for 100 ppm P, there was a lot less wear and pitting than TCP at 100 ppm P and suggests that additive X is more active at protecting the surface and works at lower concentrations.

Test time (seconds) / Test Oil	800 ppm P (X) + Base oil	2000 ppm P (X) + Base oil	4200 ppm P (X) + Base oil
0			
621			
1521			
2421			
3321			

4221			
7821			
12042			
15642			
19863			

		179	
23463			
27684			
31284			
35505			
39105			

43326			
46926			
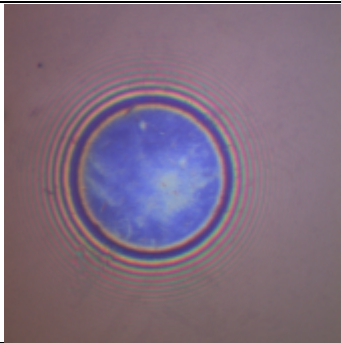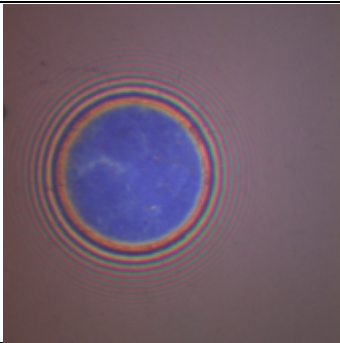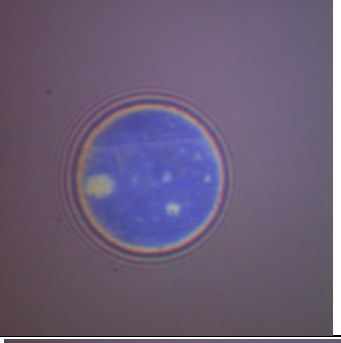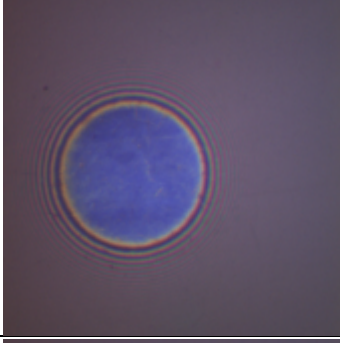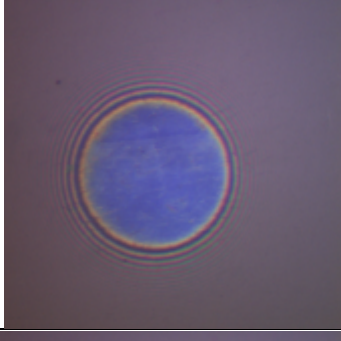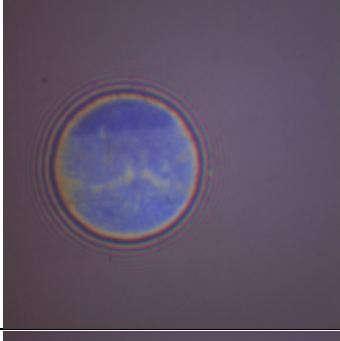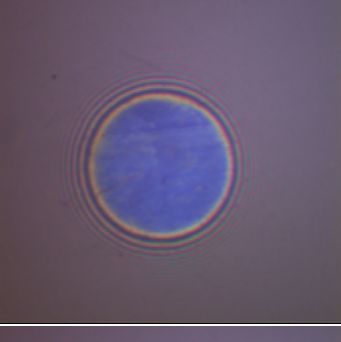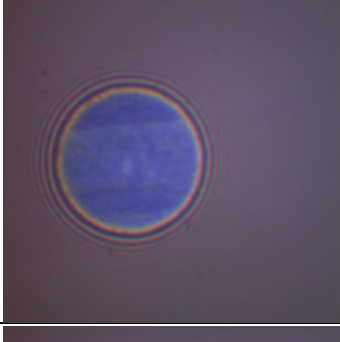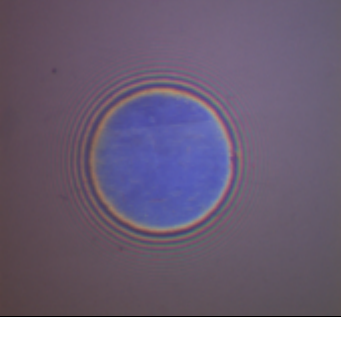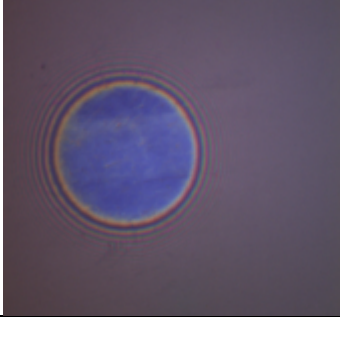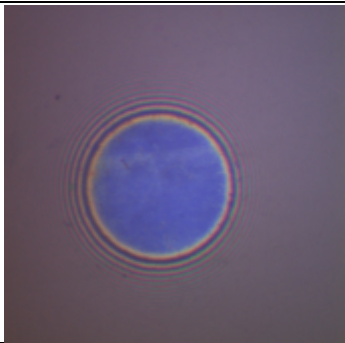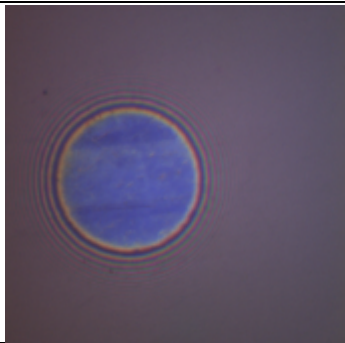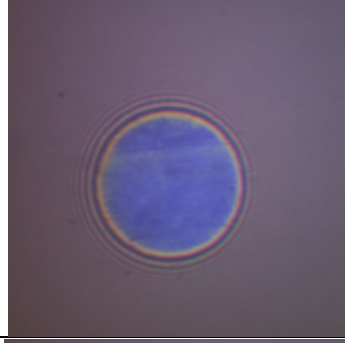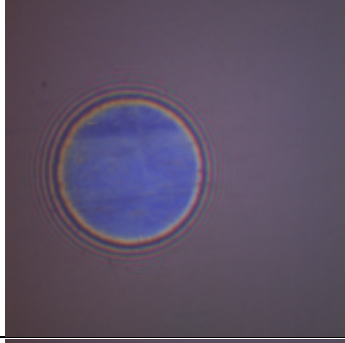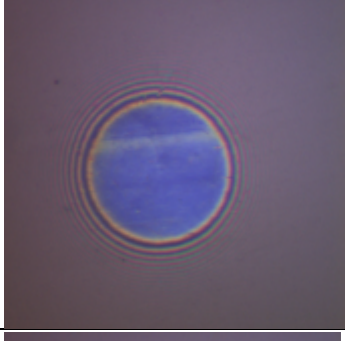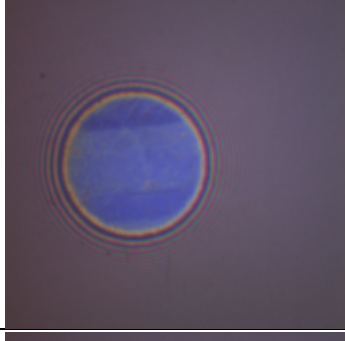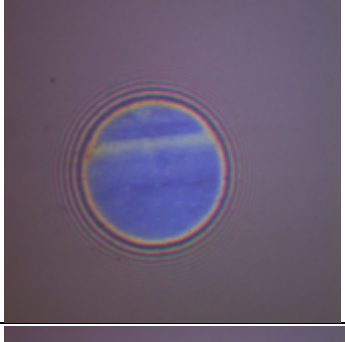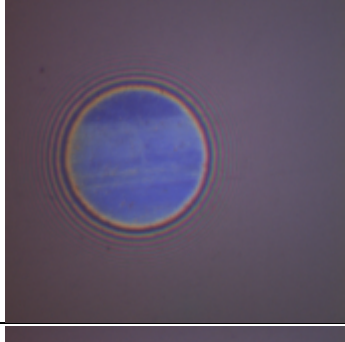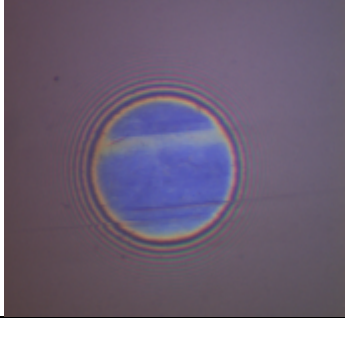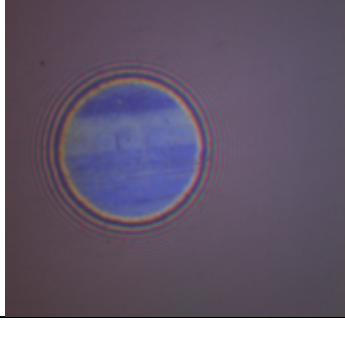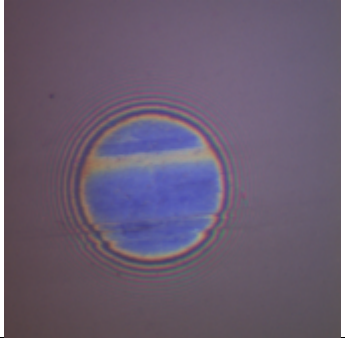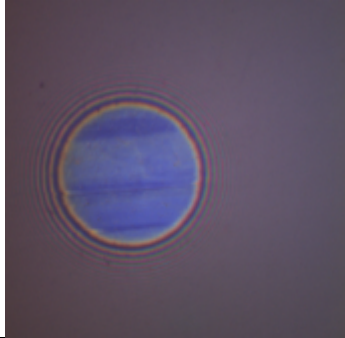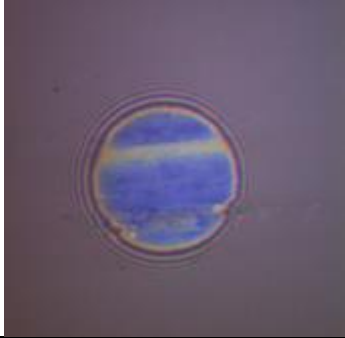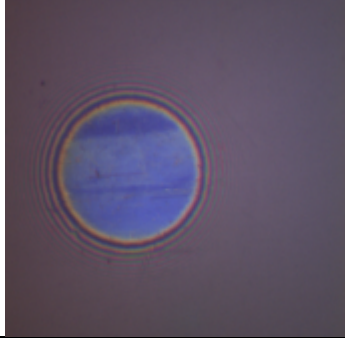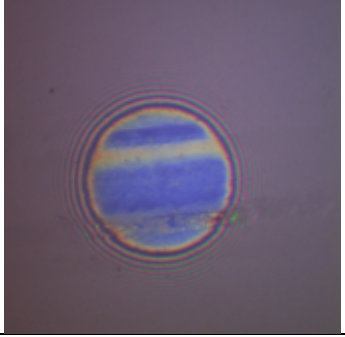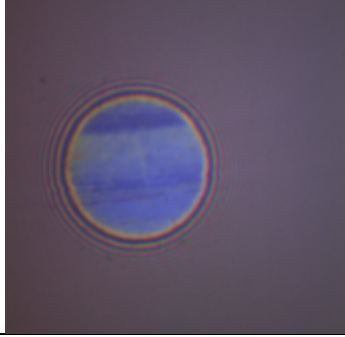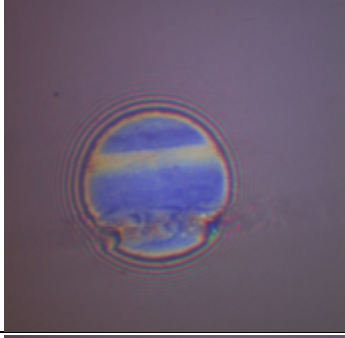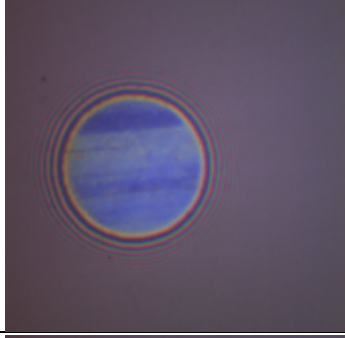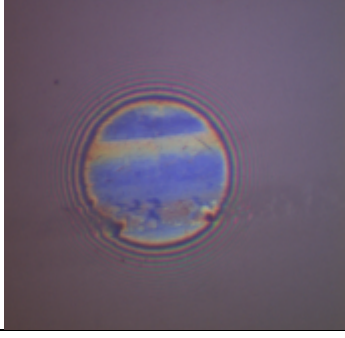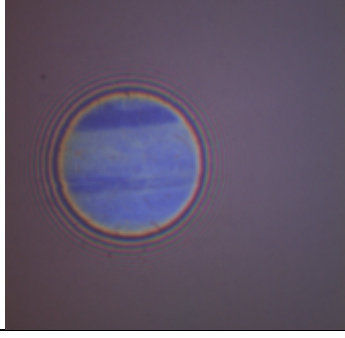
Figure 5-28 - Interferometer images from the MTM-SLIM for different concentrations of additive X in base oil.

Test time (seconds)/ Test Oil	100 ppm P (X) + Base oil	200 ppm P (X) + Base oil
0		
621		
1521		
2421		
3321		

181

4221		
7821		
12042		
15642		
19863		

23463		
27684		
31284		
35505		
39105		

43326		
46926		

Figure 5-29 - Interferometer images from the MTM-SLIM for different lower concentrations of additive X.
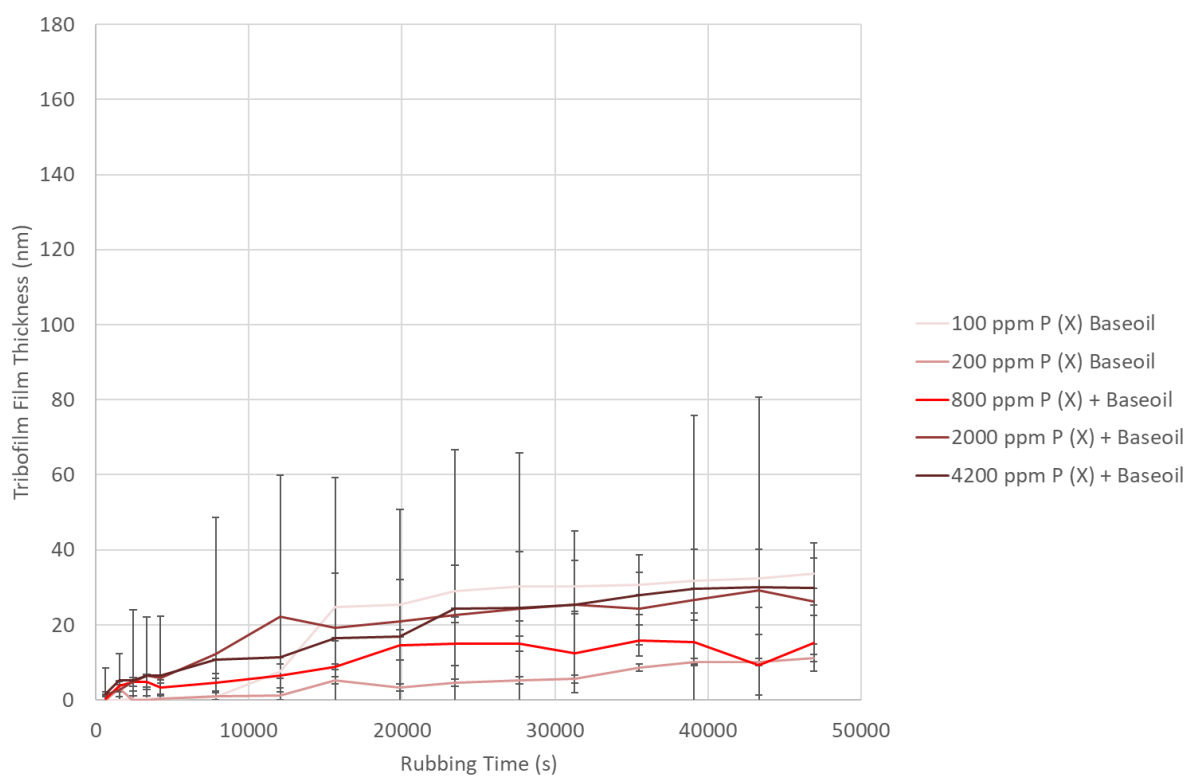
Figure 5-30 – Mean film thickness of additive X tribofilms from different concentration solutions against the rubbing time.

Stribeck Curve Analysis

This section will interpret the Stribeck curves produced from the MTM-SLIM. However, only the initial and final Stribeck curves were shown instead of all seven for each test as all show a gradual transition from the initial to final Stribeck curve and do not add extra information as shown in Figure 5-31. (The 1-7 labelling of the curves corresponds to the sequence of when the Stribeck curves were measured, where 1 was the first curve at 0 hours, 2 at 2 hours, 3 at 4 hours, 4 and 6 hours, 5 at 8 hours, 6 at 10 hours and then the final curve 7 at 12 hours.)
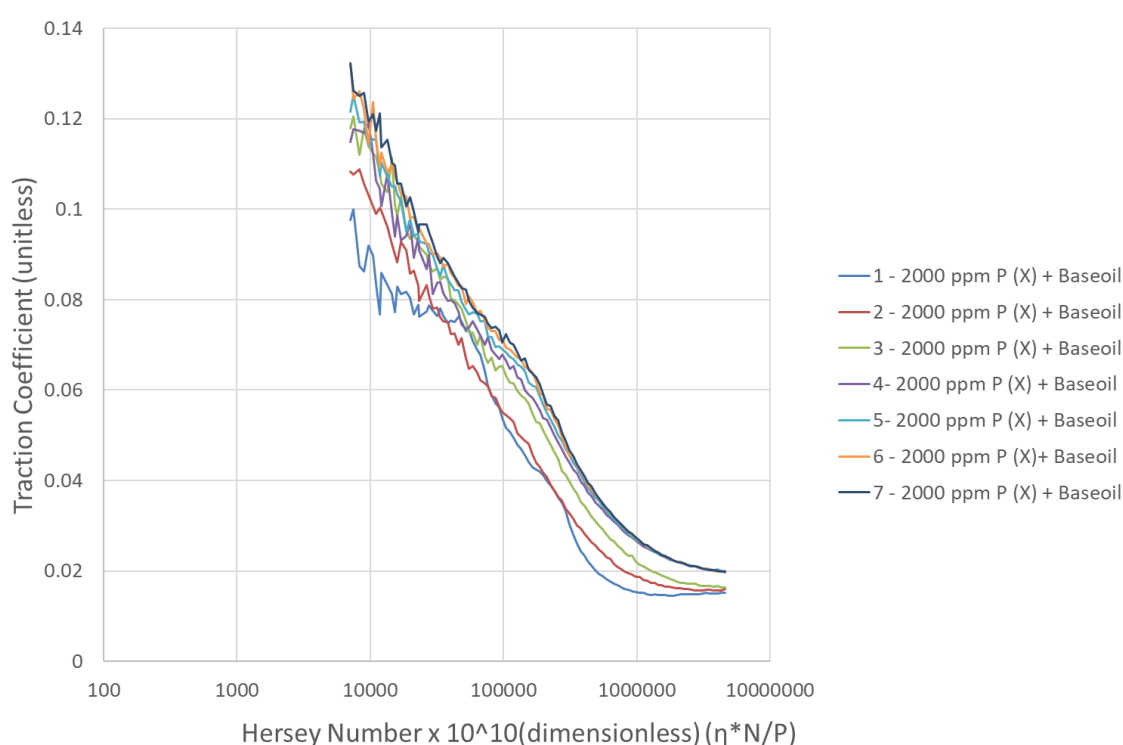
Figure 5-31 – Stribeck curves throughout the whole MTM-SLIM test for one lubricant candidate where a Stribeck curve was recorded initially and then every 2 hours.

Most Stribeck curves show an increase in friction across all regimes, but some do not as will be discussed for ZDDP. It should be noted that all Stribeck tests shoul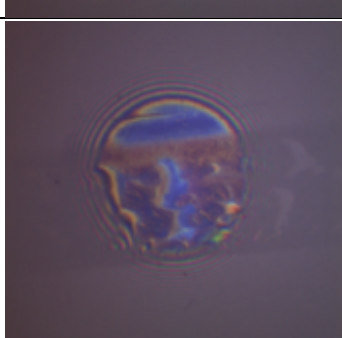d reach the EHD as calculated from the lambda ratio shown in Chapter 3. But many of the curves do not appear to flatten out at higher Hersey numbers, which, suggest they may not yet have reached the EHD regime. All the Stribeck curves have been plotted against the Hersey number and are therefore,

normalised for viscosity allowing the effect of the additive on friction to be examined. In general, it can also be seen that the error bars are larger for the final Stribeck curve, but this is expected due to the differing amount of wear on the surface for repeat tests.
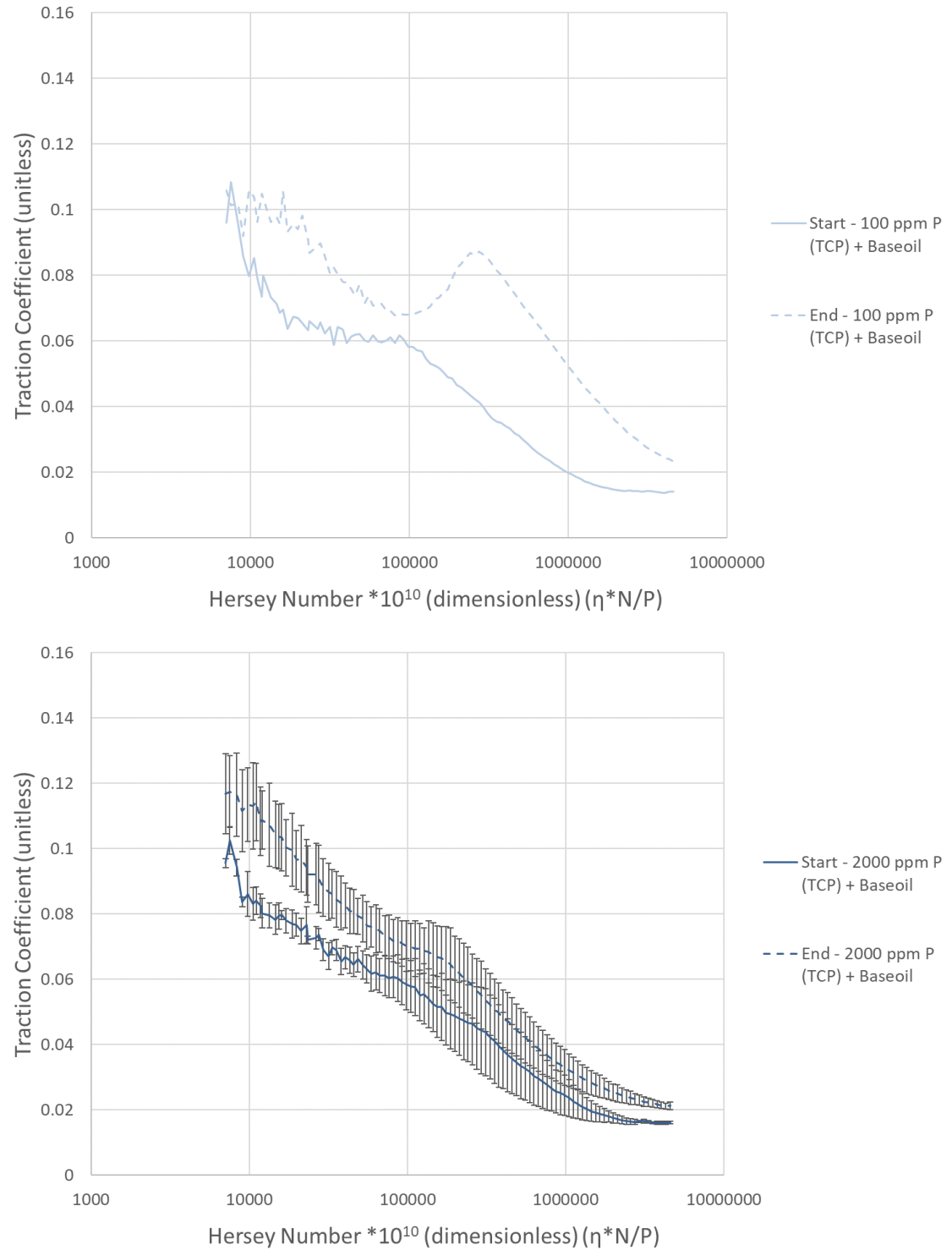
Figure 5-32- Initial and final Stribeck curves for 100 ppm P (TCP) and 2000 ppm P (TCP) showing the variation in friction across the lubrication regimes from the start to the end of the wear test.

Figure 5-32 displays the Stribeck curves for TCP at 100 ppm P and 2000 ppm P. Only a few Stribeck curves at certain concentrations are shown for each additive due to them showing a similar trend of an increase in friction from the initial to final curve and are all in Appendix 8. There is a larger increase in friction across all regimes for 100 ppm P and this is most likely due to the severe wear and pitting seen in Figure 5-22. The "hump" in the curve cannot currently be explained. This hump could mark the transition from the boundary to mixed regimes as the introduction of the lubricant film between the surfaces may have some interaction that initially leads to an increase in friction before it decreases and this hump seem more prominent in the latter Stribecks of the tests suggesting rougher surfaces may increase the size of this hump. There are no error bars for this test as only one test was completed.

Figure 5-33 displays the Stribeck curves for additive X at 100 ppm P and 2000 ppm P. There is less separation between the initial and final Stribeck curves than TCP potentially due to there being less wear and pitting on the 100 ppm P (X) test.
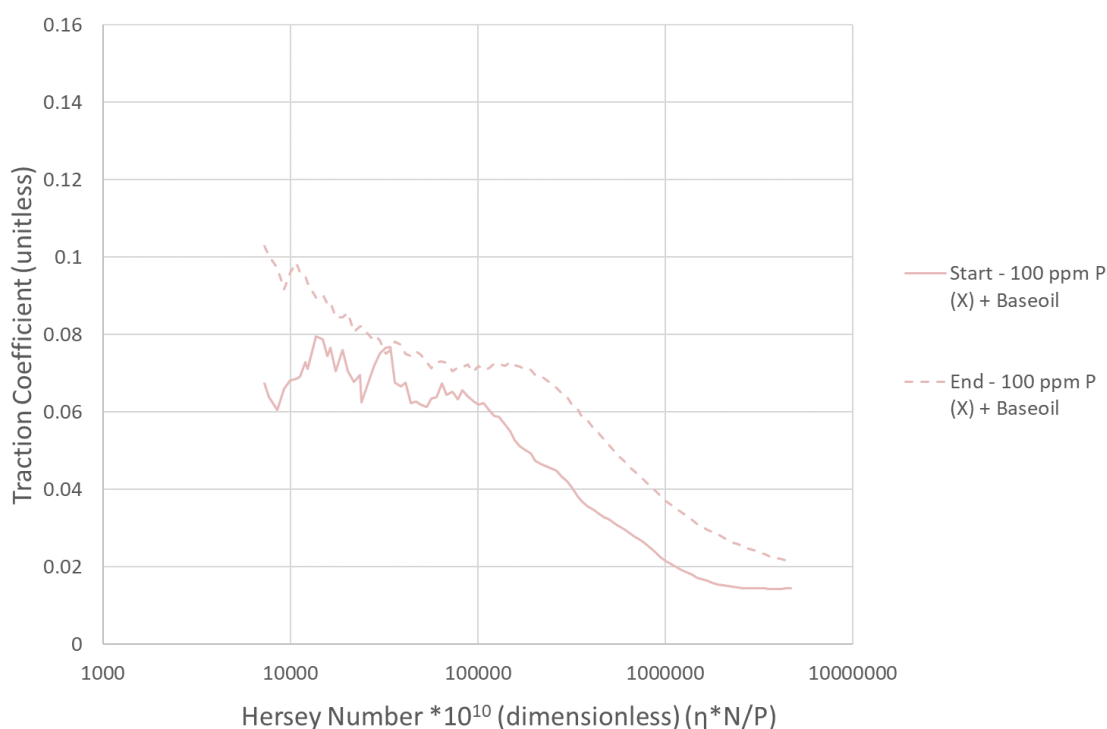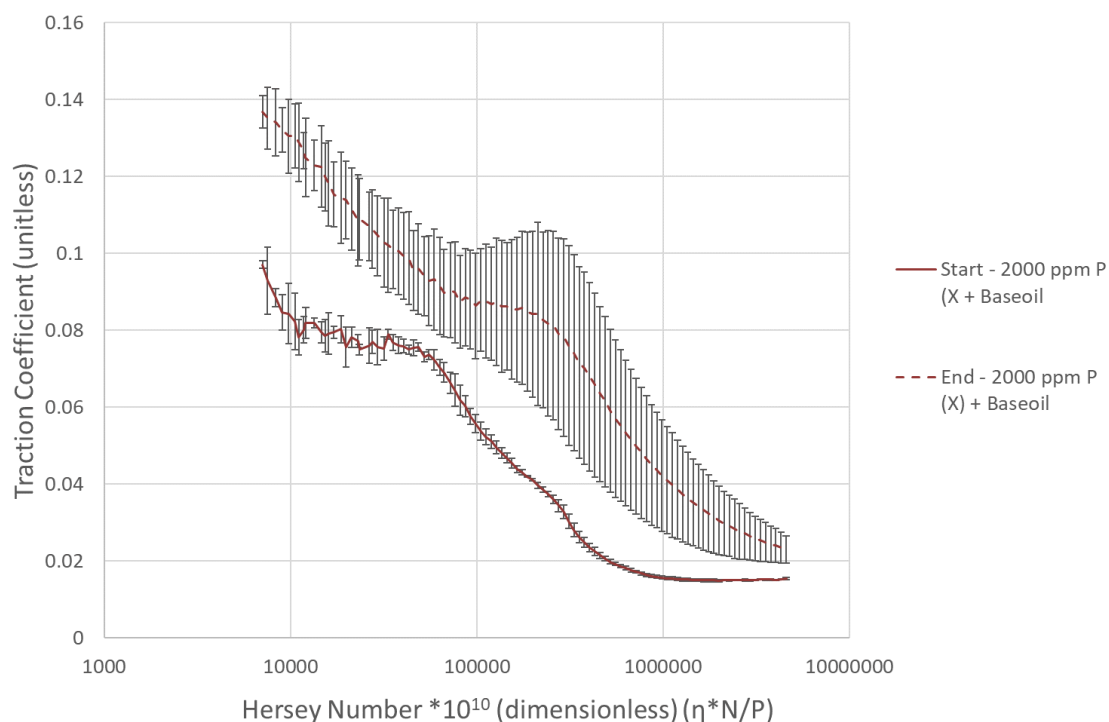
Figure 5-33 - Initial and final Stribeck curves for 100 ppm P (X) and 2000 ppm P (X) showing the variation in friction across the lubrication regimes from the start to the end of the wear test.

Figure 5-34 displays the Stribeck curves for base oil and 2000 ppm P (ZDDP). The base oil shows a much larger separation from the initial to final Stribeck curve and this is most likely due to the worn and pitted rough surface giving rise to higher friction.

ZDDP has a different trend to the ashless additives in that the boundary friction decreases throughout the test, however, the mixed friction increases. This was seen with both concentrations; however, the error is quite large. This is in agreement with the MPR section which, showed that friction for ZDDP in the boundary regime decreases.
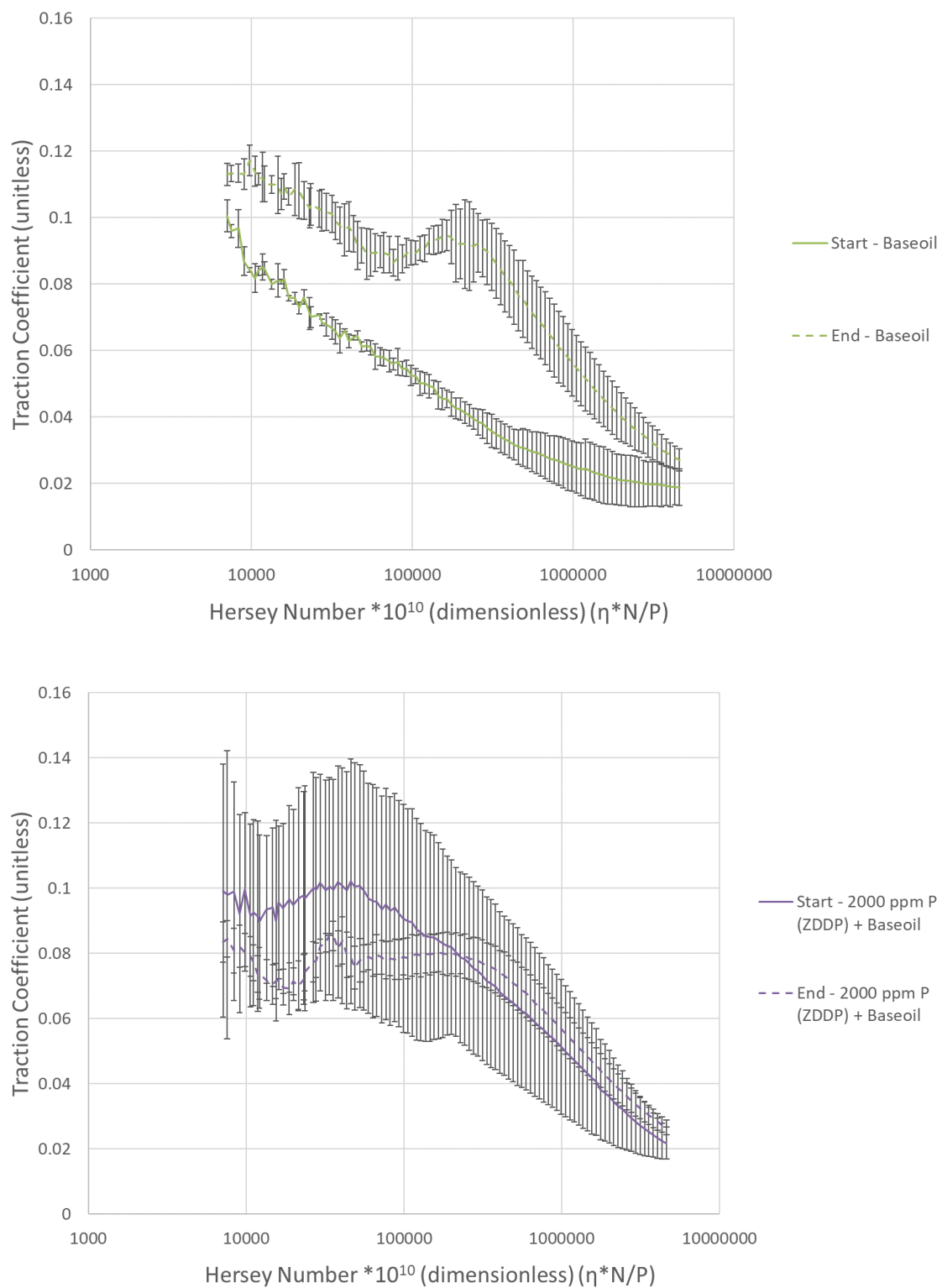
Figure 5-34 - Initial and final Stribeck curves for base oil and 2000 ppm P (ZDDP) showing the variation in friction across the lubrication regimes from the start to the end of the wear test.

Figure 5-35 shows the Stribeck curves comparing all the concentrations of TCP in the initial and final Stribeck curves. The error bars have been omitted from this section to allow better visualization of the Stribeck curves, but these can be seen in the previous figures.

There is minimal separation between the different concentrations of TCP in the initial figure, but there is some separation in the final Stribeck curves. Most are lower than the base oil throughout the test except 100 ppm P which, had similar wear, but 4200 ppm P has similar friction too. This may suggest that the concentration can be too high which, can lead to friction increasing. However, the data sets are very similar and limited conclusions can be drawn.
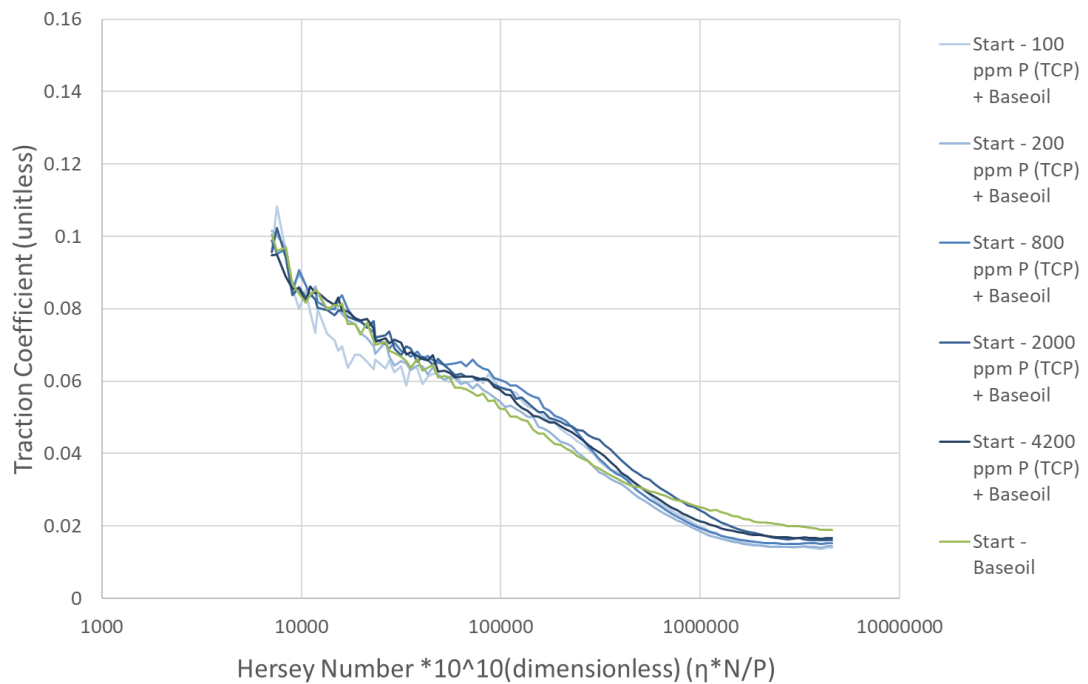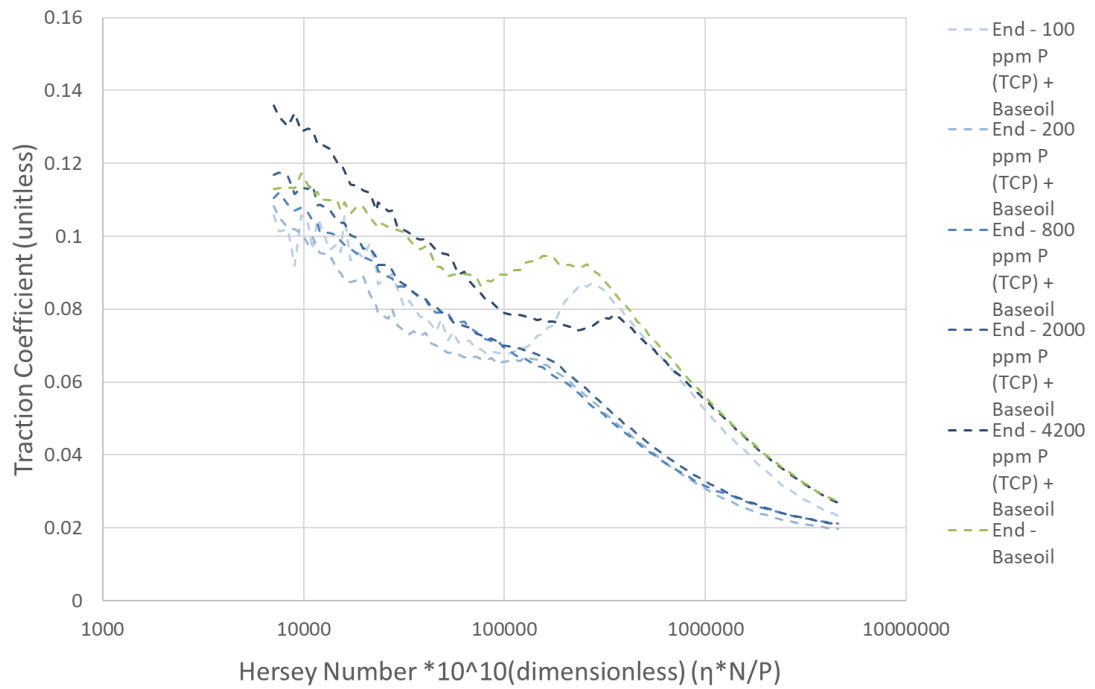
Figure 5-35 - Initial and final Stribeck curves for all concentrations of TCP and base oil showing the variation in friction across the lubrication regimes from the start to the end of the wear test and between different TCP concentrations.

Figure 5-36 shows the Stribeck curves comparing all the concentrations of TCP in the initial and final Stribeck curves. Very similar curves were obtained at the start of test, but the base oil has higher friction at higher Hersey numbers, however, as per previous the Stribeck curve for base oil, it is not outside of the error bar range. There are larger differences in the final Stribeck curves, however, there is no trend with concentration and the base oil has the highest friction.
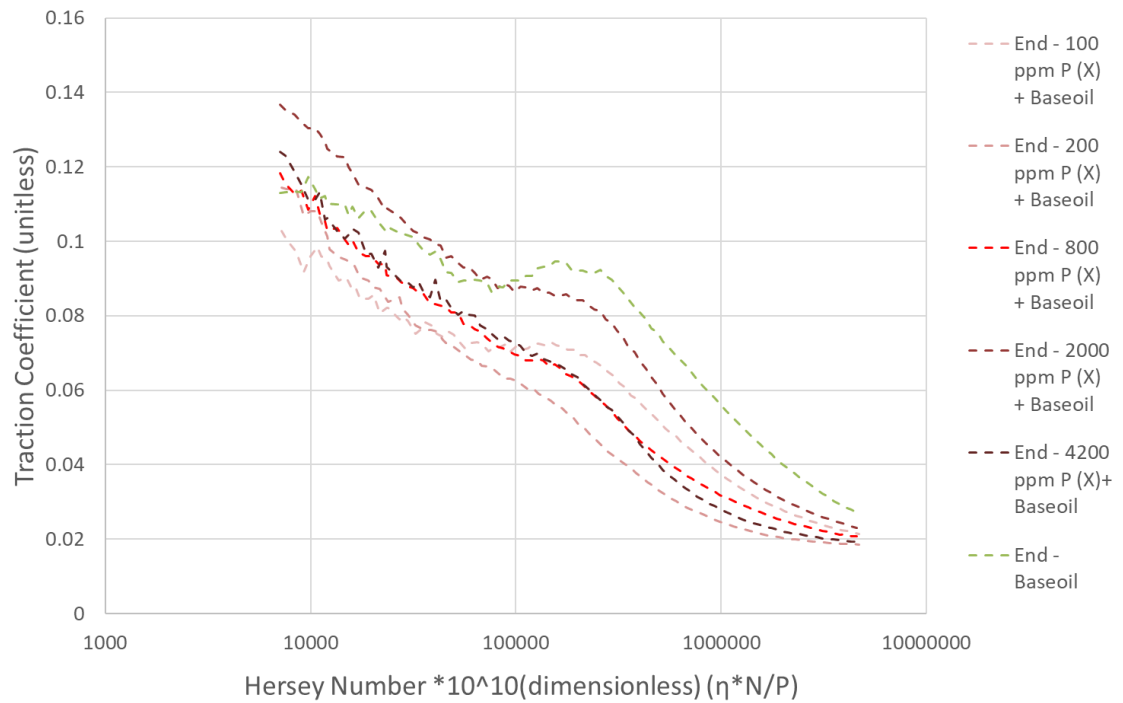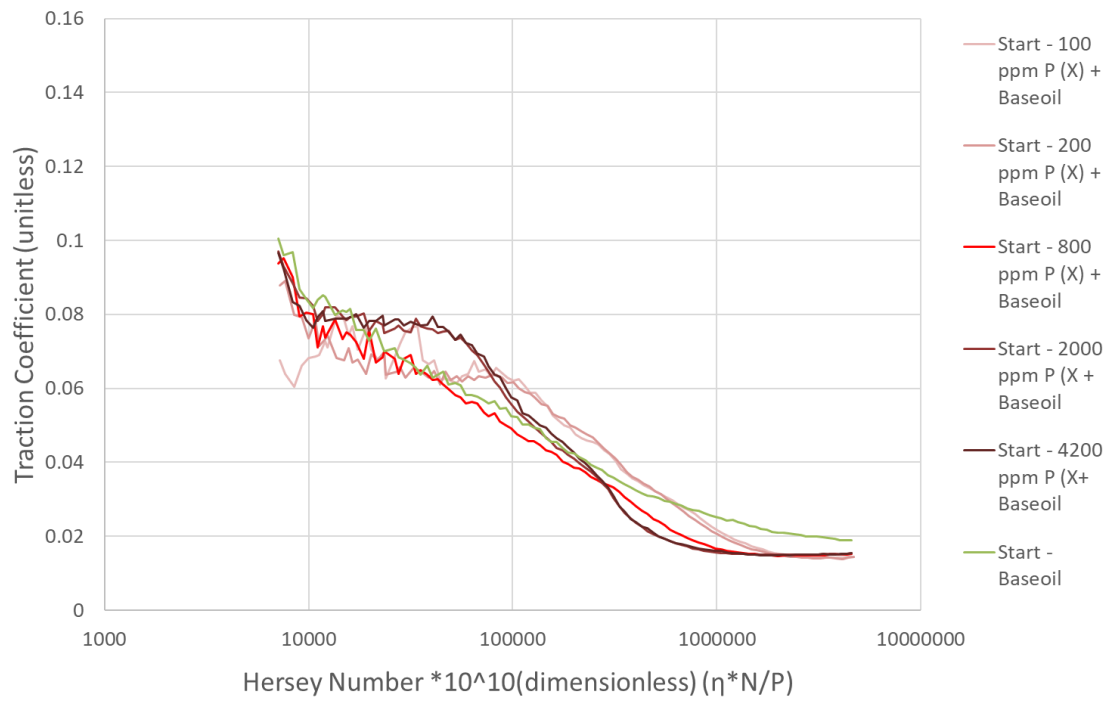
Figure 5-36 - Initial and final Stribeck curves for all concentrations of additive X and base oil showing the variation in

friction across the lubrication regimes from the start to the end of the wear test and between different TCP concentrations.

Figure 5-37 shows the Stribeck curves comparing all the concentration of ZDDP in the initial and final Stribeck curves. At the start of the test, there is a trend of increasing friction from base oil to 800 ppm P to 2000 ppm P. In the final Stribeck curves, the friction in the boundary regime has decreased significantly for both ZDDP concentrations resulting in lower friction as opposed to the base oil which, increased towards the end of the test and this results in all the curves converging at higher Hersey numbers. Again, the results agree with the MPR results for decreasing friction for ZDDP in the boundary regime. However, the boundary friction is lowest for 800 ppm P suggesting a higher concentration may increase friction in the boundary regime.
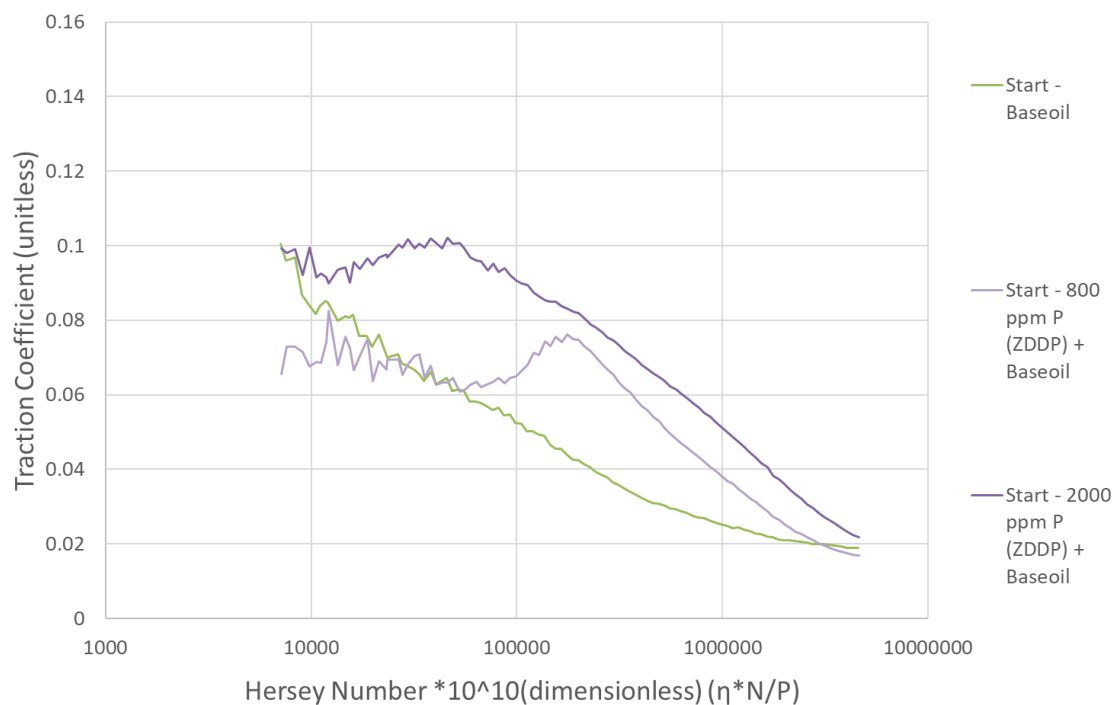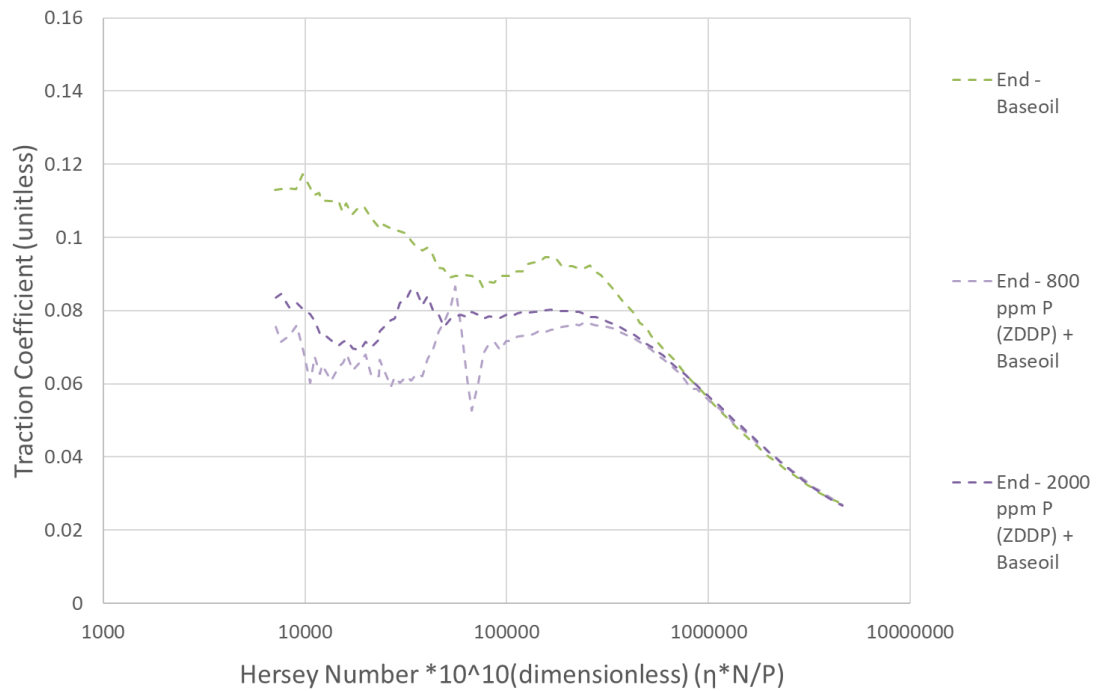
Figure 5-37 - Initial and final Stribeck curves for all concentrations of ZDDP and base oil showing the variation in friction across the lubrication regimes from the start to the end of the wear test and between different TCP concentrations.

Figure 5-38 compares the initial and final Stribeck curves comparing all the additives at 800 ppm P. In the initial Stribeck curves, the boundary friction is similar but ZDDP has the highest mixed to EHD friction with TCP and additive X performing similarly, as also seen in the final Stribeck curves. They both increase marginally in friction from the initial Stribeck curves, but the ZDDP final Stribeck curve remains the same as the initial Stribeck curve. But in the final Stribeck curves, since TCP and additive X have shifted, ZDDP has the lowest boundary friction but highest mixed friction.
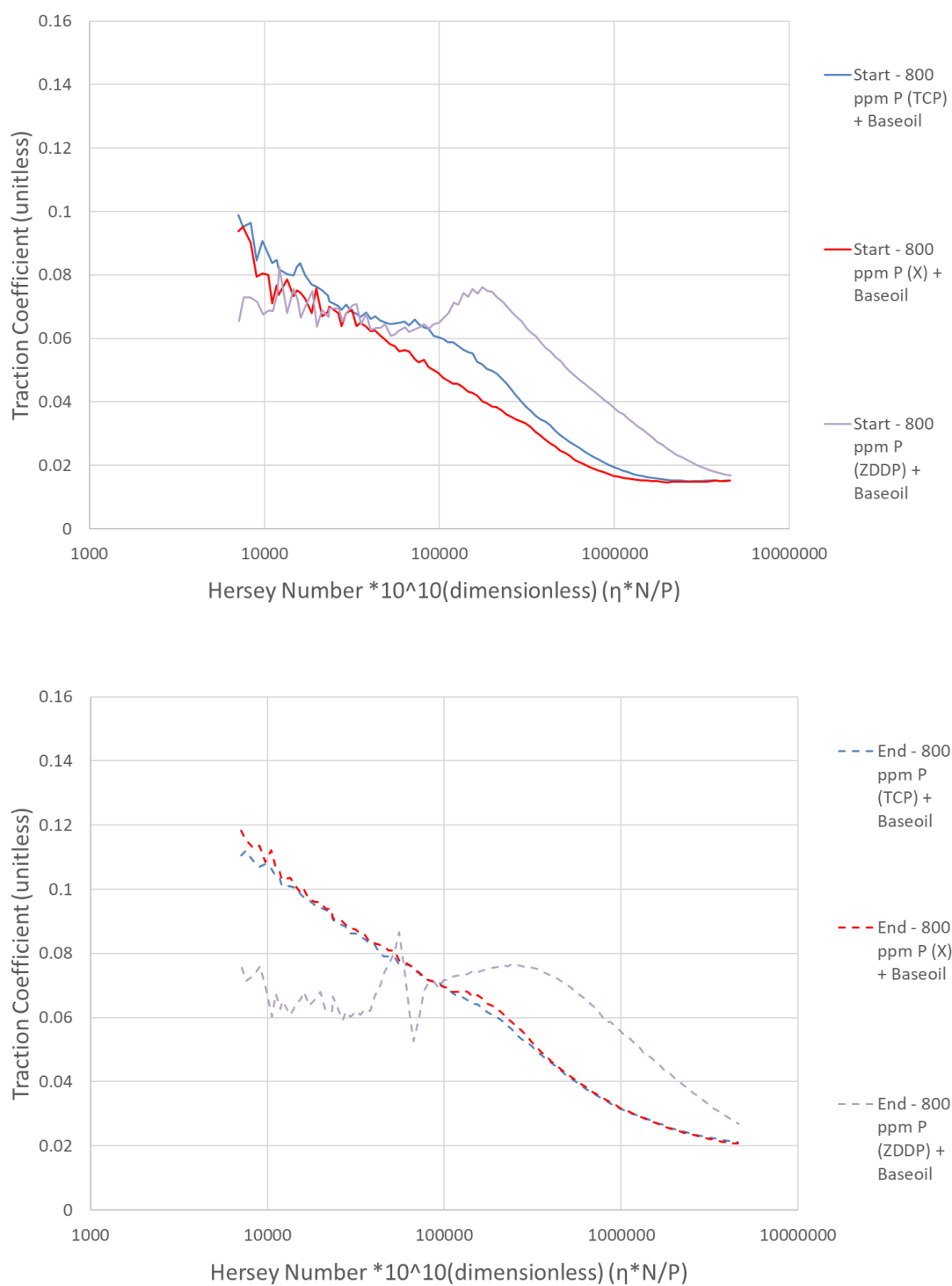
Figure 5-38 – Comparison between the different anti-wear additives at 800 ppm P at the start and end of the test.

Figure 5-39 compares the initial and final Stribeck curves comparing all the additives at 2000 ppm P. ZDDP has the highest friction in the initial Stribeck curves and the ashless additives are similar. However, in the final curves, there appears to be more separation of the ashless additive curve at higher concentrations as shown from additive X having higher friction than TCP across all regimes. ZDDP also has lower friction in boundary, but higher friction than the ashless additive curves at higher Hersey numbers.

Overall, it can be seen from the MTM-SLIM Stribeck analysis that most show an increase in friction for the initial Stribeck curve to the final Stribeck curve. The 100 ppm tests revealed higher friction difference for TCP than additive X as expected from the excessive wear seen for the TCP test, confirming that additive X is more active than TCP at lower concentrations. The base oil had the highest friction on the final Stribeck curve, due to the wear produced and a similar trend was seen for 100 ppm P (TCP). ZDDP had a slightly different trend showing high friction in the boundary regime but low friction in the mixed/EHD regime in the initial Stribeck curve but then the boundary friction decreases and the friction at high Hersey numbers increases.

Friction results also highlighted that a there may be an effect of friction increasing once the concentration increases but this point differs for different additives. TCP had a friction increase at 4200 ppm P, X at 2000 ppm P and 2000 ppm P for ZDDP. However, this trend is not too strong for additive X. The difference in additive performance is more prominent at higher concentrations as shown from difference between 800 ppm P and 2000 ppm P.

The order of friction in the final Stribeck curves in the boundary regime for 2000 ppm starting from the lowest is ZDDP<TCP<X. The order of friction in the final Stribeck curves in the mixed/ EHD regime for 2000 ppm P starting from the lowest is TCP<X<ZDDP
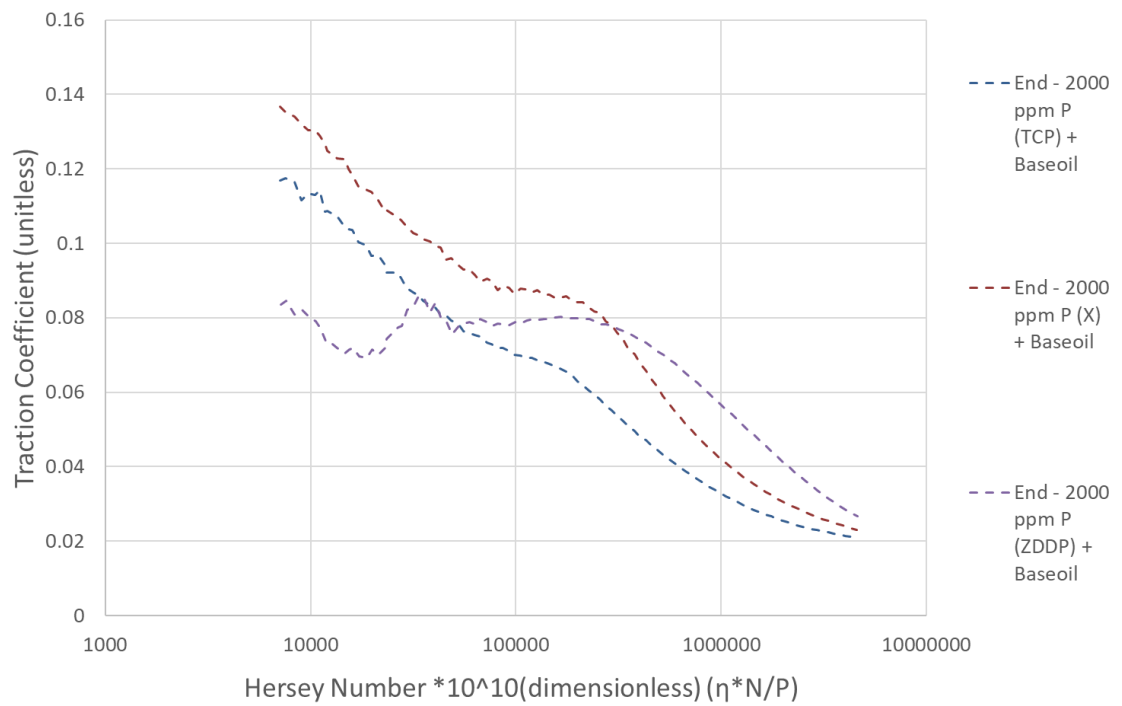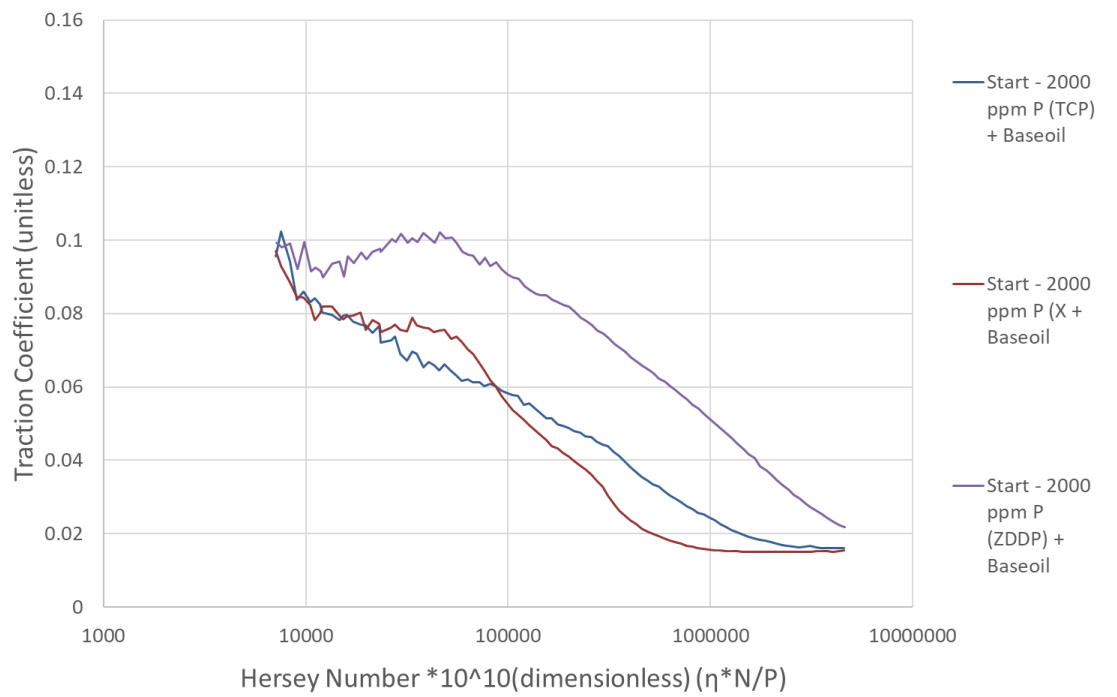
Figure 5-39 – Comparison between the different anti-wear additives at 2000 ppm P at the start and end of the test

Overall Friction Analysis

This section discusses the traction coefficients that are measured throughout the entire test and as can be seen from Figure 5-40, the Stribeck curves taken at specific what appear as vertical lines. However, it is the boundary friction that is being interpreted in this section.

Figure 5-40 shows the overall friction for all the concentrations of TCP and base oil. They all start in a similar range at the beginning of the test, but the cases for base oil, 100 ppm and 4200 ppm then increase. This is most likely due to the increased wear with the base oil and 100 ppm tests. However, the 4200 ppm P plot is a surprising result as not a lot of wear was seen, which, could suggest too much TCP could increase boundary friction.
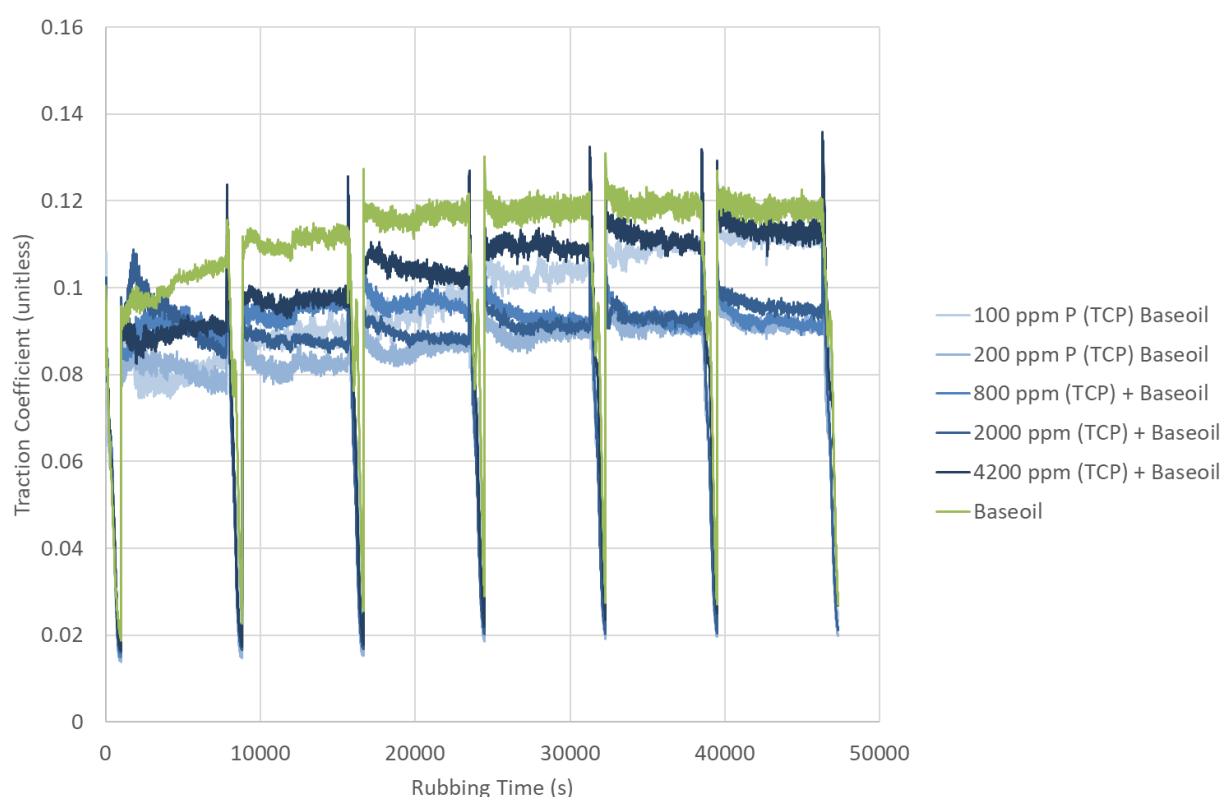
Figure 5-40 – The overall friction throughout the test for all concentrations of TCP and base oil.

Figure 5-41 shows the overall friction for all the concentrations of additive X and base oil. Again, they all start with similar friction, but then the base oil increases the most. But 2000

ppm P and 4200 ppm P also increase by a similar amount to the base oil whilst the other lower concentrations have a smaller increase in traction coefficient.

This data suggests there may be an optimum concentration for anti-wear additives before friction increases as minimal wear was seen with these tests, as shown from Figure 5-22. This could also back up that additive X is a more active anti-wear additive than TCP as it provides more protection at lower concentrations and promotes micropitting more.
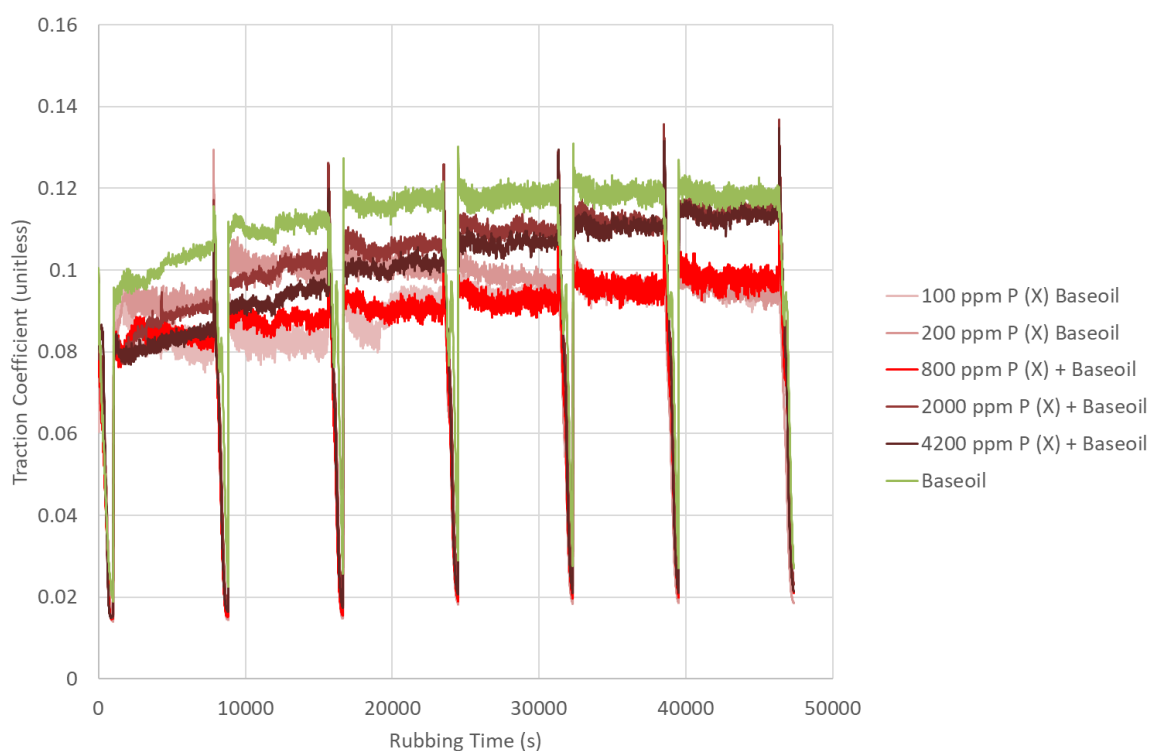
Figure 5-41 - The overall friction throughout the test for all concentrations of additive X and base oil.

Figure 5-42 shows the overall friction for all the concentrations of ZDDP and base oil. Initially ZDDP has a much higher friction than all these other tests with 800 ppm P being the highest and then this trend flips as the rubbing time increases resulting in the base oil having the highest friction and 800 ppm P ZDDP having the lowest. This suggests increasing the concentration of ZDDP could give an initially lower friction but increase the friction in the long run. It may be that due to the quick formation of the ZDDP tribofilm, it could give rise to an initially rough

surface giving rise to initially high friction and then decreases as more tribofilm forms and plastic deformation occurs to give a smoother surface as suggested by Ueda and Spikes (184).

These friction results agree with the MPR results in that the ZDDP gives rise to a decrease in friction in the boundary regime.
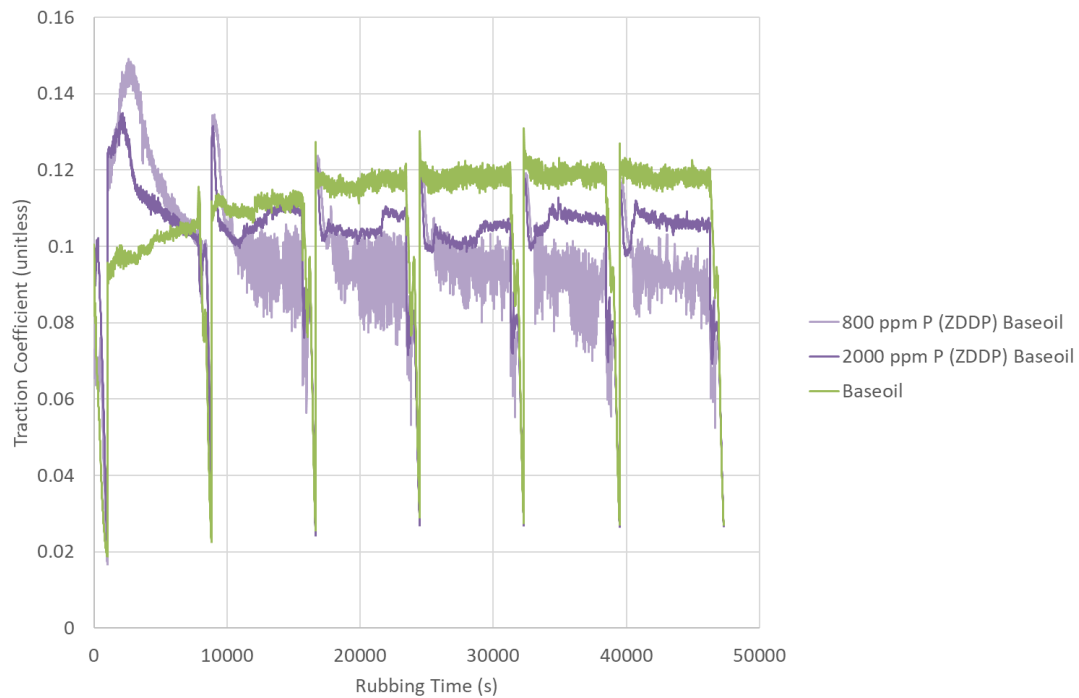
Figure 5-42 – The overall friction throughout the test for all concentrations of ZDDP and base oil.

Figure 5-43 compares the overall friction for the different anti-wear additives at 800 ppm P. ZDDP initially has the highest friction but then decreases and they all have a similar measured friction by the end of the test.
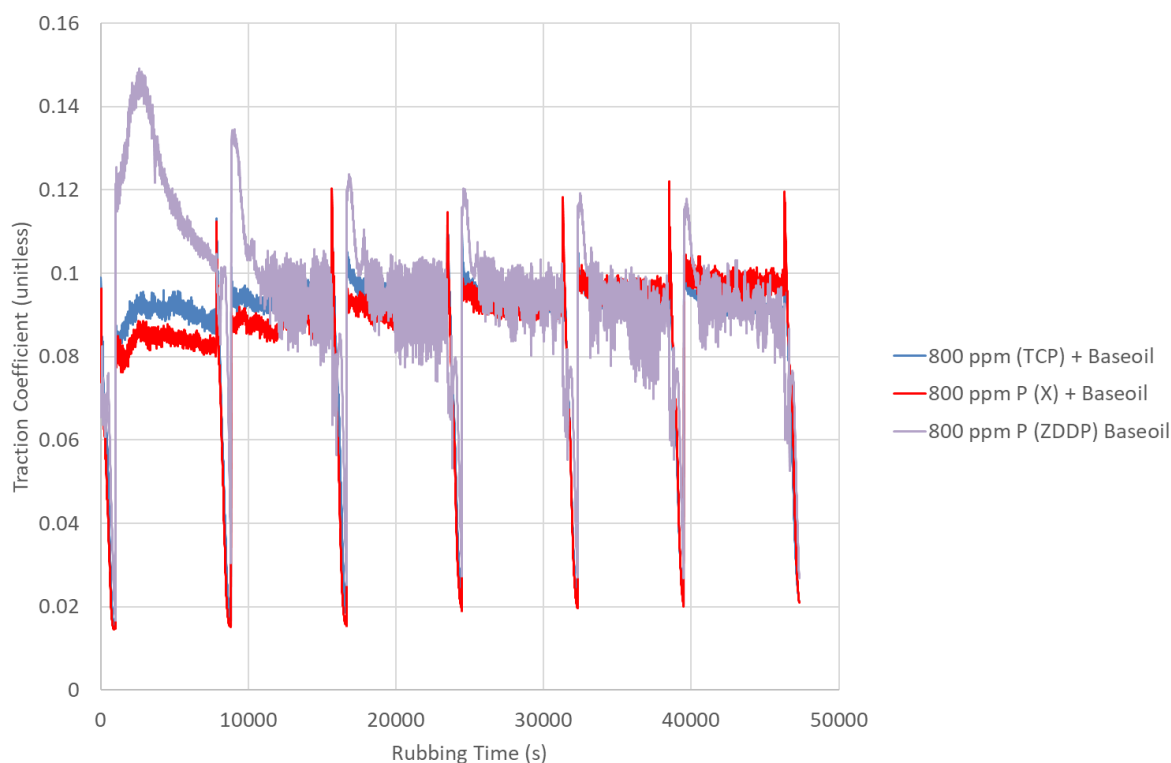
Figure 5-43 – The overall friction throughout the test for all the different anti-wear additives at 800 ppm P.

Figure 5-44 compares the overall friction for the different anti-wear additives at 800 ppm. There is more separation at 2000 ppm P than at 800 ppm P. However, a different trend is seen with additive X initially being the lowest followed by TCP and then ZDDP.

But then towards the end of the test, TCP has the lowest followed by ZDDP and then additive X. Again, there could be an effect of an optimum concentration for different additives as at 4200 ppm P (TCP), there was an increase in friction. However, with additive X the results have shown this additive to be more active/ stronger at lower concentrations than TCP and hence, at 2000 ppm it has higher friction as it does for 4200 ppm. However, previous results would have expected ZDDP to be the lowest, however, this too could be an effect of concentration as 800 ppm P had a lower friction than 2000 ppm P.
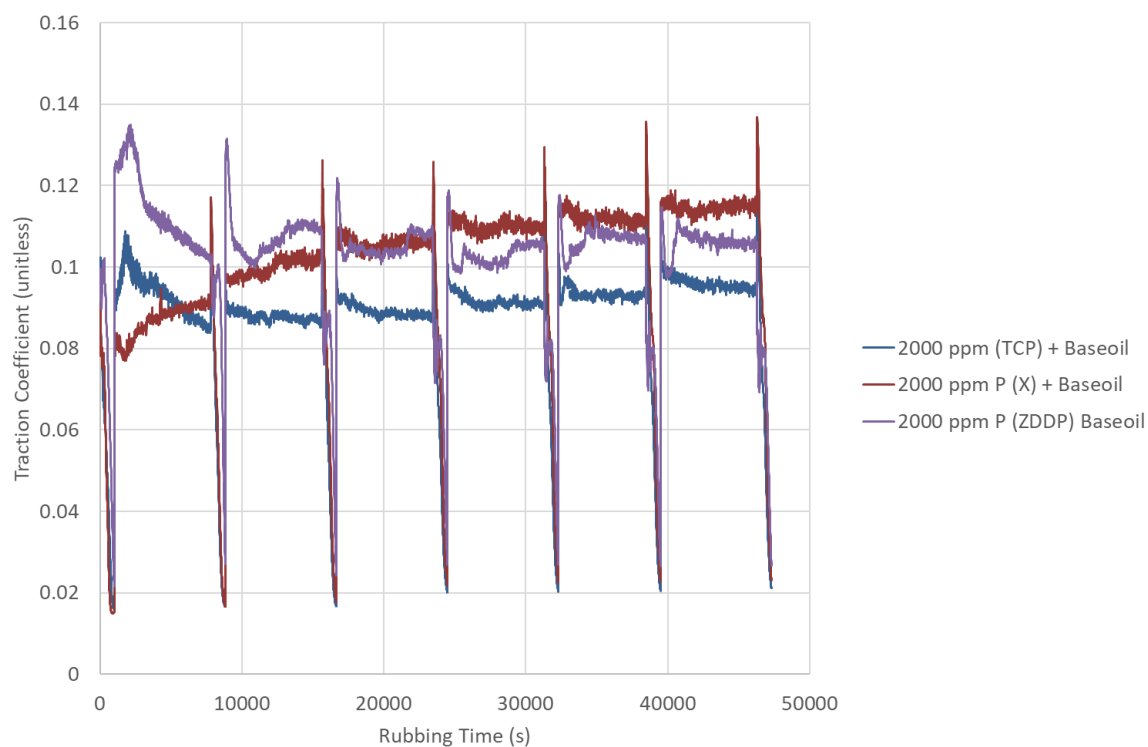
Figure 5-44 – The overall friction throughout the test for all the different anti-wear additives at 2000 ppm P.

5.3 Conclusions

Overall, it has been shown that a variety of methods have been used to evaluate three different anti-wear additives at different concentrations to understand whether ashless additives also promote micropitting like it has been shown for ZDDP.

From the MPR results, the wear track images found that micropitting was produced with the characteristic "V" shape pit pointing in the direction of friction, opposite to the rolling direction. TCP showed a slower progression and a smaller amount of micropitting compared to the other additives, but there did not appear to be an effect of concentration. The tribofilm also appeared coloured on the surface and the micropits were larger than those produced for ZDDP. Additive X showed a faster progression of micropitting and more micropitting than TCP, but less than ZDDP which, appears to increase slightly with increasing concentration. The micropits were a similar size to TCP, but larger than those produced from ZDDP and the tribofilm produced a

202

coloured surface on the wear track. ZDDP showed the fastest progression and a larger amount of micropitting, which, appeared to increase with concentration. The micropits were smaller than those produced for the other additives. It is possible the faster action of ZDDP results in forming smaller micropits due to forming lots of adjacent micropits simultaneously that intercept and therefore are prevented from growing into a larger micropit. Base oil had the slowest progression of micropitting, but quickly propagated into more severe failures like macropitting and produced no colours on the surface.

The overall friction results found that the boundary friction was mostly similar in the 0.1 range and no effect of additive concentration was seen. TCP had the highest friction followed by additive X, then base oil and then ZDDP. Unlike in the literature, a higher friction for ZDDP was not seen in the MPR. However, an initial increase was seen in the MTM-SLIM tests during tribofilm formation, but this was not seen in the MPR tests. This potentially suggests that there could be a slight loss in efficiency for the ashless additives in comparison to base oil alone and ZDDP and base oil. However, this marginal increase friction is the consequence of these additive providing better protection.

The track width results demonstrated that TCP had the lowest increase in track width and showed no effect of concentration. Additive X has some effect of concentration showing an increasing track width increase with high additive X concentrations. The base oil had the second highest track width increase. However, ZDDP had the highest track width increase, which, increased with higher concentrations. This highlighted that despite not progressing to more severe failure modes like base oil, a substantial amount of wear was seen from extensive micropitting alone showing the dangers of micropitting.

It was found from the MPR Stribeck curves that TCP had the highest friction followed by additive X and then ZDDP which, was comparable with base oil. The separation of Stribeck curves was more pronounced at higher concentrations.

From the roughness results it was found that the counterface rings which, are harder and rougher than rollers resulted in a decrease in roughness for all oils. The base oil test had the lowest average ring roughness and was similar to TCP. Additive X had a slightly higher roughness, but ZDDP had the highest. This agrees with theory of ZDDP protecting asperities early, which, prevents running in by protecting asperities and therefore, roughness which, promotes micropitting. The rollers displayed a mix of results due to severity of damage and method of roughness could capture or miss pits depending on where the Talysurf took the profile which, could therefore, affect the measurement. However, ZDDP has a lower roughness than everything which, suggests the extensive small micropitting led to a relatively smooth surface.

From the MTM-SLIM results, the wear track images revealed that the base oil shows severe wear and pitting and the direction of the pits are in agreement with the MPR in terms of the "V" shape pit pointing in the direction of friction, opposite to the rolling direction. The ashless additives show minimal wear with only some abrasion showing protection of the surface. As the concentration is decreased, 100 ppm P (TCP) has wear just like base oil, but additive X only shows some initiation of that kind of wear, suggesting that additive X is more effective at protecting the surface at lower concentrations. ZDDP visually affects the surface more than the others as shown from more discolouration of the wear track, but no pitting was seen.

The interferometry images found that the base oil produces a very misshapen and dark contact clearly indicating wear as confirmed by the optical images. TCP forms a very thin tribofilm of maximum thickness ~30 nm, which, also forms slowly, but it still sufficient enough for the wear not to progress into the failure mode seen with base oil except for 100 ppm. Additive X arguably forms a slightly thicker tribofilm as seen from the images, however, the measurements show the thickness is similar to TCP. ZDDP forms a very thick tribofilm ~80-140 nm very quickly in comparison.

The Stribeck curves showed that most show an increase in friction for the initial Stribeck curve to the final Stribeck curve. 100 ppm tests revealed higher friction difference for TCP than additive X as expected from the excessive wear seen for the TCP test, confirming that additive X is more active than TCP at lower concentrations. The base oil had the highest friction on the final Stribeck curve, due to the wear produced and a similar trend was seen for 100 ppm P (TCP). ZDDP had a slightly different trend showing high friction in the boundary regime, but low friction in the mixed/EHD regime in the initial Stribeck curve, but then the boundary friction decreases and the friction at high Hersey numbers increases. Friction results also highlighted that there may be an effect of friction increasing once the concentration increases, but this point differs for different additives. TCP had a friction increase at 4200 ppm P, X at 2000 ppm P and 2000 ppm P for ZDDP. However, this trend is not too strong for additive X. Difference in additive performance is more prominent at higher concentrations as shown from the difference between 800 ppm P and 2000 ppm P. The order of friction in the final Stribeck curves in the boundary regime for 2000 ppm starting from the lowest is ZDDP<TCP<X. The order of friction in the final Stribeck curves in the mixed/ EHD regime for 2000 ppm P starting from the lowest is TCP<X<ZDDP.

The overall friction results showed that for TCP, the highest boundary friction was found for concentrations of 100 ppm P and 4200 ppm P, which, were the same magnitude as base oil. This was expected for 100 ppm P as this has a lot of wear and pitting like the base oil test, but the 4200 ppm P may be due to the high concentration of TCP. Additive X showed a higher boundary friction for 2000 ppm P and 4200 ppm P as the same magnitude as the base oil again showing a higher concentration could lead to increased friction, but as additive X is more active, this occurs at lower concentrations than for TCP. ZDDP had a lower boundary friction for 800 ppm P than 2000 ppm P, which, are both lower than base oil and ZDDP also initially increases in boundary friction before it decreases. This effect is not seen with the ashless additives. At

800 ppm P, the boundary friction was similar for all additives except for the initial increase for ZDDP. However, at 2000 ppm P, there was more separation and the order of boundary friction starting with the lowest was TCP<ZDDP<X, this is a different trend from what was observed from the Stribeck curves.

Overall, it can be seen that TCP and additive X promote micropitting to a much lesser extent than ZDDP. This could be attributed to their slower and thinner tribofilm formation that allows surfaces to "run-in" and, therefore, do not maintain high asperity contact pressures as aggressively as ZDDP. This delays the onset of micropitting initiation however, micropitting does seem to initiate earlier than for the base oil tests as the protection is sufficient to protect against more severe failure modes.

Chapter 6.   The Friction and Tribofilm Evaluation of Commercially Available Fully Formulated Lubricants

6.1 Introduction

As shown from Chapter 4 and Chapter 5, the individual components of a lubricants' formulation have significant effects on the friction in different lubrication regimes and also on the type and amount of wear produced.

The next two chapters uses the knowledge acquired from the previous chapters on base oils and anti-wear additives to aid in the understanding of the tribological performance of a range of fully formulated commercially available lubricants with respect to PGB applications and their effect on friction across a range of lubrication regimes will be investigated along with the tribofilms these formulations produce. This information will be used to identify whether current lubricants are suitable for the PGB in the UltraFan© by using the MTM to create representative conditions to understand the performance of different formulations. Consequently this will enable designers to deduce whether current lubrication solutions are suitable to satisfy this highly loaded gear box or whether mitigations like the previously discussed dual oil system would be necessary to meet the requirements of the PGB and high temperature core as discussed in section 0.

The lubricants chosen for investigation in this Chapter have a range of different physical properties and chemistries to investigate whether different properties offer specific benefits over others and details of these can be seen in 3.2.2 in the Commercially Available Full Formulation Lubricants section. This includes a range of kinematic viscosities and different additives packages, thus giving a range of load carrying capabilities and tribological properties.

6.2 Results & Discussion

6.2.1 MTM Evaluation

Effect of Temperature on Commercially Available Lubricant Performance

Stribeck curves for lubricants A-D can be seen in Figure 6-1 to Figure 6-4. They all follow the same trend with temperature: as the temperature increases, the traction coefficient decreases. However, normalising the Stribeck curves for viscosity by plotting them against the Hersey number, only accounts for shifting the curves laterally. As the temperature increases, the friction decreases because of a decrease in the viscosity of the lubricant, thus less resistance to shear. Also, a lower viscosity forms a thinner lubricant film and is less effective at separating opposing surface asperities resulting in the surfaces contacting, which, could therefore, give rise to higher traction coefficients.

The difference in viscosity is the dominant effect which, seems to be dictating the traction coefficient in these Stribeck curves. This trend is also more apparent on the right-hand side of the Stribeck curves in the mixed/ EHD regimes (depending on the lambda ratios as shown in Chapter 3). In the boundary regime on the left-hand side of the Stribeck curves there is less separation as this regime is less influenced by viscosity and more influenced by the additive package in accordance with the literature information (3,7). As these graphs are comparing the same lubricants at different temperatures, they all have the same additive package.

The error bars of the standard deviation are displayed on the data points on the Stribeck curves which, are taken from a mean average of three tests. As no surface is identical, it is expected that asperity contact in the boundary regime will lead to more varied traction coefficients which, results in the boundary regime having larger error bars.
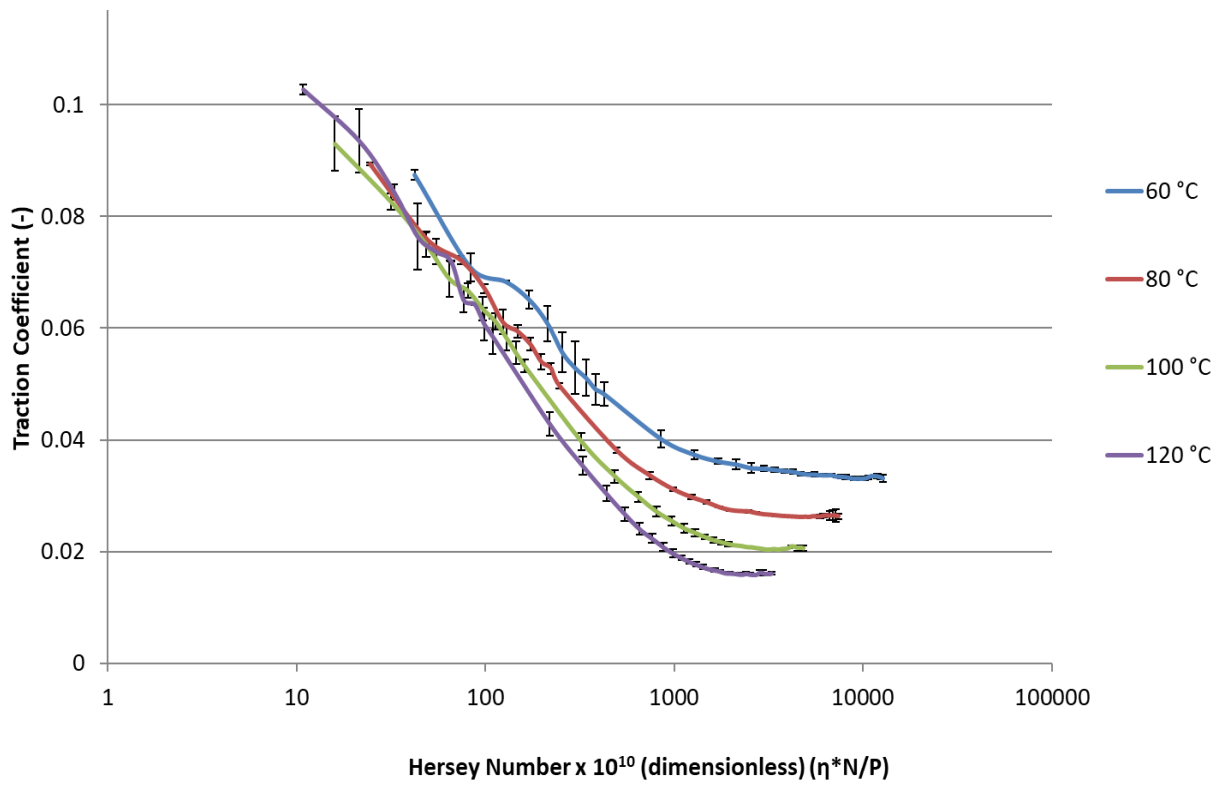
Figure 6-1 – Stribeck curves for Lubricant A at a range of temperatures.
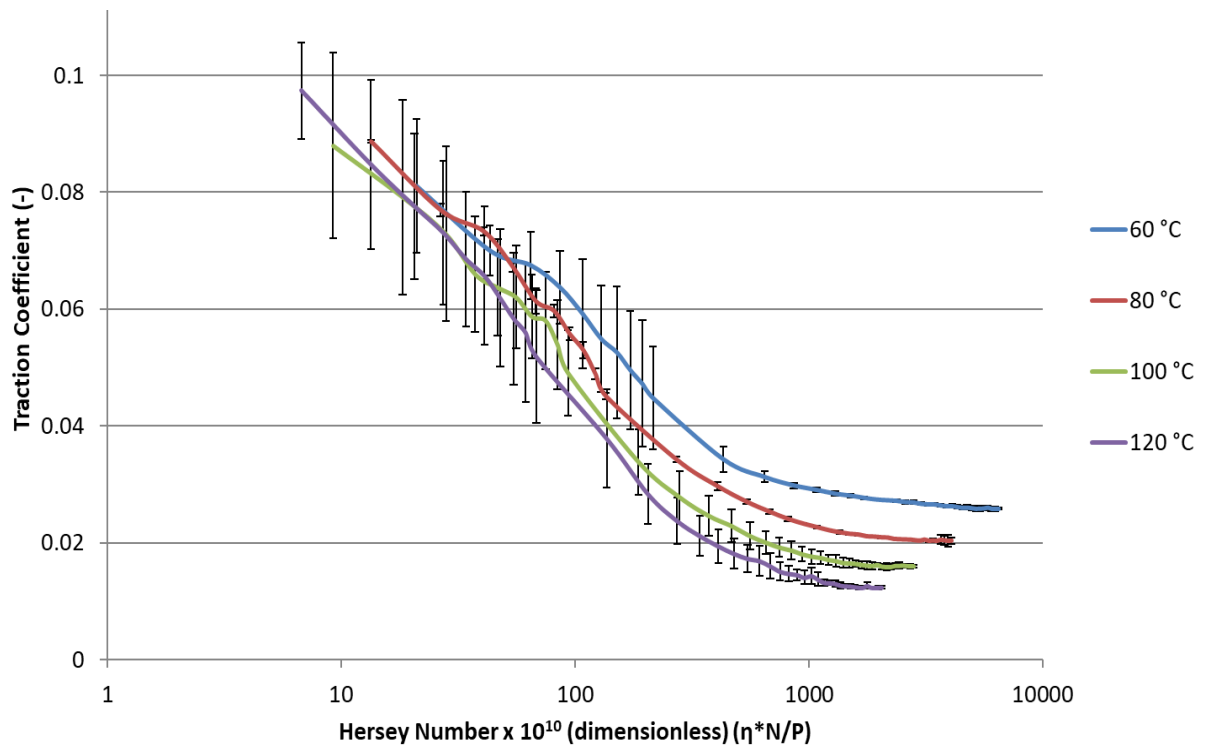
Figure 6-2 - Stribeck curves for Lubricant B at a range of temperatures.

209
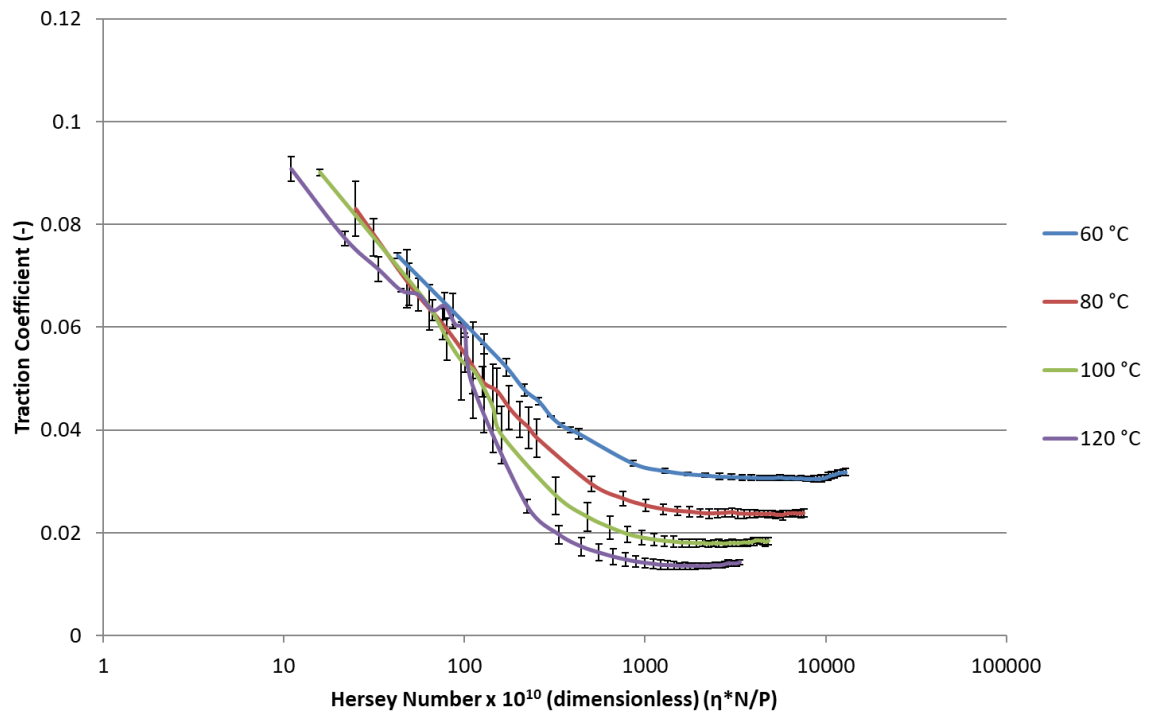
Figure 6-3 - Stribeck curves for Lubricant C at a range of temperatures.
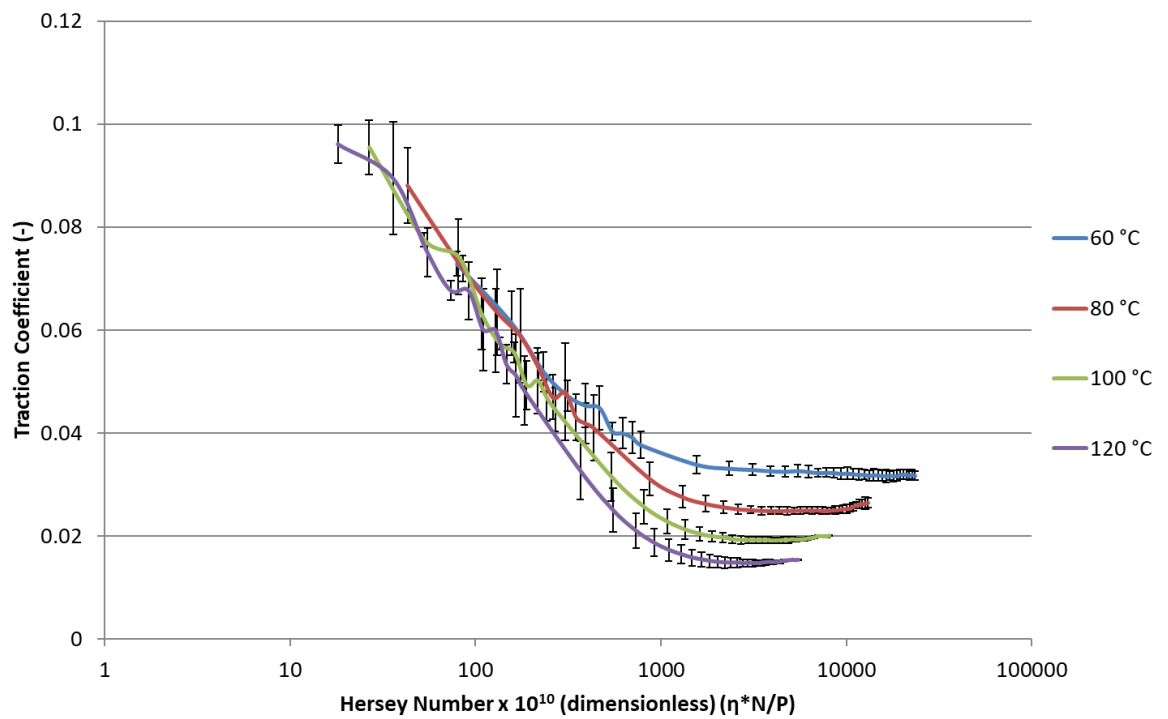
Figure 6-4 - Stribeck curves for Lubricant D at a range of temperatures.

210

Comparison of Oil Brands at the Same Temperature

The Stribeck curves comparing lubricants A-D are shown in Figure 6-5 to Figure 6-8 respectively. These have also been normalised for viscosity by plotting them against the Hersey number. There is less separation in the EHD/ mixed regime on the right-hand side of the curves in comparison to the boundary regimes on the left. This potentially suggests that despite a difference in base oil package, the difference in additive package is causing the largest difference in the boundary regime. However, as shown from Chapter 4, the difference in base oils can still contribute here too.

The error bars also overlap in these graphs showing that the differences in formulation are not producing a distinct trend. However, there is a trend of low to high friction in the boundary regime from Lubricant B to C to A to D. It is likely these differences are from difference in additive package as shown in Chapter 3. However, due to the difference in types and amounts of different additives, it is difficult to deduce the sources of the difference in friction. It is likely, as shown in Chapter 5, that certain additive may give rise to increased friction if the additive forms a rough tribofilm, but this needs further investigation.

It can also be seen that there is less convergence at lower temperatures for lubricant B on the right-hand side of the graph suggesting that the difference in base oil package may be more apparent at low temperatures. Whilst this separation is likely to be influenced by viscosity, it is also likely that the difference in the base oils of the formulated lubricants also contributes as shown in Chapter 4. Chapter 3 lists the available information on base oil packages between the test lubricants. It can be seen from this table that all of the oil have different base oil packages, some of which, are similar to those used in Chapter 4. In Chapter 4 it was demonstrated that different molecular chemistries can influence friction even when independent of viscosity. Here, lubricant B with a base oil package comprised mostly of NPG and TMP seems to have a lower traction coefficient than the other lubricants containing MONOPE, DIPE and high

molecular weight TMP. This contradicts the findings in Chapter 4 as friction decreased as the number of ester groups increases. There could be molecular differences that result in similar frictional effects, for example, the use of TMP rather than MONOPE would increase friction but using longer chains would, therefore, decrease friction again. Despite lubricant B having a lower friction in the mixed regime at lower temperature tests due to having base oil package comprised of NPG and TMP, this suggests the other lubricants (A and C) may have branching present.

Due to the complexity in the many different formulation differences between these lubricants it is difficult to identify the root cause of the frictional differences. However, on balance, lubricants A and C have lower friction that the other lubricants, suggesting these may potentially result in lower and less severe wear mechanisms that the other lubricants.
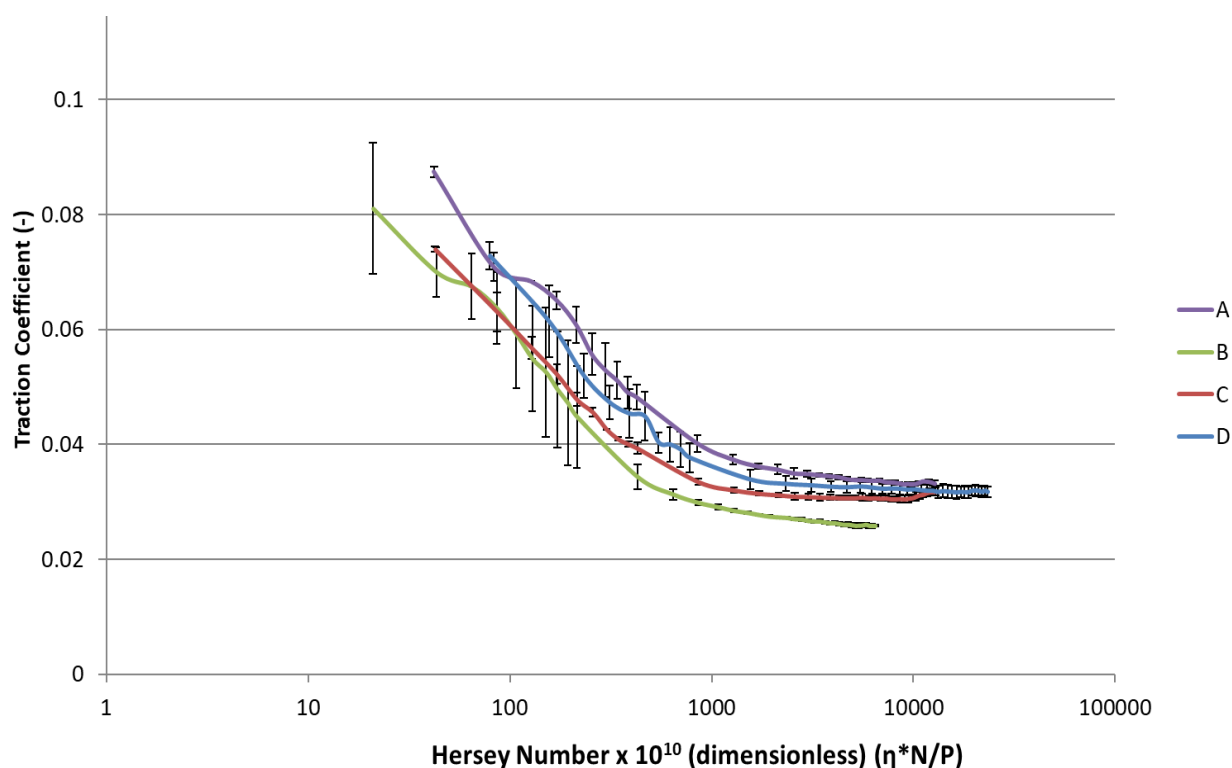
Figure 6-5 - Stribeck curves at 60 °C for lubricants A-D.
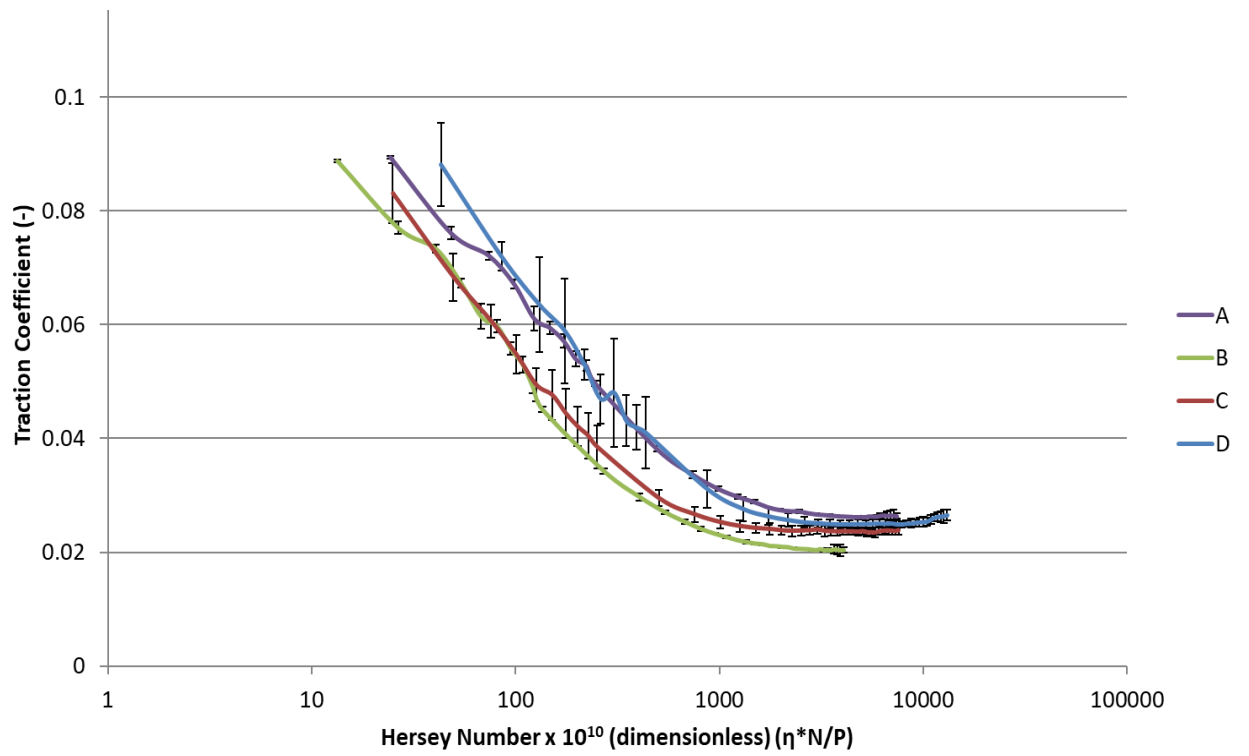
Figure 6-6 - Stribeck curves at 80 °C for lubricants A-D.
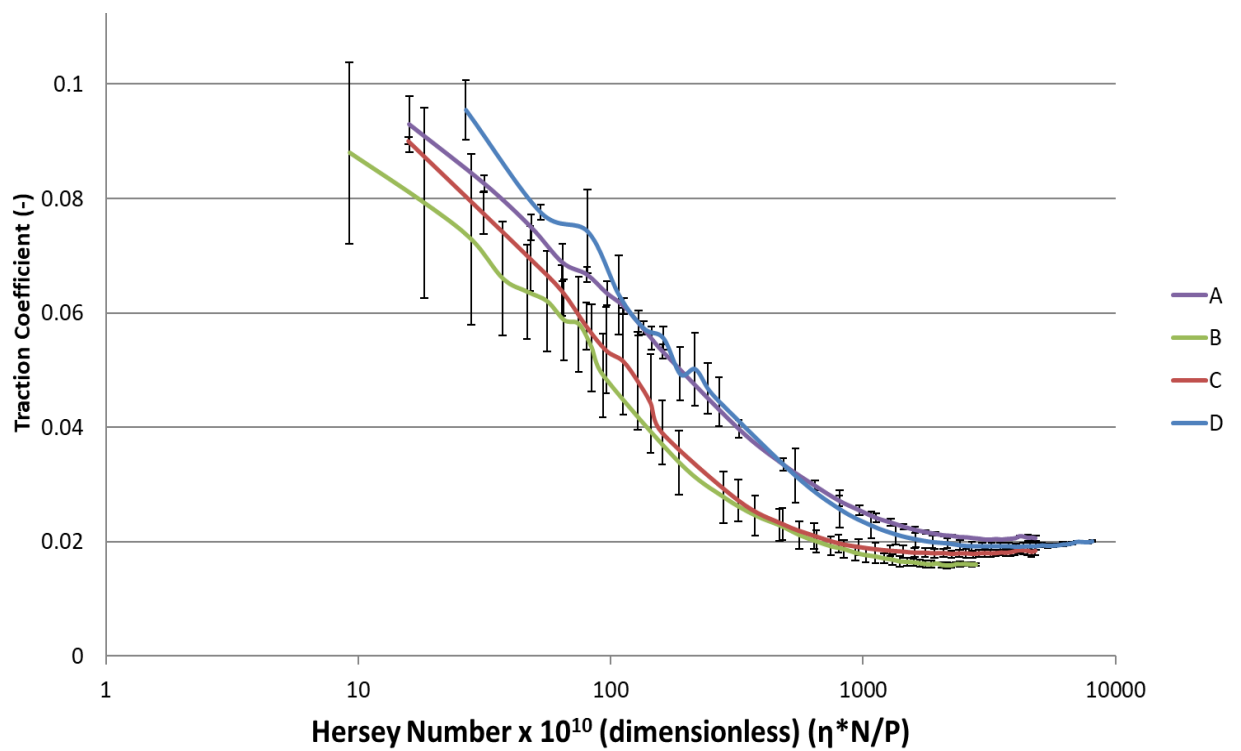
Figure 6-7 - Stribeck curves at 100 °C for lubricants A-D.

213
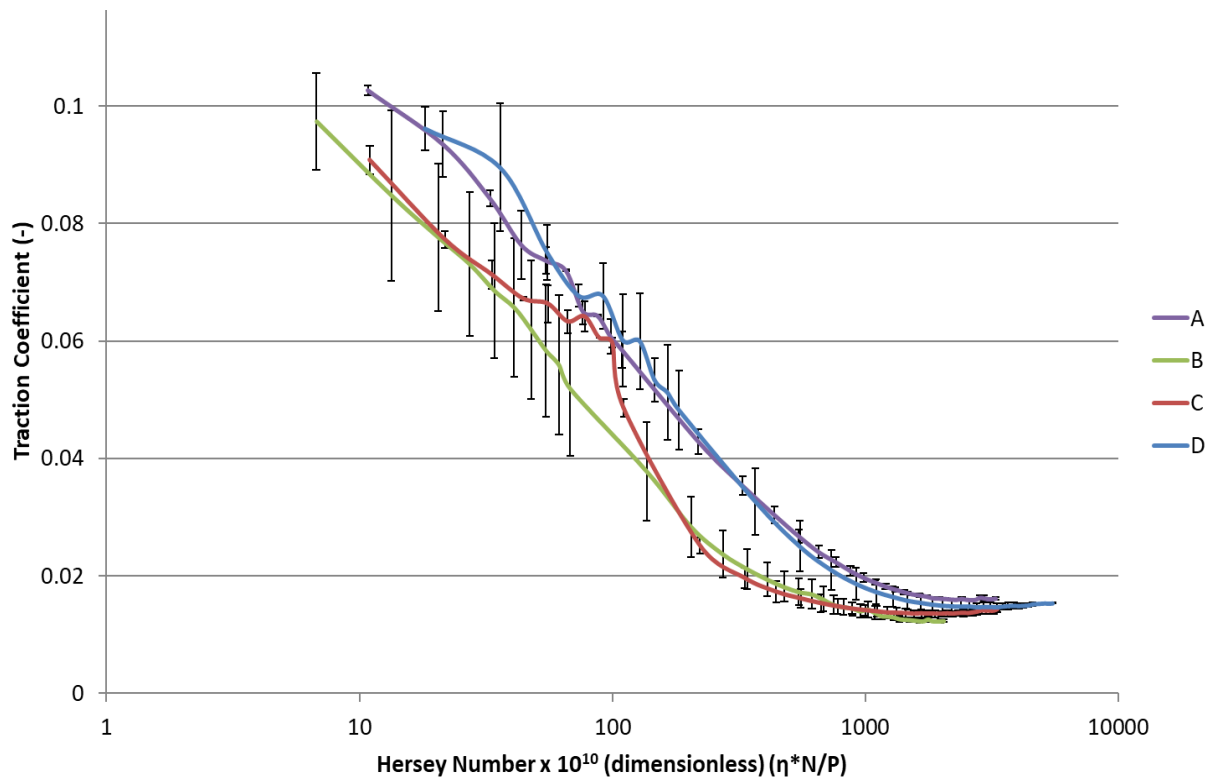
Figure 6-8 - Stribeck curves at 120 °C for lubricants A-D.

6.2.2 MTM-SLIM Evaluation

Lubricants A-D were evaluated with the MTM-SLIM to understand differences in the behaviour of boundary additives under the chosen conditions. This section will evaluate test results from a constant wear test at low entrainment speeds to promote tribofilm formation and monitor its formation over time under boundary conditions. Understanding of tribofilm formation will contribute to further understanding of how specific wear mechanisms are affected, in particular micropitting.

Optical Microscope Wear Track Images

Images of the wear tracks on the MTM ball and discs can be seen in Figure 6-9. It is very apparent that the wear tracks for lubricant C show that barely any wear has been produced in comparison to the other lubricants. Lubricant D seems to show slightly less wear than lubricants

A and B with only abrasive scoring on the wear track visible. Lubricants A and B show the most surface damage with abrasion and potentially some minor pitting. However, in comparison to wear produced in MPR tests, the wear produced on the MPR specimens is minimal. Figure 6-9 also shows the rolling direction of the ball and the disc and the direction of the frictional force. However, this is usually more useful to consider when pitting is present as the direction of the pit is dependent under the frictional direction (183).

Note the difference in microscopy images in comparison to chapter 5, a different microscope was used that had dark field mode which, gave better visualisation of some for the wear features as opposed to bright field imaging in these images.
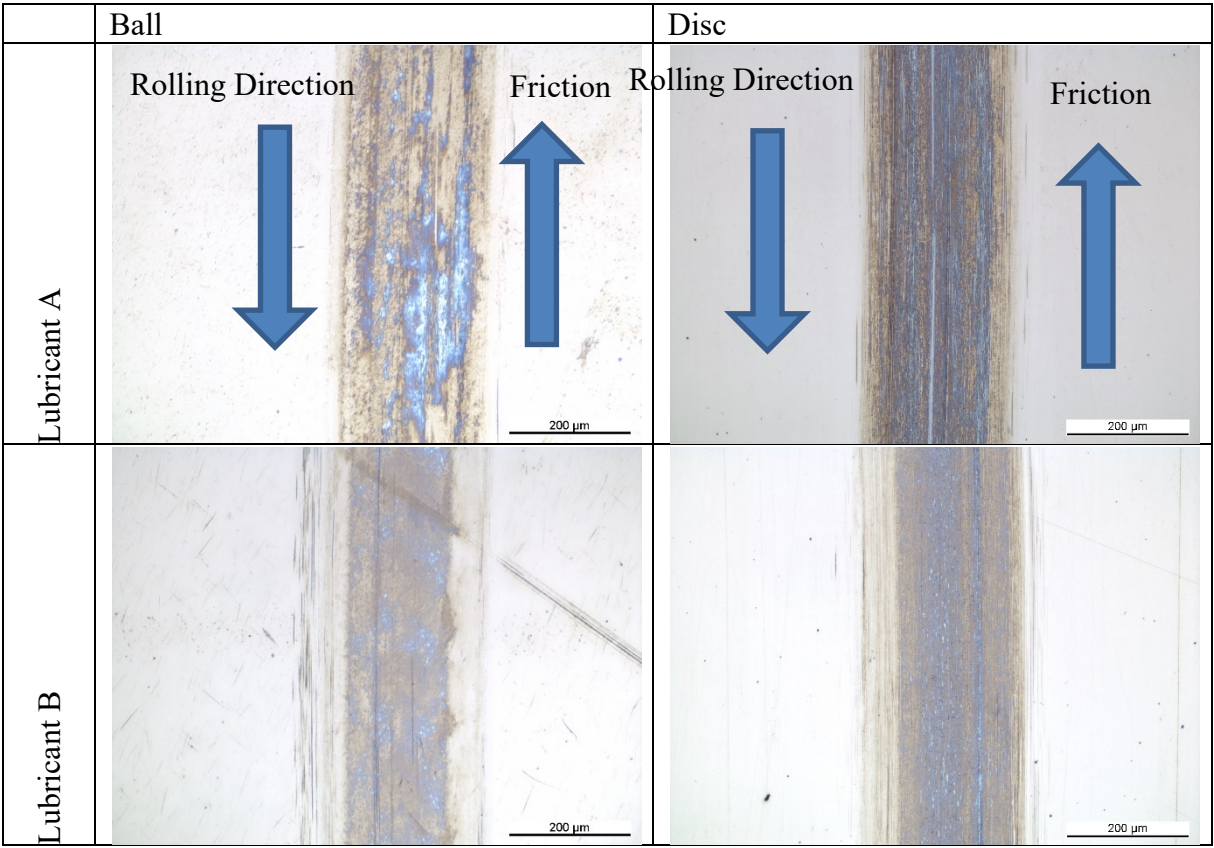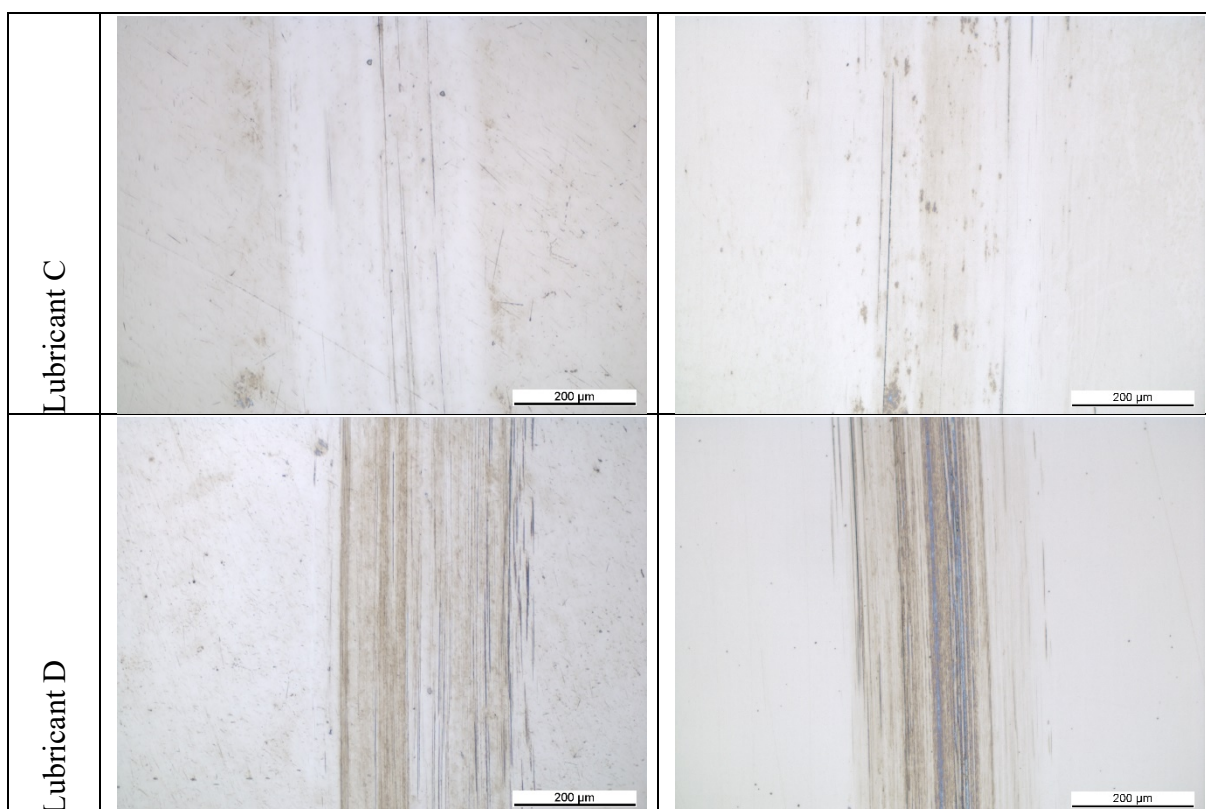
Figure 6-9 – Wear track optical microscope images of ball and disc specimens from the MTM-SLIM tests.

Tribofilm Evaluation

Figure 6-11, Figure 6-13, Figure 6-15 and Figure 6-17 show the SLIM interferometric images through the duration of the wear test for the completing three runs for each lubricant. Figure 6-10, Figure 6-12, Figure 6-14 and Figure 6-16 show the recorded film thicknesses for each test throughout the total rubbing time.

In comparison to the SLIM images in Figure 5-23 with ZDDP, the tribofilms formed are much thinner for all test lubricants as expected for ashless additives (38,166). However, the interferometry images show poor repeatability with the same lubricant. However, all lubricants also seem to demonstrate a gradual formation, removal and reformation process throughout all the tests.

In Figure 6-11, SLIM041 for lubricant A appears to be different to the other repeats as there is a faster build-up of a film but also appears to show an abrasive line horizontally throughout

216

the Hertzian contact. As shown in Chapter 3, loss of an entirely circular contact patch with interruptions as the edges of the Newton rings is indicative of wear on the surface. But the maximum tribofilm produced by lubricant A is of a similar magnitude of thickness of <40 nm as shown in Figure 6-10 for all three tests. This value is in agreement with the literature (38,166). Also, the tribofilm morphology also appears to be slightly patchy in places during formation similar to tribofilms produced by ZDDP but gradually forms a thicker smoother film as the film develops (29,164,185). However, despite the gradual formation, removal and reformation of the tribofilm, except with the abrasive scoring line in SLIM041, there appears to be no excessive wear distorting the interferometry images as in Figure 5-23 for the SLIM tests using base oil.
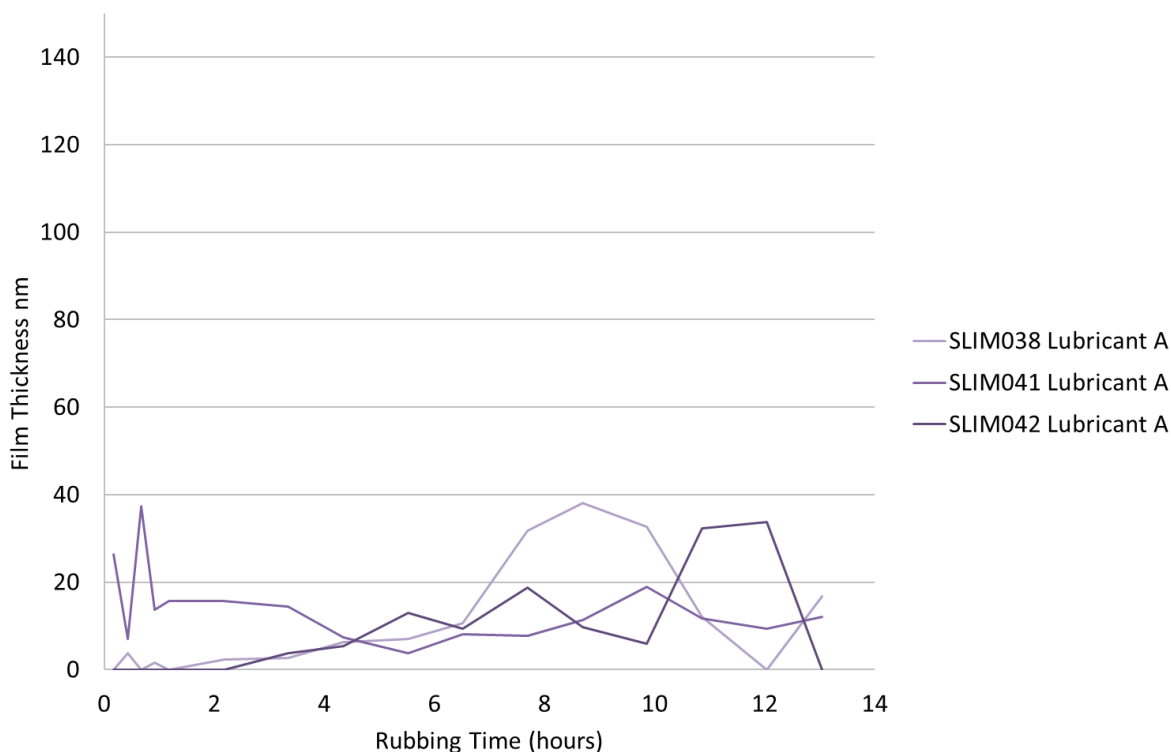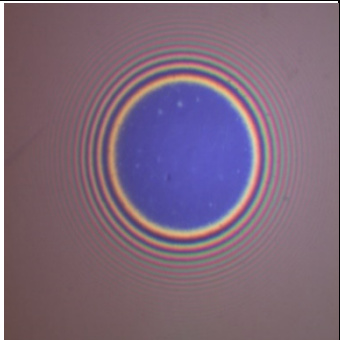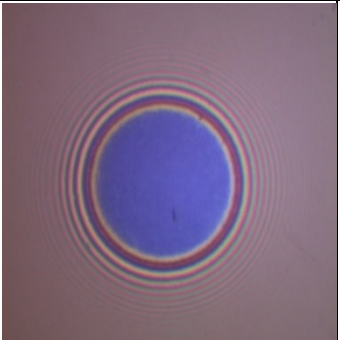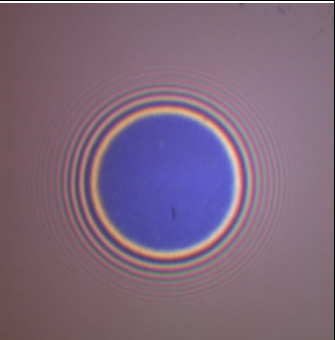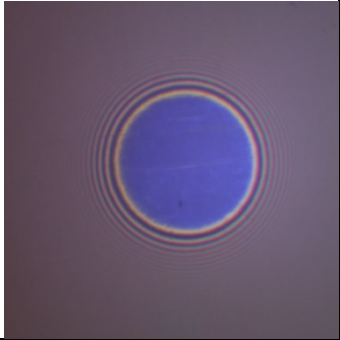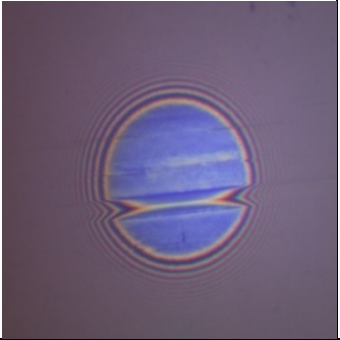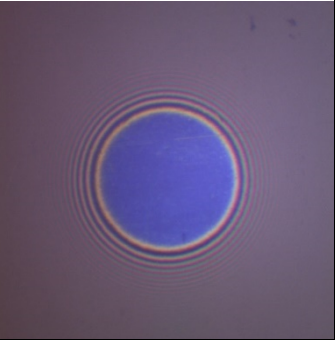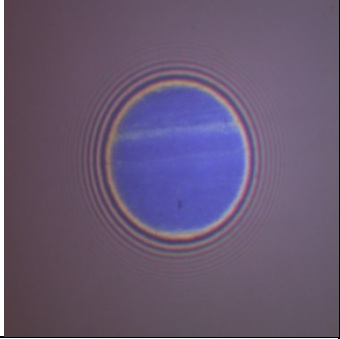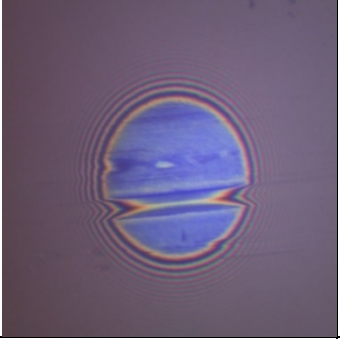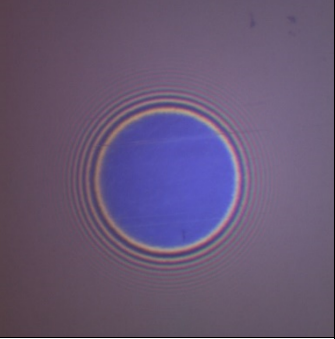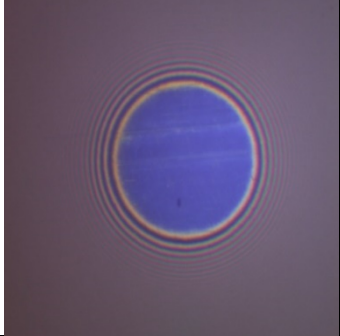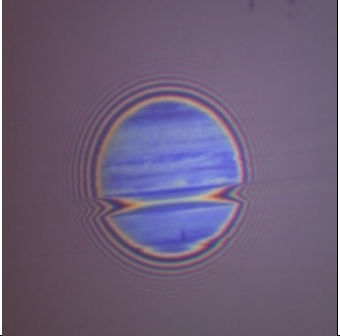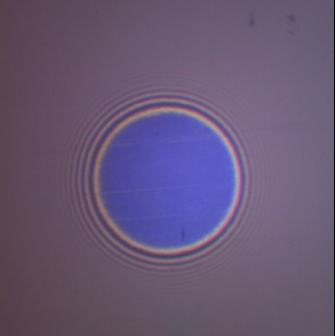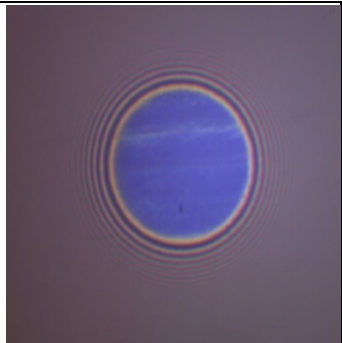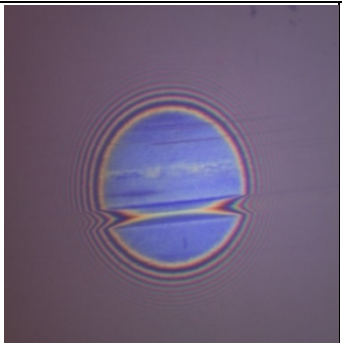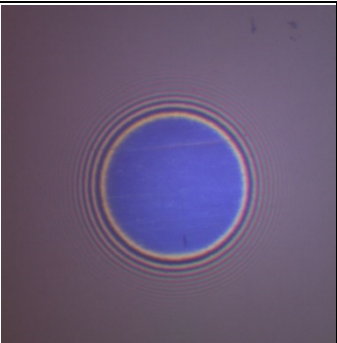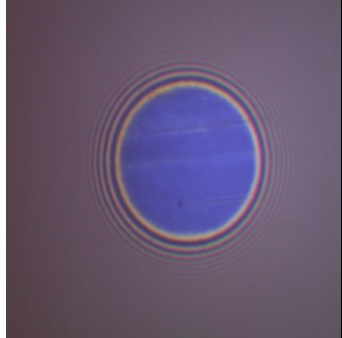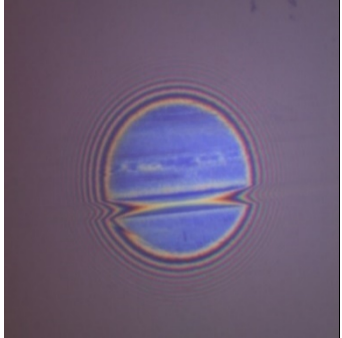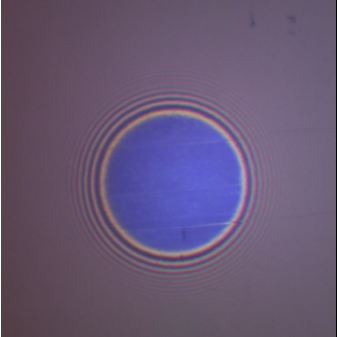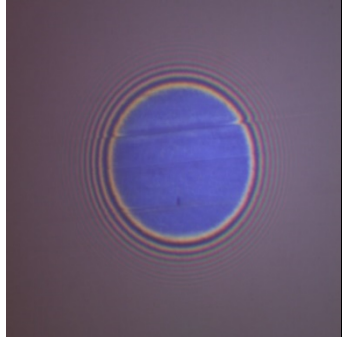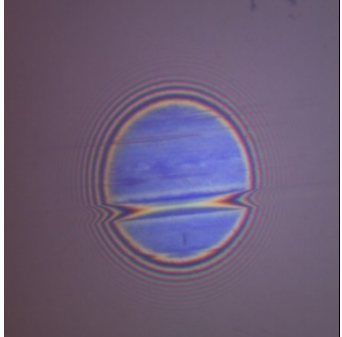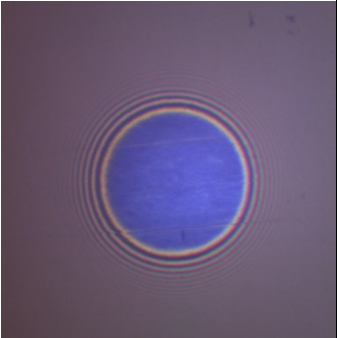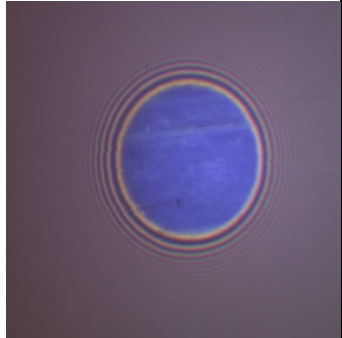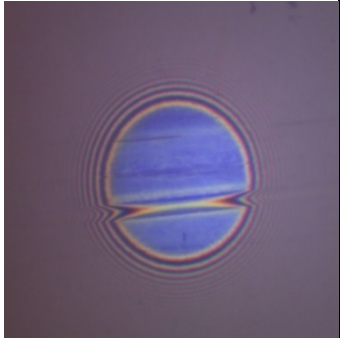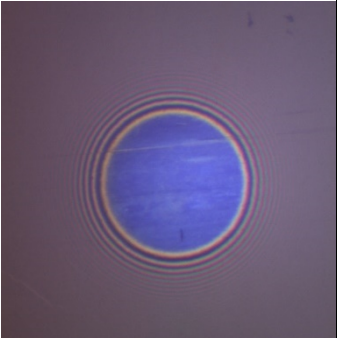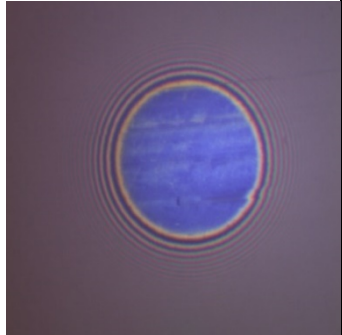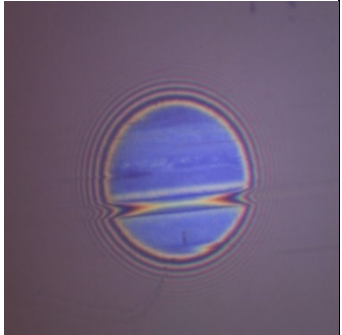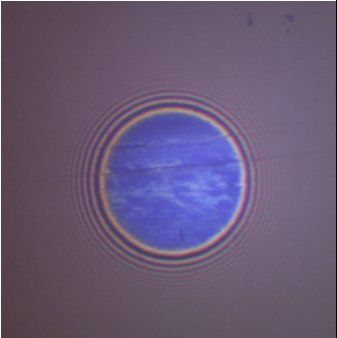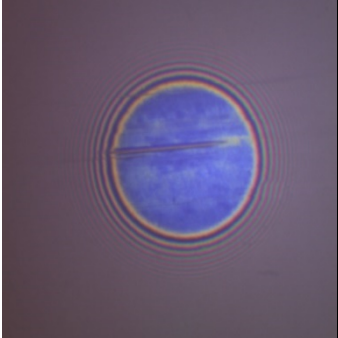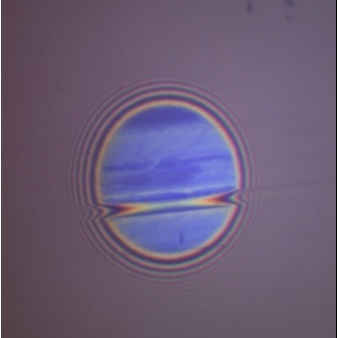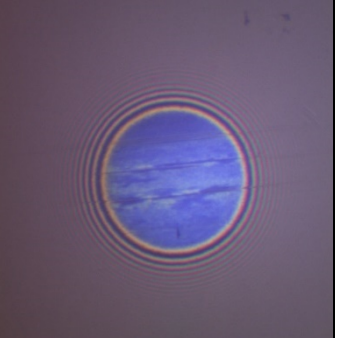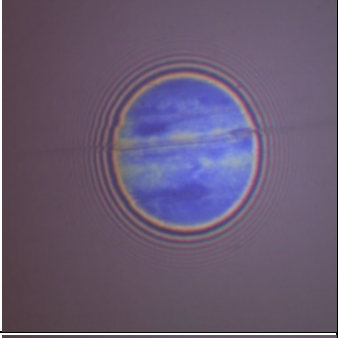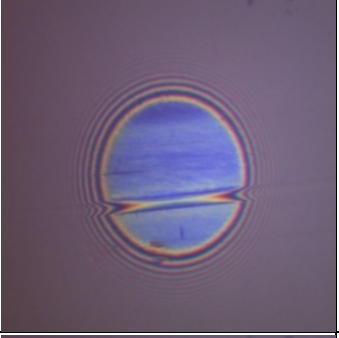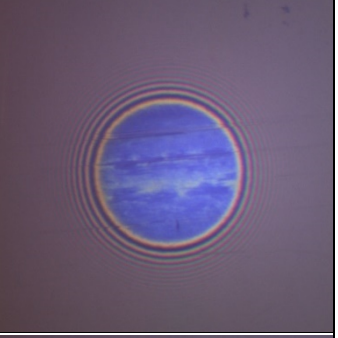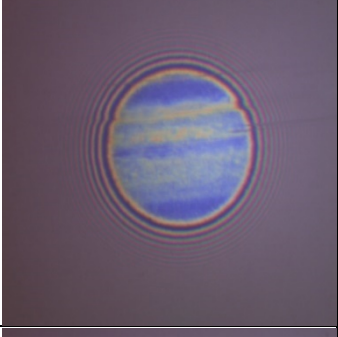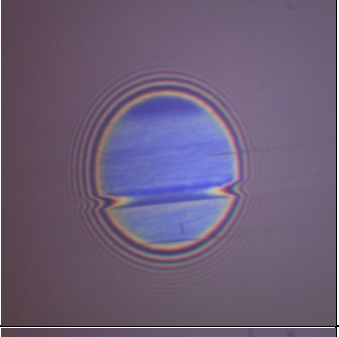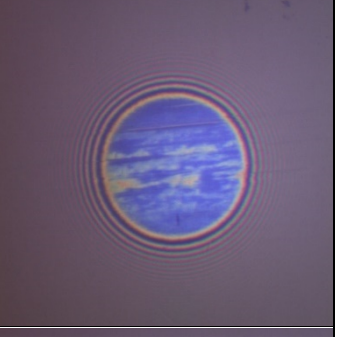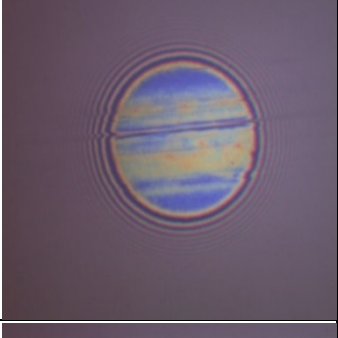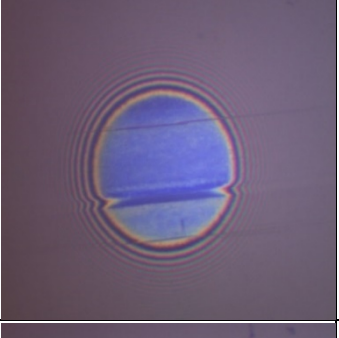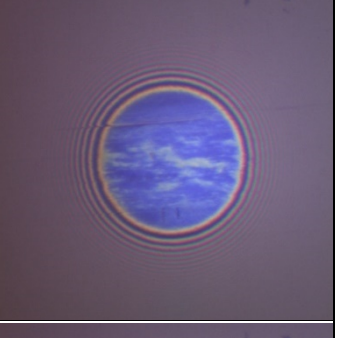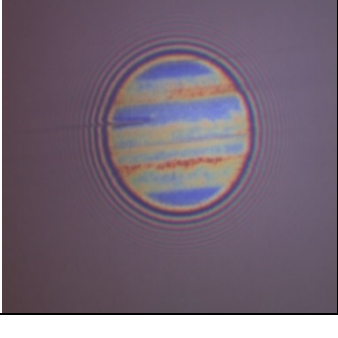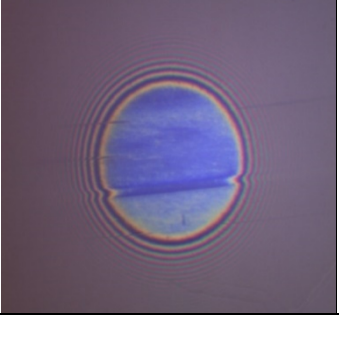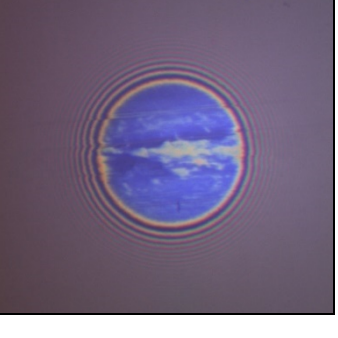
Figure 6-10 – Graph showing the tribofilm thicknesses produced by lubricant A throughout each test.

Test time (seconds) / Test Number	SLIM038	SLIM041	SLIM042
0			
621			
1521			
2421			

3321			
4221			
7821			
12042			
15642			

19863			
23463			
27684			
31284			
35505			

39105			
43326			
46926			

Figure 6-11 - Interferometer images from the MTM-SLIM for 3 repeats for Lubricant A.

Again, differences between the repeats with lubricant B can be seen in Figure 6-13. SLIM037 seems to develop a film that is sustained longer than the other tests before the film is then removed. As shown from Figure 6-12, they also produce tribofilm no thicker than 40 nm again synonymous with tribofilm thickness of TCP reported in the literature (38,166). It can also be seen SLIM044 appeared to form only a very thin film ~10 nm, despite using the same lubricant and conditions. Maybe there could be subtle differences in the specimen surfaces that prevent or promote the initiation of film formation. However, this will need to be investigated further.
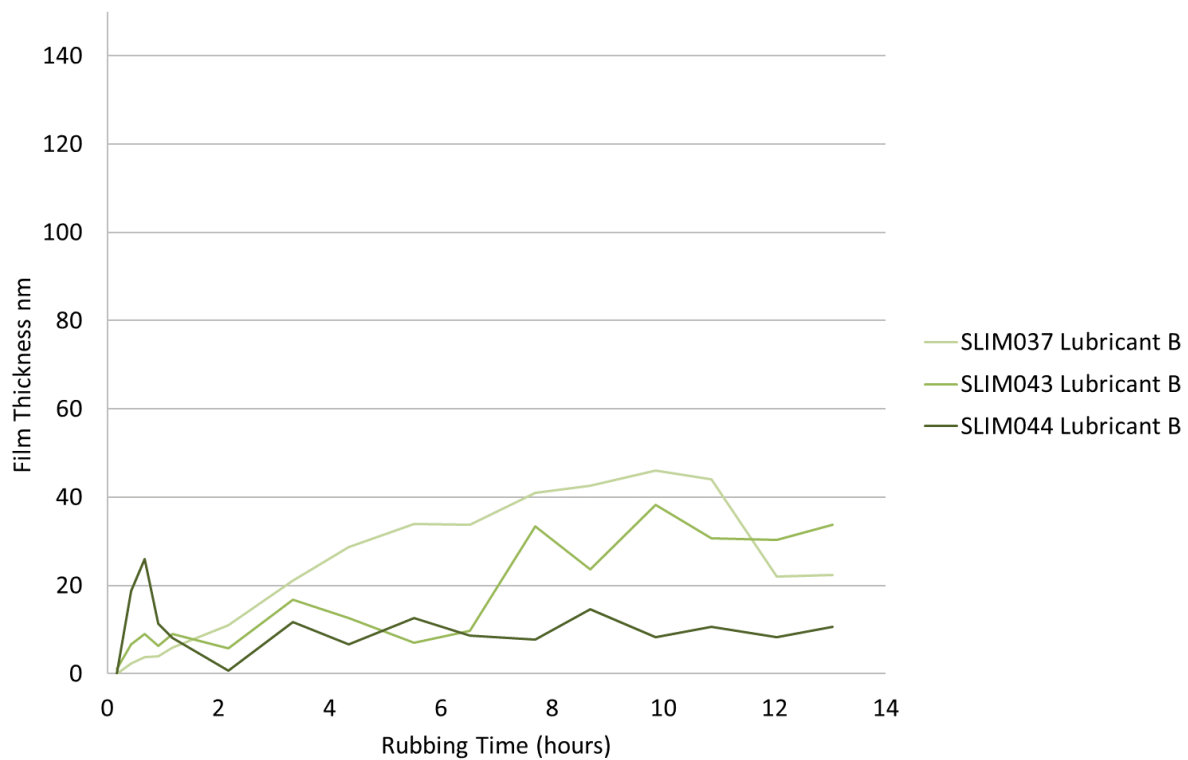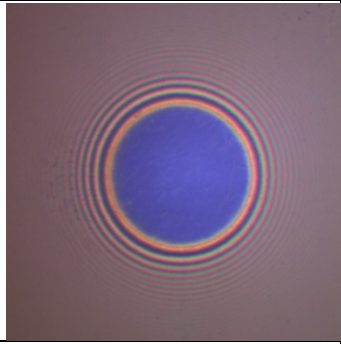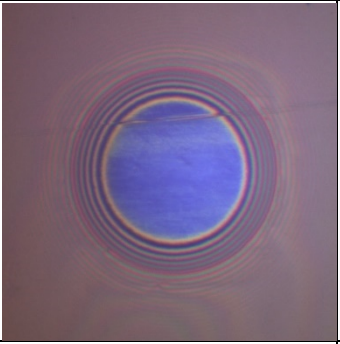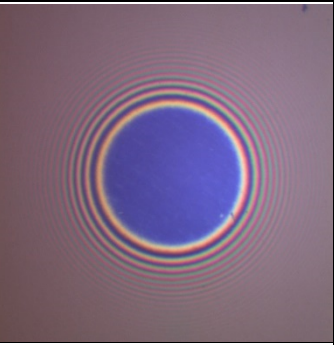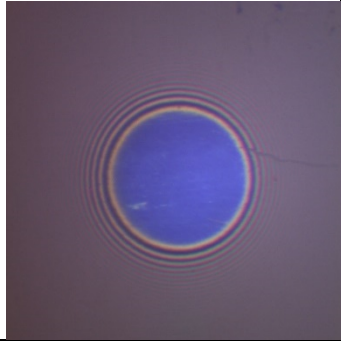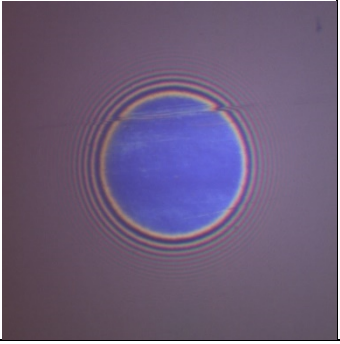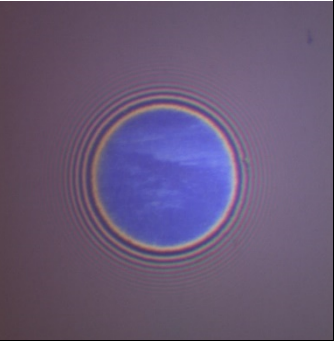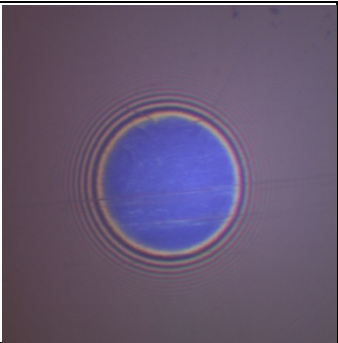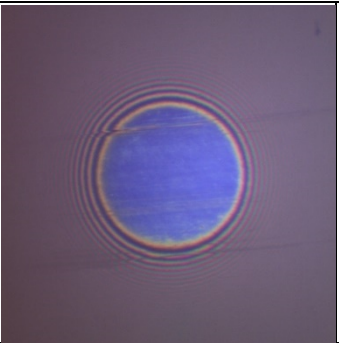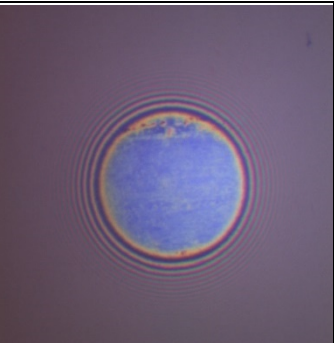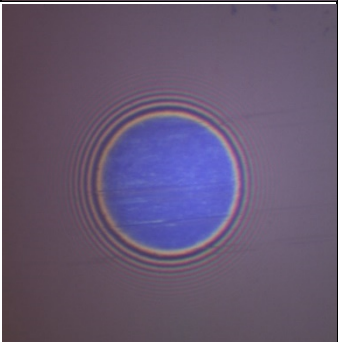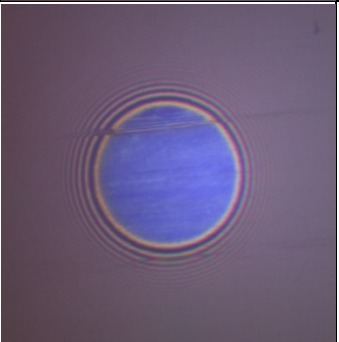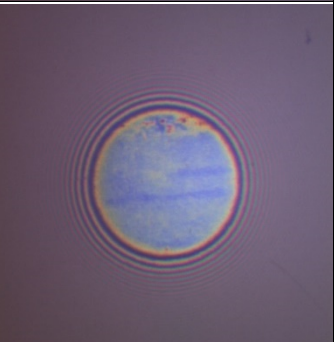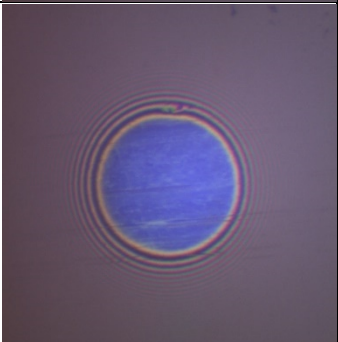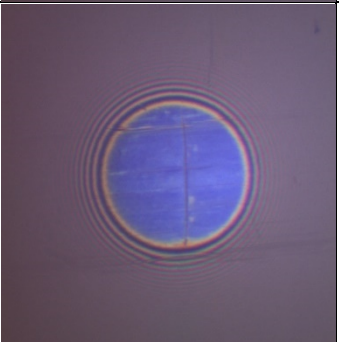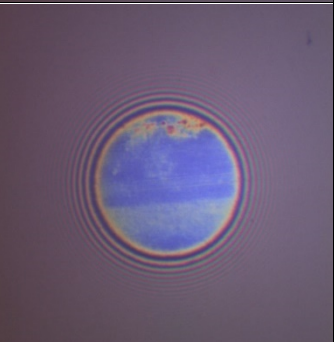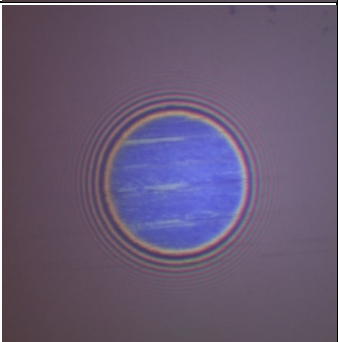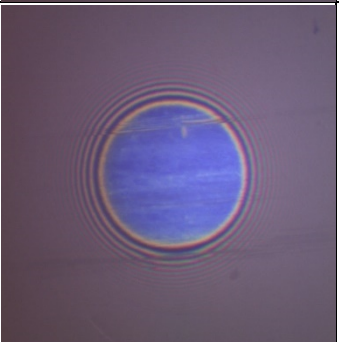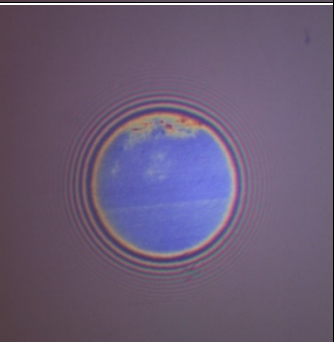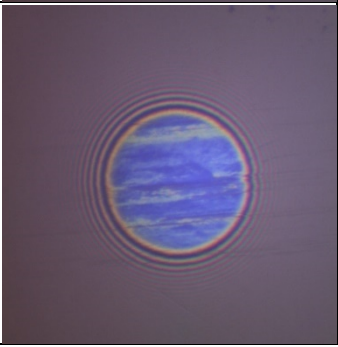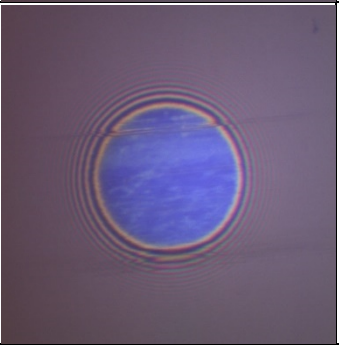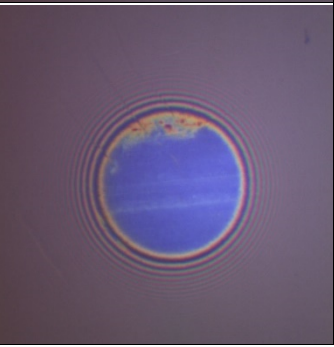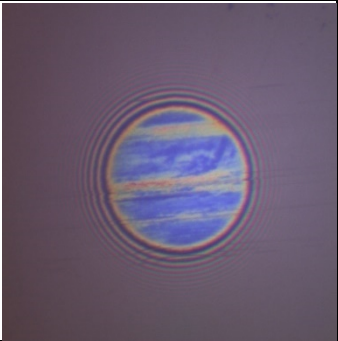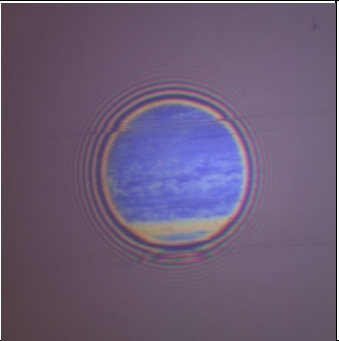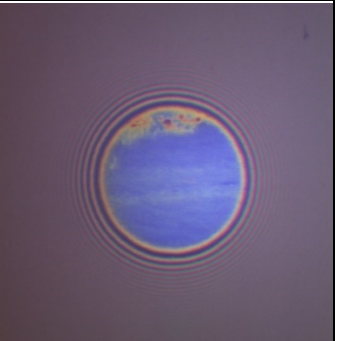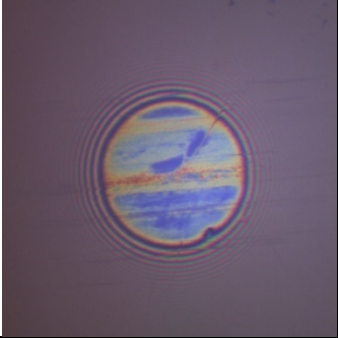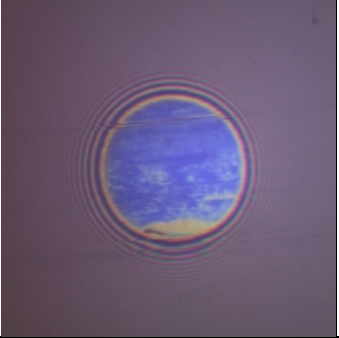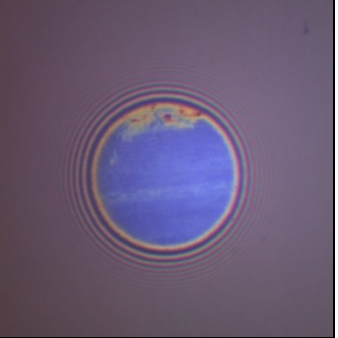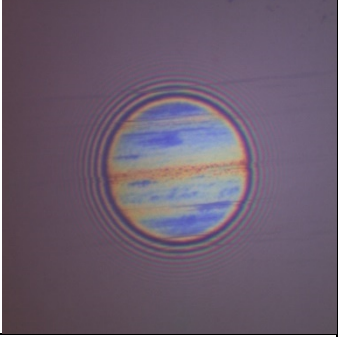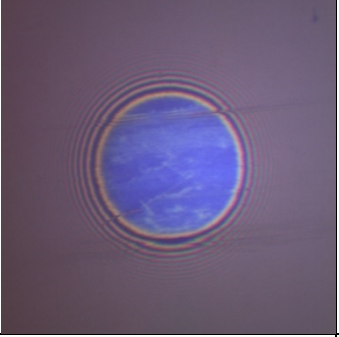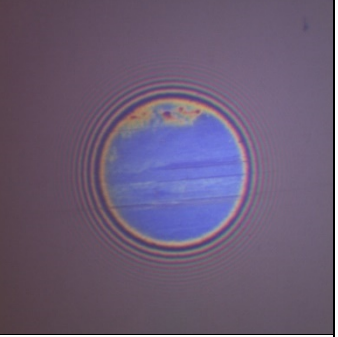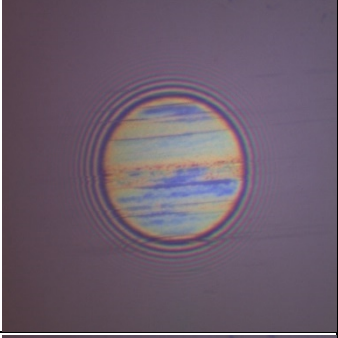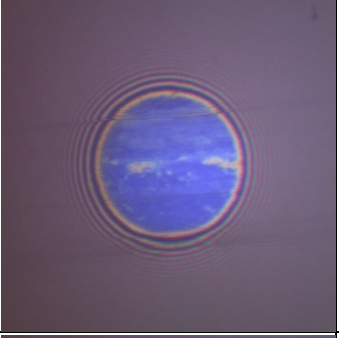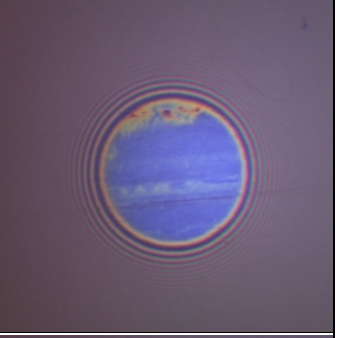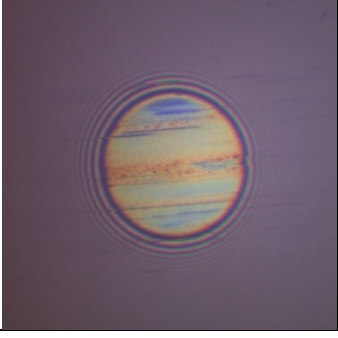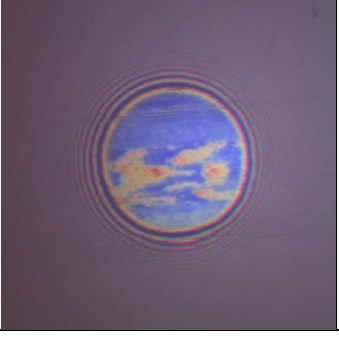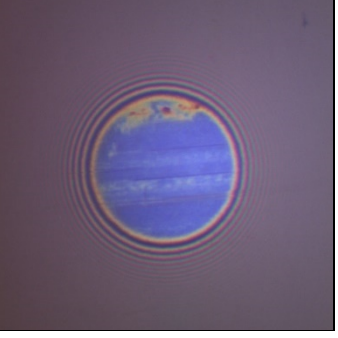
Figure 6-12 – Graph showing the tribofilm thicknesses produced by lubricant B throughout each test.

Test time (seconds) / Test Number	SLIM037	SLIM043	SLIM044
0			
621			

1521			
2421			
3321			
4221			
7821			

12042			
15642			
19863			
23463			
27684			
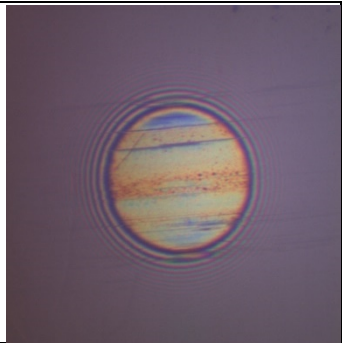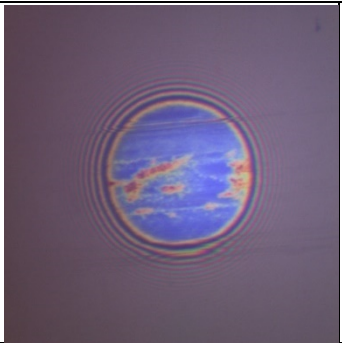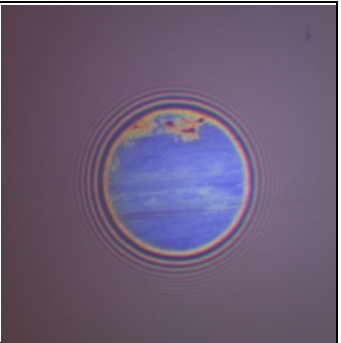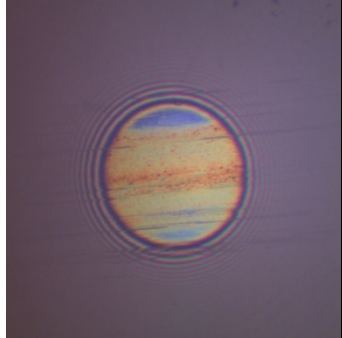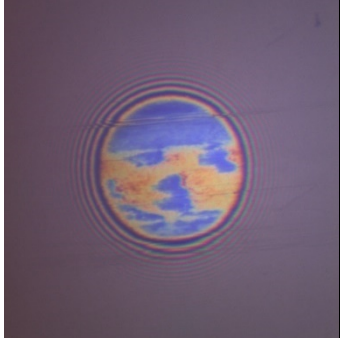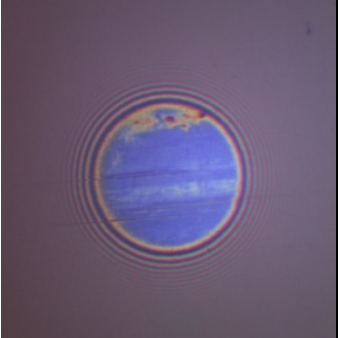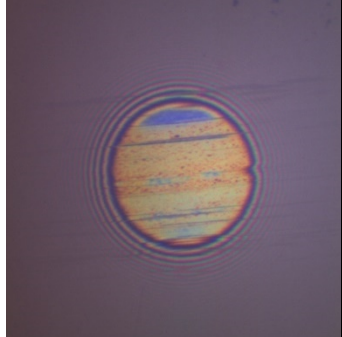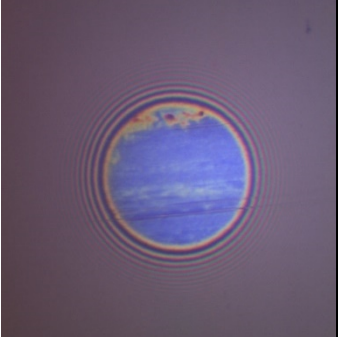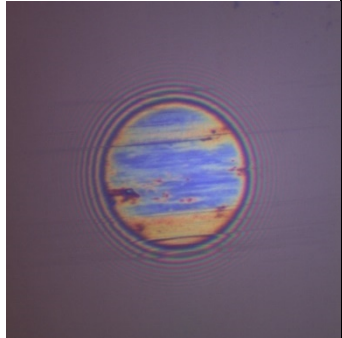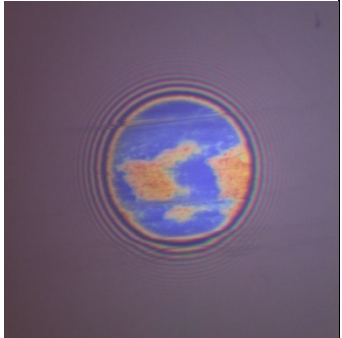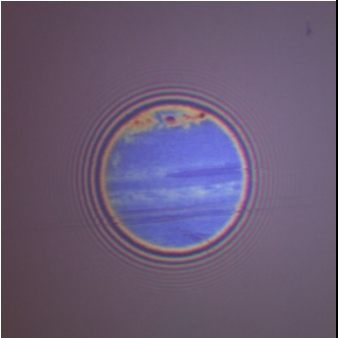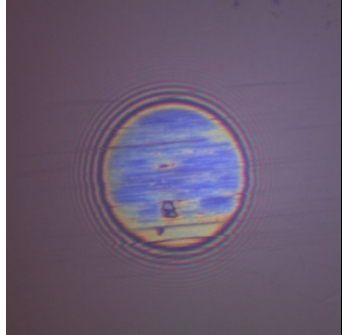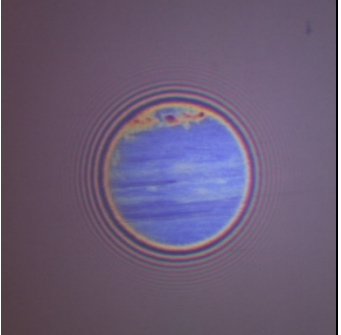
		225	
31284			
35505			
39105			
43326			
46926			

Figure 6-13 - Interferometer images from the MTM-SLIM for 3 repeats for Lubricant B.

In Figure 6-15, all the interferometry images for the tests with lubricant C show a misshapen Hertzian contact, which, would suggest that wear was occurring or something else is preventing a smooth circular contact with the mapper window. However, this minimal wear was seen in the wear track image in Figure 6-9, but, the measured tribofilm thickness was a similar thickness to the other lubricants tested as shown in Figure 6-14. Some potential theories for this are:

1. There is no tribofilm present and wear is giving rise to the misshapen contact. However, this is unlikely due to the image of the wear track of the ball with lubricant C showing little wear and the interferometry images are not accompanied by dark colours, which, can be misinterpreted as a thick anti-wear tribofilm as shown in Chapter 3.

2. The tribofilm is opaque and the light cannot pass through the tribofilm and is reflecting off the surface of the tribofilm instead with which, the mapper window is making irregular contact. The SLIM method relies upon the tribofilm being translucent such that a light wave can pass through, reflect off the steel surface and recombine with another light wave that has been reflected off the chromium layer to produce the interference image (38,93,94). Work needs to be done to understand how the light interacts with different types of film and whether different films have different degrees of translucency/ opacity and/ or refractive index.

3. The surface of the steel has been softened by the EP additive in lubricant C resulting in deformation of the ball on the surface of the mapper window resulting in the irregular contact patch. It has been reported later in 7.2 in the Hardness section that lubricant C softens the steel more than lubricant A therefore, backing up this theory.

However, SLIM026 and SLIM027 show some patches of yellow areas that could be small islands of tribofilm, but these are not present in SLIM036. These areas are producing films in of the same magnitude as those seen in lubricants A and B. Whereas SLIM036 shows very little or no tribofilm present. There is also the added complexity that a replacement mapper

window was required for SLIM036 in which, the colour produced by the window were marginally different to the other images but this should have produced the same results as an alternative calibration file was used for that mapper window.
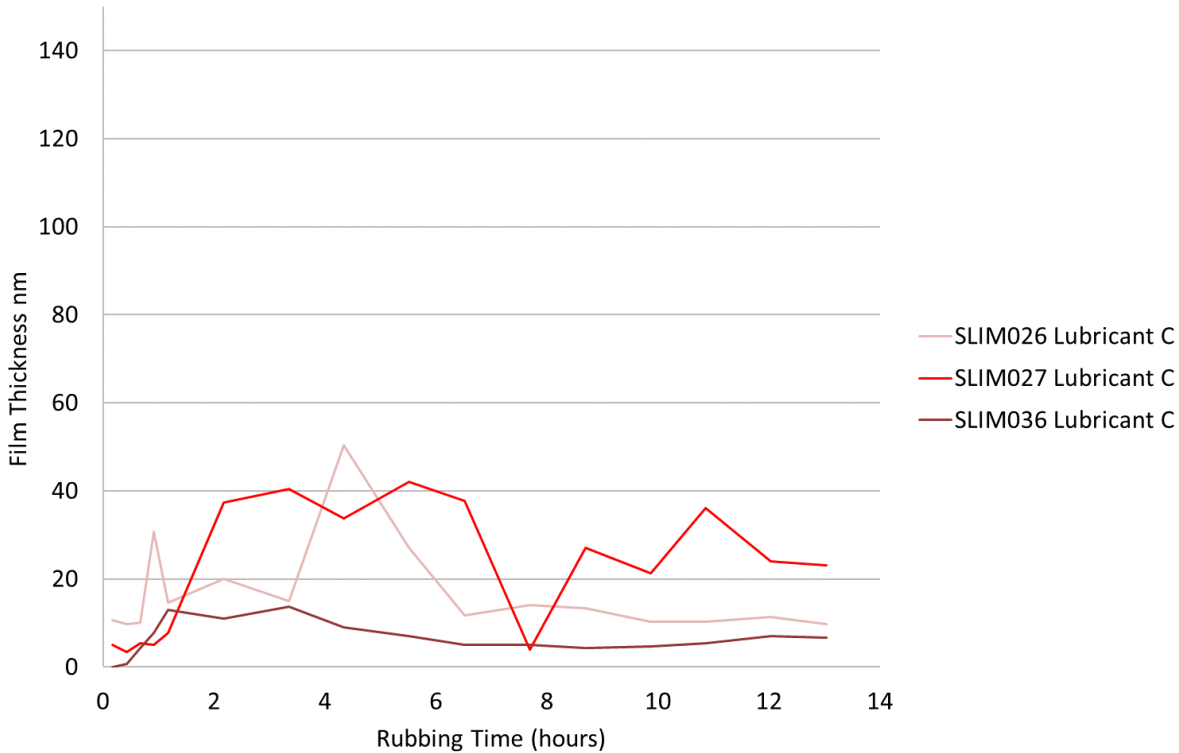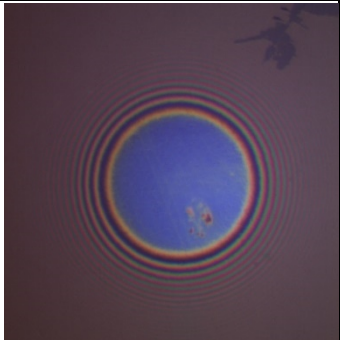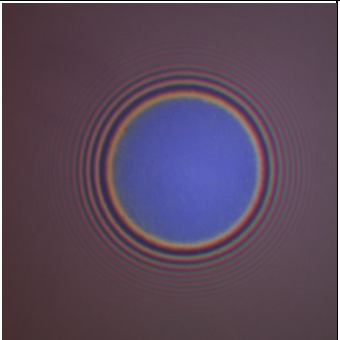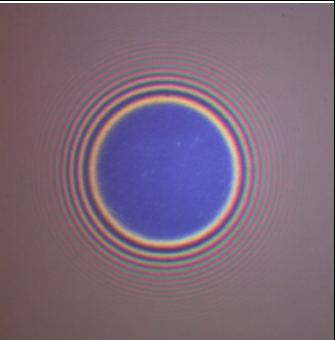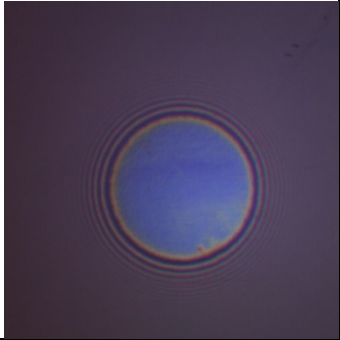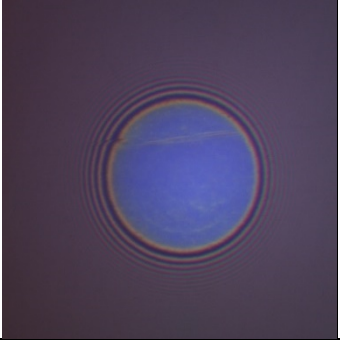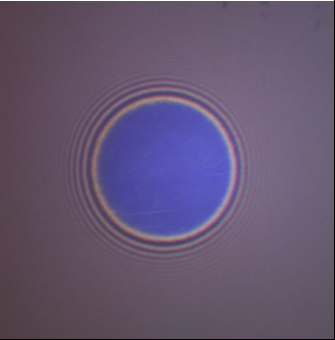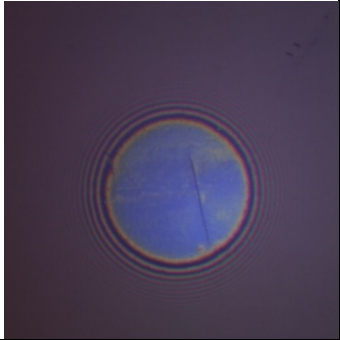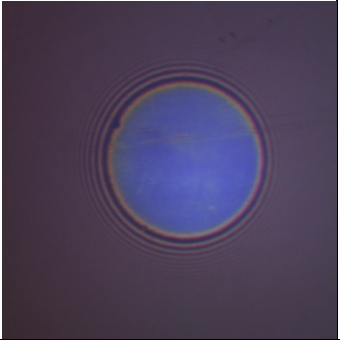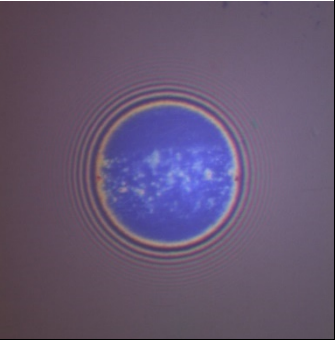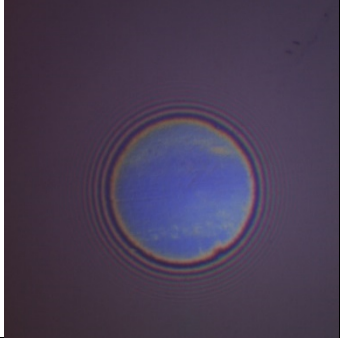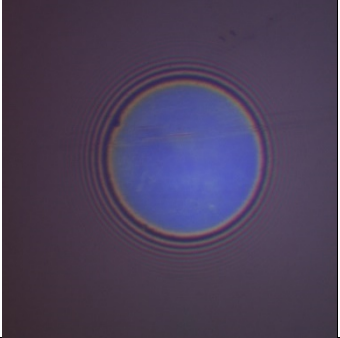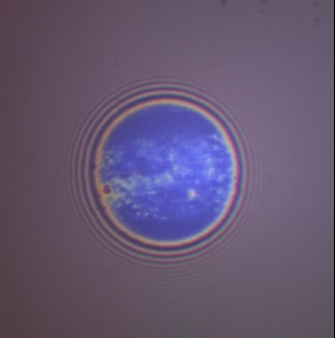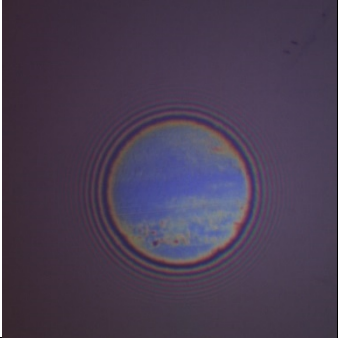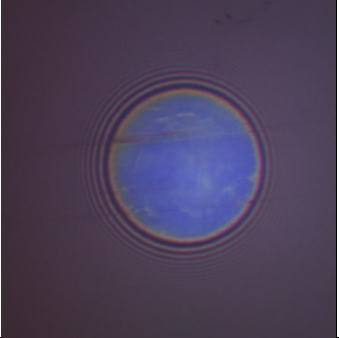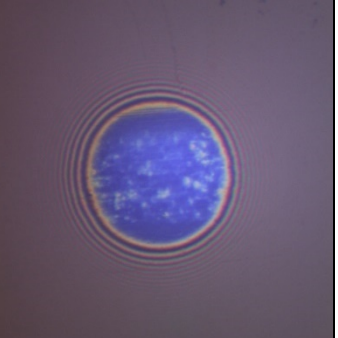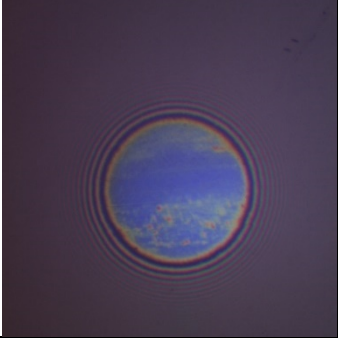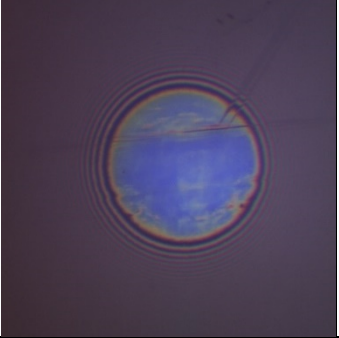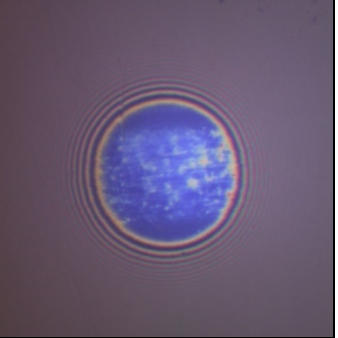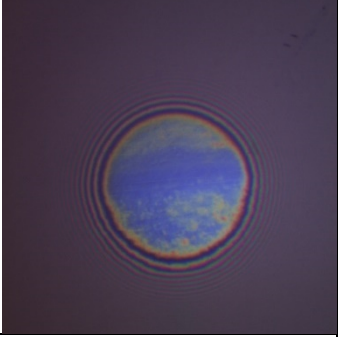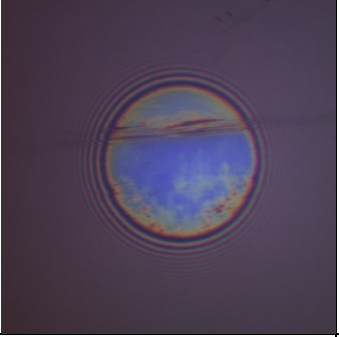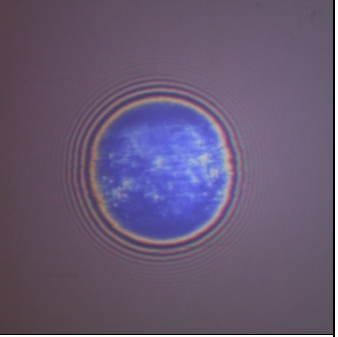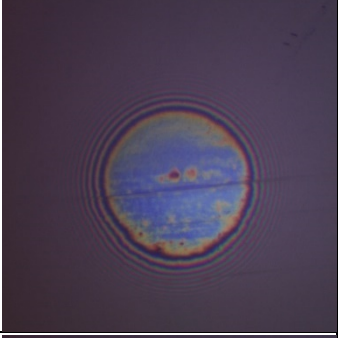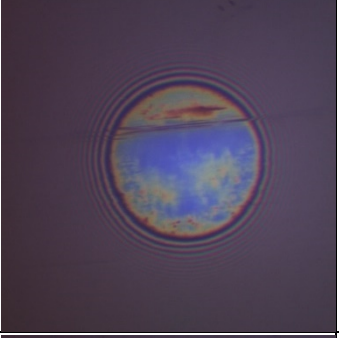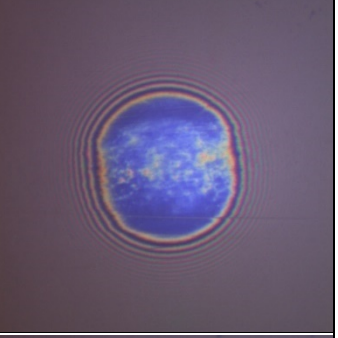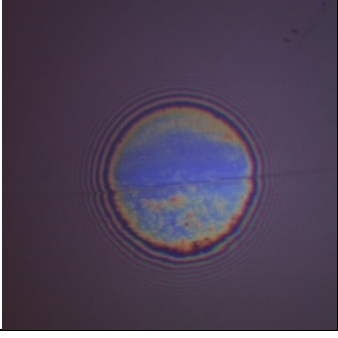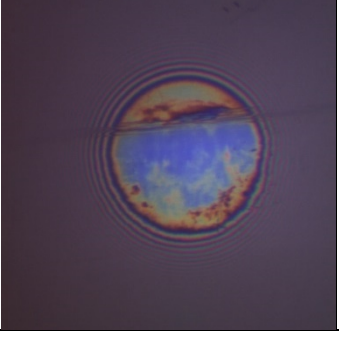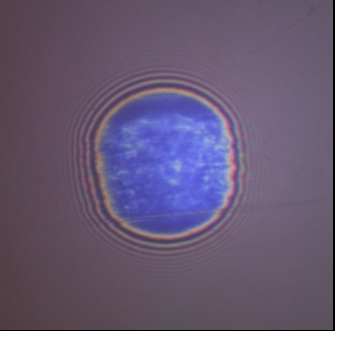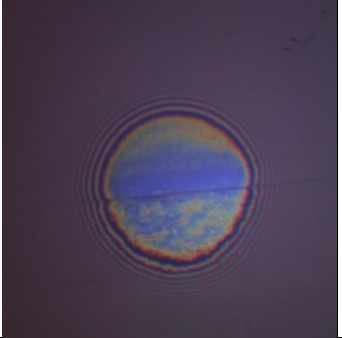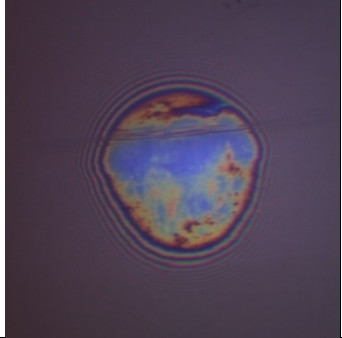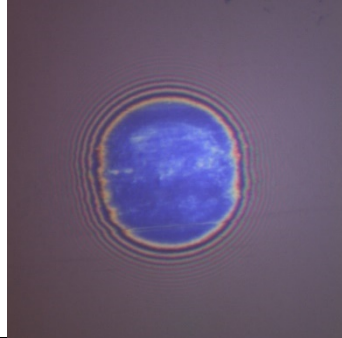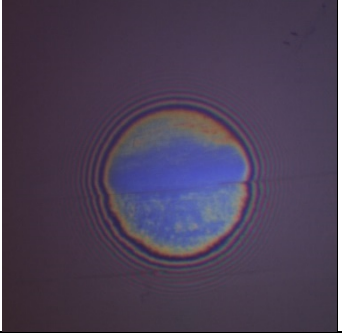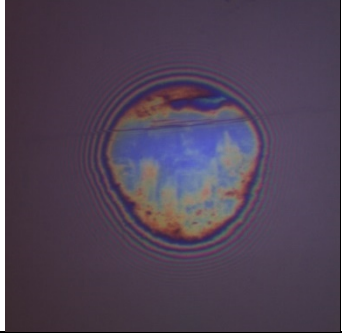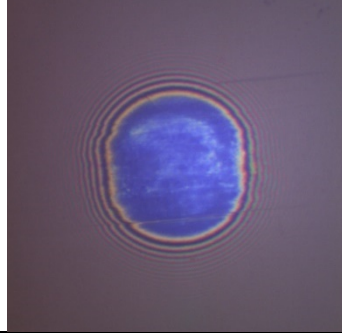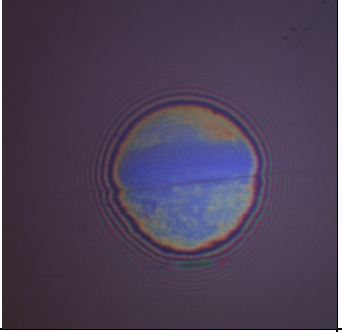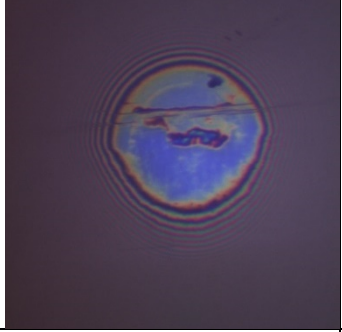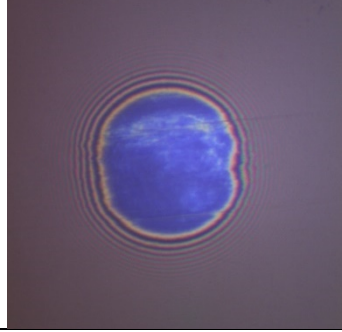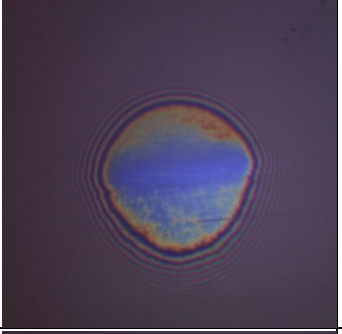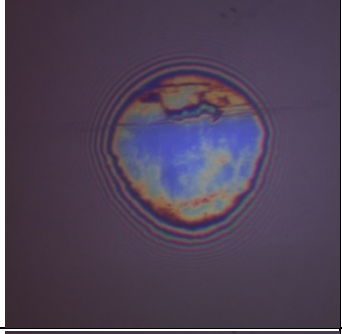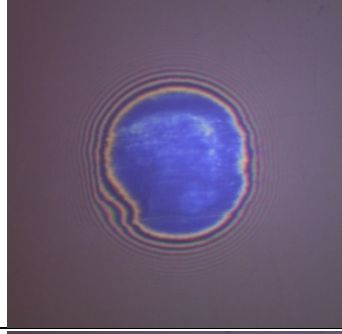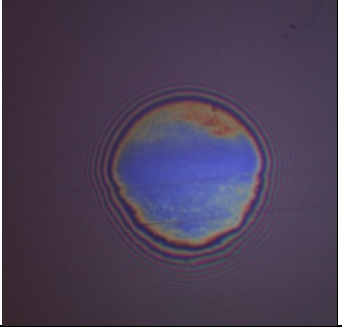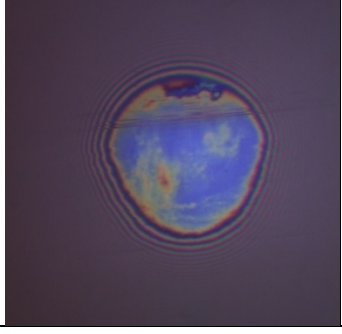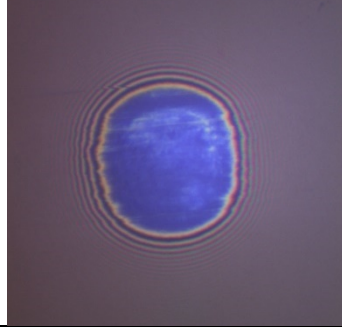
Figure 6-14 – Graph showing the tribofilm thicknesses produced by lubricant C throughout each test.

Test time (seconds) / Test Number	SLIM026	SLIM027	SLIM036
0			
621			
1521			
2421			

3321			
4221			
7821			
12042			
15642			

19863			
23463			
27684			
31284			
35505			

39105			
43326			
46926			

Figure 6-15 - Interferometer images from the MTM-SLIM for 3 repeats for Lubricant C.

Figure 6-17 shows the interferometry images for lubricant D for all the repeats and the film thickness is shown in Figure 6-16 . The repeat SLIM images appear similar to each other suggesting similar performance between all tests for Lubricant D. Lubricant D produces a low film thickness as shown in Figure 6-16 however, SLIM028 has a larger film thickness than the other tests which, can be seen in the images as there appears to be more tribofilm present in that test. However, all the tests show the same morphology of a thin tribofilm present with abrasive score lines through the contact which, even penetrate through the Newton rings suggesting the abrasion is present on the wear track as confirmed in the wear track images in Figure 6-9. These results suggest the tribofilm from lubricant D is different to the other lubricants in that it may not be strong enough to prevent abrasion. But it could also

be the case that as this is a highly viscous gear oil, these conditions may be insufficient to fully activate the EP and anti-wear additives in this lubricant formulation to chemically react and protect the surface.
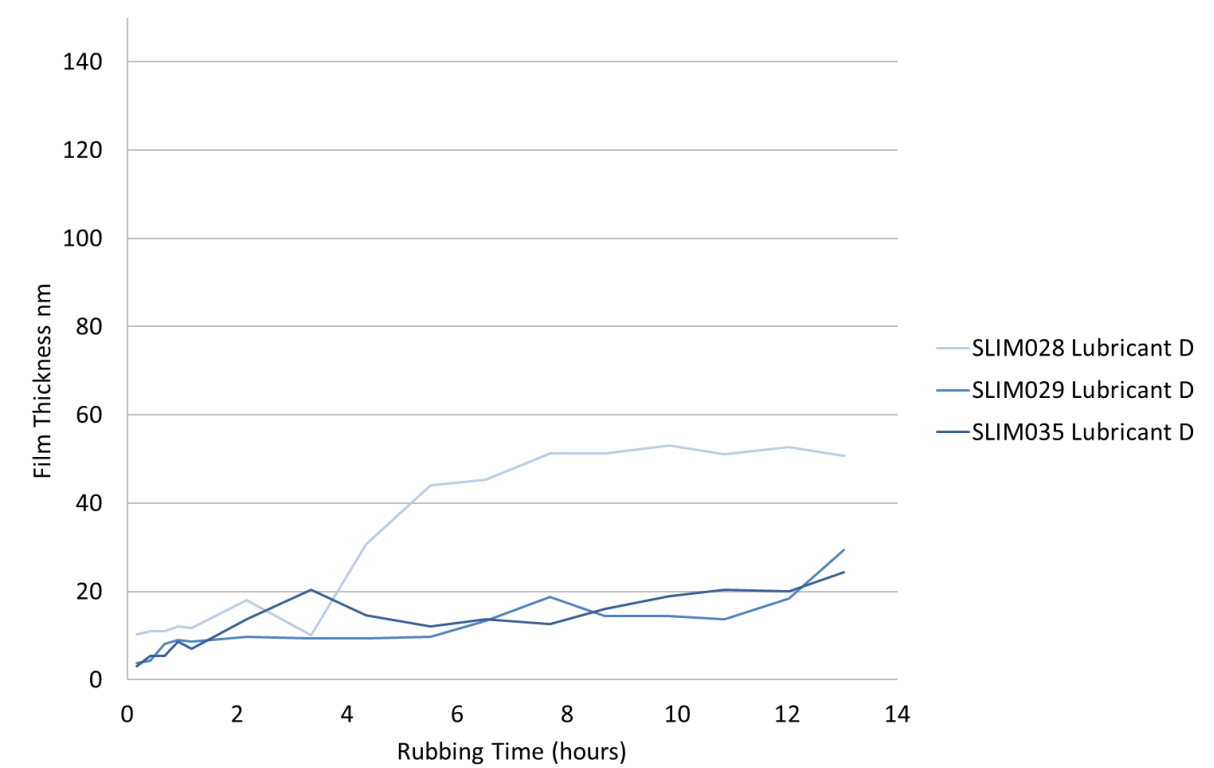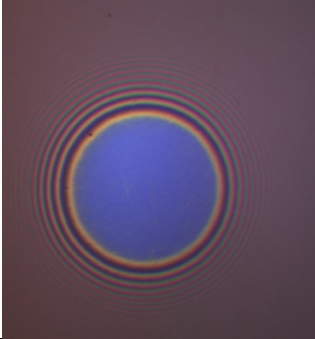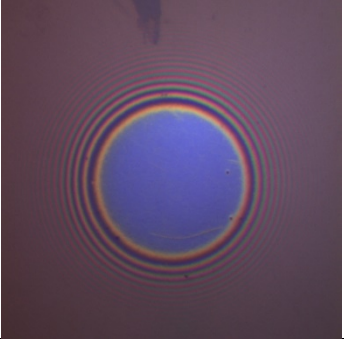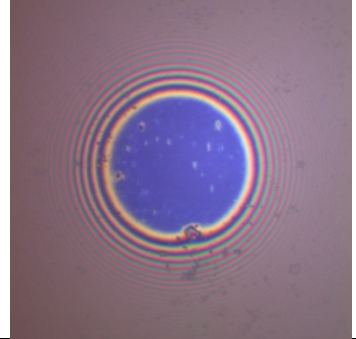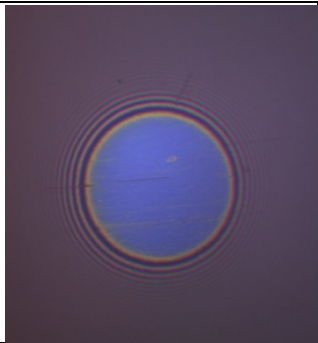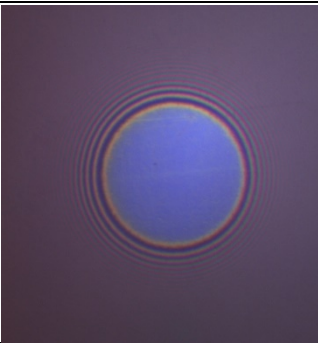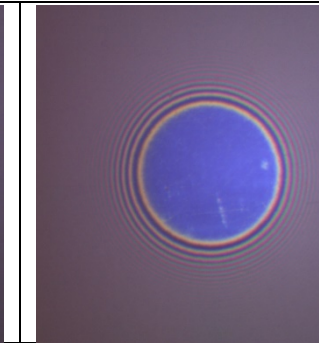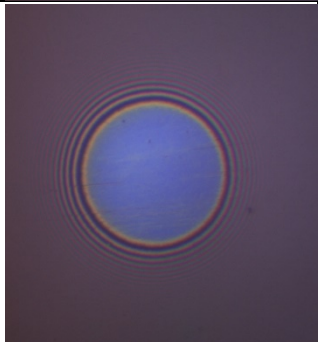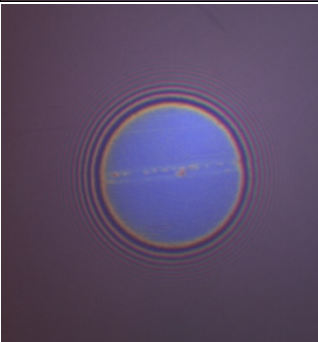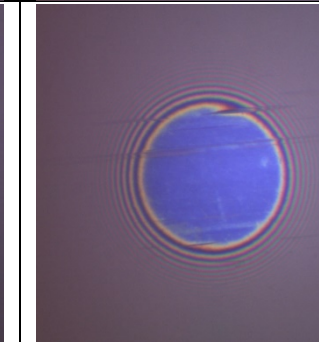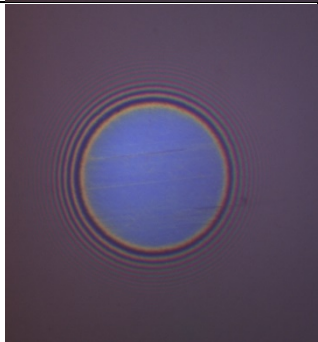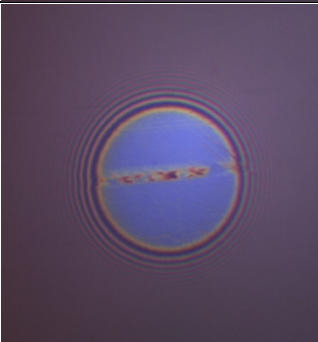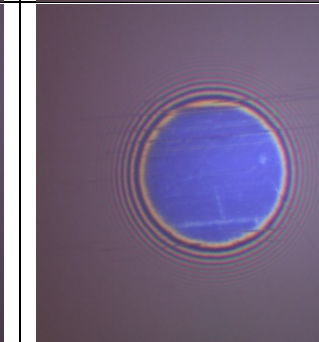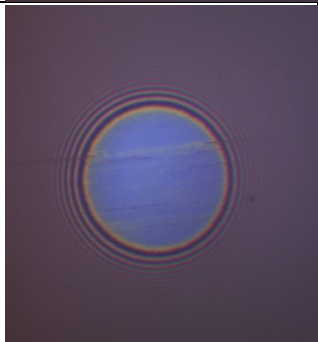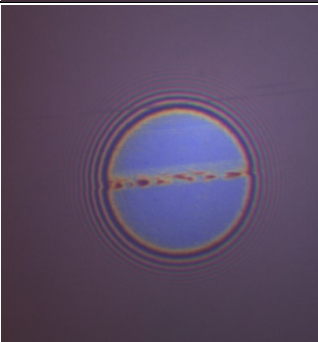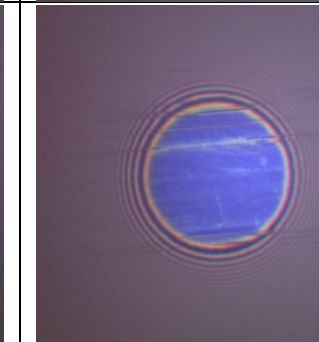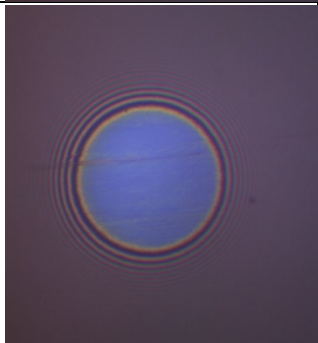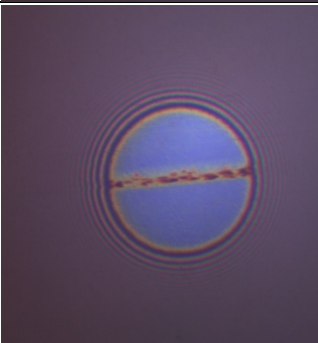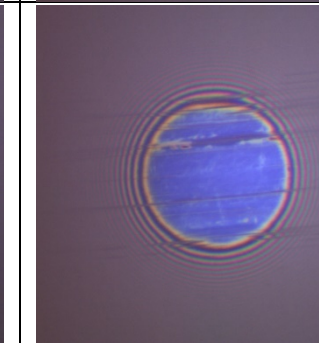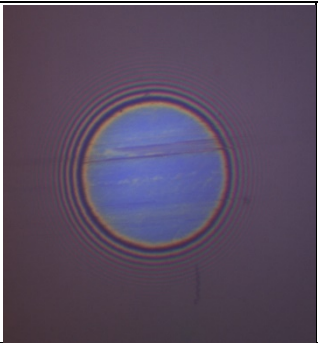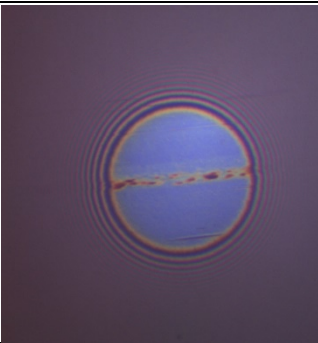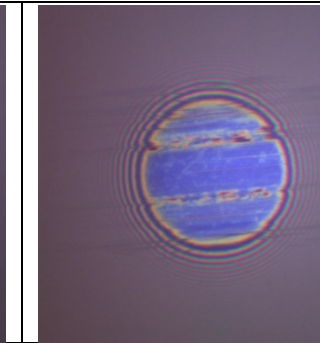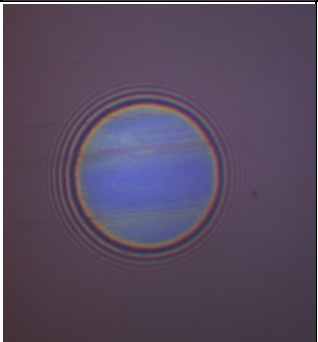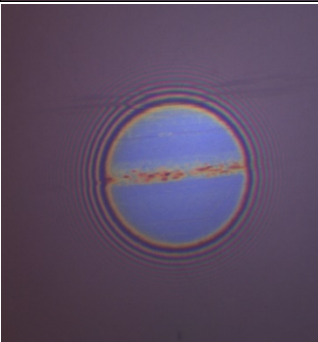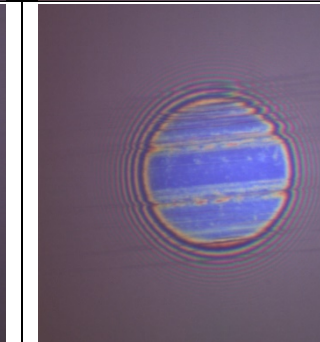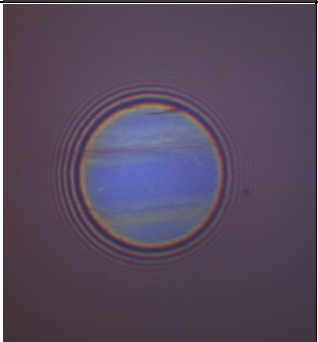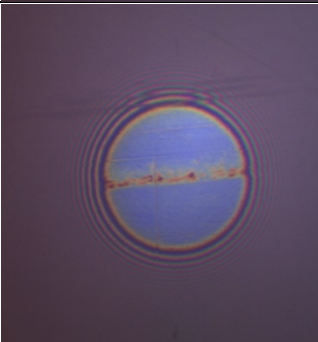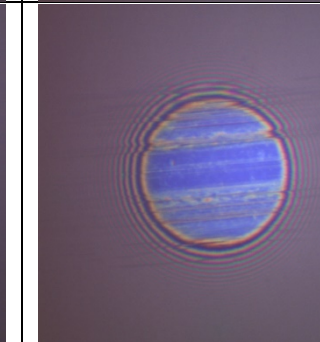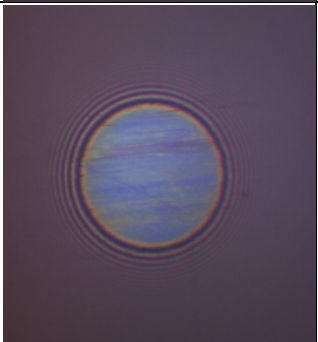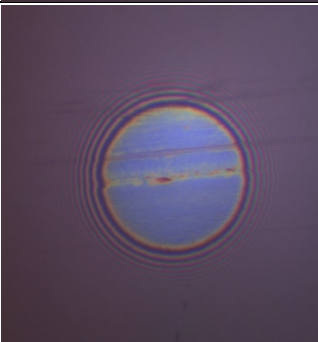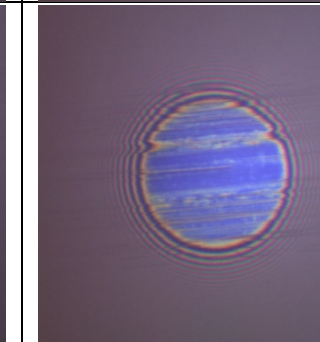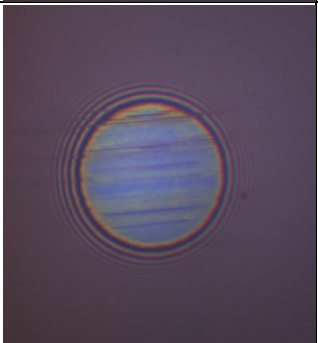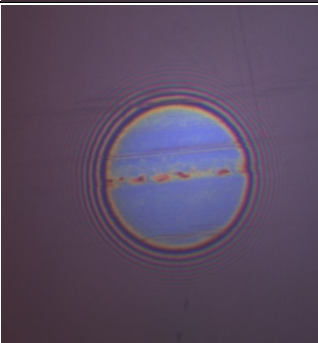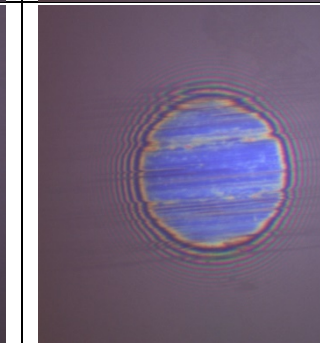
Figure 6-16 – Graph showing the tribofilm thicknesses produced by lubricant D throughout each test.
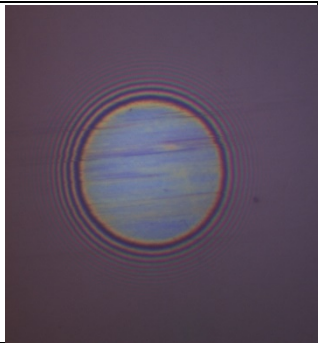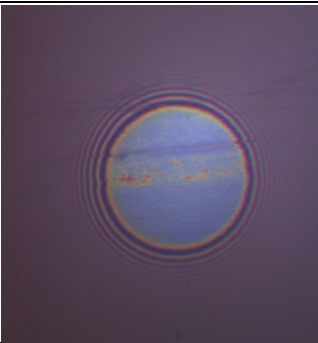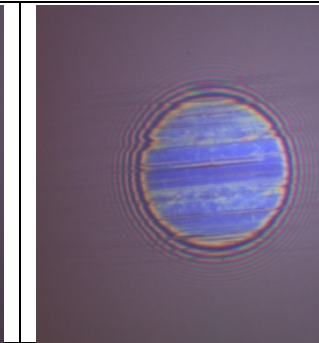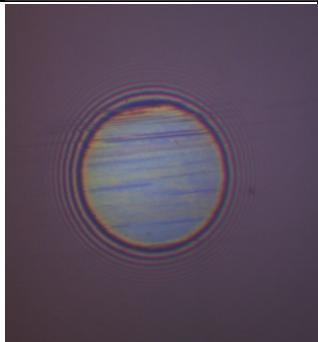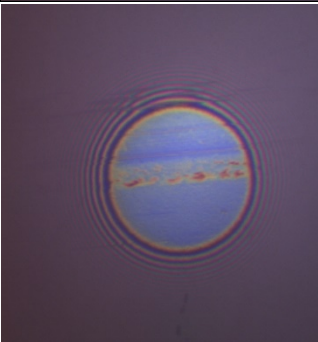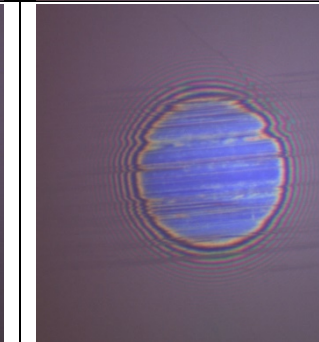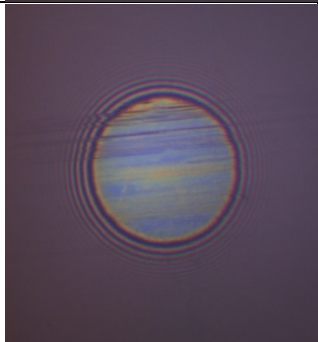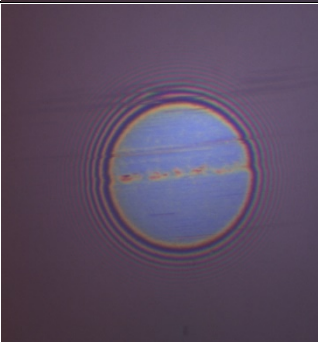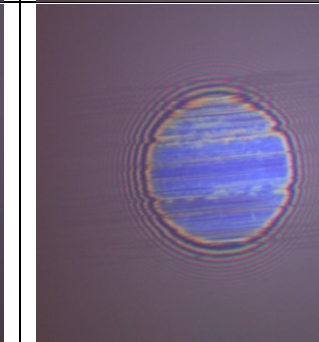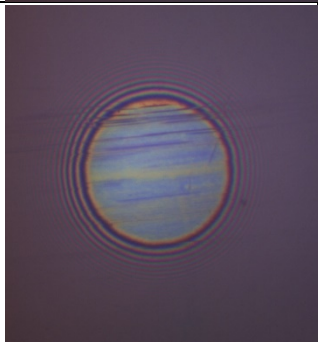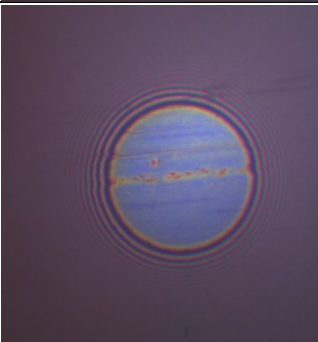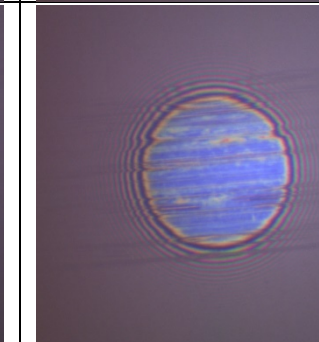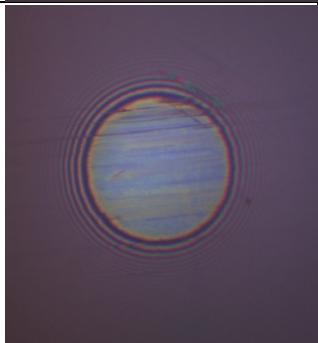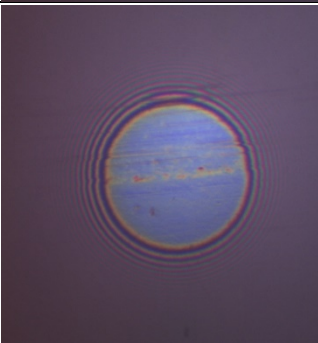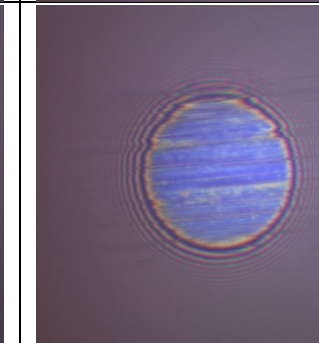
Test time (seconds)/ Test Number	SLIM028	SLIM029	SLIM035
0			

621			
1521			
2421			
3321			
4221			

7821			
12042			
15642			
19863			
23463			

27684			
31284			
35505			
39105			
43326			

Figure 6-17 - Interferometer images from the MTM-SLIM for 3 repeats for Lubricant D.

Graphs comparing the mean average film thickness throughout the tests and the mean average maximum tribofilm thickness can be seen in Figure 6-18 and Figure 6-19 respectively. The results show that virtually all the oils form very thin films that slowly build up to maximum thicknesses between 30 - 40 nm. As the thickness resolution is between 25 - 30 nm, this technique cannot distinguish which, lubricant quantitatively produces a thicker film, however, from the images it could be argued that lubricants A and B form marginally thicker tribofilms (35,93,94).

From the images, Lubricants A and B perform similarly as there is a slow build-up of a thin patchy film that is regularly sheared off before reforming. However, this still prevents excessive wear, like what is seen with the base oil in Figure 5-23. Lubricant C appears to generate much less wear than the other lubricants, but, a misshapen Hertzian contact patch on the SLIM image is present which, suggests wear. Again, there is no excessive wear as is observed for the base oil in Figure 5-23. Therefore, there must be another reason for the misshapen contact such as the way the collimated light refracts off the EP tribofilm or whether the oil is having a different effect on the substrate steel like softening the surface.

Lubricant D also forms a thin tribofilm but appears to not protect against abrasion under these conditions. It could be that the tribofilm is weaker in comparison to the tribofilms generated from the other lubricants or that the conditions are not harsh enough to initiate the action of the EP additives present in this particular gear oil. More work would be needed to clearly deduce

236

what is responsible for these results by isolating particular additives in the base oil as has been done in Chapter 5 with anti-wear additives and gradually increase the complexity by introducing other additives into the mix to understand the synergistic effect of multiple additives. It is also clear that the types of additive do not seem to be having an affect on the thickness of the tribofilms produced within the resolution of the SLIM.
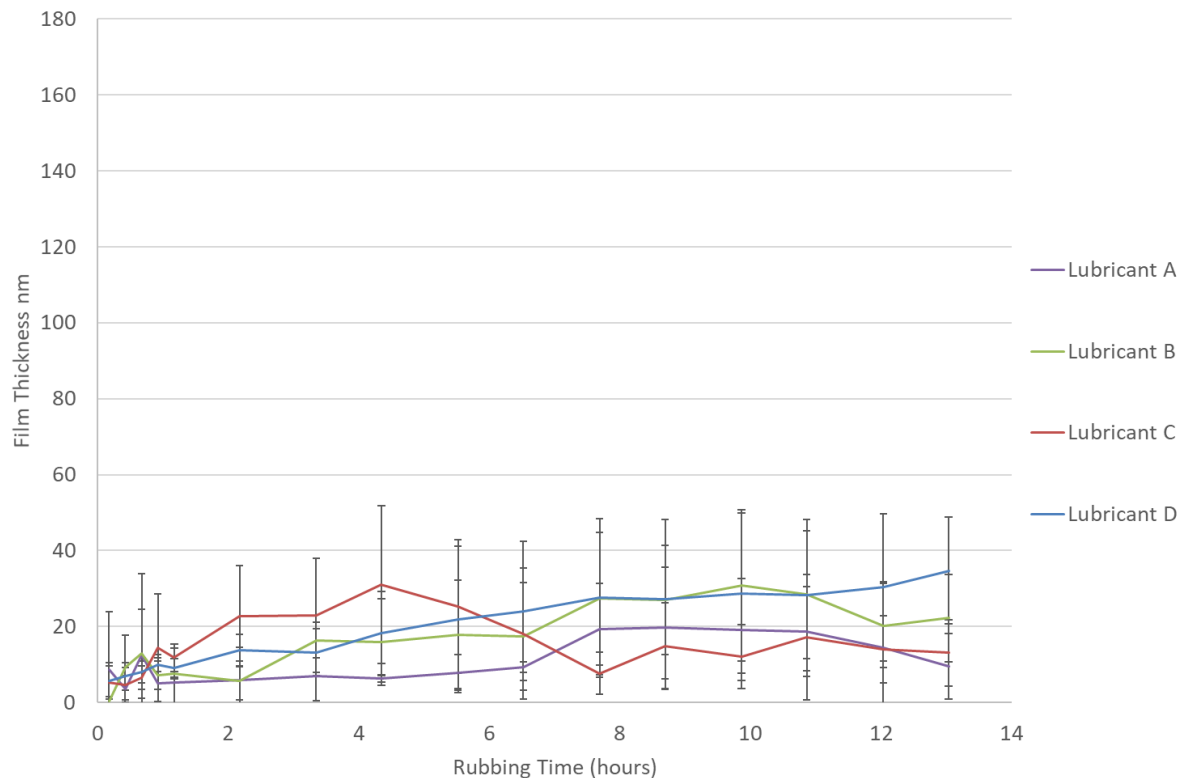
Figure 6-18 The mean average film thickeness for each lubricant throughout the total rubbing time.
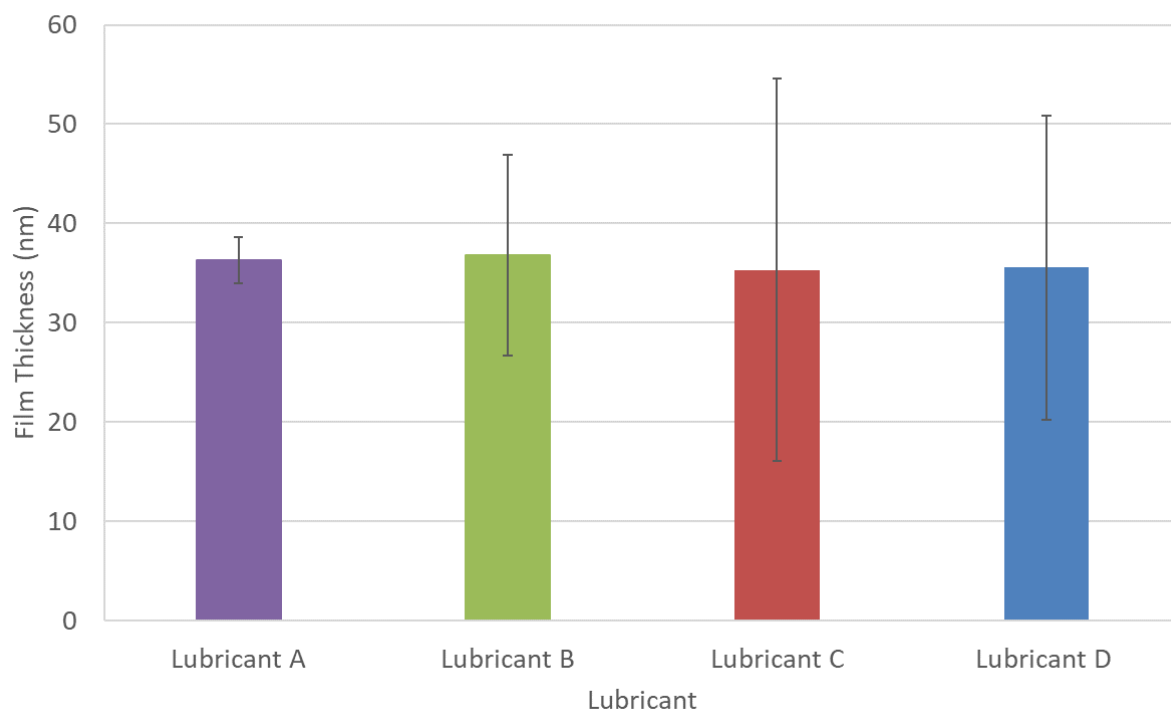
Figure 6-19 – The mean average maximum tribofilm thicknesses produced during the entrie test duration.

Stribeck Curve Analysis

The following section analyses the Stribeck curves produced for lubricants A-D throughout the SLIM test. As shown in Chapter 3, these Stribeck curves differ from the MTM Stribeck curves seen in the previous section in that a marginally lower contact pressure was used for the SLIM i.e. tests of 0.96 GPa instead of 1.01 GPa; the temperature is constant at 100 °C and Stribeck curves are recorded at specific intervals throughout the boundary wear test to monitor changes in the Stribeck curves over time.

All of the Stribeck curves for one test for each of the lubricants A-D can be seen in Figure 6-20, Figure 6-21, Figure 6-22 and Figure 6-23 respectively. Lubricants A, B and D show the same trend in that the initial Stribeck curve has a lower traction coefficient than subsequent tests. It is likely that the increased wear of the surface is leading to a rougher surface which, is therefore, producing higher friction over time. Some studies have also suggested that ZDDP tribofilms

238

have led to increased friction due to its patchy morphology, however, it has yet to be confirmed as to whether thinner ashless anti-wear additives also give rise to this increase in friction (160,186).

The Stribeck curves for lubricant C remain very similar throughout the entire test suggesting there is no wear of the surface. These theories are confirmed by considering the images in Figure 6-9 which, shows minimal wear for lubricant C in comparison to the other lubricants. Therefore, it is likely these results are a result of running in, where eventually an equilibrium is reached where any further change in the Stribeck curves are minimal. Lubricant D appears to run in faster than lubricants A and B potentially suggesting that lubricants A and B provide more protection or that a tribofilm from lubricant D forms more quickly which, results in lower friction. However, it is difficult to make further conclusions without more information of the additives and further examination into testing individual additives.
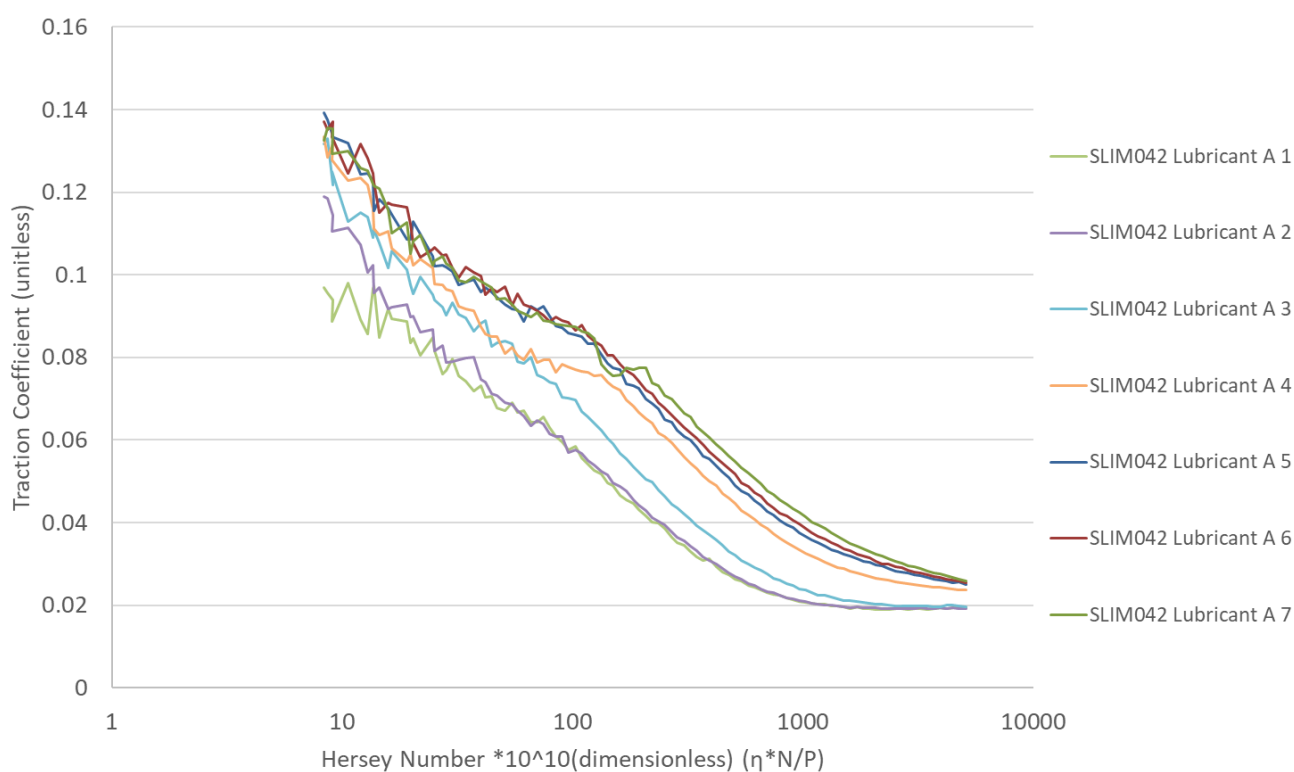
Figure 6-20 – Stribeck curves thoughout the boundary SLIM test for Lubricant A.

239
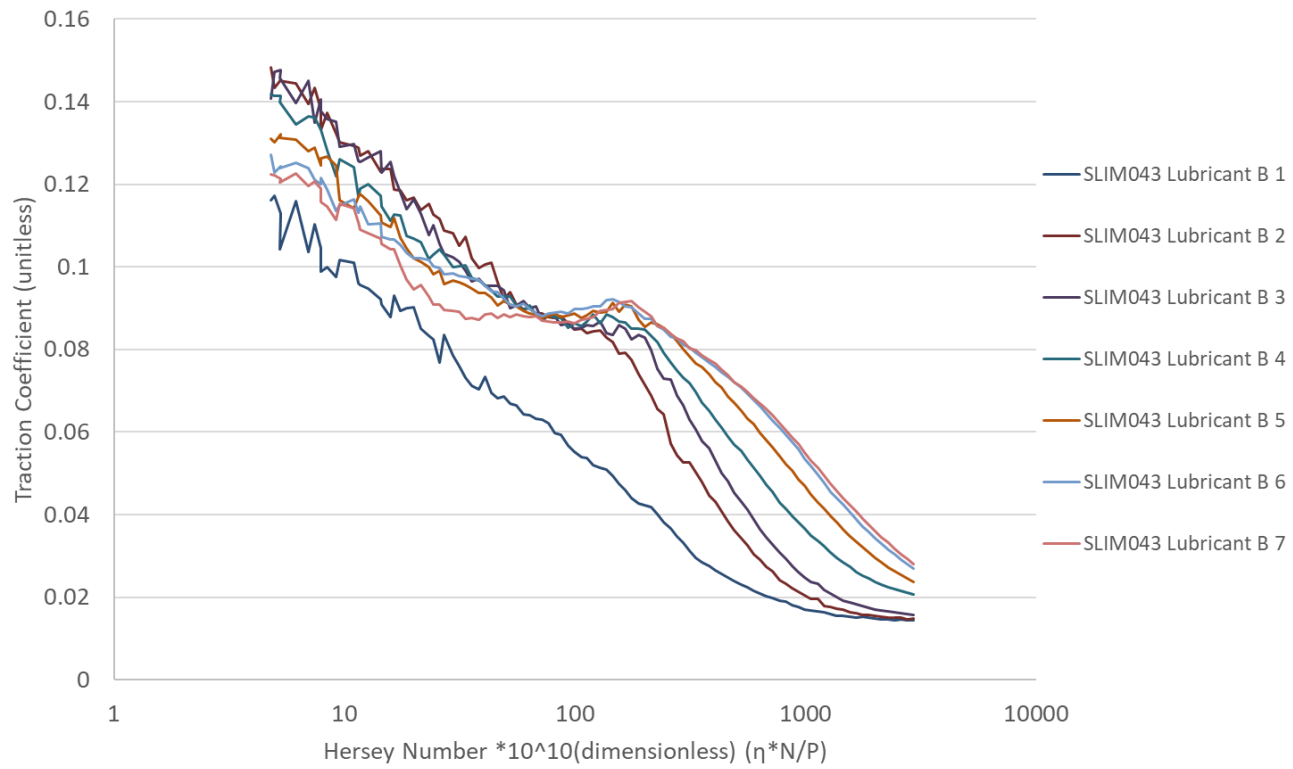
Figure 6-21 – Stribeck curves thoughout the boundary SLIM test for Lubricant B.
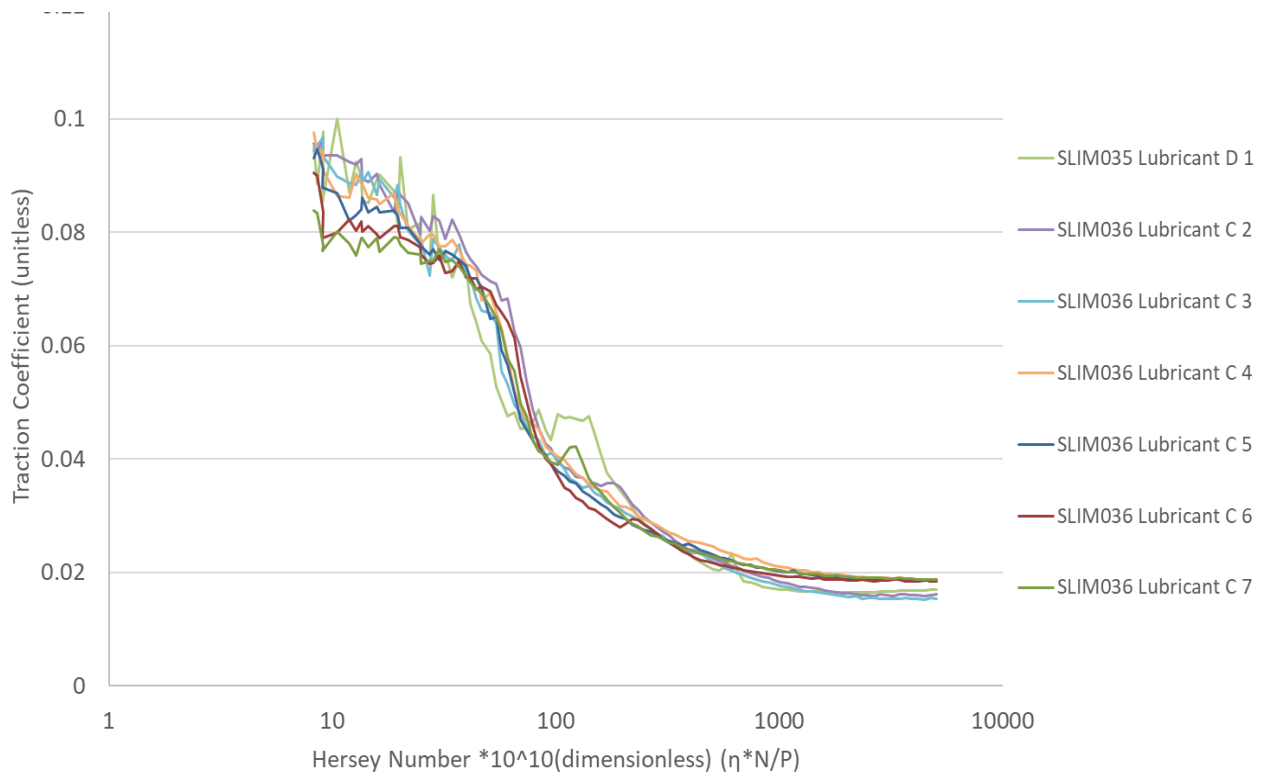
Figure 6-22 – Stribeck curves thoughout the boundary SLIM test for Lubricant C.

240
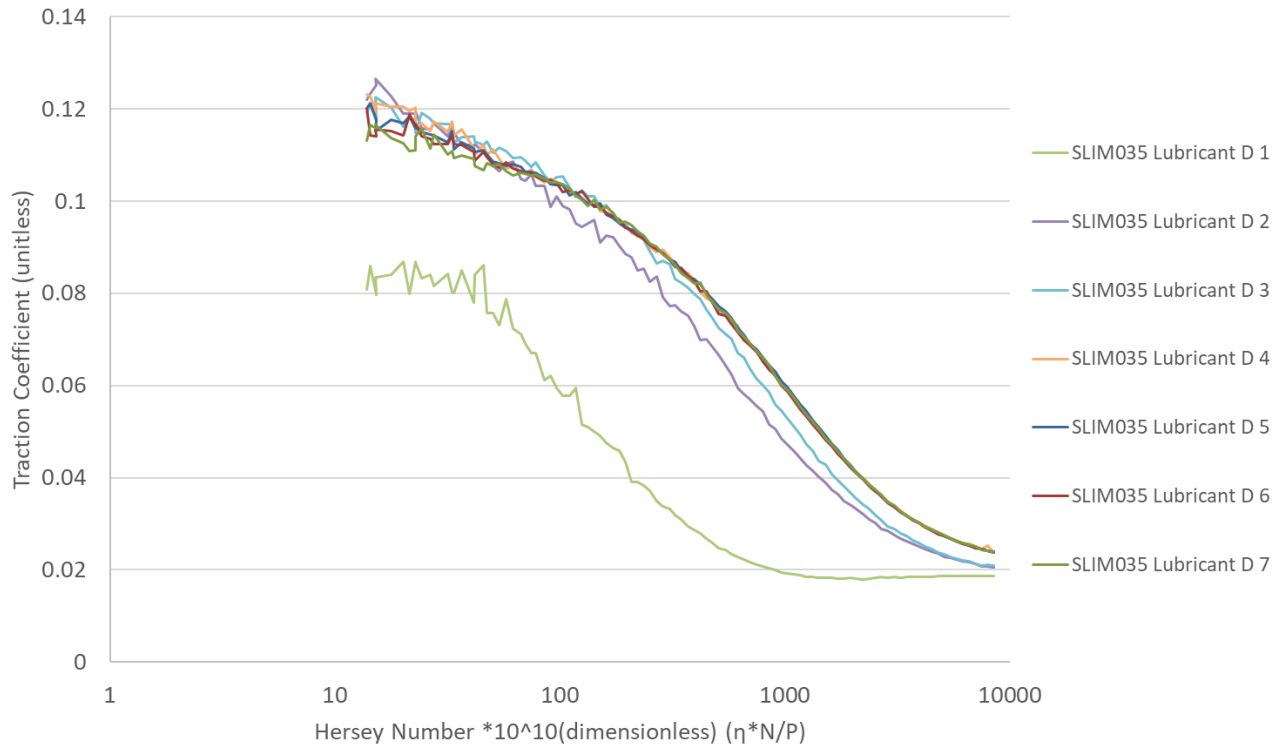
Figure 6-23 – Stribeck curves thoughout the boundary SLIM test for Lubricant D.

Figure 6-24, Figure 6-25, Figure 6-26 and Figure 6-27 show the average initial and final Stribeck curves for lubricants A-D respectively. The error bars show the repeatability of these measurements throughout the tests using the standard deviation. Generally, it can be seen that the initial Stribeck curve is more repeatable than the final curve, which, is most likely due to different amounts of wear in repeat measurements. This also highlights again the difference between lubricant C and the other lubricants, as an increase in friction between the initial and final Stribeck curve is not observed. It can also be seen that there is generally more error in the boundary regime, which, is expected due to surface to surface contact with varying degrees of wear between repeats giving rise to a wider range of traction coefficients.
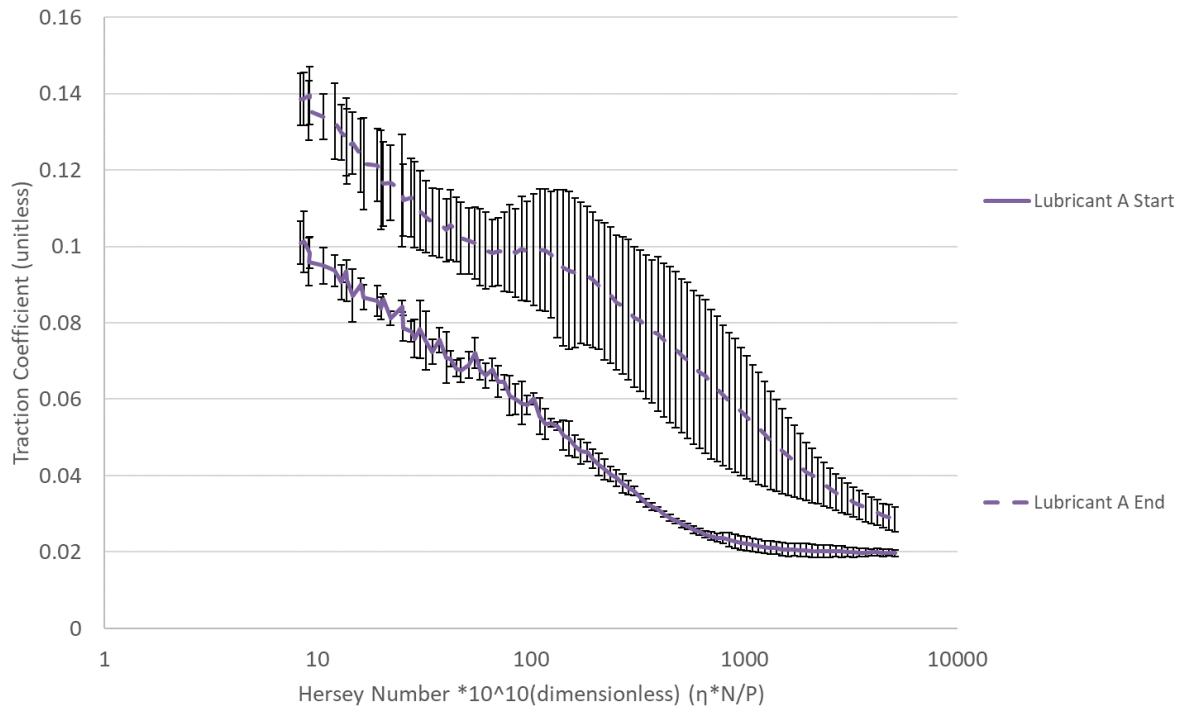
Figure 6-24 – Graph showing the average intial and final stribeck curves for the repeat SLIM tests for Lubricant A.
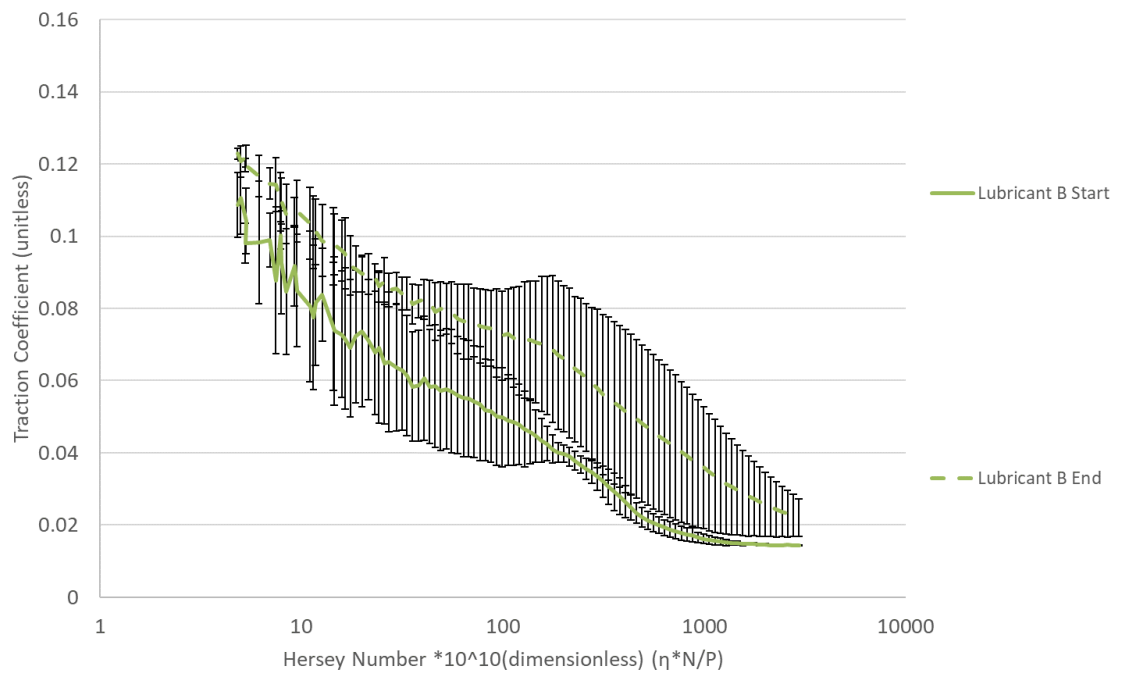
Figure 6-25 – Graph showing the average intial and final stribeck curves for the repeat SLIM tests for Lubricant B.
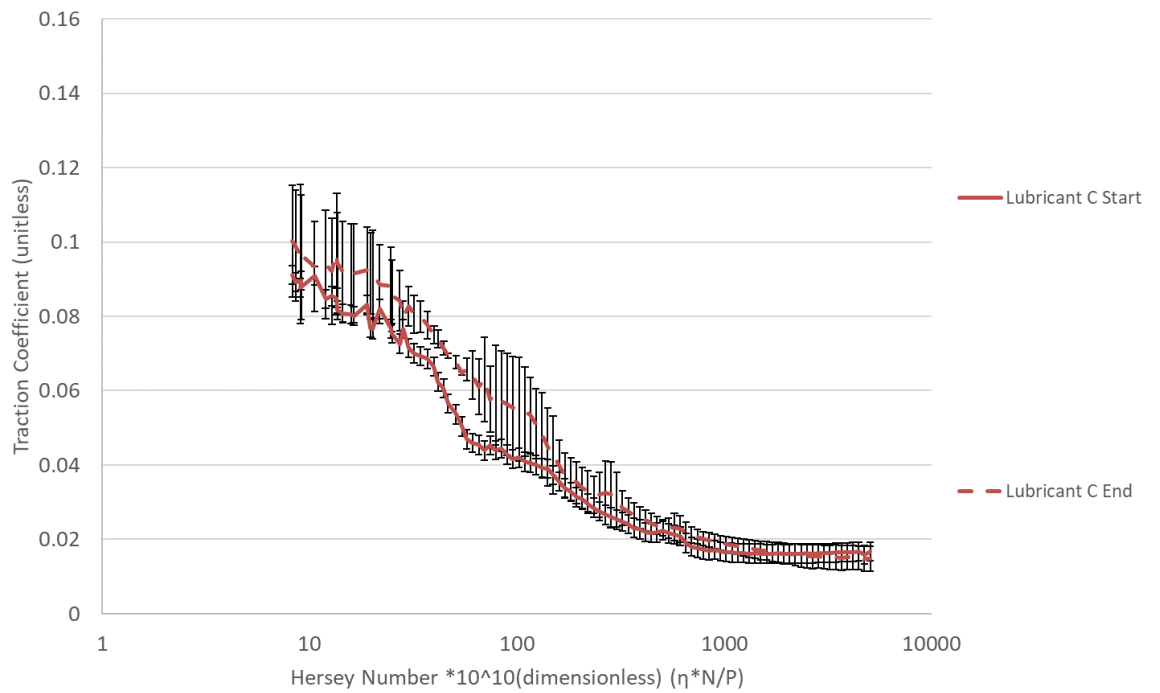
Figure 6-26 – Graph showing the average intial and final stribeck curves for the repeat SLIM tests for Lubricant C.
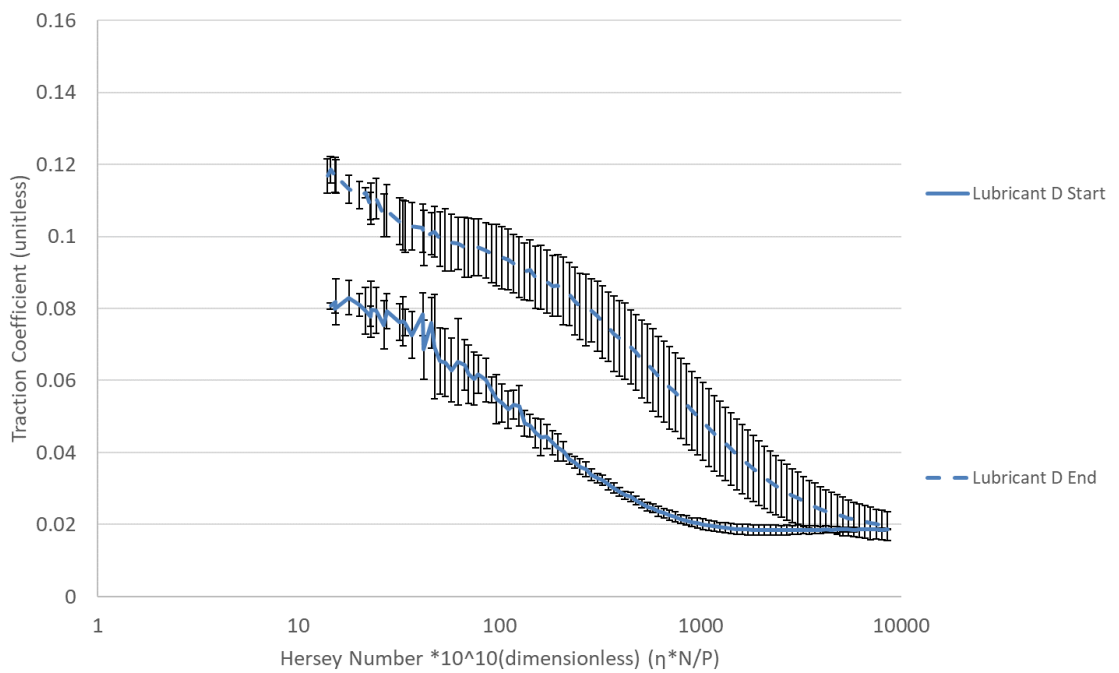
Figure 6-27 – Graph showing the average intial and final stribeck curves for the repeat SLIM tests for Lubricant D.

243

Graphs comparing Stribeck curves for lubricants A-D at the start and end of the SLIM tests are presented in Figure 6-28 and Figure 6-29 respectively. These curves have been again normalised for viscosity by plotting against the Hersey number. The initial Stribeck curves show very little variation as the beginning of the test which, is expected as the surfaces are smooth and unworn. Whereas as the end of the SLIM test, there is a distinct separation between the different lubricants with lubricant A having the highest friction, followed closely by lubricant D, then lubricant B and finally lubricant C having the lowest friction. It is most likely these results are due to the amount of wear on the surface as shown in Figure 6-9, where lubricant C has minimal wear and lubricant B appears to have a smoother wear track than lubricants A and D, which, show more irregular wear and abrasion respectively. However, this would need to be confirmed with a roughness measurement.

It can also be seen that for the final Stribeck curves, all the lubricants do not appear to reach the EHD regime where the curve plateaus at high speeds. All of the lubricants should be capable of reaching the EHD regime under these conditions as shown in Chapter 3, where the lambda ratio curves reach the EHD at 100 °C. This is most likely due to the increase in roughness of the surface as a result of wear.
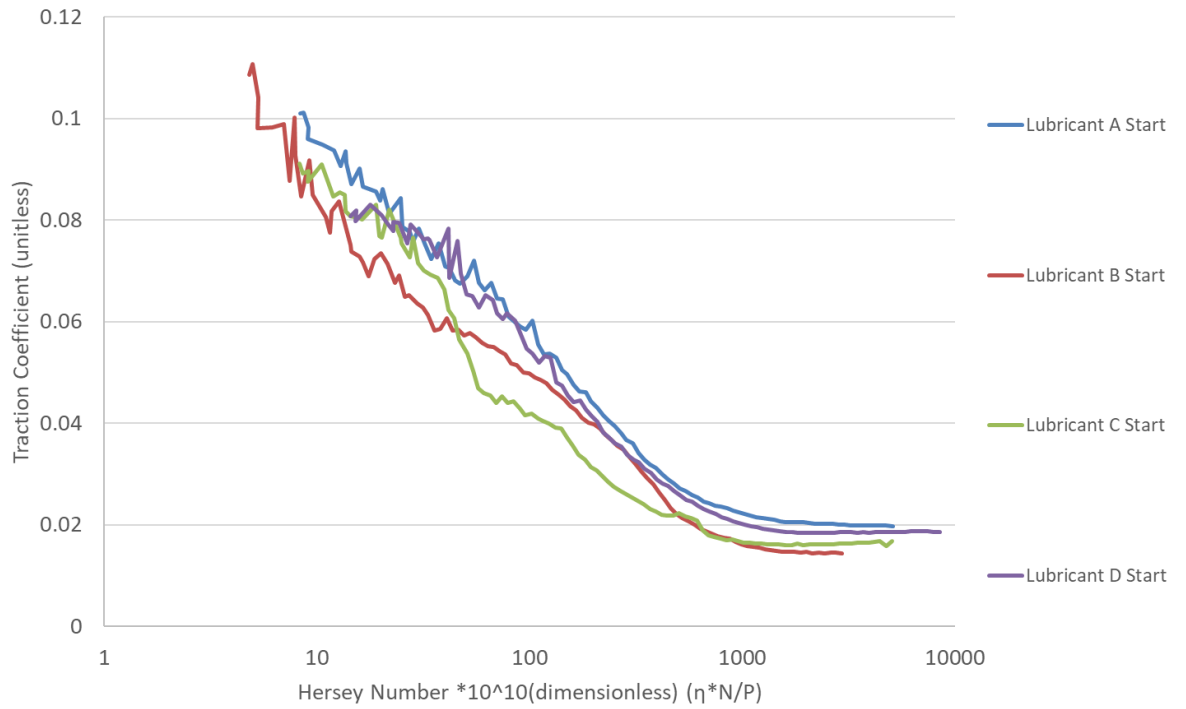
Figure 6-28 – Graph showing the average intial stribeck curves for the repeat SLIM tests for Lubricants A-D.
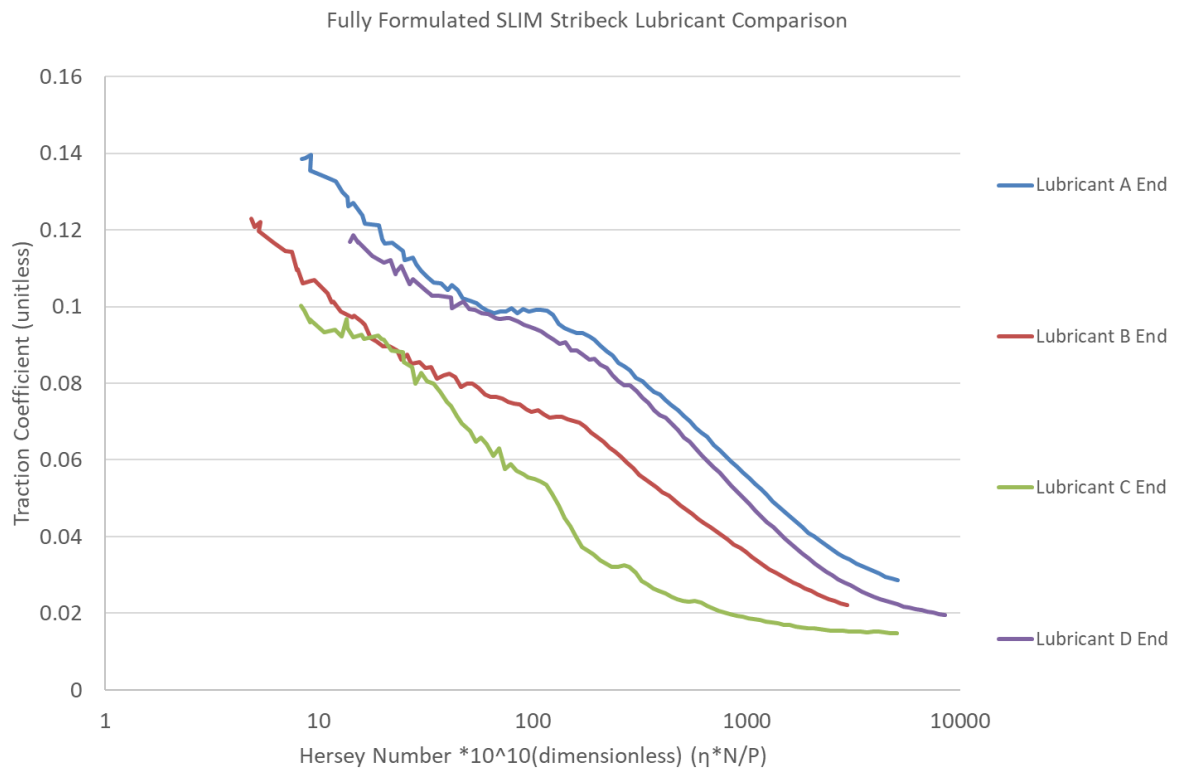
Figure 6-29 – Graph showing the average final stribeck curves for the repeat SLIM tests for Lubricants A-D.

Overall Friction Analysis

The traction coefficient was also recorded for the entire duration of the wear test as well as the Stribeck curves which, can be seen from Lubricant A-D in Figure 8-12, Figure 8-13, Figure 8-14 and Figure 8-15 in Appendix 9.

The sharp spikes in these graphs show where the Stribeck curves were recorded which, were discussed in the previous section. These graphs show that there is a degree of variability in the traction coefficient at the beginning of the test, which, is expected during the running in process, but there is also a difference in this boundary friction throughout the entire SLIM tests for the repeats. As mentioned in Chapter 4, it is expected there will be more variation in the boundary regime as it is impossible to have exactly the same surface for each test and as a result they will wear in slightly different ways giving rise to increased friction.

Figure 6-30 shows the average friction throughout the SLIM test for all lubricants. The graph shows that the traction coefficient gradually changes over time resulting in a clear separation between the different lubricants. It is well known that viscosity tends to have less of an influence in the boundary regime (7). It can be seen that lubricant A results in an increase in friction from 0.09 to 0.12, lubricant B remains relatively constant at throughout 0.10, lubricant D increases from 0.08 to 0.10 and lubricant C initially increases from 0.08 to 0.95, but then decreases to 0.06. These results again back up the Stribeck curve results and the wear track image in that lubricant A appears to produce the most wear, followed by lubricant D and B and lubricant C has very little wear. The fact that lubricant C decreases in friction suggests that the additives in lubricant C are giving rise to a frictional decrease if there is no change in the surface from wear. This suggests that the anti-wear film from lubricant C may not be visible in the interferometry images.
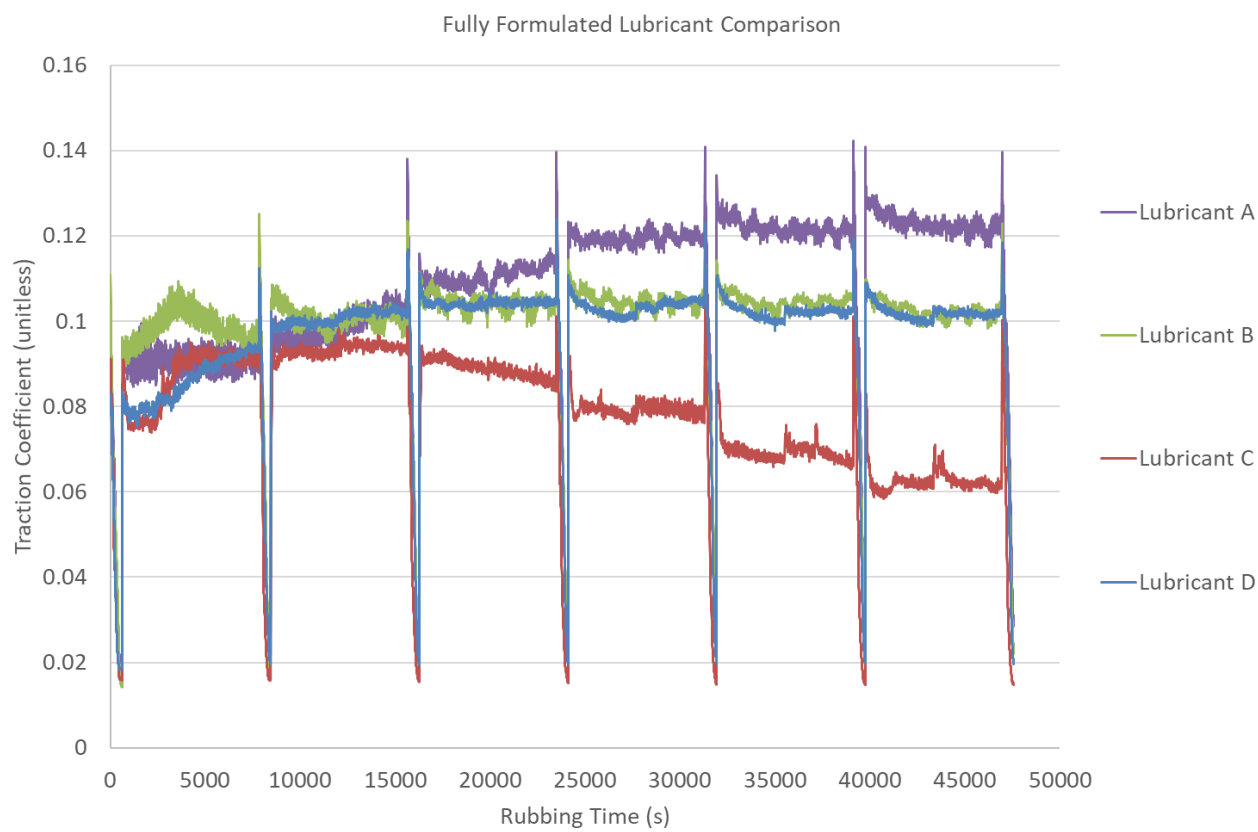
Figure 6-30 – Graph of the average friction against the rubbing time throughout the SLIM tests for Lubricants A-D.

6.3   Conclusions

A series of experiments carried out using the MTM found that Lubricant B and C had the lowest friction across the boundary and mixed lubrication regimes and the lubricants performed similarly at higher Hersey numbers. This is due to the differences in base oil packages where it is likely that lubricant A and D have more branched base oils giving rise to higher friction. This could also be due to differences in the additive package. However, it is difficult to make further conclusions without more formulation information or simpler lubricants to reduce the number of variables.

A wider study was conducted on an MTM-SLIM to further evaluate lubricants A-D through studying the tribofilms produced by each lubricant. The optical microscopy images of the wear

track on the ball and disc specimens revealed lubricant A had the most wear, then B, then D which, had mainly fine abrasive wear and then C which, has very little wear on the surface. The SLIM images showed that all lubricants slowly formed films, following a mechanism of gradual formation, shearing off and then reformation. This thickness of the ashless tribofilms did not exceed 40 nm and resolution of the technique cannot distinguish which, lubricant forms thicker tribofilms. Lubricants A and B gradually form thin patchy tribofilms with little/ no distortion of the Hertzian contact on the SLIM image. Lubricant C forms a misshapen contact which, would normally suggest wear, but there was no wear on the surface. This suggested that the EP additive derived tribofilm may interact differently with light than the phosphorus based anti-wear additive and that the softening of the surface could also play a part in the misshapen Hertzian contact on the mapper window. Lubricant D also formed very thin tribofilms but did not seem to protect the surface from abrasion as abrasive scoring was seen on the SLIM image and was also seen in the wear track.

Stribeck curves on the MTM-SLIM tests showed that lubricants A, B and D show an increase in roughness with subsequent Stribeck curves, whereas Stribeck curves for lubricant C remain contact throughout subsequent curves. This was most likely due to lubricant C resulting in very little wear in comparison to the other lubricants, resulting in very little variation in surface roughness. Comparison of the final Stribeck curves allowed differentiation of lubricants, showing that the order of friction across the lubrication regimes went from high to low went lubricant A, then D then B and finally C which, followed the order of wear severity.

Overall friction in the boundary regime for the whole MTM-SLIM test confirmed same results with high to low friction in the order A, B and D the same and then C. Lubricant C was the only one to decrease in friction, which, could indicate an underlying mechanism with the EP additive which, decreases friction.

Chapter 7.   The Micropitting Evaluation of Commercially

Available Fully Formulated Lubricants for PGB Applications

7.1 Introduction

As shown from Chapter 6, commercially available formulations have substantially different characteristics which, affects both friction and the type of tribofilms produced which, consequently affects the wear. This chapter will utilize this understanding to obtain their influence on micropitting under representative PGB conditions. Micropitting is a prevalent failure mechanism in gears and the wrong lubricant could inadvertently promote micropitting initiation leading to early propagation of the wear into more severe failures ultimately resulting in reduced component life and potentially compromised safety of the aircraft.

Chapter 5 highlighted the effect of anti-wear additives on micropitting showing that whilst they may protect against scuffing type failures, early protection of asperities with strong additives can protect asperities too early, preventing the running in process resulting in maintaining high asperity contact pressures that promote micropitting. Although Chapter 5 showed that this effect was much less severe for additives used in aviation lubricants, it remains to be seen as to whether there is a synergistic affect with other additives in the formulation that could accelerate micropitting.

This chapter will use an MPR as discussed in section 3.1.3 to evaluate the micropitting propensity of lubricants A-D on two different gear steels; MSRR 6010 and P53 which, are both potential candidates as PGB material. Details of which, are shown in 3.2.1 in the MPR Specimens section.

7.2   Results & Discussion

Lubricants A-D have been evaluated on their influence on micropitting propensity, wear generation and their influence on boundary friction on two steels: MSRR6010 and Pyrowear 53. These are presented in the following section.

Wear Track Image Analysis

Figure 7-1 and Figure 7-2 present optical microscope images of the wear tracks from wear tests conducted with four different lubricants on MSRR6010 and P53 respectively. The images were comparable for the repeat tests of each lubricant and hence, images from only one test are shown. Images were selected from four of eleven steps to allow better visualisation of the progression of wear. High definition camera images of the roller specimens were also acquired to better visualise the wear produced and to identify the true colour of the wear tracks and these can be seen in Figure 7-3 and Figure 7-4. It should also be noted for these images that the optical images were taken at a different orientation to the HD camera images. This was unintentional and a result of an external source taking the camera images. The impact this has on the image is that the micropits are the opposite way round for each method as illustrated in Figure 7-5.

Lubricant A shows a gradual increase in micropitting throughout the test. Lubricant B shows very minimal wear and micropitting but the micropits present are of a similar size to lubricant A. Lubricant C exhibits a polishing effect on the surface, which, appears to slow down the onset of micropitting. But when the micropits do form they appear to be larger than the micropits formed from tests with the other oils. The polishing effect that lubricant C exhibits can be more easily seen in Figure 7-3 and Figure 7-4, as a very polished and smoothened surface has been produced. Figure 7-3 also highlights that there could be some localised micro-scuffing present as shown from the small vertical features in the wear track.
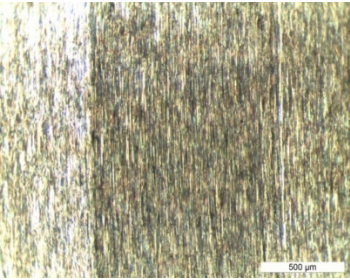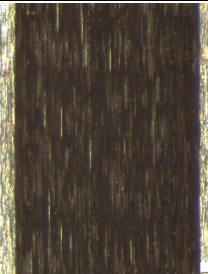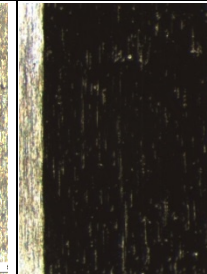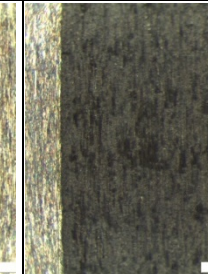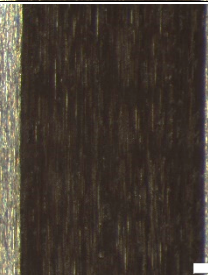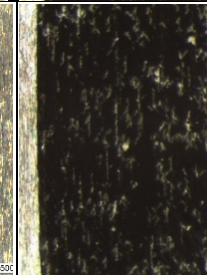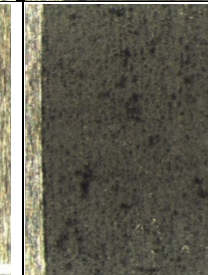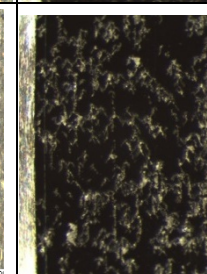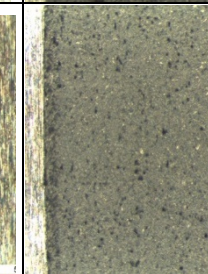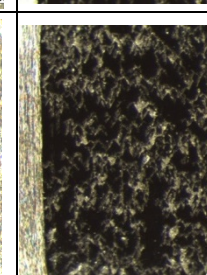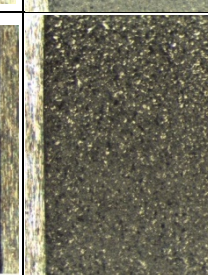
250

Lubricant	Lubricant A	Lubricant B	Lubricant C	Lubricant D
Unworn Specimen				
Step 2 – 440 k cycles				
Step 5 – 1760 k cycles				
Step 8 – 3080 k cycles				
Step 11 – 4400 k cycles				

Figure 7-1 – Optical microscope images of the wear track of the MSRR6010 chamfered rollers for each lubricant.
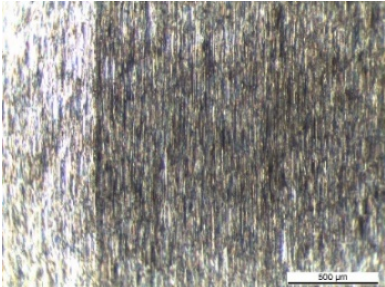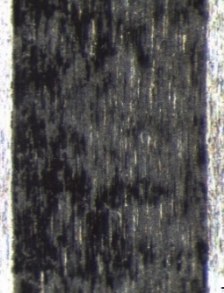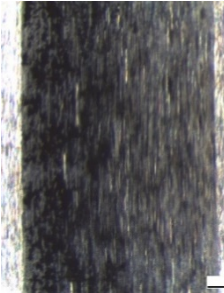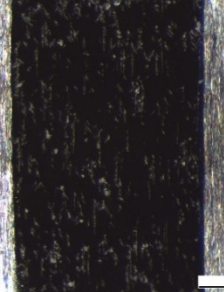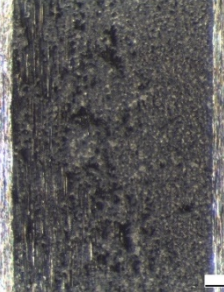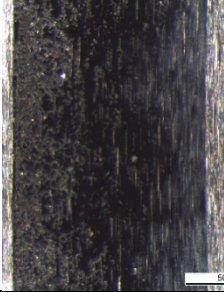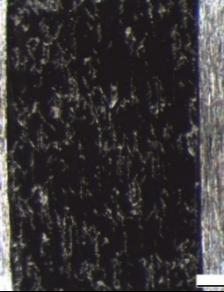
Lubricant	Lubricant A	Lubricant B	Lubricant C	Lubricant D
Unworn Specimen				
Step 2 – 440 k cycles				
Step 5 – 1760 k cycles				
Step 8 – 3080 k cycles				
Step 11 – 4400 k cycles				

Figure 7-2 – Optical microscope images of the wear track of the P53 chamfered rollers for each lubricant.

Lubricants	Wear track Image	Zoomed in Wear track image
Lubricant A		
Lubricant B		
Lubricant C		
Lubricant D		

Figure 7-3 – High definition images of the wear tracks of the MSRR6010 roller specimens.

Lubricants	Wear track Image	Zoomed in Wear track image
Lubricant A		
Lubricant B		
Lubricant C		
Lubricant D		

Figure 7-4 – High definition images of the wear tracks of the P53 roller specimens.
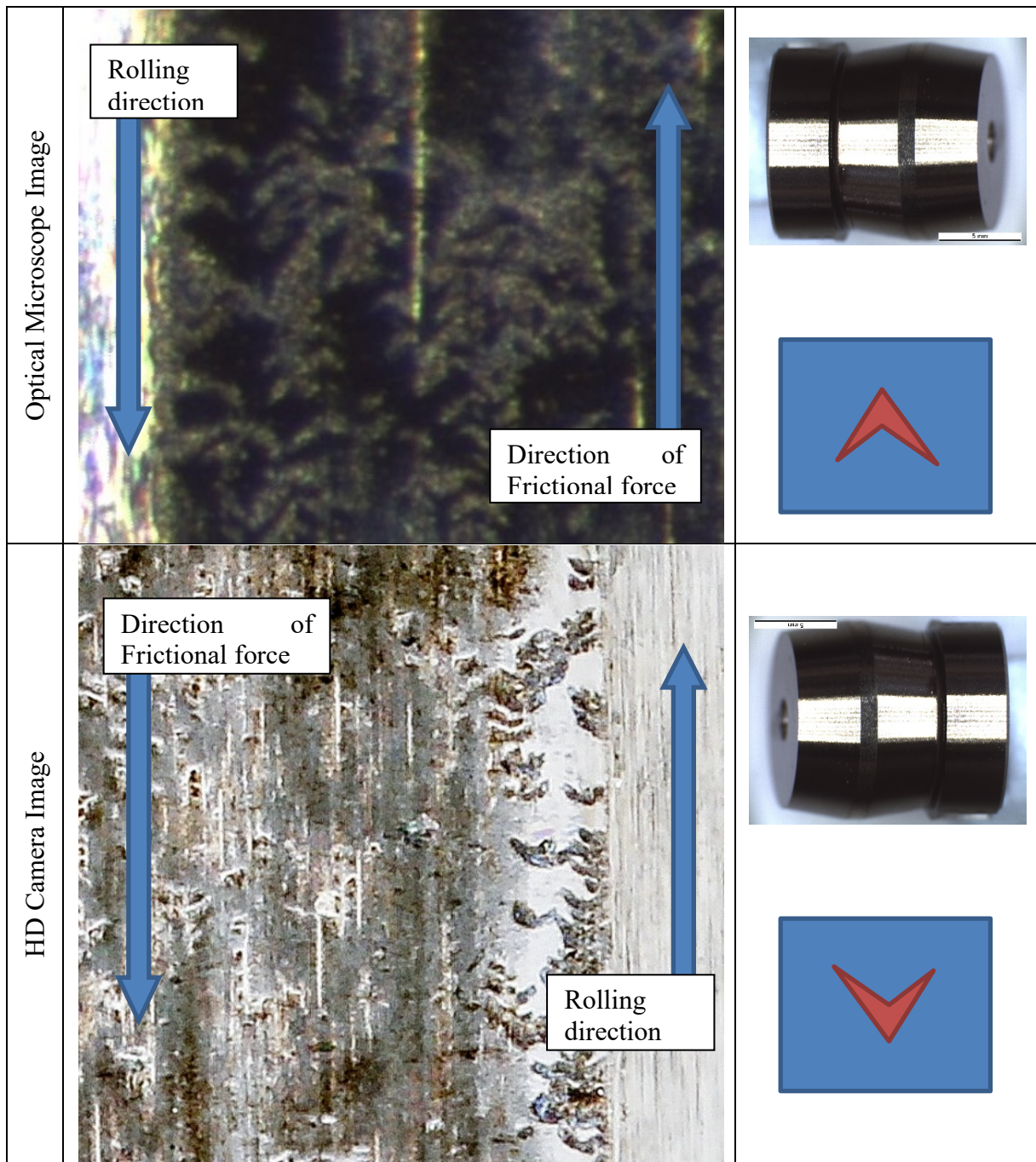
Figure 7-5 – Table showing the orientation of micropitting with respect to roller orientation, rolling direction and frictional force.

The test with lubricant D has the most severe wear as micropitting occurs very quickly, smaller than those produced from lubricants A and B and then progresses into severe wear and material loss as shown later from the Mass Loss results. Therefore, it is evident that lubricant D has the worst performance at these test conditions.

The colours produced on the wear tracks from tests with lubricant A and lubricant B have varying hues of browns and oranges. It is difficult to decipher whether these colours are a result of the oil or due to a thermal effect of the steel on wearing.

For MSRR 6010, it is instantly evident from the images that the lubricants appear to affect the surface of the specimens in different ways. As shown and discussed for Figure 5-2, it is likely this could be an effect of the anti-wear additives left of the surface, due to there being no dispersion colour effect in the HD image of the wear track for the base oil. However, the HD image of the wear track from the MPR test with just base oil in Figure 5-2 produces no array of spectral colours in the wear track suggesting the additives are responsible for dispersing the light producing this effect.

For P53, overall, there was less surface damage in comparison to MSRR 6010 and micropits formed more slowly. This is most likely due to the P53 being softer and the P53 rings being initially smoother as shown in Chapter 3.

Lubricant C exhibits the same polishing wear in P53 as in MSRR 6010 as the wear track appears smoothened and shiny in appearance. This also seems to have delayed the onset of micropitting formation however, the micropits appear larger in size in comparison to micropitting tests with other oils. But there is less micropitting in P53 most likely due to the difference in roughness and hardness.

The amount of micropitting on P53 with lubricant A was similar to MSRR6010 where a moderate amount of micropitting had been produced but it propagated at a slower rate than with MSRR 6010. Micropitting also initiates at the edge of the wear track where the chamfer begins, this is expected due to edge effects that are commonly seen with these type of micropitting experiments where there is a higher stress concentration at the edge of the wear track (179,181) and this is commonly seen throughout these wear tests.

Lubricant B performed differently on P53 in comparison to MSRR6010 as there was much less surface damage and minimal micropitting. Lubricant D also performed differently on P53 compared to MSRR 6010 as there was a moderate amount of small micropitting that initiated earlier than the other oils but did not propagate into the extensive wear seen on MSRR6010. Overall, the most micropitting was found with lubricant A or lubricant D however, lubricant C presented with fewer but larger micropits which, propagated more slowly than the other oils.

For the micropitting test with lubricant A, the images in Figure 7-2 show that there is more micropitting on the P53 rollers than on the MSRR6010 rollers. This differs from what is shown in the optical microscope images, but the HD images give a better overview of the wear track and clearly show there is more micropitting. Also, there is a repeating pattern on the wear track around the circumference of the roller where micropits have clustered. This has been detected previously and is thought to be due to the rig itself vibrating at a certain frequency due to the parameters of the test, i.e. the rotation speeds of the specimens. However, this is not believed to affect the outcome of the test. It can also be seen that there is a brownish colour to the wear track, which, is believed to be the remnants of boundary additives bound to the surface.

The P53 wear track using lubricant B showed minimal damage and as with lubricant A, there was a slight repeating pattern on the wear track, which, is again expected to be due to rig vibration. Also, the yellow/ brown staining on the wear track is assumed to be bound boundary additives on the surface.

The HD images for lubricant D show much less severe wear than on the MSRR6010 specimens and the specimens appear moderately micropitted as opposed to extensive wear. From these images, lubricant A appears to be the most damaged followed by lubricant D, then lubricant C and then finally lubricant B has the least damage.

Quantification of micropitting using image analysis

ImageJ was used to conduct image analysis on the microscopy images from the micropitting pitting tests. This analysis allowed the amount of micropitting on the surface of the wear tracks to be quantified allowing the different lubricants to be evaluated on the micropitting propensity. In comparison to the image analysis in 5.2.1 in the Micropitting Quantification Using Image Analysis section, this micropitting image analysis was performed on the final step of full formulation tests instead of step 2 on the anti-wear additive and base oil blend tests. This is due to the full formulation tests having less severe wear and micropitting formation occurring more slowly than on the gear steels using full formulation lubricants. Whilst this could be due to the full formulation providing more protection than the anti-wear additive and base oil blends, it is more likely that the tests with the candidate gear steels are more resistant to micropitting due to the ring and the roller having a smaller difference in hardness than on the standard 16MnCr5 specimens. The standard specimens are created this way such that the roller is softer ensuring that the majority of the wear and micropitting damage is concentrated onto the central roller specimen (106,150).

Figure 7-6 shows a bar chart summarising the average micropitting quantification of the final step of the micropitting tests for lubricants A-D on MSRR6010 and P53. For MSRR6010, Lubricant D has the most pitting on the surface as also confirmed from the microscopy images, followed by lubricant A, the lubricant C and then lubricant B. Whereas on P53, lubricant A had the most micropitting followed by lubricant D, then lubricant B and then lubricant C. However, once again the error bars need to be considered as they are quite large on the P53 specimens. However, it is clear that the lubricants A and D seem to cause more micropitting than lubricants B and C. It has already been highlighted that lubricant C exhibits a polishing effect on the wear track that delays the initiation of micropitting but forms larger micropits in the long run. Lubricant B forms less micropitting than lubricants A and D as expected from the microscopy

images. Lubricant B seems to have a better resistance to micropitting in comparison to lubricants A and D despite having a lower viscosity. Lubricant A produces more micropitting than B and C for both steels showing a worse tribological performance despite A and B having similar anti-wear additive packages. Lubricant D performs the worse on both steels despite being the most viscous and being a gear oil. It may be that lubricant D required more severe operating conditions to initiate additive action, which, results in excessive wear. This could also be an effect of the anti-wear additive rapidly forming a tribofilm which, results in the quick protection of surface asperities, which, prevents "running-in" as shown for ZDDP (157,179). It can also be seen that lubricant B with MSRR6010 does not have an error bar. This is because a repeat has been omitted from the results as mentioned earlier due to the wear track containing heavy micropitting at a skewed angle.

However, there remains some ambiguity in this method that requires further development to improve the accuracy of the micropitting quantification through image analysis. As this method identifies micropits through the micropits having a different colour and contrast to the rest of the wear track, it will recognise other features as a micropit which, contribute to the total percentage area. Therefore, this method requires further optimisation to isolate micropits in the quantification of micropits on the surface. Also, previous results have shown that P53 appears to have less sever wear and micropitting that MSRR 6010 and lubricants A and B do not seem to follow this. This is most likely due to errors in this method.
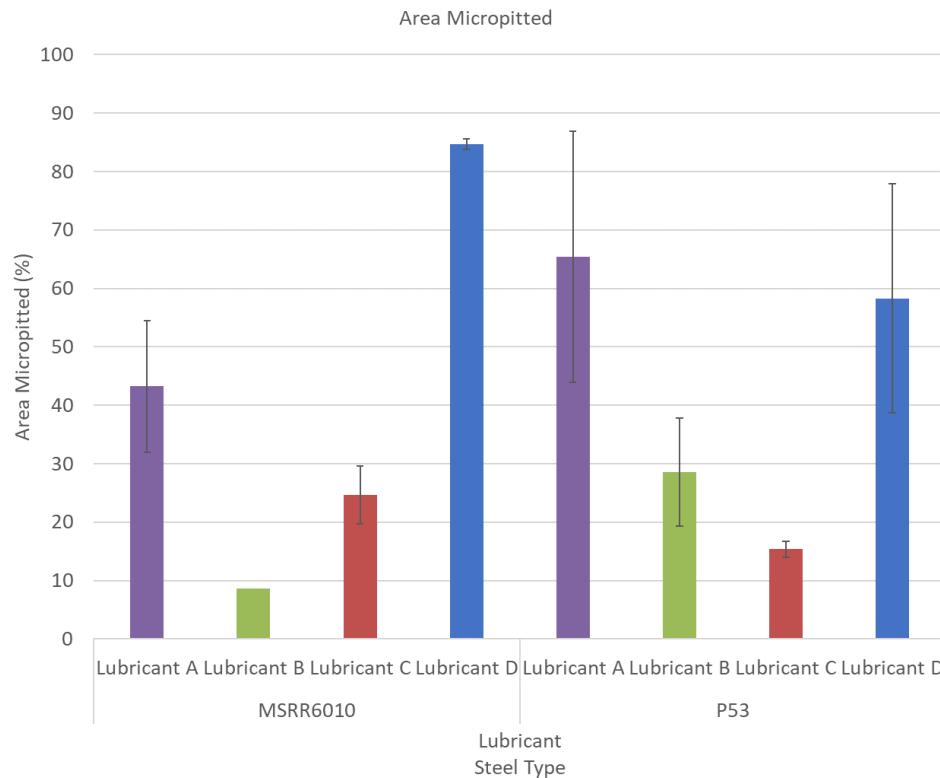
Figure 7-6 –The mean average amount of micropitting from image analysis using ImageJ after the final step of the MPR test for lubricant A-D on MSRR6010 and P53.

Friction

A graph showing the average traction coefficient of each lubricant with both MSRR6010 and P53 is shown in Figure 7-7. All the lubricants behave similarly throughout all the steps of the wear test, all having a relatively constant traction coefficient but P53 has a lower measured traction coefficient than MSRR6010, an average of ~0.09 as opposed to ~0.13 respectively. This is most likely due to the higher hardness of the MSRR6010 steel and the higher initial roughness of the MSRR 6010 rings. Also, it can clearly be seen that the difference in lubricant viscosity is having no effect on the traction coefficient in the boundary regime as expected (7). Again, there is no error bar for lubricant B due to omitting the repeat due to finding skewed micropits in the contact.
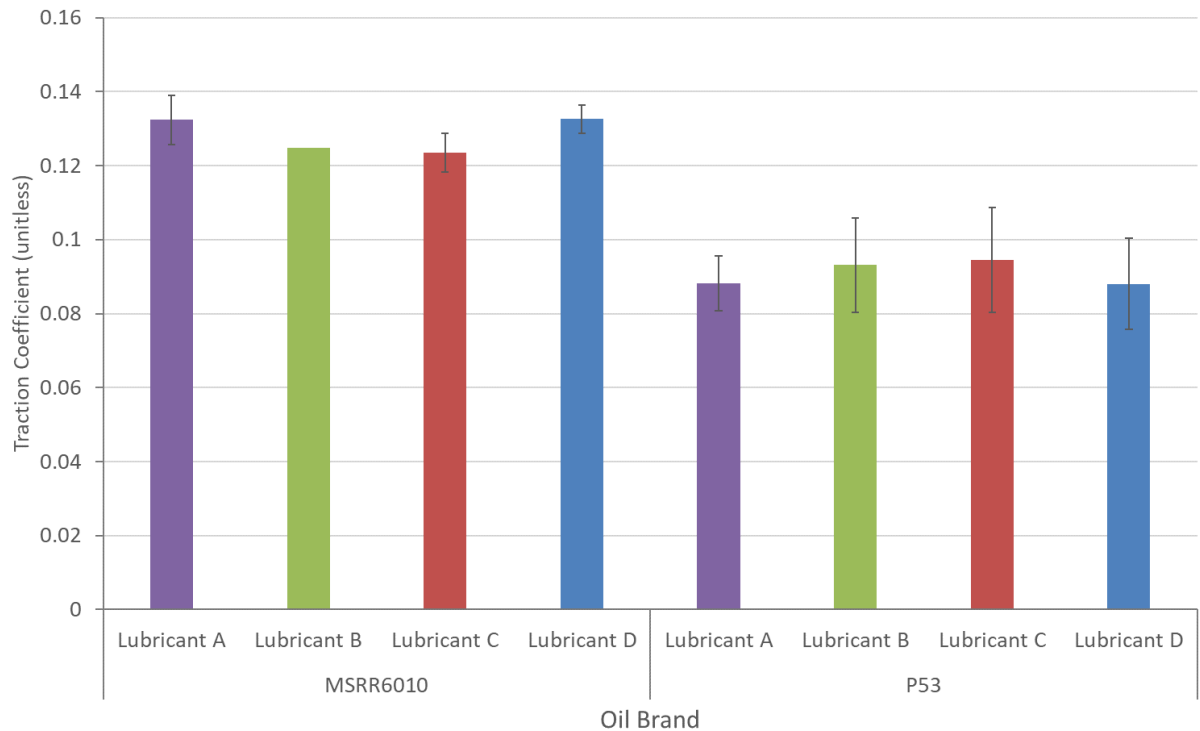
Figure 7-7 - The mean average traction coefficient for each lubricated wear test for MSRR6010 and P53 where each test is labelled according to the lubricant and steel used for the test.

Wear Track Width Increase

Figure 7-8 shows the increase in wear track width of the roller. The graph shows that there is generally a smaller increase in wear track width on the P53 steel than the MSRR6010 steel. Again, this is most likely due to the harder and rougher MSRR6010 rings wearing the central roller more than the P53 roller as shown in Table 3-12 and Table 3-13. For P53, there appears to be a slight trend in the track width data too however, there is a lot of overlap between the error bars. The trend shows an increase in track width from lubricant B to lubricant D to lubricant C to lubricant A. Again, the data shows that the difference in viscosity has no effect on the results as the highest and lowest viscosity oils (lubricant D and lubricant B) have the lowest track width increases. These results present a different trend to what is seen in the MSRR6010 steel, where lubricant D performed the worst followed by lubricant C, then A then B. Lubricants A and B are have similar track width increase results. It was expected lubricant

D would perform moderately better than the other lubricants due to having a higher viscosity which, would therefore, mean it could form a thicker film and better protect the surface. However, it is evident that the viscosity is having no effect most likely due to the wear test being conducted in the boundary lubrication regime. However, it should be considered that the increase in the P53 roller tracks are very small and resulting in overlapping error bars, so this trend does not give a strong inference on oil performance. It can be seen with lubricant C on MSRR6010 that the polishing wear seen on the wear track images still results in the second highest track width increase for that steel, showing that polishing wear is still detrimental to the surface. There is less increase in track width for lubricant C on P53, but this was similar for most oils on P53.
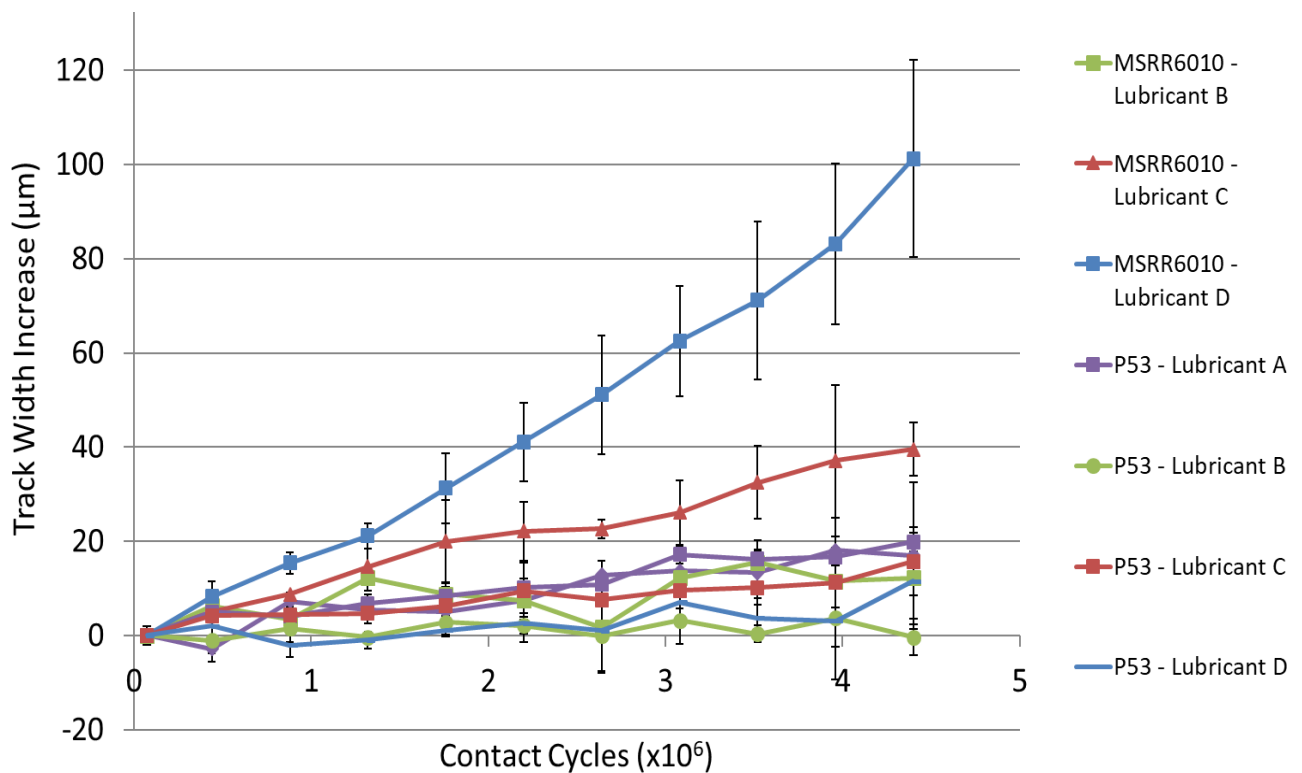
Figure 7-8 – Graph showing the increase in wear track width of the roller.

Mass Loss

Figure 7-9 shows the mean average mass loss for the MSRR6010 and P53 rollers. The P53 mass loss is lower than the MSRR6010 micropitting, which, is most likely due to the higher hardness and initial ring roughness of the MSRR6010 specimens as shown in Chapter 3. However, these mass losses are very small resulting in large error bars and the mass losses are of the same order of magnitude as the uncertainty for the balance and therefore, the mass loss results do not impose a strong trend.

For MSRR6010, lubricant D has the largest mass loss followed by lubricant C, then A and then B. Lubricant D is a surprising result considering that this lubricant has the highest viscosity out of all the test candidates and has extra EP additives as well as AW additives so, therefore, it would be expected to provide a thicker film to better protect the surface. However, the viscosity clearly has no effect as lubricant D has the worst performance under these conditions.

For P53, the trend in these results show that mass loss increases from lubricant B to lubricant D to lubricant A to lubricant C, but the error bars are large for the latter two oils. This differs from MSRR6010 in that lubricant D had the largest track width increase with the other oils showing similar performance. But lubricant B seems to have the lowest mass loss on both steels, therefore, showing better performance than the other lubricants.

Lubricant C for both steels has a relatively high mass loss in comparison to the other lubricants again suggesting that the polishing wear is still detrimental to the surface.
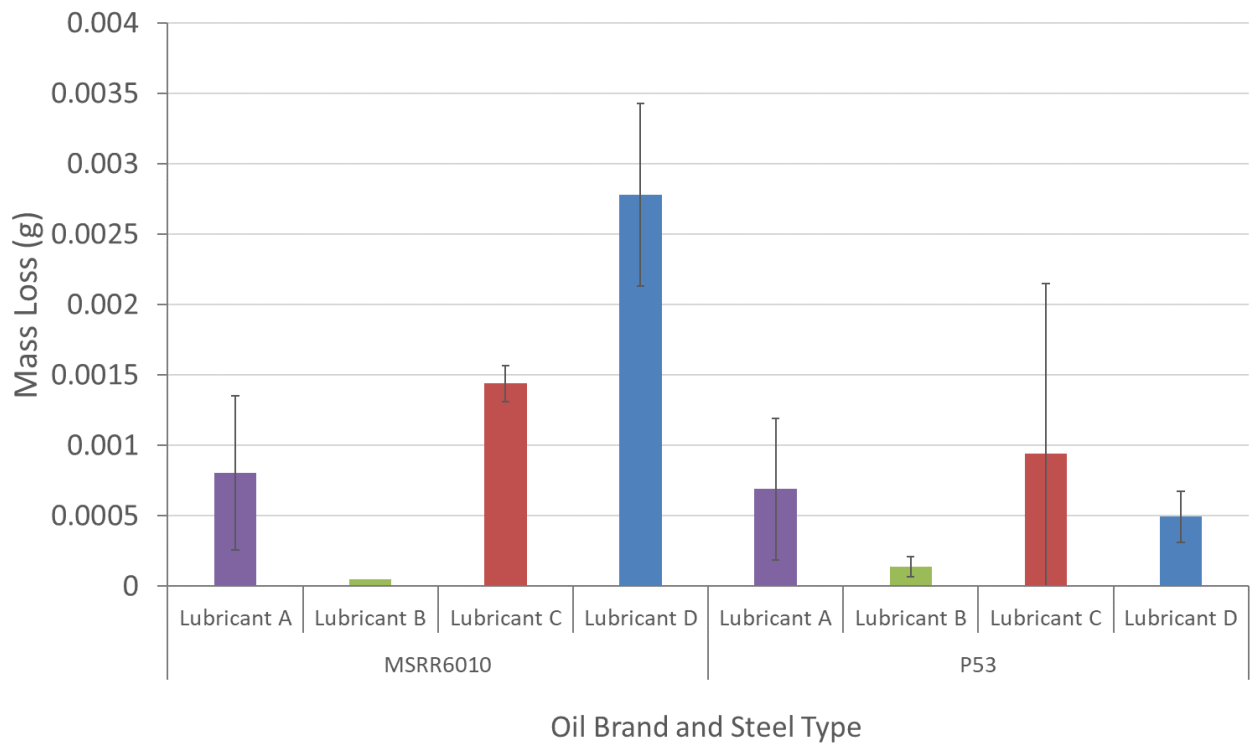
Figure 7-9 - The mean average overall mass loss from the wear tests conducted with different lubricant formulations on MSRR6010 and P53. The bars also each have error bars of the standard deviation.

Stribeck Analysis

The Stribeck curves for the start and end Stribeck curves can be seen from MSRR6010 and P53 in Figure 7-10 to Figure 7-13 respectively. The results are similar to those obtained by the MTM in that there is a similar behaviour between all lubricant candidates.

It can also be seen that as the entrainment speed is increased and therefore, the Hersey number, there is only a slight decrease in traction coefficient. This is due to this test operating in the boundary regime throughout the entire range of the Stribeck curve, due to the line contact geometry used in the MPR giving rise to a larger contact area than a point contact. Even higher entrainment speeds and Hersey numbers or a lower surface roughness would be required to reach the EHD regime. It is in the EHD regime where the difference in viscosity would have more of an effect, however, as the Stribeck curves are plotted against the Hersey number, the graphs have been normalised against viscosity.

264

For MSRR6010, the Stribeck curves in both graphs are similar except for lubricant B in which, the traction coefficient decreased by 0.2 at low speeds, but this may be due to running in of the specimens. Lubricant C also has the lowest friction at high Hersey numbers in the final Stribeck curves showing that the excessive smoothening seen in the microscopy wear images could be responsible for the decrease in friction. There is also less error in comparison to the P53 Stribeck curves. Again, lubricant B has no error bars due to the repeat being omitted due to the skewed micropits in the contact.

This differs from the SLIM Stribeck curves where an increase in traction coefficient was produced, but this is due to the MTM specimens being smoother than MPR specimens in which, wear results in an increase in roughness. Whereas with MPR specimens, they are initially rougher than MTM specimens and typically become smoother as wear progresses until pitting begins which, increases the roughness again.

For P53, the standard deviation throughout the start Stribeck curves is large showing the variation in the measured friction between the repeats. This could be an effect of the differing amounts of running in between repeats as there is smaller error in the final Stribeck curves. However, lubricant C has the highest friction followed by, lubricant B, then lubricant D and finally lubricant A in both Figure 7-12 and Figure 7-13.

There is no substantial change in the Stribeck curves for each lubricant between the start and end Stribeck curves except for lubricant B in which, the traction coefficient decreased by 0.1, across the whole curve and lubricant C has increased marginally across the whole curve too. For lubricant B this may be due to running in of the specimens and for lubricant C this could just be due to the larger pitting giving rise to more friction towards the end of the wear test.

The main comparison between the steels is that the friction for MSRR6010 is higher than P53 as shown in the Friction section. This backs up the fact that more extensive wear was seen with the MSRR6010 specimens.
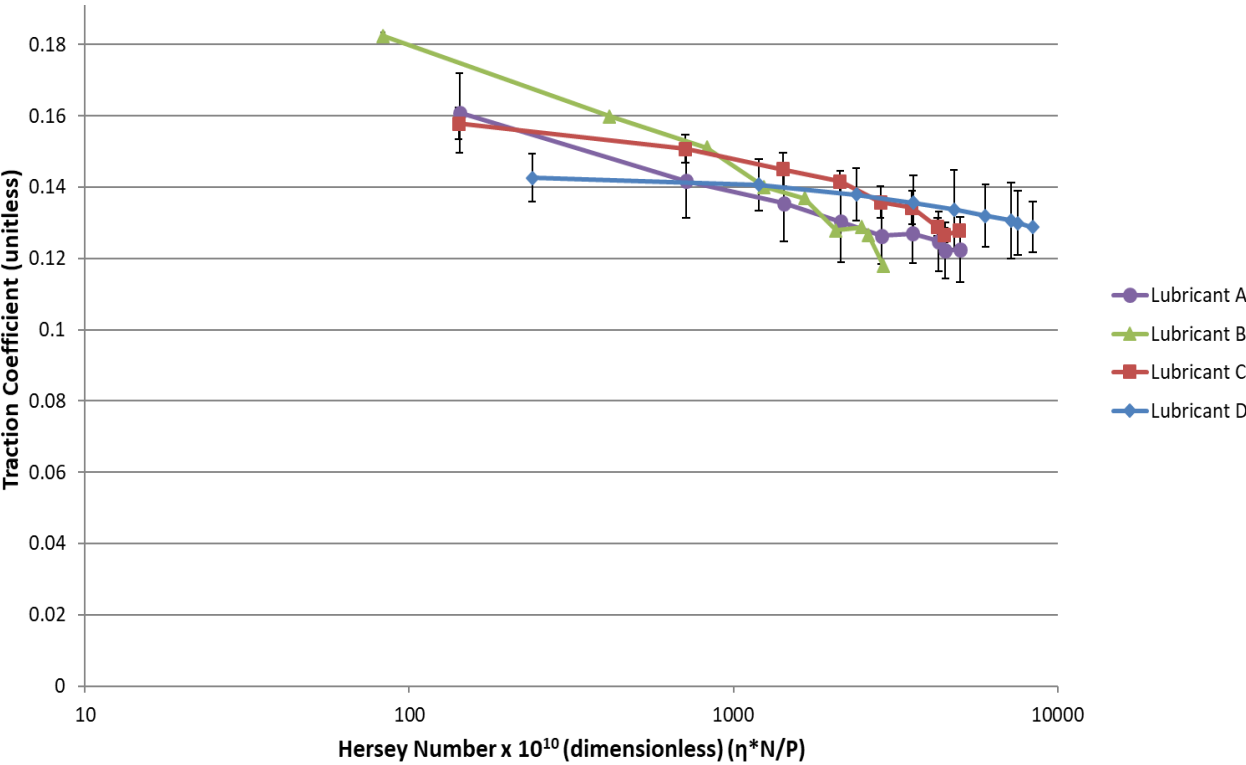
Figure 7-10 – Stribeck curves at the beginning of the wear tests for each lubricant MSRR6010.
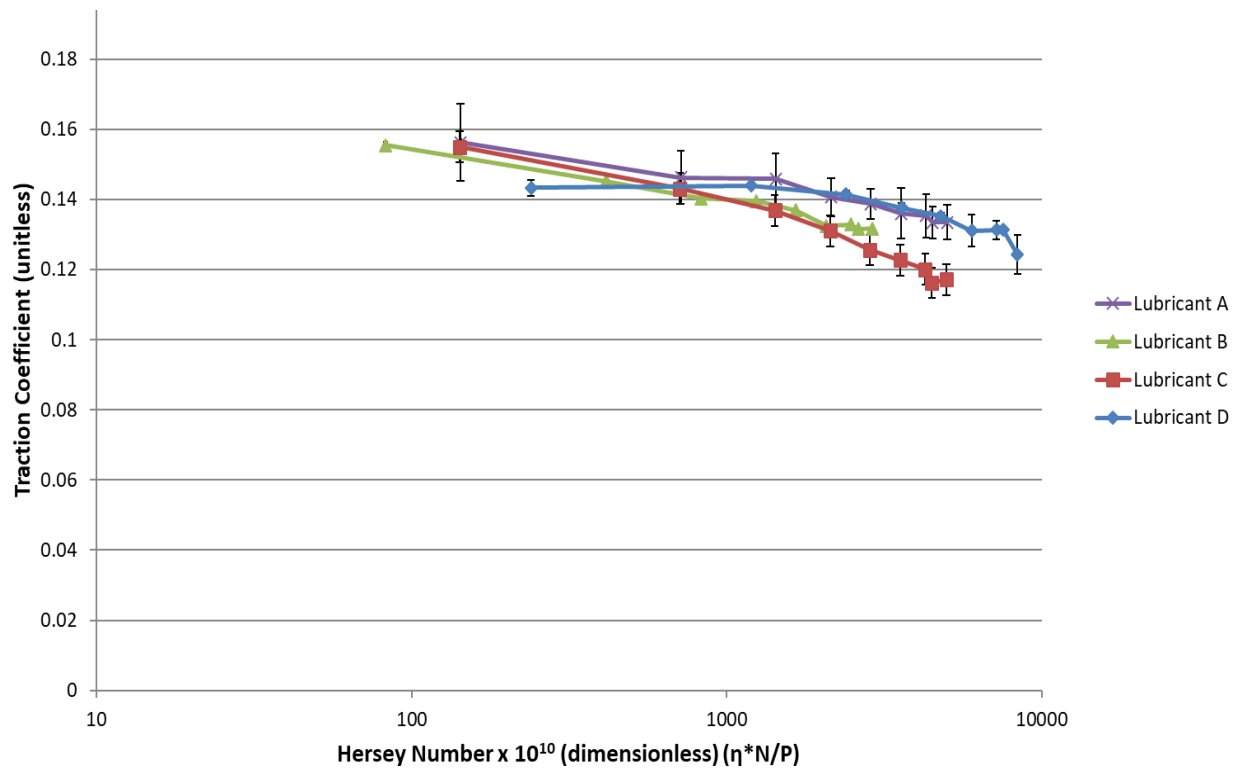
Figure 7-11 - Stribeck curves at the end of the wear tests for each lubricant for MSRR6010.
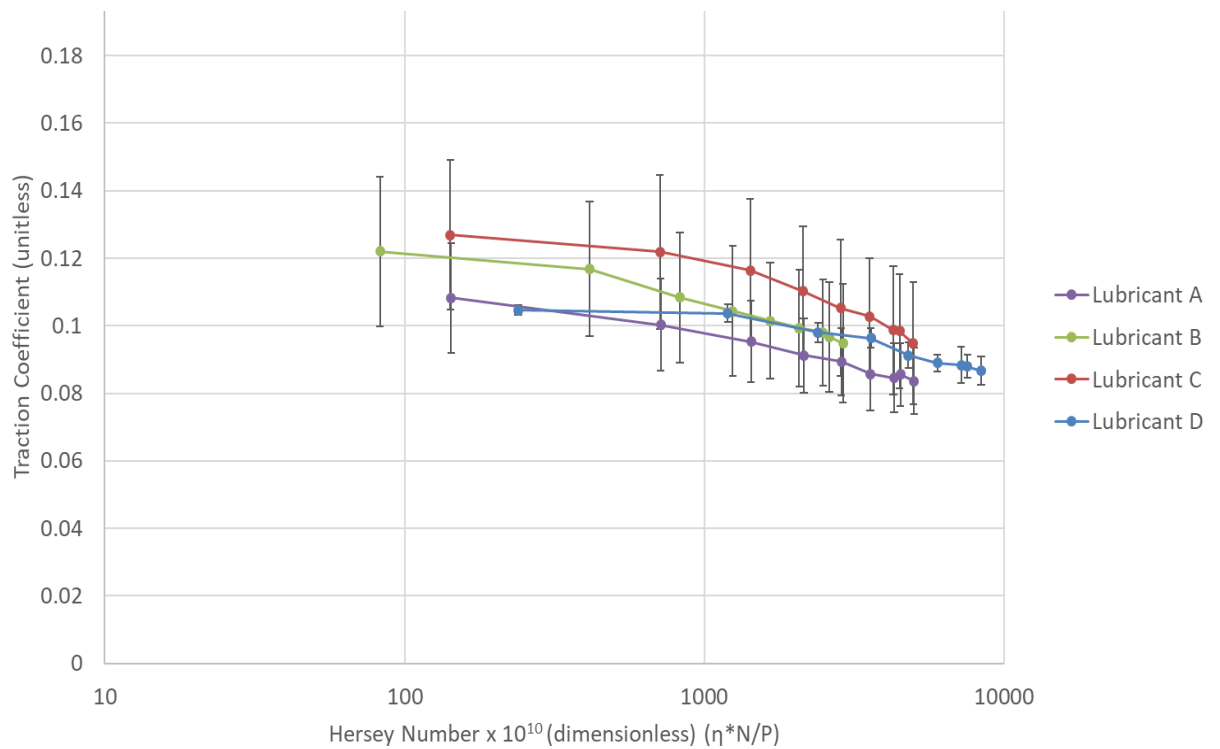
Figure 7-12 – Stribeck curves at the beginning of the wear tests for each lubricant for P53.

267
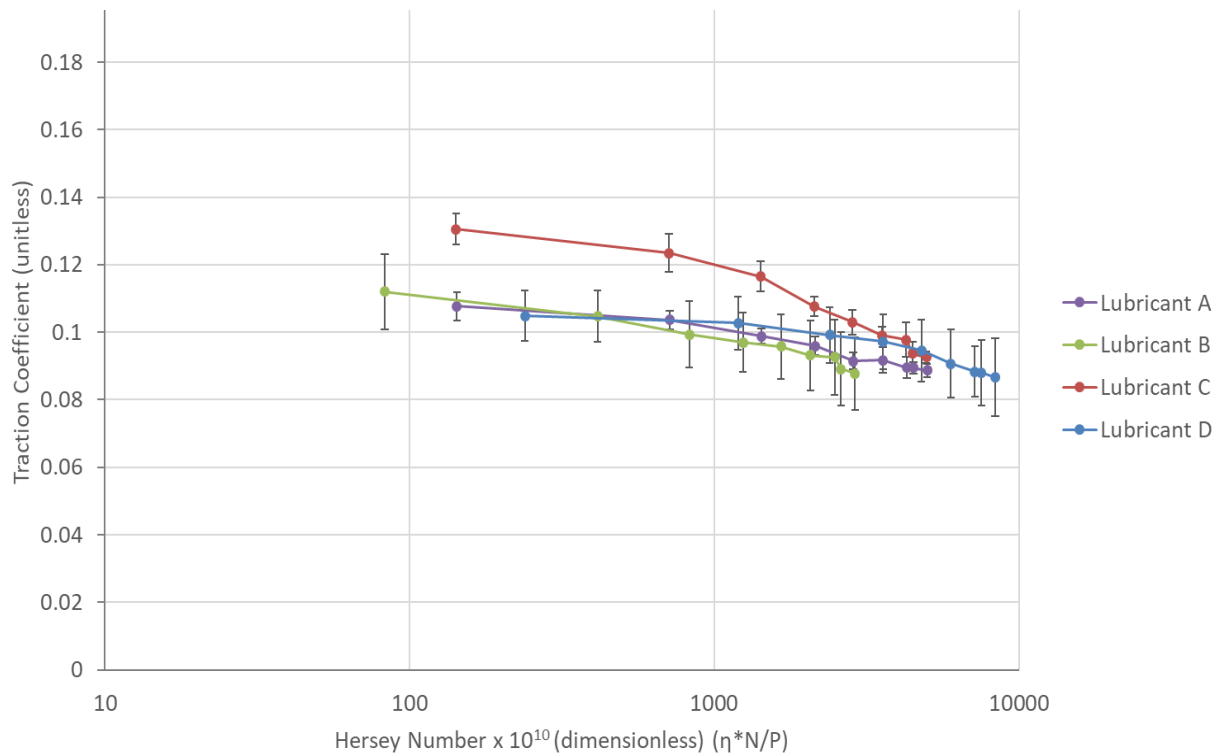
Figure 7-13 - Stribeck curves at the end of the wear tests for each lubricant for P53.

Roughness

Bar charts comparing the roughness of ring and roller specimens after the tests for MSRR6010 and P53 are shown in Figure 7-14 and Figure 7-15.

Firstly, with the ring specimens, it can be seen that there is a moderate decrease in Ra with both steels suggesting an overall smoothening throughout all tests. It can also be seen that the MSRR6010 ring was initially rougher than the P53 specimens by ~0.1 μm, and this coupled with the MSRR6010 being harder could explain the increased wear and increased rate of micropitting seen with the MSRR6010 tests.

For MSRR6010, whilst the difference in roughness is only small, it can be seen that lubricant C has the largest decrease in roughness suggesting that part of the formulation is responsible for this decrease in roughness as seen from the polishing wear in the microscopy images. There

are similarities between the results from lubricant A and lubricant B, but lubricant D has the lowest decrease in roughness, and this may be responsible for the more extensive wear seen on the roller. It may be possible that the boundary additives in lubricant D are protecting the asperities such that a rougher surface is maintained that could give rise to more wear (157,179).

With the ring specimens for P53, there is a moderate decrease in R_a suggesting an overall smoothening throughout all tests. Whilst the difference in roughness is only small, lubricant C and lubricant B have the largest decrease in roughness. This explains the polishing effect found on the lubricant C roller and it is likely the EP additive is responsible as confirmed later by XPS analysis. Despite the substrate with lubricant B having the lowest roughness suggesting that this specimen has been run in the most, lubricant B still had the lowest track width increase and mass loss which, potentially shows that an oil that allows components to run in initially will give rise to better micropitting protection. It has been discussed in various papers that certain lubricants increase micropitting by protecting asperities early in the test therefore, maintaining higher contact pressures resulting in more micropitting (157,179,187,188). However, despite the polishing seen with lubricant C, it can also be seen that larger micropits than the other oils eventually formed. It could be that the EP additive present in the formulation of lubricant C weakens the surface such that larger micropits can form however this would need to be investigated further.

Lubricant C was smoothened to a similar extent on P53 as on MSRR6010, but the other oils all resulted in smoother surfaces on the P53 rings than the MSRR6010 rings.

It can be seen from Figure 7-15 that the rollers for both steels have a lower initial roughness than the ring specimens and a mixture of outcomes are seen post-test for different lubricants. For MSRR6010, lubricant C appears to dramatically roughen the surface, which, could be explained by the large micropits in the wear track. But it is clear from the images that there is a smoothening effect with lubricant C. The presence of micropits will obviously lead to an

269

increased roughness, but it can be seen that the unpitted areas are polished and smoothened. The rest of the candidates showed similar performance to each other with some appearing so show smoothening effects (lubricant A) and other roughening (lubricant B and lubricant D). However, by considering the error bars present, it can be seen that the majority of these are not very repeatable.

It can be seen from Figure 7-15 that the P53 roller has a slightly higher initial roughness than the MSRR6010 roller specimen and a mixture of outcomes are seen post-test for different lubricants. All the lubricants except lubricant B give rise to a rougher roller surface which, coincides with the amount of pitting on the surfaces of these oils. However, as lubricant B only produced a small amount of micropitting, there has been a moderate degree of running in producing a slightly smoother surface.

It should also be noted that due to the roller specimen wearing much more that the ring specimen, the roughness of the roller may not be a reliable parameter as the Ra will vary greatly depending on where the measurement is taken due to the micropitting present.

Further work is required to find different roughness parameters that better distinguish between these worn surfaces.
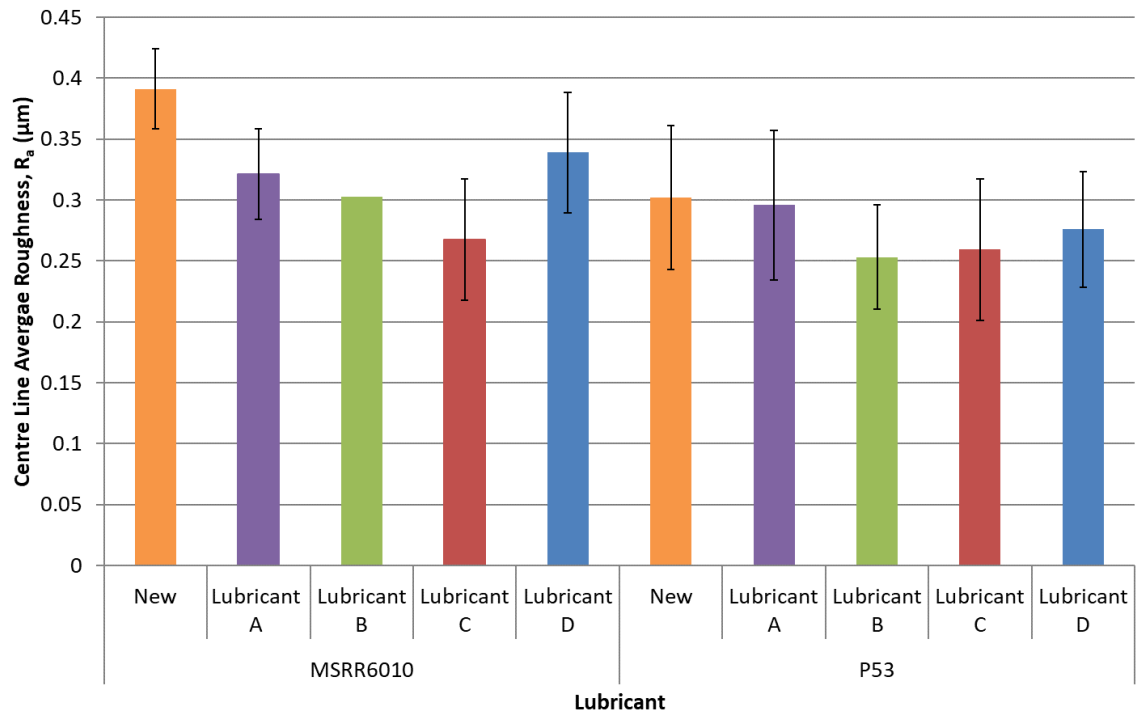
Figure 7-14 – Bar chart showing the average centre line average roughness (Ra) of the ring specimens for the wear tests from each lubricant candidate.
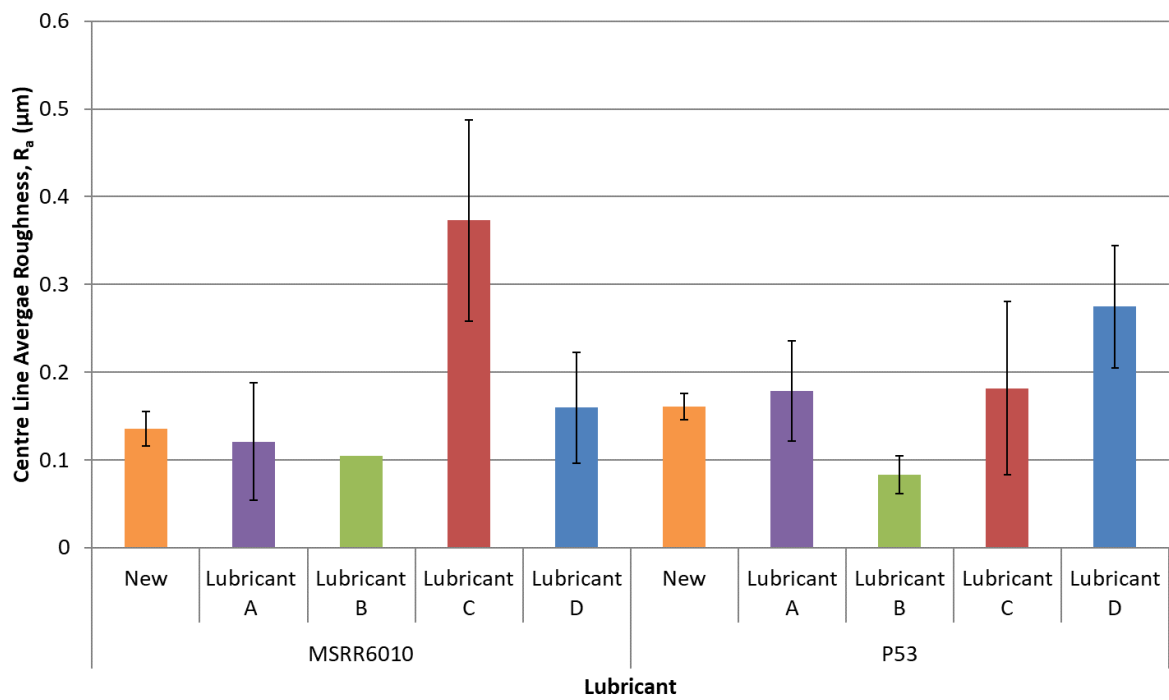
Figure 7-15– Bar chart showing the average Ra of the roller specimens for the wear tests from each lubricant candidate.

271

To confirm the smoothening effect of lubricant C, the roughness was measured using an Alicona to measure an unpitted area on the wear track on P53 (Figure 7-16). An Alicona is a Focus Variation Microscopy (FVM) technique in which a reflective optical microscope scans vertically above a sample whilst capturing images. The images are then processed in order to determine the height at which a given lateral position is most in focus. These positions with their assigned height values are then combined to produce a 3D dataset. Multiple such 3D datasets from different positions can be combined to form a 3D dataset of a surface that is larger than the field of view of the chosen objective (189).
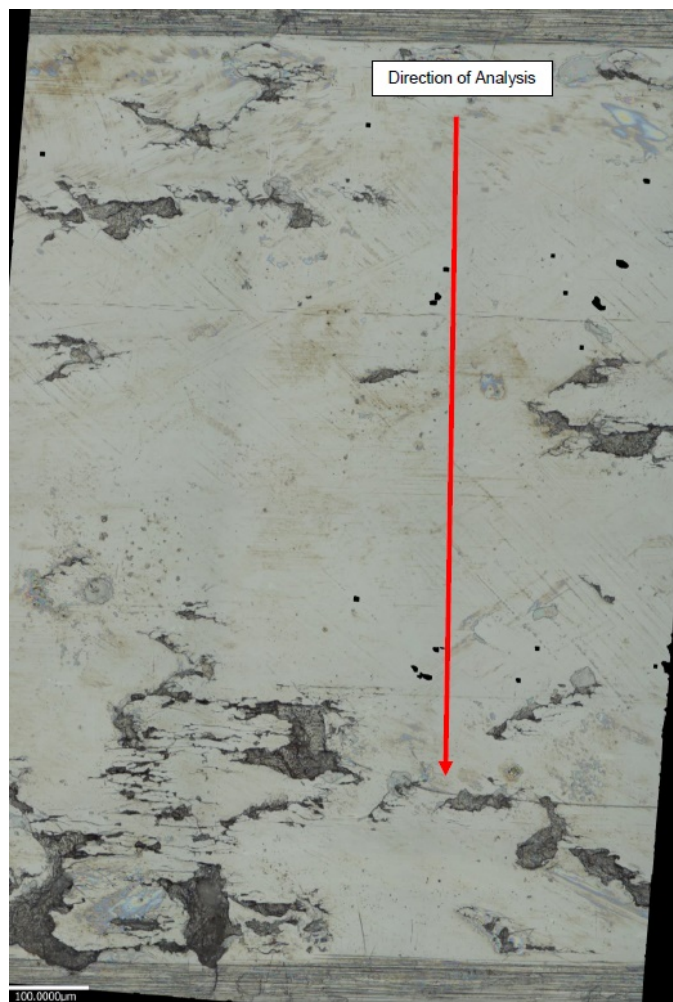
Figure 7-16 – Image showing the location on the wear track of the roller worn with lubricant C where the Alicona measured the roughness of the unpitted area.

The measured Ra was 0.06 μm and hence, this shows the surface has been smoothened. However, this polishing effect should be studied further on other steels.

XPS

The work discussed in this section was carried out by Dr Steven Hinder, the Experimental Officer and Manager of the Surface Analysis Laboratory at the University of Surrey. The interpretation of the data produced below was carried out by the author of this thesis.

Surface analysis was performed using XPS to detect the presence and concentration of different elements on the surface of the test specimens. For these results, the focus has been on the elements present in the boundary additives which, are believed to chemisorb onto the surface under high pressures and temperatures and consequently, all metal atomic abundances have not been discussed. This is being studied to deduce if these additives are influencing the different micropitting and wear characteristics produced. Information on the boundary additives present are shown in Chapter 3.

There are certain elements that are considered to be common contaminant elements, and these are carbon, oxygen and chlorine and therefore, potentially give rise to misleading results. Therefore, carbon and oxygen will not be discussed, but chlorine has been analysed as it is known to be present and surface active in the EP additive of lubricant C. Silicon was not analysed either due to silicon being present in small quantities in both steel alloys and in the anti-foamant additive in some of the formulations.

Despite omitting MPR058 from the rest of the interpretation, it has been left in the XPS section as only one roller specimen was submitted for each oil with each steel. However, MPR058 was only excluded due to it being in the rig in the incorrect orientation, which, resulted in excessive wear and micropitting. Therefore, chemically it should still be representative of how lubricant

B interacts with the surface and the elements left on the surface are assumed to be the same for repeats. All of the XPS results can be seen in Appendix 10.

The main findings of these results were that chlorine and higher levels of nitrogen were detected for lubricant C which, indicated the presence of the EP on the surface which, is most likely responsible for the polishing effect produced. Also, high levels of phosphorus were found in all tests showing all phosphorus based anti-wear additives have some surface interaction and the higher concentration of phosphorus in the wear track suggested higher pressures assist in its chemisorption with the surface. Nitrogen was also detected on the surface for all tests and is present in many parts of each lubricant's formulation showing that other additives are also surface active, and the surface is not dominated by the anti-wear additive.

Hardness

Many sections in this chapter have discussed the smoothening and polishing effect of lubricant C, however, there is limited information in the literature about a potential mechanism for this effect. As confirmed by the XPS analysis, it is assumed that the EP additive in lubricant C is responsible for the polishing effect. It has been reported in the literature that the EP additive has had a softening effect on bronze (50,190). Consequently, the hardness in and out of the wear tracks of some 16MnCr5 specimens was also tested with Lubricants A and C and the results can be seen in Table 7-1. These results were obtained by Intertek (an analytical laboratory company used by and embedded within Rolls-Royce) using a Vickers Hardness Machine, with a Diamond Indenter using a load of 10 kg.

Table 7-1 – Table showing the hardness results for roller specimens tested with lubricant A and C both inside and outside of the wear track.

Vickers Hardness H_V	Lubricant A		Lubricant C	
	Inside the wear track	Outside the wear track	Inside the wear track	Outside the wear track
	691, 701, 699	711, 720, 716	664, 664, 668	674,681,689

By comparing these to the initial hardness of a 16MnCr5 roller of an average of 709 HV, it can be seen that for both lubricants, the micropitting test and the lubricant give rise to softening of the steel in the wear track and outside of the wear track, but to a lesser extent. However, lubricant C has an increased effect of softening the steel in comparison to lubricant A. It also seems to be accelerated in the harsh conditions within the wear track, as softening still occurs outside of the wear track even in the absence of higher temperatures and a high contact pressure.

However, it is understood that measuring the hardness on a rough worn surface will measure relatively soft anyway and hence is likely to incur error and it not strongly validated. But these results weakly suggest a potential mechanism by which, the EP additive in lubricant C gives rise to polishing and a slower onset of micropitting, but larger micropits in the long term. More work needs to be done to isolate the specific EP additive in the base oil to confirm the polishing, micropitting and softening effects. Additionally, more work needs to be done to understand the effect on the steel at a microstructural level but also on a chemical level and XPS depth profiling could provide as insight to the effect this additive is having on the steel. It is not currently expected that the other gear steels would perform differently with respect to hardness due to them having similar chemical compositions. The 16MnCr5 steel also has a higher tempering temperature than the other steels meaning it should be less resistant to any microstructural changes at the surface.

7.3 Conclusions

Lubricants A-D were evaluated on their micropitting propensity under representative conditions on two different gear steels. There was generally less micropitting and wear on the P53 steel compared to the MSRR6010 steel, most likely due to the lower hardness of the P53 steel and the initially lower roughness of the P53 rings, this was reflected in the measured friction being

0.2 lower than MSRR6010. On MSRR6010, lubricant D was the most worn having progressed from rapid micropitting to extensive wear. Then lubricant A had the most micropitting, followed by lubricant C showing signs of polishing wear and larger micropitting and then finally lubricant B had minimal micropitting.

For P53, a similar trend was seen with lubricant D having the most micropitting followed closely by lubricant A, lubricant C showed the same polishing wear with larger micropits and lubricant B was the least pitted. The marginally larger micropits and polishing wear found with lubricant C has been attributed to the Cl based EP additive in its formulation as detected by XPS.

The larger amount of wear and micropitting with MSRR6010 was also confirmed by the higher average traction coefficient of ~0.13 as opposed to ~0.09. This was also explained by the higher hardness of the P53 steel specimens and the higher initial surface roughness of the P53 rings. Similar frictional differences were found in the Stribeck curves for the MPR tests on both steels with MSRR6010 having a higher friction than P53.

The difference between the initial and final Stribeck curves revealed a running-in effect on the MPR specimens as the friction decreased over time which, differs from the MTM Stribeck curves where friction increased over time due to the smooth specimens becoming rougher over time.

The mass loss and track width increase results revealed similar trend with the P53 steel generally having less wear than the MSRR6010. However, the main difference was that for both steels, lubricant C demonstrated a substantial track width increase and mass loss suggesting that polishing wear is detrimental to the surface and can result in significant mass loss and therefore, component profile deviation.

The roughness results confirmed the significant polishing and smoothening effect of lubricant C as shown for the larger decrease in R_a in comparison to the other lubricants. The rings for all steel resulted in smoothening throughout the test.

The roller roughness did not confirm the smoothening effect of lubricant C due to the extensive pitting on the surface, but an Alicona was used to measure the roughness of an unpitted area of the wear track confirming the smoothening effect.

The XPS results provided a useful insight into which, components of each lubricant formulation were present on the surface and could therefore, be attributed to its specific kind of wear. The presence of chlorine and higher levels of nitrogen indicated the presence of the EP in lubricant C on the surface, which, is most likely responsible for the polishing effect produced. High levels of phosphorus were found in all tests showing all phosphorus based anti-wear additives have some surface interaction and the higher concentration of phosphorus in the wear track suggested higher pressures assist in its chemisorption with the surface. Nitrogen was also seen in all tests and is present in many parts of each lubricant's formulation. Higher levels were found for lubricant, which, again confirms the presence of the EP additive on the surface.

Hardness tests on the wear track of steel roller tested with lubricant C and lubricant A revealed that lubricant C substantially softens steel, which, could be a contributing factor to the polishing wear mechanism.

Chapter 8.   Conclusions and Future Work

8.1   Conclusions

The tribological performance of gas turbine lubricants have been extensively studied. The MTM-SLIM and MPR were found to be useful tribological testing rigs that allowed the tribological effect of differences in the lubricant formulation to be detected. In particular, this thesis allowed different lubricant formulations to be evaluated under representative PGB conditions, which, enabled further understanding into the friction and what wear mechanisms (i.e. micropitting) that are prevalent in that environment.

This thesis evaluated the effect of individual components of a lubricant formulation on friction and wear respectively, as well as the impact that the full formulation has on tribological performance.

Polyol ester base oils were studied by investigation of the effect of differences in molecular structure on friction. In particular this study understood the well-known effect of viscosity on friction and aimed to isolate the impact of the molecular structure by studying each base oil at the same viscosity. It was found that increasing the chain length, the number of ester groups and the degree of linearity (decreasing the amount of branching) led to a decrease in friction across all lubrication regimes.

This effect was attributed to improved molecular packing efficiency of larger and more linear chains; however, further work is required to completely confirm this hypothesis.

Anti-wear additives were also investigated with a focus on whether aviation ashless additives promote a common wear mechanism seen on the dedenda of gear teeth called micropitting via a similar mechanism to that shown for a common automotive anti-wear additive (ZDDP).

It was found that the ashless additives in this study (TCP and Additive X) promote micropitting to a much lesser extent than ZDDP but also still protect against more severe failure modes (like macropitting) in comparison to the base oil alone.

The mechanism of ZDDP micropitting promotion was attributed to rapid tribofilm formation resulting in protection of surfaces too early, which, prevents the running-in process, which, maintains localised high asperity contact pressures, which, results in faster micropitting formation in a high pressure and high sliding environment. Whereas, TCP and Additive X formed much thinner tribofilms that formed at a slower rate and therefore, it is hypothesised that these ashless additives allow the running process to occur, but then encourage micropitting formation later after significant tribofilm formation. Whilst these additives still formed micropits earlier than the base oil, they still protect against more severe failure modes which, reinforces the theory that anti-wear additive protection requires a careful balance of properties specific for an operating environment to protect against micropitting, without comprising protection against other severe failure modes.

Finally, current full formulation lubricants were evaluated under representative PGB conditions. Four lubricants were chosen that covered a variety of parameters from differences in physical properties like kinematic viscosity, but also in terms of formulation with different lubricants having different additive packages.

It was found that Lubricant B with the lowest viscosity performed the best, as it had low friction in the MTM tests, developed a thin anti-wear tribofilm in the SLIM tests without excessive wear, but also resulted in the least amount of micropitting in the MPR tests. It was expected that the lowest viscosity would have the worst performance due to forming a thinner lubricant film than the more viscous lubricants, how the viscosity had little effect in all of these tests in the boundary lubrication regime.

Lubricant A would be the second-best lubricant candidate because whilst this oil showed more micropitting damage than lubricant B, it still had less damage than lubricant D. On the MTM it had higher friction than other oils and the SLIM revealed it formed a thin tribofilm without excessive wear. As shown from Chapter 5, ashless anti-wear additives like TCP do not pose a significant risk to micropitting, as they do not perform as strongly as ZDDP which, prevents the running-in of components, maintaining high asperity contact pressure accelerating micropitting. This lubricant is also approved to SAE AS5780 and is already known to offer enhanced thermal capabilities.

Lubricant C despite producing low friction and minimal wear on the MTM, it is clear that the chlorinated EP additive poses a potential risk to engine components through polishing wear mechanisms, which, can give risk to significant material loss and therefore, component profile deviation. This additive needs to be isolated and tested further to confirm the action of this particular additive and also if the polishing occurs due to softening of the metal substrate.

Lubricant D seemed to perform the worst, producing the most wear and also micropitting quicker than the other lubricant candidates. It was previously assumed this lubricant would offer more protection than the other lubricants due to its higher viscosity and it being a gear oil with specific anti-wear and EP additives to provide enhanced protection. However, it is likely that the conditions within these tests may not be severe enough to provide the mechanochemical conditions necessary for the additives in this gear oil to activate to provide protection.

8.2 Impact on the Business

Overall, test methods have been developed to aid the understanding of how lubricant formulations affect the tribological performance under representative conditions.

Whilst the investigation into base oil molecular structure led to a more fundamental understanding of how subtle changes in molecular chemistry can affect friction, it gave an insight to how changes in base oil chemistry could impact friction despite having similar viscosity.

The micropitting risk of current anti-wear additives in aviation were shown to be much less severe than the common automotive additive ZDDP. It was shown to allow "running-in" of component surfaces that resulted in a reduction in local high asperity contact pressures that accelerate micropitting. The importance of having the right balance of anti-wear properties was highlighted which, shows that protection against micropitting and scuffing can often be compromising properties. Whilst it is importance for lubricant formulators to continue to improve anti-wear properties, an additive that is too strong and forms tribofilm too quickly could promote micropitting whilst protecting against scuffing.

The evaluation of a lubricant with respect to the PGB showed that a lower viscosity lubricant offered improved tribological properties over other candidates. However, the optimal tribological benefits would need to be balanced with understanding its thermal capabilities which, are suspected to be worse with it having a lower viscosity. There would also be significant challenges to using this lubricant in a civil aviation gas turbine as it not currently approved as the civil aviation lubricant specification unless its thermal capabilities were deemed adequate. A lower viscosity oil could also offer extra efficiency benefits as it has less resistance to shear resulting in lower operational losses.

Overall, this thesis highlighted the importance of choosing an appropriate lubricant for a specific environments. In particular, how certain anti-wear additives can promote different wear mechanisms. It has been shown how an anti-wear additive like ZDDP that reacts with a surface quickly results in accelerated micropitting whilst protecting again other wear mechanisms like scuffing. Whilst there are other additives in a lubricants formulation that have not been evaluated, this thesis investigates the mechanism of anti-wear additives that would be beneficial in the understand of boundary additives in general. However, the true effect of the additives would need to be individually evaluated and then together with the other additives to understand what synergistic effects they have together in the formulation.

It has also been shown how variable the results are depending on the other test parameters. ZDDP in the literature has been shown to both increase and decrease friction and this is entirely due to the difference in other test parameters used. The surface roughness is a key factor to consider in a tribological environment and a smooth surface would drive down contact pressures and significantly reduce the micropitting risk.

This thesis only focuses on steel substrates as this is the main material used throughout aviation transmission systems. However, introducing coatings could significantly affect the way the lubricant and the additives behave. Hence, such coating would need to be evaluated with these oils to understand whether they provide the same level of effectiveness in comparison to steel.

8.3 Future Work

This thesis covered a broad range of tribological areas and has highlighted a range of areas for future work. The potential avenues for future work have been split according to the corresponding chapter in this thesis.

Future work for the investigation into aviation base oils in Chapter 4 could include:

- Further understanding of the rheology of aviation lubricants under representative shear rates experienced in oil system environments. The parallel plate rheometer cannot reach shear rates high enough for the EHD conditions seen in the Stribeck curve due to the oil being centrifugally flung out of the gap of the rheometer. Ultrahigh shear viscometers have been used in the past that address this issue (191).

- Further understand the synergistic effect of more complex base oils with mixtures of chain lengths, branching and number of ester groups. Whilst this chapter conclusions showed the effects of varying certain characteristics of the molecule structure, base oils used in aerospace formulations contain a mixture of chain lengths, branching and number of ester groups as this offers improved pour point capabilities and avoids the needs for costly separation processes. This could be done by formulating base oils with specific ratios of different structures to understand how this impacts friction.

- To explore whether traction curves of the base oils offer any further information than the Stribeck curves discussed.

- To look into confirming the packing efficiency argument potentially through the use of absorption theory using a quartz crystal microbalance (QCM) to confirm whether longer and straighter molecular structures pack more efficiently than smaller and bulkier branched structures whilst keeping the viscosity constant.

Future work for the investigation into aviation anti-wear additives in Chapter 5 could include:

- Use other techniques to further characterise the micropits formed by different additives and also develop improved image analysis to quantify micropitting and its progression. This could include using high resolution non-contact (Alicona or Wyko Veeco interferometer) or contact (AFM) optical instrument to characterise the micropits which, could capture the size, morphology and depth of the pits in relation to the specific additive used to create the pit.

- Understand the synergistic effect of aerospace anti-wear additives with other common components of aviation lubricant formulations to understand if the combination of additives is beneficial or detrimental to micropitting.

- Also deduce whether other additives in an aviation lubricant formulation alone contribute to micropitting.

- Understand how degradation of the oil and additive affects tribological performance as this would be more representative of engines in service in which, the lubricant has a long lifetime. There has been a study looking at the mild degradation of di-2-ethylhexyl sebacate and how it affects wear performance. It was found that initially the wear of steel specimens increased, but as the oxidation progressed further, the wear performance actually improved from new oil. This would be a complex study as not only does the chemistry of the lubricant change under degradation, the physical properties change too like the viscosity, therefore, it would be useful to understand how tribological performance changes as the lubricant degrades (26,192).

- Aviation anti-wear additives and their corresponding tribofilms could be further studied. The MTM-SLIM, whilst being useful at monitoring the film in-situ and understanding wear performance, struggles to detect such thin films. Therefore, a technique like that used by Rydel *et al* where an AFM was used to measure ZDDP thickness by measuring

the profile with the tribofilm film, chemically removing the tribofilm using EDTA and oxalic acid and then remeasuring the same profile to get another measure of the thickness (36,100,101). This could potentially confirm the measurement produced by the MTM-SLIM.

- The adsorption behaviour could also be studied using a quartz crystal microbalance like Yungk *et al* to understanding the anti-wear additive adsorption mechanism, however, this could be difficult to combine with the necessary contact conditions required for film formation (193).

Future work for the investigation into fully formulated aviation lubricants in Chapter 6 and Chapter 7 could include:

- To further explore the difference in behaviour of the EP additive in lubricant C in comparison to TCP by isolating this additive in Base oil and confirming this additive is responsible for the results produced. This would confirm if a softening and/ or polishing mechanism is occurring that gives rise to minimal wear in the MTM-SLIM tests, result in delayed onset of micropitting in the MPR tests but also gives rise to polishing wear which, produces significant material loss.

- Further characterisation of different tribofilms using methods such as the film thickness method detailed by Rydel *et al* to confirm film thickness but also explore other methods to characterise different films (100).

- To understand what microstructural changes these lubricants impose on the steel through SEM analysis.

- To explore how current commercially available lubricants interact with different materials as most lubricants are formulated to be used with steels.

References

1. Rolls-Royce. The Jet Engine. 5th Edition. Rolls-Royce plc, editor. Chichester, West Sussex: John Wiley & Sons Inc.; 2015. 288 p.

2. Torbacke M, Rudolphi ÅK, Kassfeldt E. Lubricants : Introduction to Properties and Performance. 1st ed. John Wiley & Sons, Incorporated; 2014. 219 p.

3. Mortier RM, Fox MF, Orszulik S. Chemistry and Technology of Lubricants. Dordrecht: Springer Netherlands; 2011. (SpringerLink: Springer e-Books).

4. ASTM International. ASTM D2509: Standard Test Method for Measurement of Load-Carrying Capacity of Lubricating Grease (Timken Method). ASTM Int. 2017;8.

5. Williams JA. Engineering Tribology. Cambridge: Cambridge University Press; 2005.

6. Jost HP. Working Group., Great Britain. Department of Education and Science. Lubrication Engineering (Education and Research): Lubrication (tribology) : education and research. Jost HP, editor. London: H.M.S.O.; 1966. p. 79.

7. Hutchings IM. Tribology : Friction and Wear of Engineering Materials. 1st Edition. Hutchings I, editor. Oxford: Butterworth-Heinemann; 1992. 280 p.

8. Bowden FP. The friction and lubrication of solids / by F.P. Bowden and D. Tabor. Part 2. Tabor D (David), editor. Oxford: Clarendon Press; 1964.

9. Amonton G. De la résistance causée dans les machines. Mem l'Académie des Sci. 1699;275–82.

10. Bowden FP. The friction and lubrication of solids / by F.P. Bowden and D. Tabor. Part 1. Tabor D (David), editor. Oxford: Clarendon Press; 1950.

11. Rabinowicz E. Friction and wear of materials. 2nd ed. New York : Wiley; 1995.

12. Stachowiak G, Batchelor AW. Engineering Tribology. 3rd ed. Butterworth-Heinemann; 2011. 830 p.

13. Oila A. Micropitting in Phenomena Related and Case Carburised Gears Adrian Oila A Thesis Submitted for the Degree of Doctor of Philosophy July 2003. University of Newcastle Upon Tyne; 2003.

14. Way S. Pitting due to rolling contact. J Appl Mech. 1935;57:49–58.

15. Olver A V. The mechanism of rolling contact fatigue: an update. J Eng Tribol. 2005;219(5):313–30.

16. Littmann WE, Widner RL. Propagation of contact fatigue from surface and subsurface origins. Trans ASME. 1996;88(3):624–36.

17. Benyajati C, Olver A V, Hamer J. An experimental study of micropitting, using a new miniature test-rig.

18. Clarke A, Evans HP, Snidle RW. Understanding micropitting in gears. Proc Inst Mech Eng Part C J Mech Eng Sci. 2015;230(7–8):1276–89.

19. Baker R. PCS Instruments: Scuffing Investigation. San Francisco: SAE E-34 Propulsion Lubricants Committee; 2016. p. 15.

20. Peng B, Huang G, Kadiric A. An Experimental Study of the Onset of Scuffing Using a New Contra-rotation Test Method. San Francisco: SAE E-34 Propulsion Lubricants Committee; 2016. p. 39.

21. PCS. PCS Intruments Products [Internet]. PCS Instruments. 2016 [cited 2016 Feb 3].

Available from: http://pcs-instruments.com/products/

22.   Airey J, Spencer M, Greenwood R, Simmons M. The Effect of Gas Turbine Lubricant Base Oil Molecular Structure on Friction. Tribol Int. 2020;146(June):11.

23.   Shell Aviation Limited. The AeroShell Book. Aviation. 2003;196.

24.   Spencer M, Shepherd T, Greenwood R, Simmons M. An Assessment of the Influence of Gas Turbine Lubricant Thermal Oxidation Test Method Parameters Towards the Development of a New Engine Representative Laboratory Test Method. SAE Int J Aerosp. 2013;6(2):2013-01–9004.

25.   Bakunin VN, Parenago OP. A Mechanism of Thermo-oxidative degradation of polyol ester lubricants.pdf. J Synth Lubr. 1992;9(2):18.

26.   Spencer MR. Gas turbine lubricant evaluation. The University of Birmingham; 2014.

27.   Stachowiak G, Batchelor AW. Chapter 8: Boundary and Extreme Pressure Lubrication. In: Engineering Tribology. 2011. p. 425–84.

28.   Soltanahmadi S, Morina A, van Eijk MCP, Nedelcu I, Neville A. Tribochemical study of micropitting in tribocorrosive lubricated contacts: The influence of water and relative humidity. Tribol Int. 2017;

29.   Topolovec-Miklozic K, Forbus TR, Spikes HA. Film thickness and roughness of ZDDP antiwear films. Tribol Lett. 2007;26(2):161–71.

30.   Taylor L, Dratva A, Spikes HA. Friction and Wear Behavior of Zinc Dialkyldithiophosphate Additive. Tribol Trans. 2000;43(3):469–79.

31.   Fujita H, Spikes HA. Study of zinc dialkyldithiophosphate antiwear film formation and

removal processes, part II: Kinetic model. Tribol Trans. 2005;48(4):567–75.

32. Hsu SM, Gates RS. Boundary lubricating films: Formation and lubrication mechanism. Tribol Int. 2005;38(3):305–12.

33. Cen H, Morina A, Neville A. Effect of slide to roll ratio on the micropitting behaviour in rolling-sliding contacts lubricated with ZDDP-containing lubricants. Tribol Int. 2018;

34. Kapadia R, Glyde R, Wu Y. In situ observation of phosphorous and non-phosphorous antiwear films using a mini traction machine with spacer layer image mapping. Tribol Int. 2007;

35. Topolovec-Miklozic K, Forbus TR, Spikes HA. Film thickness and roughness of ZDDP antiwear films. Tribol Lett. 2007;

36. Rydel JJ, Pagkalis K, Kadiric A, Rivera-Díaz-Del-Castillo PEJ. The correlation between ZDDP tribofilm morphology and the microstructure of steel. 2017;

37. Zhang J, Spikes H. On the Mechanism of ZDDP Antiwear Film Formation. Tribol Lett. 2016;

38. Benedet JFL. Low and Zero SAPS Antiwear Additives for Engine Oils. Imperial College of Science, Technology and Medicine, London; 2012.

39. Johnson D, Bachus M, Hils J. Interaction between Lubricants Containing Phosphate Ester Additives and Stainless Steels. Lubricants. 2013;1(2):48–60.

40. Sheasby JS, Caughlin T a., Mackwood W a. The effect of steel hardness on the performance of antiwear additives. Wear. 1996;201(1–2):209–16.

41. Gauthier A, Montes H, Georges J. Boundary Lubrication with Tricresylphosphate (TCP).

Importance of Corrosive Wear. ASLE Trans. 1982;(25):445–55.

42. Perez JM, Ku CS, Pei P, Hegemann BE, Hsu SM. Characterization of Tricresylphosphate Lubricating Films by Micro- Fourier Transform Infrared Spectroscopy. Tribol Trans. 1990;(33):131–9.

43. Godfrey D. The Lubrication Mechanism of Tricresyl Phosphate on Steel. ASLE Trans. 1965;(8):1–11.

44. Saba CS, Forster NH. Reactions of aromatic phosphate esters with metals and their oxides. Tribol Lett. 2002;12(2):135–46.

45. Sasaki K, Inayoshi N, Tashiro K. Friction-induced dynamic chemical changes of tricresyl phosphate as lubricant additive observed under boundary lubrication with 2D fast imaging FTIR-ATR spectrometer. Wear. 2010;268(7–8):911–6.

46. Hsu SM, Gates RS. Boundary lubricating films: Formation and lubrication mechanism. In: Tribology International. 2005.

47. Wright J. Extreme Pressure Additives in Gear Oils [Internet]. Machinery Lubrication. 2019 [cited 2019 Jun 20]. p. 1. Available from: https://www.machinerylubrication.com/Read/1406/extreme-pressure-additives

48. Canter N. Additives for Metalworking Fluids. In: Booser R, editor. Tribology Data Handbook. CRC Press; 1997. p. 862–71.

49. Noria Corporation. Limitations of Extreme Pressure Additives [Internet]. Machinery Lubrication. 2019 [cited 2018 Jun 10]. p. 1. Available from: https://www.machinerylubrication.com/Read/29031/extreme-pressure-additives

50. Cash W. The Effects of EP Additives on Gearboxes [Internet]. Machinery Lubrication India. 2019 [cited 2019 Jun 20]. p. 1. Available from: http://machinerylubricationindia.com/current-issue/97-magazine/2014/mar-apr/197-the-effects-of-ep-additives-on-gearboxes

51. Cober G. Avoiding Common Gearbox Lubrication Problems. Machinery Lubrication. 2019. p. 1.

52. Wan Y, Amerongen E V, Lankamp H. I fatigue life of rolling bearings.

53. Nixon HP, Zantopulos H. Lubricant additives, Friend or Foe, What the equipment design engineer needs to know. Journal of the Society of Tribologists and Lubrication Engineers. 1995;(October):815–22.

54. Evans RD, More KL, Darragh C V., Nixon HP. Transmission electron microscopy of boundary-lubricated bearing surfaces. Part II: Mineral oil lubricant with sulfur- and phosphorus-containing gear oil additives. Tribol Trans. 2005;

55. SAE. SAE AS5780 Specification for Aero and Aero-Derived Gas Turbine Engine Lubricants. SAE Int J Aerosp. 2013;(B):20.

56. Easa. European Aviation Safety Agency Certification Specifications for Engines. 2010.

57. U.S. Department of Transportation FAA (FAA). Advisory Circular Subject: Approval of Propulsion Fuels, Additives, and Lubricating Oils. 2018.

58. Rolls-Royce Plc. Rolls-Royce UltraFan© [Internet]. https://www.rolls-royce.com. Derby: Rolls-Royce; 2016 [cited 2017 Apr 21]. Available from: https://www.rolls-royce.com/products-and-services/civil-aerospace/future-products.aspx#section-overview

59. Inc HI. Honeywell Aerospace Engines [Internet]. https://aerospace.honeywell.com. 2018 [cited 2018 Nov 26]. Available from: https://aerospace.honeywell.com/en/products/engines/tfe731-turbofan-engine

60. United Technologies Corporation - Pratt & Whitney Division. Pratt & Whitney PW1000G [Internet]. 2017 [cited 2017 Jan 4]. p. 1. Available from: http://www.pw.utc.com/Content/PurePowerPW1000G_Engine/pdf/B-1-1_PurePowerEngineFamily_SpecsChart.pdf

61. Hart K. Gas Turbine Oil Systems Analysis – Advanced Course. University of Hertfordshire; 2008.

62. Zhang Y, Finger S, Behrens S. Introduction to Mechanisms: Gears [Internet]. Carnegie Mellon University. 2019 [cited 2019 Jun 20]. p. 1. Available from: https://www.cs.cmu.edu/~rapidproto/mechanisms/chpt7.html#HDR103C

63. Gangadhar Bhavi I. Design and analysis of crown pinion of a differential gear box for reduced number of teeth to improve torque transmitted [Internet]. The International Journal of Robotics Research. 2014 [cited 2019 Jun 20]. p. 189–95. Available from: https://www.researchgate.net/publication/280033279_DESIGN_AND_ANALYSIS_OF_CROWN_PINION_OF_A_DIFFERENTIAL_GEAR_BOX_FOR_REDUCED_NUMBER_OF_TEETH_TO_IMPROVE_TORQUE_TRANSMITTED/figures?lo=1

64. International Organization for Standardization. ISO 10825: Gears — Wear and damage to gear teeth. International Organization for Standardization; 1995.

65. Gopinath PK, Mayuram PMM. NPTEL Course Machine Design II Lecture 6 Gear Failure. Madras, India: Indian Institute of Technolog; 2019.

66.   Beckman M. Gear Failure Analysis. Tribology and Lubrication Technology Magazine, STLE Publication,. 2019 Apr;24–32.

67.   Rexnord Industries LLC Gear Group. Failure Analysis Gears-Shafts-Bearings-Seals. Vol. 2, Rexnord. 1978. p. 1–20.

68.   Cheng HS. Cheng CRC Book Gears Ch 29. In: Bharat Bhushan, editor. Modern Tribology Handbook. CRC Press; 2001. p. 1095.

69.   Bergseth E. On tribological design in gear tooth contacts. Royal Institute of Technology Stockholm; 2012.

70.   Tallian TE. On Competing Failure Modes in Rolling Contact. ASLE Trans. 1967;10:418–39.

71.   Skurka JC. Elastohydrodynamic Lubrication of Roller Bearings. J Lubr Technol. 1970;92(2):281–91.

72.   Rantala J. Roughness Parameters. Electronic Coolings. 2016. p. 1.

73.   Gordon England. Vickers Hardness Test [Internet]. 2016 [cited 2017 Jan 5]. p. 1. Available from: http://www.gordonengland.co.uk/hardness/vickers.htm

74.   Hooke C. A review of the paper "A numerical solution to the elastohydrodynamic problem" by D. Dowson and G.R. Higginson. Proc Inst Mech Eng Part C J Mech Eng Sci. 2009;223(1):49–63.

75.   (NPFC) M and GS& S (Naval P and FC. FED-STD-791: Federal Standard Testing Method Of Lubricants, Liquid Fuels, And Related Products: Method 6508 Load Carrying Capacity Of Lubricating Oils (Ryder Gear Machine). Military and Government Specs &

Standards (Naval Publications and Form Center) (NPFC); 2007. p. 460.

76. SAE International. SAE ARP6255: Aviation Lubricant Tribology Evaluator (ALTE) Method to Determine the Lubricating Capability of Gas Turbine Lubricants. SAE International; 2013. p. 9.

77. SAE International. SAE ARP6156: WAM High Speed Load Capacity Test Method. SAE International; 2017. p. 18.

78. Brujan E. Cavitation in Non-Newtonian Fluids: With Biomedical and Bioengineering Applications. 1st ed. Springer Science & Business Media; 2010. 269 p.

79. Stenberg C. Cross-linkers, rheology modifiers and lubricants: impact on water retention and rheology of coating colours at various shear rates. [Karlstads]: Karlstads Univiersity; 2016.

80. Muraki M. Molecular structure of synthetic hydrocarbon oils and their rheological properties governing traction characteristics. Tribol Int. 1987;20(6):347–54.

81. Moore AJ. The behaviour of lubricants in elastohydrodynamic contacts. Proc Inst Mech Eng Part J J Eng Tribol. 1997;211(Part J):91–106.

82. Malkin AY, Isayev A. 3.1 Newtonian and Non-Newtonian Liquids. In: Rheology - Concept, Methods, and Applications. 3rd ed. Knovel; 2019.

83. Lotfizadehdehkordi B. Rheology and Tribology of Lubricants With Polymeric Viscosity Modifiers. 2015;

84. ASTM International. ASTM D4683: Standard Test Method for Measuring Viscosity of New and Used Engine Oils at High Shear Rate and High Temperature by Tapered

Bearing Simulator Viscometer at 150 °C. ASTM Int. 2019;12.

85. Kew Engineering Ltd. Automotive Fluids - Lubricating Oils & Greases, Fuels, Coolants & Brake Fluids [Internet]. Kew Engineering Ltd. 2009 [cited 2019 Jun 20]. Available from: https://www.kewengineering.co.uk/Auto_oils/oil_viscosity_explained.htm

86. PCS Instruments. MTM [Internet]. pcs-instruments.com. 2015 [cited 2015 Oct 8]. Available from: https://pcs-instruments.com/product/mtm/

87. Hamrock BJ, Schmid SR, Jacobson BO. Elastohydrodynamic Lubrication of Elliptical Conjunctions. In: Fundamentals of Fluid Film Lubrication. 2nd ed. CRC Press; 2004. p. 35.

88. Hamrock BJ, Schmid SR, Jacobson BO. Film Thicknesses for Different Regimes of Fluid Film Lubrication. In: Fundamentals of Fluid FIlm Lubrication. 2nd ed. CRC Press; 2004. p. 23.

89. ASTM International. ASTM D341-09: Standard Practice for Viscosity-Temperature Charts for Liquid Petroleum. ASTM Int West Conshohocken, PA. 2009;

90. Walker DL, Student G, Sanborn ; D M, Winer AO. Molecular Degradation of Lubricants in Sliding Elastohydrodynamic Contacts. J Lubr Technol. 1975;97(3):390–5.

91. Mackenzie K, Jemmett AE. Polymer shear stability. Wear. 1971;17(5–6):389–368.

92. Minitab. Minitab 18: Stat Guide. Minitab; 2019.

93. Cann PM, Spikes HA, Hutchinson J. The Development of a Spacer Layer Imaging Method (SLIM) for Mapping Elastohydrodynamic Contacts. Tribol Trans.

1996;39(4):915–21.

94.   Spikes HA, Cann PM. The development and application of the spacer layer imaging method for measuring lubricant film thickness H A Spikes and. Proc Inst Mech Eng. 2001;2015(Part J):261–78.

95.   Hollis B. Physics of Sound: Interference [Internet]. method-behind-the-music.com. [cited 2019 Aug 25]. p. 1. Available from: https://method-behind-the-music.com/mechanics/images/interfere-6135388d.png

96.   Spikes H. Stress-augmented thermal activation: Tribology feels the force. Friction. 2018;6(1):1–31.

97.   Shimizu Y, Spikes HA. The Influence of Slide–Roll Ratio on ZDDP Tribofilm Formation. Tribol Lett. 2016;64(2):1–11.

98.   Brow RK, Tallant DR, Myers ST, Phifer CC. The short-range structure of zinc polyphosphate glass. J Non Cryst Solids. 1995;191:45–55.

99.   Fujita H, Glovnea RP, Spikes HA. Study of zinc dialkydithiophosphate antiwear film formation and removal processes, part I: Experimental. Tribol Trans. 2005;48(4):558–66.

100.   Jelita Rydel J, Vegter RH, Rivera-Díaz-Del-Castillo PEJ. Tribochemistry of bearing steels: A new AFM method to study the material-tribofilm correlation. Tribol Int. 2016;

101.   Rydel JJ. Tribochemistry of bearing steels. University of Cambridge; 2016.

102.   Sayles RS, Macpherson PB. Influence of wear debris on rolling contact fatigue. Roll Contact Fatigue Test Bear Steels Symp, (Phoenix, US.a May 12-14, 1981), JJC Hoo

(Astm Publ. 1982;ASTM STP 7:255–74.

103. Nikas GK, Sayles RS, Ioannides E. Effects of debris particles in sliding/rolling elastohydrodynamic contacts. Proc Inst Mech Eng Part J J Eng Tribol. 1998;212(5):333–42.

104. Olver A V. Testing Transmission Lubricants: The Importance of Thermal Response. Proc Inst Mech Eng Part G J Aerosp Eng. 1991;

105. Sanchez-Rubio M, Chinas-Castillo F, Ruiz-Aquino F, Lara-Romero J. A new focus on the Walther equation for lubricant viscosity determination. Lubr Sci. 2006;18:95–107.

106. Rycerz P, Kadiric A. The Influence of Slide–Roll Ratio on the Extent of Micropitting Damage in Rolling–Sliding Contacts Pertinent to Gear Applications. Tribol Lett. 2019;67(2):1–20.

107. Morales-Espejel GE, Brizmer V. Micropitting modelling in rolling–sliding contacts: Application to rolling bearings. Tribol Trans. 2011;

108. Tung SC, McMillan ML. Automotive tribology overview of current advances and challenges for the future. Tribol Int. 2004;37(7):517–36.

109. American Petroleum Institute. Engine Oil Licensing and Certification System, Annex E - API base oil interchangeability guidelines for passenger car motor oils and diesel engine oils. Washington; 2017.

110. Zhang J, Tan A, Spikes H. Effect of Base Oil Structure on Elastohydrodynamic Friction. Tribol Lett. 2017;65(13):1–24.

111. Hentschel KH. The influence of molecular structure on the frictional behaviour of

lubricating fluids. J Synth Lubr. 1985;2(3):143–74.

112. Hentschel KH. The influence of molecular structure on the frictional behaviour of lubricating fluids 2: low coefficients of traction. J Synth Lubr. 1985;2(3):238–60.

113. Hirst W, Moore AJ. Elastohydrodynamic lubrication at high pressures. II. Non-Newtonian behaviour. Proc R Soc A. 1979;365(1723):537–65.

114. Gentle CR, Cameron A. An investigation of traction in elastohydrodynamic point contacts using optical interferometry. ASLE Trans. 1975;18(3):222–8.

115. Biresaw G, Bantchev GB. Elastohydrodynamic (EHD) Traction Properties of Seed Oils. Tribol Lubr Technol. 2013;12.

116. LaFountain AR, Johnston GJ, Spikes HA. The elastohydrodynamic traction of synthetic base oil blends. Tribol Trans. 2001;44(4):648–56.

117. Gunsel S, Korcek S, Smeeth M, Spikes HA. The elastohydrodynamic friction and film forming properties of lubricant base oils. Tribol Trans. 1999;42(3):559–69.

118. Chang H-S, Spikes HA, Bunemann TF. The shear stress properties of ester lubricants in elastohydrodynamic contacts. J Synth Lubr. 1992;9(2):91–114.

119. Beeck O, Givens JW, Smith AE. On the Mechanism of Boundary Lubrication. I. The Action of Long-Chain Polar Compounds. Source Proc R Soc London Ser A, Math Phys Sci. 1940;177(968):90–102.

120. Frewing JJ. The Influence of Temperature on Boundary Lubrication. Proc R Soc London. 1942;181(984):23–42.

121. Frewing JJ. The Heat of Adsorption of Long Chain Compounds and their Effect on

Boundary Lubrication. Proc R Soc London. 1944;182(990):270–85.

122. Beltzer M, Jahanmir S. Role of Dispersion Interactions Between Hydrocarbon Chains in Boundary Lubrication. ASLE Trans. 1986;30(1):47–54.

123. Beltzer M, Jahanmir S. Effect of Additive Molcular Structure on Friction. Lubr Sci. 1988;1(1):3–26.

124. Jahanmir S, Beltzer M. Effect of Additive Molecular Structure on Friction Coefficient and Adsorption. J Tribol. 1986;108:550–74.

125. Davidson JE, Hinchley SL, Harris SG, Parkin A, Parsons S, Tasker PA. Molecular Dynamics Simulation to Aid the Rational Design of Organic Friction Modifiers. J Mol Graph Model. 2006;25(4):495–506.

126. Hardy WB, Doubleday I. Boundary Lubrication - The Paraffin Series. In: Proceedings of the Royal Society London. London; 1922. p. 49–68.

127. Okabe H, Masuko M, Sakurai K. Dynamic Behaviour of Surface Adsorbed Molecules Under Boundary Lubrication. ASLE Trans. 1980;24(4):476–473.

128. Askwith TC, Cameron A, Crouch RF. Chain Length of Additives in Relation to Lubricants in Thin Film and Boundary Lubrication. In: Proceedings of the Royal Society of London Series A, Mathematical and Physical. London: Royal Society; 1966. p. 500–19.

129. Konishi M, Washizu H. Understanding the effect of the base oil on the physical adsorption process of organic additives using molecular dynamcis. Tribol Int. 2019;(August 2018):1–7.

130. Kus M, Kalin M. Influence of additives and their molecular structure on the static and dynamic wetting of oil on steel at room temperature. Appl Surf Sci. 2019;490(June):420–9.

131. Housel T. Synthetic Esters: Engineered to Perform [Internet]. Machinery Lubrication, Noria Corporation. 2019 [cited 2019 May 5]. p. 1. Available from: https://www.machinerylubrication.com/Read/29703/synthetic-esters-perform

132. Tsubouchi T, Hata H, Yoshida Y. Optimisation of molecular structure for traction fluids. Lubr Sci. 2004;16:393–403.

133. Washizu H, Ohmori T. Molecular dynamics simulations of elastohydrodynamic lubrication oil film. Lubr Sci. 2010 Sep;22(8):323–40.

134. Hammann WC, Schisla RM, Groenweghe L. C. D., Gash VW. Synthetic Fluids for High-capacity Traction Drives. ASLE Trans. 1970;13(2):105–16.

135. Cecil R, Pike WC, Raje NR. Development of methods for evaluating traction fluids. Wear. 1973;26(3):335–53.

136. Yoshizaki M, Naruse C, Nemoto R, Haizuka S. Study on frictional loss of spur gears (Concerning the influence of tooth form, load, tooth surface roughness, and lubricating oil). Tribol Trans. 1991;34(1):138–46.

137. Höhn B-R, Michaelis K, Doleschel A. Frictional Behaviour of Synthetic Gear Lubricants. Tribol Ser. 2001;39:759–68.

138. Martins R, Seabra J, Brito A, Seyfert C, Luther R, Igartua A. Friction coefficient in FZG gears lubricated with industrial gear oils: Biodegradable ester vs. mineral oil. Tribol Int. 2006;39(6):512–21.

139. Michaelis K, Höhn B-R, Hinterstoißer M. Influence factors on gearbox power loss. Ind Lubr Tribol. 2011;63(1):46–55.

140. Fernandes CMCG, Amaro PMP, Martins RC, Seabra JHO. Torque loss in cylindrical roller thrust bearings lubricated with wind turbine gear oils at constant temperature. Tribol Int. 2013;67:72–80.

141. Lainé E, Olver A V., Beveridge TA. Effect of lubricants on micropitting and wear. Tribol Int. 2008;

142. Balcombe R, Fowell MT, Olver A V., Ioannides S, Dini D. A coupled approach for rolling contact fatigue cracks in the hydrodynamic lubrication regime: The importance of fluid/solid interactions. Wear. 2011;271(5–6):720–33.

143. Balcombe R. A study of rolling contact fatigue cracks in lubricated contacts. Imperial College London; 2012.

144. Webster MN, Norbart CJ. An experimental investigation of micropitting using a roller disc machine. Tribol Trans. 1995;38:883–93.

145. Nakajima A, Ichimaru K, Hirano F. Effects of combination of rolling direction and sliding direction on pitting of roller. J Synth Lubr Eng. 1983;4(4):93–8.

146. Winter H, Oster P. Influence of lubrication on pitting and micropitting resistance of gears. Gear Technol. 1990;7(2):16–23.

147. Hohn BR, Oste P, Emmert S. Micropitting in case-carburised gears - FZG micropitting test. VDI Ber. 1996;1230:331–44.

148. Bull SJ, Evans JT, Shaw BA, Hofmann DA. The effect of the white layer on micropitting

and surface contact fatigue failure of nitrided gears. Proc Inst Mech Eng Part J J Eng Tribol. 1999;213:305–13.

149. Olver AV. Micropitting of gear teeth: design solutions. In: Aerotech'95, Birmingham. Birmingham: London: Institute of Mechanical Engineerin; 1995.

150. Spikes HA, Olver A V, Macpherson PB. Wear in Rolling Contacts. Vol. 112, Wear. 1986.

151. Berthe D, Flamand L, Foucher D, Godet M. Micropitting in Hertzian contacts. ASME J Lubr Technol Trans. 1980;102:478–89.

152. Zhou RS, Cheng HS, Mura T. Micropitting in rolling and sliding contact under mixed lubrication. J Tribol. 1989;111:605–13.

153. Cardis AB, Webster MN. Gear oil micropitting evaluation. Gear Technol. 2000;17(5):30–5.

154. Graham RC. Pitting of hard steel rolling-sliding elastohydrodynamically lubricated line contacts. Imperical College London; 1979.

155. Brechot P, Cardis AB, Murphy WR, Theissen J. Micropitting resistant industrial gear oils with balanced performance. Ind Lubr Tribol. 2000;52(3):125–36.

156. Nakajima A. Effect of asperity interacting frequency on surface durability. In: International symposium on gearing and power transmissions. Tokyo; 1981. p. 26.

157. Ueda M, Spikes H, Kadiric A. In-situ observations of the effect of the ZDDP tribofilm growth on micropitting. Tribol Int. 2019;138(March):342–52.

158. Trivedi HK, Forster NH, Rosado L. Rolling contact fatigue evaluation of advanced

bearing steels with and without the oil anti-wear additive tricresyl phosphate. Tribol Lett. 2011;41(3):597–605.

159. Trivedi HK, Forster NH, Rosado L. Rolling contact fatigue evaluation of advanced bearing steels with and without the oil anti-wear additive tricresyl phosphate. Tribol Lett. 2011;

160. Soltanahmadi S, Morina A, Van Eijk MCP, Nedelcu I, Neville A. Investigation of the effect of a diamine-based friction modifier on micropitting and the properties of tribofilms in rolling-sliding contacts. J Phys D Appl Phys. 2016;

161. FUJITA H, SPIKES HA. Study of Zinc Dialkyldithiophosphate Antiwear Film Formation and Removal Processes, Part II: Kinetic Model. Tribol Trans. 2005;48(4):567–75.

162. Gosvami NN, Bares JA, Mangolini F, Konicek AR, Yablon DG, Carpick RW. Mechanisms of antiwear tribofilm growth revealed in situ by single-asperity sliding contacts. Science (80-). 2015;348(6230):102–6.

163. Zhang J, Spikes H. On the Mechanism of ZDDP Antiwear Film Formation. Tribol Lett. 2016 Aug 29;63(2):24.

164. Spikes H. The history and mechanisms of ZDDP. Tribol Lett. 2004;17(3):469–89.

165. Morina A, Neville A. Tribofilms: Aspects of formation, stability and removal. J Phys D Appl Phys. 2007;

166. Guan B, Pochopien BA, Wright DS. The chemistry, mechanism and function of tricresyl phosphate (TCP) as an anti-wear lubricant additive. Lubr Sci. 2015;123–34.

167. Dawczyk J, Ware E, Ardakani M, Russo J, Spikes H. Use of FIB to Study ZDDP Tribofilms. Tribol Lett. 2018;66(4):1–8.

168. Jones RB, Coy RC. The chemistry of the thermal degradation of zinc dialkyldithiophosphate additives. ASLE Trans. 1981;24:91–7.

169. Sung D, Gellman AJ. The surface chemistry of alkyl and arylphosphate vapor phase lubricants on Fe foil. Tribol Int. 2002;35(9):579–90.

170. Saba CS, Forster NH. Reactions of aromatic phosphate esters with metals and their oxides. Tribol Lett. 2002;

171. Goldblatt IL, Appeldoorn JK. The Antiwear Behavior of TCP in Different Atmospheres and Different Base Stocks. A S L E Trans. 1970 Jan 1;13(3):203–14.

172. Klaus EE, Bieber HE. Effect of Some Physical and Chemical Properties of Lubricants on Boundary Lubrication. ASLE Trans. 1964;7(1).

173. Lancaster JK. A review of the influence of environmental humidity and water on friction, lubrication and wear. Tribol Int. 1990;23(6):371–89.

174. Naidu SK, Klaus EE, Duda JL. Evaluation of liquid phase oxidation products of ester and mineral oil lubricants. Ind Eng Chem Prod Res Dev. 1984;23(4):613–9.

175. Bieber HE, Klaus, EE, Tewksbury EJ. A study of tricresyl phosphate as an additive for boundary lubrication. Tribology. 1968;1(4):251.

176. Makki JF, Graham EE. Vapor Phase Deposition on High Temperature Surfaces. Tribol Trans. 1990 Jan 1;33(4):595–603.

177. Bertrand P. Reactions of tricresyl phosphate with bearing materials. Tribol Lett.

1997;3:367–77.

178. Lainé E, Olver A V., Lekstrom MF, Shollock BA, Beveridge TA, Hua DY. The effect of a friction modifier additive on micropitting. Tribol Trans. 2009;

179. Benyajati C, Olver A V, Hamer J. An experimental study of micropitting, using a new miniature test-rig. Transient Process Tribol. 2004;601–11.

180. Olver AV, Dini D, Lainé E, Beveridge TA, Hua DY. Roughness and Lubricant Chemistry Effects in Micropitting. In: AGMA Fall Technical Meeting. Detroit, MI: American Gear Manufacturers Association; 2007.

181. Rycerz P. Propagation of surface initiated rolling contact fatigue cracks in bearing steel. 2014.

182. Soltanahmadi S. Tribochemical investigation of micropitting in rolling-element bearing applications: the influence of lubricant additives and water contamination. 2017.

183. Ueda M, Spikes H, Kadiric A. In-situ observations of the effect of the ZDDP tribofilm growth on micropitting. Tribol Int. 2019;138(May):342–52.

184. Ueda M, Spikes H. Evolution of ZDDP crystallinity and its effect on film durability. Nashville, TN, USA: 74th STLE Annual Meeting and Exhibition; 2019. p. 1.

185. Dawczyk J, Morgan N, Russo J, Spikes H. Film Thickness and Friction of ZDDP Tribofilms. Tribol Lett. 2019;67(2):1–15.

186. Lainé E, Olver A V., Lekstrom MF, Shollock BA, Beveridge TA, Hua DY. The Effect of a Friction Modifier Additive on Micropitting. Tribol Trans. 2009;52(4):526–33.

187. Lainé E, Olver A V., Beveridge TA. Effect of lubricants on micropitting and wear. Tribol

Int. 2008;41(11):1049–55.

188.	Rycerz P. Propagation of surface initiated rolling contact fatigue cracks in bearing steel. Imperial College London; 2014.

189.	Piska M, Metelkova J. ON THE COMPARISON OF CONTACT AND NON-CONTACT EVALUATIONS OF A MACHINED SURFACE. MM Sci J. 2015 May 14;2014(02):476–80.

190.	Cash W. The Pros and Cons of Polishing Wear [Internet]. Machinery Lubrication India. 2019 [cited 2019 Jun 10]. p. 1. Available from: http://machinerylubricationindia.com/magazine/130-2018/sep-oct/550-the-pros-and-cons-of-polishing-wear

191.	Warrens C, Jefferies AC, Mufti RA, Lamb GD, Guiducci AE, Smith AG. Effect of oil rheology and chemistry on journal-bearing friction and wear. In: Proceedings of the Institution of Mechanical Engineers, Part J: Journal of Engineering Tribology. 2008.

192.	Wu Y, Li W, Zhang M. Oxidative degradation of synthetic ester and its influence on tribological behaviour. Tribol Int. 2013;64:16–23.

193.	Acharya B, Sidheswaran MA, Yungk R, Krim J. Quartz crystal microbalance apparatus for study of viscous liquids at high temperatures. Rev Sci Instrum. 2017;88(2).

194.	Jaeger JC. Moving sources of heat and the temperature of sliding contacts. Proc R Soe New South Wales. 1942;56:203.

195.	ASTM International. Standard Test Method for Kinematic Viscosity of Transparent and Opaque Liquids (and Calculation of Dynamic Viscosity) 1. Annu B ASTM Stand. 2010;i(C):1–10.

Appendix

Appendix 1.   Published journal article

The effect of gas turbine lubricant base oil molecular structure on friction

Jake Airey [a,b,*], Matthew Spencer [a], Richard Greenwood [b], Mark Simmons [b]

[a] Rolls-Royce plc, PO Box 31, Derby, DE24 8BJ, UK
[b] School of Chemical Engineering, University of Birmingham, Edgbaston, B15 2TT, UK

ARTICLE INFO

ABSTRACT

The effect of molecular structure of lubricant polyol ester base oils on friction was studied. A Mini-Traction Machine was used to produce Stribeck curves under representative oil system conditions. The base oils were examined independent of viscosity to isolate the impact of the molecular structure. The effect of chain length, the number of ester groups and the effect of branching were investigated. Friction decreases as the chain length increases, as the number of ester groups increases and as the amount of branching decreases. The decrease in friction as the chain length and number of ester groups increases was attributed to improved packing efficiency and that longer chains can better separate surfaces. However, branching increases friction due to hindering packing efficiency.

1. Introduction

The formulation of a lubricant requires a careful balance of different chemistries to tailor the lubricant to a specific environment thus ensuring optimal performance. The oil system of an aerospace gas turbine engine presents highly challenging conditions for a lubricant, which requires a sufficiently low pour point that it is still able to flow on start up in a cold climate at $-40\,°C$, and also possess the chemical stability to resist degradation during take-off when the engine is at full thrust with bulk oil temperatures over $200\,°C$ [1]. However, the motivation of this paper was to explore lubricant behaviour in the power gearbox environment in Rolls-Royce's new engine, the UltraFan© [2]. As the gearbox is located near the front of the engine, oil temperatures are cooler than in the core of the engine. There are many other requirements in which additives are needed to boost capability in other areas and these additives include anti-wear additives, anti-foamants, corrosion inhibitors, metal deactivators and anti-oxidants [3]. However, the largest proportion of the formulation of a gas turbine lubricant is the base oil; approximately 95% of the total. Hence the base oil governs most of the physical characteristics of the lubricant and is the focus of this study.

In most mechanical systems, low friction is desired to improve machine efficiency and limit component wear. It has been highlighted in many industries that frictional losses are a major source of energy loss and understanding of tribology can be implemented to conserve energy and therefore efficiency [4]. This is especially relevant within a gas turbine oil system where it is vital that the oil lubricates the many different components such as bearings and gears to prolong the component life and ensure the safe operation of the engine. Advances in gas turbine technology has resulted in an increase in engine oil temperature as gas turbines run hotter to increase power and efficiency. This is due to the Brayton cycle which shows thermodynamically that the power and gas turbine efficiency is proportional pressure ratio, therefore by increasing the compression ratio, this increases engine temperatures as expected from the ideal gas law [1].

Consequently, aviation lubricant technology has evolved to cope with the rise in oil system temperatures. Specifically, the type of base oil has moved away from crude oil derived mineral oils that were unstable at high temperatures resulting in excessive volatility and degradation and onto entirely synthetic polyol esters [3,5]. Base oils are categorized by the American Petroleum institute (API) and are used in many lubricant specifications worldwide [6]. The base oil categories are:

- Group I – Mineral oil-based containing <90% saturates and/or >0.03% sulphur with a viscosity index ≥ 80 and < 120.
- Group II – Mineral oil-based containing $\geq 90\%$ saturates and/or $\leq 0.03\%$ sulphur with a viscosity index ≥ 80 and < 120.
- Group III – Mineral oil-based containing $\geq 90\%$ saturates and/or $\leq 0.03\%$ sulphur with a viscosity index ≥ 80 and ≥ 120.
- Group IV – Polyalphaolefin (PAO) base oils.
- Group V – All other synthetic base stocks not included in the other groups. Therefore, aviation polyol esters are part of this group.

* Corresponding author. School of Chemical Engineering, University of Birmingham, Edgbaston, B15 2TT, UK.
  E-mail address: Jake.Airey@Rolls-Royce.com (J. Airey).

Research on how the molecular structure of the latest generation of aviation base oils influences friction is limited and inconclusive due to difficulty in acquiring base oils with a specific molecular chemistry. This is because standard production produces base oils containing mixture of chain lengths which would require a costly separation process. However, a mixture of chain lengths is beneficial as it lowers the pour point giving enhanced lower temperature capabilities as a mixture of molecule sizes hinders the close packing necessary for freezing to occur at low temperatures. Previous research in this area has mostly been done with base oils containing a mixture of molecules therefore resulting in generally assumed conclusions, especially as it is not always possible to reproduce a base oil mixture exactly. Conversely, base oils with a mixture of chain lengths are more relevant to lubricants used in real applications and hence, trends drawn from simplified single molecule compounds have to be balanced with understanding how mixtures of different size base oil molecules synergistically affect friction [7].

Previous trends in the effect of base oil types on friction have been reviewed. It is well known that a higher kinematic viscosity results in higher elastohydrodynamic (EHD) friction due to the higher viscosity fluid having more resistance to shear [3,8]. However, this research focuses on the effect of molecular chemistry on friction when the effect of viscosity is removed by testing the oils at the same viscosity by varying the test temperature for each oil.

Most papers evaluating base oils relate the molecular characteristics to EHD friction as this is the regime where additives have little influence and the properties of the base oil dominate [7,9–17]. It is also useful to understand how various fluids behave in high speed conditions. Conversely, there has also been extensive work looking at how the molecular structure of fatty acid friction modifier (FAFM) additives affect friction, but this is mostly for the boundary regime as they are added as boundary additives to reduce boundary and mixed friction beyond the capabilities of low viscosity grade oils [4,18]. Consequently, by considering the effect of base oils properties in the EHD regime and FAFM in the boundary regime, these trends provide a useful insight into the expected behaviour of polyol base oils across a range of lubrication regimes.

FAFM are believed to readily adsorb on to a surface either via dipole interactions (Frewing [19,20]) or via hydrogen bonding interaction (Beltzer et al. [21–23] and also by Davidson et al. [24]). Friction trends for FAFM are well documented and it has been shown that friction decreases as chain length increases [25,26], in unsaturated chains, trans isomers give rise to lower friction than cis isomer due to straighter chains [27] and that polarity is also a dominant factor [19,20]. It has also been demonstrated that branching leads to higher friction due to creating an irregular profile of molecular repulsion and deep interaction zone that gives rise to high friction and has weak cohesive forces between adjacent chains in the monolayer resulting in increased vulnerability to shear [19–23,27]. The has also been shown the adsorption of FAFM additives is easier with branched base oils as the owing to their irregular profile which results in a decrease in traction coefficient in the boundary regime [28]. Hence despite this paper observing the effect of different base oil molecular structures on friction, their behaviour with additives should also be considered when creating a lubricant formulation.

Consequently, some of the trends seen with friction modifiers may be synonymous to polyol ester base oils, however due to the difference in structure, location of the polar functional group in the molecule and the difference in reactivity between a carboxylic acid and an ester group, care needs to be taken in how transferrable these trends are. Polyol esters associate with metal surfaces due to their polarity as well and increasing chain length and decreasing branching also decreases boundary friction. However, the shielding from attached carbon chains around the ester group will result in a decrease in their surface activity and could hinder monolayer formation leading to a decrease in the applicability of the branching trend seen with FAFMs [29].

Contrariwise, there has been a wide range of research investigating

base oils, but this mostly related to EHD performance [7,9–17]. Tsubouchi proposed five molecular properties that are likely to increase friction in traction fluids [30]. The first is high molecular stiffness caused by structures with restricted molecular mobility due to a high proportion of unsaturated bonds or complex ring structures as this hinders molecular slip as molecules cannot deform and rotate easily which can also give rise to molecular entanglement. Through various studies, it is believed that EHD friction is influenced mostly by the flexibility and structure of individual molecules as this will affect how molecular layers shear over one another under high pressure. Washizu and Ohmori confirmed this using molecular dynamics simulations [31]. This was seen by Zhang et al. where it was shown that flexible groups and linear molecules favoured low friction which allowed more free movement and prevented molecular entanglement [7]. Synthetic esters are an example of a flexible molecule as the ester bond allows free rotation of substituents. Hentschel et al. also discovered that bulkier and more irregular shaped cyclic structures gave rise to more steric hindrance hindering fluidity due to neighbouring molecule interlocking resulting in higher friction in comparison to regular spherical and ellipsoidal rings [10].

The second was large molecule size as it was believed this produces more steric hinderance. More specifically, this is referring to the degree of branching and linearity of molecule, how much free space a molecule occupies and how it interacts with neighbouring layers. Zhang et al. showed that bulky cyclo-hexyl rings and methyl branches gave higher EHD friction due to hindering movement against neighbouring layers [7]. While linear chains favour low friction as they interact less with neighbouring layers. An NPG based polyol ester with a branched substituent gave higher friction than a linear one containing a double bond. It was also found that the friction of polyglycols was strongly influenced by the amount of branching, with more propylene instead of ethylene units resulting in more branching and therefore higher friction [7]. This was confirmed by Hentschel who suggested the low friction of polyglycols was caused by the low degree of branching resulting in a thread-like structure which allowed the polyglycols chains to align which minimal interaction with other layers [11]. These results were confirmed by Hirst and Moore [12]. Further confirming that bulkier molecules give a higher EHD friction, Hammann et al. showed that molecules with one or two cyclohexyl rings gave high EHD friction [32]. Cecil et al. confirmed this result by finding that paraffinic mineral oils gave a lower EHD friction than naphthenic, the latter having more saturated rings substituents [33]. The paper also showed that glycol compounds produced a lower friction than the mineral oils tested. A similar study was also performed by Hirst and Moore where EHD friction was higher for molecules containing multiple side chains and saturated rings, but it was found to be lower for polyglycols [12]. It was also found that friction was found to be lower for benzene ring containing base oils where the substituents were located para to one another (substituents on opposite carbons on the 6-membered ring) as opposed to ortho and meta (substituents on the adjacent carbon or the second carbon around the 6-membered ring) due to the molecule being more linear [12]. Another study discovered that EHD friction increased with increased degree of branching. Friction data was analysed using a viscoelastic Eyring model and it was noted that the Eyring stress decreased with the degree of branching and with molecular volume [34]. LaFountain et al. measured the EHD friction properties of three base oils a found that the EHD friction increased from PAO (polyalphaolefins) to diesters to alkylated aromatic base oils [15]. This again confirmed that bulkier molecules can give rise to higher friction. Zhang et al. reported a general trend with base oil group with group 1 having the highest friction, then group 2 and then groups 3 and 4 which also follows the trend of decreasing proportion of cyclic and branched components [7].

However, an increase in the size of the molecule can also decrease friction if the larger molecule can pack more efficiently than the smaller molecule. With regards to base oils seen in aviation lubricants, Chang utilized an in-contact temperature rise mapping method to measure the

2

shear stress properties of a range of ester base oils and it was found that pentaerythritol esters had a lower shear stress than trimethylolpropane (TMP) based esters. The paper also noted that more branching lead to an increase in shear stress [17].

The third molecular characteristic was short alkyl chains resulting in a poor molecular packing efficiency. Zhang et al. showed an increase in chain length from adipic to azelaic to sebacic acid results in decreasing friction [7,30].

The fourth factor was a high melting point, but this may just be due to larger molecules and molecules with more polar atoms resulting in stronger intermolecular bonding as they inherently have a higher melting point [30].

The fifth molecular characteristic is low molecular polarity as high polarity gives rise to repulsion between neighbouring molecules preventing close packing and aiding the molecules sliding over one another [30]. It was found that solvent treated mineral base oils gave a higher friction than hydrotreated oils and that the lowest friction was produced by group III and group IV base oils therefore showing the introduction of polar water resulted in lower friction than those treated with organic non-polar solvents [16].

There have also be other studies that observed the loss of torque and efficiency of real bearings and gears and found that the synthetic base oils tested; PAOs, polyglycols and esters produced a reduction in torque in comparison to other mineral oils. This could be due to a few characteristics such as molecular packing efficiency, polarity or bulky substituents, but it is difficult to make further deductions without more detail on the molecular chemistry of the mineral oils, but is likely to be due to a higher proportion of cyclic and branched substituents [35–39]. When compared the synthetic base oils to each other, the literature sources found opposing results in that Yoshizaki et al. found PAO to give a lower friction than polyglycols whereas the opposite was found by Höhn et al. This may be due to differences in the PAOs and polyglycols tested hence the reason for the difficulty in understanding trend with base oils and the necessity for control of base oil production for research purposes [35,36].

The above literature shows that the effect of molecular structure on base oils in the EHD regime and FAPM in the boundary regime have similar trends but differ the mechanism behind the frictional effects. The literature suggests that low friction is favoured by longer chain lengths, linear molecules, less branching and therefore less bulky molecules. The aim of this paper is to deduce whether the molecular structure of the aviation derived base oils influences friction following the trends previously outlined in the literature but also to further confirm the trends seen in the literature with lubricants with known specific molecular structures. Specifically, the effect of varying the alkyl chain length on the end groups on the polyol esters, the number of ester groups in the polyol ester and the introduction of branching to these structures on friction is explored. This was done by producing Stribeck curves to compare the different base oils over a range of temperatures. To deduce whether the molecular structure still influences friction when independent of viscosity, the different base oils were compared by testing each oil at a specific temperature to attain the same kinematic viscosity.

For this testing a Mini-Traction machine (MTM) was chosen as it allowed the quick production of Stribeck curves at specific temperatures under specific point contact conditions representative of cooler gearbox environments near the front of the engine.

2. Experimental

2.1. Mini traction machine

An MTM (developed by PCS instruments) was used to evaluate the tribological performance of the oils. The MTM uses a ball on a disc configuration, each component with a specific rotational speed (and therefore entrainment speed (U)) to achieve the defined slide-roll ratio (SRR).

U and the SRR are defined by equations (1) and (2) where u_1 and u_2 are the surface velocities of surface 1 and 2 respectively.

$$U = \frac{|u_1 - u_2|}{2} \tag{1}$$

$$SRR = \frac{|u_1 - u_2|}{U} \tag{2}$$

The contact between the ball and the disc is submerged in a reservoir of lubricant (approximately 35 mL) and the ball rotates against the disc at an inclined axis to eliminate spin in the contact. The speed of both ball and disc are controlled independently and driven by separate motors, which allows different combinations of surface speeds and SRR to be set by the operator. The load and lubricant temperature can also be controlled and the traction coefficient (friction) is measured. A schematic of the MTM can be seen in Fig. 1.

Specifications of the test specimens are shown in Table 1, both of which showed minimal wear throughout the Stribeck tests.

2.2. Test conditions

The MTM was used to produce Stribeck curves at a range of temperatures. The range of bulk oil test temperatures were chosen to understand the effect of the temperature and viscosity on friction, cover a range of oil temperatures that could be seen during service in the front of the engine and also to test specific base oils at specific kinematic viscosities. Whilst gas turbine oil systems exceed these temperatures in the core of an engine, the focus was on understanding base oil behaviour in a cooler gearbox environment. The MTM also has the limitation of a maximum bulk oil temperature of 150 °C however, the temperatures chosen were adequate for demonstrating the effect of base oil molecular structure on friction. Testing at core engine temperatures would also introduce the complication of lubricant degradation which would affect tribological behaviour through an increase in viscosity and the formation of carbon deposits [40]. Each of these tests was completed three times to confirm repeatability and all Stribeck curves have been plotted with error bars of one standard deviation for each data point. Representative gas turbine oil system contact conditions were used for Stribeck analysis are shown in Table 2 where the contact pressure was calculated using the formulae for a Hertzian point contact [41].

It should be noted in these tests, the type of EHD lubrication seen at high entrainment speeds was hard viscous EHD lubrication as the steel specimens used have a high elastic modulus, the viscosity changes in the contact due to the high contact pressures and the contact is elastically deforms due to the high contact pressure in the non-conformal contact [42,43].

Two different methods of normalising for viscosity were applied to the tests to isolate the effect of the molecular structure on friction. One method involved plotting the measured traction coefficient against the Hersey number (3) where μ is the dynamic viscosity, N the entrainment speed in revolutions per second and p_0 is the maximum contact pressure.
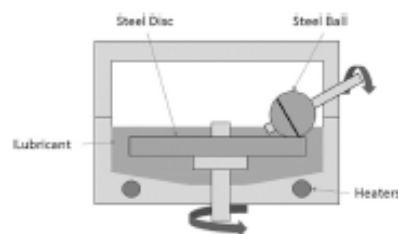
Fig. 1. Configuration of the MTM showing the rotational directions of the ball and disc.

Table 1
Specification of test specimens.

Property	MTM Standard Disc	MTM Drilled Ball
Dimensions (diameter)	46 mm	¾" (19.05 mm)
Material	AISI 52100	AISI 52100
Surface Finish, R_a	<0.01 μm	<0.02 μm
Hardness, H_v	720–780	800–920

Table 2
Conditions used for Stribeck analysis.

Parameter	Value
Applied Load	40 N
Contact Pressure	1.01 GPa
Slide-to-Roll Ratio (SRR)	50%
Entrainment Speed	0–3 m/s

$$Hersey\ Number = \frac{\mu \times N}{P0} \tag{3}$$

The dynamic viscosities were calculated using densities supplied by the manufacturer and the calculated kinematic viscosities.

The second method involved testing each lubricant by carrying out experiments at different temperatures for each oil so that they all had the same kinematic viscosity. This was done using data from measurements of kinematic viscosity and ASTM D341 [44]. The viscosities selected were chosen as the calculated test temperature required for each oil was within the temperature range capability of the MTM.

Another consideration worth noting is shear stability of the base oil molecules. Walker et al. showed by sampling the base oil through a small hole, that polymeric base oils can break down into smaller molecules in EHD contacts [45]. They suggested that polymeric scission will begin to occur in linear hydrocarbon polymers if shear stress x molecular weight^2 $>1 \times 10^{14}$ dyne/cm^2, but this is generally only a concern for much larger base oil molecules and hence, the shear stability of the base oils tested in this study was assumed not to be an issue [46].

Also, due to the low roughness of the superfinished specimens (R_a < 0.01 μm for the disc and R_a < 0.02 μm for the ball), very minimal wear was produced for all tests and therefore the wear was not investigated.

2.2.1. Test lubrication regimes

Using the supplied pressure-viscosity coefficients, the fluid film thickness and therefore lambda ratio, the lubrication regimes can be estimated for each oil over the range of speeds seen in the Stribeck test. The film thicknesses were calculated using formulae derived by Dowson and Higginson 1977 [41,47]. These calculations utilized the data provided by the manufacturer to calculate the dynamic viscosity at each test temperature to give a more accurate estimate of the film thickness and therefore the lambda ratio.

Hence from Fig. 2, it can be seen from the plot of lambda ratio against the Hersey number that neopentyl glycol with chains of n-C7 (NPG C7, the lowest viscosity base oil in this study) does not reach the EHD regime with the conditions used. Therefore, whilst previous studies have only compared the effect of base oil structure on EHD friction, the results presented in this paper observe the effect of the molecular structure across a range of lubrication regimes as not all the oils will reach the EHD regime at higher entrainment speeds due to specific lubricant properties and limitations of the test rig. However, the results across the range of conditions seen in this study give an insight into the behaviour of different base oils on friction.

2.3. Test fluids

A variety of group V base oils were acquired of known chemical composition and molecular structure with no additives and these variations were selected to test the behaviour of a variety of realistic types of polyols. The base oils tested are all polyol ester type lubricants as this are currently the most commonly used base oil in aviation lubricants primarily due to their superior high temperature capability [40]. The esters were made through standard esterification reaction of the polyol with excess acids. The synthesis is monitored by testing the hydroxyl value (a measure of the content of free hydroxyl groups in a chemical substance) and the purity of the products are confirmed by the hydroxyl value, measurement of the total acid number (a measure of acidity) and by gas chromatography.
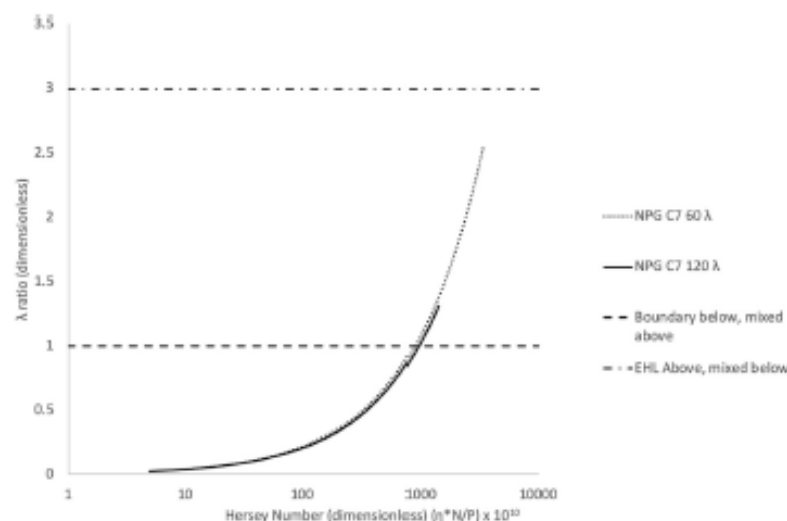
Fig. 2. Lambda ratio against the Hersey number for the NPG C7 base oil showing that it does not reach the EHD regime at test temperature for the test conditions used.

2.3.1. Varied chain length and ester base oils

The molecular structure of the base oils used to look at the effect of chain length and the number of ester groups are shown in Fig. 3.

The base oils represent esters typically seen in aerospace lubricants and have representative chain lengths. The two parameters considered are the chain length of the substituent end groups on the esters and the amount of ester groups on the molecule. The chain lengths of the pentaerythritol base oils vary by increments of two carbons. These variations were selected as they were readily available from the supplier.

Tests have shown that the base oils tested are Newtonian up to shear rates of 200 s^{-1} due to the measurement limitation of the cone and plate rheometer centrifugally forcing out low viscosity fluids at high shear rates. But it is assumed that these base oils are all Newtonian in the EHD regime as well as shown by Moore 1997 [9].

2.3.2. Varied degree of branching base oils

The molecular structure of these base oils used to look at branching can be seen in Fig. 4. This was done by synthesizing polyol pentaerythritol esters with different ratios of straight and branched acids to vary the amount of branching the final lubricant formulation. The acids used were octanoic acid (NC8) for the linear chains and 2-ethy hexanoic acid (EH) for the branched chains. Hence due to the difficulty in forcing esterification to react at a specific alcohol group on a pentaerythritol, base oils g., h. and i. are most likely not only the structures depicted but are mixture of order combinations depending on the available alcohols for the esterification reaction. However, due to controlling the ratios of the alcohol reactants, the total ratio of linear to branched chains will still be the percentages stated.

2.3.3. Physical properties of the base oils

A table showing the physical properties of the base oils can be seen in Table 3.

3. Results and discussion

3.1. The effect of chain length and the number of ester groups on friction

This section will interpret the tribological properties of the base oils in Fig. 3 in which the chain length and the number of ester groups in the polyol ester have been varied.

3.1.1. Effect of temperature

The normalised Stribeck curves solely showing the MONOPE C7 base oil are shown in Fig. 5. The other base oils displayed similar trends.

Generally, it is known that a higher viscosity results a lower traction coefficient in the boundary regime due to the fluid forming a thicker oil film to protect asperities, but a lower viscosity will result in a lower traction coefficient at high speeds as a thinner fluid is sheared more easily [49]. As the temperature is varied, this results in a viscosity change, which alters the performance in the boundary and EHD regimes and the general trend is the friction decreases from low to high temperature due to the difference in viscosity and temperature effects.

Normalisation of the Stribeck curves would lead to a single master curve if viscosity was the sole parameter governing frictional characteristics, but the fact that there is still separation of results in Fig. 5 shows that another variable as well as viscosity is contributing to the underlying tribological behaviour. Also, it should be noted that this method of normalising for viscosity can only shift curves laterally on the Stribeck graph and can therefore not account for the lower traction coefficients produced for the higher temperature tests because of the decreased viscosity.

Therefore, Fig. 5 shows a decrease in traction coefficient as the temperature is increased which is due to the increased temperature resulting in a decrease in viscosity and hence the fluids are sheared more easily. Prior to normalisation of the Stribeck curves, higher viscosities would favour a lower traction coefficient in the boundary regime however, normalisation results in shifting of the curves as the tests have been normalised for viscosity. The separation in the curves is also larger for the test fluids that have a larger difference in viscosity across the range of test temperatures.

3.1.2. Comparison at constant temperature

Fig. 6 shows that when the base oils are compared at a constant temperature, separation of the Stribeck curves only emerges at the higher temperatures (120 °C). At the lower test temperature of 60 °C there is no significant trend. By considering the viscosities of each of these oils at each test temperature, there is a larger difference in kinematic viscosity at the lower test temperature. Hence it can be seen that at 120 °C, this has the smallest range of viscosities of 2.83 cSt whereas at 60 °C the range is 12.04 cSt. Consequently, at low temperatures, viscosity dominates the behaviour leading to similar curves due to normalising for viscosity by plotting the traction coefficient against the Hersey number. When the difference in viscosity in minimised, a difference in friction emerges due to other underlying variables in the system, namely the difference in molecular structure.

The order of the friction decreased from NPG C7 to TMP C7 to MONOPE C5 to MONOPE C7 and then to MONOPE C9. Hence, this indicates an effect of molecular structure on friction. The results show that friction decreases with an increase in both the number of ester groups and the chain length. It is likely this is due to the larger molecules being able to pack more efficiently and separate the surfaces due to their larger size. Larger chains can better separate surfaces since they take up more space thus providing improved support, but this can often come with increased friction if larger bulkier molecules have more difficulty moving which can mask this effect.

However, at high test temperatures at high entrainment speeds, the pentaerythritol base oils converge, and the neopentyl and trimethylol base oils remain separated from them. This suggests that the pentaerythritol base oils behave similarly at higher entrainment speeds regardless of their difference in chain length as they reach the EHD regime and that the neopentyl and trimethylol base oils require higher speeds to reach the same traction coefficient. Hence this shows that the effect of the number of ester groups potentially has a larger impact on the molecular packing than differences in substituent chain length.

Fig. 3. Molecular structure of the base oils tested. a. polyol ester made from pentaerythritol with chains of n-C9 (MONOPE C9), b. polyol ester made from pentaerythritol with chains of n-C7 (MONOPE C7), c. polyol ester made from pentaerythritol with chains of n-C5 (MONOPE C5), d. polyol made from trimethylol propyl with chains of n-C7 (TMP C7) and e. polyol ester made neopentyl glycol with chains of n-C7 (NPG C7).

311
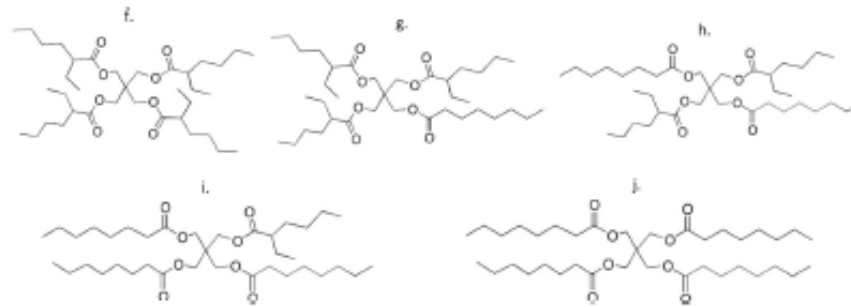
Fig. 4. Molecular structure of the base oils used to observe the tribological effect of molecular branching. f. polyol ester made from pentaerythritol with chains of all (MONOPE EH), g. polyol ester made from pentaerythritol with 25% chains being NC8 and 75% of chains being EH (MONOPE NC8:EH 25:75), h. polyol ester made from pentaerythritol with a 50:50 ratio of EH and NC8 chains (MONOPE NC8:EH 50:50), i. polyol ester made from pentaerythritol with 75% chains being NC8 and 25% of chains being EH (MONOPE NC8:EH 75:25) and j. polyol ester made from pentaerythritol with chains of all NC8 chains (MONOPE NC8).

Table 3
Table showing the kinematic viscosities at 40 °C and 100 °C for the base oils and their viscosity index calculated using ASTM D2270 [48].

Base oil	Kinematic Viscosity at 40 °C, cSt	Kinematic Viscosity at 100° C, cSt	Viscosity Index
NPG C7	5.6	1.9	124
TMP C7	13.9	3.4	124
MONOPE C5	15.3	3.6	119
MONOPE C7	21.1	4.6	135
MONOPE C9	30.5	6.0	146
MONOPE EH 100	44.1	6.2	84
MONOPE NC8: EH 25:75	35.5	5.7	101
MONOPE NC8: EH 50:50	31.0	5.5	115
MONOPE NC8: EH 75:25	27.5	5.3	130
MONOPE NC8 100	25.5	5.2	142

3.1.3. Comparison at constant kinematic viscosity

When tested at a constant viscosity, there is a clear separation of Stribeck curves across each of the different test viscosities, but there appears to be a slightly larger separation on the lowest viscosity graph; Fig. 7. The order from high to low friction is marginally different to the same temperature Stribeck curves as the trend now goes NPG C7, MONOPE C5, TMP C7, MONOPE C7 and then MONOPE C9. Therefore, the MONOPE C5 and TMP C7 have swapped. However, this is since they have very similar molecular weights and therefore viscosity and have performed very similarly throughout all the tests.

Despite this marginal change in frictional order, the same trend can clearly be observed, showing that as both chain length, and the number of ester groups increases, the friction decreases. This reinforces the theory that viscosity is not the only factor influencing friction and that the molecular structure has a substantial effect which is revealed after viscosity has been eliminated as a variable. It is likely this is due to the larger molecules being able to pack more efficiently, which results in less frictional resistance and be able to separate the rubbing surfaces more effectively because of their increasing size.

Another observation is that the pentaerythritol base oils do not completely converge at high entrainment speeds as they did when all

Fig. 5. Normalised Stribeck curves of the MONOPE C7 base oil at a range of temperatures.

6
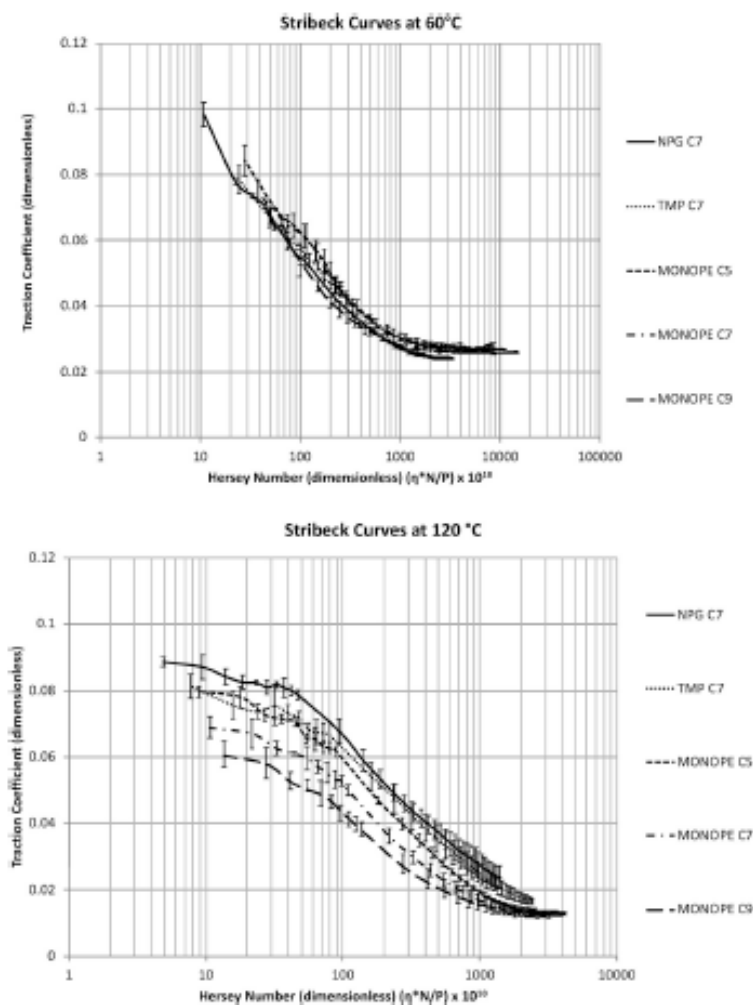
Fig. 6. Normalised Stribeck curves comparing the different base oils at 60°C and 120°C.

compared at the same test temperature. This could be due to increasing chain length effect being more apparent at the same viscosity and potentially requires higher entrainment speeds to converge. Again, the effect of the number of ester groups potentially has a larger impact on the molecular packing than differences in substituent chain length as there is a larger separation between the NPG C7, TMP C7 and MONOPE C7 than each of the MONOPE curves.

3.2. The effect of molecular branching on friction

This section will interpret the tribological properties of the base oils in Fig. 4 in which the amount of molecular branching has been varied.

3.2.1. Effect of temperature

Fig. 8 shows Stribeck curves for the MONOPE NC8:EH 25:75 base oil at a range of test temperatures (the other base oils display similar trends). Again typically, friction decreases as the temperature increases,

which is due to the viscosity decreasing with increasing temperature and results in less friction due to lower viscosity fluids having a lower resistance to shear. There is also more separation in the EHD regime due to the physical properties of the lubricant like viscosity having more influence in the EHD regime than in the boundary regime. However just as in Fig. 5, normalisation of the Stribeck curves would lead to a single master curve if viscosity was the only factor governing frictional characteristics, but the fact that there is still separation of results shows that another variable as well as viscosity is contributing to the underlying tribological behaviour. But this method of normalising for viscosity can only shift curves laterally on the Stribeck graph and can therefore not account for the lower traction coefficients produced for the higher temperature tests as a result of the decreased viscosity. Hence these Stribeck curves still show a trend of decreasing friction with increasing temperature and therefore viscosity.

7
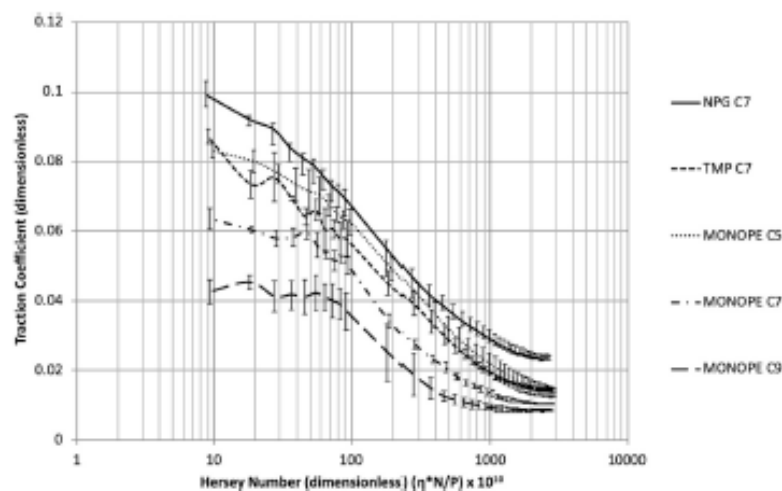
Fig. 7. Normalised Stribeck curves comparing the different base oils at a kinematic viscosity of 2.9 cSt by varying the test temperature for each base oil.
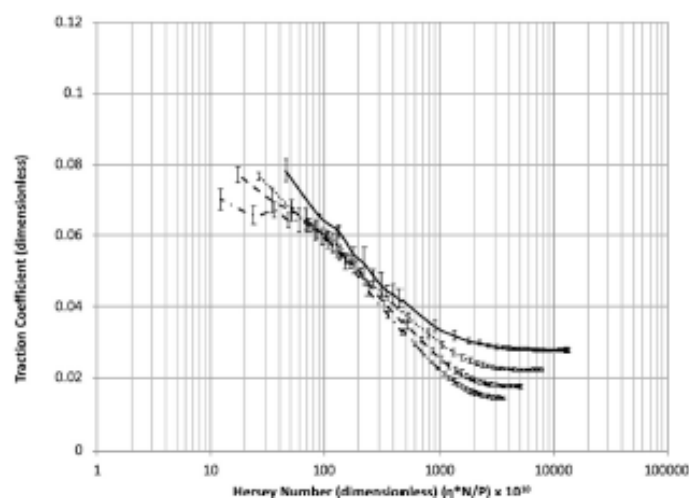
Fig. 8. Stribeck curves for NC8:EH 27:25 at a range of test temperatures.

3.2.2. Comparison at constant temperature

When comparing the base oils at the same temperature, there is a distinct and repeatable separation between the Stribeck curves following a trend of low to high friction as the proportion of branching (from EH chains) increases (as shown in Fig. 9 for both 60 °C and 120 °C). At constant test temperatures, each of the test fluids has a different kinematic viscosity however plotting against the Hersey number normalises for viscosity and hence the trends seen must be due to differences in molecular chemistry. In this case, as the amount of molecular branching increases, the friction increases across all lubrication regimes. Unlike in Fig. 6, this trend can be seen at the lower and higher test temperatures and it is clearer to see at lower test temperatures. This could potentially suggest that branching may have a more significant effect on friction than the molecular variables studied earlier.

3.2.3. Comparison at constant kinematic viscosity

There is clear separation of Stribeck curves when tested at a constant kinematic viscosity across each of the different test viscosities, but unlike in Fig. 7, this separation remains present at each of the test kinematic viscosities as shown in Fig. 10. Again, friction increases with the amount of branching present in the base oil. This reinforces the theory that viscosity is not the only factor influencing friction and that the molecular structure has a substantial effect too which is remains present after viscosity has been eliminated as a variable. Branching leads to more interference with molecular packing, which results in more frictional resistance. It is also clear that this effect is present across all lubrication regimes.

Hence this shows that the inclusion of branching may inverse the trends seen with the previous oils where increasing chain length and increasing the number of ester groups decreased friction potentially due

8

314
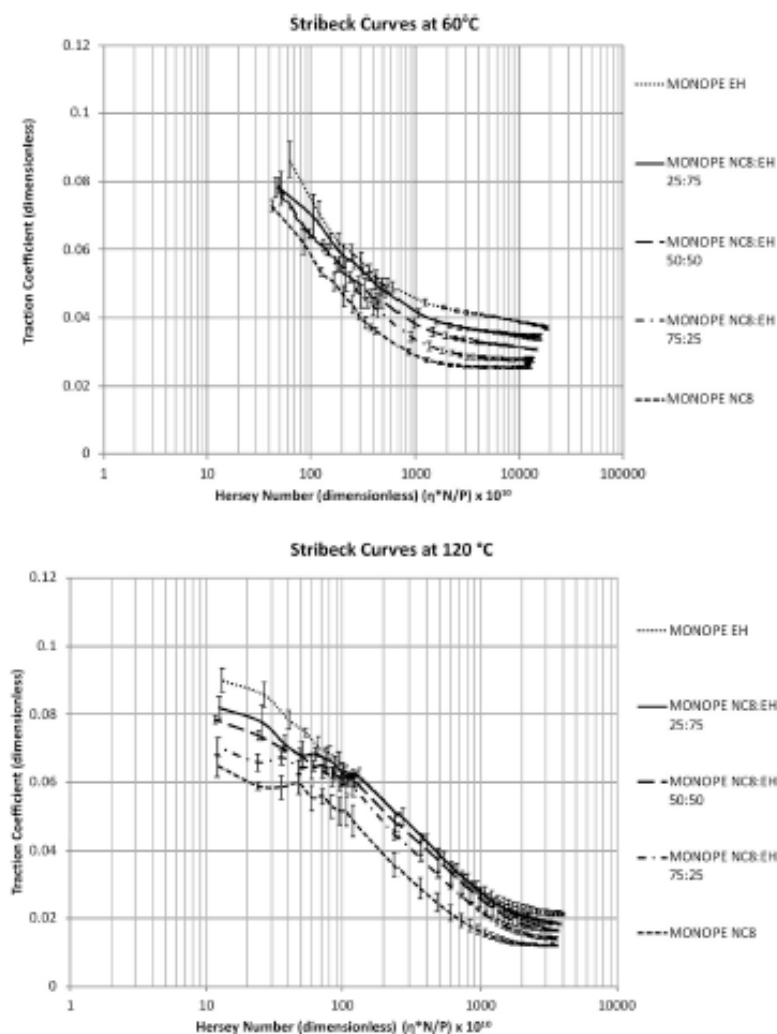
Fig. 9. Normalised Stribeck curves comparing the linear vs. branched base oils at 60 °C and 120 °C.

to larger molecules being able to pack more efficiently and better support load. It may be that the inclusion of branched side chain prevents the larger molecule packing as efficiently giving rise to more steric hinderance as the molecules get larger with more branching.

4. Conclusions

Stribeck curves have been produced for a range of base oils with specific molecular structures to understand the effect of molecular structure on friction. Whilst changes to molecular structure influence the viscosity of the fluid, the base oils were also tested at the same viscosity by varying the temperature of each test. The results showed the molecular structure has a substantial impact on the measured friction across all lubrication regimes. The viscosity behaviour is as expected with an increase in viscosity leading to an increase in friction as a higher

viscosity fluid incurs more resistance to shear. After viscosity was eliminated as a variable through plotting Stribeck curves against the Hersey number and by conducting wears tests at the same viscosity, the first two molecular variables explored were; the effect of chain length and the influence of the number of ester groups on friction. It was shown that the friction decreases across all lubrication regimes as the chain length increases and by increasing the number of ester groups which is most likely due to larger molecules being able to pack more efficiently and separate the contacting surfaces. Larger chains can separate surfaces better since they take up more space thus providing improved support, but this can often come with increased friction if larger bulkier molecules have more difficulty moving which can mask this effect. It was also seen that the number of ester groups potentially has more of an effect on friction that the substituent chain length as the pentaerythritol base oils converge when compared at the same temperature, but the TMP and

9

Fig. 10. Normalised Stribeck curves comparing the different base oils at kinematic viscosities of 3 cSt and 7 cSt by varying the test temperature for each base oil.

NPG oils remain separated. This suggested that the pentaerythritol base oils behave very similarly at high entrainment speeds regardless of their difference in chain length. In addition, the effect of molecular branching was explored which showed that the friction increased as the proportion of branching on the ester substituents increased. Consequently, the inclusion of branched side chains prevents the larger molecules packing as efficiently, giving rise to more steric hinderance as the molecules get larger with more branching giving rise to increased friction.

Overall, these results agree with the literature in that low friction is favoured by longer chain lengths, increasing the number of ester groups (within a polyol ester) and maintaining a linear molecule. Branching leads to producing a bulkier molecule which gives rise to high friction whereas, whilst increasing the chain length and the number of ester groups increases the size of the molecule, the molecule remains linear and flexible giving rise to improved load carrying capacity and packing efficiency which reduces friction.

Future work could look into confirming the packing efficiency argument potential through the use of absorption theory using a quartz crystal microbalance (QCM) to confirm whether longer and straighter molecular structures pack more efficiently than smaller and bulkier branched structures whilst keeping the viscosity constant.

10

316

Declaration of competing interest

Acknowledgments

References

[1] Rolls-Royce. The jet engine. fifth ed. Chichester, West Sussex: John Wiley & Sons Inc.; 2015.

[2] Rolls-Royce Plc. Rolls-royce UltraFan®. https://WwwRolls-RoyceCom.2016. https://www.rolls-royce.com/products-and-services/civil-aerospace/future-products.aspx#section-overview. accessed April 21, 2017.

[3] Mortier RM, Fox MF, Orszulik S. Chemistry and technology of lubricants. Dordrecht: Springer Netherlands; 2011.

[4] Tung SC, McMillan ML. Automotive tribology overview of current advances and challenges for the future. Tribol Int 2004;37:517–36. https://doi.org/10.1016/j.triboint.2004.01.013.

[5] Shell Aviation Limited. The AeroShell Book. Aviation; 2003. p. 196.

[6] American Petroleum Institute. Engine Oil Licensing and Certification System, Annex E - API base oil interchangeability guidelines for passenger car motor oils and diesel engine oils. 2017. Washington.

[7] Zhang J, Tan A, Spikes H. Effect of base oil structure on elastohydrodynamic friction. Tribol Lett 2017;65:1–24. https://doi.org/10.1007/s11249-016-0791-7.

[8] Williams JA. Engineering tribology. Cambridge: Cambridge University Press; 2005.

[9] Moore AJ. The behaviour of lubricants in elastohydrodynamic contacts. Proc Inst Mech Eng J J Eng Tribol 1997;211:91–106. https://doi.org/10.1243/1350650971542345.

[10] Hentschel KH. The influence of molecular structure on the frictional behaviour of lubricating fluids. J Synth Lubr 1985;2:143–74. https://doi.org/10.1002/jsl.3000020205.

[11] Hentschel KH. The influence of molecular structure on the frictional behaviour of lubricating fluids 2: low coefficients of traction. J Synth Lubr 1985;2:238–60. https://doi.org/10.1002/jsl.3000020304.

[12] Hirst W, Moore AJ. Elastohydrodynamic lubrication at high pressures. II. Non-Newtonian behaviour. Proc R Soc A 1979;365:537–65. https://doi.org/10.1098/rspa.1979.0033.

[13] Gentle CR, Cameron A. An investigation of traction in elastohydrodynamic point contacts using optical interferometry. ASLE Trans 1975;18:222–8. https://doi.org/10.1080/05698197508982764.

[14] Biresaw G, Bantchev GB. Elastohydrodynamic (EHD) traction properties of seed oils. Tribol Lubr Technol 2013;12. https://doi.org/10.1080/10402001003599769.

[15] LaFountain AR, Johnston GJ, Spikes HA. The elastohydrodynamic traction of synthetic base oil blends. Tribol Trans 2001;44:648–56. https://doi.org/10.1080/10402000108982506.

[16] Guneel S, Korcek S, Smeeth M, Spikes HA. The elastohydrodynamic friction and film forming properties of lubricant base oils. Tribol Trans 1999;42:559–69. https://doi.org/10.1080/10402009908982255.

[17] Chang H-S, Spikes HA, Bunemann TF. The shear stress properties of ester lubricants in elastohydrodynamic contacts. J Synth Lubr 1992;9:91–114. https://doi.org/10.1002/jsl.3000090202.

[18] Beeck O, Givens JW, Smith AE. On the mechanism of boundary lubrication. I. The action of long-chain polar compounds. Source Proc R Soc London Ser A, Math Phys Sci 1940;177:90–102. https://doi.org/10.1098/rspa.1940.0112.

[19] Frewing JJ. The influence of temperature on boundary lubrication. Proc R Soc Lond 1942;181:23–42. https://doi.org/10.1098/rspa.1942.0056.

[20] Frewing JJ. The heat of adsorption of long chain compounds and their effect on boundary lubrication. Proc R Soc Lond 1944;182:270–85. https://doi.org/10.1098/rspa.1944.0004.

[21] Beltzer M, Jahanmir S. Role of dispersion interactions between hydrocarbon chains in boundary lubrication. ASLE Trans 1986;30:47–54. https://doi.org/10.1080/05698198708981729.

[22] Beltzer M, Jahanmir S. Effect of additive molecular structure on friction. Lubr Sci 1988;1:3–26. https://doi.org/10.1002/ls.3010010103.

[23] Jahanmir S, Beltzer M. Effect of additive molecular structure on friction coefficient and adsorption. J Tribol 1986;108:550–74. https://doi.org/10.1115/1.3261129.

[24] Davidson JE, Hinchley SL, Harris SG, Parkin A, Parsons S, Tasker PA. Molecular dynamics simulation to aid the rational design of organic friction modifiers. J Mol Graph Model 2006;25:495–506. https://doi.org/10.1016/j.jmgm.2006.03.006.

[25] Hardy WB, Doubleday I. Boundary lubrication - the paraffin series. London: Proc. R. Soc. London; 1922. p. 49–68. https://doi.org/10.1201/9781420050448.ch4.

[26] Okabe H, Masuko M, Sakurai K. Dynamic behaviour of surface adsorbed molecules under boundary lubrication. ASLE Trans 1980;24. https://doi.org/10.1080/05698198108983044. 476–473.

[27] Askwith TC, Cameron A, Crouch RF. Chain length of additives in relation to lubricants in thin film and boundary lubrication. Proc. R. Soc. London. Ser. A, Math. Phys, vol. 291. London: Royal Society; 1966. p. 500–19.

[28] Konishi M, Washizu H. Understanding the effect of the base oil on the physical adsorption process of organic additives using molecular dynamics. Tribol Int 2019: 1–7. https://doi.org/10.1016/j.triboint.2019.01.027.

[29] Housel T. Synthetic esters: engineered to perform vol. 1. Mach Lubr Noria Corp; 2019. https://www.machinerylubrication.com/Read/29703/synthetic-esters-perform. accessed May 5, 2019.

[30] Tsubouchi T, Hata H, Yoshida Y. Optimization of molecular structure for traction fluids. Lubr Sci 2004;16:393–403.

[31] Washizu H, Ohmori T. Molecular dynamics simulations of elastohydrodynamic lubrication oil film. Lubr Sci 2010;22:323–40. https://doi.org/10.1002/ls.126.

[32] Hammann WC, Schisla RM, Groenweghe LCD, Gash VW. Synthetic fluids for high-capacity traction drives. ASLE Trans 1970;13:105–16. https://doi.org/10.1080/05698197008972287.

[33] Cecil R, Pike WC, Raje NR. Development of methods for evaluating traction fluids. Wear 1973;26:335–53. https://doi.org/10.1016/0043-1648(73)90186-5.

[34] Muraki M. Molecular structure of synthetic hydrocarbon oils and their rheological properties governing traction characteristics. Tribol Int 1987;20:347–54. https://doi.org/10.1016/0301-679X(87)90063-6.

[35] Yoshizaki M, Naruse C, Nemoto R, Haizuka S. Study on frictional loss of spur gears (Concerning the influence of tooth form, load, tooth surface roughness, and lubricating oil). Tribol Trans 1991;34:138–46. https://doi.org/10.1080/10402009108982021.

[36] Höhn B-R, Michaelis K, Doleschel A. Frictional behaviour of synthetic gear lubricants. Tribol Ser 2001;39:759–68. https://doi.org/10.1016/S0167-8922(01)80156-5.

[37] Martins R, Seabra J, Brito A, Seyfert C, Luther R, Igartua A. Friction coefficient in FZG gears lubricated with industrial gear oils: biodegradable ester vs. mineral oil. Tribol Int 2006;39:512–21. https://doi.org/10.1016/j.triboint.2005.03.021.

[38] Michaelis K, Höhn B-R, Hinterstoißer M. Influence factors on gearbox power loss. Ind Lubr Tribol 2011;63:46–55. https://doi.org/10.1108/00368791111101830.

[39] Fernandes CMCG, Amaro PMP, Martins RC, Seabra JHO. Torque loss in cylindrical roller thrust bearings lubricated with wind turbine gear oils at constant temperature. Tribol Int 2013;67:72–80. https://doi.org/10.1016/j.triboint.2013.06.016.

[40] Spencer M, Shepherd T, Greenwood R, Simmons M. An assessment of the influence of gas turbine lubricant thermal oxidation test method parameters towards the development of a new engine representative laboratory test method. SAE Int J Aerosp 2013;6. https://doi.org/10.4271/2013-01-9004. 2013-01-9004.

[41] Stachowiak G, Batchelor AW. Engineering tribology. third ed. Butterworth-Heinemann; 2011.

[42] Hamrock BJ, Schmid SR, Jacobson BO. Elastohydrodynamic lubrication of elliptical conjunctions. Fundam. Fluid film lubr. second ed. CRC Press; 2004. p. 35.

[43] Hamrock BJ, Schmid SR, Jacobson BO. Film thicknesses for different regimes of fluid film lubrication. Fundam. Fluid film lubr. second ed. CRC Press; 2004. p. 23.

[44] ASTM International. ASTM D341-09: standard practice for viscosity-temperature charts for liquid Petroleum. West Conshohocken, PA: ASTM Int; 2009. https://doi.org/10.1520/D0341-09.2.

[45] Walker DL, Student G, Sanborn DM, Winer AO. Molecular degradation of lubricants in sliding elastohydrodynamic contacts. J Lubr Technol 1975;97:390–5. https://doi.org/10.1115/1.3452614.

[46] Mackenzie K, Jemmett AE. Polymer shear stability. Wear 1971;17. https://doi.org/10.1016/0043-1648(71)90045-7. 389–368.

[47] Hooke C. A review of the paper "A numerical solution to the elastohydrodynamic problem" by D. Dowson and G.R. Higginson. Proc Inst Mech Eng C J Mech Eng Sci 2009;223:49–63. https://doi.org/10.1243/09544062JMES1002.

[48] ASTM International. ASTM D2270-10: standard practice for calculating viscosity index from kinematic viscosity at 40 °C and 100 °C. PA: ASTM Int West Conshohocken; 2016. https://doi.org/10.1520/D2270-10R16.

[49] Hutchings IM. Tribology : friction and wear of engineering materials. first ed. Oxford: Butterworth-Heinemann; 1992.

317

Appendix 2.   Calculation for temperature rise at the MPR contact inlet

Due to the conditions within the contact, the actual temperature of the lubricant in the inlet will increase in comparison to the bulk. Therefore, this temperature rise can be calculated which, allows a more accurate calculation of the viscosity of the fluid in the contact and therefore, the film thickness. This can be estimated using Jaegers theory of moving hot spots as reviewing my Olver (104,194). The equations are based on a model that assumes that frictional heat is created in the contact between both specimens and is then conducted away into the surfaces of the specimens (188). Jaegers theory of moving hot spots proposed three different equations for the temperature rise in the contact depending on the geometry of the contact. The was one for infinite roller where $l \rightarrow \infty$, one for a thin disc where the disc radius is more than the width and one for small discs with a thick shaft where the width of the disc is less than the disc radius which, is less than the shaft length. It is recognised that the complex geometry of the MPR contact does not fit perfectly into one of these categories due to the roller and disc falling into different categories, the thin disc equation was used a good assumption of temperature rise in the contact (106,181).

$$Thin\ Discs,\ M_R = \left\{ 8.88(hk)^{\frac{1}{2}} l^{\frac{1}{2}} R \frac{I_1(nR)}{I_0(nR)} \right\}^{-1}$$

$$where\ n = \left(\frac{2h}{kl} \right)^{-1}$$

$$B_i = \frac{1}{2bl} \frac{1}{k_i} \left(\frac{\chi_i b}{u_i} \right)^{\frac{1}{2}} where\ i = 1,\ 2\ (Roller\ or\ ring)$$

$$\alpha = \frac{1.06B_2 + M_2}{1.06(B_1 + B_2) + M_1 + M_2}$$

$$Inlet\ Temperature\ (Contact\ Temp),\ (T_C)_1 = (W\mu\Delta u) \times \alpha \times (1.60B_1 + M_1) + T_A$$

ρ is the steel density, b is the contact half width, l is axial length of contact, k is the steel thermal conductivity, Cp is the specific heat capacity of steel, X is the thermal diffusivity, u_1 and u_2 are the surface speeds of the roller and ring respectively, Δu (u_1-u_2) is the sliding speed, μ is the coefficient of friction, T_A is the ambient temperature, W is the total load, h is the convective heat transfer coefficient and I_1 and I_o are Bessel Functions.

The equations below show how the convective heat transfer coefficient was calculated based on the equations for forced convection heat transfer past plane surfaces for laminar flow (104) and also the thermal diffusivity.

$$Reynold\ number,\ (N_{RE})_L = \frac{UL}{\upsilon}$$

$$Prandtl\ Number,\ N_{PR} = \frac{\eta C_p}{k}$$

$$Nusselt\ Number,\ (N_{NU})_L = 0.664(N_{RE})_L^{\frac{1}{2}}(N_{PR})^{\frac{1}{3}}$$

$$Nusselt\ Number,\ (N_{NU})_L = \frac{hL}{k}$$

$$Convective\ Heat\ Transfer\ Coefficient,\ h = \frac{(N_{NU})_L k}{L}$$

$$Thermal\ Diffusivity, X = \frac{k}{\rho C_p}$$

ρ is the oil density, U is the fluid free stream velocity, L is the plate length, υ is the kinematic viscosity, η is the dynamic viscosity, k is the oil thermal conductivity at 100°C and C_p is the specific heat capacity at 100°C. Once the temperature rise had been calculated, the Walther equation could be used to calculate the kinematic viscosity at that temperature (105). The Walther equation is also the basis of method ASTM D341 which, was used to calculate the kinematic viscosities of the oils used in Chapter 4 and this calculation is shown in Appendix 4.

Appendix 3. Kinematic Viscosities of the base oils

Table 8-1 shows the measured kinematic viscosities of the base oils used for investigating chain length and the number of ester groups and Table 8-2 shows the variation in molecular weight between these base oils.

Table 8-1 – Table listing some of the measured properties of the base oils investigating chain length and the number of esters in a polyol ester (Figure 3-23).

Ester description	Kinematic Viscosity at 40 °C (cSt)	Kinematic Viscosity at 100 °C (cSt)
MONOPE with all n-C5 acid	15.4	3.6
MONOPE with all *n*-C7 acid	21.3	4.6
MONOPE with all *n*-C9 acid	30.3	5.9
TMP with all *n*-C7 acid	14.0	3.4
NGP with all *n*-C7 acid	5.6	1.9

Table 8-2 – Table displaying the number of each element in the compound and hence, the molecular weights of the base oils.

Ester description	Carbon	Hydrogen	Oxygen	Molecular Weight g/mol
MONOPE with all n-C5 acid	41	76	8	472.619
MONOPE with all *n*-C7 acid	33	60	8	584.835
MONOPE with all *n*-C9 acid	25	44	8	697.051
TMP with all *n*-C7 acid	27	50	6	470.691
NGP with all *n*-C7 acid	19	36	4	328.493

Table 8-3 shows the measured kinematic viscosities of the base oils used for investigating the effect of molecular branching.

Table 8-3 - Table listing some of the measured properties of the base oils investigating the degree of molecular branching in a polyol ester (Figure 3-24).

Ester description	Kinematic Viscosity at 40 °C (cSt)	Kinematic Viscosity at 100 °C (cSt)
MONOPE with all NC8	25.52	5.24

MONOPE with NC8: EH of 75:25	27.53	5.33
MONOPE with NC8: EH of 50:50	30.99	5.5
MONOPE with NC8: EH of 25:75	35.48	5.74
MONOPE with all NC8	44.12	6.24

The kinematic viscosities for the formulated oils provided are shown in Table 8-4 with their

corresponding viscosities at 40 and 100 °C.

Table 8-4- Table of the fully formulated blends viscosities at 40 and 100°C.

	Kinematic Viscosity at 40 °C (cSt)/ (mm^2/ s)	Kinematic Viscosity at 100 °C (cSt))/ (mm^2/ s)
High	66.1	8.04
Medium High	52.4	6.93
Medium Low	31.5	4.99
Low	12.6	3.08

Appendix 4.   Temperature and viscosity prediction using ASTM D341

The ASTM method D341 was used to calculate the temperature at which, each oil has certain viscosity (89). The example shown here is for the MONOPE C9 base oil, but the same method was done for the other base oils too. To predict the temperatures and kinematic viscosities, at least two measured viscosities are needed for each oil at known temperatures. Using equations (8-1), (8-2) and (8-3), the kinematic viscosities can be calculated by plotting a line of LogT against LogLogZ as shown in Figure 8-1.

$$LogLogZ = A - BLogT \qquad \text{(8-1)}$$
$$Z = v + e^{(-1.47 - 1.84v - 0.51v^2)} \qquad \text{(8-2)}$$
$$v = (Z - 0.7) + e^{(0.7487 - 3.295(Z-0.7) + 0.6119(Z-0.7)^2 - 0.3193(Z-0.7)^3)} \qquad \text{(8-3)}$$
$$\text{(8-4)}$$

Temperature (°C)	LogT (T converted into K)	Kinematic Viscosity (cSt)	LogLogZ
40	2.4958	30.5	0.1744
100	2.5719	5.99	-0.0833
108.9	2.5821	5.407	-0.1047

Table 8-5 - Table showing the measured kinematic viscosities and at measured temperatures and the calculated values for LogT and LogLogZ.

The kinematic viscosities at 40 and 100°C were provided by the supplier and the viscosity at 108.9°C was measured using ASTM D445 to confirm the oil had a viscosity of 5 cSt and also to gather another data point to feed back into the viscosity prediction to improve its accuracy (195).

Graph of LogT against LogLogZ to predict kinematic viscosities at certain temperatures using ASTM D341

$y = -3.289x + 8.3821$
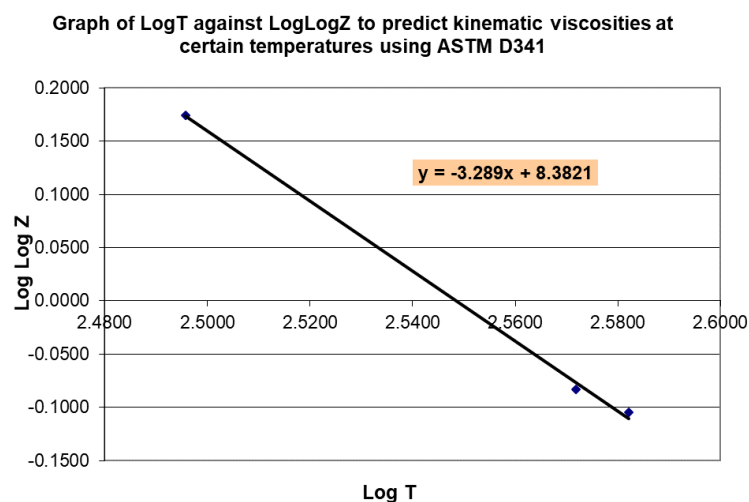
Figure 8-1 - Graph of LogT against LogLogZ to predict kinematic viscosities at certain temperatures using ASTM D341.

Consequently, the kinematic viscosity can be estimated at the test temperatures using ASTM D341 and these can be seen in Table 8-6.

Table 8-6 – The estimated kinematic viscosities using ASTM D341 of the base oils at the temperatures tested.

Ester description	Kinematic Viscosity cSt			
	60 °C	80 °C	100 °C	120 °C
PE with all n-C5 acid	8.48	5.29	3.92	2.65
PE with all *n*-C7 acid	11.40	6.95	4.66	3.36
PE with all *n*-C9 acid	15.65	9.33	6.14	4.35
TMP with all *n*-C7 acid	7.82	4.94	3.41	2.51
NGP with all *n*-C7 acid	3.61	2.54	1.91	1.52

The lubricants were also tested at the same viscosity by varying the test temperature for each base oil. These temperatures were also calculated using ASTM D341 and can be seen in Table 8-7.

Table 8-7 – Table showing the calculated temperatures at which, the base oils have the following viscosities.

Ester description	Temperature at which, the lubricant has a kinematic viscosity of (°C)		
	2.9 cSt	5 cSt	7.3 cSt
PE with all n-C5 acid	113.8	82.5	65.9

PE with all *n*-C7 acid	130.2	96.2	77.8
PE with all *n*-C9 acid	149	111.5	91.3
TMP with all *n*-C7 acid	110.1	79.4	62.7
NGP with all *n*-C7 acid	71.9	44.8	30

This same method was applied to the base oils using for the branching study and their calculated kinematic viscosities can be seen in Table 8-8 and Table 8-9.

Table 8-8 – The estimated kinematic viscosities for the base oils for the branching study using ASTM D341 of the base oils at the temperatures tested.

Ester description	Kinematic Viscosity cSt			
	60 °C	80 °C	100 °C	120 °C
MONOPE with all NC8	13.27	7.93	5.24	3.73
MONOPE with NC8: EH of 75:25	13.93	8.18	5.33	3.75
MONOPE with NC8: EH of 50:50	15.07	8.6	5.5	3.82
MONOPE with NC8: EH of 25:75	16.53	9.16	5.74	3.93
MONOPE with all NC8	19.32	10.26	6.24	4.18

Table 8-9 – Table showing the calculated temperatures at which, the base oils have the following viscosities.

Ester description	Temperature at which, the lubricant has a kinematic viscosity of (°C)		
	3 cSt	5 cSt	7cSt
MONOPE with all NC8	134.9	102.5	85.6
MONOPE with NC8: EH of 75:25	135.0	103.4	86.8

MONOPE with NC8: EH of 50:50	135.7	104.9	88.7
MONOPE with NC8: EH of 25:75	136.9	106.8	91.0
MONOPE with all NC8	140.1	110.5	95.0

This same method was applied to the fully formulated lubricants and their calculated kinematic viscosities can be seen in Table 8-10 and Table 8-11.

Table 8-10 - The estimated kinematic viscosities for the fully formulated lubricants using ASTM D341 at the temperatures tested.

Lubricant	Kinematic Viscosity cSt			
	60 °C	80 °C	100 °C	120 °C
Low	7.05	4.5	3.14	2.33
Medium Low	14.48	7.99	5.01	3.43
Medium High	22.31	11.65	6.99	4.63
High	27.15	13.79	8.1	5.28

Table 8-11 - Table showing the temperatures at which, the fully formulated lubricants have a kinematic viscosity of 5 cSt.

Oil	Temperature at which, the oil has a kinematic viscosity of 5 cSt (°C)
High	122.8
Medium High	115.9
Medium Low	100.6
Low	74.9

Appendix 5. Calculation of the dynamic viscosities required for the Hersey Number

The density of these fluids was also required such that their dynamic viscosity could be calculated which, was needed to calculate the Hersey number. Whilst it is recognised that density varies with temperature; the densities could not be acquired for the different fluids at different temperatures. Hence, the room temperature density for each fluid was used for all calculations with the assumption that they densities remains different to each of the fluids. This method is only shown for the base oils in Figure 3-23 and the same method was used for all the other base oils in the study.

Table 8-12 –Densities pure base oils.

	NPG, all C7 acids	TMP, all C7 acids	PE, all C5 acids	PE, all C7 acids	PE, all C9 acids
Density of Liquids, 15.6 °C	0.9291	0.9628	1.022	0.9809	0.9569

The dynamic viscosity has been calculated from the density multiplied by the kinematic viscosities in Table 8-6 and then converted from cP to Pa. s by multiplying by 10^{-3}. These dynamic viscosities can be seen in Table 8-13. The density will change with temperature, but only the density at 15.6 °C could be acquired and hence, the dynamic viscosities have been estimated using this.

Table 8-13 – Dynamic viscosities at of the pure base oils at a range of temperatures.

Pa. s	Dynamic Viscosity Pa. s			
	60 °C	80 °C	100 °C	120 °C
NPG, all C7 acids	0.003354	0.00236	0.001775	0.001412
TMP, all C7 acids	0.007529	0.004756	0.003283	0.002417
PE, all C5 acids	0.008667	0.005406	0.004006	0.002708
PE, all C7 acids	0.011182	0.006817	0.004571	0.003296
PE, all C9 acids	0.014975	0.008928	0.005875	0.004163

Hence, the dynamic viscosities can also be calculated for when they were all tested at different

temperature to achieve the same kinematic viscosity, these can be seen in Table 8-14.

Table 8-14 - Dynamic viscosities calculated from the kinematic viscosity.

Ester description	Dynamic viscosities calculated from the kinematic viscosity (Pa. s)		
	2.9 cSt	5 cSt	7.3 cSt
NPG, all C7 acids	0.00269439	0.0046455	0.0074606
TMP, all C7 acids	0.00279212	0.004814	0.00702844
PE, all C5 acids	0.0029638	0.00511	0.0074606
PE, all C7 acids	0.00284461	0.0049045	0.00716057
PE, all C9 acids	0.00277501	0.0047845	0.00698537

This same method was applied to the branched base oils and the densities and dynamic viscosity

data can be seen in Table 8-15, Table 8-16 and Table 8-17.

Table 8-15 –Densities pure base oils.

	MONOPE with all NC8	MONOPE with NC8: EH of 75:25	MONOPE with NC8: EH of 50:50	MONOPE with NC8: EH of 25:75	MONOPE with all EH
Density of Liquids, 15.6 °C	0.968	0.968	0.967	0.966	0.966

Table 8-16 – Dynamic viscosities at of the pure base oils at a range of temperatures.

Pa. s	Dynamic Viscosity Pa. s			
	60 °C	80 °C	100 °C	120 °C
MONOPE with all NC8	0.0128	0.0077	0.0051	0.0036
MONOPE with NC8: EH of 75:25	0.0135	0.0079	0.0052	0.0036
MONOPE with NC8: EH of 50:50	0.0146	0.0083	0.0053	0.0037
MONOPE with NC8: EH of 25:75	0.016	0.0088	0.0055	0.0038
MONOPE with all EH	0.0187	0.0099	0.006	0.004

Table 8-17 - Dynamic viscosities calculated from the kinematic viscosity.

Ester description	Dynamic viscosities calculated from the kinematic viscosity (Pa. s)		
	2.9 cSt	5 cSt	7.3 cSt
MONOPE with all NC8	0.0028072	0.00484	0.0070664
MONOPE with NC8: EH of 75:25	0.0028072	0.00484	0.0070664
MONOPE with NC8: EH of 50:50	0.0028043	0.004835	0.0070591
MONOPE with NC8: EH of 25:75	0.0028014	0.00483	0.0070518
MONOPE with all NC8	0.0028014	0.00483	0.0070518

This same method was applied to the fully formulated lubricants and the densities and dynamic viscosity data can be seen in Table 8-18, Table 8-19 and Table 8-20.

Table 8-18 –Densities of the fully formulated lubricants.

	Low	Medium Low	Medium High	High
Density of Liquids (specific gravity, unitless) 15.56 °C	0.9669	0.9661	0.9677	0.9676

Table 8-19 – Dynamic viscosities at of the fully formulated lubricants at a range of temperatures.

Pa. s	Dynamic Viscosity Pa. s			
	60 °C	80 °C	100 °C	120 °C
Low	0.006816645	0.00435105	0.003036066	0.002252877
Medium Low	0.013989128	0.007719139	0.004840161	0.003313723
Medium High	0.021589387	0.011273705	0.006764223	0.004480451
High	0.02627034	0.013343204	0.00783756	0.005108928

Table 8-20 - Dynamic viscosities for the fully formulated lubricants calculated from the kinematic viscosity.

Lubricant Pa.s	Dynamic viscosities calculated from the kinematic viscosity (Pa. s)
	5 cSt
Low	0.00501531
Medium Low	0.004956093
Medium High	0.004858822
High	0.004872834

Appendix 6.   Estimation of the pressure viscosity coefficient at different test temperatures

The pressure viscosity coefficients (PVC) have also been supplied for these oils (Table 8-21) and have been used to calculate the film thickness and the therefore, the lambda ratio. This parameter also varies with temperature and the PVC at different temperatures has been estimated by plotting the known PVC against temperature and using the equation of the line to calculate the other temperatures. These can be seen in Table 8-22 and the graph of the plotted pressure viscosity coefficients can be seen in Figure 8-2. For most of the base oils, the PVC increases as temperature decreases except for TMP n-C7, this is not currently understood.

Table 8-21 – Supplied PVC of the pure base oils.

Pressure-Viscosity Coefficient, x 10^{-8} m^2/N	NPG, all C7 acids	TMP, all C7 acids	PE, all C5 acids	PE, all C7 acids	PE, all C9 acids
at 40°C	0.67	1.07	2.28	2.18	0.92
at 70°C	0.63	1.13	1.57	1.49	0.72
at 100°C	0.6	1.18	1.21	1.13	0.6
at 130°C	0.58	1.22	0.99	0.92	0.52

Table 8-22 – Estimated pressure viscosity coefficients that have been calculated from the line equations in Figure 8-2.

PVC estimation (based on line equations) x 10-8 m^2/N	NPG, all C7 acids $y = -0.001x+0.705$	TMP, all C7 acids $y = 0.0017x+1.0083$	PE, all C5 acids $y = 31.087x^{-0.706}$	PE, all C7 acids $y = 32.713x^{-0.731}$	PE, all C9 acids $y = 1.1531e^{-0.006x}$
60	0.65	1.11	1.53	1.44	0.77
80	0.63	1.14	1.15	1.08	0.68
100	0.60	1.18	1.21	1.13	0.60
120	0.58	1.21	0.77	0.72	0.54
30	0.68				
44.8	0.66				
71.92	0.63				
62.7		1.11			
79.4		1.14			
110.1		1.19			

65.9			1.39		
82.8			1.11		
113.79			0.81		
77.8				1.11	
96.2				0.90	
130.2				0.66	
91.25					0.63
111.5					0.56
149					0.46
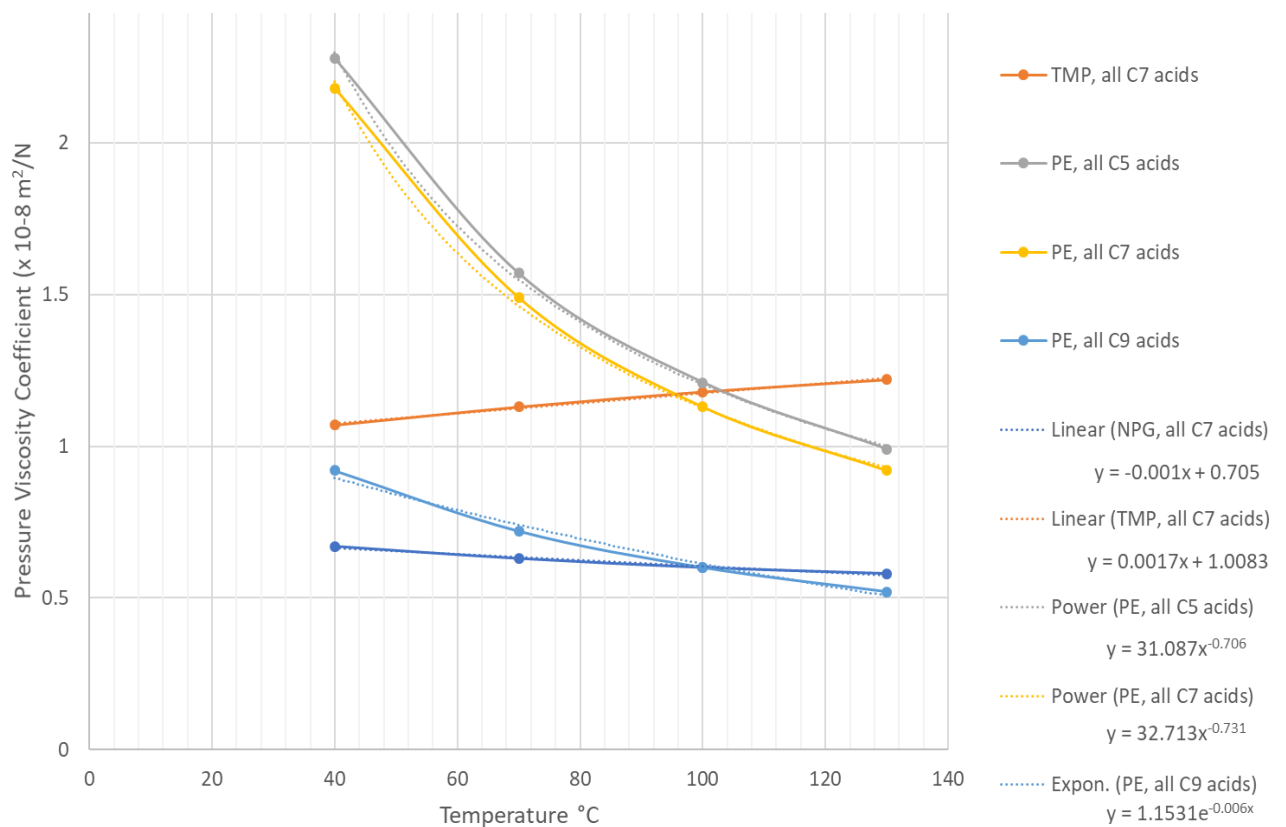
Figure 8-2 – Graph showing the pressure viscosity coefficients for the pure base oils plotted against the temperature. These were fit to line equations that allowed the estimation of the PVC at other temperatures.

The pressure-viscosity coefficients could not be acquired for the other base oils tested but is expected as they are more viscous fluids that they should all reach the EHD regime and the high entrainment speeds used during these tests on the MTM.

Appendix 7. Base Oil Rheology

The base oils were tested using a Bohlin Gemini HR Nano Rotonetic Drive 2 rheometer with a cone on plate configuration. The parameters for the rheometer can be seen in Table 8-23. The cone attachment was a 40 mm stainless steel cone with a 4 ° angle. The tested conducted used a controlled shear stress ramp up to a shear rate of 200 s^{-1} and then back down to check for hysteresis. Temperature was controlled using the Peltier plate attachment.

All the base oils were tested at 25 °C but only 2 of the base oils were tested at a range of temperatures to show to show that there is no effect with temperature and viscosity influencing non-Newtonian behaviour. The base oils tested were the NPG C7 base oil shown in Figure 3-23 and the "High" formulated lubricant. The rationale was that if these were Newtonian, the base oils in between this viscosity range with a similar chemistry are also Newtonian.

Table 8-23 – Table showing the parameters for the Bohlin Gemini HR Nano Rotonetic Drive 2 rheometer.

Parameter	Value
Torque Range in controlled stress & rate viscometry:	10nNm to 200mNm
Torque Range in controlled stress & strain oscillation:	3nNm to 200mNm
Torque resolution:	Better than 1nNm
Position resolution:	50nrad
Frequency range:	1µHz to 150Hz
Controlled speed range (CR mode):	0.01mrad s-1 to 600rad s-1
Measurable speed range (CS mode):	10nrad s-1 to 600rad s-1
Normal force N1 measurement range:	0.001N to 20N (50N optional)
Step change in strain:	<10ms
Temperature controls: Peltier Plate:	-30ºC to 200ºC
Nominal operating voltage	110 or 220V
Size (with Peltier plate)	52cm (H) x 33cm (W) x 37cm (D)
Weight (with Peltier plate)	28kg

It can be seen from Figure 8-3 and Figure 8-4 that the lowest and highest viscosity lubricants in this study are Newtonian and therefore, all the base oils used in this study can be assumed to

be Newtonian. The graphs are expected to be noisier at lower speeds and more so with less viscous fluids however, it can be seen at higher shear rates, the viscosity remains relatively constant with shear thus suggesting Newtonian behaviour.

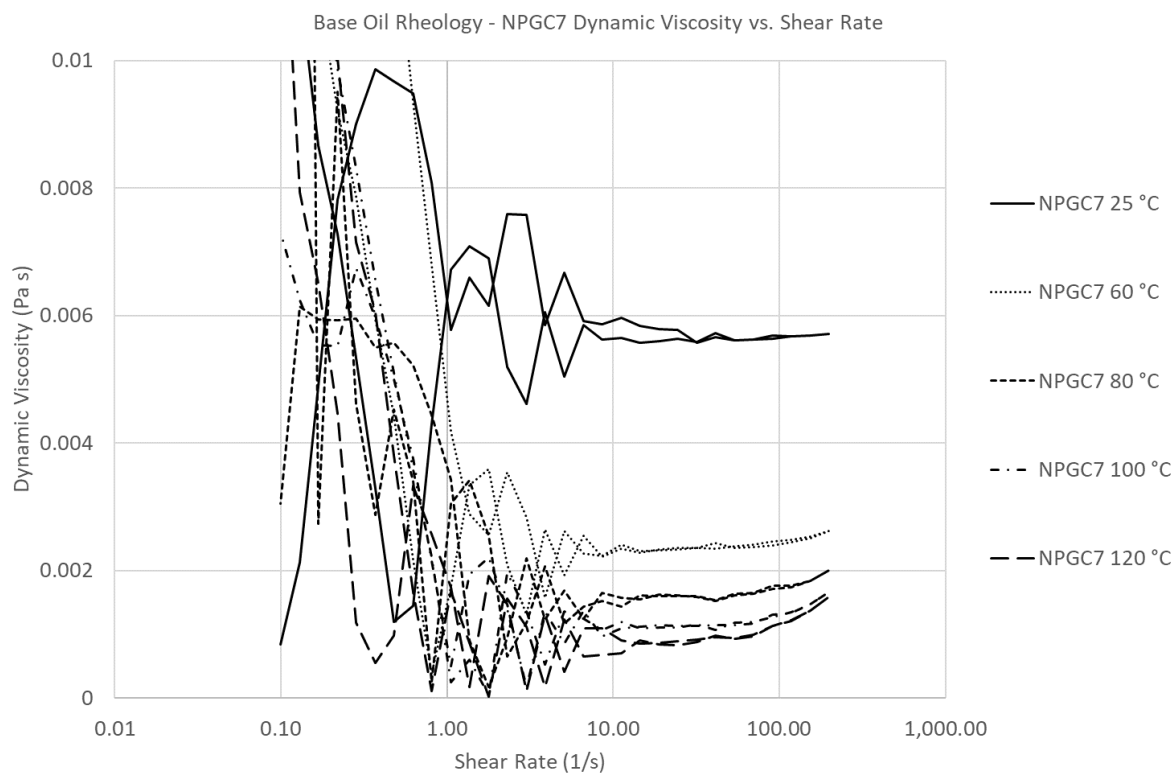Base Oil Rheology - NPGC7 Dynamic Viscosity vs. Shear Rate
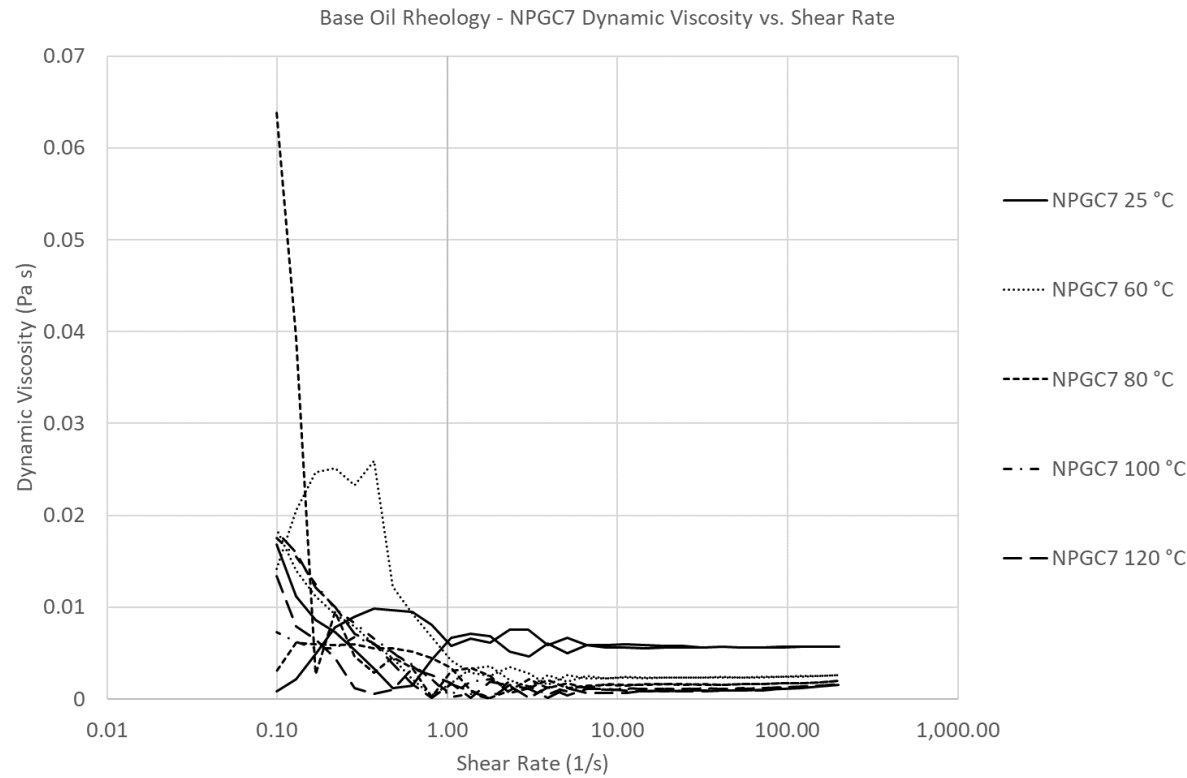
Figure 8-3 – Graph showing the measured dynamic viscosity against shear rate for NPGC7 showing Newtonian behaviour.
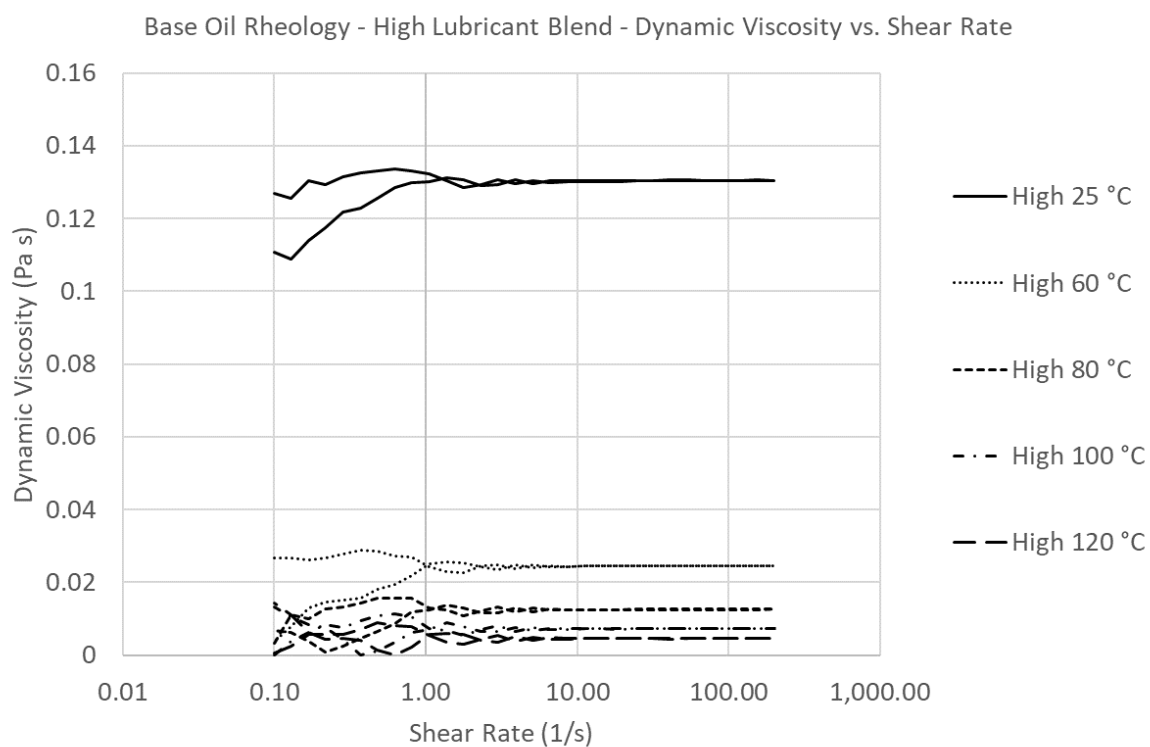

Figure 8-4 – Graph showing the measured dynamic viscosity against shear rate for the High lubricant blend showing

Newtonian behaviour.

333

Appendix 8.   Extra Stribeck Curves for the different anti-wear additive concentrations

Figure 8-5 - Initial and final Stribeck curves for 200 ppm P (TCP) and Base oil showing the variation in friction across the lubrication regimes from the start to the end of the wear test.
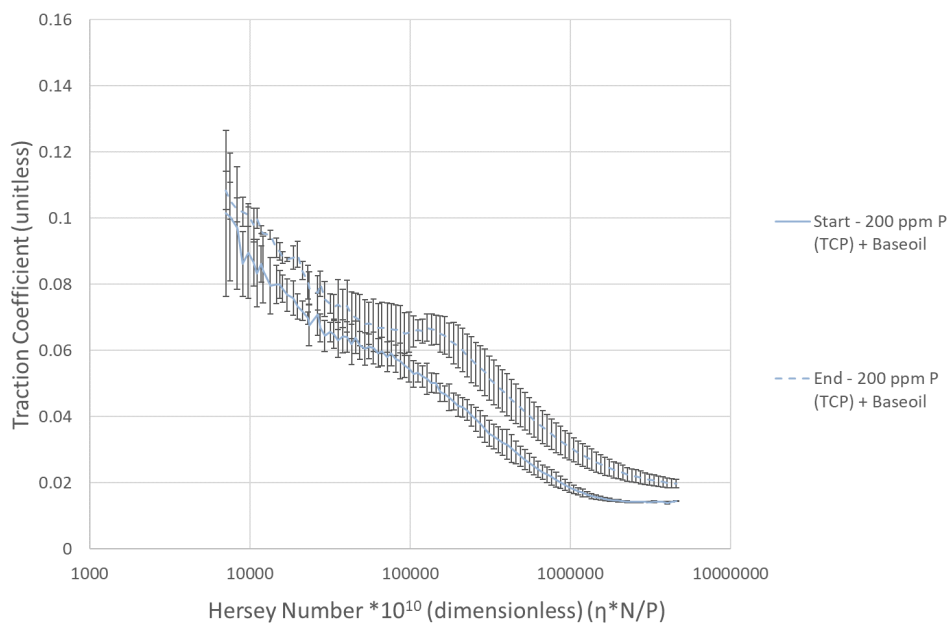

Figure 8-6 - Initial and final Stribeck curves for 800 ppm P (TCP) and Base oil showing the variation in friction across the lubrication regimes from the start to the end of the wear test.

Figure 8-7 - Initial and final Stribeck curves for 4200 ppm P (TCP) and Base oil showing the variation in friction across the lubrication regimes from the start to the end of the wear test.
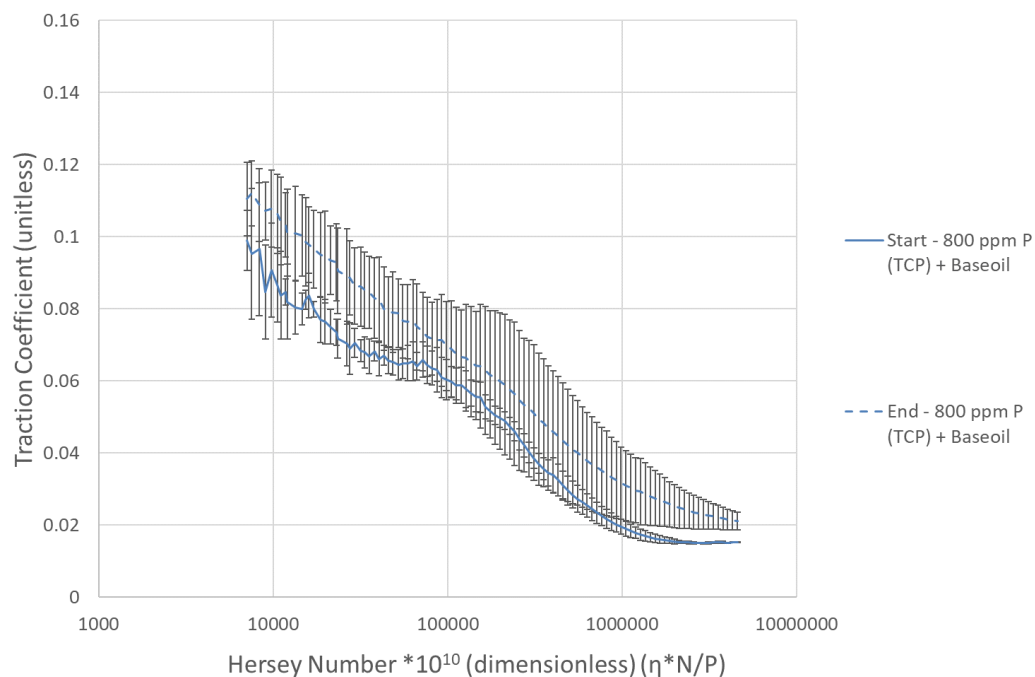

Figure 8-8 -- Initial and final Stribeck curves for 200 ppm P (X) and Base oil showing the variation in friction across the lubrication regimes from the start to the end of the wear test.

335

Figure 8-9 - Initial and final Stribeck curves for 800 ppm P (X) and Base oil showing the variation in friction across the lubrication regimes from the start to the end of the wear test.
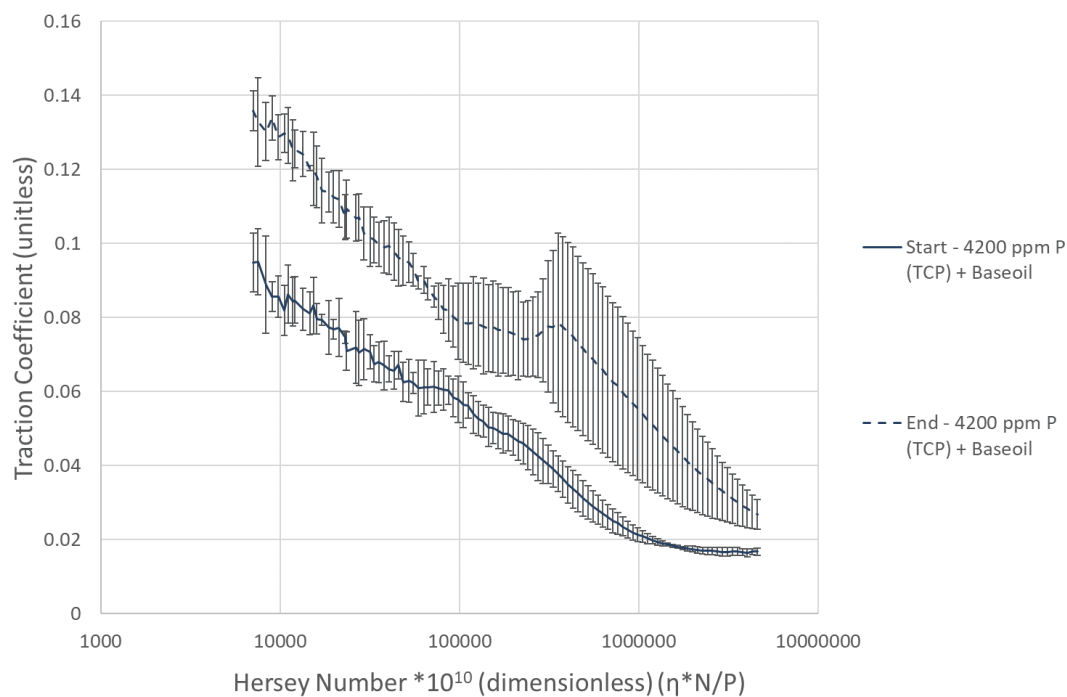

Figure 8-10 - Initial and final Stribeck curves for 4200 ppm P (X) and Base oil showing the variation in friction across the lubrication regimes from the start to the end of the wear test.
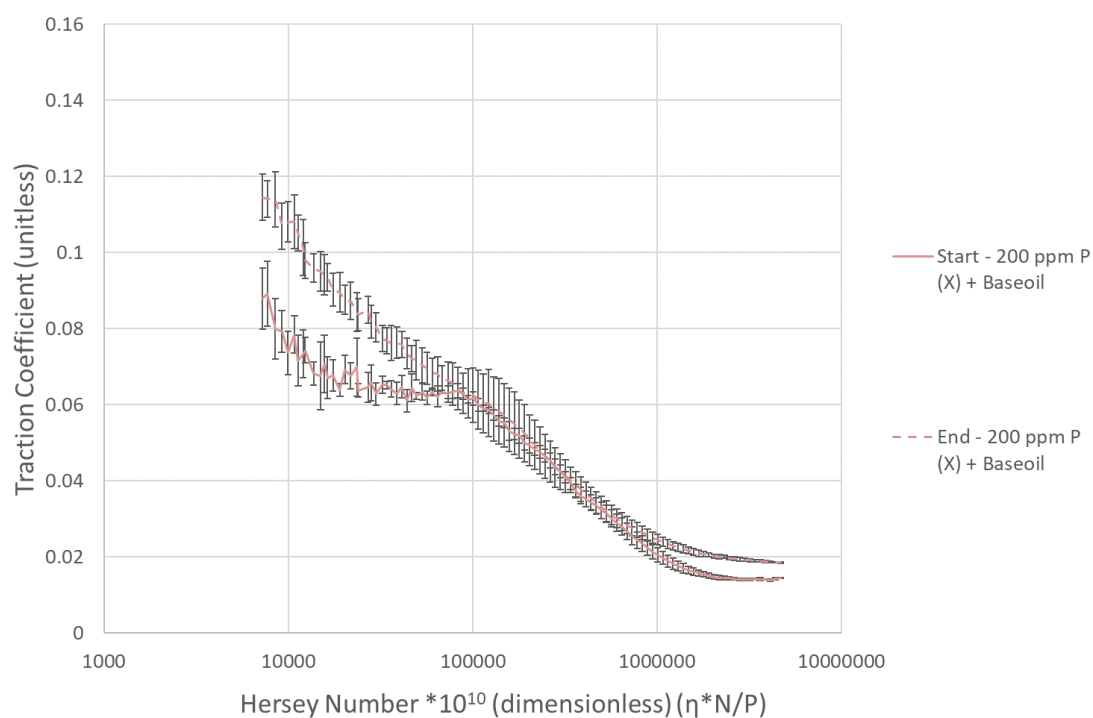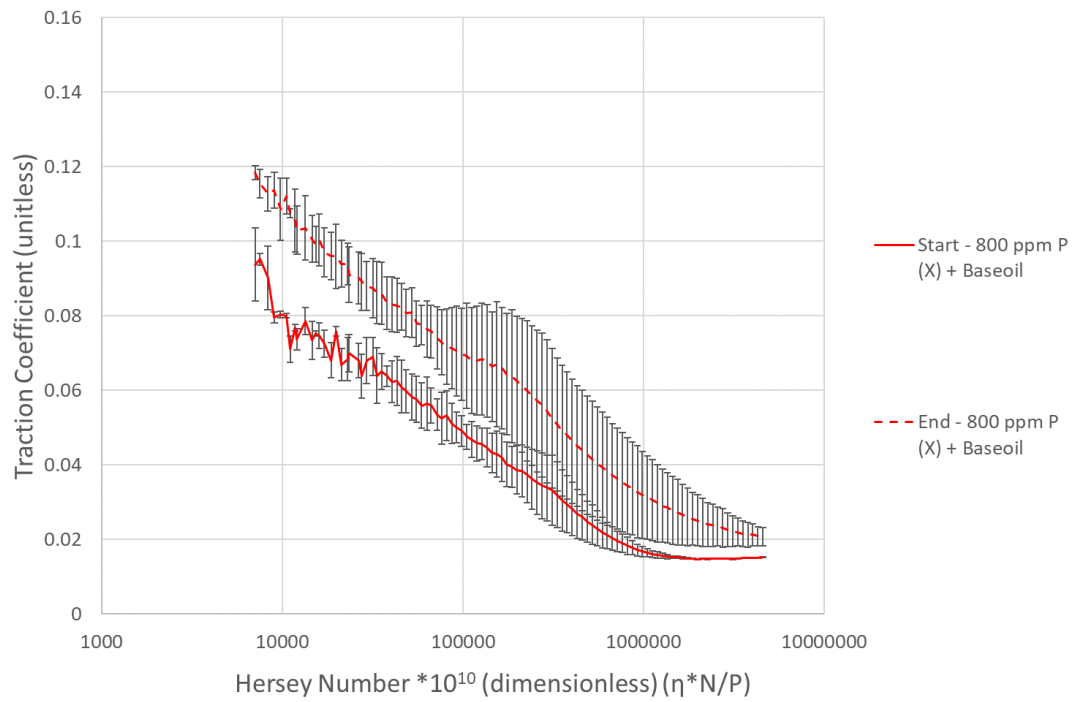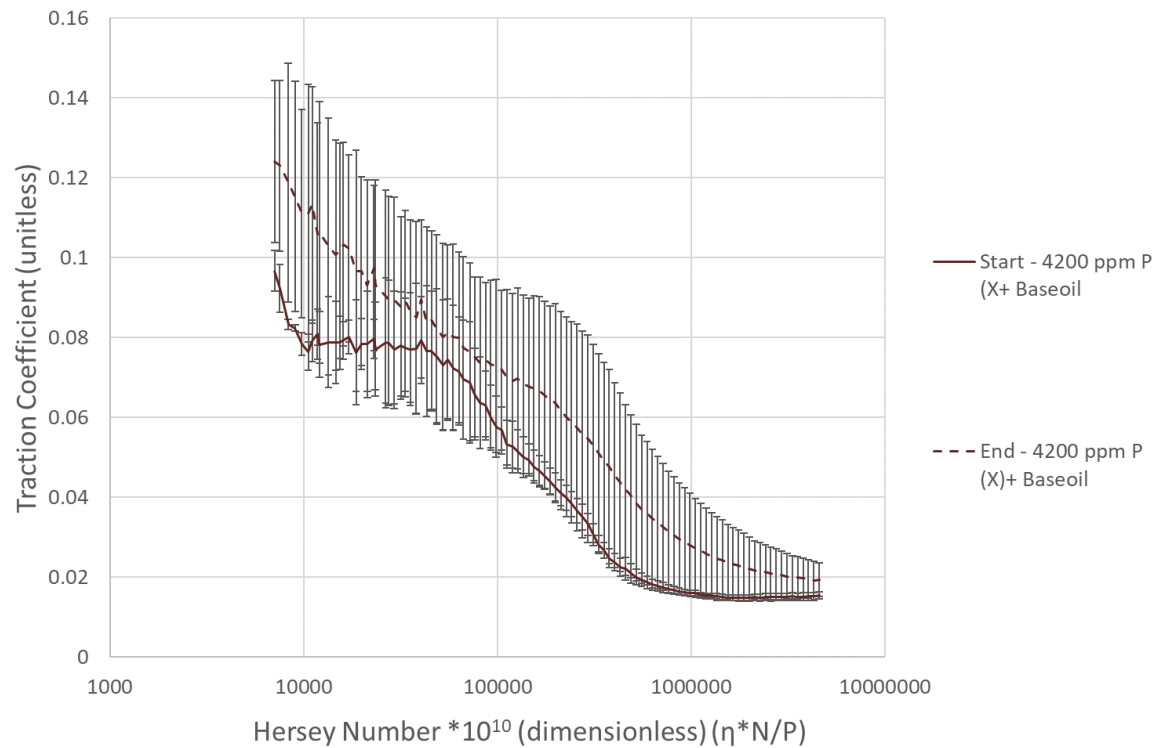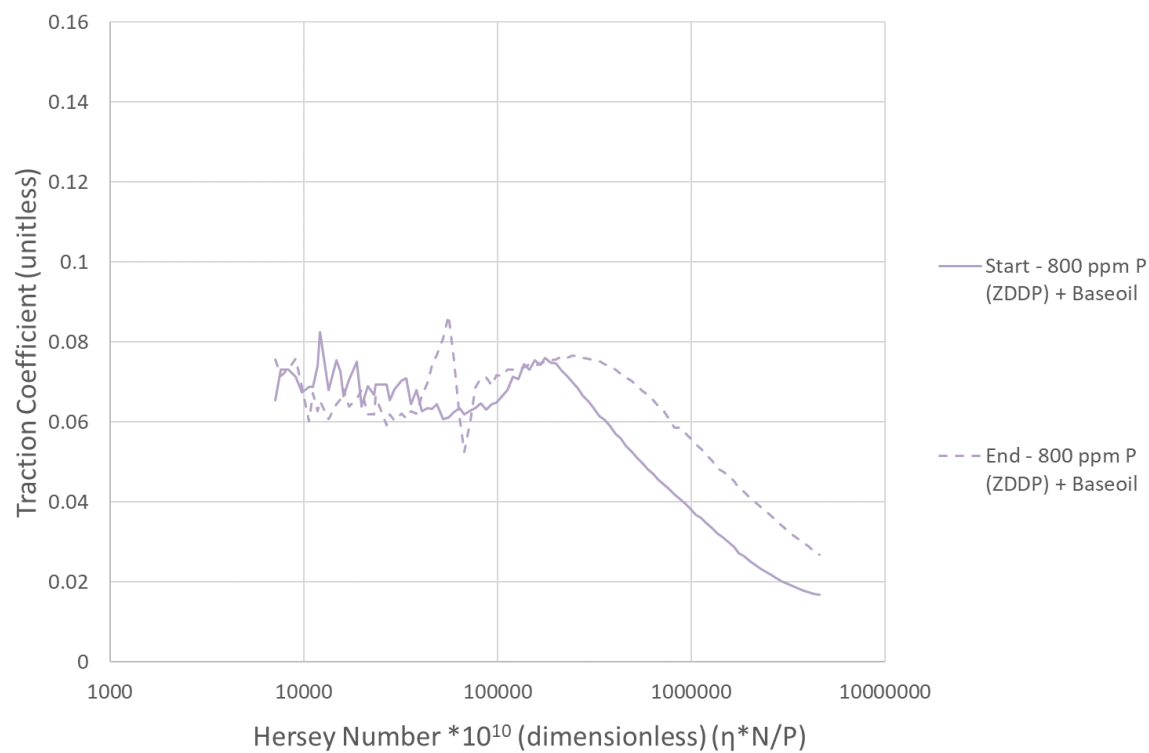
Figure 8-11 - Initial and final Stribeck curves for 800 ppm P (ZDDP) and Base oil showing the variation in friction across the lubrication regimes from the start to the end of the wear test.

Appendix 9. Overall SLIM friction graphs for each lubricant

Figure 8-12 – Graph of the friction against the rubbing time throughout the SLIM tests for the repeat tests with Lubricant A.

Figure 8-13 – Graph of the friction against the rubbing time throughout the SLIM tests for the repeat tests with Lubricant B.

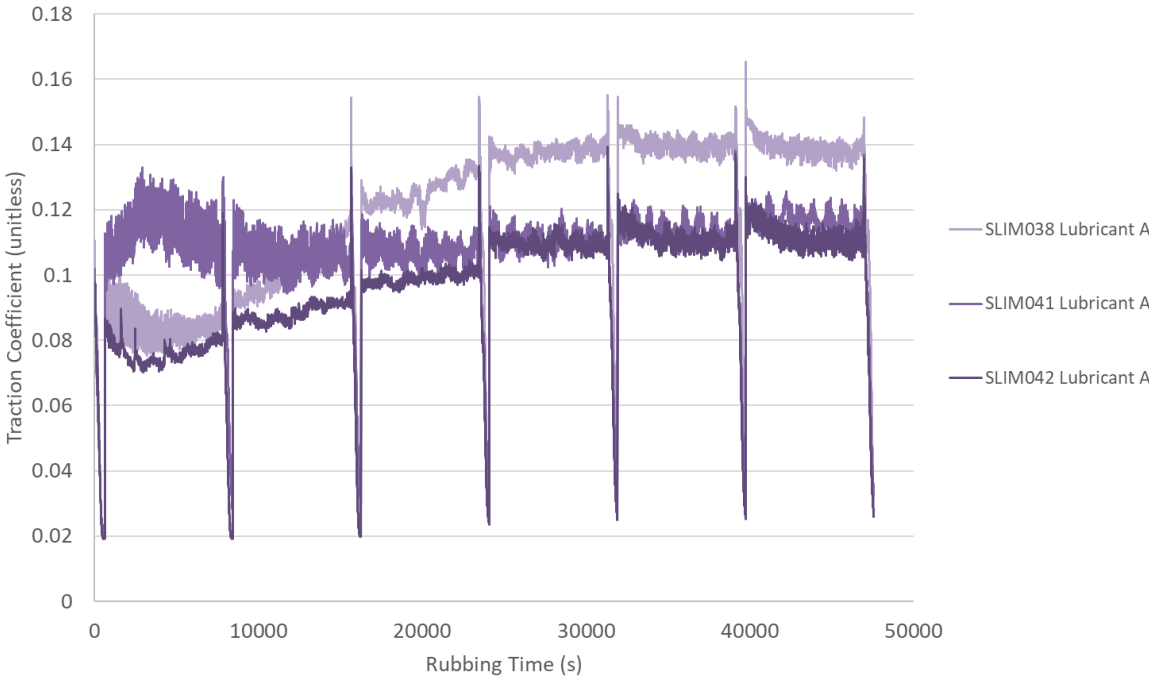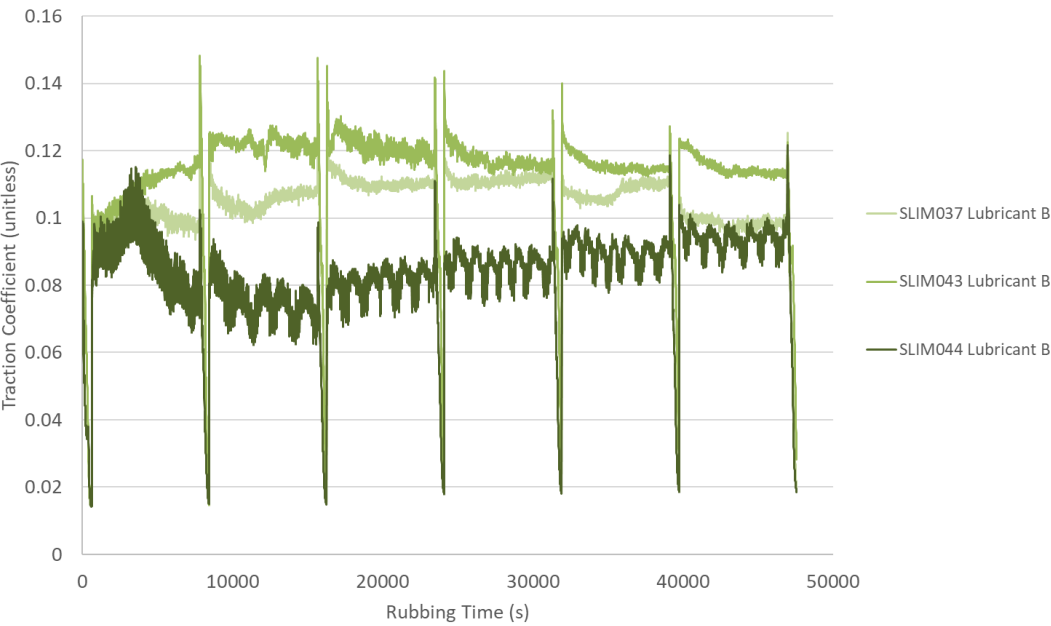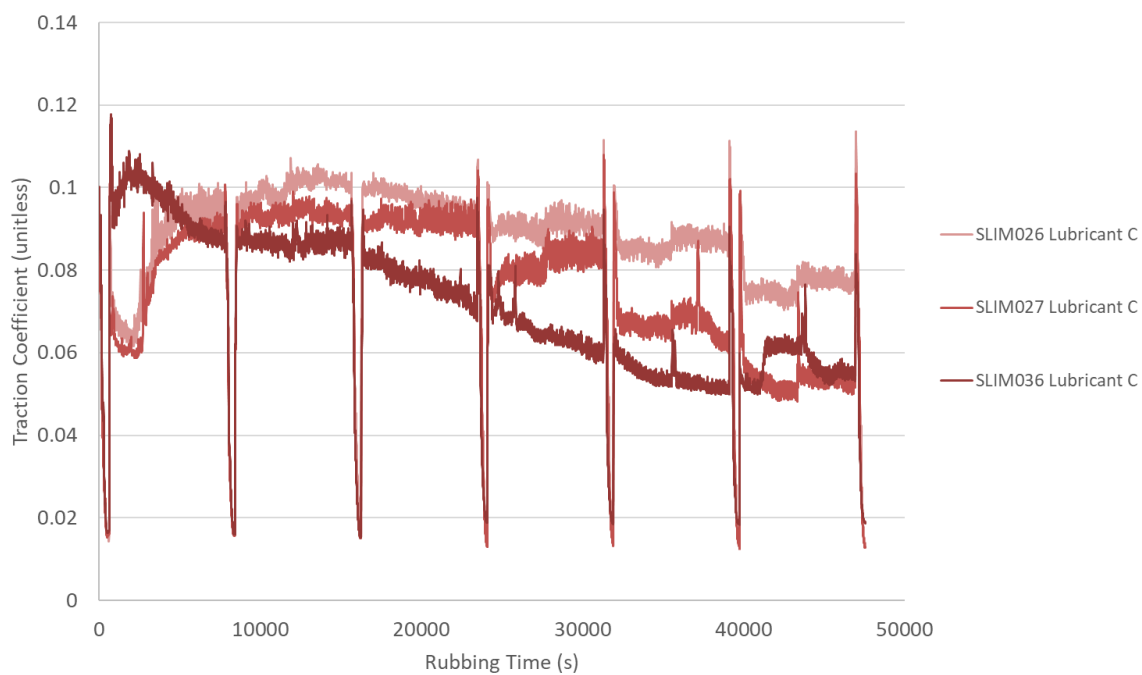Figure 8-14 – Graph of the friction against the rubbing time throughout the SLIM tests for the repeat tests with Lubricant C.
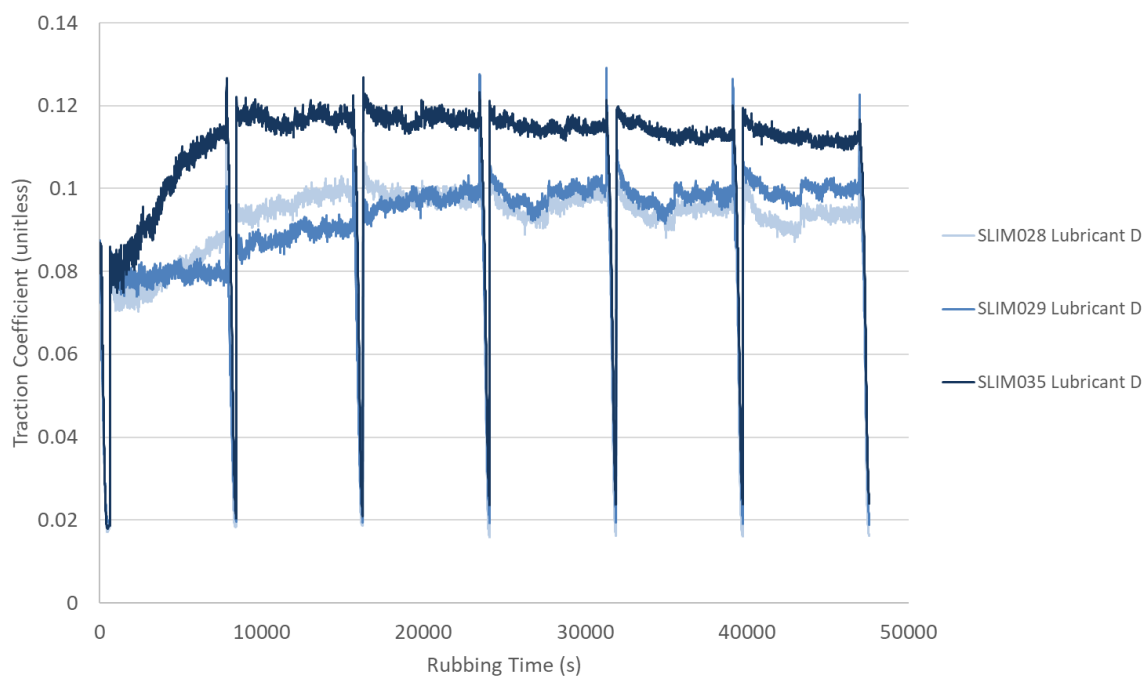

Figure 8-15 – Graph of the friction against the rubbing time throughout the SLIM tests for the repeat tests with Lubricant D.

Appendix 10. XPS

Figure 8-16 shows the atomic abundance of chlorine (Cl) through the quantification of the Cl 2p binding energy peaks for each wear test. The tests using lubricant C on both steels have detected Cl both inside and outside of the wear track as expected due to the presence of the chlorinated EP additive. It can also be seen it is present as an organic chloride as shown from the binding energy corresponding to the chemical state regions shown in Table 8-24 suggesting it is present on the surface as a breakdown product of the extreme pressure additive which, is a chlorine containing compound. It could also be suggested that the Cl can bind more easily to the P53 rather than the MSRR6010 as the Cl abundance is higher on both the body and the wear track on P53 than MSRR6010.
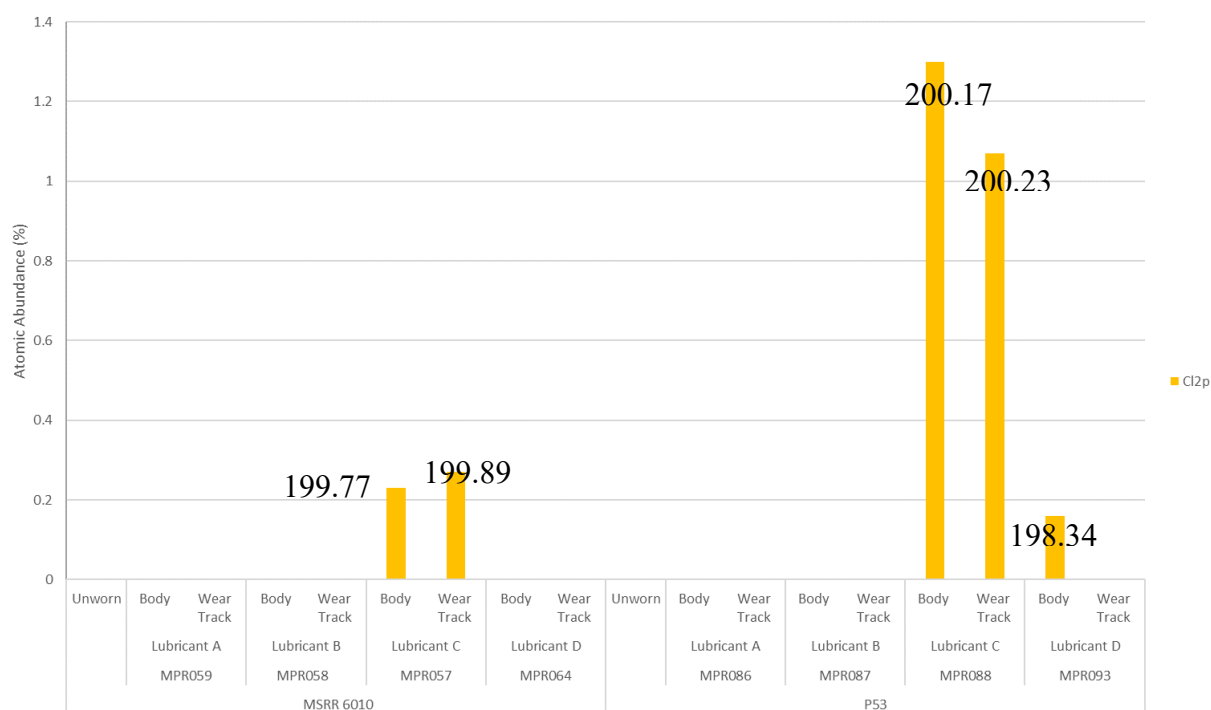

Figure 8-16 – XPS results showing the concentration of chlorine due to emission of a photoelectron from a 2p orbital for both the MSRR6010 and P53 steels both on the wear track and outside of the wear track.

340

Table 8-24 – Table showing different characteristics XPS binding energies for specific chemical states of chlorine (Thermo Fisher Scientific Inc., 2019).

Chemical state	Binding energy Clp3/2 / eV
Organic Cl	200
Metal chloride	~198.5–199

However, it has also been detected in the body of the P53 test with lubricant D but is believed this could be a contaminant as chlorine is a common contaminant in the form of salt transferred from skin. This is confirmed for MPR093 as shown from binding energy of 198.34 being close to the metal chloride region, again confirming it could be there in the presence of a salt.

Figure 8-17 compares the surface concentration of nitrogen on all the wear test specimens. The concentrations for lubricant C are highest for both steels suggesting the amine EP additive mentioned earlier reacts with the surface more than the other nitrogen containing surface additives. It was also noted that all the tests (except MPR088) had a higher concentration of nitrogen in the wear track than the body suggesting the harsher conditions in the wear contact encouraged the nitrogen to bind to the surface. It is not understood why nitrogen has been detected in both unworn steels as nitrogen should not be present in either of the steel alloys however, this could just be contamination. Therefore, this suggests if nitrogen is already present in prior to the wear test, there may not be a significant amount from the other oils formulations that are binding to the surface however, most of the oils do have a higher concentration than the unworn steels. Also, it may be possible the reason nitrogen is present with other formulations is that is part of the metal deactivator additive, however, this should be investigated further as it may be that this additive could also contribute to micropitting propensity.

All the binding energies for the nitrogen peaks were close to 400 eV suggesting nitrogen is present in the form organic amine (-C-NH$_2$, Table 8-25) as expected from all the nitrogen

containing boundary additives in the formulations. It could be suggested nitrogen binds more strongly to P53 than MSRR6010 too.
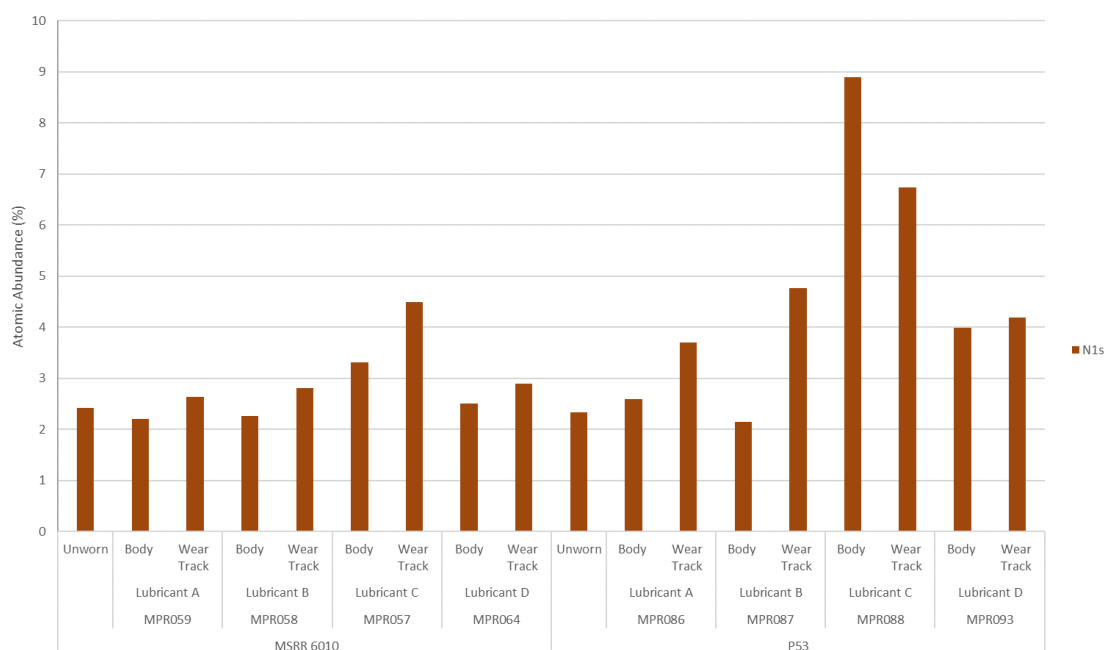

Figure 8-17 – XPS results showing the concentration of nitrogen due to emission of a photoelectron from a 1s orbital for both the MSRR6010 and P53 steels both on the wear track and outside of the wear track.

Table 8-25 – Table showing different characteristics XPS binding energies for specific chemical states of nitrogen (Thermo Fisher Scientific Inc., 2019).

Chemical state	Binding energy Mg1s / eV
Metal nitrides	~397
NSi3 (Si3N4)	398.0
NSi2O	399.9
NSiO2	402.5
C-NH2	~400
Nitrate	>405

It is clear from Figure 8-18 that phosphorus has originated from the lubricant as there is no phosphorus present in the unworn specimens. It should also be noted that phosphorus is only present in the anti-wear additives in all the lubricants formulations. The phosphorus concentration is higher in the wear track for most of the tests backing up the theory that anti-wear and extreme pressure additive require high pressure conditions to chemisorb onto the wear track.

For MSRR6010, the highest concentrations of phosphorus are highest in the wear track of the test with the most damage. However, P53 does not follow this trend as lubricant B has the least micropitting and has the second highest concentration of phosphorus in the wear track. It could be argued that phosphorus adheres better to P53 than MSRR6010. All the binding energies for phosphorus were close to 133 eV and therefore, phosphorus was present in the form of a phosphates as shown from Table 8-26.
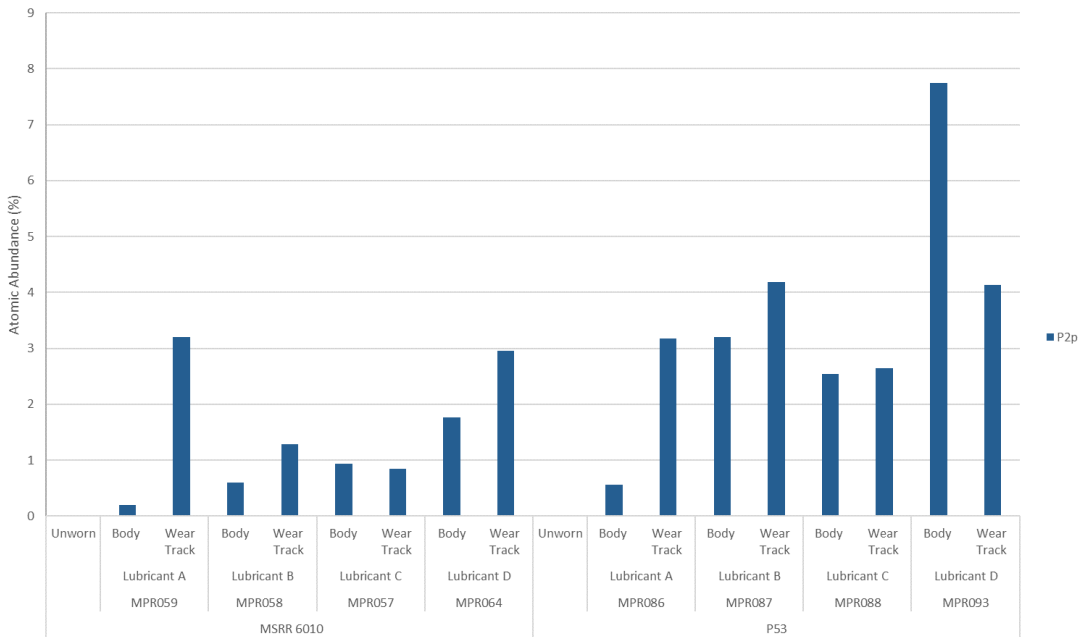

Figure 8-18 – XPS results showing the concentration of phosphorus due to emission of a photoelectron from a 2p orbital for both the MSRR6010 and P53 steels both on the wear track and outside of the wear track.

Table 8-26 – Table showing different characteristics XPS binding energies for specific chemical states of phosphorus (Thermo Fisher Scientific Inc., 2019).

Chemical state	Binding energy Clp3/2 / eV
Metal phosphide	~128.5
Metal phosphate	~133